

Electronic Thesis and Dissertation Repository

---

10-20-2022 10:00 AM

# The Coordination Chemistry and Reactivity of Pd Phosphine 1-Azaallyl Complexes

Kyle M. Jackman, *The University of Western Ontario*

Supervisor: Blacquiere, Johanna, M., *The University of Western Ontario*

A thesis submitted in partial fulfillment of the requirements for the Doctor of Philosophy degree  
in Chemistry

© Kyle M. Jackman 2022

Follow this and additional works at: <https://ir.lib.uwo.ca/etd>

 Part of the [Inorganic Chemistry Commons](#)

---

## Recommended Citation

Jackman, Kyle M., "The Coordination Chemistry and Reactivity of Pd Phosphine 1-Azaallyl Complexes"  
(2022). *Electronic Thesis and Dissertation Repository*. 8926.  
<https://ir.lib.uwo.ca/etd/8926>

This Dissertation/Thesis is brought to you for free and open access by Scholarship@Western. It has been accepted for inclusion in Electronic Thesis and Dissertation Repository by an authorized administrator of Scholarship@Western. For more information, please contact [wlsadmin@uwo.ca](mailto:wlsadmin@uwo.ca).

## Abstract

Structurally responsive ligands (SRLs) are a class of ligands that change their coordination mode with a metal centre, which permits reactions that are difficult with non-SRLs, allow access to unique mechanisms, and allow isolation of unusual coordination complexes. The 1-azaallyl (1-AzA) family of SRLs are capable of isomerizing between  $\eta^3$ -NCC and  $\kappa^1$ -N modes that occupy two and one coordination sites, respectively. This thesis investigates a new class of phosphine 1<sup>^</sup>AzA (P<sup>^</sup>AzA) ligands and the reactivity of their coordination complexes with palladium.

The first-generation P<sup>^</sup>AzA ligand contains a phenyl linkage between the two heteroatoms and affords a [Pd<sup>II</sup>(CH<sub>3</sub>)(P<sup>^</sup>AzA)]<sub>2</sub> dimer when coordinated to Pd. Thermolysis of the dimer results in the formation of two new Pd complexes, a [Pd<sup>I</sup>(P<sup>^</sup>AzA)]<sub>2</sub> dimer and a mononuclear [Pd<sup>II</sup>(P<sup>^</sup>AzA)<sub>2</sub>] complex via a unique mechanism. Distinct coordination modes of the 1-AzA are observed in all three complexes, and a previously unreported coordination mode is observed in the [Pd<sup>I</sup>(P<sup>^</sup>AzA)]<sub>2</sub> dimer. The formation of both Pd complexes is accompanied by difficult Csp<sup>3</sup>-Csp<sup>3</sup> cross coupling, directly caused by the structurally responsive 1-AzA. The 1-AzA reduces barriers required for the reductive elimination step, and maintains the unusual dinuclear motif throughout the reaction. A direct synthesis for the [Pd<sup>I</sup>(P<sup>^</sup>AzA)]<sub>2</sub> dimer is also reported, and this complex is catalytically active for Kumada cross-coupling. Experimental evidence suggests the dinuclear Pd structure is maintained throughout the reaction mechanism. Thus, the phenyl-linked P<sup>^</sup>AzA ligand has been established as beneficial for fundamental reactivity proceeding via unusual mechanisms.

The second-generation P<sup>^</sup>AzA ligands contain a 1,8-naphthalene or 2,2'-biphenyl backbone. A P<sup>^</sup>AzA complex with the naphthalene backbone can only be isolated with the 1-AzA coordinated  $\kappa^1$ -N. When the biaryl ligand is coordinated to Pd the first example of a Pd(P<sup>^</sup>AzA) complex with the 1-AzA coordinated  $\eta^3$ -NCC coordination is observed. The bite angle of the biaryl ligand is ca. 15° larger than the naphthalene ligand, likely due to the increased distance between P and N, as well as rotation between the two aryls. The increased bite angle for the biaryl ligand allows for the isolation of the 1-Aza in the  $\eta^3$ -NCC coordination mode, and a new ligand design strategy method for isolating Pd complexes in this coordination mode has therefore been reported.

## Keywords

Organometallic • Catalysis • Coordination Chemistry • Structurally Responsive Ligands • Cross-coupling • Polymerization • Reductive Elimination • Mechanistic Studies • Palladium • 1-Azaallyl

## Summary for Lay Audience

Catalysis is the process of increasing the rate of a chemical reaction by using an additive that is regenerated after each individual reaction takes place. Catalysts allow you to make molecules that are difficult or are inefficiently produced via other methods. It is one of the most important chemical discoveries in modern history, and it is so impactful that it is estimated that 90% of all commercial products use a catalyst at some point in the production chain. Transition metal catalysts are comprised of two equally important parts, the metal centre and the ligands that are bound to the metal centre, together these species form a transition metal complex. Structurally responsive ligands can change the way that they are bound to the metal centre, allowing for multiple different types of bonding to occur. These changes in binding can have a profound impact on the reactions that can be permitted by the complex and these transition metal complexes can consequently perform reactions difficult with other methods. Furthermore, the changes in binding allow for the isolation of a variety of unique and novel transition metal complexes. Together, these advantages could allow the synthesis of new and impactful fine chemicals and reduce the number of steps required to synthesize a plethora of natural products.

This thesis describes the synthesis and reactivity of a new series of ligands that contain phosphorus and a structurally responsive functional group. How the ligands are bound to the transition metal palladium is thoroughly explored, and new ligand design strategies influencing metal-ligand binding are discussed. Additionally, direct evidence of the beneficial effects of the structural responsiveness of the ligand is reported as it makes fundamental reaction steps easier, and it is shown to allow unusual reaction pathways where it is key in maintaining the catalyst structure.

## Co-Authorship Statement

This thesis involves work from two previously published manuscripts in Chapters 2, and 3. Manuscripts of the work in Chapter 4 and 5 are in preparation and will be submitted shortly.

Chapter 1 and 6 were written by KMKJ and edited by JMB.

The work presented in Chapter 2 was co-authored by Kyle M. K. Jackman, Benjamin J. Bridge, Ethan R. Sauvé, Christopher N. Rowley, Cameron H. M. Zheng, James M. Stubbs, Paul D. Boyle, and Johanna M. Blacquiere.<sup>1</sup> KMKJ performed 70% of the experimental work and

spectral characterization. CNR performed DFT analysis. PDB collected and solved the X-ray crystallographic data. KMKJ and JMB prepared and edited the document.

The work presented in Chapter 3 was co-authored by Kyle M. K. Jackman, Guangchao Liang, Paul D. Boyle, Paul M. Zimmerman, and Johanna M. Blacquiere.<sup>2</sup> KMKJ performed all experimental work and spectral characterization. GL performed all computational analysis. PDB and KJ collected and solved the X-ray crystallographic data. KMKJ and JMB prepared and edited the introduction, experimental results, discussion, and conclusions. The computational sections were prepared by GL and edited together with PMZ. JMB and PMZ refined and edited the manuscript.

The work in Chapter 4 was co-authored by Kyle M.K. Jackman, Soumik Das, Ethan L. Lidsky, Emily Traver, Paul D. Boyle, Paul M. Zimmerman, and Johanna M. Blacquiere. KMKJ performed 95% of the experimental work and spectral characterization data. ELL and ET contributed to the synthesis of the target compound **4-2**. SD performed computational analysis under the guidance of PMZ; however, these results were not included in the thesis. PDB collected and solved the X-ray crystallographic data. KMKJ prepared the document, JMB edited the document.

The work in Chapter 5 was co-authored by Kyle M.K. Jackman, Leslie Kelley, Paul D. Boyle, and Johanna M. Blacquiere. KMKJ performed 80% of the experimental work and spectral characterization. LK contributed to some of the synthesis and characterization of the biaryl ligand (**5-L5a**, **H(5-L5)**, and **5-L5**) and its coordination complexes (**5-7**). LK also performed polymerization with **5-7**. PDB collected and solved the X-ray crystallographic data. KMKJ prepared the document, some sections of which included contributions from the 4491 thesis of LK. JMB edited the document.

## References

1. Jackman, K. M. K.; Bridge, B. J.; Sauvé, E. R.; Rowley, C. N.; Zheng, C. H. M.; Stubbs, J. M.; Boyle, P. D.; Blacquiere, J. M., *Organometallics* **2019**, *38*, 1677-1681.
2. Jackman, K. M. K.; Liang, G.; Boyle, P. D.; Zimmerman, P. M.; Blacquiere, J. M., *Dalton Trans.* **2022**, *51*, 3977-3991.



## Acknowledgements

Holy cannoli I can't believe I made it this far, this is insane. I started at Western way back in 2013 when I was just a wee baby. Now in 2022 I'm old and bitter and wish I could just go back and do the 9 years all over again the exact same way.

First and foremost, I would like to give an enormous thank you to Johanna Blacquiere, who I have been lucky enough to have as my supervisor for the last 6(!) years. Thank you for your patience, your guidance, and your belief in me. I still remember you telling me in your office that you had every confidence that I could do a PhD, and I had never had someone I respected so much put so much confidence in me and that moment was when I began to believe in myself.

I would like to thank all the wonderful people who have come and gone from the lab throughout my tenure. James, thanks for taking me under your wing when I first started and showing me the ins and outs of fantasy hockey. Sorry I'm better than you are at it now. Scott, it's always entertaining finding one of your surprise memes on proper procedures. Nick, Matt, there was never a dull moment when the two of you were in the office, you two were attached at the hip so you get the same sentence. Meagan, Ben, Amrit, thanks for always being down for a trip to the Grad Club. Shagana and Megan thanks for helping me enjoy the last little bit of my PhD. JW, I hope you bring the children back to Chernobyl. And of course, my partner in crime over the last 6 years Devon. It's going to be very weird not working with you, I wish you the best of luck buddy.

Thanks to my mom and dad, Sam and Derek, and my brother Noah. I'm very thankful for every opportunity I got to go home and disconnect from chemistry. Thank you to my writing partner, Rudy. I used to be annoyed that he napped all the time, but it was super convenient for writing this document.

And of course, my love, my best friend, my fiancé, Courtney. You have been my rock for 7 years, and without you I don't know if I would be sitting here writing this document. You inspire me every day to be the best version of myself, and I want to be the best version of myself for you. I'm sorry that you've had to deal with thesis-le over the last few weeks/months, but I have a good feeling we won't have to simultaneously go through a thesis finale, a move, a job hunt, and planning a wedding again. I love you Schmobe, thank you for putting up with my bs throughout this journey and I can't wait for the next step in our lives together.

Thank you Western, it's been the best 9 years of my life, but it's time to move on.

# Table of Contents

|   |              |
|---|--------------|
| <b>Abstract .....</b>   | <b>i</b>     |
| <b>Co-Authorship Statement .....</b>  | <b>ii</b>    |
| <b>Acknowledgements .....</b>   | <b>iv</b>    |
| <b>Table of Contents .....</b>  | <b>v</b>     |
| <b>List of Tables .....</b>   | <b>ix</b>    |
| <b>List of Figures .....</b>  | <b>ix</b>    |
| <b>List of Schemes .....</b>  | <b>xii</b>   |
| <b>List of Abbreviations .....</b>  | <b>xvi</b>   |
| <b>List of Complexes .....</b>  | <b>xviii</b> |
| <b>1.0 Introduction .....</b>   | <b>1</b>     |
| 1.1 Catalysis, and its Impact on Society .....  | 1            |
| 1.2 Transition Metal Catalyzed Cross Coupling Reactions .....   | 2            |
| 1.3 Catalysis using Palladium .....   | 4            |
| 1.3.1 Palladium Catalyzed Cross-Coupling .....  | 4            |
| 1.3.2 Palladium Catalyzed Polymerization .....  | 7            |
| 1.4 Dinuclear Group 10 Complexes .....  | 12           |
| 1.5 Structurally Responsive Ligands .....   | 16           |
| 1.6 1-Azaallyls as Ligands in Organometallic Chemistry .....  | 21           |
| 1.7 Phosphine 1-Azaallyl Ligands .....  | 24           |
| 1.8 Scope of Thesis .....   | 25           |
| 1.9 References .....  | 27           |
| <b>2.0 Csp<sup>3</sup>-Csp<sup>3</sup> Coupling with a Pd<sup>II</sup> Complex Bearing a Structurally Responsive Ligand .....</b> | <b>32</b>    |
| 2.1 Introduction .....  | 32           |
| 2.2 Results and Discussion .....  | 33           |
| 2.3 Conclusion .....  | 37           |
| 2.4 Experimental .....  | 38           |
| 2.4.1 – General Considerations .....  | 38           |

|   |           |
|---|-----------|
| 2.4.2 – Synthesis of PdCl(CH <sub>3</sub> )(H[2-L1]), 2-1.....                                    | 39        |
| 2.4.3 – Synthesis of Pd(CH <sub>3</sub> )(L1), 2-2, via deprotonation of 2-1.....                 | 40        |
| 2.4.4 – Synthesis of K[2-L1].....   | 41        |
| 2.4.5 – Synthesis of Pd(CH <sub>3</sub> )(L1), 2-2, via metalation of K[2-L1].....                | 41        |
| 2.4.6 – Synthesis of Pd(CH <sub>3</sub> )(py)(2-L1), 2-3.....                                     | 42        |
| 2.4.7 – Synthesis of [Pd(L1)] <sub>2</sub> , 2-4 and Pd(L1) <sub>2</sub> , 2-5.....               | 42        |
| 2.4.8 – Independent Synthesis of 2-5.....   | 43        |
| 2.4.9 – GC-MS and GC-FID Procedures.....  | 44        |
| 2.4.9.1 – Procedure for Ethane Calibration by GC-FID.....   | 44        |
| 2.4.9.2 – Procedure for Ethane Quantification by GC-FID for Heated Samples of 2-2.....            | 45        |
| 2.5 References.....   | 45        |
| <b>3.0 Changes in Ligand Coordination Mode Induce Bimetallic C-C Coupling Pathways.....</b>       | <b>48</b> |
| 3.1 Introduction.....   | 48        |
| 3.2 Results.....  | 52        |
| 3.2.1 Non-Structurally Responsive Phosphine-Amido Complex.....                                    | 52        |
| 3.2.2 Assessment of a Monomer-Dimer Equilibrium with 3-1.....                                     | 54        |
| 3.2.3 Formation of the Methane as a By-Product.....   | 55        |
| 3.2.4 Possible Pathways for C-C Reductive Elimination.....  | 58        |
| 3.2.5 Reaction Order and Eyring Analysis of Reductive Elimination.....                            | 59        |
| 3.2.6 Relationship between Reductive Elimination Products 3-2 and 3-3.....                        | 60        |
| 3.2.7 Assessment of a Radical Pathway to Reductive Elimination.....                               | 61        |
| 3.2.8 Assessment of a Monometallic Reductive Elimination Pathway.....                             | 62        |
| 3.2.9 Assessment of Bimetallic Pathways to Reductive Elimination.....                             | 64        |
| Path C1: Ethane Formation from an Asymmetric Methyl-Bridged Dimer.....                            | 64        |
| Path C2: Formation of Ethane and Product 3-3 from Bimetallic Dimethyl Intermediate 8a5.....       | 66        |
| Path C3: Formation of Ethane and PdI Dimer 3-2 from a Ligand-Bridged Bimetallic Intermediate..... | 68        |
| 3.3 Discussion.....   | 70        |
| 3.3.1 Monometallic Route to Methane By-Product.....   | 70        |
| 3.3.2 Bimetallic CH <sub>3</sub> Transfer.....  | 71        |
| 3.3.3 Bimetallic 1,1-Reductive Elimination.....   | 73        |
| 3.4 Conclusions.....  | 74        |
| 3.5 Experimental.....   | 75        |

|  |           |
|--|-----------|
| 3.5.1 Synthetic Procedures .....   | 75        |
| 3.5.1.1 General Considerations.....  | 75        |
| 3.5.1.2 Ligand Synthesis .....   | 77        |
| 3.5.1.2.1 Synthesis of $\text{Ph}_2\text{P}(\text{o-C}_6\text{H}_4)\text{NH}(\text{i-Bu})$ , <b>H[3-L2]</b> :.....           | 77        |
| 3.5.1.2.2 Synthesis of $\text{K}[\text{Ph}_2\text{P}(\text{o-C}_6\text{H}_4)\text{N}(\text{i-Bu})]$ , <b>K[3-L2]</b> : ..... | 78        |
| 3.5.1.3 Complex Synthesis .....  | 78        |
| 3.5.1.3.1 Synthesis of $\text{Sn}(\text{CD}_3)_4$ : .....  | 78        |
| 3.5.1.3.2 Synthesis of $\text{Pd}(\text{CD}_3)\text{Cl}(\text{COD})$ : .....   | 79        |
| 3.5.1.3.3 Synthesis of $[\text{Pd}(\text{CD}_3)(\mathbf{3-L1})_2]$ , <b>3-1-d6</b> : .....                                   | 80        |
| 3.5.1.3.4 Synthesis of $[\text{Pd}(\text{CH}_3)(\mathbf{3-L2})_2]$ , <b>3-4</b> :.....                                       | 80        |
| 3.5.1.3.5 Synthesis of $[\text{Pt}(\text{CH}_3)(\mathbf{3-L1})_2]$ , <b>3-5</b> :.....                                       | 81        |
| 3.5.1.3.6 Synthesis of $\text{Pt}(\mathbf{3-L1})_2$ , <b>3-6</b> : .....   | 82        |
| 3.5.1.3.7 Synthesis of $\text{K}[\text{Pd}(\text{CH}_3)_2(\mathbf{3-L1})]$ , <b>K[3-7]</b> : .....                           | 82        |
| 3.5.1.3.8 Attempted Synthesis of $[\text{Pd}(\mathbf{3-L1})_2\text{Pd}(\text{CH}_3)_2]$ , <b>3-8</b> : .....                 | 83        |
| 3.5.1.3.8.1 Room Temperature:.....   | 83        |
| 3.5.1.3.8.2 0 °C:.....   | 84        |
| 3.5.2 Experimental Procedures .....  | 84        |
| 3.5.2.1 Kinetic Data: .....  | 84        |
| 3.5.2.1.1 Rate Data: .....   | 84        |
| 3.5.2.1.2 Eyring Analysis.....   | 84        |
| 3.5.2.2 Radical Tests .....  | 85        |
| 3.5.2.3 Crossover Experiments .....  | 85        |
| 3.5.2.3.1 Filled Tube Experiment .....   | 85        |
| 3.5.2.3.2 GC-MS Analysis .....   | 86        |
| 3.5.2.4 General Thermolysis Procedure .....  | 86        |
| 3.5.2.5 Relationship between 3-4 and 3-5 .....   | 86        |
| 3.5.3 Computational Details .....  | 87        |
| 3.6 References.....  | 87        |
| <b>4.0 Evidence of an On-Cycle Dinuclear <math>\text{Pd}^{\text{I}}</math> Catalyst for Kumada Cross-Coupling .....</b>      | <b>91</b> |
| 4.1 Introduction.....  | 91        |
| 4.2 Results .....  | 93        |
| 4.2.1 Improved Synthesis of <b>4-2</b> .....   | 93        |
| 4.2.2 Kumada Cross Coupling .....  | 94        |

|  |            |
|--|------------|
| 4.2.3 Determination of Catalyst and Substrate Order .....  | 97         |
| 4.2.4 Assessment of Decomposition Products of <b>4-2</b> as Catalytically Active species .....           | 99         |
| 4.2.5 Attempted Synthesis of Reaction Intermediates .....  | 100        |
| 4.2.6 Comparison of Kumada Coupling with <b>4-2</b> and <b>4-10</b> .....                                | 102        |
| 4.3 Conclusion .....   | 103        |
| 4.4 Experimental Section.....  | 104        |
| 4.4.1 General Considerations.....  | 104        |
| 4.4.2 Improved Synthesis of [Pd <sup>I</sup> ( <b>4-L1</b> )] <sub>2</sub> , <b>4-2</b> .....            | 105        |
| 4.4.3 Synthesis of [Pd(I)(Ph)( <b>H(4-L1)</b> )], ( <b>4-10</b> ).....                                   | 106        |
| 4.4.4 General Procedure for Kumada Coupling Catalysis.....   | 107        |
| 4.4.5 General Procedure for Variable Time Normalization Analysis (VTNA) .....                            | 108        |
| 4.5 References.....  | 109        |
| <b>5.0 Assessing the Influence of Wider Bite Angles on P<sup>^</sup>AzA Coordination Chemistry .....</b> | <b>111</b> |
| 5.1 Introduction.....  | 111        |
| 5.2 Result and Discussion.....   | 116        |
| 5.2.1 Ligand Synthesis .....   | 116        |
| 5.2.1.1 Phosphin(it)e-Amine Synthesis ( <b>5-L4a</b> , <b>5a</b> , and <b>6a</b> ).....                  | 117        |
| 5.2.1.2 Phosphin(it)e-Imine Synthesis ( <b>H[5-L4, 5, and 6]</b> ).....                                  | 118        |
| 5.2.1.3 Phosphine-Imine Deprotonation .....  | 120        |
| 5.2.2 Palladium Complex Synthesis.....   | 122        |
| 5.2.2.1 Synthesis of Pd Phosphine-Imine Complexes <b>5-4</b> and <b>5-5</b> .....                        | 122        |
| 5.2.2.2 P <sup>^</sup> AzA Complex Synthesis .....   | 124        |
| 5.2.3 Ethylene Homopolymerization .....  | 126        |
| 5.3 Conclusions.....   | 127        |
| 5.4 Experimental .....   | 128        |
| 5.4.1 Synthetic Procedures .....   | 128        |
| 5.4.1.1 General Considerations.....  | 128        |
| 5.4.1.2 Ligand Synthesis .....   | 129        |
| 5.4.1.2.1 Phosphinite-Amine Synthesis ( <b>5-L4a</b> ) .....   | 129        |
| 5.4.1.2.2 Attempted Phosphinite-Imine Synthesis ( <b>H[5-L4]</b> ) .....                                 | 130        |
| 5.4.1.2.3 Naphthalene Phosphine-Imine Synthesis ( <b>H[5-L5]</b> ).....                                  | 131        |
| 5.4.1.2.4 Biaryl Phosphine-Imine Synthesis ( <b>H[5-L6]</b> ).....                                       | 131        |
| 5.4.1.3 P <sup>^</sup> AzA Ligand Synthesis .....  | 132        |

|   |            |
|---|------------|
| 5.4.1.2.3.1 Biaryl P <sup>^</sup> AzA Synthesis ( <b>K[5-L6]</b> ).....         | 132        |
| 5.4.1.3. Complex Synthesis .....  | 133        |
| 5.4.1.3.1 Phosphine-Imine Complex Synthesis .....                               | 133        |
| 5.4.1.3.1.1 Naphthalene P <sup>^</sup> I Complex Synthesis ( <b>5-4</b> ) ..... | 133        |
| 5.4.1.3.1.2 Biaryl P <sup>^</sup> I Complex Synthesis ( <b>5-5</b> ).....       | 134        |
| 5.4.1.3.2 P <sup>^</sup> AzA Complex Synthesis .....                            | 135        |
| 5.4.1.3.2.1 Naphthalene P <sup>^</sup> AzA Synthesis ( <b>5-6</b> ) .....       | 135        |
| 5.4.1.3.2.2 Biaryl P <sup>^</sup> AzA Synthesis ( <b>5-7</b> ).....             | 136        |
| 5.5 References.....   | 136        |
| <b>6.0 Conclusions and Future Work .....</b>                                    | <b>138</b> |
| 6.1 Summary and Conclusion .....  | 138        |
| 6.2 Future Work .....   | 140        |
| <b>Appendices.....</b>  | <b>144</b> |
| Appendix A: Supplementary Information for Chapter 2 .....                       | 144        |
| Appendix B: Supplementary Information for Chapter 3 .....                       | 181        |
| Appendix C: Supplementary Information for Chapter 4 .....                       | 238        |
| Appendix D: Supplementary Information for Chapter 5 .....                       | 262        |
| Appendix E Copyright Material and Permissions .....                             | 292        |
| Appendix F Curriculum Vitae .....   | 293        |

## List of Tables

|  |    |
|--|----|
| <b>Table 4.1.</b> Reaction optimization and control reactions for Kumada coupling between <b>4-4a</b> and PhMgBr at 0.1 mol% <b>4-2</b> , at varying times and temperatures..... | 95 |
|--|----|

## List of Figures

|   |    |
|---|----|
| <b>Figure 1.1.</b> a) Energy profile for a hypothetical reaction with (orange line) and without (blue line) a catalyst. b) A generic catalytic cycle for the hypothetical reaction in a). .....   | 2  |
| <b>Figure 1.2.</b> A series of ligands coordinated to Pd <sup>II</sup> that have successfully been employed for the copolymerization of ethylene with polar comonomers. <sup>46, 95, 96</sup> .....   | 10 |
| <b>Figure 1.3.</b> $\alpha$ -diimine complexes used to investigate steric ( <b>O/P</b> ) <sup>101, 102</sup> effects on chain-walking and copolymerization activity, and a benchmark $\alpha$ -diimine complex ( <b>Q</b> ). <sup>102</sup> .....   | 11 |
| <b>Figure 1.4.</b> a) Phosphine-sulfonate Pd <sup>II</sup> complexes ( <b>R, S, T</b> ) used to investigate how linear polyethylene is formed with the phosphine-sulfonate complexes. <sup>105</sup> b) complexes used to investigate the impact of changing the backbone ( <b>U, V</b> ) on the copolymerization of ethylene with polar co monomers. <sup>107</sup> .... | 12 |

|   |    |
|---|----|
| <b>Figure 1.5.</b> A selection of isolated dinuclear Pd and Ni complexes. M = Pd/Ni. <sup>116, 117</sup> .....  | 13 |
| <b>Figure 1.6.</b> The different Pd <sup>II</sup> and Ni <sup>II</sup> $\alpha$ -diimine complexes synthesized for investigations of SRL impact on ethylene polymerization (left). Reversible coordination of the morpholine moiety in the secondary coordination sphere (right). <sup>131</sup> .....  | 18 |
| <b>Figure 1.7.</b> General illustration of the diverse range of bimetallic (left) and monometallic (right) coordination modes of the 1-AzA group. <sup>142</sup> .....  | 21 |
| <b>Figure 1.8.</b> A selection of group 10 1-AzA complexes. R = Si(CH <sub>3</sub> ) <sub>3</sub> . <sup>143, 145</sup> .....   | 23 |
| <b>Figure 2.1.</b> Displacement ellipsoid (50% probability) plots of <b>2-4</b> (left) and <b>2-5</b> (right). Hydrogen atoms have been omitted for clarity. Selected bond distances (Å): 2-4 Pd <sup>I</sup> -Pd <sup>I</sup> 2.6109(7), Pd <sup>I</sup> -N <sup>1</sup> 2.061(3), Pd <sup>I</sup> -Pd <sup>I</sup> 2.3136(9), Pd <sup>I</sup> -C <sup>1</sup> 2.308(3), Pd <sup>I</sup> -C <sup>2</sup> 2.205(3), C <sup>1</sup> -C <sup>2</sup> 1.396(4); 2-5 Pd <sup>I</sup> -P <sup>1</sup> 2.2383(10), Pd <sup>I</sup> -P <sup>2</sup> 2.2437(10), Pd <sup>I</sup> -N <sup>1</sup> 2.088(3), Pd <sup>I</sup> -N <sup>2</sup> 2.091(3), N <sup>1</sup> -C <sup>7</sup> 1.408(4), N <sup>2</sup> -C <sup>29</sup> 1.389(4)..... | 37 |
| <b>Figure 2.2.</b> General labeling scheme for the phosphine imine ligand <b>H[2-L1]</b> . This scheme will be used consistently for all compounds throughout the experimental. In cases where H <sup>3</sup> and C <sup>3</sup> atoms are non-equivalent H <sup>3</sup> and H <sup>3'</sup> , C <sup>3</sup> and C <sup>3'</sup> are used to distinguish between the two sites.....  | 39 |
| <b>Figure 3.1.</b> a) <sup>2</sup> H NMR spectra following the thermolysis of <b>3-5</b> in C <sub>6</sub> D <sub>6</sub> (top), and C <sub>6</sub> H <sub>6</sub> (bottom), spectra zoomed in to show $\delta_D = 6.00 - 0.00$ (92.1 MHz, C <sub>6</sub> H <sub>6</sub> ). b) <sup>2</sup> H NMR spectrum following the thermolysis of <b>3-5</b> in C <sub>6</sub> D <sub>6</sub> , spectrum zoomed in to show $\delta_D = 8.50 - 5.50$ (92.1 MHz, C <sub>6</sub> H <sub>6</sub> ). .....   | 58 |
| <b>Figure 3.2.</b> a) Plot of Ln[ <b>3-1</b> ] vs time for two reactions in which the initial concentrations of <b>3-1</b> were 22 mM (red) and 62 mM (blue). b) Eyring plot of the rate constants acquired from heating a solution of <b>3-1</b> (16 mM) in benzene from 40 to 70 °C. ....   | 60 |
| <b>Figure 3.3.</b> General labelling scheme for a) phosphine 1-azaallyl (P <sup>^</sup> AzA) ligand <b>3-L1</b> ; b) phosphine amine ligand <b>H[3-L2]</b> ; c) P <sup>^</sup> AzA ligand <b>3-L1</b> . This scheme will be used consistently for all compounds throughout the experimental. The denotations H <sup>3</sup> , H <sup>3'</sup> , C <sup>3</sup> , and C <sup>3'</sup> are used to distinguish between cases where atoms H <sup>3</sup> and C <sup>3</sup> are not equivalent. ....   | 77 |
| <b>Figure 4.1.</b> Examples of dinuclear Pd <sup>I</sup> dimer complexes including halide bridged <b>4-A</b> and <b>4-B</b> .....   | 92 |
| <b>Figure 4.2.</b> Halide exchange reaction with A and aryl halides. ....   | 92 |
| <b>Figure 4.3.</b> Kumada coupling between PhMgBr and aryl bromides <b>4-4b-g</b> using 0.1 mol % <b>2</b> at 60 °C. .  | 96 |
| <b>Figure 4.4.</b> Kumada coupling between PhBr and various C <sub>sp</sub> <sup>3</sup> hybridized Grignard reagents using 1.0 mol % <b>4-2</b> . <sup>a</sup> : <b>4-4a</b> used as the coupling partner. ....  | 97 |
| <b>Figure 4.5.</b> Three plausible pathways for activation of a $\mu$ -X Pd <sup>I</sup> dimer to enter a catalytic cycle. Path a) Direct entry of the dinuclear complex that operates as an on-cycle catalyst. Expected order of <b>4-2</b> = 1.0. Path b) Nucleophile assisted fragmentation <sup>16</sup> which results in disproportionation to active Pd <sup>0</sup> (L) and Pd <sup>II</sup> LX <sub>2</sub> byproduct. Expected order of <b>4-2</b> = 1.0. Path c) Homolytic cleavage of the dinuclear Pd <sup>I</sup> structure to give Pd <sup>I</sup> LX monomers, followed by reduction to give 2 active Pd <sup>0</sup> catalysts. Expected order in <b>4-2</b> = 0.5. ....  | 97 |
| <b>Figure 4.6</b> Variable time normalization analysis: (left) concentration of <b>4-4f</b> and PhMgBr kept constant at 210 and 315 mM respectively. Concentration of <b>4-2</b> changed from 210 $\mu$ M (green), 520 $\mu$ M (red), and 830 $\mu$ M (blue). Consumption of <b>4-4f</b> is being tracked. (right) concentration of <b>4-2</b> and PhMgBr kept constant at 210 $\mu$ M and 315 mM respectively. Concentration of <b>4-4f</b> changed from 50 mM (blue), 110 mM (red), and 220 mM (green). Formation of <b>4-5f</b> is being tracked. Reactions ran in duplicate. ....   | 98 |

- Figure 4.7.** (Top) General reaction scheme for Kumada coupling of **4-4a** with PhMgBr or MeMgBr at 0.1 and 1.0 mol% respectively. Bar graph showing product formation vs. catalyst used, filled bar = formation after 24 h, unfilled and filled bar together = formation after 48 h. (Left) R = Ph 0.1 mol% catalyst used. i = 0.1 mol% of complex **4-2** heated for 3 h at 60 °C. ii = 0.1 mol% complex **4-2** heated for 24 h at 70 °C (Right) R = Me. .... 100
- Figure 4.8.** Thermal displacement plot of **4-10**. Displacement ellipsoid (50% probability). All hydrogen atoms and have been omitted for clarity. P(1)-Pd(1)-N(1) = 82.36(1)°, C(10)-Pd(1)-I(1) = 89.53(1)°, N(1)-C(1)-C(2) = 121.80(6)°, C(1)-C(2)-C(3) = 106.10(6)°,  $\tau^4 = 0.16$ ,<sup>31</sup> N(1)-C(1) = 1.326(7) Å, C(1)-C(2) = 1.486(1) Å, Pd(1)-P(1) = 2.231(1) Å, Pd(1)-N(1) = 2.201(4) Å, Pd(1)-I(1) = 2.654(7) Å, Pd(1)-C(10) = 2.008(5) Å..... 101
- Figure 4.9.** Consumption of **4-4a** (solid line) and formation of **4-5a** (dotted line) following Kumada coupling with PhMgBr as the Grignard reagent, using 0.1 mol% **4-2** (red), 0.1 mol% **4-10** (grey), and 0.2 mol% **4-10** (black)..... 103
- Figure 4.10.** General labelling scheme for a) phosphine 1-azaallyl (P<sup>AzA</sup>) ligand **4-L1**; b) phosphine amine ligand **H[4-L2]**; c) P<sup>AzA</sup> ligand **4-L1**. This scheme will be used consistently for all compounds throughout the experimental. The denotations H<sup>3</sup>, H<sup>3'</sup>, C<sup>3</sup>, and C<sup>3'</sup> are used to distinguish between cases where atoms H<sup>3</sup> and C<sup>3</sup> are not equivalent..... 105
- Figure 5.1.** a) Selected monoanionic ligand groups: 1-AzA (**A**), allyl (**B**), carboxylate (**C**) and a Pd 1-AzA catalyst (**D**) used in Suzuki-Miyaura coupling catalysis. <sup>i</sup>Pr = 2,6-diisopropylphenyl. .... 111
- Figure 5.2.** Representative scheme for a migratory-insertion polymerization mechanism, showing isomerization of the 1-AzA between  $\kappa^1$ -N and  $\eta^3$ -NCC potentially stabilizing the low coordinate species **E**..... 112
- Figure 5.3.** Three P<sup>AzA</sup> ligands that have been designed thus far, a phenyl linked ligand **5-L1**, and two alkyl linked ligands **5-L2** and **5-L3**. .... 112
- Figure 5.4.** Isolated Ru(**L1**) complexes showing  $\kappa^1$ -N (**E** and **F- $\kappa$** ) and  $\eta^3$ -NCC (**F- $\eta$** ). .... 114
- Figure 5.5.** Pd(**H(5-L1)**) complex **J** and its thermal ellipsoid plot. Thermal ellipsoids are shown at the 50% probability level. For clarity, all hydrogens and phenyl substituents have been omitted. P(1)-Pd(1)-N(1) = 80.10(2)°, C(27)-Pd(1)-Cl(1) = 90.35(3)°, N(1)-C(1)-C(2) = 124.85(9)°, C(1)-C(2)-C(3) = 109.10(1)°,  $\tau^4 = 0.10$ ,<sup>13</sup> N(1)-C(1) = 1.284(1) Å, C(1)-C(2) = 1.488(2) Å, Pd(1)-P(1) = 2.190(7) Å, Pd(1)-N(1) = 2.199(9) Å, Pd(1)-Cl(1) = 2.381(7) Å, Pd(1)-C(27) = 2.038(1) Å..... 116
- Figure 5.6.** The three ligands designed to have wider bite angles compared to **5-L1**. .... 117
- Figure 5.7.** <sup>1</sup>H NMR spectrum of H[5-L6] in CDCl<sub>3</sub> with an example of the tautomerization between H[5-L6b] and H[5-L6c]. .... 120
- Figure 5.8.** Thermal ellipsoid plot of **5-5b**, for clarity only one unit of crystallized **5-5b** is shown, additionally and all hydrogens except for the N-H and all phenyl substituents were omitted. Thermal ellipsoids are shown at the 50% probability level. Only values for A crystal are reported. P(1)-Pd(1)-N(1) = 95.18(4)°, C(27)-Pd(1)-Cl(1) = 91.68(5)°, N(1)-C(1)-C(2) = 125.67(2)°, C(1)-C(2)-C(3) = 119.31(2)°,  $\tau^4 = 0.07$ ,<sup>13</sup> N(1)-C(1) = 1.440(2) Å, C(1)-C(2) = 1.332(3) Å, Pd(1)-P(1) = 2.208(9) Å, Pd(1)-N(1) = 2.248(2) Å, Pd(1)-Cl(1) = 2.387(1) Å, Pd(1)-C(27) = 2.035(2) Å..... 124



## List of Schemes

|  |    |
|--|----|
| <b>Scheme 1.1.</b> The proposed catalytic cycle for a typical cross coupling reaction involving a $M^{0/II}$ catalytic cycle. $R^{v'n}$ = alkyl or aryl. ....  | 2  |
| <b>Scheme 1.2.</b> Ni catalyzed doubly enantioconvergent cross-coupling by Fu, resulting in excellent stereo-control over vicinal coupling partners. <sup>36</sup> .....   | 3  |
| <b>Scheme 1.3.</b> The proposed catalytic cycle for a) a typical cross coupling reaction involving a $Pd^{0/II}$ catalytic cycle. $R^{v'n}$ = alkyl or aryl. ....  | 5  |
| <b>Scheme 1.4.</b> The previous route for the synthesis of Ceralasterib <b>D</b> , and the recently developed plant-scale synthesis of <b>D</b> utilizing a Suzuki-Miyaura coupling with a $Pd(dppf)Cl_2$ catalyst. <sup>66</sup> .....  | 6  |
| <b>Scheme 1.5.</b> a) First example of palladium catalyzed $Csp^3-Csp^3$ cross-coupling using bulky trialkyl phosphines as ligands reported by Fu. <sup>70</sup> b) $Csp^3-Csp^3$ cross-coupling of i) allylic and ii) benzyl bromides with diborylmethane using different Pd catalysts. <sup>70,72</sup> .....  | 7  |
| <b>Scheme 1.6.</b> The migratory-insertion mechanism for olefin polymerization including typical decomposition routes $\beta$ -hydride elimination, chain walking, $\beta$ -halogen elimination, and chelate formation. $\textcircled{P}$ = polymer chain, R = H or a functional group, X = halogen. ....  | 8  |
| <b>Scheme 1.7.</b> Proposed mechanism for Kumada coupling using $[Ni^I]_2$ dimer <b>X</b> as the precatalyst. ....   | 14 |
| <b>Scheme 1.8.</b> Left: Buchwald-Hartwig Amination with $Pd^I$ dimer <b>Z</b> and right: aminocarbonylation with $Pd^{II}$ dimer <b>AA</b> . ....   | 15 |
| <b>Scheme 1.9.</b> Suzuki Miyaura coupling using halogen bridged $Pd^I$ dimers <b>AC</b> and <b>AD</b> reported by Schoenebeck. ....   | 16 |
| <b>Scheme 1.10.</b> General depiction of reversible changes in coordination by SRLs, left = denticity ( $\kappa$ ), right = hapticity ( $\eta$ ). ....   | 16 |
| <b>Scheme 1.11.</b> a) Changes in coordination mode of an acetate ligand from $\kappa^2-OO$ to $\kappa^1-OO$ during deprotonation in the proposed mechanism for CMD. <sup>126</sup> b) Indenyl slippage from $\eta^5$ to $\eta^3$ in a generic Mo complex. DG = directing group. <sup>128</sup> .....  | 17 |
| <b>Scheme 1.12.</b> Alkyne cyclotrimerization catalyzed by Ni complexes bearing ligands with dynamic ( <b>AG<sub>i</sub></b> ) and static ( <b>AG<sub>ii/iii</sub></b> ) coordination modes. <sup>132</sup> .....  | 19 |
| <b>Scheme 1.13.</b> Proposed mechanism for alkyne cyclotrimerization catalyzed by a structurally responsive Ni complex analogous to <b>AG<sub>i</sub></b> . <sup>133</sup> .....   | 20 |
| <b>Scheme 1.14.</b> Different coordination modes observed with N,N'-dimethyl-2,11-diaza[3.3]pyridinophane ligands coordinated to Pd and Ni allowing for the isolation of complexes bearing unusual metal oxidation states (left). <sup>137-139</sup> Oxidatively induced reductive elimination of ethane starting from $Pd^{II}$ and $Ni^{II}$ complexes (right). <sup>139-141</sup> ..... | 21 |
| <b>Scheme 1.15.</b> General depiction of the isomerization from $\eta^3-NCC$ to $\kappa^1-N$ , which opens a coordination site for substrate binding. ....   | 22 |
| <b>Scheme 1.16.</b> Synthesis of two different $P^{\wedge}AzA$ Pd complexes using a lithium transfer reagent. <sup>143</sup> .....   | 23 |
| <b>Scheme 1.17.</b> Proposed interconversion between different isomers of 1-AzA Ni complex <b>AN</b> . R = $Si(CH_3)_3$ . <sup>145</sup> .....   | 24 |
| <b>Scheme 1.18.</b> Synthetic pathway used to obtain $Ru(P^{\wedge}AzA)$ complex <b>AQ</b> . <sup>148</sup> .....  | 24 |
| <b>Scheme 1.19.</b> a) Coordination of phosphine-imine ligand <b>H[L2]</b> to Pd affording <b>AR</b> , and subsequent deprotonation in coordinating solvent to afford bicyclic $Pd^{II}$ complex <b>AT</b> . b) Coordination of phosphine-imine ligand <b>H[L3]</b> to Pd to afford <b>AS</b> and attempted deprotonation with $Li[HMDS]$ in coordinating solvent. <sup>149</sup> .....    | 25 |

|   |    |
|---|----|
| <b>Scheme 2.1.</b> Synthesis of Phosphine-Imine Complex <b>2-1</b> . Displacement ellipsoid (50% probability) plot of <b>2-1</b> (right). All hydrogen atoms have been omitted for clarity, except those on C <sup>1A</sup> , C <sup>2A</sup> and C <sup>11A</sup> . .33  | 33 |
| <b>Scheme 2.2.</b> a) Formation of <b>2-2</b> via deprotonation of <b>2-1</b> *the yield decreases for scales >50 mg. Displacement ellipsoid (50% probability) plot of <b>2-2</b> . All hydrogen atoms have been omitted. b) Deprotonation of <b>H[2-L1]</b> with KH to afford <b>K[2-L1]</b> followed by coordination to PdCl(CH <sub>3</sub> )(COD) to afford <b>2-2</b> or metalation of <b>K[2-L1]</b> ..... 34 | 34 |
| <b>Scheme 2.3.</b> Lewis acidic and reductive elimination reactivity of <b>2-2</b> . .... 36  | 36 |
|   |    |
| <b>Scheme 3.1.</b> General Mechanisms for Monometallic (left) and Bimetallic (right) Palladium Catalyzed C-C Bond Formation. .... 49  | 49 |
| <b>Scheme 3.2.</b> Formation of Bimetallic Pd Products following C-C Bond Formation from Monometallic Precursors. .... 50   | 50 |
| <b>Scheme 3.3.</b> Bimetallic Alkyl Transfer and Reductive Elimination. .... 51   | 51 |
| <b>Scheme 3.4.</b> C-C Reductive Elimination from a Pd <sup>II</sup> Dimer ( <b>3-1</b> ), Showing Changes in Ligand Coordination Mode. Yields of <b>3-2</b> and <b>3-3</b> are 35 and 50%, respectively based on starting ligand. .... 52  | 52 |
| <b>Scheme 3.5.</b> Synthesis of Phosphine-Amido Complex, <b>3-4</b> , (left) and thermal displacement plot of <b>3-4</b> (right). Displacement ellipsoid (50% probability) plot of <b>3-4</b> . All hydrogen atoms, and a THF molecule that co-crystallized in the unit cell have been omitted for clarity. .... 53   | 53 |
| <b>Scheme 3.6.</b> Thermolysis of Phosphine-Amido Complex, <b>3-4</b> ..... 54  | 54 |
| <b>Scheme 3.7.</b> Computed dissociation of dimer <b>3-1</b> to monomers <b>m1</b> . Free energies are given in kcal/mol. .... 54   | 54 |
| <b>Scheme 3.8.</b> Thermolysis of <b>3-1</b> and <b>3-1-d<sub>6</sub></b> for H/D Crossover Test. .... 55   | 55 |
| <b>Scheme 3.9.</b> Formation of methane from monomer <b>m1</b> . Free energies are relative to dimer <b>3-1</b> and are given in kcal/mol..... 56   | 56 |
| <b>Scheme 3.10.</b> Preparation of Pt <sup>II</sup> Dimer, <b>3-5</b> . .... 56   | 56 |
| <b>Scheme 3.11.</b> Thermolysis of Pt(II)-CH <sub>3</sub> Dimer <b>3-5</b> to Afford Pt <sup>II</sup> complex <b>3-6</b> (left) and thermal displacement plot of <b>3-6</b> (right). Displacement ellipsoid (50% probability) plot of <b>3-6</b> . All hydrogen atoms have been omitted for clarity. .... 57  | 57 |
| <b>Scheme 3.12.</b> Proposed General Pathways for Reductive Elimination from <b>3-1</b> . .... 59   | 59 |
| <b>Scheme 3.13.</b> Thermolysis of <b>3-2</b> and <b>3-3</b> ..... 61   | 61 |
| <b>Scheme 3.14.</b> Reaction of <b>3-1</b> with H-Atom Donors. .... 62  | 62 |
| <b>Scheme 3.15.</b> Calculated energetics for methyl radical formation. Free energies are relative to dimer <b>3-1</b> and given in kcal/mol. .... 62   | 62 |
| <b>Scheme 3.16.</b> Synthesis of Dimethyl Monomer <b>K[3-7]</b> ..... 63  | 63 |
| <b>Scheme 3.17.</b> a) Thermolysis of <b>K[3-7]</b> ; and b) Computed energies for C-C and C-H bond formation from <b>[3-7]</b> <sup>-</sup> . Selected atom distances are given in Å. .... 63  | 63 |
| <b>Scheme 3.18.</b> Path C1: Ethane formation from a pseudo methyl-bridged dimer <b>d1a</b> . Selected atom distances in monomer <b>m1</b> are given in Å. Computed oxidation states of Pd atoms from LOBA analysis are given in purple. ΔG in kcal mol <sup>-1</sup> . .... 65   | 65 |
| <b>Scheme 3.19.</b> Path C2: Ethane formation from a bimetallic dimethyl intermediate <b>8a5</b> . Computed oxidation states of Pd atoms from LOBA analysis are given in purple. ΔG in kcal mol <sup>-1</sup> ..... 67  | 67 |
| <b>Scheme 3.20.</b> Attempted Formation of <b>3-8</b> . Conditions: (i) 15 equiv [Pd(CH <sub>3</sub> ) <sub>2</sub> (cod)], C <sub>6</sub> D <sub>6</sub> , rt; (ii) 2.0 equiv [Pd(CH <sub>3</sub> ) <sub>2</sub> (cod)], C <sub>6</sub> D <sub>6</sub> , rt; (iii) 2.5 equiv [Pd(CH <sub>3</sub> ) <sub>2</sub> (cod)], C <sub>7</sub> D <sub>9</sub> , 0 °C. .... 68  | 68 |

|   |     |
|---|-----|
| <b>Scheme 3.21.</b> Path C3: Ethane formation from ligand-bridged dimer. Computed oxidation states of Pd atoms from LOBA analysis <sup>63</sup> (except those of dimer <b>3-2</b> ) are given in purple. $\Delta G^\circ/\Delta G^\ddagger$ are in kcal mol <sup>-1</sup> .   | 70  |
| <b>Scheme 3.22.</b> Competing pathways from monomer <b>m1</b> that can lead to methane formation through methyl transfer (left) or C-H activation (right), as well as the pathway affording ethane and <b>3-3</b> (centre).   | 71  |
| <b>Scheme 3.23.</b> (a) The pathways of methyl transfer, and (b) geometric parameters of the Pd-CH <sub>3</sub> -Pd fragments in the transition states.   | 72  |
| <b>Scheme 3.24.</b> Three proposed operative bimetallic Csp <sup>3</sup> -Csp <sup>3</sup> coupling pathways (C1-C3) from <b>3-1</b> , showing the reductive elimination step to give ethane, and complex <b>3-2</b> , or <b>3-3</b> and Pd(0). Colours depict the different coordination modes for the 1-azaallyl group of <b>3-L1</b> : $\mu$ -N (blue), $\kappa^1$ -N (pink), $\eta^3$ -NCC (red) and $\mu$ -( $\kappa^1$ -N, $\eta^2$ -CC) (green). $\Delta G$ values shown are in kcal/mol and the values are relative to <b>3-1</b> at 0 kcal/mol.  | 74  |
| <b>Scheme 4.1.</b> Kumada coupling using <b>4-B</b> as a precatalyst in 2.5 mol%.   | 93  |
| <b>Scheme 4.2.</b> Previously established Csp <sup>3</sup> -Csp <sup>3</sup> coupling beginning from <b>1</b> to give ethane, <b>4-2</b> , and <b>4-3</b> . Yields shown were obtained by <sup>31</sup> P{ <sup>1</sup> H} NMR spectroscopy.  | 93  |
| <b>Scheme 4.3.</b> a) Improved synthesis of complex <b>4-2</b> starting from a Pd <sup>I</sup> dimer precursor. Isolated yields are shown. b) Attempted synthesis of <b>4-2</b> using non-coordinating solvent (ie. THF) <b>4-3</b> and <b>4-4</b> . In-situ yields relative to <b>K[4-L1]</b> are shown.   | 94  |
| <b>Scheme 4.4.</b> General scheme for the Kumada coupling between <b>4-4a</b> and PhMgBr with varying loadings of <b>4-2</b> , and temperatures.  | 95  |
| <b>Scheme 4.5.</b> a) Addition of PhI (2.0 equiv) to <b>4-2</b> at room temperature resulting in 46% conversion in-situ to <b>4-10</b> . b) Independent synthesis of <b>4-10</b> via coordination of <b>H(4-L1)</b> to PdIPh(TMEDA).  | 101 |
| <b>Scheme 5.1.</b> The two paths that have been successfully used to obtain a P <sup>AzA</sup> -metal complex beginning from <b>P<sup>A</sup>I</b> . Path <b>a</b> : deprotonation of the <b>P<sup>A</sup>I</b> followed by coordination to M generating <b>M(P<sup>AzA</sup>)</b> . Path <b>b</b> : Coordination of <b>P<sup>A</sup>I</b> to M followed by deprotonation affording <b>M(P<sup>AzA</sup>)</b> . Alternatively, the deprotonation can be attempted in the presence of a Lewis base (:LB) affording a Lewis base stabilized <b>M(P<sup>AzA</sup>)</b> complex <b>M(P<sup>AzA</sup>)(LB)<sub>n</sub></b> . | 113 |
| <b>Scheme 5.2.</b> a) Coordination of <b>H[5-L1]</b> to Pd via path <b>a</b> to afford P <sup>AzA</sup> complex <b>5-1</b> in excellent yields. Thermolysis of <b>5-1</b> gives dinuclear <b>5-2</b> and mononuclear <b>5-3</b> , each with distinct coordination modes of the 1-AzA.   | 115 |
| <b>Scheme 5.3.</b> Attempted synthesis of a P <sup>AzA</sup> complex containing a) ethyl linked ligand <b>5-L2</b> . Coordination of <b>H[5-L2]</b> to Pd affording <b>G</b> , followed by attempted deprotonation with Li[HMDS]. b) propyl linked ligand <b>5-L3</b> . Coordination of <b>H[5-L3]</b> to Pd generates <b>H</b> . Complex <b>H</b> is treated with Li[HMDS] in pyridine affording <b>I</b> .  | 115 |
| <b>Scheme 5.4.</b> Synthesis of phosphinite-amine precursor <b>5-L4a</b> .  | 117 |
| <b>Scheme 5.5.</b> Synthesis of phosphine-amine precursor <b>5-L5a</b> .  | 117 |
| <b>Scheme 5.6.</b> Synthesis of <b>5-6La</b> following literature procedures.   | 118 |
| <b>Scheme 5.7.</b> Attempted synthesis of phosphinite-imine <b>H[5-L4]</b> instead affording <b>5-L4b</b> .   | 119 |
| <b>Scheme 5.8.</b> Synthesis of phosphine-imine precursor <b>H[5-L5]</b> .  | 119 |
| <b>Scheme 5.9.</b> Synthesis of <b>H[5-L6]</b> from precursor <b>5-L6a</b> . <b>H[5-L6]</b> is in equilibrium with tautomers <b>H[5-L6a]</b> and <b>H[5-L6b]</b> .  | 119 |

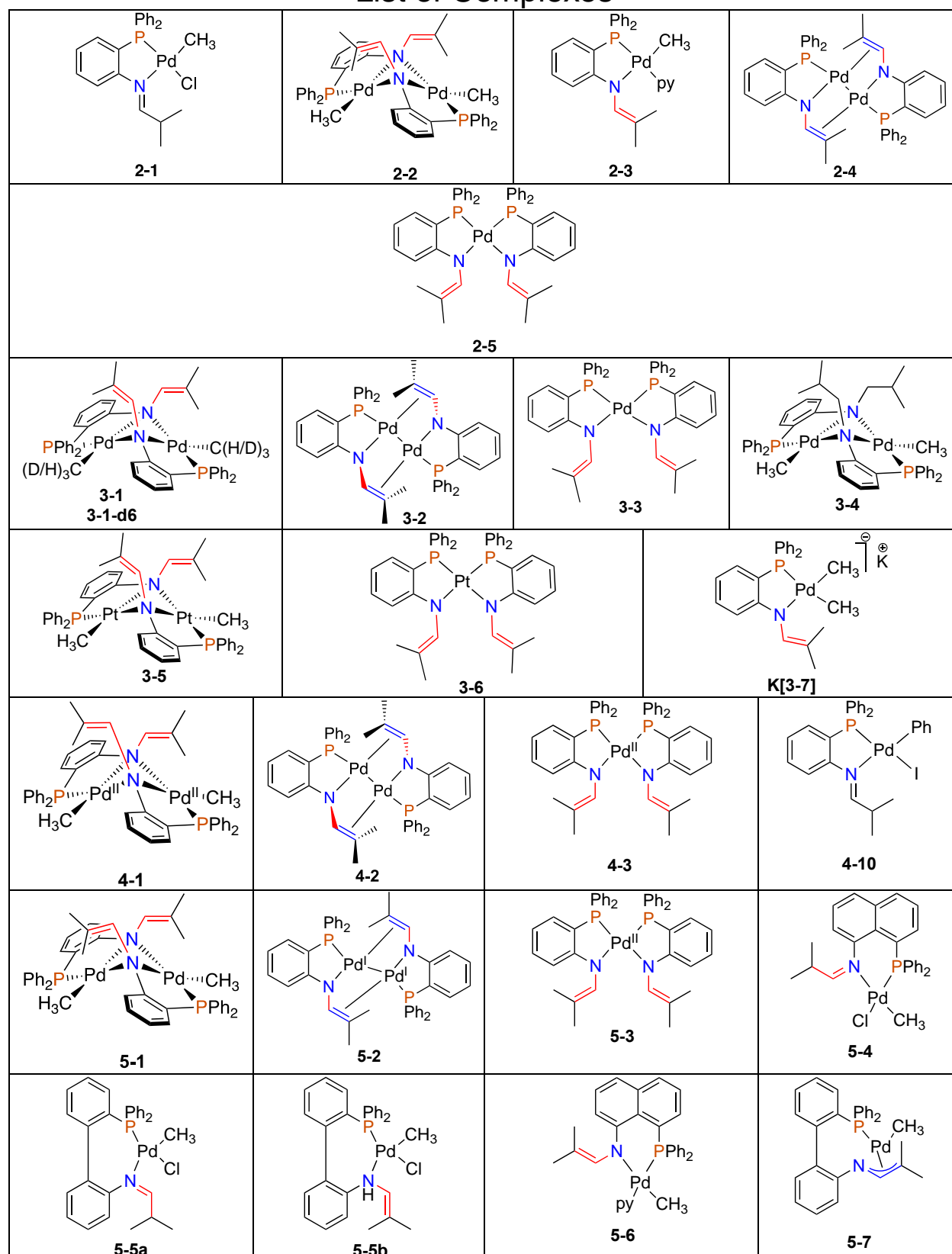
|   |     |
|---|-----|
| <b>Scheme 5.10.</b> Attempted deprotonation of <b>H[5-L5]</b> to give <b>Y[5-L5]</b> Y = Li/K, Base = H, <sup>t</sup> BuOK, <sup>n</sup> Bu, <sup>t</sup> Bu, N(Si(CH <sub>3</sub> ) <sub>2</sub> ), N(CH <sub>2</sub> (CH <sub>3</sub> ) <sub>2</sub> ). .....   | 121 |
| <b>Scheme 5.11.</b> Synthesis of <b>K[5-L6]</b> via deprotonation of the two tautomers of <b>H[5-L6]</b> with KH. ....  | 121 |
| <b>Scheme 5.12.</b> Coordination of <b>H[5-L5]</b> to [PdCl(CH <sub>3</sub> )(COD)] affording <b>5-4</b> . Thermal Ellipsoid plot of <b>5-4</b> . Thermal ellipsoids are shown at the 50% probability level. For clarity, all hydrogens have been omitted. P(1)-Pd(1)-N(1) = 81.94(3)°, C(27)-Pd(1)-Cl(1) = 89.08(4)°, N(1)-C(1)-C(2) = 124.31(1)°, C(1)-C(2)-C(3) = 109.03(1)°, τ <sup>4</sup> = 0.06, <sup>13</sup> N(1)-C(1) = 1.280(1) Å, C(1)-C(2) = 1.490(2) Å, Pd(1)-P(1) = 2.206(7) Å, Pd(1)-N(1) = 2.144(9) Å, Pd(1)-Cl(1) = 2.371(7) Å, Pd(1)-C(27) = 2.060(1) Å..... | 122 |
| <b>Scheme 5.13.</b> Coordination of H[5-L6] to PdCl(CH <sub>3</sub> )(COD) affording 5-5. ....  | 123 |
| <b>Scheme 5.14.</b> Deprotonation of <b>5-4</b> with Li[HMDS] in pyridine, affording P <sup>^</sup> AzA complex <b>5-6</b> in 70% yield with the 1-AzA coordinated κ <sup>1</sup> -N. ....  | 125 |
| <b>Scheme 5.15.</b> Synthesis of P <sup>^</sup> AzA complex <b>5-7</b> via coordination of <b>K[5-L6]</b> . The 1-AzA moiety is proposed to be coordinated η <sup>3</sup> -NCC. ....  | 125 |
| <b>Scheme 5.16.</b> Synthesis of polyethylene catalyzed by <b>5-7</b> . ....  | 126 |
| <br>  |     |
| <b>Scheme 6.1.</b> Left: Current P <sup>^</sup> AzA ligands bearing phenyl phosphine substituents. Right: Future phosphine substituents that should be investigated including electron rich and poor groups. X = X-type ligand. ....  | 141 |
| <b>Scheme 6.2.</b> Left: Current P <sup>^</sup> AzA ligands bearing methyl substituents at the C <sup>2</sup> position and its coordination complex with Pd. Right: Phenyl substitution at C <sup>2</sup> and the proposed change in Pd product selectivity favouring formation of the Pd <sup>I</sup> dimer instead of the mononuclear Pd <sup>II</sup> complex. ....  | 141 |
| <b>Scheme 6.3.</b> Left: Biaryl P <sup>^</sup> AzA complex used for homopolymerization of ethylene. Right: Future polyethylene polymerization using the other P <sup>^</sup> AzA ligands reported in this document and their P <sup>^</sup> I analogues. ....   | 142 |
| <b>Scheme 6.4.</b> Left: Currently synthesized P <sup>^</sup> AzA ligands and their coordination complexes with Pd. Right: Currently synthesized P <sup>^</sup> AzA ligands and future work of coordinating them to Ni. ....  | 142 |
| <b>Scheme 6.5.</b> Left: Kumada coupling using a [Pd <sup>I</sup> (P <sup>^</sup> AzA)] <sub>2</sub> dimer reported in chapter 4. Right: Different potential cross coupling uses for the [Pd <sup>I</sup> (P <sup>^</sup> AzA)] <sub>2</sub> including Suzuki-Miyaura cross coupling and Buchwald-Hartwig Amination. ....   | 143 |

## List of Abbreviations

|                             |   |
|-----------------------------|---|
| 9-BBN                       | 9-Borabicyclo[3.3.1]nonane                  |
| Å                           | Angstrom                                    |
| a,b,c $\alpha,\beta,\gamma$ | Unit Cell Constants                         |
| Ar                          | Aryl  |
| ATR                         | Ataxia Telangiectasia and Rad3-related      |
| AzA                         | 1-Azaallyl                                  |
| Bn                          | Benzyl                                      |
| cal                         | Calories                                    |
| cm                          | Centimeters                                 |
| COD                         | 1,5-Cyclooctadiene                          |
| COSY                        | Correlation Spectroscopy                    |
| Cp                          | Cyclopentadiene                             |
| Cy                          | Cyclohexane                                 |
| DCM                         | Dichloromethane                             |
| DFT                         | Density Functional Theory                   |
| DME                         | Dimethoxyethane                             |
| DOSY                        | Diffusion Ordered Spectroscopy              |
| Dppf                        | 1,1-Bis(Diphenylphosphino)ferrocene         |
| Dppm                        | 1,1-Bis(Diphenylphosphino)methane           |
| eq / equiv                  | Equivalents                                 |
| Et <sub>2</sub> O           | Diethyl ether                               |
| FID                         | Flame Ionization Detection                  |
| FTIR                        | Fourier-Transformed Infrared Spectroscopy   |
| FWHM                        | Full Width Half Max                         |
| g                           | Grams                                       |
| G                           | Gibbs Free Energy                           |
| GC                          | Gas Chromatography                          |
| glyme                       | Dimethoxyethane                             |
| H                           | Enthalpy                                    |
| h                           | Hours                                       |
| HDPE                        | High Density Polyethylene                   |
| HMBC                        | Heteronuclear Multiple-Bond Correlation     |
| HMDS                        | Hexamethyldisilylamide                      |
| HSQC                        | Heteronuclear Single-Quantum Correlation    |
| Hz                          | Hertz                                       |
| <sup>i</sup> Pr             | Isopropyl                                   |
| IR                          | Infrared                                    |
| K                           | Kelvin                                      |
| L                           | Ligand                                      |
| LDPE                        | Low Density Polyethylene                    |
| LOBA                        | Localized Orbital Bonding Analysis          |
| MALDI                       | Matrix Assisted Laser Desorption Ionization |
| Me                          | Methyl                                      |
| MeCN                        | Acetonitrile                                |

|                    |  |
|--------------------|--|
| mg                 | Milligrams   |
| MHz                | Megahertz  |
| mL                 | Milliliter   |
| mol                | Moles  |
| MS                 | Mass Spectroscopy  |
| MW                 | Molecular Weight   |
| NBO                | Natural Bond Order   |
| <sup>n</sup> Dec   | n-Decyl  |
| <sup>n</sup> Hex   | n-Hexyl  |
| nm                 | Nanometer  |
| NMR                | Nuclear Magnetic Resonance   |
| <i>o</i>           | Ortho  |
| OAc                | Acetate  |
| P <sup>^</sup> AzA | Phosphine 1-Azaallyl   |
| P <sup>^</sup> I   | Phosphine Imine  |
| PE                 | Polyethylene   |
| PEPPSI             | Pyridine-Enhanced Precatalyst Preparation Stabilization and Initiation |
| Ph                 | Phenyl   |
| PhCN               | Benzonitrile   |
| ppm                | Parts Per Million  |
| prod               | Product  |
| py                 | Pyridine   |
| rds                | Rate Determining Step  |
| S                  | Entropy  |
| s                  | Seconds  |
| SRL                | Structurally Responsive Ligand   |
| sub                | Substrate  |
| <sup>t</sup> Bu    | Tert-butyl   |
| <sup>t</sup> BuO   | Tert butoxide  |
| TEMPO              | (2,2,6,6-Tetramethylpiperidin-1-yl)oxidanyl                            |
| THF                | Tetrahydrofuran  |
| T <sub>m</sub>     | Melting Temperature  |
| TOF                | Time of Flight   |
| TON                | Turnover Number  |
| UATR               | Universal Attenuated Total Reflection                                  |
| VTNA               | Variable Time Normalization Analysis                                   |
| τ                  | Geometry Index   |
| ‡                  | Transition State   |
| °                  | Degrees  |

## List of Complexes

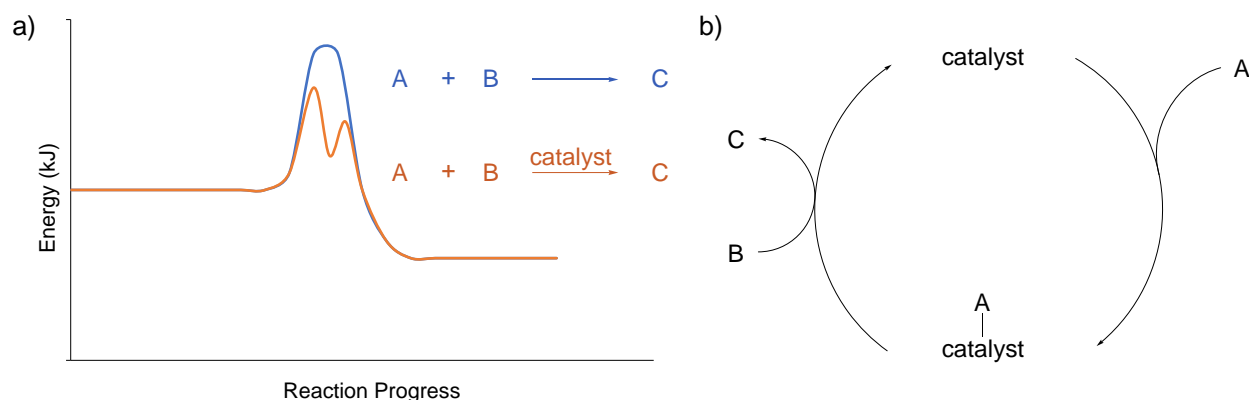


## 1.0 Introduction

### 1.1 Catalysis, and its Impact on Society

Catalysis is arguably the most important process in the world; enzymes perform catalytic reactions that sustain life, and it is estimated that 90% of all commercial products utilize a catalyst at some point in the production chain.<sup>1,2</sup> Since catalysts do not alter reaction equilibria the advantage of catalysis is primarily kinetic,<sup>3</sup> the phenomenon operates by lowering activation barriers and accelerating reaction times (Figure 1.1a).<sup>4</sup> Catalytic reactions can be defined as either homogeneous or heterogeneous. In a homogeneous reaction, the substrate and catalyst are in the same phase (e.g., dissolved in a liquid) while in a heterogeneous reaction the two species are in different phases (e.g., solid and gas).<sup>1, 5</sup> While heterogeneous catalysis is predominantly used industrially, the distinct advantage of homogeneous catalysis lies in its generally well defined mechanisms, allowing for easy catalyst modification and thus extraordinary selectivity for specific products.<sup>6</sup> In a general cycle (Figure 1.1b), a substrate (A) will interact with the catalyst, the catalyst then facilitates either an intramolecular reaction within A, or an intermolecular reaction with another substrate (B), and the product (C) is released. Upon product release the original catalyst structure is regenerated. While the structure of the catalyst will often change to promote steps throughout the catalytic cycle, one of the key concepts of catalysis is that the structure of the catalyst returns to its original form upon product release.<sup>1, 4, 5</sup> In an ideal scenario, a catalyst can therefore permit a reaction an infinite number of times, being regenerated after each individual turnover.<sup>5</sup> Although, this is not the case in reality, since side reactions often lead to irreversible changes in the chemical structure that do not allow the catalyst to re-enter the cycle, resulting in catalyst deactivation. The term turnover number (TON) can therefore be used as an indication of the lifetime of the catalyst.<sup>7</sup> The TON is the number of times a catalyst can operate in a catalytic cycle before it becomes deactivated. A large TON indicates a stable and robust catalyst, and as such high TONs are desirable.

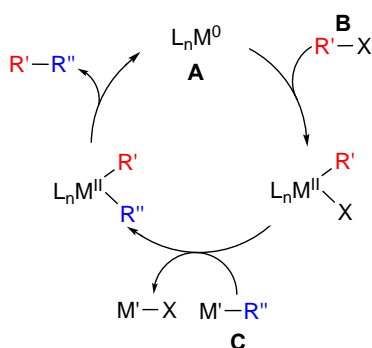




**Figure 1.1.** a) Energy profile for a hypothetical reaction with (orange line) and without (blue line) a catalyst. b) A generic catalytic cycle for the hypothetical reaction in a).

## 1.2 Transition Metal Catalyzed Cross Coupling Reactions

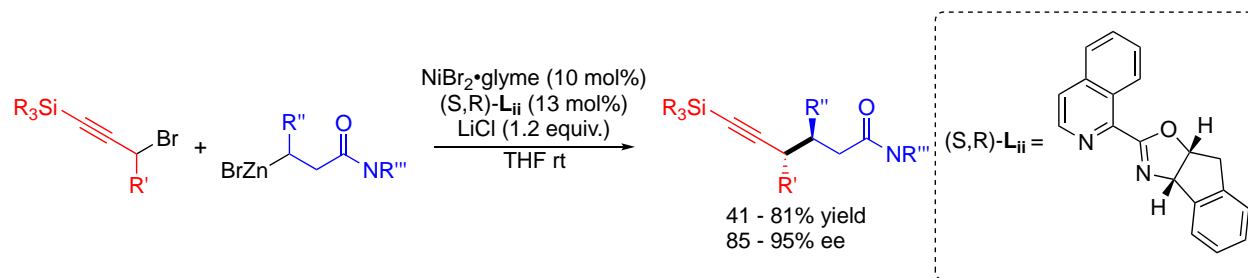
A cross-coupling reaction is a process in which two organic fragments are brought together to form a new bond through the aid of a catalyst (Scheme 1.1).<sup>8-10</sup>. Compared to other synthetic methods, cross-coupling reactions are highly reliable and reproducible, which is a major factor in the widespread use of these methods for the formation of new molecules.<sup>11</sup> A cross-coupling reaction generally requires three components.<sup>7</sup> The first component is a metal catalyst to facilitate the reaction (**A**).<sup>12</sup> Second, an electrophilic organic species (**B**) is required, this is most often an organohalide,<sup>12, 13</sup> however thioesters,<sup>14</sup> thioethers,<sup>15, 16</sup> mesylates,<sup>17</sup> and triflates<sup>18, 19</sup> have also been successfully used. And finally, a stoichiometric organometallic coupling partner is required (**C**), several different metals can fill this role including magnesium,<sup>20</sup> tin,<sup>21, 22</sup> lithium,<sup>20, 23, 24</sup> zinc,<sup>20, 25, 26</sup> and boron.<sup>12, 27-29</sup>



**Scheme 1.1.** The proposed catalytic cycle for a typical cross coupling reaction involving a  $M^{0/II}$  catalytic cycle.  $R^{''}$  = alkyl or aryl.

The first examples of cross coupling reactions were mediated by the metals sodium, lithium, and magnesium.<sup>7, 30</sup> However, in the early 20<sup>th</sup> century it was discovered that transition metals, specifically copper, were exceptional at facilitating many of these transformations.<sup>30</sup> Transition metals possess several characteristics that make them desirable as catalysts, including readily accessible and unfilled d orbitals, as well as low transition state barriers between a wide range of oxidation states. As a consequence, these atoms can operate in reduction/oxidation (redox) cycles,<sup>5</sup> which is key to facilitating fundamental organometallic reaction steps such as oxidative addition and reductive elimination.<sup>12, 31</sup>

Today, several different transition metals are used for cross-coupling.<sup>9, 32</sup> One popular choice is nickel, a first row group 10 transition metal.<sup>9, 33</sup> The toxicity of nickel is lower than other transition metals,<sup>34</sup> and compared to other group 10 metals such as palladium, nickel has a slower rate of undesirable  $\beta$ -hydride elimination of alkyl-[Ni] intermediates.<sup>33, 35</sup> Nickel has also been shown to facilitate rapid oxidative addition, especially with challenging substrates such as  $Csp^3$  electrophiles. Fu reported the significantly challenging double enantioconvergent  $Csp^3$ - $Csp^3$  coupling of racemic partners while controlling the stereochemistry at vicinal stereocenters (Scheme 1.2).<sup>36</sup> Their catalyst was generated *in-situ* by using an inexpensive<sup>37</sup>  $NiBr_2 \cdot glyme$  precatalyst with a chiral pyridine-oxazoline ligand (S,R)- $L_{ii}$ . Fu controlled the stereochemistry at both carbon atoms with good yields and excellent enantiomeric excess. The reaction was also tolerant of ethers, esters, acetals, and silicon functional groups. Unfortunately, the reaction mechanism was not reported, but it was postulated that the reaction proceeds through radicals generated by both coupling partners.



**Scheme 1.2.** Ni catalyzed doubly enantioconvergent cross-coupling by Fu, resulting in excellent stereo-control over vicinal coupling partners.<sup>36</sup>

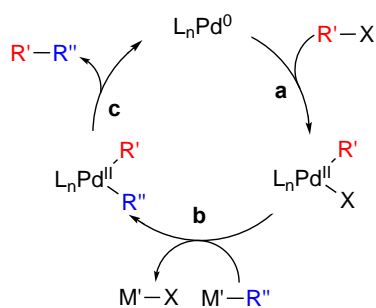
## 1.3 Catalysis using Palladium

Palladium is one of the premier transition metals for catalysis, and it has found applications in a myriad of industrial and research processes.<sup>38</sup> Palladium is a second row  $d^{10}$ -electron metal, and five different oxidation states of Pd are known (0, +1, +2, +3, +4).<sup>39, 40</sup> The oxidation states most commonly encountered for palladium are the 0, +2, and +4 oxidation states,<sup>41, 42</sup> and as such many catalytic cycles with palladium involve two electron reductions and oxidations with palladium operating in a Pd<sup>0</sup>/Pd<sup>II</sup>, or less commonly a Pd<sup>II/IV</sup> cycle.<sup>10</sup> Palladium catalyzed reactions are prevalent in the industrial synthesis of pharmaceuticals,<sup>9</sup> agrochemicals,<sup>43</sup> and fine chemicals.<sup>44</sup> Palladium has found wide spread applications in hydrogenation,<sup>5</sup> olefin polymerization,<sup>45-47</sup> and is undeniably the most important metal with respect to cross-coupling catalysis.<sup>43</sup> Despite its high cost, palladium has several advantages over other nonprecious metals that has led to its prevalence in catalysis. Palladium can promote coupling of low reactivity substrates, it permits reactions at low temperatures, and the high TONs associated with Pd systems often helps balance out the cost in large-scale applications.<sup>43, 48</sup>

### 1.3.1 Palladium Catalyzed Cross-Coupling

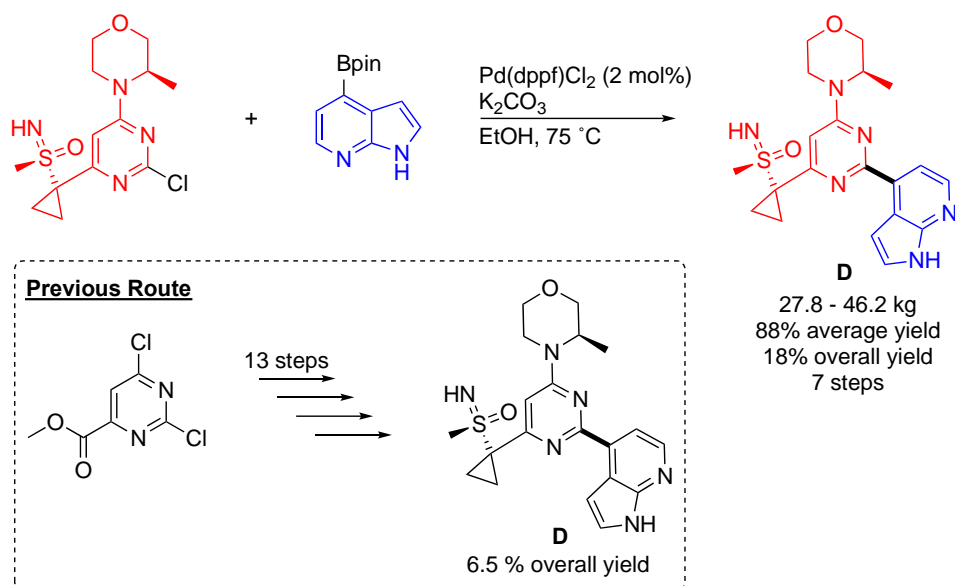
Palladium has had the largest impact on the field of cross-coupling catalysis.<sup>43, 49</sup> In 2010 the Nobel Prize in Chemistry was awarded to Negishi, Suzuki, and Heck for “Palladium-Catalyzed Cross Couplings in Organic Synthesis”.<sup>50</sup> Furthermore, a SciFinder search reveals that nearly 11,000 publications and patents have been released since 2010 regarding advances in palladium catalyzed cross-coupling. Palladium has been essential to the development of processes for the formation of new C–C and C–E (E = O, S, N) bonds, and is the main catalyst used in Heck,<sup>51, 52</sup> Suzuki,<sup>53, 54</sup> Sonogashira,<sup>55, 56</sup> Negishi,<sup>57</sup> Stille,<sup>21, 22</sup> and Kumada<sup>58</sup> couplings, as well as Buchwald-Hartwig amination (Scheme 1.3).<sup>59, 60</sup> The mechanism for cross-coupling with palladium is very similar to the representative scheme discussed in Section 1.2. The first step involves oxidative addition of the electrophile to a Pd<sup>0</sup> catalyst to afford an organometallic Pd<sup>II</sup> complex (Scheme 1.3 **a**). Next, transmetalation with an organometallic reagent occurs, exchanging an organic group for the X-type ligand from the electrophile (**b**). Finally, the catalyst facilitates the reductive elimination of the two organic fragments, and releases the newly formed product to regenerate the

$\text{Pd}^0$  catalyst (c).<sup>10</sup> Although the advent of Pd catalyzed cross coupling occurred almost 50 years ago, new and elegant examples of cross coupling with palladium are still frequently being published.<sup>9, 12, 13</sup> For example, C–C coupling pathways proceeding directly through C–H activation, instead of C–X or C–Y (Y =  $\text{BR}_2$ , SR etc.) activation, have now been established.<sup>61-63</sup> However, these pathways are often complicated by the inert nature of the C–H bond.<sup>62</sup> As a consequence,  $\text{Pd}^{\text{II}}$  catalysts instead often react preferentially with the organometallic reagents resulting in precipitation of  $\text{Pd}^0$ .<sup>62</sup>



**Scheme 1.3.** The proposed catalytic cycle for a) a typical cross coupling reaction involving a  $\text{Pd}^{0/\text{II}}$  catalytic cycle.  $\text{R}'/\text{R}''$  = alkyl or aryl.

C–C bonds make up the backbone of organic molecules, therefore, industries heavily relying on organic molecules, such as the pharmaceutical and fine-chemical industries, have benefited immensely from advancements in C–C coupling reactions. Yang reported a Suzuki coupling as a key step in their plant-scale synthesis of the ATR inhibitor Ceralasterib (**D**) (Scheme 1.4). Ceralasterib is a compound that entered clinical trials in 2019 to study the treatment of a diverse range of tumors.<sup>64, 65</sup> Previously, chemists struggled to sufficiently scale up the reaction from the gram scale to multi kilogram scale,<sup>66</sup> and the overall yield of **D** from the previously reported route was just 6.5% over 13 steps. However, by changing the synthetic approach and utilizing a Suzuki Coupling reaction as the final step, the overall yield was improved to 18% over 7 steps. Additionally, an 88% average yield for the cross coupling step was achieved.

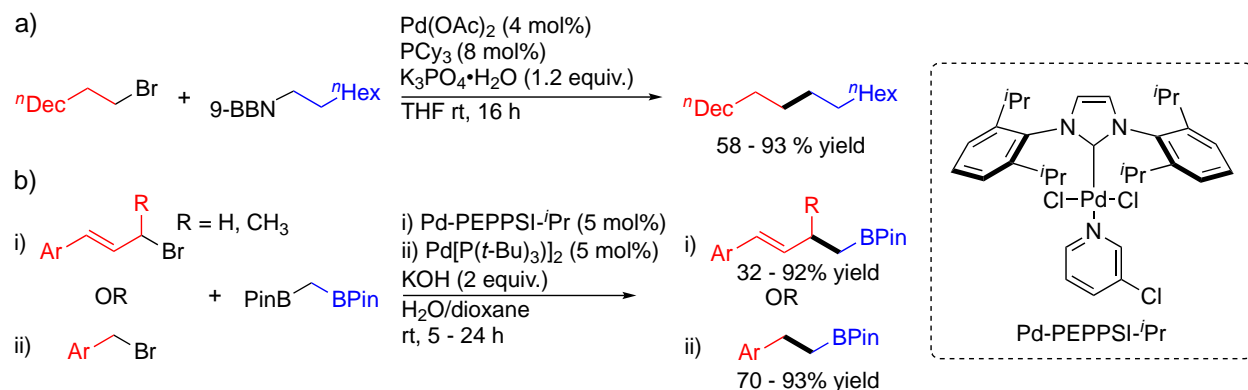


**Scheme 1.4.** The previous route for the synthesis of Ceralasterib **D**, and the recently developed plant-scale synthesis of **D** utilizing a Suzuki-Miyaura coupling with a Pd(dppf)Cl<sub>2</sub> catalyst.<sup>66</sup>

Most cross coupling reactions involve the coupling of  $Csp^2-Csp^{1/2/3}$  hybridized carbons.<sup>67</sup> While  $Csp^2-Csp^{1/2/3}$  bonds are indeed prevalent throughout organic chemistry,  $Csp^3-Csp^3$  bonds are equally as ubiquitous. Thus, there is great value in methods that can controllably make new alkyl-alkyl bonds.<sup>68,69</sup> However, coupling of  $sp^3$  hybridized orbitals is particularly challenging due to the tendency of these species to undergo  $\beta$ -hydride elimination prior to reductive elimination, as well as the decreased rate of oxidative addition of  $sp^3$  hybridized electrophiles.<sup>33</sup> A foundational report from Fu in 2001 realized the Pd catalyzed alkyl-alkyl Suzuki-Miyaura cross-coupling of unactivated alkyl bromides at room temperature by using Pd(OAc)<sub>2</sub> and bulky trialkyl phosphines, such as PCy<sub>3</sub> (Scheme 1.5a).<sup>70</sup> This reaction was compatible with substrates that were susceptible to  $\beta$ -hydride elimination, and could be performed with organoboranes instead of harsher nucleophiles such as Grignard reagents. However, the reaction was limited to primary alkyl bromides. It was proposed that electron donation from the phosphine facilitated oxidative addition, while the bulky alkyl groups prevented  $\beta$ -hydride elimination.<sup>71</sup>

Shibata built on this work a decade later, using Pd(PEPSSI-*i*Pr) and Pd[P(*t*Bu)<sub>3</sub>]<sub>2</sub> catalysts (Scheme 1.5b).<sup>72</sup> A variety of electrophilic benzyl and allylic bromides were successfully cross-coupled with diborylmethane in a water/dioxane mixture at room temperature with good functional group tolerance. Notably, the process was not limited to primary alkyl bromides, as the cross-coupling of secondary  $sp^3$  allyl bromides was also carried out with yields ranging from 32 – 92%.

It was suggested that strong electron donation from the NHC ligand in Pd(PEPPSI-*i*Pr) gave a  $\pi$ -allylpalladium intermediate with the electrophile. This intermediate is more stable than the  $\sigma$ -bound intermediate when other chelating ligands are used, thus improving the rate of reaction. Finally, steric bulk from the NHC ligands was proposed to promote reductive elimination of the cross-coupled product.

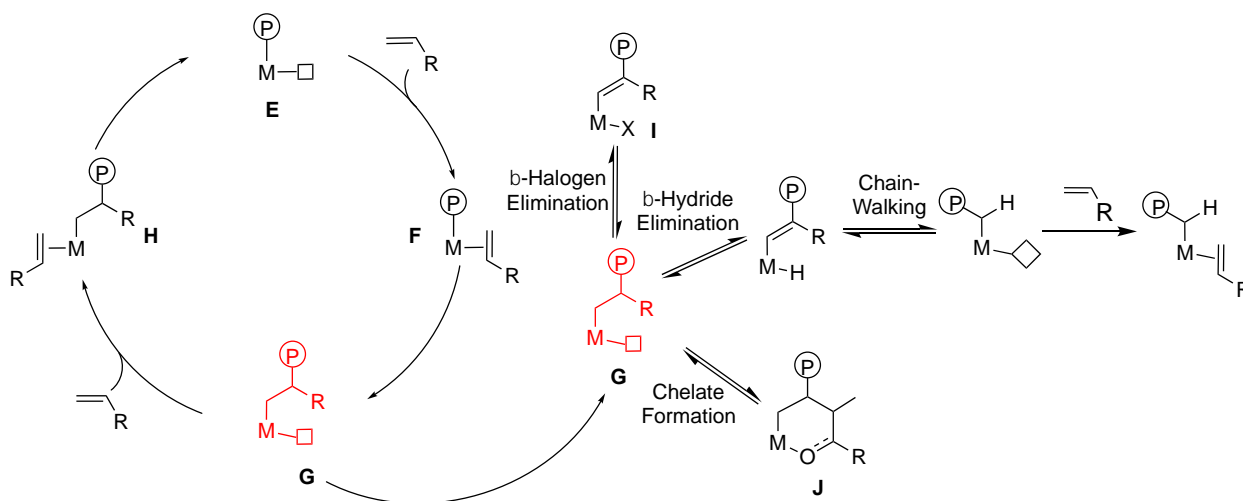


**Scheme 1.5.** a) First example of palladium catalyzed  $Csp^3-Csp^3$  cross-coupling using bulky trialkyl phosphines as ligands reported by Fu.<sup>70</sup> b)  $Csp^3-Csp^3$  cross-coupling of i) allylic and ii) benzyl bromides with diborylmethane using different Pd catalysts.<sup>70, 72</sup>

### 1.3.2 Palladium Catalyzed Polymerization

Polymers have applications in every facet of life,<sup>73</sup> including electronics, packaging, transportation, and textiles.<sup>74</sup> Each year over 400 million tonnes of plastic are produced worldwide, and it is estimated that by 2050 annual plastic production will reach 1.1 billion tonnes.<sup>75</sup> Polyethylene (PE) accounts for over 30% of plastics produced, with over 100 million tonnes being synthesized each year.<sup>75,76</sup> PE is the simplest hydrocarbon polymer consisting of repeating units of ethylene. There are many different types of PE, but the two most common types are low density polyethylene (LDPE) and high density polyethylene (HDPE).<sup>76</sup> Industrially, LDPE is generally produced using free radical polymerization,<sup>77, 78</sup> which is a poorly controlled method of polymerization.<sup>79,80</sup> Alternatively, the key to producing HDPE is to ensure that the amount of branching in the polymer chain is minimal, and this is most often achieved using a transition metal catalyst.<sup>81</sup> Industrially, HDPE is typically formed through a migratory insertion mechanism (Scheme 1.6) mediated by a group four Ziegler-Natta or Kaminsky metallocene catalyst such as  $\text{TiCl}_4$  or  $[\text{Zr}(\text{Cl}_2)(\text{Cp}_2)]$  respectively.<sup>81-83</sup>

The first step in this mechanism is initiation by a cocatalyst, such as methylaluminoxane. The initiator abstracts two halogens and installs an alkyl group on the catalyst. This generates a spot for the polymer chain to grow (Scheme 1.6, **E**,  $\text{\textcircled{P}}$ ), as well as an open coordination site for a monomer to bind to the catalyst center (**E**,  $\square$ ). Monomer coordination then occurs through the olefin's  $\pi$ -system (**F**).  $\pi$ -Coordination is favourable due to electron donation from the olefin's  $\pi$ -bonding orbital into an empty orbital on the metal, which strengthens the olefin-metal bond and weakens the C=C bond. Additionally, the metal donates electron density back into the olefin's  $\pi^*$ -antibonding orbital which also weakens the C=C bond and helps to improve the rate of the subsequent step, monomer insertion. Upon insertion an unstable three coordinate intermediate is formed (**G**). Ideally, another monomer coordinates to the metal centre (**H**) and the catalyst cycle continues. However, due to the reactive nature of **G** undesirable side reactions are common, resulting in low MW and disperse branching densities. One of these pathways is  $\beta$ -hydride elimination, which creates highly branched polymers through a process known as chain-walking. Chain-transfer can also occur following  $\beta$ -hydride elimination, which leads to low MW polymers. Additional deactivation pathways include  $\beta$ -halogen elimination with halogenated monomers (**I**) and chelate formation with polar monomers (**J**). Both pathways can lead to catalyst deactivation and termination of the growing polymer chain.



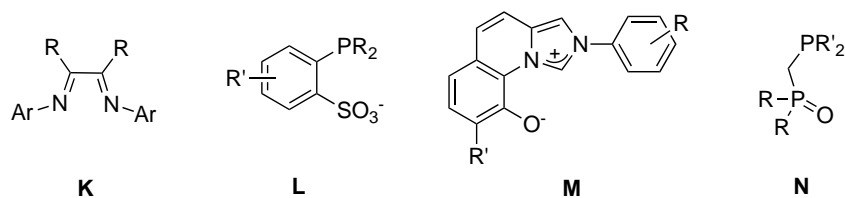
**Scheme 1.6.** The migratory-insertion mechanism for olefin polymerization including typical decomposition routes  $\beta$ -hydride elimination, chain walking,  $\beta$ -halogen elimination, and chelate formation.  $\text{\textcircled{P}}$  = polymer chain, R = H or a functional group, X = halogen.

Copolymerization is the polymerization of two or more distinct monomers, and for copolymerization with ethylene typically one of the monomers is polar.<sup>84</sup> Tuning the monomers,

varying the functional groups, and altering the amount of polar comonomer present leads to a variety of different polymeric structures with distinct functional properties such as adhesion, chemical stability, and dyeability.<sup>84</sup> For example, the copolymer of ethylene and vinyl acetate, poly(ethylene vinyl-acetate),<sup>85</sup> is used to make hot melt adhesives or protective foams in sporting equipment.<sup>86</sup> Comonomer incorporations are highly substrate dependent, but can range anywhere from 0 – 50%. However, the vast majority of transition metal catalyzed routes typically have below 10% comonomer incorporation, and comonomer incorporations labeled as ‘high’ are typically greater than 10%.<sup>87-89</sup> Although, due to the high oxophilicity of early transition metals, the Ziegler-Natta and Kaminsky catalysts used to generate homopolymers of ethylene tend to become poisoned by the heteroatoms in polar co-monomers, limiting their applications in copolymerization.<sup>45</sup> Therefore, functional polymers are mainly produced industrially through free-radical polymerization, leading to substantial branching and dispersed MWs.<sup>90</sup> This is amplified by the high pressures and temperatures required, which also inflates costs. Another popular method of installing polar functionalities to polymer backbones is through post polymerization modifications.<sup>91</sup> However, the upgrading of alkanes is a difficult process due to the inert nature of the C–H bond.<sup>92</sup>

For some time, late transition metals were not significantly applied to polymerization as they were generally considered inferior to early-transition metal catalysts due to their facile ability to undergo  $\beta$ -H elimination.<sup>93</sup> It was widely believed that this tendency would result in chain transfer and thus low MW polymers. Although, late transition metals have significantly reduced oxophilicity and increased functional group tolerance compared to early transition metals, making them attractive as candidates for copolymerization with polar monomers.<sup>94</sup> The late transition metals are also good at back donation into the  $\pi^*$  orbitals of the bonded olefin, which weakens the olefin’s  $\pi$  bond and activates the olefin. Several ligands including  $\alpha$ -diimine (Figure 1.2 **K**), phosphine sulfonate (**L**), imidazoquinolate (**M**), and bisphosphine ligands (**N**) have been coordinated to Pd and the complexes have successfully copolymerized ethylene with polar monomers



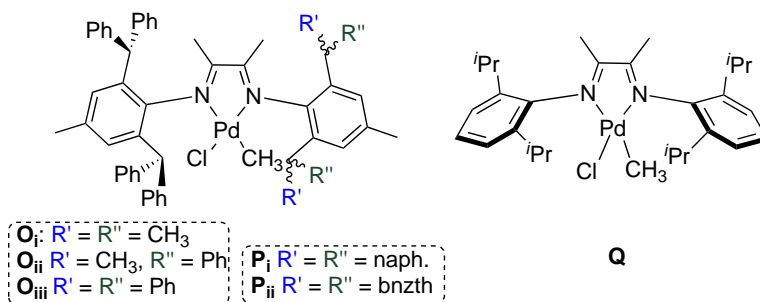


**Figure 1.2.** A series of ligands coordinated to Pd<sup>II</sup> that have successfully been employed for the copolymerization of ethylene with polar comonomers.<sup>46, 95, 96</sup>

Considerable work from Brookhart has shown that cationic group 10 transition metals coordinated by  $\alpha$ -diimine ligands (Figure 1.2 **K**) are highly active catalysts for polymerization. These catalysts are also electrophilic, which allows for a higher rate of olefin insertion.<sup>97</sup> Furthermore, by employing bulky  $\alpha$ -diimine ligands the axial positions on the metal centre are blocked. In these complexes the aryl groups lie roughly perpendicular to the metal-diimine plane, therefore the *ortho*- substituents considerably crowd the axial site. This protection helps to significantly reduce chain transfer,<sup>93</sup> and high MW polymers can be obtained. Mechanistic and computational work from Brookhart have revealed that in the 16 e<sup>-</sup> catalyst resting state the monomer and growing polymer chain occupy *cis*- equatorial sites on the metal centre.<sup>98</sup> Upon migratory insertion, the resulting low-coordinate complex (ie. **G**) is susceptible to chain transfer through exchange with an incoming monomer from the axial position. Through Brookhart's ligand design this process is prevented, negating chain transfer and allowing the formation of high MW polymers.

Highly branched PE is often obtained with these complexes (80 per 1000 carbons); chain-walking is a characteristic feature of these species due to the high rates of  $\beta$ -H elimination and hydride-reinsertion.<sup>46, 89, 99</sup> However, chain-walking can be controlled by modulating ethylene pressure, reaction temperature, and catalyst structure.<sup>100</sup> For example, the Chen group recently reported two examples where increased steric bulk greatly reduced polymer branching densities.<sup>101,102</sup> A series of  $\alpha$ -diimine ligands were synthesized in which the steric bulk at both *ortho* positions of one N-aryl substituent was systematically increased in size and the ligands were coordinated to Pd<sup>II</sup> (Figure 1.3 **O/P**). The complex with the least sterically bulky R groups **O<sub>i</sub>** generated PE with branching densities as high as 117 branches per 1000.<sup>101</sup> Alternatively, complex **P<sub>ii</sub>** generated polymers with branching densities as low as 13 branches per 1000 carbons.<sup>102</sup> It was proposed that the bulky substituents facilitate ethylene coordination, and prevented chain walking. Complexes **P<sub>i</sub>** and **P<sub>ii</sub>** were also used for the copolymerization of ethylene with a series of polar

monomers. These complexes were highly active for the copolymerization of ethylene with carboxylic acids, esters, and alcohols, and generated polymers with high MW, reduced branching (10 – 38 branches per 1000), and comonomer incorporation ranging from 0.06 to 6.67%. Comparatively, a benchmark  $\alpha$ -diimine Pd<sup>II</sup> complex **Q** was deactivated when copolymerization was attempted with the same polar monomers.<sup>102</sup>

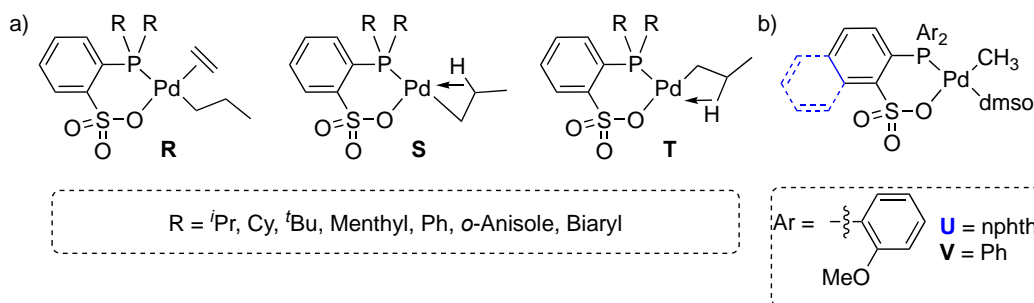


**Figure 1.3.**  $\alpha$ -diimine complexes used to investigate steric (**O/P**)<sup>101, 102</sup> effects on chain-walking and copolymerization activity, and a benchmark  $\alpha$ -diimine complex (**Q**).<sup>102</sup>

The Drent-type phosphine-sulfonate ligands are one of the most successful ligand families for copolymerization of ethylene and polar monomers (Figure 1.2 L).<sup>46, 89</sup> The phosphine-sulfonate catalysts are noted for their highly linear PE, and offer two distinct advantages.<sup>89</sup> First, the Pd<sup>II</sup> complex is neutral and electron rich, which allows for good functional group tolerance.<sup>103</sup> This is especially true compared to the Brookhart-type ligands, where the active catalysts are charged and electrophilic.<sup>93</sup> Second, computational investigations on this ligand family suggest that the lone pair on the ligated oxygen of the  $-SO_3^-$  moiety prevents olefin to metal  $\pi$ -donation, and promotes metal to olefin  $\pi$ -backdonation, activating the monomer for polymerization.<sup>104</sup>

Recently, Nozaki investigated the mechanism by which the phosphine-sulfonate complexes generate linear polyethylene.<sup>105</sup> Specifically, they investigated the effect of sterics and electronics from the phosphine on polymer linearity (Figure 1.4). They found that complex **R** is the key intermediate for both  $\beta$ -H elimination and linear chain growth. Insertion of the monomer into the growing polymer chain occurs from **R**, which results in the three-coordinate complex **S**.  $\beta$ -H elimination occurs from **S**, as there is a vacant site *cis* to the polymer chain where the  $\beta$ -H can coordinate. When significantly bulky phosphine substituents were used ( $R = ^iPr, Ph, Menthyl$ )  $\beta$ -H elimination was prevented, and linear polyethylene was afforded. Additionally, complex **R** can undergo a *cis/trans* isomerization to afford **T**. In complex **T** there is once again a vacant site *cis* to the growing polymer chain. Thus,  $\beta$ -H elimination can again occur from **T**. However, steric and electronic inhibition both play a key role in preventing the formation of **T**. The trans-effect has

been noted as a key factor in these complexes by Frenking;<sup>106</sup> indeed, when a strong and sterically bulky substituent was used the formation of the *trans*-P-Pd-H (i.e. **T**) complex was significantly reduced, as well as the *cis*-P-Pd-H complex (i.e. **S**).



**Figure 1.4.** a) Phosphine-sulfonate Pd<sup>II</sup> complexes (**R**, **S**, **T**) used to investigate how linear polyethylene is formed with the phosphine-sulfonate complexes.<sup>105</sup> b) complexes used to investigate the impact of changing the backbone (**U**, **V**) on the copolymerization of ethylene with polar co monomers.<sup>107</sup>

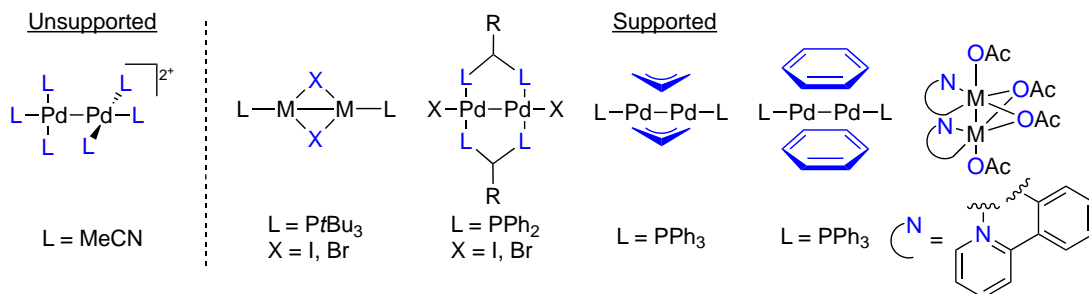
Chen has investigated the impact of backbone alteration on phosphine-sulfonate systems.<sup>107</sup> They synthesized a phosphine-sulfonate ligand with the  $-\text{PR}_2$  and  $-\text{SO}_3$  moieties at the 1,2 positions on a naphthalene backbone (Figure 1.4 **U**), and compared its performance to the phenyl linked analogue (Figure 1.4 **V**) toward the generation of PE, and the copolymerization of ethylene with polar monomers. For the homopolymerization of ethylene, complex **U** is an order of magnitude more active in comparison to **V**. Furthermore, complex **U** produced very high MW polymers (17300 g/mol) with low MW distributions. For the copolymerization of ethylene and methyl acrylate, comonomer incorporation of 40% was obtained with **U**, which is among the highest reported in the literature. Furthermore, **U** generated the highest MW copolymers of all the complexes reported in this study (6900 g/mol). Unfortunately, the authors did not provide rationale for the improved reactivity of **U** compared to **V**.

Unfortunately, the  $\alpha$ -diimine and phosphine-sulfonate ligands have not gained much attention industrially. One large drawback particularly for the  $\alpha$ -diimine systems is an inverse relationship between catalyst activity and temperature. At higher temperatures the catalysts tend to become far less active, which limits their scope industrially.<sup>100</sup>

## 1.4 Dinuclear Group 10 Complexes

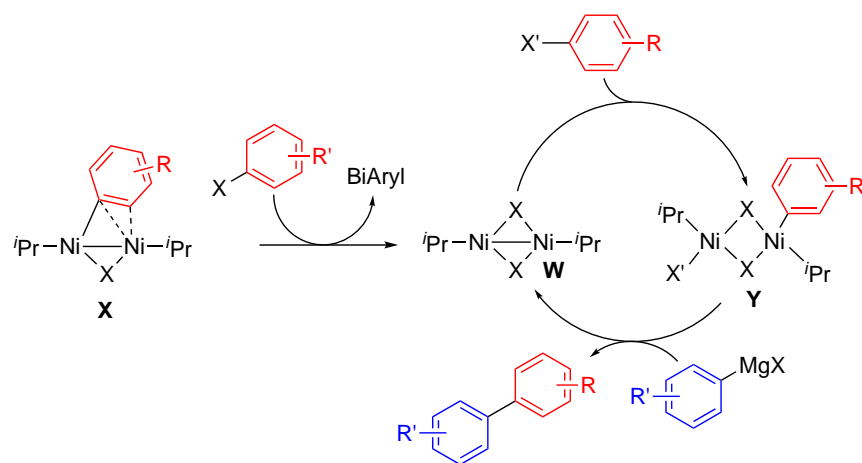
The vast majority of reported catalysts are monometallic species, and this is mostly due to their simple design, and ease of synthesis.<sup>108</sup> Dinuclear complexes require special ligand design,

requiring multiple binding motifs, or bridging anionic ligands, and their syntheses are often complicated, leading to low product yields.<sup>108</sup> However, catalysis using homo- and heterobimetallic complexes has gained considerable attention recently, as metal-metal cooperativity has been shown to promote unique reaction pathways, and in some cases allows for improved reactivity compared to monometallic catalysts.<sup>109-112</sup> Dinuclear complexes have been reported as precatalysts, active catalysts, as well as on-cycle intermediates in catalytic cycles.<sup>113-115</sup> There are several examples of dinuclear complexes containing nickel and palladium (Figure 1.5), as well as reports on their reactivity. Most commonly, dinuclear complexes are supported through bridging supporting ligands such as bisphosphines, allyls, and even halides. Though there are also rare examples of dinuclear Pd complexes in which the ligands are simple monodentate species (i.e. acetonitrile).



**Figure 1.5.** A selection of isolated dinuclear Pd and Ni complexes. M = Pd/Ni.<sup>116, 117</sup>

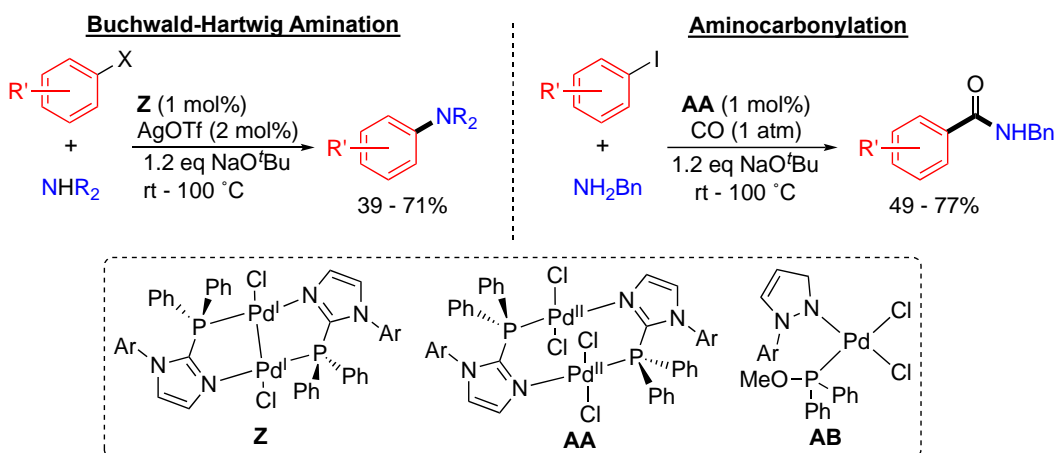
Matsubara proposed a  $[\text{Ni}^{\text{I}}(\mu\text{-X})(\text{IPr})_2]$  (**W**) dimer (IPr = 1,3-bis(2,6-diisopropylphenyl)imidazol-2-ylidene, X = F, Cl, Br) as the catalytically active species in the Kumada cross coupling of PhMgBr and aryl halides at room temperature (Scheme 1.7).<sup>118</sup> The precatalyst **X** is a Ni<sup>I</sup> dimer bridged through a chloride and tolyl group, coordinated  $\mu\text{-Cl}$  and  $\mu\text{-}\eta^2\text{-C}_6\text{H}_4(\text{CH}_3)$ , respectively. DFT calculations, and stoichiometric and kinetic experiments imply that the dimeric Ni framework remains intact throughout the catalytic process, and that the reaction proceeds in a Ni<sup>I/III</sup> cycle. The process is initiated by oxidative addition of one equivalent of aryl halide to the precatalyst **X**, reductively eliminating a homocoupled organic product and forming the proposed active catalyst **W**. Oxidative addition of the aryl halide occurs at one Ni centre, and the halide from the electrophile bridges the two metal centres giving **Y**. Transmetalation with PhMgBr then occurs followed by reductive elimination of biaryl, reforming **W**.



**Scheme 1.7.** Proposed mechanism for Kumada coupling using  $[\text{Ni}^{\text{I}}]_2$  dimer **X** as the precatalyst.

Recently, Michaelis reported the synthesis and reactivity of bimetallic  $\text{Pd}^{\text{I}}$  and  $\text{Pd}^{\text{II}}$  complexes coordinated by 2-phosphinoimidazole ligands (Scheme 1.8, **Z**, **AA**, respectively).<sup>116</sup> By altering the number of chloro- ligands coordinated to the Pd centre, they could change the oxidation state on Pd from +1 in **Z**, to +2 in **AA**. They found both complexes were active catalysts for an  $\alpha$ -arylation reaction, affording complete conversion to the desired naphthalene product in 1 h by GC-FID. Under the same conditions a similar monometallic  $\text{Pd}^{\text{II}}$  complex **AB** was inactive. Mechanistic and DFT studies suggested that the bimetallic motif was maintained throughout the reaction. Additionally, Michaelis compared reactivity between **Z** and **AA** in different C–N cross coupling reactions.<sup>119</sup> **Z** was more active for Buchwald-Hartwig amination, reaching complete conversion of the benchmark substrate in 4 h, while **AA** only reached 45% conversion under the same amount of time. This is consistent with previous reports, which have shown that  $\text{Pd}^{\text{I}}$  dimers such as **AC** often outperform  $\text{Pd}^{\text{II}}$  catalysts in some Suzuki couplings and Buchwald-Hartwig aminations.<sup>117</sup> The  $\text{Pd}^{\text{I}}$  dimers often act as a source of the true highly reactive monometallic  $\text{Pd}^{\text{0L}}$  catalysts in these reactions (*vide infra*).<sup>120</sup> NMR studies suggested that the binuclear structure remains largely intact throughout the reaction, which the authors suggest may be important to the high catalyst activity observed. Additionally, the lower oxidation state of **Z** was proposed to accelerate oxidative addition, resulting in higher activity compared to **AA**. Contrarily **AA** is more active than **Z** in aminocarbonylation reactions between aryl iodides and amines in the presence of CO. However, NMR studies for the aminocarbonylation reaction revealed significant amounts of free ligand, suggesting decomposition had occurred to afford  $\text{Pd}^{\text{0}}$  nanoparticles. Indeed, when a

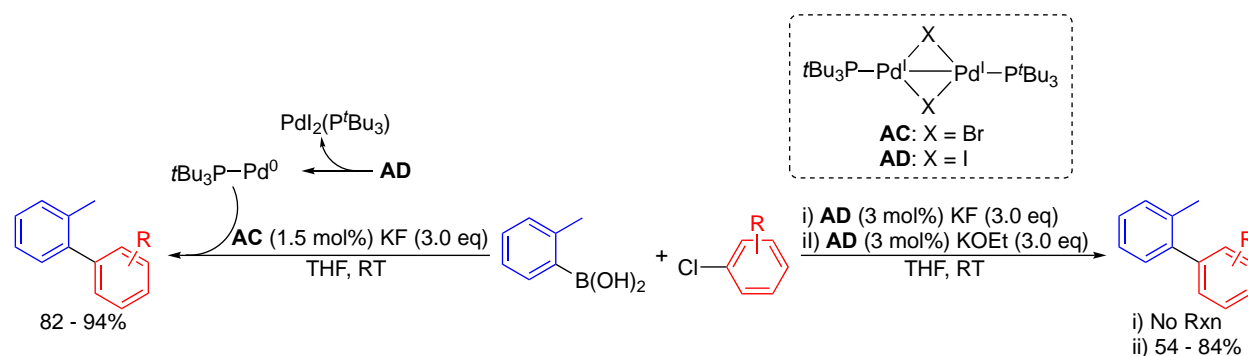
drop of Hg was added to the reaction mixture,<sup>121</sup> conversion was dramatically reduced, and less than 5% conversion was observed in 90 minutes. In this scenario it was therefore proposed the dimers **Z** and **AA** simply serve as precatalysts to Pd<sup>0</sup> nanoparticles. The authors suggest that decomposition of **AA** is more rapid than **Z**, which results in the higher performance observed.



**Scheme 1.8.** Left: Buchwald-Hartwig Amination with Pd<sup>I</sup> dimer **Z** and right: aminocarbonylation with Pd<sup>II</sup> dimer **AA**.

Schoenebeck has made significant contributions to the study of Pd<sup>I</sup> dimers, particularly in terms of elucidating the role of Pd<sup>I</sup> dimers in catalytic cycles. In 2012, they discovered that a *Csp*<sup>2</sup>–*Csp*<sup>2</sup> Suzuki Miyaura reaction proceeded in the presence of 1.5 mol% of Pd<sup>I</sup> dimer **AC**.<sup>122</sup> However, through a combination of experiments and computations it was concluded that **AC** cleaves to form Pd black and mononuclear Pd<sup>0</sup>(P<sup>t</sup>Bu<sub>3</sub>)<sub>2</sub>, the latter of which serves as the true active catalyst (Scheme 1.9, left). With the aid of the Mayr parameter (*N*),<sup>123, 124</sup> they determined that activation of dimers **AC** and **AD** was consistent with nucleophile-induced fragmentation.<sup>120</sup> Thus, catalyst nuclearity could be controlled by tuning the nucleophilicity of the additives. Previously, no reactivity was observed when **AD** had been used for Suzuki-Miyaura cross coupling. However, by changing the base from KF (*N* = 9) to KO<sup>t</sup>Bu (*N* = 16.1) efficient cross-coupling of aryl boronic acids and aryl halides was achieved (Scheme 1.9, right). This reaction was also remarkably air and moisture stable, as no efforts were made for water and oxygen exclusion. Additionally, they considered the direct use of a nucleophilic coupling partner rather than a nucleophilic activating agent. This would result in direct metal-substrate coordination rather than requiring an initial halide removal step. They hypothesized that Grignard reagents would be sufficiently nucleophilic

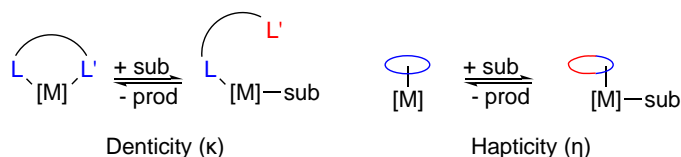
to serve this purpose. Indeed, efficient Kumada Coupling was observed using **AD** between aryl halides and aryl Grignard reagents. Again, no care was taken to ensure water and oxygen were excluded from the reaction. Remarkably the reactions were not impeded, and reached completion in 5 min. Additionally, the reaction was tolerant of electron-rich and poor aryl halides, as well as functionalities typically incompatible with Grignard reagents such as esters.



**Scheme 1.9.** Suzuki Miyaura coupling using halogen bridged  $\text{Pd}^{\text{I}}$  dimers **AC** and **AD** reported by Schoenebeck.

## 1.5 Structurally Responsive Ligands

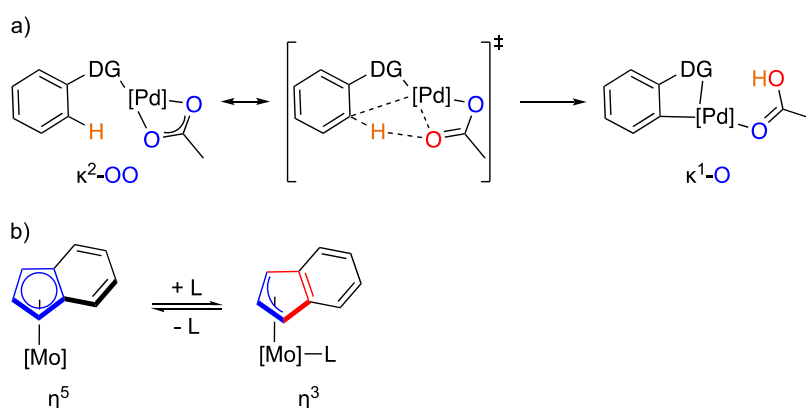
Structurally responsive ligands (SRLs) are ligands that can reversibly change their coordination mode depending on the overall coordination sphere of the metal (Scheme 1.10).<sup>125</sup> SRLs are advantageous in catalysis as they offer a means to stabilize low coordinate species, while still allowing for an open coordination site for substrate binding (Scheme 1.10).<sup>125</sup>



**Scheme 1.10.** General depiction of reversible changes in coordination by SRLs, left = denticity ( $\kappa$ ), right = hapticity ( $\eta$ ).

SRLs operate through one of two main ways, or in some cases through a combination of both. The first type of response is through changes in denticity, which is a change in the number of non-contiguous nuclei that are coordinated between the metal and ligand (denoted by  $\kappa$ ) (Scheme 1.10, left).<sup>125</sup> A classic example of a change in ligand denticity is in the proposed mechanism for concerted metalation deprotonation (CMD), where an acetate ligand changes from  $\kappa^2\text{-OO}$  to  $\kappa^1\text{-}$

O to help facilitate the deprotonation and metalation steps of C-H activation (Scheme 1.11 a).<sup>126</sup> A reversible change in ligand denticity is often referred to as ligand hemilability.<sup>127</sup> The other possible response is through changes in ligand hapticity, which is a change in coordination through a  $\pi$ -system (denoted by  $\eta$ ) (Scheme 1.10, right).<sup>125</sup> For example, the indenyl ligand can undergo an isomerization from  $\eta^5$  to  $\eta^3$  opening a coordination site to bind an exogenous ligand (Scheme 1.11 b).<sup>128</sup> Colloquially known as the indenyl effect, this phenomenon is well established and has been shown in many cases to have a positive influence on catalysis by increasing substitution rates. There are several other examples of ligands that undergo changes in hapticity, including 1,3-butadiene and benzene which isomerize between  $\eta^2$  or  $\eta^4$  and between  $\eta^6$ ,  $\eta^4$ , or  $\eta^2$ , respectively.<sup>129</sup> SRLs have also been shown to promote fundamental catalytic processes such as oxidative addition and reductive elimination.<sup>125</sup> SRLs therefore have the capacity to control selectivity, access new reaction pathways, prevent undesirable processes, and enhance the rate of reactions.

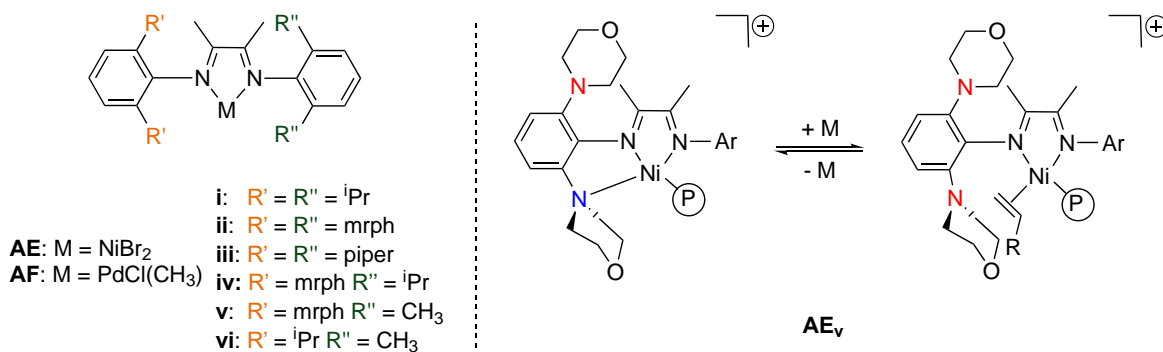


**Scheme 1.11.** a) Changes in coordination mode of an acetate ligand from  $\kappa^2$ -OO to  $\kappa^1$ -OO during deprotonation in the proposed mechanism for CMD.<sup>126</sup> b) Indenyl slippage from  $\eta^5$  to  $\eta^3$  in a generic Mo complex. DG = directing group.<sup>128</sup>

The use of SRLs in polymerization highlight the positive impacts of this class of ligand.<sup>130, 131</sup> In 2017 Chen used a series of group 10  $\alpha$ -diimine catalysts for the copolymerization of ethylene with polar monomers (Figure 1.6).<sup>131</sup> A morpholine (**AE<sub>ii</sub>**) or piperidine (**AE<sub>iii</sub>**) moiety in the second-coordination sphere generated highly linear PE (<1 branch per 1000). This is a drastic improvement from classic Brookhart-type catalysts which often have branching densities greater than 80 branches per 1000 carbons.<sup>99</sup> Comparatively, **AE<sub>i</sub>** with two *i*Pr substituents produced polymers with 63 branches per 1000 carbons. Additionally, [**AF<sub>iv</sub>**]<sup>+</sup> was also efficient at the copolymerization of ethylene with polar monomers, while no copolymers were obtained with structurally static [**AF<sub>i</sub>**]<sup>+</sup>. Complex [**AF<sub>iv</sub>**]<sup>+</sup> also successfully copolymerized allyl chloride and



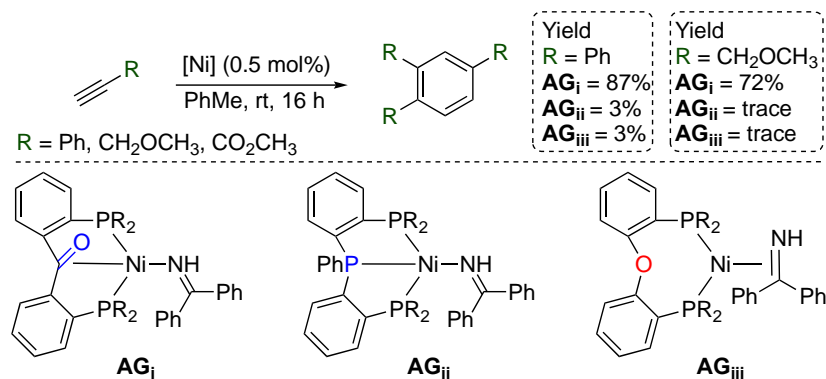
ethylene, with high comonomer incorporation (10.3%)<sup>88</sup> and high MW ( $6.0 \times 10^4 \text{ g}\cdot\text{mol}^{-1}$ ). Allyl alcohol, allyl ether, allyl acetate, and allylbenzene were also successfully copolymerized with ethylene by  $[\text{AF}_{\text{iv}}]^+$ . Polymerization pathways with  $\text{AE}_{\text{v}}$  and  $\text{AE}_{\text{vi}}$  were compared computationally. Ethylene coordination was less favourable with  $\text{AE}_{\text{v}}$  by  $16.7 \text{ kcal}\cdot\text{mol}^{-1}$ , consistent with competitive coordination between N and ethylene in  $\text{AE}_{\text{v}}$ . Furthermore, the energy barrier for branch formation with  $\text{AE}_{\text{v}}$  was determined to be  $18.1 \text{ kcal}\cdot\text{mol}^{-1}$ , whereas branch formation is  $6 \text{ kcal}\cdot\text{mol}^{-1}$  more favourable with  $\text{AE}_{\text{vi}}$ . More importantly, this step with  $\text{AE}_{\text{v}}$  is endergonic by  $5.7 \text{ kcal}\cdot\text{mol}^{-1}$  and therefore thermodynamically unfavourable, while this step with  $\text{AE}_{\text{vi}}$  is exergonic by  $1.2 \text{ kcal}\cdot\text{mol}^{-1}$ . Thus, it was proposed that reversible coordination of the nitrogen atom was stronger than  $\beta\text{-H}$  and  $\beta\text{-X}$  coordination, but weaker than ethylene coordination. Consequently, allowing for a reduction in polymer branching, and a greater tolerance towards polar additives. Computationally the morpholine substituent was also determined to have a steric advantage. Formation of branched Ni-alkyl intermediates with  $\text{AE}_{\text{v}}$  was calculated to be  $5.5 \text{ kcal}\cdot\text{mol}^{-1}$  higher in energy compared to the analogous linear Ni-alkyl intermediates.



**Figure 1.6.** The different Pd<sup>II</sup> and Ni<sup>II</sup>  $\alpha$ -diimine complexes synthesized for investigations of SRL impact on ethylene polymerization (left). Reversible coordination of the morpholine moiety in the secondary coordination sphere (right).<sup>131</sup>

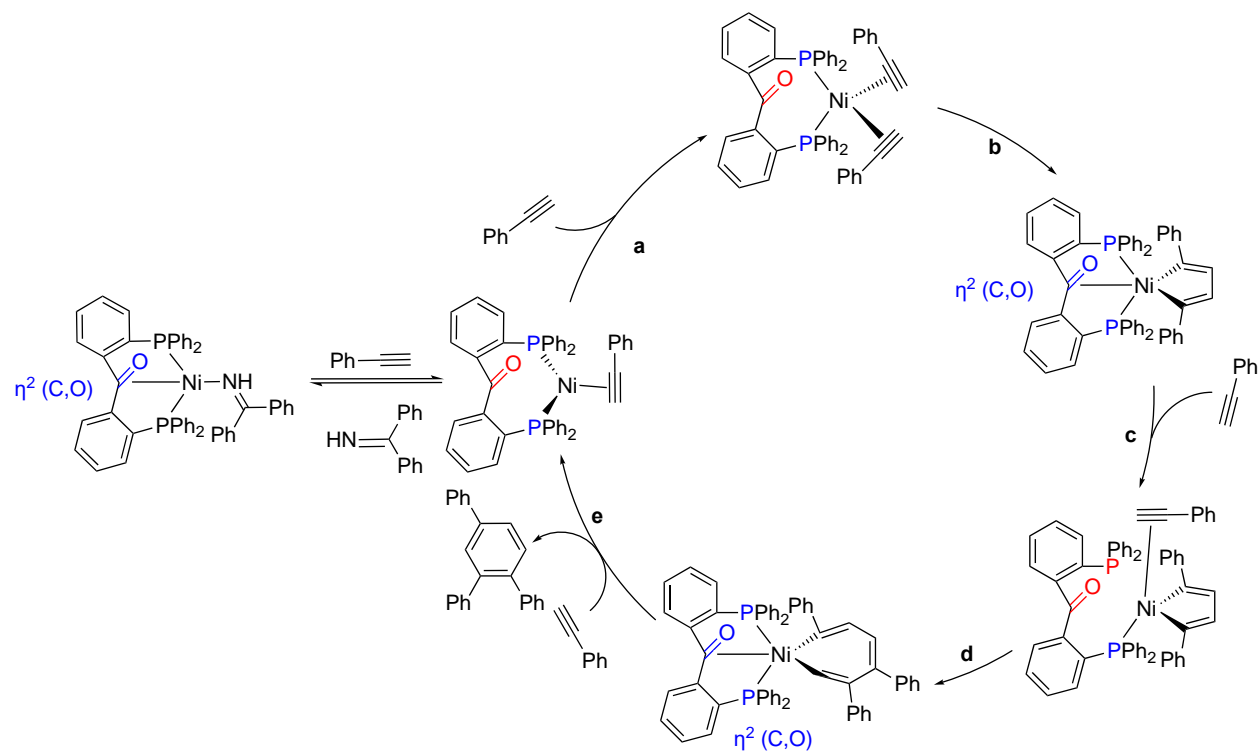
An SRL was also found to be advantageous when coordinated to Ni for the [2+2+2] cyclotrimerization of alkynes, an atom economic route to forming substituted benzenes (Scheme 1.12).<sup>132, 133</sup> Selectivity is often a challenge in these reactions, and a specific problem that nickel catalysts often have is the insertion of a fourth alkyne to make a tetrameric cyclooctatetraene.<sup>134</sup> Three different Ni complexes were isolated;  $\text{AG}_{\text{i}}$ ,  $\text{AG}_{\text{ii}}$ , and  $\text{AG}_{\text{iii}}$  each with different coordinative moieties in the ligand backbone, resulting in distinct coordination at each Ni centre. Complex  $\text{AG}_{\text{ii}}$  and  $\text{AG}_{\text{iii}}$ 's coordination modes are tridentate ( $\kappa^2\text{-PPP}$ ) and bidentate ( $\kappa^3\text{-PP}$ ), respectively. Complex  $\text{AG}_{\text{i}}$  bears a hemilabile carbonyl which can undergo reversible  $\eta^2\text{-CO}$  coordination. Of

the three complexes, **AG<sub>i</sub>** was the most selective for the 1,2,4-trimer and consequently the highest yielding with phenyl acetylene (R = Ph) and methyl propiolate (R = CO<sub>2</sub>CH<sub>3</sub>). Additionally, **AG<sub>i</sub>** was the only complex able to catalyze the cyclotrimerization of methyl propargyl ether (R = CH<sub>2</sub>OCH<sub>3</sub>).<sup>132</sup>



**Scheme 1.12.** Alkyne cyclotrimerization catalyzed by Ni complexes bearing ligands with dynamic (**AG<sub>i</sub>**) and static (**AG<sub>ii/iii</sub>**) coordination modes.<sup>132</sup>

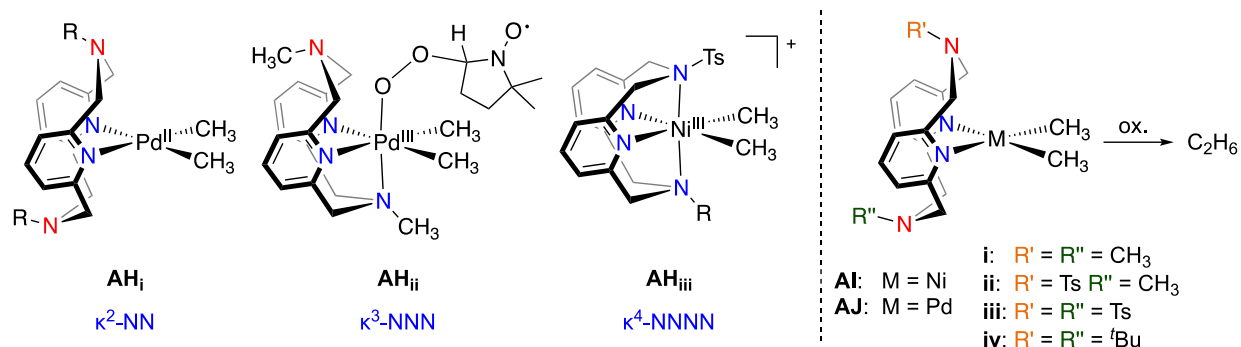
The authors also attempted to elucidate the benefit of the structurally responsive ketone computationally using a truncated version of **AG<sub>i</sub>** with phenyl substituents on the phosphine.<sup>133</sup> Their mechanism was proposed using data from the computations, paired with their previous experimental observations (Scheme 1.13). Changes in ketone coordination mode are evident throughout the proposed mechanism. Notably, the catalyst resting state is in equilibrium between a  $\kappa^2\text{-PP}:\eta^2\text{-C=O}$  and  $\kappa^2\text{-PP}$  coordination mode, which facilitates substrate coordination. The structurally responsive function of the ligand is most pronounced in the oxidative coupling step (**a**), which happens to be the rate-determining step (rds). The reversible coordination of the carbonyl helps to stabilize the key metallacyclopentadiene intermediate, and the activation barrier with the carbonyl moiety is 5.9 kcal•mol<sup>-1</sup> lower than with a structurally static analogue of **AG<sub>ii</sub>**. The positive impact of reversible C=O coordination was also noted in allowing the stepwise coordination and insertion of the third alkyne into the dimer to form a metallacycloheptatriene (**c** – **d**). The pathway opened through reversible C=O coordination is lower in energy by ca. 8 kcal•mol<sup>-1</sup> compared to the Diels-Alder type mechanism that **AG<sub>ii</sub>** was calculated to proceed through. These key computational findings support the experimental observations of improved yields and higher selectivity for the [2+2+2] cyclotrimerization of alkynes with an SRL catalysts.



**Scheme 1.13.** Proposed mechanism for alkyne cyclotrimerization catalyzed by a structurally responsive Ni complex analogous to **AG<sub>i</sub>**.<sup>133</sup>

SRLs can also be used to stabilize metals in uncommon oxidation states, allowing for their direct analysis and isolation.<sup>135-138</sup> Several examples use a *N,N'*-R<sub>2</sub>-2,11-diaza[3.3]pyridinophane ligand coordinated to dimethyl Ni or Pd (Scheme 1.14).<sup>138, 139</sup> These ligands have static  $\kappa^2$ -N,N coordination through the pyridine rings, however the amine groups are capable of reversible coordination, allowing for three distinct coordination modes through N:  $\kappa^2$ ,  $\kappa^3$ , and  $\kappa^4$  (Scheme 1.14).<sup>138</sup> The changes in coordination mode have allowed for the isolation of Ni complexes in the unusual +3 oxidation state, as confirmed by X-ray crystallography of **AH<sub>iii</sub>**.<sup>138</sup> The Ni<sup>III</sup> complex **AH<sub>iii</sub>** was also able to undergo oxidant-induced *Csp*<sup>3</sup>-*Csp*<sup>3</sup> reductive elimination of ethane. The authors assessed the impact of the N-R group by comparing both the yield of ethane, and the selectivity towards ethane with either **AI<sub>i</sub>**, **AI<sub>ii</sub>**, or **AI<sub>iii</sub>**. The highest yielding complex **AI<sub>iii</sub>** had two electron-withdrawing tosyl substituents appended to N and achieved 96% yield of ethane and 0% methane. The authors suggest that the electron withdrawing substituents destabilize the Ni<sup>III</sup> intermediate that forms upon 1 e<sup>-</sup> oxidation and allows for rapid reductive elimination to give ethane. Similar studies with **AJ<sub>ii</sub>**, a Pd analogue of **AI<sub>ii</sub>**, have revealed the need for fine tuning both the ligand denticity and donating ability of the amines.<sup>140</sup> A balancing act is required to ensure that

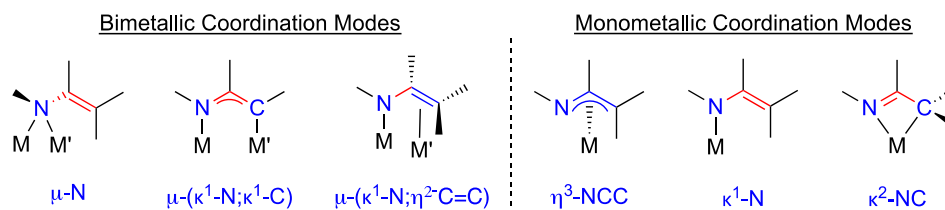
the Pd<sup>III</sup>-superoxo intermediate can be formed, but the Pd<sup>IV</sup> species is unstable enough that it undergoes reductive elimination. Complex **AJ<sub>ii</sub>** could produce ethane in 99% yield with 0% methane at rt, compared to complex **AJ<sub>iv</sub>** which required heating at 110 °C for 60 h to achieve yields of 90% ethane with 10% methane.<sup>140, 141</sup>



**Scheme 1.14.** Different coordination modes observed with N,N'-dimethyl-2,11-diaza[3.3]pyridinophane ligands coordinated to Pd and Ni allowing for the isolation of complexes bearing unusual metal oxidation states (left).<sup>137-139</sup> Oxidatively induced reductive elimination of ethane starting from Pd<sup>II</sup> and Ni<sup>II</sup> complexes (right).<sup>139-141</sup>

## 1.6 1-Azaallyls as Ligands in Organometallic Chemistry

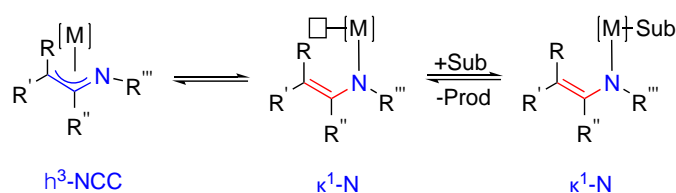
The 1-azaallyl (1-AzA) group (Figure 1.7) is isoelectronic to many common SRLs such as carboxylates, allyls, and amidates,<sup>127</sup> however it has received far less attention as a ligand in organometallic chemistry. In these systems, a negative charge is delocalized throughout the NCC backbone, allowing it to adopt a wide variety of coordination modes. Indeed, a range of coordination modes have been observed in metal 1-AzA complexes, (Figure 1.7).<sup>142-147</sup>



**Figure 1.7.** General illustration of the diverse range of bimetallic (left) and monometallic (right) coordination modes of the 1-AzA group.<sup>142</sup>

The diverse coordination modes are heavily influenced by the metal and sterics of the groups appended to the NCC backbone. In low coordination environments sterically hindered 1-AzA ligands coordinated to M<sup>II</sup> (M = group 2, 13, 14) prefer κ<sup>2</sup>-NC coordination modes instead of η<sup>3</sup>-NCC.<sup>142</sup> Alternatively, a κ<sup>1</sup>-N coordination mode is often observed in monometallic

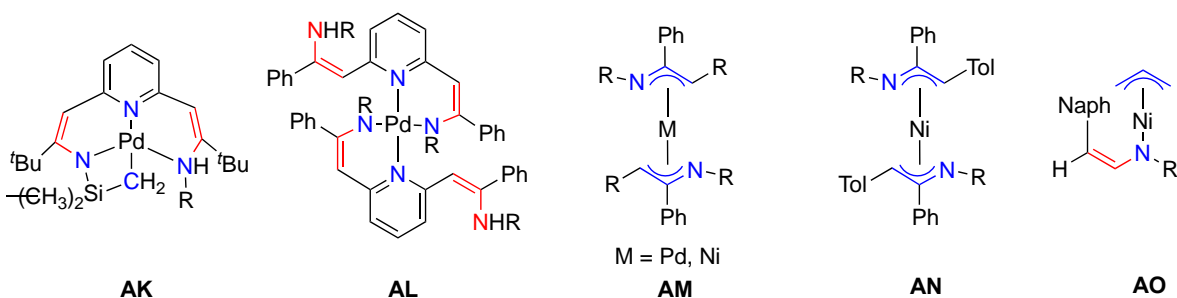
complexes in the presence of neutral donors such as THF and pyridine.<sup>142</sup> One isomerization of interest is the change from  $\kappa^1\text{-N}$  to  $\eta^3\text{-NCC}$  (Scheme 1.15). These modes occupy one and two coordination sites respectively, and are commonly observed in monometallic complexes.<sup>142</sup> In a catalytic cycle the moiety could change from  $\eta^3\text{-NCC}$  to  $\kappa^1\text{-N}$  to allow substrate coordination, and once product release or monomer insertion has occurred then the ligand can change back to  $\eta^3\text{-NCC}$  to stabilize the low-coordinate intermediate. The  $\kappa^1\text{-N}$  to  $\eta^3\text{-NCC}$  isomerization has been observed in  $\text{Ni}^{\text{II}}$  complexes coordinated by 1-AzA ligands (*vide infra*),<sup>145</sup> and is identical to the  $\eta^3\text{-CCC}$  to  $\kappa^1\text{-C}$  slippage observed with allyl metal complexes that allows for facile C–C bond formation.<sup>142</sup>



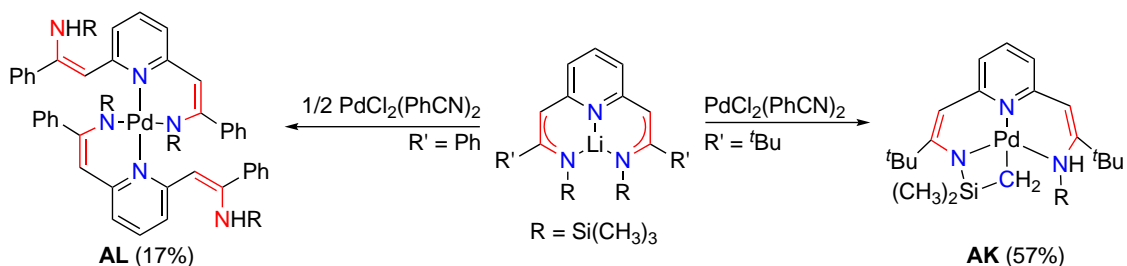
**Scheme 1.15.** General depiction of the isomerization from  $\eta^3\text{-NCC}$  to  $\kappa^1\text{-N}$ , which opens a coordination site for substrate binding.

There are several methods to prepare transition-metal 1-AzA complexes.<sup>142</sup> One method is to generate the alkali metal salt through deprotonation of the  $\beta$ -carbon of the imine precursor with a strong alkali base such as KH or Li[HMDs]. These alkali-AzA salts are effective transfer reagents and have been used for the synthesis of several f- and d-block metal complexes.<sup>142</sup> Coordination of the salt to a transition metal precursor allows for isolation of the desired transition metal-AzA complex. Alternatively, an imine ligand can be coordinated to the metal centre followed by deprotonation with a strong base such as KH or KO<sup>t</sup>Bu.<sup>142</sup>

There are several examples of 1-AzA group 10 complexes (Figure 1.8).<sup>142, 143, 145</sup> Layh reported the synthesis of square-planar  $\text{Pd}^{\text{II}}(1\text{-AzA})$  complexes using a lithium transfer reagent (Scheme 1.16).<sup>143</sup> Depending on the stoichiometry of ligand to  $\text{Pd}^{\text{II}}$  precursor in solution, two distinct complexes were obtained. If one equivalent of  $\text{PdCl}_2(\text{PhCN})_2$  was used, complex **AK** was produced in which the ligand is tetradentate, and each AzA moiety is coordinated  $\kappa^1\text{-N}$  through the nitrogen. Alternatively, using  $\frac{1}{2}$  an equivalent of  $\text{PdCl}_2(\text{PhCN})_2$  results in generation of bis-ligated complex **AL**. In complex **AL** the ligand is bidentate, and each 1-AzA moiety is coordinated  $\kappa^1\text{-N}$  through the nitrogen, similar to **AK**. In this report, the 1-AzA moiety was only observed in the  $\kappa^1\text{-N}$  coordination mode.<sup>143</sup>

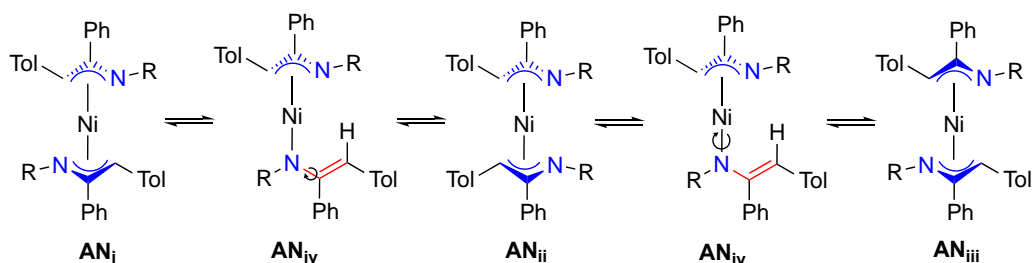


**Figure 1.8.** A selection of group 10 1-AzA complexes. R = Si(CH<sub>3</sub>)<sub>3</sub>.<sup>143, 145</sup>



**Scheme 1.16.** Synthesis of two different P<sup>AzA</sup> Pd complexes using a lithium transfer reagent.<sup>143</sup>

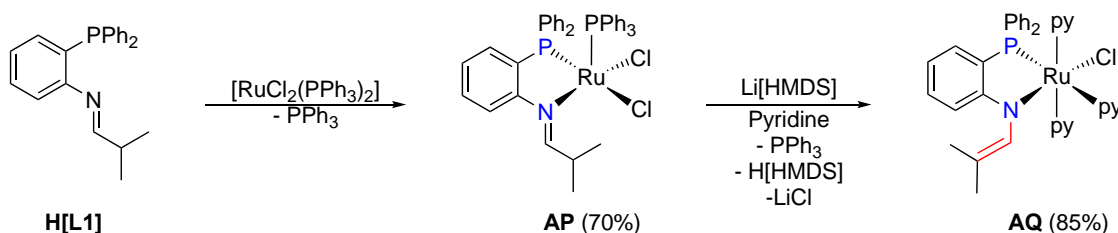
Lappert has been able to coordinate a myriad of 1-AzA ligands to transition metals using their lithium or potassium salts.<sup>145</sup> This includes several examples of group 10 AzA complexes with Pd and Ni such as **AM**, **AN**, and **AO** (Figure 1.8). Bis-ligated **AM** and **AN** were prepared using 2 equivalents of the Li[AzA] salt and reacting with PdCl<sub>2</sub>(COD) or NiBr<sub>2</sub>(DME). Complex **AO** was prepared following a 2:1 reaction between the K[AzA] salt and a common Ni-allyl precursor [Ni(η<sup>3</sup>-allyl)(μ-Cl)]<sub>2</sub>. Complexes **AM** and **AN** exhibit η<sup>3</sup>-NCC coordination of the 1-AzA moiety, while in complex **AO** the 1-AzA group is coordinated κ<sup>1</sup>-N and the allyl ligand remains coordinated η<sup>3</sup>-CCC. NMR spectroscopy of **AN** also revealed that 3 isomers, **AN<sub>i</sub>**, **AN<sub>ii</sub>**, and **AN<sub>iii</sub>**, exist in solution in a 16:8:1 ratio, respectively. Unsurprisingly, complex **AN<sub>i</sub>** is the most abundant, in which there is the least steric clash between the trisilylmethyl substituents on N, and there is a staggered arrangement of the AzA backbones. Furthermore, it was determined that the three species interconvert with one another in a rapid fluxional process (Scheme 1.17). The proposed pathway involves η<sup>3</sup> to κ<sup>1</sup> slippage. However, the κ<sup>1</sup> species was not observable by NMR spectroscopy. Oligomers were obtained when compound **AN** was used for the polymerization of ethylene, however there was no mention of polymer MW, polydispersity, branching, or T<sub>m</sub>.<sup>145</sup>



**Scheme 1.17.** Proposed interconversion between different isomers of 1-AzA Ni complex **AN**. R = Si(CH<sub>3</sub>)<sub>3</sub>.<sup>145</sup>

## 1.7 Phosphine 1-Azaallyl Ligands

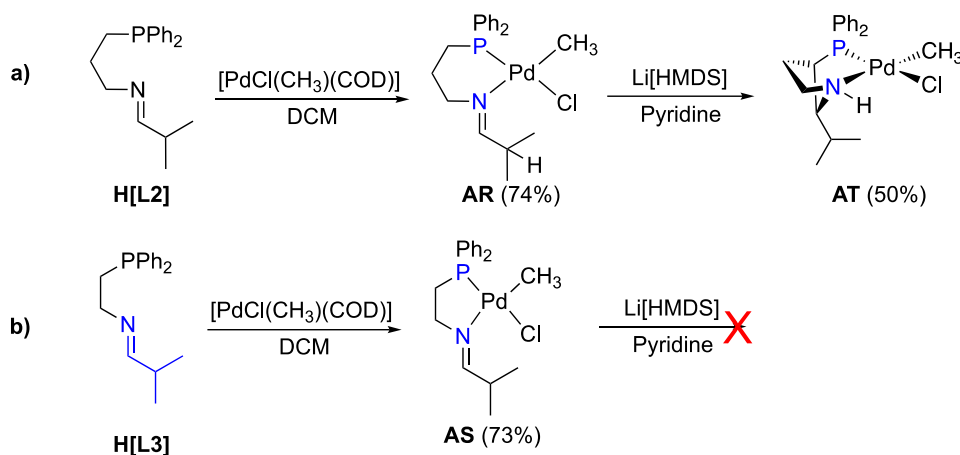
In 2017, the Blacquiere group reported the synthesis of the first phosphine 1-AzA ligand (P<sup>^</sup>AzA) (Scheme 1.18).<sup>148</sup> These ligands contain a soft phosphine donor and a structurally responsive 1-AzA moiety. The phosphine is structurally static and anchors the ligand to the metal centre, while the AzA moiety has the potential to change coordination mode to help influence reactivity. Ligand **H[L1]** is a phosphine-imine (P<sup>^</sup>I) precursor for a P<sup>^</sup>AzA ligand, and it contains a phenyl linkage between the two heteroatoms to maintain rigidity of the ligand. Following a reaction with [RuCl<sub>2</sub>(PPh<sub>3</sub>)<sub>2</sub>] and **H[L1]**, complex **AP** was afforded. Deprotonation of **AP** was attempted with Li[HMDS] in non-coordinating solvents, however a complex mixture of products was obtained. Instead, **AP** was successfully deprotonated with Li[HMDS] in the presence of pyridine, affording the py analogue **AQ**. Pyridine helps to stabilize the resulting Ru(P<sup>^</sup>AzA) complex allowing for its isolation. Complex **AQ** contains the 1-AzA moiety coordinated κ<sup>1</sup>-N to the metal centre, and no other coordination modes of the 1-AzA moiety were observed.<sup>148</sup>



**Scheme 1.18.** Synthetic pathway used to obtain Ru(P<sup>^</sup>AzA) complex **AQ**.<sup>148</sup>

Another attempt to isolate a transition metal P<sup>^</sup>AzA complex involved P<sup>^</sup>I precursors **H[L2]** and **H[L3]** (Scheme 1.19).<sup>149</sup> These ligands contained flexible propyl and ethyl linkages between the two heteroatoms, which contrasts with the rigid 1,2-disubstituted aryl linkage in **H[L1]**. Several attempts were made to generate the lithium and potassium AzA salts of the ligand,

however deprotonation was not successful. Instead, the P<sup>^</sup>AzI precursors were coordinated to Pd using [PdCl(CH<sub>3</sub>)(COD)] to afford **AR** and **AS**. Deprotonation was still unsuccessful with **AS**. Although, when **AR** was reacted with Li[HMDS] in the presence of pyridine, deprotonation occurred in the ligand backbone at the carbon α- to phosphorus, affording the bicyclic structure **AT**. While a P<sup>^</sup>AzA complex was not obtained, this report suggested ligands with backbones susceptible to deprotonation are not amenable to the isolation of P<sup>^</sup>AzA species.



**Scheme 1.19.** a) Coordination of phosphine-imine ligand **H[L2]** to Pd affording **AR**, and subsequent deprotonation in coordinating solvent to afford bicyclic Pd<sup>II</sup> complex **AT**. b) Coordination of phosphine-imine ligand **H[L3]** to Pd to afford **AS** and attempted deprotonation with Li[HMDS] in coordinating solvent.<sup>149</sup>

## 1.8 Scope of Thesis

Herein, the design, synthesis, and coordination chemistry of a series of P<sup>^</sup>AzA ligands will be reported and discussed. Additionally, polymerization, cross-coupling catalysis, and fundamental reaction steps such as reductive elimination with the newly synthesized P<sup>^</sup>AzA metal complexes will be investigated.

Chapter 2 discusses the synthesis of phenyl-linked P<sup>^</sup>AzA ligand, **L1**, and its coordination to [PdCl(CH<sub>3</sub>)(COD)]. The resulting Pd(P<sup>^</sup>AzA) species is a Pd<sup>II</sup> dimer in which the P<sup>^</sup>AzA ligand bridges the Pd<sup>II</sup> centres through the anionic nitrogen in a κ<sup>1</sup>-P,μ-N coordination mode. This complex then undergoes a thermolysis reaction to form a new Csp<sup>3</sup>-Csp<sup>3</sup> bond by reductive elimination of ethane as the major product, as well as formation of minor amounts of methane. The yields of ethane and methane are quantified. Two new Pd products are formed through the thermolysis; a bis-ligated Pd<sup>II</sup>(**L1**)<sub>2</sub> monometallic complex and a [Pd<sup>I</sup>(**L1**)]<sub>2</sub> dimer. Distinct



coordination modes of the P<sup>^</sup>AzA ligand are observed in each complex. The bis-ligated species contains P<sup>^</sup>AzA moieties coordinated  $\kappa^2$ -PN, while the dimer exhibits a  $\mu$ -( $\kappa^2$ -PN, $\eta^2$ -CC) coordination mode. The  $\mu$ -( $\kappa^1$ -N, $\eta^2$ -CC) motif, where the N lone pair and C-C  $\pi$ -bond are simultaneously coordinated to two different metal centres is the first example of a 1-AzA moiety coordinated in this fashion.

Chapter 3 extensively investigates the mechanism by which  $C_{sp^3}$ - $C_{sp^3}$  reductive elimination of ethane occurs from the  $[Pd^{II}(\mathbf{L1})(CH_3)]_2$  dimer using a combined experimental and computational approach. Through the synthesis of non-SRL analogues, potential reaction intermediates, and isotopically labelled species, it is revealed that the versatile coordination chemistry of P<sup>^</sup>AzA ligand **L1** promotes bimetallic C-C bond formation. The P<sup>^</sup>AzA moiety adopts various coordination modes to maintain the bimetallic structure during the C-C bond forming mechanism. The process involves intramolecular methyl transfer and 1,1-reductive elimination from one palladium centre. Furthermore, it is determined that the minor byproduct methane is likely formed through a monometallic intermediate that is susceptible to solvent C-H activation. The capacity of **L1** to adopt different coordination modes promotes the observed C-C coupling mechanism through bimetallic pathways unattainable with statically-coordinated ligands.

Chapter 4 examines the improved synthesis of the  $[Pd^I(\mathbf{L1})]_2$  dimer, through coordination of the K[**L1**] salt to a known  $[Pd^I]_2$  dimer precursor. The resulting synthetic pathway is a more selective, higher yielding, and less technically demanding means of acquiring the  $[Pd^I(\mathbf{L1})]_2$  dimer, compared to the previous procedure. Furthermore, the applicability of  $[Pd^I(\mathbf{L1})]_2$  toward catalytic Kumada coupling of Grignard reagents and aryl bromides was investigated. Stoichiometric reactions and variable time normalization analyses (VTNA) were carried out in conjunction with computational analysis to determine if the mechanism for C-C coupling is dinuclear or mononuclear.

In Chapter 5, three new P<sup>^</sup>AzA ligands are designed and synthesized in which the backbone linkage between the P and N nuclei has been changed. Backbones which would likely result in an increased P-Pd-N bite angle were chosen to try and observe a species with an  $\eta^3$ -NCC coordination mode. These ligands contain naphthyl, biaryl, and phosphinite backbones. The coordination chemistry of each ligand will be discussed, and where a coordinatively-unsaturated P<sup>^</sup>AzA complex could not be obtained, analogous Lewis-base stabilized species were synthesized. The

obtained complexes, as well as the Pd<sup>II</sup> dimer coordinated with ligand **L1**, are utilized for the polymerization of ethylene.

Chapter 6 provides a summary and conclusions of the reported work. Furthermore, future work for this project is also discussed in this section.

## 1.9 References

1. Bhaduri, S.; Mukesh, D., *Homogenous Catalysis: Mechanisms and Industrial Applications*. John Wiley & Sons: New Jersey, 2014.
2. de Vries, J. G.; Jackson, S. D., *Catal. Sci. Technol.* **2012**, *2*, 2009.
3. Greco, F. A., *J. Chem. Educ.* **1986**, *63*, 382.
4. Hanefeld, U.; Lefferts, L., *Catalysis: An Integrated Textbook for Students*. John Wiley & Sons: New Jersey, 2018.
5. Shriver, D. F.; Weller, M. T.; Overton, T.; Rourke, J.; Armstrong, F. A., *Inorganic Chemistry*. Freeman: 2014.
6. Fadhel, A. Z.; Pollet, P.; Liotta, C. L.; Eckert, C. A., *Molecules* **2010**, *15*, 8400-8424.
7. Johansson Seechurn, C. C. C.; DeAngelis, A.; Colacot, T. J., *New Trends in Cross-Coupling: Theory and Applications*. The Royal Society of Chemistry: United Kingdom, 2014.
8. Ruiz-Castillo, P.; Buchwald, S. L., *Chem. Rev.* **2016**, *116*, 12564-12649.
9. Jana, R.; Pathak, T. P.; Sigman, M. S., *Chem. Rev.* **2011**, *111*, 1417-1492.
10. Liu, C.; Zhang, H.; Shi, W.; Lei, A., *Chem. Rev.* **2011**, *111*, 1780-1824.
11. Molander, G.; Wolfe, J. P.; Larhed, M., *Science of Synthesis: Cross-Coupling and Heck-Type Reactions*. Thieme: Stuttgart, Germany, 2013.
12. Korch, K. M.; Watson, D. A., *Chem. Rev.* **2019**, *119*, 8192-8228.
13. Petrone, D. A.; Ye, J.; Lautens, M., *Chem. Rev.* **2016**, *116*, 8003-8104.
14. Cherney, A. H.; Reisman, S. E., *Tetrahedron* **2014**, *70*, 3259-3265.
15. Yu, Y.; Liebeskind, L. S., *J. Org. Chem.* **2004**, *69*, 3554-3557.
16. Ma, Y.; Cammarata, J.; Cornella, J., *J. Am. Chem. Soc.* **2019**, *141*, 1918-1922.
17. Dooleweerd, K.; Fors, B. P.; Buchwald, S. L., *Org. Lett.* **2010**, *12*, 2350-2353.
18. Neely, J. M.; Bezdek, M. J.; Chirik, P. J., *ACS Cent. Sci.* **2016**, *2*, 935-942.
19. Schoenebeck, F.; Houk, K. N., *J. Am. Chem. Soc.* **2010**, *132*, 2496-2497.
20. Klatt, T.; Werner, V.; Maximova, M. G.; Didier, D.; Apeloig, Y.; Knochel, P., *Chem. Eur. J.* **2015**, *21*, 7830-7834.
21. Cordovilla, C.; Bartolomé, C.; Martínez-Ilarduya, J. M.; Espinet, P., *ACS Catal.* **2015**, *5*, 3040-3053.
22. Devendar, P.; Qu, R.-Y.; Kang, W.-M.; He, B.; Yang, G.-F., *J. Agric. Food. Chem.* **2018**, *66*, 8914-8934.
23. Hazra, S.; Johansson Seechurn, C. C. C.; Handa, S.; Colacot, T. J., *ACS Catal.* **2021**, *11*, 13188-13202.
24. Giannerini, M.; Fañanás-Mastral, M.; Feringa, B. L., *Nat. Chem.* **2013**, *5*, 667-672.
25. Hofmayer, M. S.; Hammann, J. M.; Lutter, F. H.; Knochel, P., *Synthesis* **2017**, *49*, 3925-3930.

26. Miao, W.; Zhao, Y.; Ni, C.; Gao, B.; Zhang, W.; Hu, J., *J. Am. Chem. Soc.* **2018**, *140*, 880-883.
27. Suzuki, A., *Pure Appl. Chem.* **1985**, *57*, 1749-1758.
28. Zaborova, E.; Deschamp, J.; Guieu, S.; Blériot, Y.; Poli, G.; Ménand, M.; Madec, D.; Prestat, G.; Sollogoub, M., *Chem. Commun.* **2011**, *47*, 9206-9208.
29. Osakada, K.; Nishihara, Y., *Dalton Trans.* **2022**, *51*, 777-796.
30. Johansson Seechurn, C. C. C.; Kitching, M. O.; Colacot, T. J.; Snieckus, V., *Angew. Chem. Int. Ed.* **2012**, *51*, 5062-5085.
31. Harper, M. J.; Arthur, C. J.; Crosby, J.; Emmett, E. J.; Falconer, R. L.; Fensham-Smith, A. J.; Gates, P. J.; Leman, T.; McGrady, J. E.; Bower, J. F.; Russell, C. A., *J. Am. Chem. Soc.* **2018**, *140*, 4440-4445.
32. Chen, J.-Q.; Dong, Z.-B., *Synthesis* **2020**, *52*, 3714-3734.
33. Kranthikumar, R., *Organometallics* **2022**, *41*, 667-679.
34. Reddy, M. M.; Reddy, K. H.; Reddy, M. U., *Pharmaceut. Reg. Affairs* **2016**, *5*, 1-8.
35. Diccianni, J. B.; Diao, T., *Trends in Chem.* **2019**, *1*, 830-844.
36. Huo, H.; Gorsline, B. J.; Fu, G. C., *Science* **2020**, *367*, 559-564.
37. Nickel (II) Bromide Ethylene Glycol Dimethyl Ether Complex – <https://www.sigmaaldrich.com/CA/en/product/aldrich/406341> (accessed Apr. 19, 2022).
38. Della Ca', N., *Catalysts* **2021**, *11*, 588.
39. Crabtree, R. H., *The Organometallics Chemistry of the Transition Metals*. John Wiley & Sons: New Jersey, 2014.
40. Cotton, F. A.; G., W.; Murillo, C. A.; Bochmann, M., *Advanced Inorganic Chemistry*. John Wiley & Sons: Toronto, 1999.
41. Khusnutdinova, J. R.; Rath, N. P.; Mirica, L. M., *J. Am. Chem. Soc.* **2010**, *132*, 7303-7305.
42. Powers, D. C.; Benitez, D.; Tkatchouk, E.; Goddard, W. A.; Ritter, T., *J. Am. Chem. Soc.* **2010**, *132*, 14092-14103.
43. Magano, J.; Dunetz, J. R., *Chem. Rev.* **2011**, *111*, 2177-2250.
44. L. Budarin, V.; S. Shuttleworth, P.; H. Clark, J.; Luque, R., *Curr. Org. Synth.* **2010**, *7*, 614-627.
45. Ittel, S. D.; Johnson, L. K.; Brookhart, M., *Chem. Rev.* **2000**, *100*, 1169-1204.
46. Nakamura, A.; Ito, S.; Nozaki, K., *Chem. Rev.* **2009**, *109*, 5215-5244.
47. Mu, H.; Zhou, G.; Hu, X.; Jian, Z., *Coord. Chem. Rev.* **2021**, *435*, 213802.
48. Torborg, C.; Beller, M., *Adv. Synth. Catal.* **2009**, *351*, 3027-3043.
49. Köhler, K.; Wussow, K.; Wirth, A. S., Palladium-Catalyzed Cross-Coupling Reactions – A General Introduction. In *Palladium-Catalyzed Coupling Reactions*, 2013; pp 1-30.
50. The Nobel Prize in Chemistry 2010 – Press Release. [https://www.nobelprize.org/nobel\\_prizes/chemistry/laureates/2010/press.html](https://www.nobelprize.org/nobel_prizes/chemistry/laureates/2010/press.html) (accessed Apr. 9, 2022).
51. Oxtoby, L. J.; A., G. J. J.; Wisniewski, S. R.; Eastgate, M. D.; Engle, K. M., *Trends in Chem.* **2019**, *1*, 572-587.
52. Lee, A. L., *Org. Biomol. Chem.* **2016**, *14*, 5357-5366.
53. Lennox, A. J. J.; Lloyd-Jones, G. C., *Chem. Soc. Rev.* **2014**, *43*, 412-443.
54. Buchspies, J.; Szostak, M., *Catalysts* **2019**, *9*, 53.
55. Wang, D.; Gao, S., *Org. Chem. Front.* **2014**, *1*, 556-566.
56. Chinchilla, R.; Nájera, C., *Chem. Soc. Rev.* **2011**, *40*, 5084-5121.
57. Heravi, M. M.; Hashemi, E.; Nazari, N., *Mol. Divers.* **2014**, *18*, 441-472.

58. Heravi, M. M.; Zadsirjan, V.; Hajiabbasi, P.; Hamidi, H., *Monatsh. Chem.* **2019**, *150*, 535-591.
59. Dorel, R.; Grugel, C. P.; Haydl, A. M., *Angew. Chem. Int. Ed.* **2019**, *58*, 17118-17129.
60. Heravi, M. M.; Kheilkordi, Z.; Zadsirjan, V.; Heydari, M.; Malmir, M., *J. Organomet. Chem.* **2018**, *861*, 17-104.
61. Wei, Y.; Hu, P.; Zhang, M.; Su, W., *Chem. Rev.* **2017**, *117*, 8864-8907.
62. Chen, X.; Engle, K. M.; Wang, D.-H.; Yu, J.-Q., *Angew. Chem. Int. Ed.* **2009**, *48*, 5094-5115.
63. Muzart, J., *Adv. Synth. Catal.* **2022**, *n/a*.
64. Kwon, M.; Kim, S. T.; Smith, S.; Smith, C.; Mortimer, P. G.; LoembE, B.; Kozarewa, I.; Dean, E.; Lee, J., *J. Clin. Oncol.* **2021**, *39*, 9514-9514.
65. Miller, A. L.; Garcia, P. L.; Yoon, K. J., *Pharmacol. Res.* **2020**, *155*, 104740.
66. Goundry, W. R. F.; Dai, K.; Gonzalez, M.; Legg, D.; O’Kearney-McMullan, A.; Morrison, J.; Stark, A.; Siedlecki, P.; Tomlin, P.; Yang, J., *Org. Process Res. Dev.* **2019**, *23*, 1333-1342.
67. Campeau, L.-C.; Hazari, N., *Organometallics* **2019**, *38*, 3-35.
68. Fu, G. C., *ACS Cent. Sci.* **2017**, *3*, 692-700.
69. Choi, J.; Fu, G. C., *Science* **2017**, *356*.
70. Netherton, M. R.; Dai, C.; Neuschütz, K.; Fu, G. C., *J. Am. Chem. Soc.* **2001**, *123*, 10099-10100.
71. Kambe, N.; Iwasaki, T.; Terao, J., *Chem. Soc. Rev.* **2011**, *40*, 4937-4947.
72. Endo, K.; Ohkubo, T.; Ishioka, T.; Shibata, T., *J. Org. Chem.* **2012**, *77*, 4826-4831.
73. Chu, M.; Liu, Y.; Lou, X.; Zhang, Q.; Chen, J., *ACS Catal.* **2022**, *12*, 4659-4679.
74. Geyer, R.; Jambeck, J. R.; Law, K. L., *Sci. Adv.* **2017**, *3*, e1700782.
75. Drowning in Plastics – Marine Litter and Plastic Waste. <https://wedocs.unep.org/xmlui/bitstream/handle/20.500.11822/36964/VITGRAPH.pdf> (Accessed 2022)
76. Zhu, T.; Li, X.; Zhao, X.; Zhang, X.; Lu, Y.; Zhang, L., *Polym. Test.* **2022**, *106*, 107460.
77. Malpass, D. B., *Introduction to Industrial Polyethylene: Properties, Catalysts, and Processes*. John Wiley & Sons: New Jersey, 2010.
78. Ye, Z.; Xu, L.; Dong, Z.; Xiang, P., *Chem. Commun.* **2013**, *49*, 6235-6255.
79. Hawker, C. J., *Trends Polym. Sci.* **1996**, *4*, 183-188.
80. Dai, S.; Chen, C., *Macromolecules* **2018**, *51*, 6818-6824.
81. Resconi, L.; Cavallo, L.; Fait, A.; Piemontesi, F., *Chem. Rev.* **2000**, *100*, 1253-1346.
82. Kaminsky, W., *J. Chem. Soc., Dalton Trans.* **1998**, 1413-1418.
83. Kaminsky, W., *J. Polym. Sci., Part A: Polym. Chem.* **2004**, *42*, 3911-3921.
84. Tan, C.; Zou, C.; Chen, C., *Macromolecules* **2022**, *55*, 1910-1922.
85. Khan, U.; May, P.; Porwal, H.; Nawaz, K.; Coleman, J. N., *ACS Appl. Mater. Interfaces* **2013**, *5*, 1423-1428.
86. Jacobs, M. A.; Kemmere, M. F.; Keurentjes, J. T. F., *Polymer* **2004**, *45*, 7539-7547.
87. Popeney, C.; Guan, Z., *Organometallics* **2005**, *24*, 1145-1155.
88. Mu, H.; Pan, L.; Song, D.; Li, Y., *Chem. Rev.* **2015**, *115*, 12091-12137.
89. Wang, J.; Wang, L.; Yu, H.; Ullah, R. S.; Haroon, M.; Zain-ul-Abdin; Xia, X.; Khan, R. U., *Eur. J. Inorg. Chem.* **2018**, *2018*, 1450-1468.

90. Hagmna, J. F.; Crary, J. W.; Mark, H. F.; Bikales, N. M.; Overberger, C. G.; Menges, G.; Kroschowiz, J. I., *Encyclopedia of Polymer Science and Engineering*. John Wiley & Sons: New Jersey, 1985.
91. Luckham, S. L. J.; Nozaki, K., *Acc. Chem. Res.* **2021**, *54*, 344-355.
92. Franssen, N. M. G.; Reek, J. N. H.; de Bruin, B., *Chem. Soc. Rev.* **2013**, *42*, 5809-5832.
93. Camacho, D. H.; Guan, Z., *Chem. Commun.* **2010**, *46*, 7879-7893.
94. Boffa, L. S.; Novak, B. M., *Chem. Rev.* **2000**, *100*, 1479-1494.
95. Nakano, R.; Nozaki, K., *J. Am. Chem. Soc.* **2015**, *137*, 10934-10937.
96. Mitsushige, Y.; Yasuda, H.; Carrow, B. P.; Ito, S.; Kobayashi, M.; Tayano, T.; Watanabe, Y.; Okuno, Y.; Hayashi, S.; Kuroda, J.; Okumura, Y.; Nozaki, K., *ACS Macro Letters* **2018**, *7*, 305-311.
97. Johnson, L. K.; Killian, C. M.; Brookhart, M., *J. Am. Chem. Soc.* **1995**, *117*, 6414-6415.
98. Tempel, D. J.; Johnson, L. K.; Huff, R. L.; White, P. S.; Brookhart, M., *J. Am. Chem. Soc.* **2000**, *122*, 6686-6700.
99. Dai, S.; Sui, X.; Chen, C., *Angew. Chem. Int. Ed.* **2015**, *54*, 9948-9953.
100. Qasim, M.; Bashir, M. S.; Iqbal, S.; Mahmood, Q., *Eur. Polym. J.* **2021**, *160*, 110783.
101. Dai, S.; Zhou, S.; Zhang, W.; Chen, C., *Macromolecules* **2016**, *49*, 8855-8862.
102. Dai, S.; Chen, C., *Angew. Chem. Int. Ed.* **2016**, *55*, 13281-13285.
103. Birajdar, R. S.; Chikkali, S. H., *Eur. Polym. J.* **2021**, *143*, 110183.
104. Nozaki, K.; Kusumoto, S.; Noda, S.; Kochi, T.; Chung, L. W.; Morokuma, K., *J. Am. Chem. Soc.* **2010**, *132*, 16030-16042.
105. Nakano, R.; Chung, L. W.; Watanabe, Y.; Okuno, Y.; Okumura, Y.; Ito, S.; Morokuma, K.; Nozaki, K., *ACS Catal.* **2016**, *6*, 6101-6113.
106. Rezabal, E.; Ugalde, J. M.; Frenking, G., *J. Phys. Chem. A* **2017**, *121*, 7709-7716.
107. Wu, Z.; Chen, M.; Chen, C., *Organometallics* **2016**, *35*, 1472-1479.
108. Li, G.; Zhu, D.; Wang, X.; Su, Z.; Bryce, M. R., *Chem. Soc. Rev.* **2020**, *49*, 765-838.
109. Cooper, B. G.; Napoline, J. W.; Thomas, C. M., *Catalysis Reviews* **2012**, *54*, 1-40.
110. Powers, I. G.; Uyeda, C., *ACS Catal.* **2017**, *7*, 936-958.
111. Pye, D. R.; Mankad, N. P., *Chemical Science* **2017**, *8*, 1705-1718.
112. Farley, C. M.; Uyeda, C., *Trends in Chem.* **2019**, *1*, 497-509.
113. Hazari, N.; Hruszkewycz, D. P., *Chem. Soc. Rev.* **2016**, *45*, 2871-2899.
114. Xu, W.; Li, M.; Qiao, L.; Xie, J., *Chem. Commun.* **2020**, *56*, 8524-8536.
115. Diccianni, J.; Lin, Q.; Diao, T., *Acc. Chem. Res.* **2020**, *53*, 906-919.
116. Ence, C. C.; Martinez, E. E.; Himes, S. R.; Nazari, S. H.; Moreno, M. R.; Matu, M. F.; Larsen, S. G.; Gassaway, K. J.; Valdivia-Berroeta, G. A.; Smith, S. J.; Ess, D. H.; Michaelis, D. J., *ACS Catal.* **2021**, *11*, 10394-10404.
117. Fricke, C.; Sperger, T.; Mendel, M.; Schoenebeck, F., *Angew. Chem. Int. Ed.* **2021**, *60*, 3355-3366.
118. Matsubara, K.; Yamamoto, H.; Miyazaki, S.; Inatomi, T.; Nonaka, K.; Koga, Y.; Yamada, Y.; Veiros, L. F.; Kirchner, K., *Organometallics* **2017**, *36*, 255-265.
119. Martinez, E. E.; Moreno, M. R.; Barksdale, C. A.; Michaelis, D. J., *Organometallics* **2021**, *40*, 2763-2767.
120. Aufiero, M.; Scattolin, T.; Proutière, F.; Schoenebeck, F., *Organometallics* **2015**, *34*, 5191-5195.
121. Finney, E. E.; Finke, R. G., *Inorg. Chim. Acta* **2006**, *359*, 2879-2887.
122. Proutiere, F.; Aufiero, M.; Schoenebeck, F., *J. Am. Chem. Soc.* **2012**, *134*, 606-612.

123. Maji, B.; Stephenson, D. S.; Mayr, H., *ChemCatChem* **2012**, *4*, 993-999.
124. Mayr, H.; Ammer, J.; Baidya, M.; Maji, B.; Nigst, T. A.; Ofial, A. R.; Singer, T., *J. Am. Chem. Soc.* **2015**, *137*, 2580-2599.
125. Blacquiere, J. M., *ACS Catal.* **2021**, *11*, 5416-5437.
126. Wang, L.; Carrow, B. P., *ACS Catal.* **2019**, *9*, 6821-6836.
127. Drover, M. W.; Love, J. A.; Schafer, L. L., *Chem. Soc. Rev.* **2017**, *46*, 2913-2940.
128. Trost, B. M.; Ryan, M. C., *Angew. Chem. Int. Ed.* **2017**, *56*, 2862-2879.
129. Calhorda, M. J.; Romão, C. C.; Veiros, L. F., *Chem. Eur. J.* **2002**, *8*, 868-875.
130. Sauthier, M.; Leca, F.; Toupet, L.; Réau, R., *Organometallics* **2002**, *21*, 1591-1602.
131. Li, M.; Wang, X.; Luo, Y.; Chen, C., *Angew. Chem. Int. Ed. Engl.* **2017**, *56*, 11604-11609.
132. Orsino, A. F.; Gutiérrez del Campo, M.; Lutz, M.; Moret, M.-E., *ACS Catal.* **2019**, *9*, 2458-2481.
133. Orsino, A. F.; Moret, M.-E., *Organometallics* **2020**, *39*, 1998-2010.
134. Wang, C.; Xi, Z., *Chem. Commun.* **2007**, 5119-5133.
135. Ruan, J.; Wang, D.; Vedernikov, A. N., *Organometallics* **2020**, *39*, 142-152.
136. Khusnutdinova, J. R.; Qu, F.; Zhang, Y.; Rath, N. P.; Mirica, L. M., *Organometallics* **2012**, *31*, 4627-4630.
137. Maleckis, A.; Sanford, M. S., *Organometallics* **2011**, *30*, 6617-6627.
138. Smith, S. M.; Rath, N. P.; Mirica, L. M., *Organometallics* **2019**, *38*, 3602-3609.
139. Peng, Q.; Wang, Z.; Zarić, S. D.; Brothers, E. N.; Hall, M. B., *J. Am. Chem. Soc.* **2018**, *140*, 3929-3939.
140. Schultz, J. W.; Rath, N. P.; Mirica, L. M., *Inorg. Chem.* **2020**, *59*, 11782-11792.
141. Tang, F.; Zhang, Y.; Rath, N. P.; Mirica, L. M., *Organometallics* **2012**, *31*, 6690-6696.
142. Caro, C. F.; Lappert, M. F.; Merle, P. G., *Coord. Chem. Rev.* **2001**, *219-221*, 605-663.
143. Bowen, R. J.; Fernandes, M. A.; Layh, M., *J. Organomet. Chem.* **2004**, *689*, 1230-1237.
144. Leung, W.-P.; Chiu, W.-K.; Mak, T. C. W., *Organometallics* **2014**, *33*, 225-230.
145. Avent, A. G.; Hitchcock, P. B.; Lappert, M. F.; Sablong, R.; Severn, J. R., *Organometallics* **2004**, *23*, 2591-2600.
146. Gu, D.; Yi, C.; Ren, W., *Inorg. Chem.* **2019**, *58*, 9260-9269.
147. Bowen, R. J.; Fernandes, M. A.; Gitari, P. W.; Layh, M.; Moutloali, R. M., *Eur. J. Inorg. Chem.* **2005**, *2005*, 1955-1963.
148. Stubbs, J. M.; Firth, K. F.; Bridge, B. J.; Berger, K. J.; Hazlehurst, R. J.; Boyle, P. D.; Blacquiere, J. M., *Dalton Trans.* **2017**, *46*, 647-650.
149. Jackman, K. M. K.; Fogh, A. A.; Stubbs, J. M.; Blacquiere, J. M., *J. Organomet. Chem.* **2019**, *880*, 56-61.

## 2.0 $Csp^3$ - $Csp^3$ Coupling with a Pd<sup>II</sup> Complex Bearing a Structurally Responsive Ligand

A dimer with two Pd<sup>II</sup>-CH<sub>3</sub> fragments is stabilized by the bridging coordination of the supporting P<sup>^</sup>AzA ligand. Heating the complex results in  $Csp^3$ - $Csp^3$  bond formation and the release of ethane. Two different palladium products are generated, each with distinct coordination modes of the P<sup>^</sup>AzA ligand.

### 2.1 Introduction

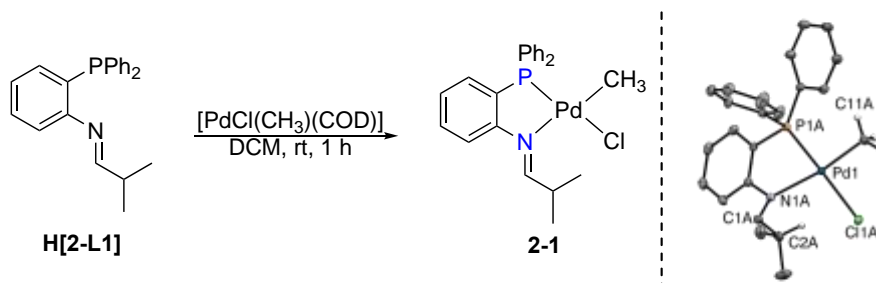
Ligands that exhibit a diversity of coordination modes are well known in coordination chemistry and transition-metal catalysis.<sup>1-4</sup> A change in ligand denticity or hapticity to a lower coordination number can promote binding of an exogenous ligand (i.e. a substrate for catalysis). Thus, a mode with a higher coordination number can stabilize latent low-coordinate complexes. This is particularly attractive in catalysis in which such intermediates are often both key active catalysts and precursors to decomposition pathways. Structural changes in ligand coordination can also promote reactivity distinct from substitution reactions. Palladium catalyzed direct arylation reactions depend on the isomerization of a carboxylate ligand from  $\kappa^2$ -*O,O* to  $\kappa^1$ -*O*.<sup>5-6</sup> The released oxygen atom acts as an intramolecular base, which lowers the activation barrier for Ar-H bond activation. Alternatively, isomerization of multidentate *N*-donor ligands to a higher coordination number (i.e.  $\kappa^2$ -*N,N* to  $\kappa^3$ -*N,N,N*) promotes oxidation of Ni<sup>II</sup>.<sup>7-9</sup> The higher coordination number stabilizes the uncommon Ni<sup>III</sup> or Ni<sup>IV</sup> intermediates, which can subsequently undergo reductive elimination to give new C-E bonds (E = C, O, N). Despite these prominent cases, examples in which structurally responsive ligands promote reactivity beyond substitution reactions remains limited.

The 1-AzA functionality can coordinate to metals through a diversity of modes, in which  $\eta^3$ -*N,C,C* binding is the most common among late-transition metals.<sup>10-11</sup> A reversible change between the  $\eta^3$ -*N,C,C* and  $\kappa^1$ -*N* coordination modes was proposed for a bis-1-AzA Ni<sup>II</sup> complex.<sup>11</sup> We hypothesized that a structurally responsive 1-AzA ligand could engender unusual and unexpected reactivity. To this end, we designed phosphine imine ligand **H[2-L1]** (Scheme 2.1, left), a pro-ligand to a phosphine 1-AzA ligand (**2-L1**) by deprotonation at C<sup>2</sup>.<sup>12</sup> Previously, we

showed that an octahedral ruthenium complex with **2-1** exhibited only a  $\kappa^2$ -*P,N* coordination mode. Herein, we report a palladium complex with ligand **2-1** that exhibits both changes in ligand coordination and an unusual  $Csp^3$ - $Csp^3$  bond-forming reaction.

## 2.2 Results and Discussion

The pro-ligand **H[2-L1]**<sup>12</sup> reacts rapidly at room temperature with  $PdCl(CH_3)(COD)$  to give **2-1**, the structure of which was confirmed by single crystal X-ray crystallography (Scheme 2.1). The complex has a slightly distorted square planar geometry, as evidenced by a  $\tau_4$  value<sup>13</sup> of 0.10 (for a perfect square plane,  $\tau_4 = 0$ ). A weak<sup>14</sup> hydrogen bond ( $X \cdots A = 3.5498(24)$  Å,  $X-H-A$  bonding angle  $134.6^\circ$ ) is observed between the chloride ligand ( $C1^{1A}$ ) and the methine proton (on  $C^{2A}$ ). This is also observed in solution where the diamagnetic anisotropy of the chloride lone pairs<sup>15-16</sup> shifts the  $H^2$  resonance downfield by ca. 2 ppm relative to the analogous signal in **H[2-L1]**.

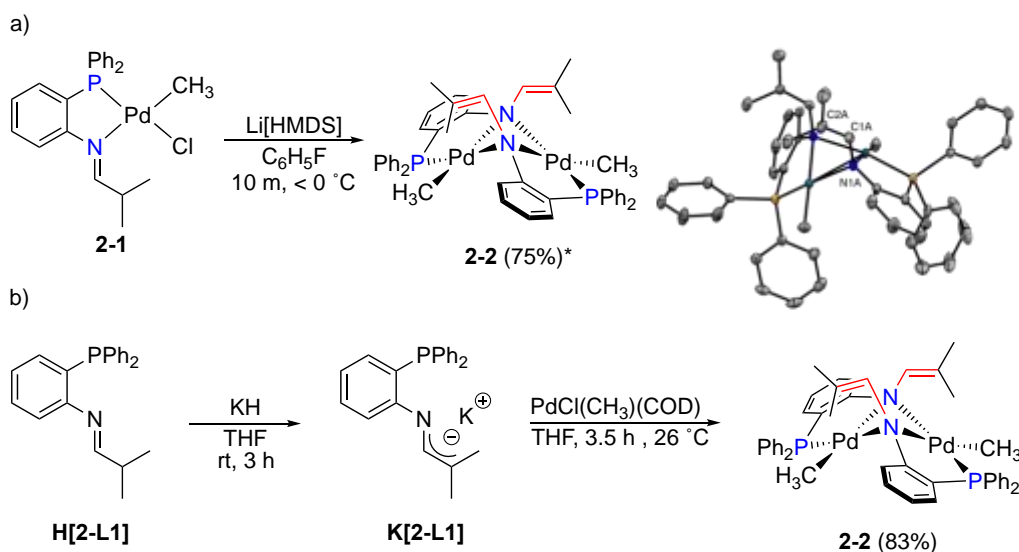


**Scheme 2.1.** Synthesis of Phosphine-Imine Complex **2-1**. Displacement ellipsoid (50% probability) plot of **2-1** (right). Hydrogen atoms have been omitted for clarity, except those on  $C^{1A}$ ,  $C^{2A}$  and  $C^{11A}$ . The hydrogen atoms were introduced at idealized positions and were allowed to ride on the parent atom.

Deprotonation of **2-1** with  $Li[HMDS]$  in non-coordinating fluorobenzene gave rapid and quantitative formation of **2-2**, observed as a singlet at 43.7 ppm in the  $^{31}P\{^1H\}$  NMR spectrum (Scheme 2.2, a). Scale-up of **2-2** via this route consistently gave low yields and Pd black was observed during the work-up, likely due to the instability of **2-2** to excess base or the conjugate acid  $H[HMDS]$ . Instead, **2-2** was obtained cleanly and in very good yield (>80%) from metallation of the deprotonated ligand salt **K[2-L1]** (Scheme 2.2, b). The identity of **2-2** was assigned as a dimer in which ligand **2-L1** bridges the two metal centres through a  $\mu$ -( $\kappa^1$ -*P*, $\kappa^2$ -*N*) coordination mode. Only a single set of ligand resonances are observed by  $^1H$  NMR spectroscopy, which indicates **2-2** has  $C_2$  symmetry in solution. Unequivocal evidence for the *cis*-disposition of the phosphine and methyl ligands is provided by the characteristically small coupling constant ( $^3J_{HP} =$



1.3 Hz)<sup>17-19</sup> for the methyl doublet at  $\delta_{\text{H}} = 0.51$ . The absence of a signal for the methine proton ( $\text{H}^2$ ) is consistent with ligand deprotonation to give the anionic 1-AzA<sup>10-11</sup> moiety. The two methyl groups ( $\text{H}^3$  and  $\text{H}^{3'}$ ) of ligand **H[2-L1]** are no longer equivalent and both are observed as singlets. The signal for  $\text{H}^{3'}$  is broad at room temperature ( $\omega_{1/2} = 169$  Hz), which is likely due to a weak agostic bonding to the axial site of palladium. A  $^1\text{H}$ - $^{13}\text{C}$  HSQC NMR experiment reveals a correlation from each methyl to the quaternary carbon  $\text{C}^2$  at 117.2 ppm (see Figure 2.2 for numbering). The location of this signal suggests that the carbon atoms of the 1-AzA moiety are not bound to the metal centre.<sup>11-12, 20-21</sup> A  $^1\text{H}$  DOSY NMR analysis (Figure A.23) of **2-2** revealed that the compound diffuses at a similar rate to a related dimer (**2-4**, *vide infra*) and slower than a monomer (**2-3**, *vide infra*). This supports the assignment of **2-2** as a dimer in solution.



**Scheme 2.2.** a) Formation of **2-2** via deprotonation of **2-1** \*the yield decreases for scales >50 mg. Displacement ellipsoid (50% probability) plot of **2-2**. All hydrogen atoms have been omitted. b) Deprotonation of **H[2-L1]** with KH to afford **K[2-L1]** followed by coordination to  $\text{PdCl(CH}_3\text{)(COD)}$  to afford **2-2** or metalation of **K[2-L1]**.

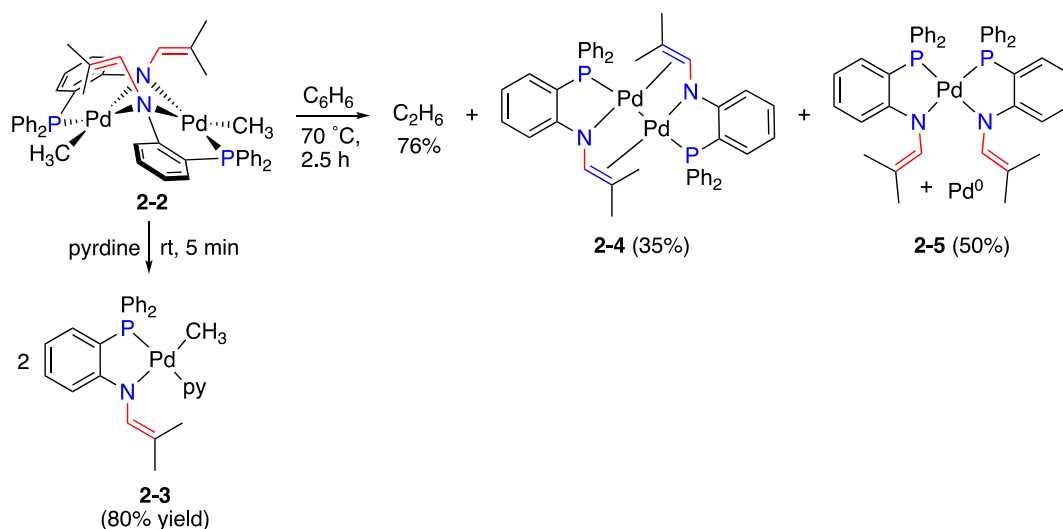
DFT calculations were conducted to compare the stability of a dimer to a monomeric complex, in which the fourth coordination site is occupied by a  $\delta$ -agostic interaction with the ligand methyl substituent. The dimer is more stable than the agostic monomer ( $\Delta G^\circ = -8.8 \text{ kcal mol}^{-1}$ ), which further supports the structural assignment of **2**. Structures of dimer **2-2** in which the  $\text{H}^{3'}$  protons bind agostically to one or both of the axial palladium sites are only 1.4 and 2.7  $\text{kcal mol}^{-1}$  higher in Gibbs energy, respectively, than the structure without agostic interactions. The close energies are in line with the broad signal for  $\text{H}^{3'}$  in the room temperature  $^1\text{H}$  NMR spectrum.

Single crystals were obtained by slow evaporation of a solution of **2-2** in a mixture of toluene and Et<sub>2</sub>O (Scheme 2.2). Two different dimer structures were found in the unit cell that differ by the position of the carbon framework of the 1-AzA unit, due to rotation about the N-C bond. Only one of the dimers is depicted in Scheme 2.2 and discussed here, but the other has very similar bond parameters. The dimeric structure shows two slightly distorted square planar Pd environments (Pd<sup>1A</sup>  $\tau^4 = 0.14$ ; Pd<sup>2A</sup>  $\tau^4 = 0.11$ ) that are bridged by the anionic nitrogen atoms of ligand **2-L1**. The Pd<sup>1A</sup>-N<sup>1A</sup>-Pd<sup>2A</sup> and Pd<sup>1A</sup>-N<sup>2A</sup>-Pd<sup>2A</sup> angles are 78.02(7) and 78.14(7), respectively, which gives a folded Pd<sub>2</sub>N<sub>2</sub> cycle and an angle between the square planes of 107.85°. The carbon frameworks of both of the 1-AzA groups are found in axial positions with respect to this ring. The Pd<sup>1A</sup>-Pd<sup>2A</sup> distance (2.7635(7) Å) is within the van der Waals radius (3.26 Å)<sup>22</sup> and is in a range consistent with a d<sup>8</sup>-d<sup>8</sup> interaction.<sup>23-24</sup> However, the large angle between the square planes is expected to minimize Pd-Pd bonding.<sup>25</sup>

Compound **2-2** readily reacts with pyridine to give adduct **2-3** (Scheme 2.3). Coordination of pyridine was evident from the <sup>1</sup>H NMR spectrum of isolated **2-3** in which signals for bound-pyridine are observed. The ligand in **2-3** adopts a  $\kappa^2$ -P,N coordination mode according to the chemical shift for C<sup>2</sup> ( $\delta_C$  118.5). Single crystals of **2-3** were obtained; while the structure was not of sufficient quality to refine the data, it did confirm the indicated connectivity. The facile formation of **2-3** indicates that the stabilizing bridging interaction of **2-2** is easily displaced and this is confirmed by DFT in which **2-3** is calculated to be more stable than **2-2** ( $\Delta G^\circ = -1.2$  kcal mol<sup>-1</sup>).

At room temperature in benzene **2-2** slowly evolves ethane, which is observed both as a dissolved gas by <sup>1</sup>H NMR spectroscopy and in the gas phase by GC-MS analysis of the headspace. Heating **2-2** at 70 °C for 2.5 h and analysis by calibrated GC-FID gives a yield of ca. 76% ethane. The Pd-based products from ethane release are two compounds, **2-4** and **2-5**, generated in a similar overall yield of 85% (35 and 50% yield, respectively, based on starting ligand **H[2-L1]**; Scheme 2.3). <sup>1</sup>H NMR analysis of **2-4** and **2-5** confirms that neither has retained the Pd-Me functionality, a requirement for ethane release. NMR analysis of **2-4** is consistent with a Pd<sup>I</sup>-Pd<sup>I</sup> dimer; such compounds are well known<sup>26-29</sup> and one electron reduction of palladium is consistent with a net bimolecular reductive elimination of ethane. Structural assignment of **2-4** was confirmed crystallographically, in which a bridging,  $\mu$ -( $\kappa^2$ -P,N, $\eta^2$ -C,C), coordination mode for ligand **2-L1** is evident (Figure 2.1). The C<sup>1</sup>-C<sup>2</sup> bond length (1.396(4) Å) is ca. 0.07 Å longer than the analogous

bond in **2-2** ( $C^{1A}-C^{2A} = 1.333(4) \text{ \AA}$ ) due to the  $\pi$ -backbonding from the  $Pd^I$  center. Expected Pd-Pd distances can be estimated from Pd-CH<sub>3</sub> bond lengths of **2-2**.<sup>27</sup> The experimental Pd-Pd length for **2-4** of 2.6109(7)  $\text{\AA}$  is nearly 0.1  $\text{\AA}$  longer than the predicted length. This is likely due to the geometric constraints imposed by the bridging 1-AzA group. The  $\pi$ -coordination of the 1-AzA group is confirmed by  $^{13}C\{^1H\}$  NMR spectroscopy that showed a signal for  $C^2$  at 74.5 ppm, significantly upfield of the expected location for a  $\kappa^1-N$  coordination mode of the 1-AzA fragment.

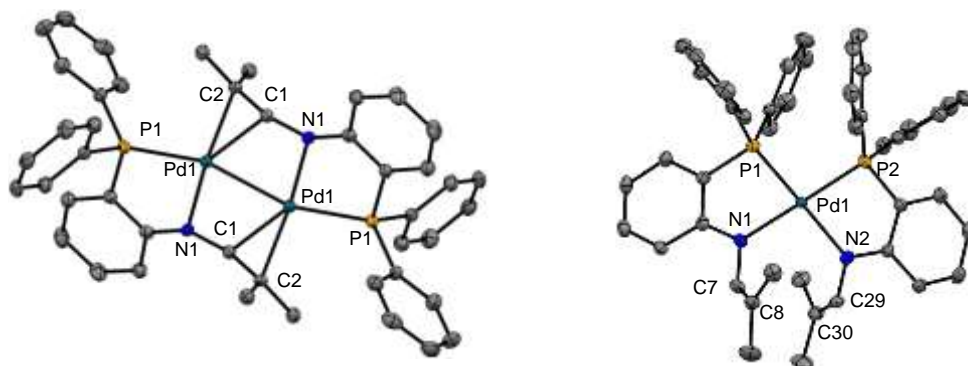


**Scheme 2.3.** Lewis acidic and reductive elimination reactivity of **2-2**.

An independent reaction of  $PdCl_2(COD)$  with 2 equiv. of **K[2-L1]** confirmed that product **2-5** is  $Pd(2-L1)_2$ . The generation of  $Pd^{II}$  from reductive elimination of **2-2** is accompanied by the formation of Pd black.  $^1H$ - $^{13}C$  HMBC NMR analysis of **2-5** reveals that  $C^2$  has  $\delta_C = 118.4$ , which is consistent with a  $\kappa^1-N$  coordination mode for the 1-AzA group. Attempted crystallization of **2-2** over several days afforded X-ray quality crystals of **2-5** (Figure 2.1). The phosphine groups are *cis*-disposed and the geometry is distorted square planar ( $\tau_4 = 0.16$ ) due to the steric repulsion of the 1-AzA groups.

A few examples of C-C bond formation from  $Pd^{II}$  mono-methyl or -alkyl complexes have been reported. Light-induced homolytic cleavage of Pd-alkyl bonds leads to radical C-C coupling.<sup>30</sup> Alternatively, oxidation of  $Pd^{II}-CH_3$  induces methyl transfer and reductive elimination from a high-valent  $Pd^{IV}(CH_3)_2$  intermediate.<sup>31-32</sup> In the present case, radical C-C coupling is improbable since the Pd products **2-4** and **2-5** are likewise afforded on heating **2-2** in the presence of 3 equiv TEMPO $\cdot$  as a radical trap<sup>33-34</sup> (**2-4**, 20%; **2-5**, 40%) or in the dark (**2-4**, 27%; **2-5**, 50%). The second pathway is even more unlikely given that no oxidant is present. No intermediates are

observed in the conversion of **2-2** to **2-4** and **2-5**, suggesting a bimolecular mechanism<sup>35-36</sup> is followed for reductive elimination. This could involve methyl-transfer<sup>36-37</sup> between Pd centres and subsequent reductive elimination<sup>38-39</sup> from a Pd<sup>II</sup>(CH<sub>3</sub>)<sub>2</sub> fragment as part of a dimer or as a monomeric intermediate. Regardless of the exact reaction path, we propose that the capacity of ligand **2-L1** to coordinate through three distinct coordination modes is important for the observed reactivity. Recently, reductive elimination of ethane was observed as a side reaction from a Pd<sup>II</sup>-CH<sub>3</sub> complex with a diphosphazane monoxide ligand. On reductive elimination the ligand isomerized from a  $\kappa^2$ -P,O to a  $\mu$ -( $\kappa^2$ -P,O, $\kappa^1$ -O') mode in the Pd<sup>I</sup>-Pd<sup>I</sup> dimer product.<sup>40</sup> This suggests that the reductive elimination reactivity observed here is general to other complexes with structurally responsive ligands.



**Figure 2.1.** Displacement ellipsoid (50% probability) plots of **2-4** (left) and **2-5** (right). Hydrogen atoms have been omitted for clarity. Selected bond distances (Å): **2-4** Pd(1)-Pd(1) 2.6109(7), Pd<sup>I</sup>-N<sup>I</sup> 2.061(3), Pd(1)-P(1) 2.3136(9), Pd(1)-C(1) 2.308(3), Pd<sup>I</sup>-C<sup>2</sup> 2.205(3), C(1)-C(2) 1.396(4); **2-5** Pd(1)-P(1) 2.2383(10), Pd(1)-P(2) 2.2437(10), Pd(1)-N(1) 2.088(3), Pd(1)-N(2) 2.091(3), N(1)-C(7) 1.408(4), N(2)-C(29) 1.389(4).

## 2.3 Conclusion

In summary, an anionic phosphine 1-AzA ligand, **K[2-L1]**, reacted with PdCl(CH<sub>3</sub>)(COD) to give a dimer, **2-2**, in which ligand **2-L1** is bound in a bridging  $\mu$ -( $\kappa^1$ -P, $\kappa^2$ -N) mode. Heating **2-2** produces ethane via  $Csp^3$ - $Csp^3$  bond formation along with two Pd products **2-4** and **2-5**. Complex **2-4** is a Pd<sup>I</sup>-Pd<sup>I</sup> dimer with  $\mu$ -( $\kappa^2$ -P,N, $\eta^2$ -C,C) binding of **2-L1** and product **2-5** is a Pd<sup>II</sup> complex with two  $\kappa^2$ -P,N bound ligands. The coordination chemistry of ligand **2-L1** is diverse and responsive. The observed chemistry is suggestive that the capacity for **2-L1** to alter its coordination mode promotes the unusual  $Csp^3$ - $Csp^3$  bond forming reaction. Ongoing studies are aimed at elucidating the mechanism for ethane formation and the role of the ligand in the process.

## 2.4 Experimental

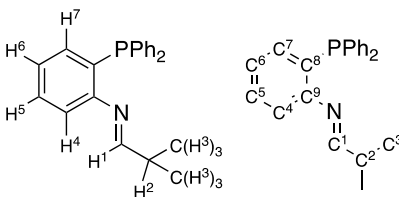
### 2.4.1 – General Considerations

Reactions were conducted in a nitrogen atmosphere glove box or using standard Schlenk line techniques under an argon atmosphere, unless otherwise indicated. Flasks, vials, and tubes were oven dried and cooled under nitrogen atmosphere prior to use. All reagents used were obtained from commercially available sources and used without further purification, unless otherwise indicated. Ethane gas was obtained from Praxair and passed through a tube filled with Drierite prior to use. The following materials were prepared following literature procedures: Pd(COD)Cl<sub>2</sub>,<sup>41</sup> PdCl(CH<sub>3</sub>)(COD),<sup>42</sup> 2-diphenylphosphinoaniline,<sup>43</sup> **H[2-L1]**.<sup>43</sup> All reaction solvents were obtained from an Innovative Technology 400-5 Solvent Purification system, dry and degassed, and stored over 4 Å molecular sieves under N<sub>2</sub> prior to use unless stated otherwise. Fluorobenzene and pyridine were dried over CaH<sub>2</sub>, distilled under vacuum, and stored over 4 Å sieves prior to use. Deuterated NMR solvents were obtained from commercial sources and stored over 4 Å sieves.

All NMR spectra were obtained on a 400 MHz Bruker or 600 MHz Varian spectrometer at 25 °C unless otherwise stated. <sup>1</sup>H and <sup>13</sup>C{<sup>1</sup>H} spectra were referenced internally, using residual solvent values, to TMS at 0 ppm as follows: benzene-*d*<sub>6</sub> (<sup>1</sup>H, 7.16 ppm; <sup>13</sup>C{<sup>1</sup>H}, 128.1 ppm), CD<sub>2</sub>Cl<sub>2</sub> (<sup>1</sup>H, 5.32 ppm; <sup>13</sup>C{<sup>1</sup>H} 52.0 ppm), toluene-*d*<sub>8</sub> (<sup>1</sup>H, 2.08 ppm), acetone-*d*<sub>6</sub> (<sup>1</sup>H, 2.05 ppm; <sup>13</sup>C{<sup>1</sup>H}, 205.9 ppm). <sup>31</sup>P{<sup>1</sup>H} spectra obtained in deuterated solvents were referenced internally to H<sub>3</sub>PO<sub>4</sub> at 0.00 ppm. <sup>31</sup>P{<sup>1</sup>H} spectra obtained in non-deuterated solvents were externally referenced to a sample of 85% H<sub>3</sub>PO<sub>4</sub>. Multiplicities are described as s (singlet), d (doublet), t (triplet), sept (septet), m (multiplet), br (broad) and ov (overlapping). X-ray diffraction measurements were made on a Bruker Kappa Axis Apex2 diffractometer at a temperature of 110 K. Infrared spectra were collected on solid samples using a PerkinElmer UATR TWO FTIR spectrometer or Bruker ALPHA II FTIR spectrometer. Elemental analysis was performed by Canadian Microanalytical Service Ltd. in Delta British Columbia. Charge-transfer Matrix Assisted Laser Desorption/Ionization mass spectrometry (MALDI) data were collected on an AB Sciex

5800 TOF/TOF mass spectrometer using pyrene as the matrix in a 20:1 molar ratio to complex. Solutions were prepared in DCM and spotted on a sample plate under an inert atmosphere and transferred to the instrument in a sealed Ziplock<sup>®</sup> bag. The instrument is equipped with a 349 nm OptiBeam On-Axis laser. The laser pulse rate was 400 Hz and data were collected in reflectron positive mode. Reflectron mode was externally calibrated at 50 ppm mass tolerance. Each mass spectrum was collected as a sum of 500 shots. Quantification of ethane was performed using an Agilent 7890a gas chromatogram with a flame ionization detector (GC-FID), fitted with HP-Plot/U column. Headspace gas chromatography – mass spectrometry (GC-MS) measurements to confirm ethane formation were obtained on a Shimadzu GCMS-QP2010 instrument, fitted with a HP-Plot/U column.

DFT calculations were performed using ORCA 4.0.1.2.<sup>44</sup> Gibbs energy corrections were determined using frequency analysis at the PBE/def2-SVP level. Structures were optimized using PBE0/def2-TZVP<sup>45</sup> with the D3 correction for dispersion with Becke-Johnson damping.<sup>46-47</sup> The solvation energy was calculated using the SMD model for benzene.<sup>48</sup>



**Figure 2.2.** General labeling scheme for the phosphine imine ligand **H[2-L1]**. This scheme will be used consistently for all compounds throughout the experimental section. In cases where  $H^3$  and  $C^3$  atoms are non-equivalent  $H^3$  and  $H^3$ ,  $C^3$  and  $C^3$  are used to distinguish between the two sites.

## 2.4.2 – Synthesis of PdCl(CH<sub>3</sub>)(H[2-L1]), **2-1**

PdCl(CH<sub>3</sub>)(COD) (100 mg, 0.377 mmol) and **H[2-L1]** (131 mg, 0.396 mmol) were weighed into a 20 mL vial. The combined reagents were dissolved in dry dichloromethane (4 mL). The pale-yellow solution was allowed to stir at room temperature for 1 h, resulting in a pale orange solution. The solvent was reduced to ca. 1 mL and 5 mL cold pentane was added to precipitate the product as an off-white solid. The remaining solvent was then decanted and **2-1** was washed with pentane (3 × 2 mL). Yield: 174 mg (94%). <sup>1</sup>H NMR (599 MHz, CD<sub>2</sub>Cl<sub>2</sub>): δ 7.80 (d, *J* = 8.3 Hz, 1H, *H*<sup>1</sup>), 7.58 – 7.51 (m, 7H, *H*<sup>5</sup> and P(Ph-*H*)), 7.46 (m, 4H, P(Ph-*H*)), 7.30 (dd, *J* = 7.3 Hz and 7.3 Hz, 1H, *H*<sup>6</sup>), 7.25 (dd, *J* = 7.9 Hz, <sup>3</sup>*J*<sub>HP</sub> = 4.5 Hz, 1H, *H*<sup>7</sup>), 7.21 (m, 1H, *H*<sup>4</sup>), 4.19 (sept, *J* = 7.8 Hz and 6.7 Hz, 1H, *H*<sup>2</sup>), 1.11 (d, *J* = 6.7 Hz, 6H, *H*<sup>3</sup>), 0.69 (d, <sup>3</sup>*J*<sub>HP</sub> = 2.8 Hz, 3H, Pd-CH<sub>3</sub>). <sup>13</sup>C{<sup>1</sup>H} NMR (151

MHz, CD<sub>2</sub>Cl<sub>2</sub>):  $\delta$  182.6 (C<sup>1</sup>), 157.0 (d, <sup>2</sup>J<sub>CP</sub> = 16.6 Hz, C<sup>9</sup>), 134.2 (d, <sup>3</sup>J<sub>CP</sub> = 12.7 Hz, P(Ph-C)), 133.6 (C<sup>5</sup>), 132.8 (C<sup>4</sup>), 131.8 (P(Ph-C)), 130.6 (d, <sup>1</sup>J<sub>CP</sub> = 46.0 Hz, C<sup>8</sup>), 129.4 (d, <sup>2</sup>J<sub>CP</sub> = 21.2 Hz, P(Ph-C)), 129.2 (d, <sup>1</sup>J<sub>CP</sub> = 53.3 Hz, P(Ph-C)), 128.7 (d, <sup>3</sup>J<sub>CP</sub> = 6.6 Hz, C<sup>6</sup>), 119.9 (d, <sup>2</sup>J<sub>CP</sub> = 8.0 Hz, C<sup>7</sup>), 34.7 (C<sup>2</sup>), 20.1 (C<sup>3</sup>), -1.7 (Pd-CH<sub>3</sub>). <sup>31</sup>P{<sup>1</sup>H} NMR (243 MHz, CD<sub>2</sub>Cl<sub>2</sub>):  $\delta$  36.2. ATR-FTIR (cm<sup>-1</sup>):  $\nu$  2964 (C<sub>sp<sup>3</sup></sub>-H), 1631 (C=C). MALDI MS (pyrene): *m/z* found 474.0, calcd. [2-1-CH<sub>3</sub>]<sup>+</sup> 474.0, [Pd(1)]<sup>+</sup> 437.1. Elem. Anal. for C<sub>23</sub>H<sub>25</sub>ClNPPd: calc'd. C 56.57, H 5.16, N 2.87; found C 56.17, H 4.99, N 2.84. Crystals suitable for single crystal X-ray diffraction were grown by layering a dichloromethane solution of **2-1** with hexanes.

### 2.4.3 – Synthesis of Pd(CH<sub>3</sub>)(L1), **2-2**, via deprotonation of **2-1**

A solution of LiHMDS (20 mg, 0.12 mmol) in fluorene (1 mL) was added dropwise to a suspension of **2-1** (50 mg, 0.10 mmol) in fluorobenzene (4 mL) in a 20 mL screw-top vial. The solution was stirred at room temperature for 10 min, during which time the colour changed from grey to bright yellow, to green, and finally orange. The resulting suspension was filtered through a glass microfiber plug to remove LiCl and the filtrate volume was reduced to 1 mL under vacuum. Cold pentane (6 mL) was added to precipitate the product as a yellow powder. The supernatant was then decanted and the resulting solid was washed with pentane (3 × 1 mL). Yield: 35 mg (75%). NOTE: The yield decreased if the scale was increased above 50 mg **2-1** due to the longer work-up time and the instability of **2-2** in the presence of either excess LiHMDS or H[HMDS]. <sup>1</sup>H NMR (599 MHz, C<sub>6</sub>D<sub>6</sub>):  $\delta$  7.89 – 7.80 (m, 4H, P(Ph-H)), 7.49 (dd, *J* = 11.6 Hz, 7.5 Hz, 4H, P(Ph-H)), 7.41 (dd, *J* = 8.4 Hz, 4.9 Hz, 2H, H<sup>5</sup>), 7.17 – 7.15 (m, 4H, P(Ph-H)), 7.12-7.07 (m, 2H, H<sup>6</sup>), 7.04 – 7.00 (m, 8H, P(Ph-H)), 6.98 – 6.95 (ov m, 4H, H<sup>4</sup>, H<sup>7</sup>), 6.64 – 6.56 (m, 2H, H<sup>1</sup>), 1.72 (s, 6H, H<sup>3</sup>), 1.45 (br s, FWHM = 169 Hz, 6H, H<sup>3</sup>), 0.51 (d, <sup>3</sup>J<sub>HP</sub> = 1.3 Hz, 6H, H<sup>1</sup>). <sup>13</sup>C{<sup>1</sup>H} NMR (151 MHz, C<sub>6</sub>D<sub>6</sub>):  $\delta$  166.6 (d, *J*<sub>CP</sub> = 19.7 Hz, C<sup>9</sup>), 141.5 (C<sup>1</sup>), 134.6 (d, *J*<sub>CP</sub> = 12.0 Hz, P(Ph-C)), 134.2 (d, *J*<sub>CP</sub> = 19.7 Hz, C<sup>8</sup>), 133.3 (d, *J*<sub>CP</sub> = 19.7 Hz, P(Ph-C)), 132.4 (C<sup>4</sup>), 131.4 (C<sup>5</sup>), 130.6 (P(Ph-C)), 129.7 (P(Ph-C)), 128.7 (d, *J*<sub>CP</sub> = 10.8 Hz, P(Ph-C)), 128.6 (d, *J*<sub>CP</sub> = 10.9 Hz, P(Ph-C)), 128.2 (C<sup>7</sup>), 120.2 (C<sup>6</sup>), 117.2 (C<sup>2</sup>) 23.8 (C<sup>3</sup>), 18.5 (C<sup>3</sup>), 1.26 (Pd-CH<sub>3</sub>). <sup>31</sup>P{<sup>1</sup>H} NMR (243 MHz, C<sub>6</sub>D<sub>6</sub>):  $\delta$  43.7. ATR-FTIR (cm<sup>-1</sup>):  $\nu$  2869 (C<sub>sp<sup>3</sup></sub>-H), 1098 (C-N). MALDI MS (pyrene): *m/z* found 435.01, calc. [2-2-CH<sub>3</sub>]<sup>+</sup> 435.05.

## 2.4.4 – Synthesis of **K[2-L1]**

A solution of **H[2-L1]** (112 mg 0.39 mmol) in THF (3 mL) was added to a suspension of KH (27 mg, 0.68 mmol) in THF (3 mL) and stirred for 3.5 h, or until the evolution of H<sub>2</sub> ceased. The solution was filtered through a glass microfiber plug to remove unreacted KH and the volume of the filtrate was reduced under vacuum to ca. 2 mL. Cold pentane (5 mL) was added with stirring to precipitate **K[2-L1]** as a yellow solid. The suspension was then filtered through a glass frit and the precipitate was washed with cold pentane (3 × 1 mL). Yield: 107 mg (86%). <sup>1</sup>H NMR (599 MHz, (CD<sub>3</sub>)<sub>2</sub>CO): δ 7.43 – 7.39 (m, 6H, P(Ph-*H*)), 7.37 – 7.31 (m, 4H, P(Ph-*H*)), 7.28 – 7.24 (m, 1H, *H*<sup>5</sup>), 6.92 – 6.88 (m, 1H, *H*<sup>6</sup>), 6.84 – 6.80 (m, 1H, *H*<sup>7</sup>), 6.68 – 6.65 (m, 1H, *H*<sup>4</sup>), 6.25 (s, 1H, *H*<sup>1</sup>), 1.66 (s, 3H, *H*<sup>3</sup>), 1.37 (s, 3H, *H*<sup>3'</sup>). <sup>13</sup>C{<sup>1</sup>H} NMR (151 MHz, (CD<sub>3</sub>)<sub>2</sub>CO) δ 148.0 (d, <sup>2</sup>*J*<sub>CP</sub> = 16.3 Hz, *C*<sup>9</sup>), 136.5 (d, *J*<sub>CP</sub> = 8.0 Hz, P(Ph-*C*)), 135.7 (d, <sup>2</sup>*J*<sub>CP</sub> = 5.3 Hz, *C*<sup>7</sup>), 134.9 (P(Ph-*C*)), 132.5 (*C*<sup>5</sup>), 130.4 (P(Ph-*C*)), 130.1 (d, <sup>2</sup>*J*<sub>CP</sub> = 7.1 Hz, P(Ph-*C*)), 122.3 (*C*<sup>1</sup>), 119.5 (*C*<sup>4</sup>), 112.3 (*C*<sup>8</sup>), 112.2 (*C*<sup>6</sup>), 111.0 (*C*<sup>2</sup>), 22.1 (*C*<sup>3</sup>), 16.4 (*C*<sup>3'</sup>). <sup>31</sup>P{<sup>1</sup>H} NMR (243 MHz, (CD<sub>3</sub>)<sub>2</sub>CO): δ – 21.5.

## 2.4.5 – Synthesis of Pd(CH<sub>3</sub>)(**L1**), **2-2**, via metalation of **K[2-L1]**

The ligand salt **K[2-L1]** (107 mg, 0.27 mmol) was suspended in fluorobenzene (3 mL) and added to a suspension of PdCl(CH<sub>3</sub>)(COD) (60 mg, 0.23 mmol) in fluorobenzene (5 mL) and allowed to stir for 30 min over which time the colour changed from grey, to yellow, to orange. The solution was then filtered through a glass microfiber plug to remove KCl, and the solvent volume was reduced to ca. 1.5 mL under vacuum. Cold pentane (5 mL) was added with stirring to precipitate **2-2** as a yellow powder. The mixture was then decanted and the powder was washed with cold pentane (3 × 1 mL). Yield: 85 mg (83%). <sup>1</sup>H and <sup>31</sup>P NMR spectroscopy data matched those for the product obtained by deprotonation of **2-1**.



## 2.4.6 – Synthesis of Pd(CH<sub>3</sub>)(py)(**2-L1**), **2-3**

In a glove box, **2-2** (20 mg, 0.044 mmol) was dissolved in pyridine (400  $\mu$ L) and stirred for 5 min to produce an orange solution. The solvent was then removed under reduced pressure, and the resulting orange solid was washed with cold pentane (3  $\times$  3 mL). Despite multiple washings, <sup>1</sup>H NMR analysis reveals that the resulting solid has 4% residual pyridine by mass, denoted by *py\** in the listed NMR spectroscopy data. Yield: 0.019 g (80%). <sup>1</sup>H NMR (599 MHz C<sub>6</sub>D<sub>6</sub>):  $\delta$  = 8.6 – 8.46 (br, 2H, *py\**), 8.36 – 8.20 (br, 2H, *py-H*) 7.94 – 7.88 (m, 4H, P(Ph-*H*)), 7.30 – 7.25 (m, 1H, *py-H*), 7.19 – 7.16 (m, 2H, *py-H*), 7.11 – 7.03 (m, 6H, P(Ph-*H*)), 7.03 – 6.95 (m, 2H, *py\**), 6.93 – 6.90 (m, 2H, *H*<sup>4</sup> and *H*<sup>7</sup>), 6.80 – 6.70 (m, 1H, *py\**). 6.48 – 6.41 (m, 2H, *H*<sup>5</sup> and *H*<sup>6</sup>) 6.35 (s, 1H, *H*<sup>1</sup>), 1.44 (ov, 6H, *H*<sup>3</sup> and *H*<sup>3'</sup>), 0.59 (d, <sup>3</sup>*J*<sub>HP</sub> = 2.1 Hz, 3H, Pd-CH<sub>3</sub>). <sup>13</sup>C{<sup>1</sup>H} NMR (151 MHz, C<sub>6</sub>D<sub>6</sub>): 165.8 (d, <sup>2</sup>*J*<sub>CP</sub> = 22.8 Hz, *C*<sup>9</sup>), 150.4 (*py\**), 135.3 (*py\**), 134.6 (s, *C*<sup>1</sup>), 134.2 – 133.7 (m, *C*<sup>8</sup> and P(Ph-*C*)) 133.8 (d, *J* = 24.2 Hz, P(Ph-*C*)) 133.7 (s, P(Ph-*C*)), 133.5 (d, <sup>2</sup>*J*<sub>CP</sub> = 1.51 Hz, *C*<sup>4</sup>), 130.2 (d, <sup>1</sup>*J*<sub>CP</sub> = 3.63 Hz, *C*<sup>7</sup>), 118.5 (s, *C*<sup>2</sup>), 114.1 (s, 113.5 (d, <sup>3</sup>*J*<sub>CP</sub> = 12.4 Hz, *C*<sup>5</sup>) 112.0 (d, <sup>2</sup>*J*<sub>CP</sub> = 8.2 Hz, *C*<sup>6</sup>) 22.1 (*C*<sup>3</sup>) 18.1 (*C*<sup>3'</sup>), -3.5 (d, <sup>2</sup>*J*<sub>CP</sub> = 6.3 Hz Pd-CH<sub>3</sub>). <sup>31</sup>P{<sup>1</sup>H} NMR (243 MHz):  $\delta$  = 45.5. ATR-FTIR (cm<sup>-1</sup>):  $\nu$  2867 (C<sub>sp</sub><sup>3</sup>-H), 1635 (C=N). MALDI MS (pyrene): *m/z* found 435.8, calc. [**2-3**-(CH<sub>3</sub>) -py]<sup>+</sup> 436.0.

## 2.4.7 – Synthesis of [Pd(**L1**)]<sub>2</sub>, **2-4** and Pd(**L1**)<sub>2</sub>, **2-5**

In a Schlenk flask, **2-2** (50 mg, 0.11 mmol) was dissolved in toluene (8.5 mL) and stirred at 70°C for 2 h under a flow of argon, over this time the colour of the solution changed from yellow to dark red. A small amount of black precipitate also formed on the walls of the flask. After 2 h, the solution was cooled, and filtered through a microfiber plug to remove any black solids and the solvent volume of the filtrate was reduced under vacuum to ca. 2 mL. With stirring, acetonitrile (ca. 4 mL) was added resulting in the precipitation of a red solid, the supernatant was decanted and the red solid was washed with cold pentane (3  $\times$  3 mL). Yield **2-4**: 12 mg (24%). <sup>1</sup>H NMR (400 MHz C<sub>6</sub>D<sub>6</sub>):  $\delta$  = 7.86 (m, 4H, P(Ph-*H*), 7.47 (m, 4H, P(Ph-*H*), 7.22 (m, 4H, P(Ph-*H*)), 7.07 (m, 8H, P(Ph-*H*), *H*<sup>6</sup>, *H*<sup>5</sup>) 6.97 (m, 2H, *H*<sup>7</sup>) 6.90 (m, 4H, P(Ph-*H*), 6.57 (m, 2H, *H*<sup>4</sup>), 5.97 (s, 2H, *H*<sup>1</sup>), 2.20 (s, 6H, *H*<sup>3</sup>), 1.58 (s, 6H, *H*<sup>3'</sup>). Due to the poor solubility of **2-4** in various deuterated solvents, a good quality <sup>13</sup>C{<sup>1</sup>H} NMR spectrum could not be obtained and as such the carbon assignments

were made based on  $^1\text{H}$ - $^{13}\text{C}$  HSQC and HMBC NMR data.  $^{13}\text{C}\{^1\text{H}\}$  NMR (151 MHz,  $\text{C}_6\text{D}_6$ ):  $\delta = 133.0$  (P(Ph-C)), 132.9 (P(Ph-C)), 129.7 ( $\text{C}^5$ ), 128.5 ( $\text{C}^6$ ), 128.4 (P(Ph-C)), 128.3 (P(Ph-C)), 117.5 ( $\text{C}^4$ ), 114.7 (P(Ph-C)), 109.0 ( $\text{C}^1$ ), 74.5 ( $\text{C}^2$ ), 27.8 ( $\text{C}^3$ ), 20.8 ( $\text{C}^3$ ).  $^{31}\text{P}\{^1\text{H}\}$  NMR (243 MHz,  $\text{C}_6\text{D}_6$ ):  $\delta = 15.0$ . ATR-FTIR ( $\text{cm}^{-1}$ ):  $\nu$  2917 ( $\text{C}_{\text{sp}^3}\text{-H}$ ), 1640 (C=C). In attempts to grow crystals of **2-2**, crystals of **2-4** suitable for X-ray diffraction were obtained by layering a benzene solution of **2-2** with pentane.

The solvent washes from the isolation of **2-4** were combined and passed through a microfiber plug to remove any minor impurities of **2-4**. The filtrate solvent was removed under reduced pressure to produce **2-5** as a dark green solid. The solid was then washed with cold pentane ( $3 \times 1$  mL). Yield **2-5**: 18 mg (36%).  $^1\text{H}$  NMR (599 MHz  $\text{C}_6\text{D}_6$ ):  $\delta = 7.23$  (m, 8H, P(Ph-*H*)), 7.13 – 7.08 (m, 2H, ( $H^5$ ), 6.87 (m, 6H, P(Ph-*H*)), 6.80 – 6.70 (ov, 12H,  $H^6$ ,  $H^7$ ,  $H^1$ , P(Ph-*H*)), 6.33 – 6.28 (m, 2H,  $H^4$ ), 1.92 (s, 6H,  $H^3$ ), 1.90 (s, 6H,  $H^3$ ).  $^{13}\text{C}\{^1\text{H}\}$  NMR (151 MHz,  $\text{C}_6\text{D}_6$ ):  $\delta = 165.8$ , ( $\text{C}^9$ ), 135.4 ( $\text{C}^1$ ), 134.1 (P(Ph-C)), 133.6 ( $\text{C}^8$ ), 133.5 (P(Ph-C)), 130.5 (P(Ph-C)), 128.5 (P(Ph-C)), 128.4 (P(Ph-C)), 118.0 ( $\text{C}^2$ ), 113.7 (P(Ph-C)), 113.4 ( $\text{C}^8$ ), 23.5 ( $\text{C}^3$ ), 18.9 ( $\text{C}^3$ ).  $^{31}\text{P}\{^1\text{H}\}$  NMR (243 MHz,  $\text{C}_6\text{D}_6$ ):  $\delta = 47.7$ . ATR-FTIR ( $\text{cm}^{-1}$ ):  $\nu$  2942 ( $\text{C}_{\text{sp}^3}\text{-H}$ ), 1652 (C=C). In attempts to grow crystals of **2-2**, crystals of **2-5** suitable for X-ray diffraction were obtained by vapour diffusion of ether into a saturated solution of **2-2** in acetonitrile at  $-35$  °C.

## 2.4.8 – Independent Synthesis of **2-5**

**K[2-L1]** (59 mg, 0.13 mmol) was suspended in benzene (3 mL) and added dropwise to a suspension of  $\text{PdCl}_2(\text{COD})$  (23 mg, 0.065 mmol) in benzene (1 mL), the vial containing the **K[2-L1]** suspension was rinsed with benzene ( $2 \times 1$  mL) and added to the reaction vial. The reaction was allowed to stir for 20 min and upon completion the dark orange solution was filtered through a microfiber plug to remove KCl. The solvent was removed under vacuum to produce **2-5** as a dark green solid. The green solid was washed with cold pentane ( $3 \times 1$  mL). Yield **2-5**: 40 mg (66%).  $^1\text{H}$  and  $^{31}\text{P}$  NMR spectroscopy data matched those for the product **2-5** obtained by heating **2-2**.

## 2.4.9 – GC-MS and GC-FID Procedures

### 2.4.9.1 – Procedure for Ethane Calibration by GC-FID

Three NMR tubes (**A-C**) containing benzene (500  $\mu\text{L}$ ) were sealed with a septum and parafilm. A known quantity of ethane (**A** = 81, **B** = 62, **C** = 42  $\mu\text{L}$ ) was added to each tube using a Gastight syringe (only used with gases) the tubes were allowed to equilibrate over an hour. With the syringe injected through the NMR tube septum of **A**, the syringe was primed (5 times) and 5  $\mu\text{L}$  of the headspace was removed and immediately injected into the GC-FID instrument. This procedure was repeated two more times on sample **A** and the area counts were averaged. Ethane gas (10  $\mu\text{L}$ ) was then injected into tube **A** via a Gastight syringe, and 5  $\mu\text{L}$  of the headspace was again added to the GC-FID instrument using the same injection procedure. The ethane addition (10  $\mu\text{L}$ ) and headspace analysis was repeated three times to give ethane added amounts of: 10, 20, 30 and 40  $\mu\text{L}$ . This analysis gave the data in Figure A.2, where volume amounts of added ethane were converted to molar amounts based on the ideal gas law. This procedure was repeated for tubes **B** and **C** to give the data in Figures A.3 and A.4, respectively. Since some portion of the ethane will be dissolved in solution, the observed area counts correspond only to headspace ethane, rather than total molar amount of ethane in the tube. Extrapolation from the generated plots (Figure A.5) gave the molar amount of ethane in found in the headspace after the initial ethane addition in **A-C**. Using the following equation, the % ethane in the headspace could be determined.

$$\% \text{ Ethane in Headspace} = \frac{\text{Extrapolated Molar Amount}}{\text{Known Molar Amount Added}} \times 100\% \quad (1)$$

The values for ethane present in the headspace were plotted relative to the known molar amount of ethane initially added to tubes **A-C** (Figure A.7). A good linear relationship was observed with an  $R^2$  value of 0.977. Using this plot the molar amount of ethane in a tube can be determined from the observed amount of ethane in the headspace. Note: Tubes of the same size and consistent solvent volumes were used in all cases.

## 2.4.9.2 – Procedure for Ethane Quantification by GC-FID for Heated Samples of 2-2

In an NMR tube, **2-2** (5.0 mg,  $8.9 \times 10^{-3}$  mmol) was dissolved in benzene (500  $\mu\text{L}$ ) and sealed with a septum and parafilm. The tube was then heated in an oil bath at 70 °C for 2.5 h. Upon completion the tubes were allowed to cool for 10 min and then a Gastight syringe was injected through the NMR tube septum, and the syringe was primed (5 times), 5  $\mu\text{L}$  of the headspace was removed and immediately injected into the GC-FID instrument. This procedure was repeated two more times and the area counts were averaged. Ethane gas (10  $\mu\text{L}$ ) was then injected into the NMR tube via a Gastight syringe and the system was allowed to equilibrate over 10 min, and 5  $\mu\text{L}$  of the headspace was again added to the GC-FID instrument using the same injection procedure. The ethane addition (10  $\mu\text{L}$ ) and headspace analysis was repeated three times to give total added ethane amounts of 10, 20, 30, and 40  $\mu\text{L}$ . This analysis gave the data in Figure A.6, where volume amounts of ethane were converted to molar amounts based on the ideal gas law. The area counts correspond to headspace ethane rather than total molar amounts of ethane in the tube. The linear relationship obtained from the calibration curve (Figure A.5) was used to determine the total molar amount of generated from heating **2-2**.

## 2.5 References

1. Adams, G. M.; Weller, A. S., *Coord. Chem. Rev.* **2018**, *355*, 150-172.
2. Drover, M. W.; Love, J. A.; Schafer, L. L., *Chem. Soc. Rev.* **2017**, *46*, 2913-2940.
3. Miller, A. J. M., *Dalton Trans.* **2017**, *46*, 11987-12000.
4. Braunstein, P.; *Angew. Chem. Int. Ed.* **2001**, *40*, 680-699.
5. Davies, D. L.; Macgregor, S. A.; McMullin, C. L., *Chem. Rev.* **2017**, *117*, 8649-8709.
6. Ackermann, L., *Chem. Rev.* **2011**, *111*, 1315-1345.
7. Camasso, N. M.; Sanford, M. S., *Science* **2015**, *347*, 1218-1220.
8. Bour, J. R.; Camasso, N. M.; Meucci, E. A.; Kampf, J. W.; Canty, A. J.; Sanford, M. S., *J. Am. Chem. Soc.* **2016**, *138*, 16105-16111.
9. Schultz, J. W.; Fuchigami, K.; Zheng, B.; Rath, N. P.; Mirica, L. M., *J. Am. Chem. Soc.* **2016**, *138*, 12928-12934.
10. Caro, C. F.; Lappert, M. F.; Merle, P. G., *Coord. Chem. Rev.* **2001**, *219-221*, 605-663.
11. Avent, A. G.; Hitchcock, P. B.; Lappert, M. F.; Sablong, R.; Severn, J. R., *Organometallics* **2004**, *23*, 2591-2600.
12. Stubbs, J. M.; Firth, K. F.; Bridge, B. J.; Berger, K. J.; Hazlehurst, R. J.; Boyle, P. D.; Blacquiere, J. M., *Dalton Trans.* **2017**, *46*, 647-650.
13. Yang, L.; Powell, D. R.; Houser, R. P., *Dalton Trans.* **2007**, (9), 955-964.

14. Steiner, T., *Angew. Chem. Int. Ed.* **2002**, *41*, 48-76.
15. Camp, A. M.; Kita, M. R.; Grajeda, J.; White, P. S.; Dickie, D. A.; Miller, A. J. M., *Inorg. Chem.* **2017**, *56*, 11141-11150.
16. Baranac-Stojanovic, M., *RSC Adv.* **2014**, *4*, 308-321.
17. Zhou, X.; Lau, K.-C.; Petro, B. J.; Jordan, R. F., *Organometallics* **2014**, *33*, 7209-7214.
18. Contrella, N. D.; Sampson, J. R.; Jordan, R. F., *Organometallics* **2014**, *33*, 3546-3555.
19. Kochi, T.; Noda, S.; Yoshimura, K.; Nozaki, K., *J. Am. Chem. Soc.* **2007**, *129*, 8948-8949.
20. Wambach, T. C.; Fryzuk, M. D., *Inorg. Chem.* **2015**, *54*, 5888-5896.
21. Friedrich, A.; Drees, M.; Käss, M.; Herdtweck, E.; Schneider, S., *Inorg. Chem.* **2010**, *49*, 5482-5494.
22. Bondi, A., *J. Phys. Chem.* **1964**, *68*, 441-451.
23. Bercaw, J. E.; Durrell, A. C.; Gray, H. B.; Green, J. C.; Hazari, N.; Labinger, J. A.; Winkler, J. R., *Inorg. Chem.* **2010**, *49*, 1801-1810.
24. Khan, M. A.; McAlees, A. J., *Inorg. Chim. Acta* **1985**, *104*, 109-114.
25. Patra, S. G.; Shee, N. K.; Drew, M. G. B.; Datta, D., *New J. Chem.* **2017**, *41*, 7384-7391.
26. Yamaguchi, Y.; Yamanishi, K.; Kondo, M.; Tsukada, N., *Organometallics* **2013**, *32*, 4837-4842.
27. Walensky, J. R.; Fafard, C. M.; Guo, C.; Brammell, C. M.; Foxman, B. M.; Hall, M. B.; Ozerov, O. V., *Inorg. Chem.* **2013**, *52*, 2317-2322.
28. Hazari, N.; Hruszkewycz, D. P., *Chem. Soc. Rev.* **2016**, *45*, 2871-2899.
29. Murahashi, T.; Kurosawa, H., *Coord. Chem. Rev.* **2002**, *231*, 207-228.
30. Fafard, C. M.; Adhikari, D.; Foxman, B. M.; Mindiola, D. J.; Ozerov, O. V., *J. Am. Chem. Soc.* **2007**, *129*, 10318-10319.
31. Lotz, M. D.; Remy, M. S.; Lao, D. B.; Ariafard, A.; Yates, B. F.; Canty, A. J.; Mayer, J. M.; Sanford, M. S., *J. Am. Chem. Soc.* **2014**, *136*, 8237-8242.
32. Sberegaeva, A. V.; Zavalij, P. Y.; Vedernikov, A. N., *J. Am. Chem. Soc.* **2016**, *138*, 1446-1455.
33. Inhibition of reactivity with TEMPO<sup>•</sup> is not conclusive evidence for a radical mechanism since competitive reaction of TEMPO<sup>•</sup> with M-H compounds is also known.<sup>34</sup>
34. Albéniz, A. C.; Espinet, P.; López-Fernández, R.; Sen, A., *J. Am. Chem. Soc.* **2002**, *124*, 11278-11279.
35. Hayashi, Y.; Nakamura, Y.; Isobe, K., *J. Chem. Soc., Chem. Commun.* **1988**, (5), 403-404.
36. Rudenko, A. E.; Clayman, N. E.; Walker, K. L.; Maclaren, J. K.; Zimmerman, P. M.; Waymouth, R. M., *J. Am. Chem. Soc.* **2018**, *140*, 11408-11415.
37. D. Fryzuk, M.; K. B. Clentsmith, G.; J. Rettig, S., *J. Chem. Soc., Dalton Trans.* **1998**, (12), 2007-2016.
38. A kinetic study<sup>39</sup> of Pd catalyzed aerobic coupling of arenes supports a mechanism involving transmetalation between two Pd(II)Ar compounds to give a Pd(II)ArAr' species that undergoes reductive elimination.
39. Wang, D.; Izawa, Y.; Stahl, S. S., *J. Am. Chem. Soc.* **2014**, *136*, 9914-9917.
40. Chen, M.; Chen, C., *Angew. Chem. Int. Ed.* **2018**, *57*, 3094-3098.
41. Wiedermann, J.; Mereiter, K.; Kirchner, K., *J. Mol. Catal. A: Chem.* **2006**, *257*, 67-72.
42. Salo, E. V.; Guan, Z., *Organometallics* **2003**, *22*, 5033-5046.
43. Stubbs, J. M.; Firth, K. F.; Bridge, B. J.; Berger, K. J.; Hazlehurst, R. J.; Boyle, P. D.; Blacquiere, J. M., *Dalton Trans.* **2017**, *46*, 647-650.
44. Neese, F., *Wiley Interdiscip. Rev. Comput. Mol. Sci.* **2011**, *2*, 73-78.

45. Schäfer, A.; Huber, C.; Ahlrichs, R., *J. Chem. Phys.* **1994**, *100*, 5829-5835.
46. Grimme, S.; Ehrlich, S.; Goerigk, L., *J. Comput. Chem.* **2011**, *32*, 1456-1465.
47. Otero-de-la-Roza, A.; Johnson, E. R., *J. Chem. Phys.* **2013**, *138*, 204109.
48. Marenich, A. V.; Cramer, C. J.; Truhlar, D. G., *J. Phys. Chem. B* **2009**, *113*, 6378-6396.

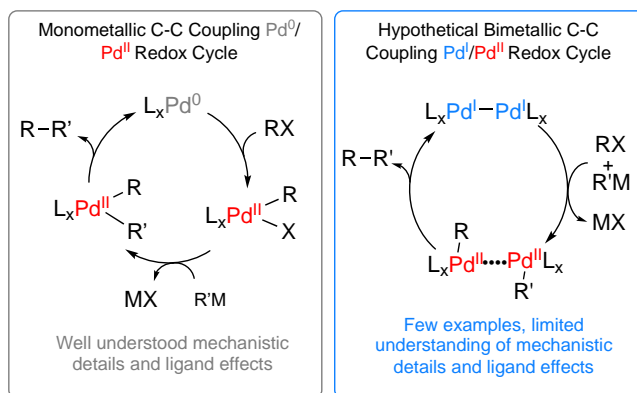
## 3.0 Changes in Ligand Coordination Mode Induce Bimetallic C-C Coupling Pathways

Carbon-carbon coupling is one of the most powerful tools in the organic synthesis arsenal. Known methodologies primarily exploit monometallic Pd<sup>0</sup>/Pd<sup>II</sup> catalytic mechanisms to give new C-C bonds. Bimetallic C-C coupling mechanisms that involve a Pd<sup>I</sup>/Pd<sup>II</sup> redox cycle, remain underexplored. Thus, a detailed mechanistic understanding is imperative for the development of new bimetallic catalysts. Previously, a Pd<sup>II</sup>-Me dimer (**3-1**) supported by **3-L1**, which has phosphine and 1-AzA donor groups, underwent reductive elimination to give ethane, a Pd<sup>I</sup> dimer, a Pd<sup>II</sup> monometallic complex, and Pd black. Herein, a comprehensive experimental and computational study of the reactivity of **3-1** is presented, which reveals that the versatile coordination chemistry of **3-L1** promotes bimetallic C-C bond formation. The phosphine 1-AzA ligand adopts various bridging modes to maintain the bimetallic structure throughout the C-C bond forming mechanism, which involves intramolecular methyl transfer and 1,1-reductive elimination from one of the palladium atoms. The minor byproduct, methane, likely forms through a monometallic intermediate that is sensitive to solvent C-H activation. Overall, the capacity of **3-L1** to adopt different coordination modes promotes the bimetallic C-C coupling channel through pathways that are unattainable with statically coordinated ligands.

### 3.1 Introduction

Palladium-catalyzed C-C bond-forming reactions have revolutionized synthetic chemistry and have been broadly adopted in pharmaceutical manufacturing.<sup>1-7</sup> The vast majority of Pd catalyzed reactions follow the same general mechanism that involves redox cycling of a monometallic catalyst between Pd<sup>0</sup> and Pd<sup>II</sup> (Scheme 3.1, left).<sup>8</sup> In contrast, there is a relative dearth of examples that involve redox cycling of a bimetallic catalyst between Pd<sup>I</sup> and Pd<sup>II</sup> (*i.e.* Scheme 3.1, right). While Pd<sup>I</sup> complexes are well established as *off-cycle* precursors to Pd<sup>0</sup> or as decomposition products,<sup>9, 10</sup> the first example of catalysis involving *on-cycle* bimetallic Pd<sup>I</sup> and Pd<sup>II</sup> complexes was shown for halide exchange of aryl iodide to aryl bromide.<sup>11, 12</sup> The dinuclear catalyst [Pd<sup>I</sup>( $\mu$ -X)Pt-Bu<sub>3</sub>]<sub>2</sub> has since been used extensively,<sup>13</sup> including in C-E (E = S, Se) bond formation that also follows a bimetallic mechanism.<sup>14-16</sup> Computational studies with other palladium complexes also support bimetallic mechanisms for pyrrole formation,<sup>17</sup> and alkene

isomerization<sup>18</sup> reactions. In the context of C-C coupling catalysis, only a few examples are known in which a bimetallic mechanism is postulated, and little mechanistic detail has been revealed.<sup>19-22</sup> Recently, bimetallic Pd<sup>I</sup> and Pd<sup>II</sup> complexes supported by bridging 2-phosphinoimidazole ligands were identified as active catalysts for  $\alpha$ -arylation to give naphthalene derivatives.<sup>22</sup> Computations supported a bimetallic mechanism with redox cycling between Pd<sup>II</sup> and Pd<sup>III</sup> or Pd<sup>IV</sup> and Ar-I oxidative addition occurred at a single Pd atom within the bimetallic framework. Of note, similar higher valent Pd<sup>II</sup>/Pd<sup>III</sup> or Pd<sup>II</sup>/Pd<sup>IV</sup> bimetallic catalytic routes are established for C-X<sup>23</sup> or C-C<sup>24, 25</sup> bond formations. Further elaboration of mechanistic understanding of bimetallic Pd<sup>I</sup>/Pd<sup>II</sup> C-C bond formation (e.g. Scheme 3.1, right), including the influence of ligand structure on reactivity, would greatly facilitate the development of the catalytic methodology.

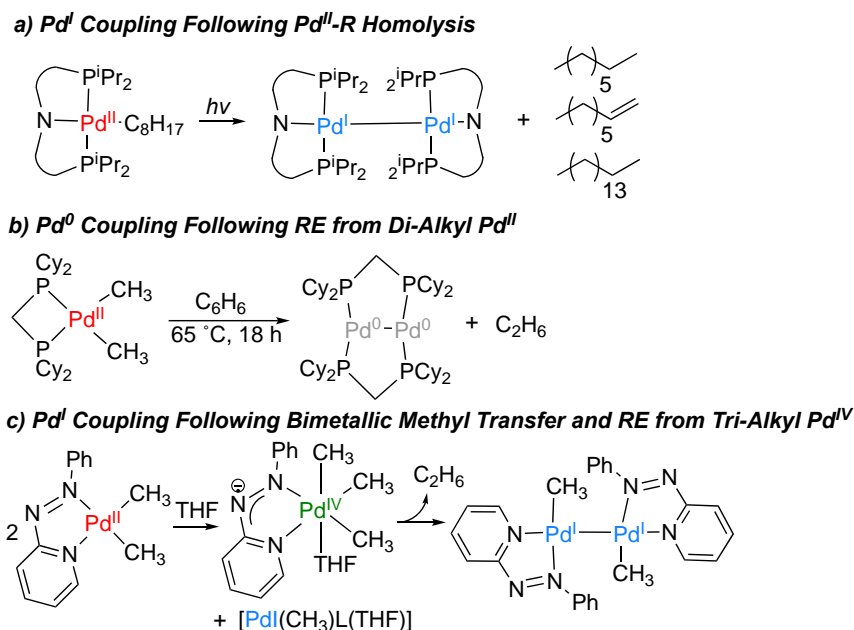


**Scheme 3.1.** General Mechanisms for Monometallic (left) and Bimetallic (right) Palladium Catalyzed C-C Bond Formation.

Reactivity of model compounds for individual reaction steps is a powerful means to gain mechanistic insight. Specifically, Pd<sup>II</sup>-R complexes with simple alkyl ligands have provided fundamental insight into the diverse mechanisms for C-C bond formation. While a number of bimetallic palladium products have been characterized, most mechanisms do not involve bimetallic intermediates for the C-C reductive elimination step. For example, bimetallic Pd<sup>I</sup> products are formed after light mediated homolysis of a Pd<sup>II</sup>-R bond of a monometallic precursor (Scheme 3.2a).<sup>26</sup> Similar coupling of the metal-based reductive elimination products can occur from Pd<sup>II</sup> dialkyl complexes following well-established monometallic 1,1-reductive elimination (Scheme 3.2b).<sup>27</sup> The resultant Pd<sup>0</sup> dimers are favoured if an appropriate bridging ligand, such as bis(dicyclohexylphosphine)methane, is employed.<sup>28</sup> Bimetallic intermediates have also been implicated in methyl transfer steps in oxidation-induced C-C bond formation.<sup>29-31</sup> Oxidation of mono or dimethyl Pd<sup>II</sup> by an exogenous oxidant or redox non-innocent ligand, induces



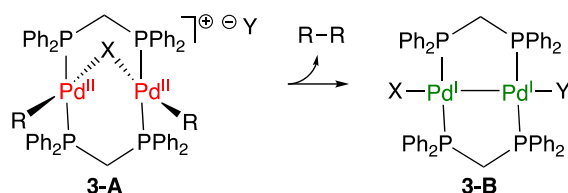
intermolecular methyl transfer between two monometallic compounds (*e.g.*, Scheme 3.2c for redox non-innocent ligand).<sup>29, 30, 31</sup> In these cases, methyl transfer involves a linear arrangement of Pd-CH<sub>3</sub>-Pd, which leads to formation of a high-valent Pd<sup>IV</sup> monometallic intermediate. Classic 1,1-reductive elimination then releases the organic product. In the case of the redox-active ligand, a Pd<sup>I</sup> dimer is formed after ligand oxidation and complex dimerization.



**Scheme 3.2.** Formation of Bimetallic Pd Products following C-C Bond Formation from Monometallic Precursors.

Only a few examples are known in which both alkyl transfer and C-C reductive elimination occur within a bimetallic palladium structure. The A-frame Pd<sup>II</sup>-R dimers, **3-A**, (R = Me, Bn, Ph) undergo C-C reductive elimination to give a Pd<sup>I</sup> dimer, **3-B** (Scheme 3.3).<sup>32, 33</sup> Notably, the narrow bite angle bis(diphenylphosphino)methane (dppm) ligand effectively stabilizes both the Pd<sup>II</sup> and Pd<sup>I</sup> bimetallic structures. Experimental mechanistic studies strongly indicated that reductive elimination proceeded via a bimetallic complex. Molecular orbital symmetry precludes a 1,2-elimination mechanism that involves a 4-centred Pd<sub>2</sub>C<sub>2</sub> transition state.<sup>34</sup> Rather, a mechanism was postulated that involves transfer of R via a bridging interaction to give a dimer with a PdR<sub>2</sub> fragment, which would undergo a classic 1,1-reductive elimination.<sup>32, 33</sup> However, the exact nature of such an intermediate, details about the methyl transfer step, the involvement of metal-metal synergy<sup>35</sup> or optimal ligand characteristics were not investigated. The methyl substituted A-frame

dimer (**3-A** where R = Me, X = Cl) gives low yields of ethane, and methane was observed as a major by-product.<sup>33</sup> Thus, the dppm ligand is not optimal to reliably promote C-C bond formation.

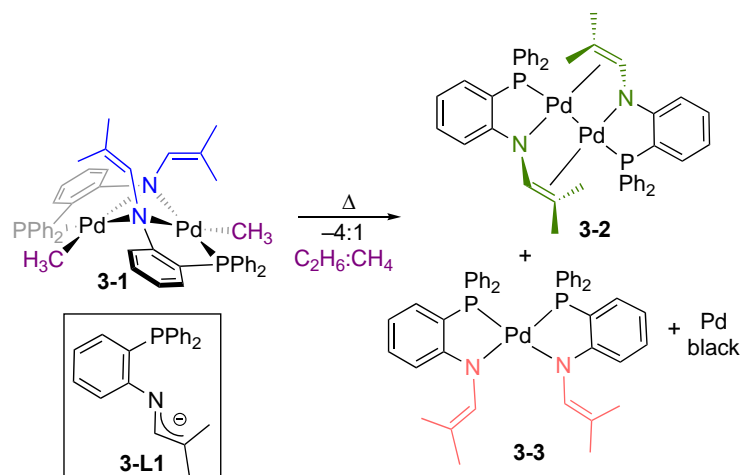


**Scheme 3.3.** Bimetallic Alkyl Transfer and Reductive Elimination.

Recently, we prepared a Pd<sup>II</sup>-methyl dimer **3-1** that bears the phosphine 1-AzA ligand, **3-L1** (Scheme 3.4).<sup>36</sup> The bridging amide nitrogen atoms enforce a bent shape to **3-1**, which is reminiscent of the A-frame dimers (**3-A**). On heating, **3-1** releases ethane without any external oxidant and the ligand **3-L1** has no apparent capacity for redox non-innocence. These observations suggest that the C-C bond forming mechanism is possibly related to the reactivity observed with the bimetallic Pd complexes, **3-A**. Reductive elimination from **3-1** is remarkably well behaved, giving high selectivity for C-C bond formation to give ethane (ca. 80%) over methane (*cf.* for **3-A** *ca.* 50% ethane; R = Me, X = Cl). This suggests that **3-A** has advantageous structural characteristics, possibly due to diverse coordination chemistry of **3-L1**. In response to the steric and electronic demands of the metal, the 1-AzA fragment in **3-L1** switches from  $\mu$ -N in **3-1** to  $\mu$ - $[\eta^2\text{-CC};\kappa^1\text{-N}]$  and  $\kappa^1\text{-N}$  modes in products **3-2** and **3-3**, respectively, which indicates that **3-L1** is structurally responsive.<sup>37</sup> We previously hypothesized that the capacity of **3-L1** to adopt these different coordination modes may *induce* C-C bond formation. This premise has been exploited extensively for decades with hemilabile ligands that promote substitution chemistry and other organometallic reactions *via* changes in ligand denticity.<sup>37-41</sup> Indeed, one of the viable catalytic pathways for bimetallic  $\alpha$ -arylation, noted above, involves a switch between  $\kappa^2\text{-P,N}$  and  $\kappa^1\text{-P}$  2-phosphinoimidazole coordination.<sup>22</sup>

The present combined experimental and computational study establishes that the structurally-responsive behaviour of the phosphine 1-AzA ligand (**3-L1**) is critical to promote bimetallic methyl transfer and C-C reductive elimination. Elucidation of optimal pathways was evaluated computationally using the Growing String Method (GSM)<sup>42-44</sup> developed by Paul Zimmerman (further details in S.I.). The computational analysis shows that the most viable mechanistic pathways are not accessible if static ligand coordination is enforced. In addition, the origin for methane as the minor by-product is identified. The presented insights reveal critical

considerations to favour productive C-C coupling pathways, which could be exploited in a bimetallic catalytic cycle involving Pd<sup>II</sup> and Pd<sup>I</sup> intermediates (e.g., **3-1** and **3-2**, respectively). Namely, a key ligand feature is the ability to readily adopt different coordination modes to maintain a bimetallic motif, which is needed to promote intramolecular methyl transfer and reductive elimination with incipient metal-metal bonding.



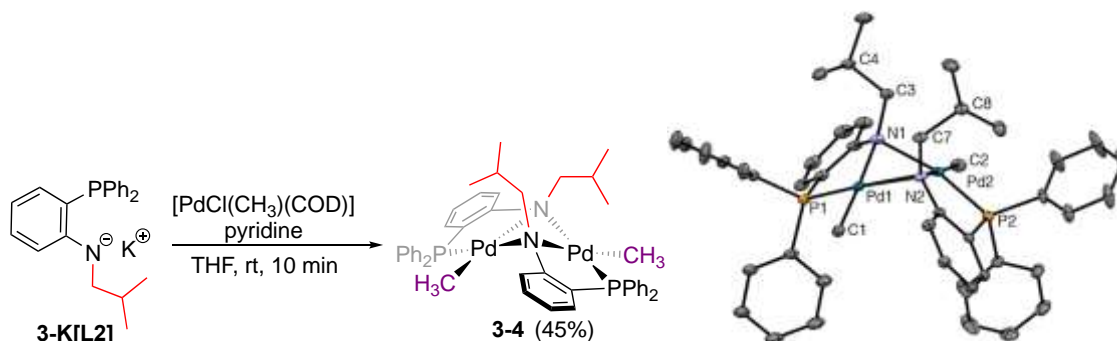
**Scheme 3.4.** C-C reductive elimination from a Pd<sup>II</sup> dimer (**3-1**), showing changes in ligand coordination mode. Yields of **3-2** and **3-3** are 35 and 50%, respectively based on starting ligand.

## 3.2 Results

### 3.2.1 Non-Structurally Responsive Phosphine-Amido Complex

During reductive elimination of ethane from **3-1**, the 1-azaallyl fragment of **3-L1** changes from  $\mu$ -N coordination mode in **3-1** to  $\mu$ -[ $\kappa^1$ -N,  $\eta^2$ -CC] and  $\kappa^1$ -N for products **3-2** and **3-3**, respectively, suggesting that changes in ligand coordination mode may *induce* C-C bond formation. We sought to probe this hypothesis by investigating the reactivity of a complex bearing **3-L2**, the reduced analogue of **3-L1**. During C-C bond formation, the ligand structure of **3-L2** would preclude formation of **3-2**, in which the alkene fragment of **3-L1** is needed to bridge the metal centres. We prepared the phosphine amido ligand **K[3-L2]** through the reduction of **H(3-L1)** with LiAlH<sub>4</sub> and deprotonation with KH. The coordination of **3-L2** to [PdCl(CH<sub>3</sub>)(COD)] was attempted at room temperature and at -30 °C. While complete consumption of **K[3-L2]** was observed by <sup>31</sup>P{<sup>1</sup>H} and <sup>1</sup>H NMR spectroscopy, the reaction consistently generated a myriad of new products. Complex **3-4** was instead prepared in 45% yield following a reaction between **K[3-L2]** and [PdCl(CH<sub>3</sub>)(COD)] in the presence of 1.3 equivalents of pyridine (Scheme 3.5). The <sup>1</sup>H

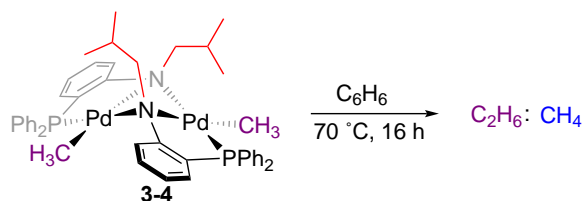
NMR spectrum of **3-4** has no signals for coordinated pyridine that would be expected for a monometallic pyridine adduct. N-H signals are absent from both the  $^1\text{H}$  NMR and the IR spectra, as expected for retention of the amido functionality. A doublet is observed in the  $^1\text{H}$  NMR spectrum for the Pd-bound methyl that has a small coupling constant ( $^3J_{\text{H-P}} = 1.8$  Hz), which is consistent with a *cis* orientation to the phosphine donor. The structure of **3-4** as a dimer was confirmed by single-crystal X-ray diffraction (Scheme 3.5). The two  $\text{Pd}^{\text{II}}$  centres adopt a distorted<sup>45</sup> square planar geometry ( $\text{Pd}(1) \tau^4 = 0.11$ ;  $\text{Pd}(2) \tau^4 = 0.13$ ), with the anionic nitrogen atoms bridging the two metal centres. Similar inequivalence of the two Pd centres was also observed in the solid-state structure of **3-1**. The  $\text{Pd}(1)\text{-N}(1)\text{-Pd}(2)$  and  $\text{Pd}(1)\text{-N}(2)\text{-Pd}(2)$  angles are  $79.44(7)$  and  $80.07(6)^\circ$ , respectively, which are ca.  $2^\circ$  larger than the analogous angles in **3-1**. The angle between the square planes of  $118.71^\circ$  is ca.  $10^\circ$  wider than that for **3-1**. Despite these minor structural deviations, complex **3-4** with an iso-butyl amido moiety is a close analogue to **3-1** with a 1-AzA group.



**Scheme 3.5.** Synthesis of Phosphine-Amido Complex, **3-4**, (left) and thermal displacement plot of **3-4** (right). Displacement ellipsoid (50% probability) plot of **3-4**. All hydrogen atoms, and a THF molecule that co-crystallized in the unit cell have been omitted for clarity.

Heating a solution of **3-4** in benzene at  $70^\circ\text{C}$  for 16 h afforded several new palladium products as judged by  $^{31}\text{P}\{^1\text{H}\}$  NMR spectroscopy. The variety of products observed from **3-4** is in contrast to reaction with **3-1**, which gives only **3-2**, **3-3** and Pd black as the metal-based products. Analysis of the headspace by GC-FID following heating of **3-4** revealed that ethane and methane were produced in 20 and 80% yields, respectively (1:4 ratio), (Scheme 3.6). This is the inverse selectivity from **3-1** that gives 76 and 24% yields of ethane and methane, respectively. The change in selectivity could reflect the inability of **3-L2** to adopt a  $\pi$ -type coordination to palladium that is essential for C-C reductive elimination. Alternatively, the alkyl substituent of the amido fragment may be more susceptible to C-H activation chemistry that leads to competitive methane formation.

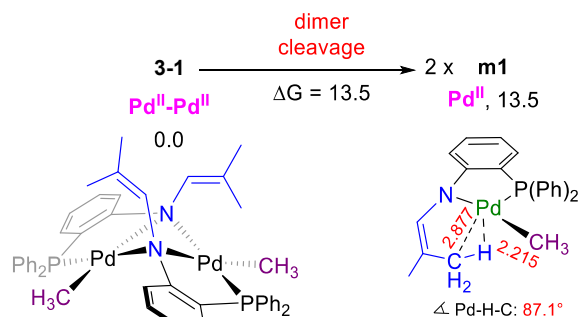
Regardless, the product distribution of **3-4** vs. **3-1** shows that the 1-AzA fragment in the latter favours C-C reductive elimination.



**Scheme 3.6.** Thermolysis of Phosphine-Amido Complex, **3-4**.

### 3.2.2 Assessment of a Monomer-Dimer Equilibrium with **3-1**

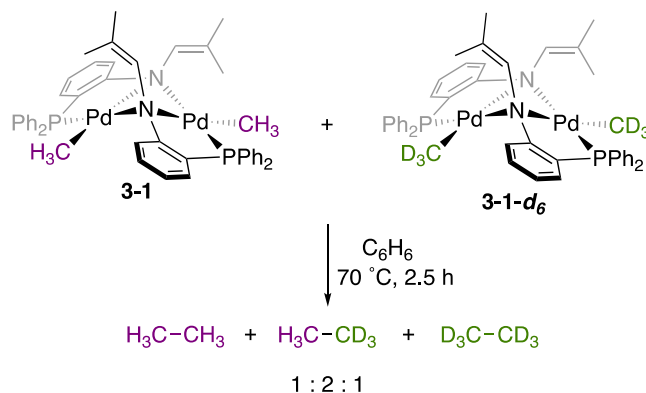
We demonstrated previously that **3-1** exists as a dimer both in the solid- and solution-states.<sup>36</sup> However, reaction chemistry of **3-1** may involve an equilibrium with a three-coordinate monomer (**m1**) (Scheme 3.7). Computed relative energies verifies that the monomers **m1** are uphill from **3-1** by 13.5 kcal/mol. This corresponds to a  $K_d$  of  $4.3 \times 10^{-3}$  M at 25 °C, which is consistent with the experimental observation that the dimer **3-1** is strongly favoured in solution. The three-coordinate metal centre in **m1** contains an agostic interaction to a methyl group of the 1-AzA group of **3-L1**, with a short Pd-H(CH<sub>3</sub>) distance (2.215 Å) and a small Pd-H-C bond angle (87.1°). This relatively weak ligation partly compensates for the missing Pd-N bond of **3-1** that must break to form the monomers.



**Scheme 3.7.** Computed dissociation of dimer **3-1** to monomers **m1**. Free energies are given in kcal/mol.

To determine if **3-1** stays intact or separates into monomers prior to reductive elimination, a crossover experiment was targeted using a 1:1 mixture of **3-1** and **3-1-d<sub>6</sub>**. First, the labeled compound **3-1-d<sub>6</sub>** was prepared in 76% yield by a reaction between **K[3-L1]** and [PdCl(CD<sub>3</sub>)(COD)]. A 1:1 mixture of **3-1** and **3-1-d<sub>6</sub>** was heated at 70 °C for 2.5 h (Scheme 3.8), following which the solution was analyzed by <sup>1</sup>H NMR spectroscopy and the headspace was

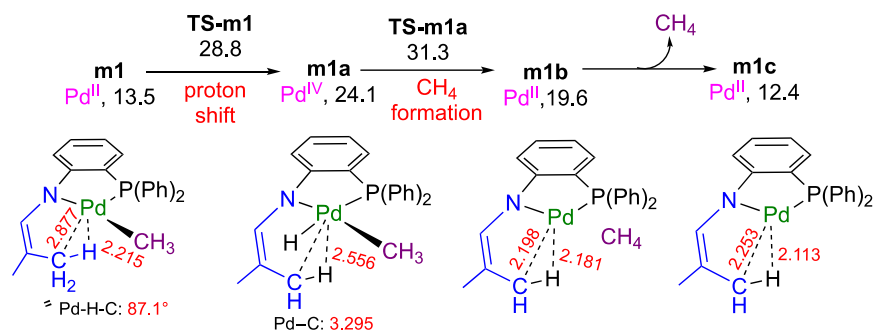
analyzed by GC-MS (Figures B.10 and B.11, respectively). The  $^1\text{H}$  NMR spectrum revealed the formation of  $\text{C}_2\text{H}_6$  and  $\text{CH}_3\text{CD}_3$  in a 1:2 molar ratio. Formation of  $\text{C}_2\text{D}_6$  was confirmed by GC-MS, which showed an approximate 1:2:1 molar ratio of  $\text{C}_2\text{H}_6$ ,  $\text{H}_3\text{C-CD}_3$  and  $\text{C}_2\text{D}_6$ . This mixture of ethane isotopologues indicates that the dimer, **3-1/3-1- $d_6$** , does cleave prior to reductive elimination. However, these experiments do not distinguish between a monomer/dimer pre-equilibrium and mechanisms that involve monomer or dimer structures *en route* to palladium products **3-2** and **3-3**.



**Scheme 3.8.** Thermolysis of **3-1** and **3-1- $d_6$**  for H/D Crossover Test.

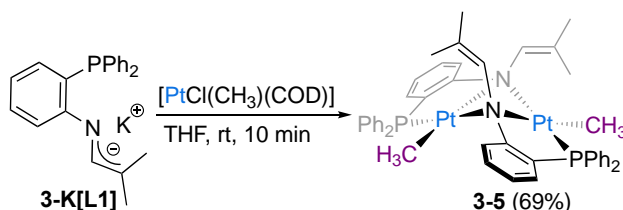
### 3.2.3 Formation of the Methane as a By-Product

The thermolysis of **3-1** gives ethane as the major product, but methane is observed in ca. 20% yield. We sought to understand how this by-product forms in order to guide future ligand redesign strategies. The viability of monomer **m1** was established above (Section 3.2.2) through experiments and computations. The monomer bears a C-H agostic bond to a methyl group of **3-L1**, and such interactions typically precede C-H bond cleavage by oxidative addition.<sup>46</sup> The route to form methane from **m1** is proposed to involve oxidative addition of the agostic C-H bond to give a square planar  $\text{Pd}^{\text{IV}}$ -hydride intermediate **m1a** through a proton shift transition state (**TS-m1**) with free energy of 28.8 kcal/mol (Scheme 3.9). Reductive elimination from the Pd-hydride **m1a** releases a methane molecule with free energy of 31.3 kcal/mol for the transition state (**TS-m1a**). An alternate concerted metallation-deprotonation route to C-H activation is possible, but the oxidative addition/reductive elimination sequence described here is more energetically viable by 3 kcal/mol (Scheme B.4). These calculations suggest that C-H activation in monomer **m1** could be the source of the observed methane by-product.



**Scheme 3.9.** Formation of methane from monomer **m1**. Free energies are relative to dimer **3-1** and are given in kcal/mol.

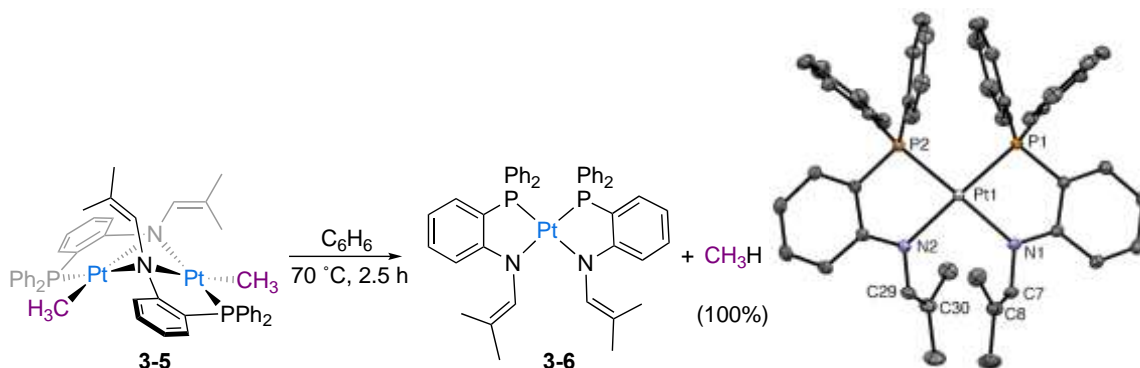
The high energy of the Pd<sup>IV</sup>-hydride intermediate **m1a**, relative to other compounds in the sequence to give methane, suggests attempts toward independent synthesis would be unsuccessful. Additionally, we noted previously that no intermediates were observed during the reductive elimination of **3-1**.<sup>36</sup> Owing to the generally higher M-L bond strengths for Pt as compared to Pd, the former can often act as more tractable versions of the less stable Pd analogues and can offer a means to isolate or observe relevant intermediates. Thus, we treated [PtCl(CH<sub>3</sub>)(COD)] with **K[3-L1]** to afford **3-5**, the Pt<sup>II</sup> analogue of **3-1** (Scheme 3.10). The <sup>31</sup>P{<sup>1</sup>H} NMR spectrum of **3-5** revealed a signal for coordinated **3-L1** at δ<sub>P</sub> = 20.2 with satellites (<sup>1</sup>J<sub>Pt-P</sub> = 4399 Hz) concordant with one-bond coupling to platinum. The carbon centre of the 1-AzA group that is *beta* to the amide nitrogen (C<sup>2</sup>) was found at 120.3 ppm. This strongly indicates that the alkene portion of **3-L1** is not involved in binding to the metal centre, which would give a significantly more upfield C<sup>2</sup> shift of ca. 40-75 ppm (Table B.1).<sup>36, 47</sup> Rather, the chemical shift is only ca. 3 ppm downfield from the analogous signal in **3-1** that has a μ-N binding mode of the 1-AzA fragment. A *cis* arrangement of the phosphine and methyl is supported by a small H-P coupling constant (<sup>3</sup>J<sub>H-P</sub> = 1.9 Hz) observed from the methyl signal in the <sup>1</sup>H NMR spectrum. Collectively, this data supports that **3-5** is a direct analogue of the Pd<sup>II</sup> dimer **3-1**.



**Scheme 3.10.** Preparation of Pt<sup>II</sup> Dimer, **3-5**.

Heating a benzene solution of **3-5** at 70 °C for 2.5 h (Scheme 3.11) gave quantitative conversion to **3-6**, which is observed in the <sup>31</sup>P{<sup>1</sup>H} NMR spectrum as a singlet at δ<sub>P</sub> = 28.0 with

satellites to platinum ( $^1J_{Pt-P} = 5208$  Hz). Complex **3-6** was isolated in a 54% yield. The beta carbon of the 1-AzA fragment ( $C^2$ ) is shifted ca. 2 ppm upfield to  $\delta_C = 119.9$ , which indicates that the 1-AzA group coordinates to platinum only through the nitrogen atom. The  $^1H$  NMR spectrum of **3-6** no longer exhibits a signal corresponding to a platinum-bound methyl. These spectroscopic features are consistent with the assignment of **3-6** as the Pt analogue of the Pd<sup>II</sup> complex **3-3**. The  $\kappa^2$ -PN coordination mode of **3-L1** and *cis* arrangement of the phosphines was confirmed by single-crystal X-ray diffraction of **3-6**. Similar to **3-3**, **3-6** adopts a distorted square planar geometry ( $\tau_4 = 0.15$ ) due to steric repulsion from the 1-AzA groups and the phenyl substituents of the phosphines. The only alkane product observed by GC-FID or  $^1H$  NMR spectroscopy was  $CH_4$ . These observations suggest that the platinum dimer **3-6** undergoes C-H activation rather than  $Csp^3-Csp^3$  reductive elimination to give ethane.

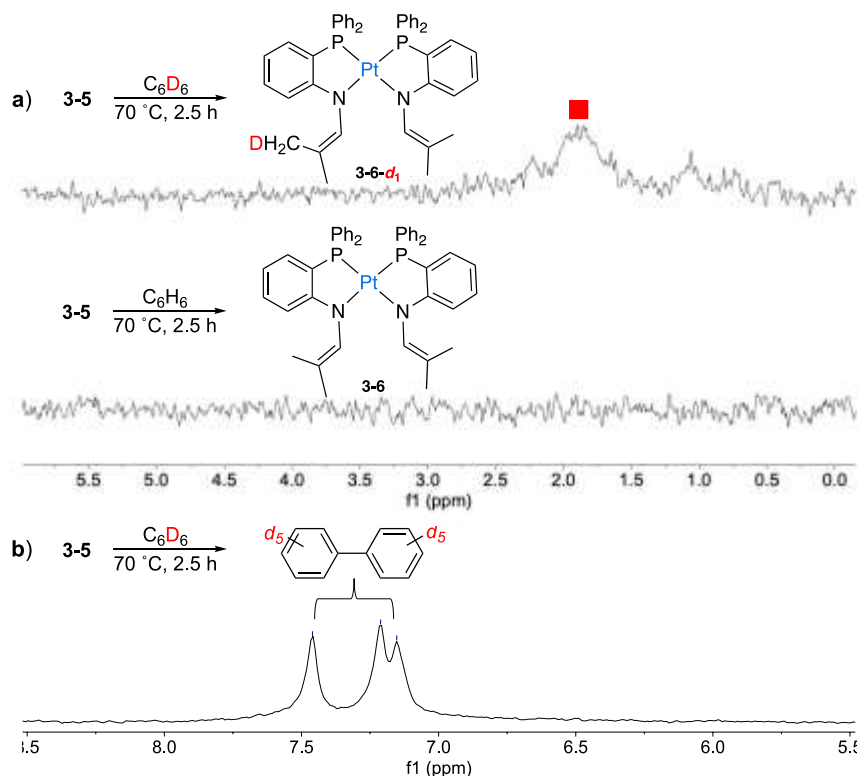


**Scheme 3.11.** Thermolysis of Pt(II)-CH<sub>3</sub> Dimer **3-5** to Afford Pt<sup>II</sup> complex **3-6** (left) and thermal displacement plot of **3-6** (right). Displacement ellipsoid (50% probability) plot of **3-6**. All hydrogen atoms have been omitted for clarity.

During the conversion of **3-5** to **3-6**, no intermediates or additional species were observed by  $^{31}P\{^1H\}$  NMR spectroscopy, which prevented direct confirmation of the Pt<sup>IV</sup> analogue of **m1a**. However, additional insight could be gained by comparison of reactions conducted in C<sub>6</sub>H<sub>6</sub> and C<sub>6</sub>D<sub>6</sub>. Heating **3-5** in C<sub>6</sub>D<sub>6</sub> again gave quantitative conversion to **3-6**. No evidence for CH<sub>3</sub>D by  $^1H$  or  $^2H$  NMR spectroscopy was observed, which suggests that the Pt-CH<sub>3</sub> fragment does not react with solvent directly to give methane. Close inspection of the  $^2H$  NMR spectrum of **3-6** synthesized in C<sub>6</sub>D<sub>6</sub> reveals a signal for a deuterated methyl of **3-L1** at ca. 2 ppm, which is not observed for samples of **3-6** prepared in C<sub>6</sub>H<sub>6</sub> (Figure 3.1a). Deuteration at this site can be rationalized by solvent activation with the Pt analogue of the proposed intermediate **m1c**, which forms after C-H activation of a **3-L1** methyl group and methane release (see Scheme 3.9). Related solvent activation was noted previously for Pt(II)-alkyl compounds,<sup>48</sup> and the palladium A-frame



complexes, **D**.<sup>33</sup> The product of solvent activation would regenerate the **3-L1** methyl group to give  $[\text{Pt}(\text{Ph})(\mathbf{3-L1})]$ , which could dimerize with another equivalent of  $[\text{Pt}(\text{Ph})(\mathbf{3-L1})]$ . From this compound biphenyl could form as a C-C coupled product, along with **3-6** (or **3-6-*d*<sub>1</sub>**) as the Pt-based product. Indeed, three signals are observed at 7.45, 7.21, and 7.13 ppm in the <sup>2</sup>H NMR spectrum from the thermolysis of **3-5** in C<sub>6</sub>D<sub>6</sub> that correspond to biphenyl-*d*<sub>10</sub> (Figure 3.1b). Furthermore, qualitative formation of biphenyl was confirmed by GC-FID, where a signal for biphenyl is consistently observed following thermolysis reactions performed in both C<sub>6</sub>H<sub>6</sub> and C<sub>6</sub>D<sub>6</sub> (Figure B.17). These observations indirectly support the proposal that methane forms from **3-1** by a sequence involving C-H activation of a methyl substituent of the 1-AzA group of **3-L1** (*i.e.*, Scheme 3.9).

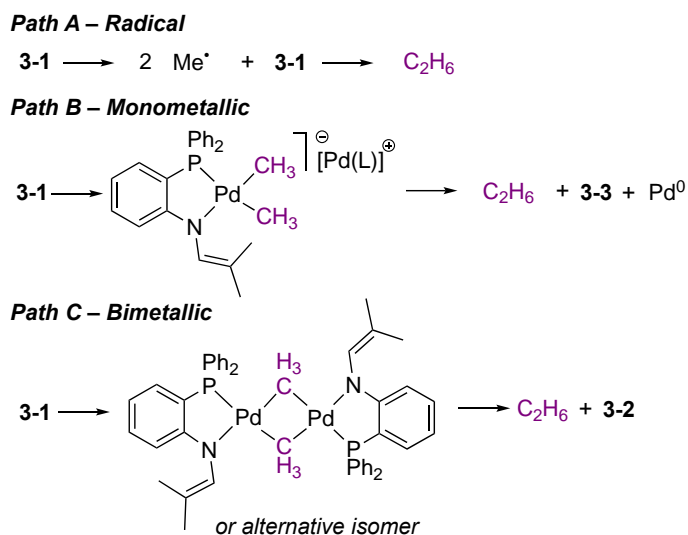


**Figure 3.1.** a) <sup>2</sup>H NMR spectra following the thermolysis of **3-5** in C<sub>6</sub>D<sub>6</sub> (top), and C<sub>6</sub>H<sub>6</sub> (bottom), spectra zoomed in to show  $\delta_D = 6.00 - 0.00$  (92.1 MHz, C<sub>6</sub>H<sub>6</sub>). b) <sup>2</sup>H NMR spectrum following the thermolysis of **3-6** in C<sub>6</sub>D<sub>6</sub>, spectrum zoomed in to show  $\delta_D = 8.50 - 5.50$  (92.1 MHz, C<sub>6</sub>H<sub>6</sub>).

### 3.2.4 Possible Pathways for C-C Reductive Elimination

Reductive elimination from **3-1** gives two different palladium products, **3-2** and **3-3**, which may mean that two distinct reaction pathways lead to C-C bond formation. To establish the mechanistic details, we considered three general reductive elimination pathways A-C (Scheme

B.12). First, despite our preliminary evidence that suggested a radical mechanism is not operative,<sup>36</sup> we considered that homolytic Pd-Me bond activation could lead to ethane and the Pd<sup>I</sup> dimer **3-2** (Scheme 3.12, Path A). Second, cleavage of dimer **3-1** and methyl transfer could give a monometallic Pd<sup>II</sup> dimethyl complex (Path B). Facile methyl transfer between bisphosphine Pd<sup>II</sup> complexes has been established<sup>49</sup> and the anionic nature of [Pd(CH<sub>3</sub>)<sub>2</sub>(**3-L1**)]<sup>-</sup> could favour reductive elimination. Third, reductive elimination could proceed via bimetallic complexes that are isomers of **3-1**, such as a methyl-bridged dimer. The monomer-dimer equilibrium established above, could be involved in Paths B or C.

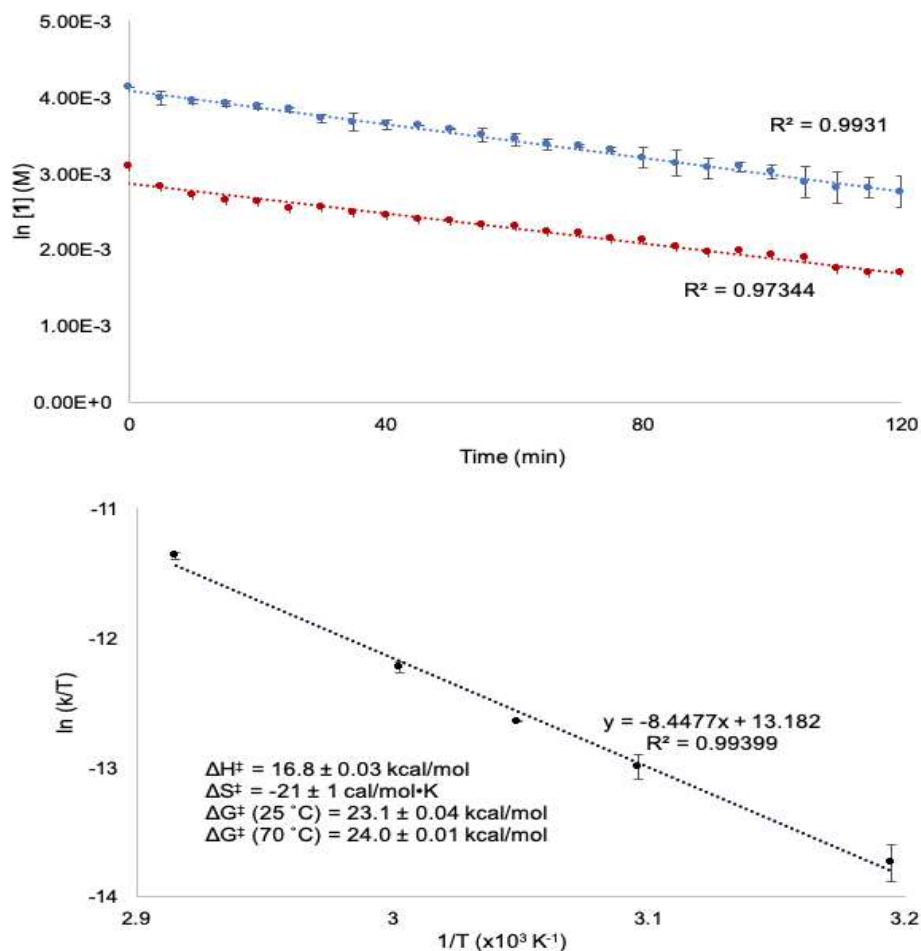


**Scheme 3.12.** Proposed General Pathways for Reductive Elimination from **3-1**.

### 3.2.5 Reaction Order and Eyring Analysis of Reductive Elimination

To determine the order for reductive elimination, two reactions at different concentrations of **3-1** in benzene (22 and 62 mM) were heated at 70 °C and monitored over time by <sup>31</sup>P{<sup>1</sup>H} NMR spectroscopy. In both cases, a plot of Ln[**3-1**] vs. time gave an excellent linear fit ( $R^2 > 0.993$ , 0.973) consistent with a reaction that is first order in **3-1** (Figure 3.2a), which is expected for all of the proposed pathways. Rate constants for the consumption of **3-1** were determined in the temperature range of 40 – 70 °C. The activation parameters calculated from an Eyring analysis were  $\Delta H^\ddagger = 16.79 \pm 0.03 \text{ kcal mol}^{-1}$  and  $\Delta S^\ddagger = -21 \pm 1 \text{ cal mol}^{-1} \text{ K}^{-1}$  (Figure 3.2b). The moderately large and negative  $\Delta S^\ddagger$  is consistent with a highly-ordered transition state with decreased translational and vibrational degrees of freedom as compared to the preceding intermediate, suggesting the formation of new bonds in the rate-determining step. Furthermore, the sign of  $\Delta S^\ddagger$  suggests that cleavage of **3-1** into two monomeric [Pd(**3-L1**)Me] fragments is not the rate-

determining step, which is consistent with other experimental and computational results. The magnitude of  $\Delta G^\ddagger$  ( $23.1 \pm 0.04 \text{ kcal mol}^{-1}$ ,  $25^\circ\text{C}$ ) is consistent with the prior observation<sup>36</sup> that the reaction can proceed at room temperature, albeit over the course of several days.

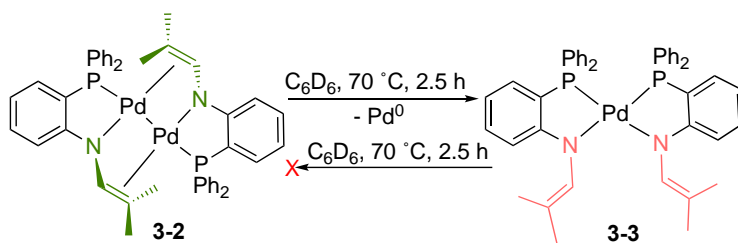


**Figure 3.2.** a) Plot of  $\text{Ln}[3-1]$  vs time for two reactions in which the initial concentrations of **3-1** were 22 mM (red) and 62 mM (blue). b) Eyring plot of the rate constants acquired from heating a solution of **3-1** (16 mM) in benzene from 40 to  $70^\circ\text{C}$ .

### 3.2.6 Relationship between Reductive Elimination Products **3-2** and **3-3**

To determine if there is a connection between the pathways affording complexes **3-2** and **3-3**, separate  $\text{C}_6\text{D}_6$  solutions were prepared containing **3-2** or **3-3** and  $\text{O=PPh}_3$  as an internal standard (Scheme 3.13). These solutions were then subjected to the conditions that give complete thermolysis of **3-1** and analyzed by  $^{31}\text{P}\{^1\text{H}\}$  and  $^1\text{H}$  NMR spectroscopy after 2.5 h. No change was

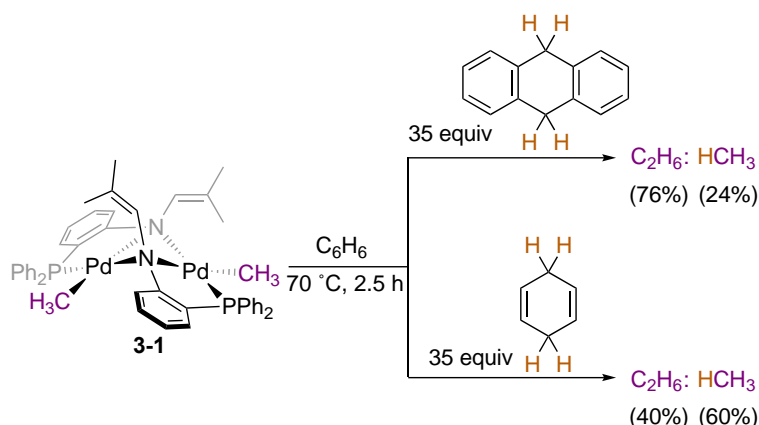
observed upon heating **3-3**. However, heating **3-2** resulted in 54% conversion to **3-3** after 2.5 h. By comparison, **3-1** completely converts to **3-2** and **3-3** within this same timeframe, during which **3-3** emerges first and the ratio of **3-2** and **3-3** is relatively static after ca. 40 min of reaction time. These observations suggest that a small percentage of **3-3** may be obtained from the thermolysis of **3-2**, but it is unlikely that this pathway exclusively accounts for **3-3**.



**Scheme 3.13.** Thermolysis of **3-2** and **3-3**.

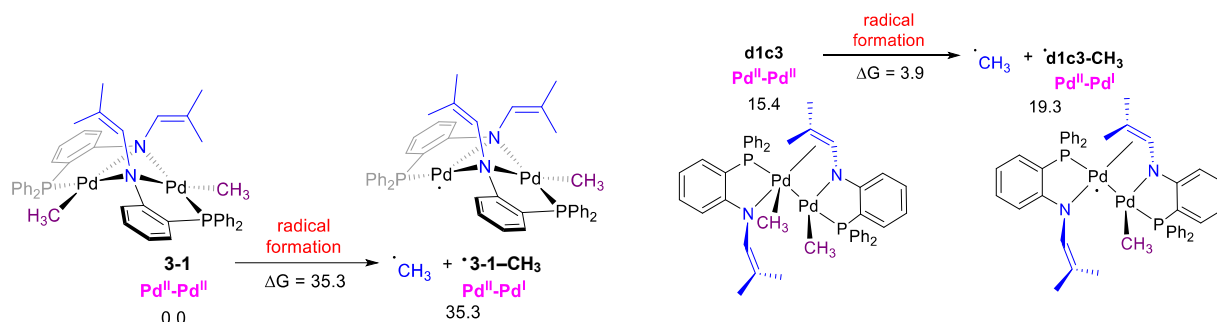
### 3.2.7 Assessment of a Radical Pathway to Reductive Elimination

Previously, we found no difference in yield of the palladium products **3-2** and **3-3** when reactions were conducted in the light or the dark.<sup>36</sup> This indicates that light mediated homolysis of the Pd-CH<sub>3</sub> bond is not a dominant pathway in ethane formation. However, a methyl-transfer step must occur prior to reductive elimination and such reactions can involve uncaged methyl radicals.<sup>31</sup> To test for radical formation, **3-1** was heated in the presence of known<sup>29, 30, 50</sup> H-atom donors 1,4-cyclohexadiene (CHD) or 9,10-dihydroanthracene (DHA), (Scheme 3.14). In the presence of DHA no change in product selectivity was observed, which indicates that H-atom abstraction did not occur and that an uncaged methyl radical (*i.e.*, Path A, Scheme 3.12) is not involved in methyl transfer. In contrast, the more potent H-atom donor CHD (c.f. BDFE<sub>(C-H)</sub>: CHD = 67.8; DHA = 76.0 kcal mol<sup>-1</sup>)<sup>50</sup> does react with **3-1** to give methane, likely via interception of an intermediate with methyl-radical character. Despite a large excess of CHD (35 equiv.) methane was not the exclusive organic product, rather ethane and methane were formed in 40 and 60 % yields, respectively. This suggests that the two palladium products are formed through distinct mechanisms, where only one has an intermediate that can be intercepted with an H-atom donor to promote homolytic Pd-CH<sub>3</sub> cleavage.



**Scheme 3.14.** Reaction of **3-1** with H-Atom Donors.

The calculated free energy for direct homolytic cleavage of the Pd-CH<sub>3</sub> bond in dimer **3-1** is 35.3 kcal/mol (Scheme 3.15), which further demonstrates that this pathway is prohibitive. As will be discussed in Section 3.2.9, a structural isomer of **3-1** that appears en route to product **3-2**, species **d1c3**, can form a methyl radical. This pathway therefore provides an intermediate that explains the observed H-atom abstraction from CHD.

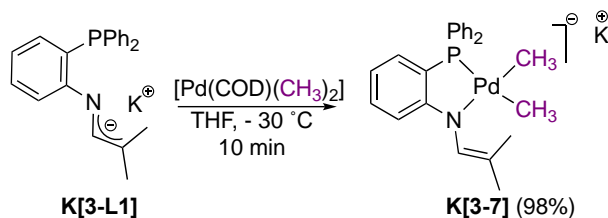


**Scheme 3.15.** Calculated energetics for methyl radical formation. Free energies are relative to dimer **3-1** and given in kcal/mol.

### 3.2.8 Assessment of a Monometallic Reductive Elimination Pathway.

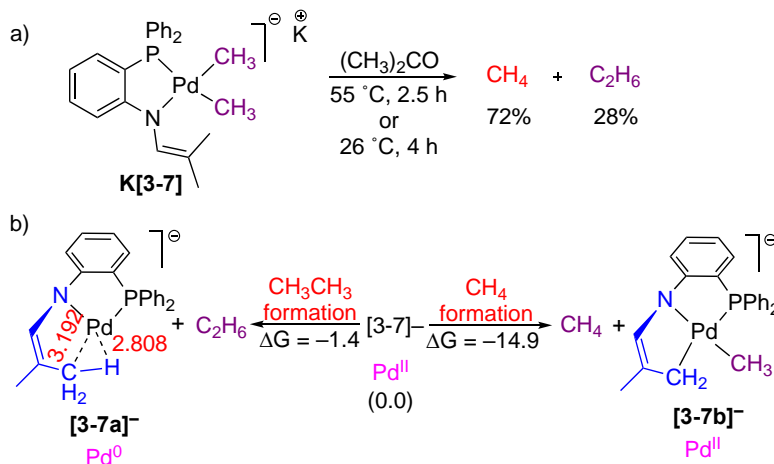
To investigate potential Path B (see Scheme 3.12), involving the monometallic intermediate [Pd(CH<sub>3</sub>)<sub>2</sub>(**3-L1**)]<sup>−</sup>, independent synthesis of a dimethyl monomer was conducted. Reaction of **K[3-L1]** and [Pd(CH<sub>3</sub>)<sub>2</sub>(COD)] at −30 °C gave **K[3-7]** in near quantitative yields (Scheme 3.16). The <sup>1</sup>H NMR spectrum of **7** reveals a pair of doublets at δ<sub>H</sub> = 0.0 and −0.05 ppm, with H–P coupling constants of <sup>3</sup>J<sub>HP</sub> = 7.2 and 7.8 Hz respectively. The similar <sup>1</sup>H chemical shifts and coupling values are consistent with other Pd(CH<sub>3</sub>)<sub>2</sub> complexes bearing asymmetric bidentate ligands.<sup>51-53</sup> The <sup>1</sup>H NMR signals correlate by <sup>1</sup>H-<sup>13</sup>C HSQC to doublets at δ<sub>C</sub> = −11.6 and 7.9,

respectively, with coupling constants of  $^2J_{\text{CP}} = 6.04$  and  $117.8$  Hz. These coupling constants are consistent with, respectively, *cis*- and *trans*-disposed methyls relative to the phosphine donor.<sup>53, 54</sup>



**Scheme 3.16.** Synthesis of Dimethyl Monomer **K[3-7]**.

Two separate solutions of **K[3-7]** in acetone-*d*<sub>6</sub> were prepared, then one was heated at 50 °C for 2.5 h and the other was left at 26 °C for 4 h (Scheme 3.17a). In both cases, the  $^{31}\text{P}\{^1\text{H}\}$  NMR spectrum revealed complete consumption of **K[3-7]** and a major product (ca. 70%) was observed at  $\delta_{\text{P}} = 40.1$ , along with several minor products. None of the observed products matched to the spectroscopic signals for **3-2** or **3-3**. The  $^1\text{H}$  NMR spectrum of the decomposition product shows a doublet at  $\delta_{\text{H}} = -1.02$ , with a small coupling constant ( $J_{\text{HP}} = 4.0$  Hz), consistent with retention of one Pd-CH<sub>3</sub> moiety. Inspection of the headspace by GC-FID revealed a 72% yield of methane, with the balance being ethane. The computed free energies for the formation of methane and ethane from **[3-7]<sup>-</sup>** are  $-14.9$  kcal/mol and  $-1.4$  kcal/mol, respectively (Scheme 3.17b). The computed preference for methane upon thermolysis of **[3-7]<sup>-</sup>**, as well as the experimental observation for the preservation of one of the Pd-CH<sub>3</sub> moieties, suggests that reductive elimination from a  $[\text{Pd}(\text{CH}_3)_2(\mathbf{3-L1})]^-$  intermediate does not occur during thermolysis of **3-1**. Incidentally, simulations also show a relatively high free energy for the formation of methyl radical (37.3 kcal/mol) from **[3-7]<sup>-</sup>**.



**Scheme 3.17.** a) Thermolysis of **K[3-7]**; and b) Computed energies for C-C and C-H bond formation from **[3-7]<sup>-</sup>**. Selected atom distances are given in Å.

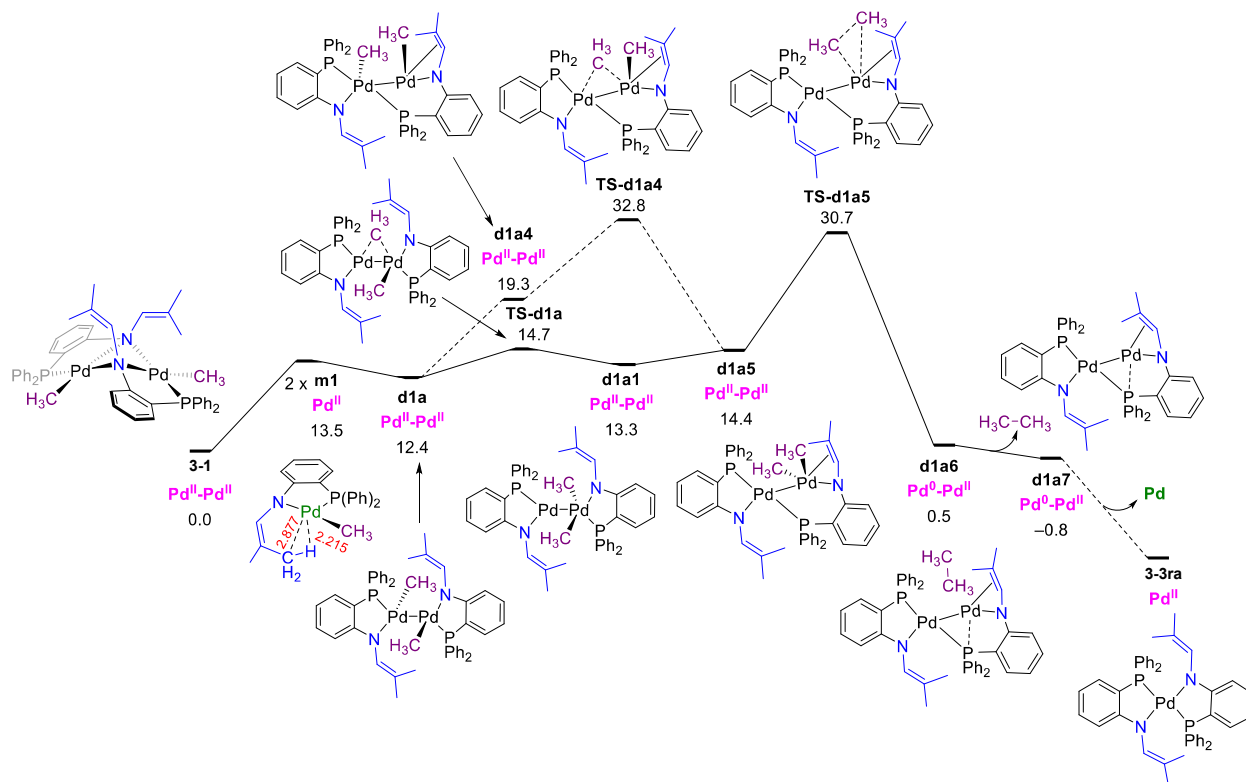
On the basis of experimental and computational studies we have discounted Path B for reductive elimination, in which ethane is formed from the dimethyl Pd<sup>II</sup> monomer [Pd(CH<sub>3</sub>)<sub>2</sub>(**3-L1**)]<sup>-</sup>.

### 3.2.9 Assessment of Bimetallic Pathways to Reductive Elimination

Based on the studies above, a bimetallic mechanism (*i.e.*, Path C in Scheme 3.12) for the formation of ethane and both palladium products **3-2** and **3-3** is most likely. Therefore, our computational efforts focused on C-C coupling pathways involving bimetallic intermediates that differ based on the coordination geometry of the **3-L1** ligand and the products formed, in which Path C1 (Scheme 3.18) and C2 (Scheme 3.19) both form Pd<sup>II</sup>(L)<sub>2</sub> (**3-3**) and Pd<sup>0</sup> as products and Path C3 (Scheme 3.20) forms Pd<sup>I</sup> dimer **3-2**. A handful of higher energy (and therefore less feasible) paths were identified and presented in the Supporting Information.

#### Path C1: Ethane Formation from an Asymmetric Methyl-Bridged Dimer

The asymmetric methyl-bridged dimer **d1a** (12.4 kcal/mol, Scheme 3.18) can form via the dimerization of two **m1** monomers. **d1a** contains Pd-C<sub>(CH<sub>3</sub>)</sub> atom distances of 2.08 and 3.11 Å (Table B.2), which suggests the asymmetric dimer **d1a** is not a classical methyl-bridged dimer with strong methyl-metal interaction.<sup>55-59</sup> From **d1a**, two different paths for the generation of ethane are possible. Both mechanisms involve reductive elimination after two methyl groups fully associate to a single Pd, and result in the formation of **3-3ra**, a geometric isomer of the experimentally observed Pd<sup>II</sup>(L)<sub>2</sub> product **3-3**. Isomer **3-3ra** is 5.3 kcal/mol higher in energy than **3-3** (Scheme B.3), and the two species are expected to be in equilibrium. Here the focus is on a pathway from **d1a** that involves an η<sup>3</sup> 1-azaallyl intermediate, since it has a lower rate-limiting barrier of 30.7 kcal/mol (Scheme 3.18) compared a second pathway at 39.5 kcal/mol (Scheme B.3).



**Scheme 3.18.** Path C1: Ethane formation from a pseudo methyl-bridged dimer **d1a**. Selected atom distances in monomer **m1** are given in Å. Computed oxidation states of Pd atoms from LOBA analysis are given in purple.  $\Delta G$  in kcal mol<sup>-1</sup>.

The favourable pathway (**3-1** → **d1a** → **d1a1** → **d1a5** → **d1a6** → **3ra**, Scheme 3.18) involves: (1) methyl transfer to form the Pd<sup>II</sup>-Pd<sup>II</sup>Me<sub>2</sub> complex **d1a1**, (2) isomerization of Pd<sup>II</sup>-Pd<sup>II</sup>Me<sub>2</sub> complex **d1a1** to form **d1a5** (3) C-C coupling to release an ethane molecule and **d1a7**, and finally (4) release of Pd<sup>(0)</sup> and a isomer of Pd<sup>II</sup>(L)<sub>2</sub> product (**3-3ra**). In the first step, electronic structure analysis suggests direct anionic methyl transfer in methyl-bridged dimer **d1a** (**TS-d1a**) leads to a Pd<sup>II</sup>-Pd<sup>II</sup>Me<sub>2</sub> dimer (**d1a1**) with a free energy barrier of 14.7 kcal/mol. Alternatively, complex **d1a4** with a coordinated η<sup>3</sup> 1-azaallyl group can appear as an intermediate for methyl transfer. The anionic methyl transfer via **TS-d1a4** has a much higher barrier than the path through **TS-d1a** (32.8 kcal/mol), but leads to the same intermediate, **d1a5**. The subsequent C-C reductive elimination from η<sup>3</sup> 1-azaallyl complex **d1a5** has a barrier of 30.7 kcal/mol, which is significantly lower than the barrier of C-C reductive elimination from κ<sup>1</sup> 1-azaallyl complex **d1a1** (39.5 kcal/mol, Scheme B.4). After ethane elimination, dissociation of one Pd atom leads to species **3-3ra**.



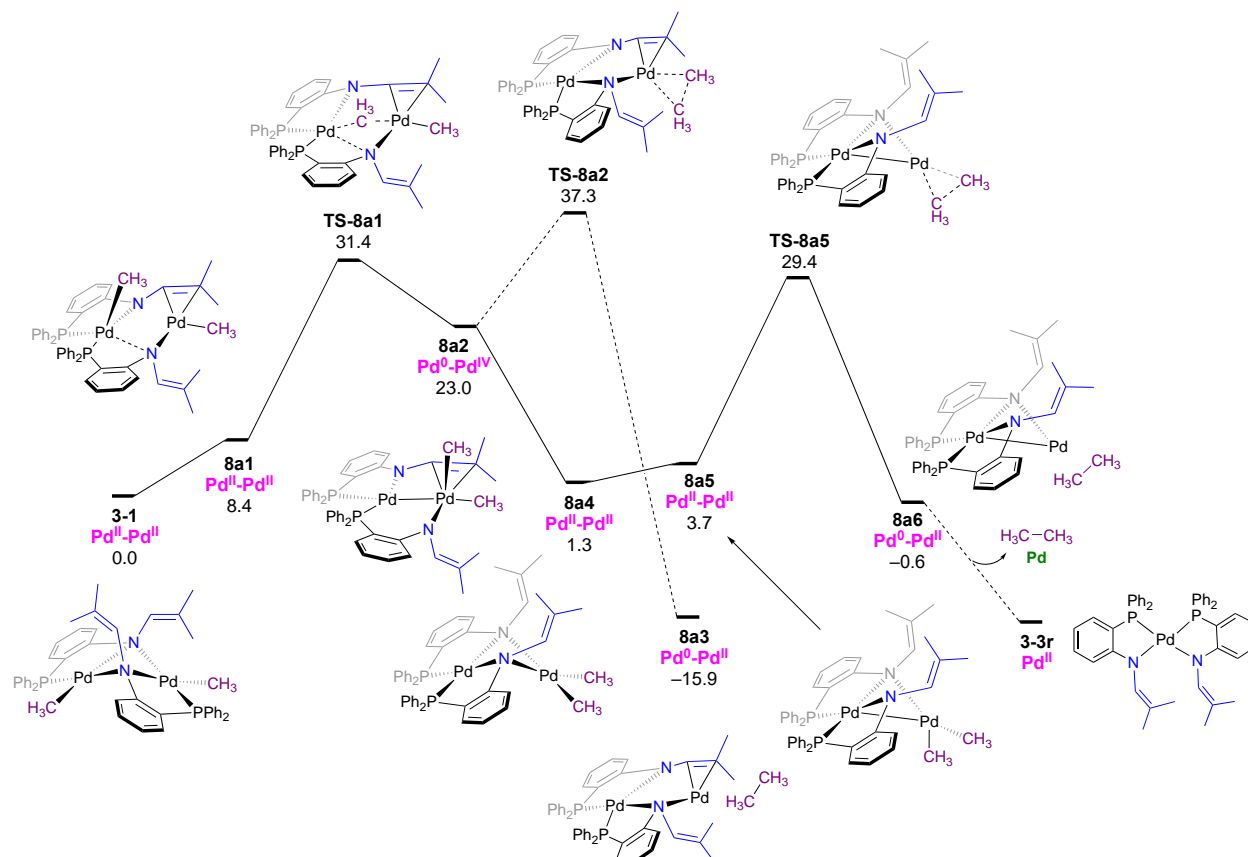
The free energy of activation for the rate-determining step (methyl transfer, **TS-d1a4**) in this anionic methyl transfer pathway is 32.8 kcal/mol, which is a little higher than the C-C coupling step (30.7 kcal/mol for **TS-d1a5**). Additional less favourable pathways with alternate conformations of the 1-azaallyl group of **3-L1** via **d1b** (a rotamer of **d1a**) are presented in Scheme B.5. The free energies of activation for the methyl transfer (**TS-d1b5**, Scheme B.5) and the C-C coupling (**TS-d1b6**, Scheme B.5) in the analogous pathways are 32.5 and 35.8 kcal/mol, respectively.

## Path C2: Formation of Ethane and Product **3-3** from Bimetallic Dimethyl Intermediate **8a5**

A bimetallic intermediate **8a5** with a Pd(Me)<sub>2</sub> moiety can also be formed without ever passing through the bridged-methyl intermediate (**8a1** → **8a2** → **8a4** → **8a5** → **8a6** → **3-3r**, Scheme 3.19). To arrive at this species, phosphine ligand migration (**3-1** → **8a1**) results in a transient Pd<sup>II</sup>-diphosphine (**8a1**) with η<sup>2</sup> 1-azaallyl coordination to one palladium centre. Intramolecular CH<sub>3</sub> transfer then generates Pd<sup>0</sup>(diphosphine)Pd<sup>IV</sup>(Me)<sub>2</sub> (**8a2**) with a barrier of 31.4 kcal/mol (**TS-8a1**), which is close to that of the rate-limiting step involved in pathway C1 (**TS-d1a4** = 32.8 kcal/mol, Scheme 3.18). These similar barriers could be explained by the similar coordination of the phosphine 1-azaallyl group. Electronic structure analysis of **8a2** suggests it is Pd<sup>0</sup>(diphosphine)Pd<sup>IV</sup>(Me)<sub>2</sub>, and this species is reached via cationic CH<sub>3</sub> transfer (**TS-8a1**) instead of anionic CH<sub>3</sub> transfer (*i.e.*, in C1 **TS-d1a** and **TS-d1a4**, see Scheme 3.18).<sup>60</sup>

After forming intermediate **8a2**, two processes may occur (Scheme 3.19): (1) direct C-C reductive elimination to release an ethane molecule (**TS-8a2**), or (2) a change in 1-azaallyl binding from η<sup>2</sup> to κ<sup>1</sup>-N to form intermediate **8a4**. The direct C-C reductive elimination from Pd<sup>0</sup>(diphosphine)Pd<sup>IV</sup>(Me)<sub>2</sub> intermediate **8a2** has a barrier of 37.3 kcal/mol (**TS-8a2**). Instead of this difficult direct C-C coupling, rearrangement of the ligand in **8a2** relaxes to the symmetric, square-planar Pd<sup>II</sup>-Pd<sup>II</sup> dimethyl intermediate **8a4**, which is over 20 kcal/mol downhill from **8a2**. **8a4** then rearranges to an asymmetric intermediate **8a5** (3.7 kcal/mol) with a distorted square-planar structure. This species is consistent with the observations of Csp<sup>3</sup>-Csp<sup>3</sup> reductive elimination from a series of square-planar *cis*-[PdMe<sub>2</sub>(PMe<sub>3</sub>)L] complex (L = CH<sub>2</sub>CH<sub>2</sub>, PMe<sub>3</sub>), where the orientation of Csp<sup>3</sup>-Csp<sup>3</sup> bond in the related transition state is perpendicular to the plane of Pd(PMe<sub>3</sub>)L.<sup>61, 62</sup> A prolonged Pd-Pd atom distance and smaller C<sub>(CH<sub>3</sub>)</sub>-Pd-C<sub>(CH<sub>3</sub>)</sub> bond angle in

tetra-coordinated intermediate **8a5** compared to those in intermediate **8a4** are observed (2.939 Å vs 2.816 Å 85.9° vs 88.4°). The barrier for the C-C reductive elimination to form an ethane molecule and Pd<sup>0</sup>-Pd<sup>II</sup> complex **8a6** is 29.4 kcal/mol (**TS-8a5**). Once ethane is released, the Pd<sup>0</sup>-Pd<sup>II</sup> complex **8a6** leads to Pd<sup>(0)</sup> and the geometric isomer of Pd<sup>II</sup>(L)<sub>2</sub> product **3-3**, species **3-3r**. After the formation of **3-3r**, ligand rotation leads to generation of the final product Pd<sup>II</sup>(L)<sub>2</sub> complex **3-3**. Other analogous pathways for the generation of ethane, Pd<sup>(0)</sup>, and Pd<sup>II</sup>(L)<sub>2</sub> via **8b1** (rotamer of **8a1**) are presented in Scheme B.7. Overall, there are two slow steps in this process: cationic methyl transfer (**TS-8a1**) and reductive elimination (**TS-8a5**), each with barriers of around 30 kcal/mol.

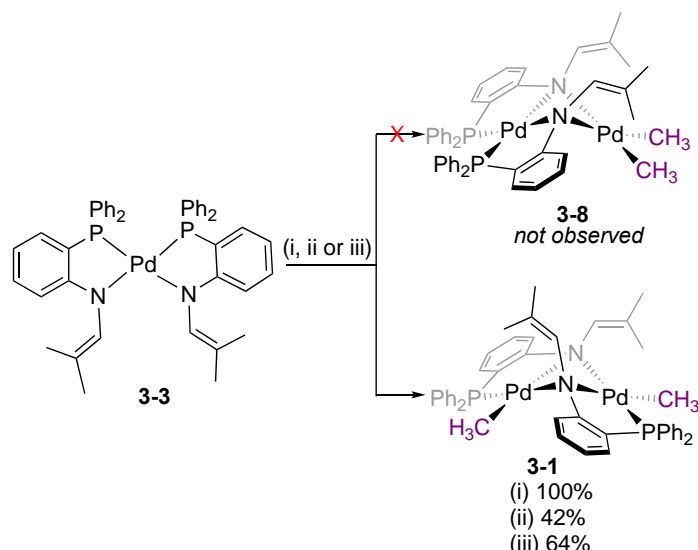


**Scheme 3.19.** Path C2: Ethane formation from a bimetallic dimethyl intermediate **8a5**. Computed oxidation states of Pd atoms from LOBA analysis are given in purple. ΔG in kcal mol<sup>-1</sup>.

Compared to the formation of ethane and Pd<sup>II</sup>(L)<sub>2</sub> (**3-3**) from a methyl-bridged dimer **d1a** (Scheme 3.18), the path with Pd<sup>II</sup>(L)<sub>2</sub>Pd<sup>II</sup>(Me)<sub>2</sub> dimethyl intermediate **8a5** (**8a1** → **8a2** → **8a4** → **8a5** → **3-3r** → **3-3**) in Scheme 3.19 has a comparable free energy barrier for the rate-determining step (31.4 kcal/mol for **TS-8a1** vs 30.7 kcal/mol for **TS-d1a5**). Alternate bimetallic structures that

involved bridging via the phosphine rather than the amido of **3-L1** were not energetically viable (Scheme B.8).

The proposed dimethyl Pd<sup>II</sup> intermediate **8a4** in Path C2 is relatively low in energy, which suggests it could be prepared independently. To this end, a solution of **3-3** was treated with [Pd(Me)<sub>2</sub>(COD)] at 0 °C (Scheme 3.20). After 4 h, <sup>31</sup>P{<sup>1</sup>H} NMR analysis revealed the formation of the Pd<sup>II</sup> dimer **3-1** as the major product in 64% yield. Higher conversion was hindered at longer times or higher temperature by the competitive thermal decomposition of [Pd(Me)<sub>2</sub>(COD)]. However, addition of excess palladium dimethyl reagent resulted in improved yields, giving **3-1** quantitatively at room temperature. In all cases, no evidence for the target bimetallic complex **3-8** was observed by <sup>31</sup>P{<sup>1</sup>H} or <sup>1</sup>H NMR spectroscopy. Given the calculated energetics, we do not expect that **3-8** rearranges to **3-1**. Rather, an alternate pathway from the reagents **3-3** and [Pd(Me)<sub>2</sub>(COD)] to **3-1** is likely operative. Unfortunately, this precludes direct experimental evaluation of **3-8** as a relevant intermediate in C-C coupling.



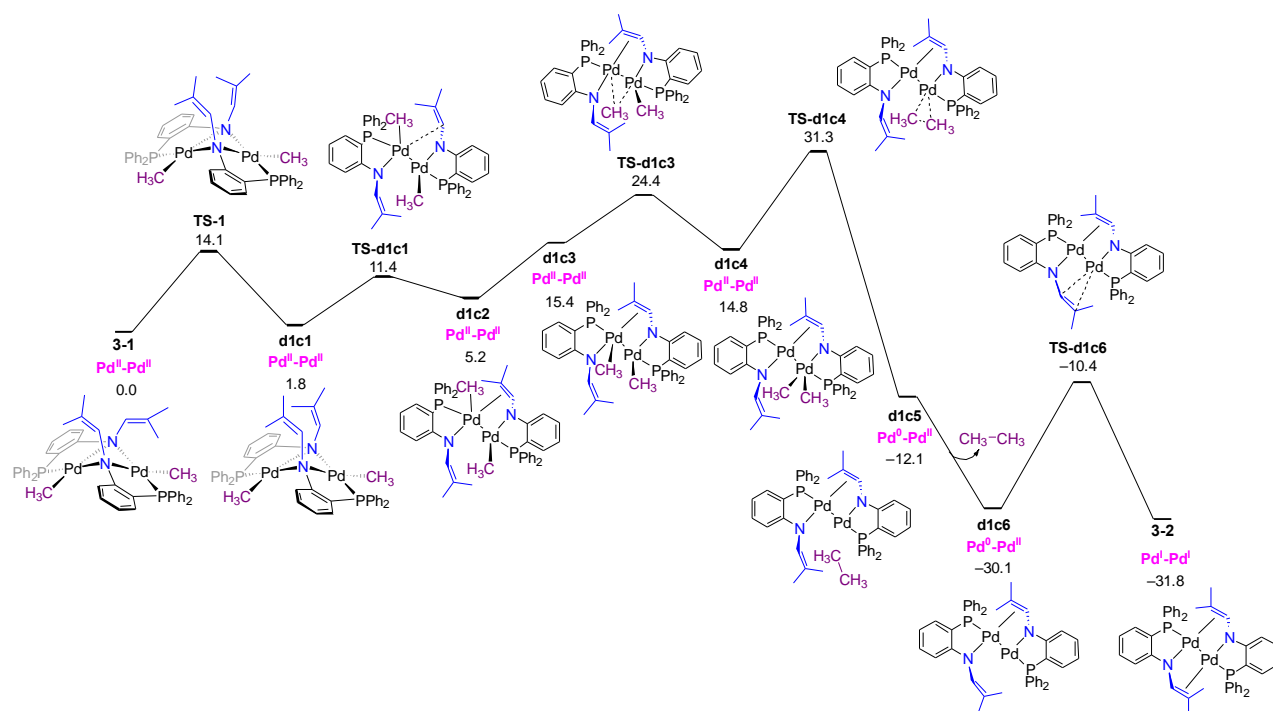
**Scheme 3.20.** Attempted Formation of **3-8**. Conditions: (i) 15 equiv [Pd(CH<sub>3</sub>)<sub>2</sub>(cod)], C<sub>6</sub>D<sub>6</sub>, rt; (ii) 2.0 equiv [Pd(CH<sub>3</sub>)<sub>2</sub>(COD)], C<sub>6</sub>D<sub>6</sub>, rt; (iii) 2.5 equiv [Pd(CH<sub>3</sub>)<sub>2</sub>(COD)], C<sub>7</sub>D<sub>9</sub>, 0 °C.

### Path C3: Formation of Ethane and PdI Dimer **3-2** from a Ligand-Bridged Bimetallic Intermediate.

Having shown possible routes for formation of products complex **3-3** (Schemes 3.18 and 3-19), the formation of dimer **3-2** and ethane is now considered. This pathway requires intramolecular CH<sub>3</sub> transfer without fragmenting the dimer into monomers, and the coordination of phosphine 1-azaallyl group has a key role in this path (Scheme 3.21). This process begins with

the rotation of phosphine 1-azaallyl anion ligand in Pd<sup>II</sup>Me(L) dimer **3-1** to form its rotamer, intermediate **d1c1**, with a barrier of 14.1 kcal/mol (**TS-1**). Next, a change in the bridging coordination mode of the 1-azaallyl fragment from  $\mu$ -N in **d1c1** to  $\mu$ -[ $\eta^2$ -CC: $\kappa^1$ -N] in **d1c2** involves a barrier of 11.4 kcal/mol for **TS-d1c1**. After reorientation of a methyl group in **d1c2** ( $E_{(\text{CH}_3)}$ -isomer), which is necessary prior to methyl transfer, Pd<sup>II</sup>Me-Pd<sup>II</sup>Me isomer **d1c3** ( $Z_{(\text{CH}_3)}$ -isomer) results. A smaller Pd-Pd-C<sub>(transferred CH<sub>3</sub>)</sub> bond angle in  $Z_{(\text{CH}_3)}$ -isomer **d1c3** compared to that in **d1c2** is observed (80.4° vs 139.1°), which is in favour of the critical methyl transfer that will lead to the generation of ethane. The homolytic breaking of Pd-Me bond in Pd<sup>II</sup>-Pd<sup>II</sup>  $Z_{(\text{CH}_3)}$ -isomer **d1c3** is uphill by 3.9 kcal/mol (Scheme B.8), which suggests the possible formation a free methyl radical. This finding suggests that **d1c3** may be the intermediate that reacts with 1,4-cyclohexadiene to give methane (*cf.* Scheme 3.14). No other more feasible homolytic breaking of Pd-Me bond in intermediates **d1a** (24.3 kcal/mol), **d1a4** (15.5 kcal/mol), **d1a5** (20.3 kcal/mol), and **5a1** (35.4 kcal/mol) are observed.

Anionic methyl transfer (**TS-d1c3**) from the Pd<sup>II</sup>Me-Pd<sup>II</sup>Me intermediate **d1c3** provides the Pd<sup>II</sup>-Pd<sup>II</sup>(Me)<sub>2</sub> dimethyl intermediate **d1c4**. The following C-C reductive elimination from **d1c4** generates an ethane molecule and Pd<sup>0</sup>-Pd<sup>II</sup> intermediate **d1c5** with an overall barrier of 31.1 kcal/mol (**TS-d1c4**) compared to Pd<sup>II</sup>Me(L) dimer **3-1**. This step is rate determining and leads to Pd<sup>I</sup>(L)<sub>2</sub> dimer complex **3-2** (31.3 kcal/mol for **TS-d1c4**), after rearrangement of the 1-azaallyl fragment (**TS-d1c6**).<sup>63</sup> Other analogous pathways for the generation of ethane and Pd<sup>I</sup>(L) dimer complex **3-2** from Pd<sup>II</sup>Me(L) dimer **3-1** are presented in the SI (Schemes B.11, and B.12).



**Scheme 3.21.** Path C3: Ethane formation from ligand-bridged dimer. Computed oxidation states of Pd atoms from LOBA analysis<sup>63</sup> (except those of dimer **3-2**) are given in purple.  $\Delta G^\circ/\Delta G^\ddagger$  are in kcal mol<sup>-1</sup>.

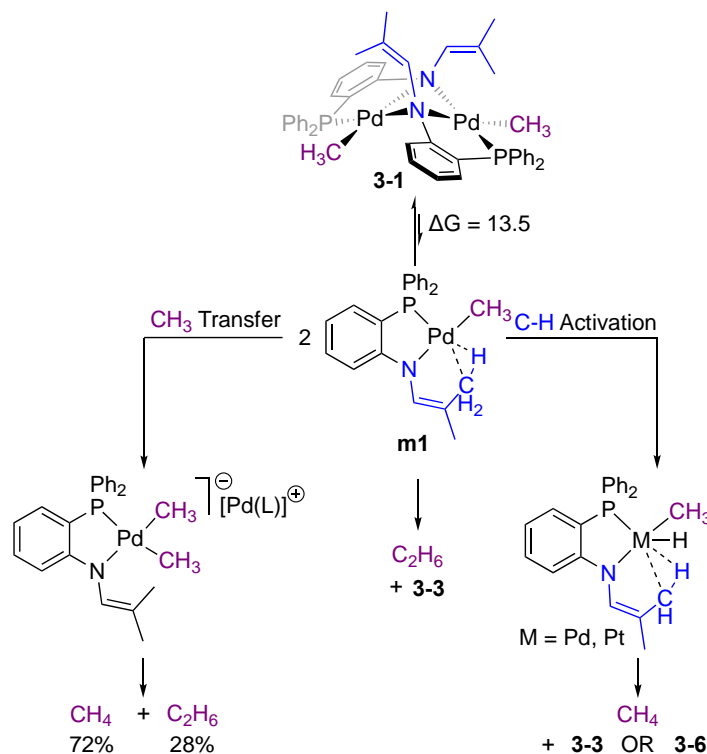
## 3.3 Discussion

### 3.3.1 Monometallic Route to Methane By-Product.

The crossover experiment with **3-1** and **3-1-d<sub>6</sub>** revealed that a monomer/dimer equilibrium is operative. This is supported by computations that show that the dimer (**3-1**) is more stable than two equiv of the monomer (**m1**) by 13.5 kcal/mol. The latter is stabilized by agostic interactions to one of the methyl substituents of the 1-Aza group of **3-L1** (Scheme 3.7).

All three of the viable C-C coupling routes follow a bimetallic mechanism and only one route, C1, relies on monomer **m1** formation via the pre-equilibrium. However, **m1** is vulnerable to several pathways that can erode selectivity for C-C bond formation to instead favour methane (Scheme 3.22). One possible pathway involves a dimethyl monomer that was shown through both experiment and computation to undergo C-C and C-H coupling, with preference for methane formation (Scheme 3.17). A second likely pathway from **m1** involves C-H oxidative addition of

the ligand to give a high-valent metal-hydride. This was indicated by computations and reactivity with **3-5**, a Pt analogue of **3-1**. Reductive elimination from **3-5** exclusively gives methane and subsequent steps involve solvent activation and formation of  $M^{II}(L)_2$  (**3-3**, M = Pd; **3-6**, M = Pt) (Scheme 3.9). From palladium monomer **m1**, the route to give methane is competitive with C-C coupling (C1). These observations indicated that the proximal methyl substituent of the 1-azaallyl moiety is vulnerable to unwanted C-H activation, and that the monomer **m1** leads to deleterious reaction pathways.



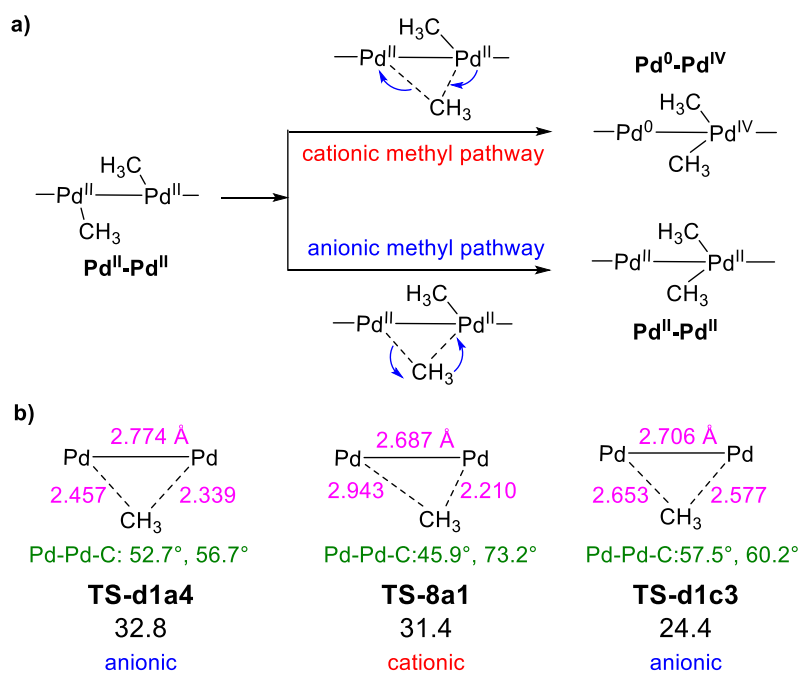
**Scheme 3.22.** Competing pathways from monomer **m1** that can lead to methane formation through methyl transfer (left) or C-H activation (right), as well as the pathway affording ethane and **3-3** (centre).

### 3.3.2 Bimetallic $\text{CH}_3$ Transfer

Experiments confirm that methyl transfer does not involve an uncaged methyl radical. Rather, the computations reveal that intramolecular Me transfer occurs within a bimetallic structure held together by the phosphine 1-azaallyl ligand (**3-L1**), which involves a transition state with a triangular arrangement of methyl and two Pd centres. This is distinct from bimolecular methyl transfer that involves a linear arrangement of Pd-Me-Pd, which leads to intermediates that undergo reductive elimination from a high-valent monometallic complex (*i.e.*, Scheme 3.2c).

Rather, intramolecular methyl transfer is unique to **3-1** and likely also the A-frame dimers, **3-A** (*i.e.*, Scheme 3.3).

Two qualitatively distinct pathways of methyl transfer are possible that involve cationic or anionic mechanisms, which were assigned based on localized orbital bonding analysis (LOBA; Scheme 3.23). Additional discussion of the limitations of the LOBA analysis and a complementary assessment are included in the Supporting Information. Cationic methyl transfer in the bimetallic Pd<sup>II</sup>-Me intermediate (**5a1**, Path C2, Scheme 3.19) leads to the mixed valent Pd<sup>0</sup>-Pd<sup>IV</sup>(Me)<sub>2</sub> complex **5a2**. Anionic methyl transfer on the other hand occurs without a change in oxidation states to reach a bimetallic dimethyl Pd<sup>II</sup>(Me)<sub>2</sub> fragment. The two anionic possibilities are realized through **TS-d1a4** (Path C1, Scheme 3.18) and **TS-d1c3** (Path C3, Scheme 3.21), and they ultimately lead to the formation of products **3-2** and **3-3**. In contrast, the cationic methyl transfer leads only to species **3-3**.



**Scheme 3.23.** (a) The pathways of methyl transfer, and (b) geometric parameters of the Pd-CH<sub>3</sub>-Pd fragments in the transition states.

The geometries for cationic and anionic methyl transfer pathways are delineated in Scheme 3.23. In the cationic path **TS-8a1**, the two Pd-C<sub>(CH<sub>3</sub>)</sub> bond distances of the transferring methyl are highly asymmetric, being 2.210 and 2.943 Å, respectively. This significantly differs from those in the anionic methyl transfers **TS-d1a4** and **TS-d1c3**, where the two Pd-C<sub>(CH<sub>3</sub>)</sub> bond distances are within approximately 0.1 Å of each other. These differing geometric characteristics, together with

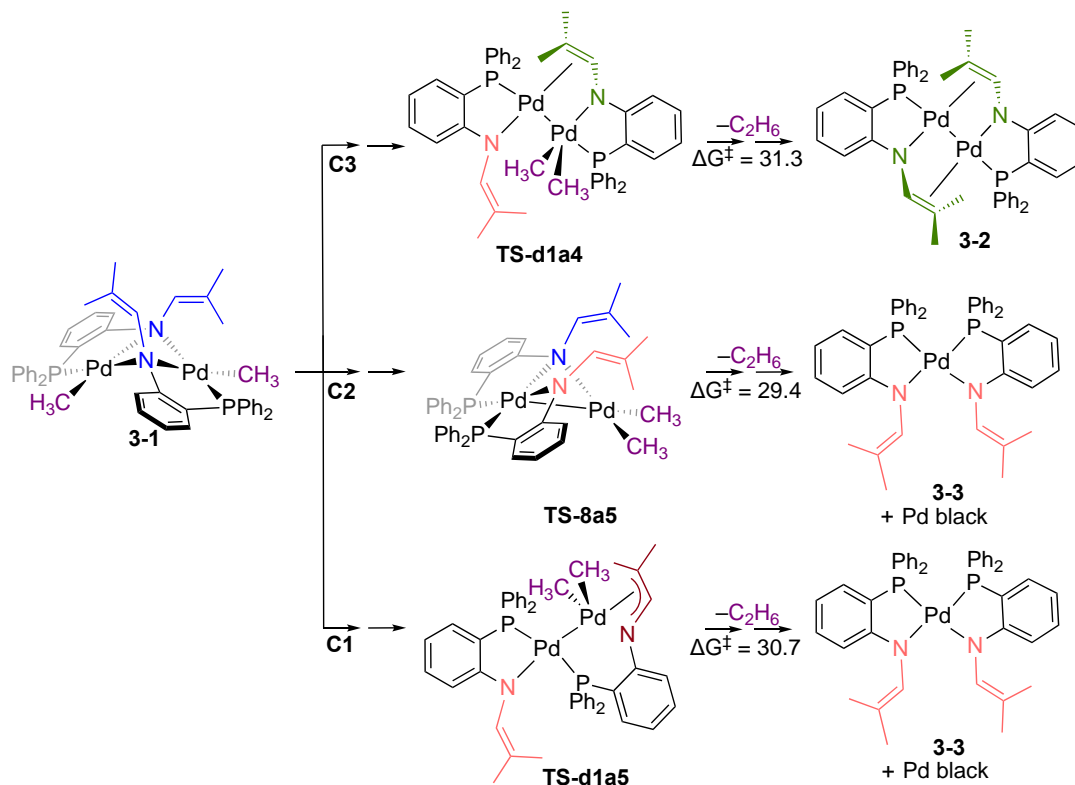
the computed oxidation states, make it clear that two very different methyl transfer mechanisms are operative.

### 3.3.3 Bimetallic 1,1-Reductive Elimination

Our initial study<sup>36</sup> confirmed the versatile coordination chemistry of phosphine 1-azaallyl ligand **3-L1**, based on the structures of **3-1** and reductive elimination products **3-2** and **3-3**. The present study shows that the changes in coordination mode *induce* C-C bond formation. In all three of the viable reaction paths, C1-C3, the 1-azaallyl coordination mode of **3-L1** alters from  $\mu$ -N to include  $\kappa^1$ -N,  $\eta^2$ -CC,  $\eta^3$ -NCC and  $\mu$ -[ $\eta^2$ -CC: $\kappa^1$ -N] (Schemes 3.18, 3.19, 3.21). The importance of the 1-azaallyl fragment to enable the C-C coupling mechanisms is supported by experimental studies with phosphine amido complex **3-8** that gives poor selectivity for C-C bond formation. The specific interactions of the 1-azaallyl group are distinct for each of Paths C1-C3 and the impact is most clearly considered for the reductive elimination step (summarized in Scheme 3.24). In C1 the PdMe<sub>2</sub> fragment of **d1a5** is ligated with an  $\eta^3$ -NCC 1-azaallyl and the barrier (**TS-d1a5**, 30.7 kcal/mol, Scheme 3.18) is lower than the analogous route with  $\kappa^1$ -N binding (**TS-d1a1**, 39.5 kcal/mol, Scheme B.4) by 8.8 kcal/mol. During reductive elimination in Path C2 (Scheme 3.19), one of the 1-azaallyl groups holds the bimetallic intermediate together via a  $\mu$ -N coordination mode. The other ligand de-coordinates from the PdMe<sub>2</sub> fragment to permit a Pd-Pd interaction giving a barrier (**TS-8a5**, 29.4 kcal/mol) that is 7.9 kcal/mol lower than an analogous structure with a retained  $\eta^2$ -CC interaction to the PdMe<sub>2</sub> moiety (**TS-8a2**, 37.3 kcal/mol). Throughout pathway C3, one **3-L1** holds the dimer together through a  $\mu$ -[ $\eta^2$ -CC: $\kappa^1$ -N] bridging coordination mode (Scheme 3.21). The alkene of this **3-L1** coordinates to the Pd without the Me groups, and the nature of the bonding interaction changes dramatically through reductive elimination. The second order perturbation energies ( $E^2$ ) from the natural bond orbital (NBO) analyses reveal that the reductive elimination precursor in **d1c4** has a relatively weak Pd-alkene interaction dominated by  $\pi_{c-c} \rightarrow d^*_{Pd}$  (5.6 kcal/mol, Scheme B.10). The analogous interaction is much stronger in intermediate **d1c5** that forms following ethane release, as evidenced by the  $E^2$  values for alkene donation to Pd ( $\pi_{c-c} \rightarrow d^*_{Pd}$ , 34.5 kcal/mol) and backdonation ( $d_{Pd} \rightarrow \pi^*_{c-c}$ , 27.6 kcal/mol, Scheme B.10). These observations, along with the short Pd-Pd distance, indicate that alkene binding significantly affects reductive elimination by modulating metal-metal synergy. The bimetallic mechanisms proposed herein—intimately dependent on changes in ancillary ligand coordination



mode—therefore complement the known monometallic mechanisms for C-C coupling at Pd (see introduction) and provide an interesting reaction motif for further development.



**Scheme 3.24.** Three proposed operative bimetallic  $Csp^3-Csp^3$  coupling pathways (C1-C3) from **3-1**, showing the reductive elimination step to give ethane, and complex **3-2**, or **3-3** and Pd(0). Colours depict the different coordination modes for the 1-azaallyl group of **3-L1**:  $\mu$ -N (blue),  $\kappa^1$ -N (pink),  $\eta^3$ -NCC (red) and  $\mu$ -( $\kappa^1$ -N,  $\eta^2$ -CC) (green).  $\Delta G$  values shown are in kcal/mol and the values are relative to **3-1** at 0 kcal/mol.

## 3.4 Conclusions

The C-C reductive elimination mechanism of a  $Pd^{II}-CH_3$  dimer (**3-2**) bearing a phosphine 1-azaallyl ligand (**3-L1**) was investigated using a combined experimental and computational approach. An equilibrium is operative between dimer **3-2** and its corresponding monomers, and the latter were deemed responsible for competing methane formation. Thus, suppression of methane to give exclusive C-C bond formation should be possible with a derivative of ligand **3-L1** that induces a greater preference for the dimeric form. A variety of evidence discounted radical or monometallic pathways for C-C bond formation. Instead, three viable bimetallic pathways were proposed and analyzed. In all cases, methyl-transfer affords a  $Pd(CH_3)_2$  fragment that undergoes 1,1-reductive elimination. A critical aspect of all three viable reductive elimination pathways is the capacity of the phosphine 1-azaallyl ligand (**3-L1**) to undergo changes in coordination mode

(i.e. five different modes identified). This structurally-responsive feature offers flexibility and versatility in the type of intermediates that can form, specifically stabilization of different bimetallic structures over undesired monometallic compounds. The changes in ligand coordination mode lowers barriers for reductive elimination, which would not be accessible with a statically-coordinated ancillary ligand. Deployment of a structurally-responsive ligand to facilitate bimetallic C-C bond formation is highly unusual and could be exploited in the emerging field of catalysis involving dinuclear Pd<sup>I</sup> and Pd<sup>II</sup> complexes as on-cycle intermediates.<sup>13</sup>

## 3.5 Experimental

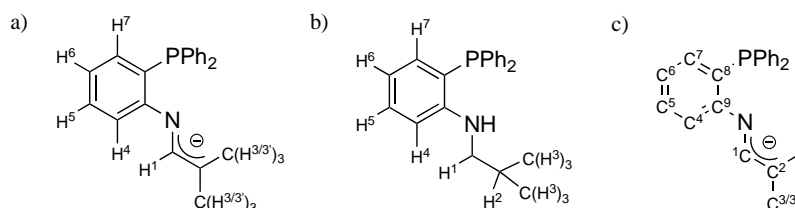
### 3.5.1 Synthetic Procedures

#### 3.5.1.1 General Considerations

Reactions were conducted in a nitrogen atmosphere glove box or using standard Schlenk line techniques under an argon atmosphere, unless otherwise indicated. All glassware was oven dried and cooled under nitrogen atmosphere prior to use unless otherwise stated. Ground-glass syringes were stored in a desiccator containing DrieRite. All reagents used were obtained from commercially available sources and used without further purification, unless otherwise indicated. Potassium Hydride was purchased from Alfa Aesar as a 30% w/w suspension in mineral oil, and was purified by filtration through a fritted funnel, the solid KH was washed with dry hexanes and diethyl ether (20 mL/g KH), the solid was dried under vacuum and stored under inert atmosphere for use. The following materials were prepared following literature procedures: PdCl(CH<sub>3</sub>)(COD),<sup>64</sup> PtCl(CH<sub>3</sub>)(COD),<sup>65</sup> 2-diphenylphosphinoaniline,<sup>47</sup> **H[3-L1]**,<sup>47</sup> **1**,<sup>36</sup> **K[3-L1]**,<sup>36</sup> and Pd(CH<sub>3</sub>)<sub>2</sub>(COD).<sup>66</sup> All reaction solvents were obtained from an Innovative Technology 400-5 Solvent Purification system, dry and degassed, and stored over activated 4 Å molecular sieves under N<sub>2</sub> prior to use, unless stated otherwise. Pyridine was dried over CaH<sub>2</sub>, distilled under vacuum, and stored over activated 4 Å sieves prior to use in an inert atmosphere. Deuterated NMR solvents were obtained from commercial sources and stored over activated 4 Å sieves in an inert atmosphere. Molecular sieves were activated by heating the sieves at 160 °C under vacuum overnight.

All NMR spectra were obtained on a 400 MHz Bruker or 600 MHz Varian spectrometer at 25 °C unless otherwise stated.  $^1\text{H}$  and  $^{13}\text{C}\{^1\text{H}\}$  spectra were referenced internally, using residual solvent values, to TMS at 0 ppm as follows: benzene- $d_6$  ( $^1\text{H}$ , 7.16 ppm;  $^{13}\text{C}\{^1\text{H}\}$ , 128.1 ppm),  $\text{CDCl}_3$  ( $^1\text{H}$ , 7.26 ppm;  $^{13}\text{C}\{^1\text{H}\}$  77.2 ppm), toluene- $d_8$  ( $^1\text{H}$ , 2.08 ppm), and acetone- $d_6$  ( $^1\text{H}$ , 2.05 ppm;  $^{13}\text{C}\{^1\text{H}\}$ , 29.8 ppm).  $^{31}\text{P}\{^1\text{H}\}$  spectra obtained in deuterated solvents were referenced internally to  $\text{H}_3\text{PO}_4$  at 0.00 ppm.  $^{31}\text{P}\{^1\text{H}\}$  spectra obtained in non-deuterated solvents were externally referenced to a sample of 85%  $\text{H}_3\text{PO}_4$ . Multiplicities are described as s (singlet), d (doublet), t (triplet), sept (septet), m (multiplet), and br (broad). Chemical shift assignments were obtained using 1D NMR spectroscopy, and hetero- and homonuclear 2D NMR spectroscopy (ie. COSY, HSQC, and HMBC). X-ray diffraction measurements were made on a Bruker Kappa Axis Apex2 diffractometer at a temperature of 110 K. Infrared spectra were collected on solid samples using a Bruker ALPHA II FTIR spectrometer. Charge-transfer Matrix Assisted Laser Desorption/Ionization (MALDI) mass spectrometry data were collected on an AB Sciex 5800 TOF/TOF mass spectrometer using pyrene as the matrix in a 20:1 molar ratio to complex. Solutions were prepared in  $\text{C}_6\text{H}_6$  and spotted on a sample plate under an inert atmosphere and transferred to the instrument in a sealed Ziplock<sup>®</sup> bag. The instrument is equipped with a 349 nm OptiBeam On-Axis laser. The laser pulse rate was 400 Hz and data were collected in reflectron positive mode unless otherwise indicated. Reflectron mode was externally calibrated at 50 ppm mass tolerance. Each mass spectrum was collected as a sum of 500 shots. The acquired data sets were plotted in Microsoft Excel, and simulations for peaks of interest were acquired from [chemcalc.org](http://chemcalc.org)<sup>6</sup> and plotted in Microsoft Excel. Quantification of ethane and methane was performed using an Agilent 7890a gas chromatogram with a flame ionization detector (GC-FID), fitted with HP-Plot/U column. GC-FID injections were performed manually using a 10  $\mu\text{L}$  Hamilton 1700 Series gas tight syringe, unless otherwise indicated. Manual injections were performed by washing the gas-tight syringe with gaseous analyte headspace ( $5 \times 10 \mu\text{L}$ ), followed by a 5  $\mu\text{L}$  gaseous headspace injection into the GC-FID instrument. Headspace gas chromatography mass spectrometry (GC-MS) measurements to confirm ethane and methane formation were obtained on a Shimadzu GCMS-QP2010 instrument, fitted with a HP-Plot/U column.

### 3.5.1.2 Ligand Synthesis



**Figure 3.3.** General labelling scheme for a) phosphine 1-azaallyl ( $P^{\wedge}AzA$ ) ligand **3-L1**; b) phosphine amine ligand **H[3-L2]**; c)  $P^{\wedge}AzA$  ligand **3-L1**. This scheme will be used consistently for all compounds throughout the experimental section. The denotations  $H^3$ ,  $H^{3'}$ ,  $C^3$ , and  $C^{3'}$  are used to distinguish between cases where atoms  $H^3$  and  $C^3$  are not equivalent.

#### 3.5.1.2.1 Synthesis of $Ph_2P(o-C_6H_4)NH(i-Bu)$ , **H[3-L2]**:

A 100 mL Schlenk flask was charged with  $LiAlH_4$  (92 mg, 2.4 mmol) and suspended in THF (8 mL). The Schlenk flask was then cooled to 0 °C and a solution of **3-L1** (200 mg, 0.60 mmol) in THF (2 mL) was added dropwise via ground-glass syringe, resulting in a colour change from clear and colourless to yellow-green. The flask was warmed to rt and stirred for 24 h. The reaction was then cooled to 0 °C, and the solution was diluted with  $Et_2O$  (10 mL). Water (0.09 mL) was added dropwise changing the solution colour from yellow-green to grey. A NaOH solution (15%, in 0.09 mL  $H_2O$ ) and additional water (0.27 mL) were added sequentially and the reaction was warmed to rt and stirred for 15 min. Anhydrous  $Na_2SO_4$  was then added and the reaction was stirred for another 15 min. The suspension was filtered, and the solvent was removed under vacuum to afford **H[3-L2]** as a clear colourless oil, which slowly solidified at room temperature to form a waxy white solid. Yield = 156 mg (78%)  $^1H$  NMR (599 MHz,  $CDCl_3$ ):  $\delta$  7.25 – 7.20 (m, 10H, P-Ph( $H$ )), 7.20 – 7.11 (m, 1H,  $H^5$ ), 6.71 (ddd,  $J = 7.7$  Hz, 6.0 Hz, 1.7 Hz, 1H,  $H^6$ ), 6.59 – 6.47 (m, 2H,  $H^4$ ,  $H^7$ ), 4.59 (br, 1H, NH), 2.83 (t,  $J = 6.1$  Hz 2H,  $H^1$ ), 1.71 (septd,  $J = 6.7$  Hz, 6.1 Hz, 1H,  $H^2$ ), 0.74 (d  $J = 6.7$  Hz, 6H,  $H^3$ ).  $^{13}C\{^1H\}$  NMR (101 MHz,  $CDCl_3$ ):  $\delta$  151.3 (d,  $^2J_{CP} = 19.2$  Hz,  $C^9$ ), 135.6 (d,  $^2J_{CP} = 8.1$  Hz,  $C^7$ ), 134.6 (d,  $J_{CP} = 5.1$  Hz, P(Ph-C)), 133.9 (d,  $J_{CP} = 19.2$  Hz, P(Ph-C)), 130.7 ( $C^5$ ), 128.8 (P(Ph-C)), 128.6 (d,  $J_{CP} = 6.1$  Hz, P(Ph-C)), 118.6 (d,  $^1J_{CP} = 10.1$  Hz,  $C^8$ ) 116.8 (d,  $^3J_{CP} = 4.0$  Hz,  $C^6$ ), 110.1 (d,  $^3J_{CP} = 2.0$  Hz,  $C^4$ ), 51.8 ( $C^1$ ), 27.8 ( $C^2$ ), 20.4 ( $C^3$ ).  $^{31}P\{^1H\}$  NMR (243 MHz,  $CDCl_3$ ):  $\delta$  -21.1. ATR-FTIR ( $cm^{-1}$ ):  $\nu$  3502 (N-H) 2944 ( $Csp^3-H$ ) ESI-MS:  $m/z$  found 334.16; calc'd **[H[3-L2]]<sup>+</sup>** 334.16.

### 3.5.1.2.2 Synthesis of K[Ph<sub>2</sub>P(*o*-C<sub>6</sub>H<sub>4</sub>)N(*i*-Bu)], **K[3-L2]**:

In a 20 mL vial, **H[3-L2]** (200 mg, 0.60 mmol) was dissolved in THF (2 mL) and added dropwise to a stirring suspension of potassium hydride (48 mg, 1.2 mmol) in THF (2 mL). The vial containing **H[3-L2]** was washed with THF (3 × 1 mL) and the mixture was stirred for 24 h. A gradual colour change was observed over the course of the first 20 min from clear and colourless, to bright yellow. Bubbles were also observed indicating the release of H<sub>2</sub>. After 24 h the reaction mixture was filtered through Celite to remove excess KH, and the reaction vial was rinsed with 0.5 mL portions of THF until the washes were no longer yellow. The washes were filtered through Celite, combined with the bulk filtrate, and the solvent was removed under vacuum to afford a yellow oil. This oil was triturated with pentane (3 × 5 mL) and dried under vacuum to give **K[3-L2]** as a yellow powder. Yield = 211 mg (95%). <sup>1</sup>H NMR (599 MHz, (CD<sub>3</sub>)<sub>2</sub>CO): δ 7.42 – 7.35 (m, 6H, P(Ph-*H*)), 7.34 – 7.27 (m, 4H, P(Ph-*H*)), 7.25 – 7.19 (m, 1H, *H*<sup>5</sup>), 6.77 – 6.73 (m, 1H, *H*<sup>6</sup>), 6.70 – 6.65 (m, 1H, *H*<sup>4</sup>), 6.59 – 6.53 (m, 1H, *H*<sup>7</sup>), 2.92 (d, *J* = 6.8 Hz, 2H, *H*<sup>1</sup>), 1.78 – 1.72 (m, 1H, *H*<sup>2</sup>), 0.81, (d, *J* = 6.8 Hz, 6H, *H*<sup>3</sup>). <sup>13</sup>C{<sup>1</sup>H} NMR (101 MHz, CDCl<sub>3</sub>): δ 151.9 (d, <sup>2</sup>*J*<sub>CP</sub> = 17.2 Hz, *C*<sup>9</sup>), 136.5 (d, <sup>2</sup>*J*<sub>CP</sub> = 8.1 Hz, *C*<sup>7</sup>), 135.1 (d, *J*<sub>CP</sub> = 5.1 Hz, P-Ph(*C*)), 134.2 (d, *J*<sub>CP</sub> = 19.2 Hz, P-Ph(*C*)), 131.5 (*C*<sup>5</sup>), 129.6 (P-Ph(*C*)), 129.4 (d, *J*<sub>CP</sub> = 14.1 Hz, *C*<sup>1</sup>) 117.3 (d, *J*<sub>CP</sub> = 3.0 Hz, *C*<sup>6</sup>), 51.9 (*C*<sup>1</sup>), 28.3 (*C*<sup>2</sup>), 20.5 (*C*<sup>3</sup>). <sup>31</sup>P{<sup>1</sup>H} NMR (243 MHz, CDCl<sub>3</sub>): δ -21.3. MALDI MS (pyrene) collected in negative ion mode *m/z* found: 255.1, calc'd [**L2**-C<sub>6</sub>H<sub>5</sub>]<sup>-</sup>: 255.1. *m/z* found: 332.2, calc'd [**3-L2**]<sup>-</sup>: 332.2.

### 3.5.1.3 Complex Synthesis

#### 3.5.1.3.1 Synthesis of Sn(CD<sub>3</sub>)<sub>4</sub>:

In a glovebox, magnesium turnings (500 mg, 21.1 mmol) and diethyl ether (7 mL) were added to a two-neck 100 mL Schlenk flask. The flask was sealed with two rubber septa, removed from the glovebox and fitted with a reflux condenser on one neck. Deuterated iodomethane (2.78 g, 19.2 mmol) was slowly added in small dropwise portions through the side arm of the flask with a ground glass syringe, while the flask was periodically warmed with a heat gun to initiate reflux. Once reflux had begun the heat was removed and the remaining iodomethane was added dropwise at a rate maintaining gentle reflux. The reaction was stirred at rt for 2 h. The reaction was then cooled down to -30 °C and a solution of SnCl<sub>4</sub> (1.00 g, 3.84 mmol) in toluene (3 mL) was added dropwise

through the side arm of the flask. The reaction was stirred for 16 h. The next day the grey mixture was quenched by slow addition of water (10 mL) at 0 °C. The suspension was filtered through a gravity funnel with a filter paper, and the filtrate was extracted with diethyl ether (3 × 5 mL), the organic layers were washed with water (3 × 10 mL) and dried over Na<sub>2</sub>SO<sub>4</sub>. The clear suspension was filtered through a gravity funnel with a filter paper and the filtrate was used immediately without further purification, a 50% yield was assumed for the subsequent reaction (*vide infra*). A 500 μL aliquot was removed and used directly for <sup>2</sup>H NMR spectroscopy. <sup>2</sup>H NMR (92.1 MHz, CH<sub>2</sub>Cl<sub>2</sub>): δ 0.62 (s, 12D, Sn-CD<sub>3</sub>). A 100 μL aliquot was diluted with 400 μL of CD<sub>2</sub>Cl<sub>2</sub>, this solution was used for <sup>119</sup>Sn{<sup>1</sup>H} NMR spectroscopy. <sup>119</sup>Sn{<sup>1</sup>H} NMR (223.8 MHz, CD<sub>2</sub>Cl<sub>2</sub>): δ – 0.67 to –1.93 (m).

### 3.5.1.3.2 Synthesis of Pd(CD<sub>3</sub>)Cl(COD):

The freshly made Sn(CD<sub>3</sub>)<sub>4</sub> solution (30 mL), and dichloromethane (60 mL) were added to a 200 mL Schlenk flask. Against a flow of argon, PdCl<sub>2</sub>(COD) (240 mg, 0.841 mmol) was added to the flask. The reaction was then allowed to stir until the colour changed from yellow to grey (ca. 16 h). The suspension was filtered through Celite, into a collection flask cooled and held at 0 °C. The reaction flask was washed with DCM (3 × 10 mL), and the washes were also filtered through Celite into the cooled collection flask. The volatiles were removed under reduced pressure at 0 °C to afford a beige powder. This powder was washed with cold diethyl ether (3 × 10 mL) to yield pure Pd(CD<sub>3</sub>)Cl(COD). The previously removed volatiles were then collected and re-reacted with PdCl<sub>2</sub>(COD) (100 mg, 0.37 mmol) as above. This was repeated until 95% of the theoretical yield based on starting (SnCD<sub>3</sub>)<sub>4</sub> was achieved. Total yield = 293 mg (61%). Note: Pd(CD<sub>3</sub>)Cl(COD) is thermally unstable and must be stored in a freezer. <sup>1</sup>H NMR (599 MHz, CDCl<sub>3</sub>): δ 5.97 – 5.85 (m, 2H, HC=CHCH<sub>2</sub>) 5.20 – 5.08 (m, 2H, HC=CHCH<sub>2</sub>), 2.75 – 2.40 (m, 8H, CHCH<sub>2</sub>CH<sub>2</sub>CH). <sup>2</sup>H NMR (92.1 MHz, CHCl<sub>3</sub>): δ 1.15 (s, Pd-CD<sub>3</sub>). <sup>13</sup>C{<sup>1</sup>H} NMR (151 MHz, CDCl<sub>3</sub>): δ 124.0 (HC=CHCH<sub>2</sub>), 100.7 (HC=CHCH<sub>2</sub>), 31.0 (CHCH<sub>2</sub>CH<sub>2</sub>CH), 27.7 (CHCH<sub>2</sub>CH<sub>2</sub>CH), 11.7 (1:3:6:7:6:3:1 sept, <sup>1</sup>J<sub>CD</sub> = 31.0 Hz, Pd-CD<sub>3</sub>). ATR-FTIR (cm<sup>-1</sup>): ν 3010 (Csp<sup>2</sup>-H), 2925 (Csp<sup>3</sup>-H). All NMR data obtained from Pd(CD<sub>3</sub>)Cl(COD) is consistent with the NMR data previously reported for its proteo analogue Pd(CH<sub>3</sub>)Cl(COD).<sup>64</sup>

### 3.5.1.3.3 Synthesis of $[\text{Pd}(\text{CD}_3)(\mathbf{3-L1})]_2$ , **3-1-*d*<sub>6</sub>**:

Prior to the beginning of the reaction, all glassware (except pipettes) and the reagents were stored in a freezer at  $-20\text{ }^\circ\text{C}$  for at least 30 minutes. In a glovebox, **K[3-L1]** (65 mg, 0.18 mmol) was dissolved in cold THF (2 mL) and added dropwise to a suspension of  $\text{PdCl}(\text{CD}_3)(\text{COD})$  dissolved in cold THF (2 mL). The reaction was stirred for 10 min and then placed in the freezer at  $-20\text{ }^\circ\text{C}$  for 10 min. The reaction was filtered through Celite into a Büchner flask. The reaction volume was reduced in the Büchner flask to ca. 2 mL and the solution was transferred to a new 20 mL vial. The reaction vial was capped and stored in the freezer at  $-20\text{ }^\circ\text{C}$  for 10 minutes. The volume was reduced to ca. 1 mL under vacuum and the solution was returned to the freezer at  $-20\text{ }^\circ\text{C}$  for 5 minutes. Cold pentane (6 mL) was added with vigorous stirring to precipitate **3-1-*d*<sub>6</sub>** as a yellow solid. The excess pentane was removed via pipette, and **3-1-*d*<sub>6</sub>** was washed with cold pentane ( $3 \times 1$  mL) and dried under vacuum. Yield = 52 mg (76%). Note: **3-1-*d*<sub>6</sub>** is thermally unstable and must be stored in a freezer, decomposition in solution occurs within 24 h at  $25\text{ }^\circ\text{C}$  while solid-state decomposition occurs over several days at  $25\text{ }^\circ\text{C}$ .  $^1\text{H}$  NMR (599 MHz,  $\text{C}_6\text{D}_6$ ):  $\delta$  7.91 – 7.83 (m, 4H, P(Ph-*H*)), 7.51 (dd,  $J = 11.6$  Hz, 7.5 Hz, 4H, P(Ph-*H*)), 7.41 (dd,  $J = 8.4$  Hz, 4.9 Hz, 2H,  $H^5$ ), 7.17 – 7.15 (m, 4H, P(Ph-*H*)), 7.12 – 7.07 (m, 2H,  $H^6$ ), 7.05 – 7.00 (m, 8H, P(Ph-*H*)), 6.99 – 6.95 (m, 4H,  $H^4$ ,  $H^7$ ), 6.64 – 6.58 (m, 2H,  $H^1$ ), 1.72 (s, 6H,  $H^3$ ), 1.42 (br s, 6H,  $H^3$ ).  $^2\text{H}$  NMR (92 MHz,  $\text{C}_6\text{H}_6$ ):  $\delta = 0.44$  (m, Pd- $\text{CD}_3$ ).  $^{31}\text{P}\{^1\text{H}\}$  NMR (243 MHz,  $\text{C}_6\text{D}_6$ ):  $\delta$  43.7 (s). MALDI MS (pyrene)  $m/z$  found 435.1, calc'd  $[\text{Pd}(\mathbf{3-L1})]^+$  435.0. All NMR data obtained from **3-1-*d*<sub>6</sub>** is consistent with the NMR data previously reported for its proteo analogue **3-1**.<sup>36</sup>

### 3.5.1.3.4 Synthesis of $[\text{Pd}(\text{CH}_3)(\mathbf{3-L2})]_2$ , **3-4**:

Prior to beginning the reaction, all glassware (except pipettes) and the reagents were stored in a freezer at  $-20\text{ }^\circ\text{C}$  for at least 30 minutes. In a 20 mL vial,  $\text{PdCl}(\text{CH}_3)(\text{COD})$  (39 mg, 0.15 mmol) was dissolved in THF (1 mL). To this vial was added 375  $\mu\text{L}$  (0.19 mmol) of a 500  $\mu\text{M}$  stock solution of pyridine in THF. Ligand **K[3-L2]** (65 mg, 0.17 mmol) was dissolved in THF (1 mL) and added dropwise to the Pd solution. The solution changed colour from yellow dark orange almost immediately. The reaction was stirred for 10 min and filtered through Celite. The vial was washed with THF ( $3 \times 1$  mL) and the washes were filtered through Celite. The filtrates were combined, and the solvent was removed under vacuum to produce a dark orange residue. Cold

pentane (5 mL) was added to dissolve the residue, and the vial was stored in the freezer at  $-20\text{ }^{\circ}\text{C}$  to produce yellow crystals of **3-4**. Yield = 35 mg (45%). **Note:** it was not possible to fully remove pyridine from the sample, ca. 20 mol% py was present as judged by  $^1\text{H}$  NMR spectroscopy. Compound **3-4** is thermally unstable and must be stored in a freezer, decomposition in solution occurs within 24 h at  $25\text{ }^{\circ}\text{C}$ , while solid state decomposition occurs over several days at  $25\text{ }^{\circ}\text{C}$ .  $^1\text{H}$  NMR (599 MHz,  $\text{C}_6\text{D}_6$ ):  $\delta$  7.96 – 7.87 (m, 8H, P-Ph(*H*)), 7.29 – 7.25 (m, 2H,  $H^5$ ), 7.12 – 7.03 (m, 14H, P-Ph(*H*),  $H^6$ ), 6.82 – 6.78 (m, 2H,  $H^4$ ), 6.37 – 6.33 (m, 2H,  $H^7$ ), 3.03 (d,  $J = 6.6$  Hz, 4H,  $H^1$ ), 1.96 (sept,  $J = 6.6$  Hz, 2H,  $H^2$ ), 0.81 (d,  $J = 6.6$  Hz, 12H,  $H^3$ ), 0.43 (d,  $J_{\text{HP}} = 1.8$  Hz, 6H, Pd- $\text{CH}_3$ ).  $^{13}\text{C}\{^1\text{H}\}$  NMR (101 MHz,  $\text{CDCl}_3$ ):  $\delta$  167.4 (d,  $J_{\text{CP}} = 23.23$  Hz,  $\text{C}^9$ ), 134.5 (P-(Ph-C)), 134.0 (d,  $J_{\text{CP}} = 53.5$  Hz, P-(Ph-C)), 133.9 (d,  $J_{\text{CP}} = 11.1$  Hz, P-(Ph-C)), 133.5 (d,  $J_{\text{CP}} = 2.0$  Hz,  $\text{C}^7$ ), 130.1 (d,  $J_{\text{CP}} = 3.0$  Hz, P-(Ph-C)), 128.6 (d,  $J_{\text{CP}} = 11.2$  Hz, P-(Ph-C)), 112.7 (d,  $J_{\text{CP}} = 57.6$  Hz,  $\text{C}^8$ ), 111.6 (d,  $J_{\text{CP}} = 13.1$  Hz,  $\text{C}^6$ ), 110.1 (d,  $J_{\text{CP}} = 9.09$  Hz,  $\text{C}^4$ ), 57.5 ( $\text{C}^1$ ), 28.2 ( $\text{C}^2$ ), 21.2 ( $\text{C}^3$ ),  $-4.6$  (d,  $J_{\text{CP}} = 6.06$  Hz, Pd- $\text{CH}_3$ ).  $^{31}\text{P}\{^1\text{H}\}$  NMR (243 MHz,  $\text{C}_6\text{D}_6$ ):  $\delta$  46.8. MALDI MS (pyrene) found 876.1, calc.  $[(\mathbf{3-4-(Me)_2}]^{+}$ : 876.1. ATR-FTIR ( $\text{cm}^{-1}$ ):  $\nu$  1451 ( $\text{C}_{\text{sp}^2}\text{-P}$ ), 1095 (C-N). Crystals suitable for X-ray diffraction were obtained by slow evaporation of pentane from a solution of **3-4** at  $-20\text{ }^{\circ}\text{C}$ , details are provided in Appendix B.

### 3.5.1.3.5 Synthesis of $[\text{Pt}(\text{CH}_3)(\mathbf{3-L1})]_2$ , **3-5**:

In two separate 20 mL vials, **K[3-L1]** (56 mg, 0.15 mmol) and  $[\text{Pt}(\text{CH}_3)\text{Cl}(\text{COD})]$  (44 mg, 0.13 mmol) were dissolved in THF (1.5 mL) and stored in a freezer at  $-20\text{ }^{\circ}\text{C}$  for ca. 10 min prior to the reaction. **K[3-L1]** was then added dropwise to a stirred solution of  $[\text{PtCl}(\text{CH}_3)(\text{COD})]$  resulting in an immediate colour change from clear to orange. The reaction was stirred for 10 minutes. The reaction was then filtered through a pipette plugged with a microfiber filter and Celite into a vial. The solvent of the filtrate was reduced under vacuum to ca. 1 mL and the vial was stored in the freezer at  $-20\text{ }^{\circ}\text{C}$  for ca. 10 min Cold pentane (10 mL) was added with vigorous stirring to precipitate **3-5** as an orange solid. The pentane was then decanted and the orange solid was washed with cold pentane ( $3 \times 1$  mL) and dried under vacuum. Yield = 47 mg (69%). **3-5** is thermally unstable and must be stored in a freezer, decomposition in solution occurs within 24 h at  $25\text{ }^{\circ}\text{C}$ , while solid state decomposition occurs over several days at  $25\text{ }^{\circ}\text{C}$ .  $^1\text{H}$  NMR (599 MHz,  $\text{C}_6\text{D}_6$ ):  $\delta$  8.10 – 7.92 (m, 4H, P-Ph(*H*)), 7.65 – 7.55 (m, 4H, P-Ph(*H*)), 7.51 (dd,  $J = 8.3, 4.8$  Hz, 2H,  $H^6$ ),



7.22 – 7.16 (m, 4H, P-Ph(*H*)), 7.09 – 7.00 (m, 8H, P-Ph(*H*)), 7.00 – 6.94 (m, 4H,  $H^{5/7}$ ) 6.67 – 6.58 (m, 2H,  $H^4$ ), 1.66 (s, 12H,  $H^{3/3'}$ ), 0.77 (d,  $^3J_{HP} = 1.9$  Hz, 6H, Pd-CH<sub>3</sub>).  $^{13}\text{C}\{^1\text{H}\}$  NMR (151 MHz, CDCl<sub>3</sub>):  $\delta$  165.4 ( $C^9$ ), 142.8 ( $C^1$ ), 134.4 (d,  $J_{CP} = 18.9$  Hz, P-Ph( $C$ )), 133.4 (d,  $J_{CP} = 16.6$  Hz, Ph( $C$ )), 132.1 (P-Ph( $C$ )), 130.9 (P-Ph( $C$ )), 130.6 (P-Ph( $C$ )), 129.9 (P-Ph( $C$ )), 128.6 ( $C$ ), 122.2 ( $C^7$ ), 120.3 ( $C^2$ ), 23.8 ( $C^3$ ), 18.35 (br,  $C^3$ ) – 15.1 (Pd-CH<sub>3</sub>).  $^{31}\text{P}\{^1\text{H}\}$  NMR (243 MHz, C<sub>6</sub>D<sub>6</sub>):  $\delta$  20.4 (s, with  $^{195}\text{Pt}$  satellites,  $^1J_{\text{P-Pt}} = 4399$  Hz). MALDI MS (pyrene)  $m/z$  found 524.1, calc. [**3-5**-(Pt(**3-L1**)(Me)<sub>2</sub>)]<sup>+</sup>: 524.1.  $m/z$  found 1049.2, calc. [**3-5**-(Me)<sub>2</sub>]<sup>+</sup>: 1049.2. ATR-FTIR (cm<sup>-1</sup>):  $\nu$  1434 (Csp<sup>2</sup>-P), 1100 (C-N).

### 3.5.1.3.6 Synthesis of Pt(**3-L1**)<sub>2</sub>, **3-6**:

In a glovebox, **3-5** (45 mg, 0.04 mmol) was dissolved in C<sub>6</sub>H<sub>6</sub> (5 mL) and added to a 25 mL Schlenk tube. The tube was sealed and removed from the box, and heated at 70 °C for 2.5 h under a flow of argon. The reaction was cooled to room temperature and the solvent was removed via vacuum to produce a dark brown residue. The residue was washed with pentane (3 × 3 mL), the washes were combined and the solvent was removed to produce a yellow solid. The solid was washed with diethyl ether (3 × 3 mL), the washes were combined and the solvent was removed to afford **3-6** as an orange solid which was dried under vacuum. Yield = 19 mg (54%).  $^1\text{H}$  NMR (599 MHz, C<sub>6</sub>D<sub>6</sub>):  $\delta$  7.34 – 7.25 (m, 4H, P-Ph(*H*)), 7.12 – 7.07 (m, 2H,  $H^5$ ), 6.96 (m, 2H,  $H^1$ ), 6.95 – 6.90 (m, 4H, P-Ph(*H*)), 6.86 – 6.80 (m, 8H, P-Ph(*H*)), 6.75 – 6.69 (m, 8H, P-Ph(*H*),  $H^{6/7}$ ) 6.35 – 6.28 (m, 2H,  $H^4$ ), 1.96 (s, 6H,  $H^{3/3'}$ ), 1.92 (s, 6H,  $H^{3/3'}$ ).  $^{13}\text{C}\{^1\text{H}\}$  NMR (151 MHz, CDCl<sub>3</sub>):  $\delta$  166.9 – 166.1 (m,  $C^9$ ), 135.9 ( $C^1$ ), 133.9 – 133.2 (m, P-Ph( $C$ ),  $C^8$ ), 132.3 (P-Ph( $C$ )), 130.4 ( $C^5$ ), 130.2 (P-Ph( $C$ )), 128.1 (P-Ph( $C$ )), 120.3 ( $C^4$ ), 117.3 (m,  $C^2$ ) 114.0 ( $C^6$ ) 113.8 – 113.5 (m,  $C^7$ ), 23.4 ( $C^3$ ), 18.5 (s,  $C^3$ ).  $^{31}\text{P}\{^1\text{H}\}$  NMR (243 MHz, C<sub>6</sub>D<sub>6</sub>):  $\delta$  28.0 (s, with  $^{195}\text{Pt}$  satellites,  $^1J_{\text{P-Pt}} = 5208$  Hz). MALDI MS (pyrene)  $m/z$  found 524.1, calc. [**3-6**-(**3-L1**)]<sup>+</sup>: 524.1.  $m/z$  found 855.2, calc. [**3-6**]<sup>+</sup>: 855.2. Crystals suitable for X-ray diffraction were obtained by solvent diffusion from a THF solution of **3-6** while using pentane as the anti-solvent at –20 °C, details are provided in Appendix B.

### 3.5.1.3.7 Synthesis of K[Pd(CH<sub>3</sub>)<sub>2</sub>(**3-L1**)], **K[3-7]**:

Prior to the beginning of the reaction, all glassware (except pipettes) and reagents were stored in a freezer at –30 °C for at least 30 minutes. In a glovebox, ligand **K[3-L1]** (78 mg, 0.21 mmol) and

Pd(CH<sub>3</sub>)<sub>2</sub>(COD) (43 mg, 0.17 mmol) were weighed out in two separate 20 mL vials. Ligand **K[3-L1]** was dissolved in THF (1 mL) and the two vials were placed in a freezer at –30 °C for ca. 15 min Cold THF (0.5 mL) was then added to dissolve Pd(CH<sub>3</sub>)<sub>2</sub>(COD), and the cold solution of **K[3-L1]** was immediately added dropwise to the solution of Pd(CH<sub>3</sub>)<sub>2</sub>(COD). The reaction vial was swirled and placed in the freezer at –30 °C for 10 min The solution was then filtered through Celite and the solvent was removed under vacuum to generate an orange residue. The residue was triturated with pentane (3 × 3 mL) to produce **K[3-7]** as a yellow crystalline solid and dried under vacuum. Yield = 87 mg (99%). **K[3-7]** is thermally unstable and must be stored in a freezer, storage longer than 2 weeks leads to decomposition even at –30 °C. <sup>1</sup>H NMR (599 MHz, (CD<sub>3</sub>)<sub>2</sub>CO): δ 7.61 (m, 4H, P-Ph(*H*)), 7.31 – 7.23 (m, 6H, P-Ph(*H*)), 6.82 – 6.76 (m, 1H, *H*<sup>5</sup>), 6.72 – 6.66 (m, 1H, *H*<sup>6</sup>), 6.20 – 6.14 (m, 1H, *H*<sup>7</sup>), 6.04 (s, 1H, *H*<sup>1</sup>) 5.79 (m, 1H, *H*<sup>4</sup>), 1.73 (s, 3H, *H*<sup>3/3'</sup>), 1.48 (s, 3H, *H*<sup>3/3'</sup>), 0.00 (d, *J* = 7.2 Hz, 3H, P-Pd-*cis*-CH<sub>3</sub>), –0.05 (d, 7.8 Hz, 3H, P-Pd-*trans*-CH<sub>3</sub>). <sup>13</sup>C{<sup>1</sup>H} NMR (151 MHz, 0 °C, (CD<sub>3</sub>)<sub>2</sub>CO): δ 165.8 (d, *J*<sub>CP</sub> = 30.2 Hz, *C*<sup>9</sup>), 138.8 (d, *J*<sub>CP</sub> = 25.7 Hz, P(Ph-C), 135.7 (*C*<sup>1</sup>), 133.9 (d, *J*<sub>CP</sub> = 13.6 Hz, *C*<sup>8</sup>), 133.3 (*C*<sup>5</sup>), 128.6 (P(Ph-C)), 128.8 (d, *J*<sub>CP</sub> = 10.6 Hz, *C*<sup>4</sup>) 127.9 (d, *J*<sub>CP</sub> = 9.1 Hz, P(Ph-C), 115.5 (d, *J*<sub>CP</sub> = 39.3 Hz P(Ph-C), 113.6 (*C*<sup>2</sup>), 112.4 (d, *J*<sub>CP</sub> = 12.1 Hz, *C*<sup>7</sup>), 107.4 (d, *J*<sub>CP</sub> = 6.0 Hz, *C*<sup>6</sup>), 21.9 (*C*<sup>3/3'</sup>), 17.7 (*C*<sup>3/3'</sup>), 7.9 (d, <sup>2</sup>*J*<sub>CP</sub> = 117.8 Hz, P-Pd-*trans*-CH<sub>3</sub>), –11.6 (d, <sup>2</sup>*J*<sub>CP</sub> = 6.04 Hz, *cis*-Pd-CH<sub>3</sub>). <sup>31</sup>P{<sup>1</sup>H} NMR (243 MHz, (CD<sub>3</sub>)<sub>2</sub>CO): δ = 22.5. ATR-FTIR (cm<sup>-1</sup>): ν 1433 (C<sub>sp</sub><sup>2</sup>-P), 1098 (C-N). MALDI MS (pyrene) collected in negative ion mode *m/z* found 330.2, calc. [**3-L1**]<sup>-</sup>: 330.1. *m/z* found 436.1, calc. [**3-7**-(Me)<sub>2</sub>]<sup>-</sup>: 436.1. *m/z* found 766.2, calc [(C<sub>22</sub>H<sub>21</sub>NP)<sub>2</sub>Pd]<sup>-</sup>: 766.2.

### 3.5.1.3.8 Attempted Synthesis of [Pd(**3-L1**)<sub>2</sub>Pd(CH<sub>3</sub>)<sub>2</sub>], **3-8**:

#### 3.5.1.3.8.1 Room Temperature:

In a glovebox, **3-3** (6 mg, 0.008 mmol) and Pd(CH<sub>3</sub>)<sub>2</sub>(COD) (Run a: 28 mg, 0.12 mmol; or Run b: 4 mg, 0.015 mmol) were weighed into two separate 4 mL vials and dissolved in C<sub>6</sub>D<sub>6</sub> (250 μL each). Complex **3-3** was then added dropwise to each of the solutions of Pd(CH<sub>3</sub>)<sub>2</sub>(COD) and the mixtures were each added to an NMR tube. The NMR tubes stood at rt for ca. 16 h total inside a glovebox and <sup>1</sup>H and <sup>31</sup>P{<sup>1</sup>H} NMR spectra were acquired on each tube after 30 minutes, 1 h, 4.5 h, and 16 h. Complete conversion from **3-3** to **3-1** was observed in Run a after 4.5 h. Complete

conversion was not observed in Run b and several new minor products were observed by  $^{31}\text{P}\{^1\text{H}\}$  NMR spectroscopy. Complex **3-8** was not observed during either reaction.

### 3.5.1.3.8.2 0 °C:

A similar procedure to the room temperature experiments was used with the following changes:  $\text{Pd}(\text{CH}_3)_2(\text{COD})$  (5 mg, 0.020 mmol), and  $\text{tol-}d_8$  was the solvent. The NMR tube stood in an ice bath held at 0 °C for 6 h total. A  $^1\text{H}$  and  $^{31}\text{P}\{^1\text{H}\}$  NMR spectrum was acquired after 30 minutes, 1 h, 4.5 h, and 6 h. Complete conversion was not observed, and conversion did not increase from 4.5 h to 6 h. Complex **3-8** was not observed during this reaction.

## 3.5.2 Experimental Procedures

### 3.5.2.1 Kinetic Data:

#### 3.5.2.1.1 Rate Data:

Two solutions of **3-1** in  $\text{C}_6\text{H}_6$  were prepared (22 mM, 62 mM) and added to two separate NMR tubes (A and B), along with a sealed capillary of triphenylphosphine oxide (TPPO) in  $\text{C}_6\text{H}_6$  (47 mM). Each NMR tube was placed into the spectrometer and an initial spectrum (time = 0,  $T_0$ ) was acquired at room temperature with the  $T_1$  relaxation delay set to 5 s. The tube was removed from the spectrometer and placed in a fridge (4 °C) while the instrument heated to 70 °C. Each tubes was placed into the spectrometer and a  $^{31}\text{P}\{^1\text{H}\}$  NMR spectrum was acquired every 5 minutes for 2 h ( $T_1$  relaxation delay of 5 s.) The consumption of **1** was monitored vs. TPPO, and plots of [**3-1**],  $\text{Ln}[\mathbf{3-1}]$ , and  $1/[\mathbf{3-1}]$  vs. Time (min) were constructed using this data. The resulting rate plot from  $\text{Ln}[\mathbf{3-1}]$  vs. Time gave an excellent linear fit, consistent with a first order reaction. These reactions were performed in duplicate.

#### 3.5.2.1.2 Eyring Analysis

An 8 mL stock solution of **3-1** in  $\text{C}_6\text{D}_6$  (80 mM) was prepared and stored in a freezer at -20 °C prior to NMR analysis. The sample was thawed and a 500  $\mu\text{L}$  aliquot was removed and added to an NMR tube, along with a sealed capillary of dimethyl terephthalate (DMTP) in  $\text{C}_6\text{D}_6$  (31 mM).

The NMR tube was then placed into an NMR spectrometer and an initial ( $T_0$ )  $^1\text{H}$  NMR spectrum was acquired at room temperature. The tube was removed from the spectrometer and placed in a fridge ( $4\text{ }^\circ\text{C}$ ) while the instrument was heated to 70, 60, 55, 50, or  $40\text{ }^\circ\text{C}$ . A  $^1\text{H}$  NMR spectrum was then acquired every 45 s for 1.15 h at the given temperature. The consumption of **3-1** was monitored vs. DMTP, and plots of  $\text{Ln}[\mathbf{3-1}]$  vs. Time (s) were constructed for each set of data at the five different temperatures. The resulting rate plots gave excellent linear fit, and the rate constants ( $k$ ) were extracted from the slope of each generated plot. An Eyring plot of  $\ln(k/T)$  vs.  $1/T$  ( $\times 10^3\text{ K}^{-1}$ ) was generated using the acquired rate constants. The  $\Delta S^\ddagger$  for the reaction was extracted from the y-intercept. The  $\Delta H^\ddagger$  for the reaction was extracted from the slope. The  $\Delta G^\ddagger$  for the reaction at  $T = 273.15$  and  $343.15\text{ K}$  was acquired using the Gibbs Free Energy formula, and the calculated values of  $\Delta H^\ddagger$  and  $\Delta S^\ddagger$ .

### 3.5.2.2 Radical Tests

Complex **3-1** (11 mg, 0.012 mmol) was dissolved in  $\text{C}_6\text{D}_6$  (500  $\mu\text{L}$ ) and the solution was added to an NMR tube along with a sealed capillary containing DMTP dissolved in  $\text{C}_6\text{D}_6$  (31 mM). The NMR tube was sealed with a rubber septum, and a  $T_0$   $^1\text{H}$  NMR spectrum was acquired at room temperature. The tube was removed from the spectrometer and 35 equiv of the selected H-atom donor (1,4-cyclohexadiene or 9,10-dihydroanthracene) was added to the tube via a 100 mM solution in  $\text{C}_6\text{D}_6$  via syringe. The NMR tube was hand swirled for 20 s and heated at  $70\text{ }^\circ\text{C}$  for 2.5 h in an oil bath. The NMR tube was cooled to room temperature and  $^1\text{H}$  and  $^{31}\text{P}\{^1\text{H}\}$  NMR spectra were acquired.

### 3.5.2.3 Crossover Experiments

#### 3.5.2.3.1 Filled Tube Experiment

Complex **3-1** (11 mg, 0.13 mmol) and **3-1-*d*<sub>6</sub>** (11 mg, 0.13 mmol) were each dissolved in  $\text{C}_6\text{D}_6$  (500  $\mu\text{L}$ ) and added to an oven-dried J. Young NMR tube. The vials were washed with  $\text{C}_6\text{D}_6$  ( $2 \times 300\text{ } \mu\text{L}$ ) and the washes were added to the NMR tube. The total volume of solution in the tube was 2.2 mL, leaving a headspace of  $< 10\%$  by volume. The tube was placed in an oil bath at  $70\text{ }^\circ\text{C}$  until the reaction was completed (ca. 2.5 h). The tube was cooled to rt and a  $^1\text{H}$  NMR spectrum was

acquired with the T1 relaxation time set to 25 s. The ratio of ethane to ethane- $d_3$  was determined by integration of the respective signals in the  $^1\text{H}$  NMR spectrum.

### 3.5.2.3.2 GC-MS Analysis

Complex **3-1** (11 mg, 0.125 mmol) and **3-1- $d_6$**  (11 mg, 0.125 mmol) were each dissolved in  $\text{C}_6\text{D}_6$  (500  $\mu\text{L}$ ) and added to an NMR tube. The NMR tube was sealed with a rubber septum cap and placed in an oil bath at 70  $^\circ\text{C}$  until the reaction was complete (ca. 2.5 h). The tube was cooled to rt and the headspace gases were injected into a GC-MS, and the chromatogram revealed an approximate 1:2:1 mixture of ethane: ethane- $d_3$ : ethane- $d_6$ .

### 3.5.2.4 General Thermolysis Procedure

Solutions of **3-1**, **3-4**, or **3-6** (6 mg, 0.007, 0.007, and 0.006 mmol) in  $\text{C}_6\text{D}_6$  (500  $\mu\text{L}$ ) or **K[3-7]** (6mg, 0.01 mmol) in acetone- $d_6$  (500  $\mu\text{L}$ ) was added to an NMR tube and the tube was sealed with a rubber septum. The NMR tube was heated in an oil bath at 70  $^\circ\text{C}$  ( $\text{C}_6\text{D}_6$ ) (Scheme B.1a), or 50  $^\circ\text{C}$  ( $(\text{CD}_3)_2\text{CO}$ ) (Scheme B.1b) for 2.5 h. The tube was cooled to room temperature and a  $^1\text{H}$  and  $^{31}\text{P}\{^1\text{H}\}$  NMR spectrum was acquired to determine if methane or ethane were formed, and to inspect the organometallic products. Using a gas-tight syringe, 7  $\mu\text{L}$  of the headspace was injected into a GC-FID. The yields of ethane and methane were determined through headspace analysis, using calibration curves generated by injection of the pure gaseous organic product into an NMR tube containing  $\text{C}_6\text{H}_6$  (500  $\mu\text{L}$ ) or acetone (500  $\mu\text{L}$ ) as previously reported.<sup>36</sup>

### 3.5.2.5 Relationship between 3-4 and 3-5

In a glovebox, complex **3-2** (3 mg, 0.003 mmol) or complex **3-3** (6 mg, 0.008 mmol) were dissolved in  $\text{C}_6\text{D}_6$  (500  $\mu\text{L}$ ) and added to an NMR tube. A sealed capillary containing DMTP (30 mM) in  $\text{C}_6\text{D}_6$  was added to the NMR tube, and the tube was sealed with a polyethylene cap, wrapped with Parafilm, and heated at 70  $^\circ\text{C}$  for 2.5 h. The NMR tube was cooled to rt, and a  $^{31}\text{P}\{^1\text{H}\}$  and  $^1\text{H}$  NMR spectrum were obtained. A relaxation delay ( $T_1$ ) of 5 s was used for the  $^{31}\text{P}\{^1\text{H}\}$  NMR experiment.

### 3.5.3 Computational Details

The proposed reaction pathways were optimized using the Growing String Method (GSM)<sup>42-44</sup> developed by the Zimmerman group, using the Q-Chem 5.2 software package<sup>64</sup>. The B97-D<sup>65, 66</sup> density functional with basis BS1 [B97-D/BS1, BS1: 6-31G<sup>67</sup> for H, C, N, LANL2DZ and fit-LANL2DZ ECP<sup>68, 69</sup> for P, and Pd] were utilized in the gas phase GSM computations. Following GSM optimizations, transition states were further refined using the B97-D density functional with basis BS2 [B97-D/BS2, BS2: 6-31G(d)<sup>67, 70</sup> for H, C, N, LANL2DZ and fit-LANL2DZ ECP for P, and Pd]. ECP fitting<sup>71</sup> for the LANL2DZ basis set of P and Pd was used via keyword fit-LANL2DZ. Frequency computations (B97-D/BS2) were performed in order to verify the nature of all stationary points. A self-consistent field convergence of  $10^{-6}$  was used for all computations. Single-point energy computations in benzene (C<sub>6</sub>H<sub>6</sub>) used the SMD model<sup>72</sup> with BS3 (def-TZVP<sup>73</sup> for H, C, N and P, def2-TZVP<sup>74</sup> and related ECP<sup>75</sup> for Pd) to model the solvation effect of the chemical reactions in solution (SMD<sub>(C<sub>6</sub>H<sub>6</sub>)</sub>-B97-D/BS3//B97-D/BS2). The energies [SMD<sub>(C<sub>6</sub>H<sub>6</sub>)</sub>-B97-D/BS3//B97-D/BS2] are determined at 1 atm and 298.15 K, and Gibbs free energies of activation ( $\Delta G^\ddagger$ ) and Gibbs free energies of reaction ( $\Delta G^\circ$ ) are given in kcal mol<sup>-1</sup>. Oxidation states were computed using localized orbital bonding analysis (LOBA)<sup>76</sup> with the method of PM localization and analyzed via Löwdin population (keywords LOBA=12, and LOBA\_THRESH=6015). The second order perturbation energies ( $E^2$ , in kcal/mol) were obtained from natural bond orbital computations (NBO 5.0 package)<sup>77</sup> incorporated in Q-Chem 5.2 package.<sup>64</sup>

Note for monomer **m1**: Two isomers of monomer **m1** and a higher energy species, **m1x**, were computed. Compared to **m1x**, a weak agostic interaction was present in isomer **m1**. The gas-phase electronic energy of **m1** is 0.3 kcal/mol higher than that of **m1x**, and the solvent-corrected Gibbs free energy of **m1** is -1.8 kcal/mol lower than that of **m1x**.

### 3.6 References

1. Gildner, P. G.; Colacot, T. J., *Organometallics* **2015**, *34*, 5497-5508.
2. Li, H.; Johansson Seechurn, C. C. C.; Colacot, T. J., *ACS Catal.* **2012**, *2*, 1147-1164.
3. Magano, J.; Dunetz, J. R., *Chem. Rev.* **2011**, *111*, 2177-2250.
4. Wu, X.-F.; Anbarasan, P.; Neumann, H.; Beller, M., *Angew. Chem. Int. Ed.* **2010**, *49*, 9047-9050.

5. Nicolaou, K. C.; Bulger, P. G.; Sarlah, D., *Angew. Chem. Int. Ed.* **2005**, *44*, 4442-4489.
6. Gensch, T.; Hopkinson, M. N.; Glorius, F.; Wencel-Delord, J., *Chem. Soc. Rev.* **2016**, *45*, 2900-2936.
7. Wencel-Delord, J.; Droge, T.; Liu, F.; Glorius, F., *Chem. Soc. Rev.* **2011**, *40*, 4740-4761.
8. Bonney, K. J.; Schoenebeck, F., *Chem. Soc. Rev.* **2014**, *43*, 6609-6638.
9. Inatomi, T.; Koga, Y.; Matsubara, K., *Molecules* **2018**, *23*.
10. Hazari, N.; Hruszkewycz, D. P., *Chem. Soc. Rev.* **2016**, *45*, 2871-2899.
11. Bonney, K. J.; Proutiere, F.; Schoenebeck, F., *Chem. Sci.* **2013**, *4*, 4434-4439.
12. Kalvet, I.; Bonney, K. J.; Schoenebeck, F., *J. Org. Chem.* **2014**, *79*, 12041-12046.
13. Fricke, C.; Sperger, T.; Mendel, M.; Schoenebeck, F., *Angew. Chem. Int. Ed.* **2021**, *60*, 3355-3366.
14. Aufiero, M.; Sperger, T.; Tsang, A. S. K.; Schoenebeck, F., *Angew. Chem. Int. Ed.* **2015**, *54*, 10322-10326.
15. Yin, G.; Kalvet, I.; Schoenebeck, F., *Angew. Chem. Int. Ed.* **2015**, *54*, 6809-6813.
16. Chen, X.-Y.; Pu, M.; Cheng, H.-G.; Sperger, T.; Schoenebeck, F., *Angew. Chem. Int. Ed.* **2019**, *58*, 11395-11399.
17. Lai, X.; Li, Y., *ChemCatChem* **2021**, *13*, 2465-2473.
18. De, S.; Sivendran, N.; Maity, B.; Pirkil, N.; Koley, D.; Gooßen, L. J., *ACS Catal.* **2020**, *10*, 4517-4533.
19. Das, R. K.; Saha, B.; Rahaman, S. M. W.; Bera, J. K., *Chem. Eur. J.* **2010**, *16*, 14459-14468.
20. Correa-Ayala, E.; Campos-Alvarado, C.; Chávez, D.; Hernández-Ortega, S.; Morales-Morales, D.; Miranda-Soto, V.; Parra-Hake, M., *Inorg. Chim. Acta* **2019**, *490*, 130-138.
21. Han, X.; Weng, Z.; Hor, T. S. A., *J. Organomet. Chem.* **2007**, *692*, 5690-5696.
22. Ence, C. C.; Martinez, E. E.; Himes, S. R.; Nazari, S. H.; Moreno, M. R.; Matu, M. F.; Larsen, S. G.; Gassaway, K. J.; Valdivia-Berroeta, G. A.; Smith, S. J.; Ess, D. H.; Michaelis, D. J., *ACS Catal.* **2021**, *11*, 10394-10404.
23. Powers, D. C.; Ritter, T., *Acc. Chem. Res.* **2012**, *45*, 840-850.
24. Maestri, G.; Motti, E.; Della Ca', N.; Malacria, M.; Derat, E.; Catellani, M., *J. Am. Chem. Soc.* **2011**, *133*, 8574-8585.
25. Cárdenas, D. J.; Martín-Matute, B.; Echavarren, A. M., *J. Am. Chem. Soc.* **2006**, *128*, 5033-5040.
26. Fafard, C. M.; Adhikari, D.; Foxman, B. M.; Mindiola, D. J.; Ozerov, O. V., *J. Am. Chem. Soc.* **2007**, *129*, 10318-10319.
27. Hartwig, J. F., *Organotransition Metal Chemistry: From Bonding to Catalysis*. University Science Books Sausalito, CA, 2010; p 1128.
28. Reid, S. M.; Mague, J. T.; Fink, M. J., *J. Am. Chem. Soc.* **2001**, *123*, 4081-4082.
29. Lanci, M. P.; Remy, M. S.; Kaminsky, W.; Mayer, J. M.; Sanford, M. S., *J. Am. Chem. Soc.* **2009**, *131*, 15618-15620.
30. Lotz, M. D.; Remy, M. S.; Lao, D. B.; Ariafard, A.; Yates, B. F.; Canty, A. J.; Mayer, J. M.; Sanford, M. S., *J. Am. Chem. Soc.* **2014**, *136*, 8237-8242.
31. Rudenko, A. E.; Clayman, N. E.; Walker, K. L.; Maclaren, J. K.; Zimmerman, P. M.; Waymouth, R. M., *J. Am. Chem. Soc.* **2018**, *140*, 11408-11415.
32. Young, S. J.; Kellenberger, B.; Reibenspies, J. H.; Himmel, S. E.; Manning, M.; Anderson, O. P.; Stille, J. K., *J. Am. Chem. Soc.* **1988**, *110*, 5744-5753.

33. Stockland, R. A.; Janka, M.; Hoel, G. R.; Rath, N. P.; Anderson, G. K., *Organometallics* **2001**, *20*, 5212-5219.
34. Trinquier, G.; Hoffmann, R., *Organometallics* **1984**, *3*, 370-380.
35. Pye, D. R.; Mankad, N. P., *Chem. Sci.* **2017**, *8*, 1705-1718.
36. Jackman, K. M. K.; Bridge, B. J.; Sauv e, E. R.; Rowley, C. N.; Zheng, C. H. M.; Stubbs, J. M.; Boyle, P. D.; Blacquiere, J. M., *Organometallics* **2019**, *38*, 1677-1681.
37. Blacquiere, J. M., *ACS Catal.* **2021**, *11*, 5416-5437.
38. Braunstein, P.; Naud, F., *Angew. Chem. Int. Ed.* **2001**, *40*, 680-699.
39. Slone, C. S.; Weinberger, D. A.; Mirkin, C. A., The Transition Metal Coordination Chemistry of Hemilabile Ligands. In *Progress in Inorganic Chemistry*, Karlin, K. D., Ed. John Wiley& Sons, Inc.: 1999; Vol. 48, pp 233-350.
40. Jeffrey, J. C.; Rauchfuss, T. B., *Inorg. Chem.* **1979**, *18*, 2658-2666.
41. Miller, E. M.; Shaw, B. L., *J. Chem. Soc., Dalton Trans.* **1974**, 480-485.
42. Zimmerman, P. M., *J. Chem. Phys.* **2013**, *138*, 184102.
43. Zimmerman, P., *Journal of Chemical Theory and Computation* **2013**, *9*, 3043-3050.
44. Zimmerman, P. M., *J. Comput. Chem.* **2015**, *36*, 601-611.
45. Yang, L.; Powell, D. R.; Houser, R. P., *Dalton Trans.* **2007**, 955-964.
46. Perutz, R. N.; Sabo-Etienne, S., *Angew. Chem. Int. Ed.* **2007**, *46*, 2578-2592.
47. Stubbs, J. M.; Firth, K. F.; Bridge, B. J.; Berger, K. J.; Hazlehurst, R. J.; Boyle, P. D.; Blacquiere, J. M., *Dalton Trans.* **2017**, *46*, 647-650.
48. Konze, W. V.; Scott, B. L.; Kubas, G. J., *J. Am. Chem. Soc.* **2002**, *124*, 12550-12556.
49. D. Fryzuk, M.; K. B. Clentsmith, G.; J. Rettig, S., *J. Chem. Soc., Dalton Trans.* **1998**, 2007-2016.
50. Warren, J. J.; Tronic, T. A.; Mayer, J. M., *Chem. Rev.* **2010**, *110*, 6961-7001.
51. Doherty, M. D.; Trudeau, S.; White, P. S.; Morken, J. P.; Brookhart, M., *Organometallics* **2007**, *26*, 1261-1269.
52. Dahan, F.; Dyer, Philip W.; Hanton, Martin J.; Jones, M.; Mingos, D. Michael P.; White, Andrew J. P.; Williams, David J.; Williamson, A.-M., *Eur. J. Inorg. Chem.* **2002**, *2002*, 732-742.
53. Smith, D. A.; Batsanov, A. S.; Costuas, K.; Edge, R.; Apperley, D. C.; Collison, D.; Halet, J.-F.; Howard, J. A. K.; Dyer, P. W., *Angew. Chem. Int. Ed.* **2010**, *49*, 7040-7044.
54. Pregosin, P. S., *NMR in Organometallic Chemistry*. Wiley-VCH Verlag &Co. KGaA: Weinheim, Germany, 2012; p 392.
55. Hayashi, Y.; Nakamura, Y.; Isobe, K., *J. Chem. Soc., Chem. Commun.* **1988**, 403-404.
56. Bursten, B. E.; Cayton, R. H., *Organometallics* **1986**, *5*, 1051-1053.
57. Wigginton, J. R.; Trepanier, S. J.; McDonald, R.; Ferguson, M. J.; Cowie, M., *Organometallics* **2005**, *24*, 6194-6211.
58. Ni, C.; Power, P. P., *Organometallics* **2009**, *28*, 6541-6545.
59. Luo, J.; Khusnutdinova, J. R.; Rath, N. P.; Mirica, L. M., *Chem. Commun.* **2012**, *48*, 1532-1534.
60. Peng, Q.; Wang, Z.; Zari c, S. D.; Brothers, E. N.; Hall, M. B., *J. Am. Chem. Soc.* **2018**, *140*, 3929-3939.
61. P rez-Rodr guez, M.; Braga, A. A. C.; Garcia-Melchor, M.; P rez-Temprano, M. H.; Casares, J. A.; Ujaque, G.; de Lera, A. R.;  lvarez, R.; Maseras, F.; Espinet, P., *J. Am. Chem. Soc.* **2009**, *131*, 3650-3657.
62. Ananikov, V. P.; Musaev, D. G.; Morokuma, K., *Eur. J. Inorg. Chem.* **2007**, *2007*, 5390-5399.



63. Gimferrer, M.; Van der Mynsbrugge, J.; Bell, A. T.; Salvador, P.; Head-Gordon, M., *Inorg. Chem.* **2020**, *59*, 15410-15420.
64. Shao, Y.; Gan, Z.; Epifanovsky, E.; Gilbert, A. T. B.; Wormit, M.; Kussmann, J.; Lange, A. W.; Behn, A.; Deng, J.; Feng, X.; Ghosh, D.; Goldey, M.; Horn, P. R.; Jacobson, L. D.; Kaliman, I.; Khaliullin, R. Z.; Kuš, T.; Landau, A.; Liu, J.; Proynov, E. I.; Rhee, Y. M.; Richard, R. M.; Rohrdanz, M. A.; Steele, R. P.; Sundstrom, E. J.; Woodcock, H. L.; Zimmerman, P. M.; Zuev, D.; Albrecht, B.; Alguire, E.; Austin, B.; Beran, G. J. O.; Bernard, Y. A.; Berquist, E.; Brandhorst, K.; Bravaya, K. B.; Brown, S. T.; Casanova, D.; Chang, C.-M.; Chen, Y.; Chien, S. H.; Closser, K. D.; Crittenden, D. L.; Diedenhofen, M.; DiStasio, R. A.; Do, H.; Dutoi, A. D.; Edgar, R. G.; Fatehi, S.; Fusti-Molnar, L.; Ghysels, A.; Golubeva-Zadorozhnaya, A.; Gomes, J.; Hanson-Heine, M. W. D.; Harbach, P. H. P.; Hauser, A. W.; Hohenstein, E. G.; Holden, Z. C.; Jagau, T.-C.; Ji, H.; Kaduk, B.; Khistyayev, K.; Kim, J.; Kim, J.; King, R. A.; Klunzinger, P.; Kosenkov, D.; Kowalczyk, T.; Krauter, C. M.; Lao, K. U.; Laurent, A. D.; Lawler, K. V.; Levchenko, S. V.; Lin, C. Y.; Liu, F.; Livshits, E.; Lochan, R. C.; Luenser, A.; Manohar, P.; Manzer, S. F.; Mao, S.-P.; Mardirossian, N.; Marenich, A. V.; Maurer, S. A.; Mayhall, N. J.; Neuscamman, E.; Oana, C. M.; Olivares-Amaya, R.; O'Neill, D. P.; Parkhill, J. A.; Perrine, T. M.; Peverati, R.; Prociuk, A.; Rehn, D. R.; Rosta, E.; Russ, N. J.; Sharada, S. M.; Sharma, S.; Small, D. W.; Sodt, A.; Stein, T.; Stück, D.; Su, Y.-C.; Thom, A. J. W.; Tsuchimochi, T.; Vanovschi, V.; Vogt, L.; Vydrov, O.; Wang, T.; Watson, M. A.; Wenzel, J.; White, A.; Williams, C. F.; Yang, J.; Yeganeh, S.; Yost, S. R.; You, Z.-Q.; Zhang, I. Y.; Zhang, X.; Zhao, Y.; Brooks, B. R.; Chan, G. K. L.; Chipman, D. M.; Cramer, C. J.; Goddard, W. A.; Gordon, M. S.; Hehre, W. J.; Klamt, A.; Schaefer, H. F.; Schmidt, M. W.; Sherrill, C. D.; Truhlar, D. G.; Warshel, A.; Xu, X.; Aspuru-Guzik, A.; Baer, R.; Bell, A. T.; Besley, N. A.; Chai, J.-D.; Dreuw, A.; Dunietz, B. D.; Furlani, T. R.; Gwaltney, S. R.; Hsu, C.-P.; Jung, Y.; Kong, J.; Lambrecht, D. S.; Liang, W.; Ochsenfeld, C.; Rassolov, V. A.; Slipchenko, L. V.; Subotnik, J. E.; Van Voorhis, T.; Herbert, J. M.; Krylov, A. I.; Gill, P. M. W.; Head-Gordon, M., *Mol. Phys.* **2015**, *113*, 184-215.
65. Becke, A. D., *The Journal of Chemical Physics* **1997**, *107*, 8554-8560.
66. Grimme, S., *J. Comput. Chem.* **2006**, *27*, 1787-1799.
67. Hehre, W. J.; Ditchfield, R.; Pople, J. A., *The Journal of Chemical Physics* **1972**, *56*, 2257-2261.
68. Hay, P. J.; Wadt, W. R., *The Journal of Chemical Physics* **1985**, *82*, 299-310.
69. Wadt, W. R.; Hay, P. J., *The Journal of Chemical Physics* **1985**, *82*, 284-298.
70. Hariharan, P. C.; Pople, J. A., *Theoretica chimica acta* **1973**, *28*, 213-222.
71. McKenzie, S. C.; Epifanovsky, E.; Barca, G. M. J.; Gilbert, A. T. B.; Gill, P. M. W., *The Journal of Physical Chemistry A* **2018**, *122*, 3066-3075.
72. Marenich, A. V.; Cramer, C. J.; Truhlar, D. G., *The Journal of Physical Chemistry B* **2009**, *113*, 6378-6396.
73. Schäfer, A.; Huber, C.; Ahlrichs, R., *The Journal of Chemical Physics* **1994**, *100*, 5829-5835.
74. Weigend, F.; Ahlrichs, R., *Physical Chemistry Chemical Physics* **2005**, *7*, 3297-3305.
75. Andrae, D.; Häußermann, U.; Dolg, M.; Stoll, H.; Preuß, H., *Theoretica chimica acta* **1990**, *77*, 123-141.
76. Thom, A. J. W.; Sundstrom, E. J.; Head-Gordon, M., *Physical Chemistry Chemical Physics* **2009**, *11*, 11297-11304.
77. Glendening, E.; Badenhoop, J., *NBO 5.0. Natural Bond Orbital Analysis Program* **2001**

## 4.0 Evidence of an On-Cycle Dinuclear Pd<sup>I</sup> Catalyst for Kumada Cross-Coupling

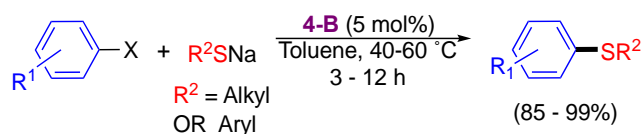
A higher yielding and faster synthesis for a Pd<sup>I</sup> dimer [Pd(**4-L1**)]<sub>2</sub> (**4-2**) is reported. Complex **4-2** is an active catalyst for Kumada coupling catalysis of aryl bromides and Grignard reagents, reaching complete consumption of the electrophile with loadings as low as 0.1 mol%. An experimental and computational approach is used to determine if the mechanism is mononuclear or dinuclear in nature. A potential route for cleavage of **4-2** to give mononuclear **4-10** was assessed. NMR studies in combination with rate analysis suggested cleavage of **4-2** is not an operative pathway. Additionally, variable time normalization analysis (VTNA) discounted a direct disproportionation route that gives two active mononuclear complexes. A non-zero order for the electrophile was attained, revealing the relevance of this substrate to the rate determining step (rds).

### 4.1 Introduction

Traditionally, palladium catalyzed cross-coupling involves a mononuclear Pd species operating in a Pd<sup>0/II</sup> redox cycle.<sup>1-3</sup> Mononuclear species dominate this space as maintaining nuclearity does not require special ligand design, and their syntheses are generally less expensive.<sup>4-6</sup> Consequently, these processes are extensively investigated, and their advantages and limitations are well understood. Processes involving dinuclear palladium complexes have been comparatively understudied, though valuable insight remains to be acquired from these mechanisms.<sup>7, 8</sup> Metal-metal synergy in dinuclear complexes can lead to improved reactivity, and can even facilitate reactions that are inaccessible to mononuclear species.<sup>8-13</sup> In addition, metal-metal synergy in dinuclear Pd complexes offer access to Pd in the unusual +1 and +3 oxidation states, which can allow entry into unique mechanisms and reactivity.<sup>14</sup> In these pathways the metal centre will most often undergo redox cycles of +/- 1.

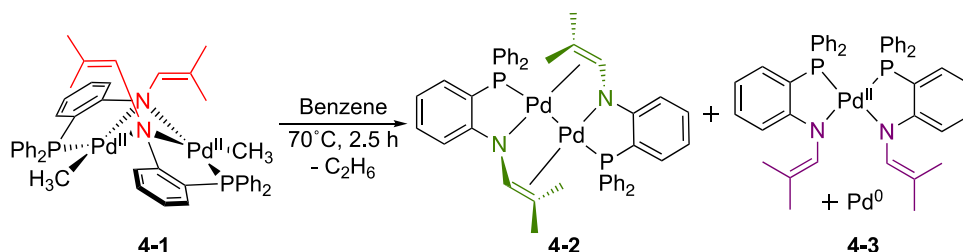
Ligands capable of securing dinuclear structures are most commonly bridging or bidentate ligands and must be able to coordinate to more than one atom simultaneously (Figure 4.1). This includes bridging halides, bidentate phosphines, allyls, and other  $\pi$ -systems. Pd<sup>I</sup> dimers bridged by monodentate halides (**4-A** and **4-B**) have shown exceeding promise in catalysis.<sup>15-18</sup> The Pd<sup>I</sup>





**Scheme 4.1.** Kumada coupling using **4-B** as a precatalyst in 2.5 mol%.

Recently, we reported a  $Csp^3$ - $Csp^3$  coupling mechanism that afforded ethane from a dinuclear  $[\text{Pd}^{\text{II}}(\text{Me})(\mathbf{4-L1})]_2$  complex **4-1** (Scheme 4.2).<sup>23</sup> One of the key aspects of this reaction was the structurally responsive phosphine 1-azaallyl ( $P^{\wedge}AzA$ ) ligand **4-L1**; its capacity to change coordination mode was revealed to be vital to  $Csp^3$ - $Csp^3$  reductive elimination. The ability to adopt various coordination modes was crucial for two reasons: (1) it reduced barriers for steps including methyl transfer between metal centres and reductive elimination and (2) it is essential for maintaining the dinuclear structure throughout the reductive elimination process. Two organometallic products are formed from this reaction: a dinuclear  $[\text{Pd}^{\text{I}}(\mathbf{4-L1})]$  dimer (**4-2**), and a mononuclear  $\text{Pd}^{\text{II}}(\mathbf{4-L1})_2$  complex (**4-3**).



**Scheme 4.2.** Previously established  $Csp^3$ - $Csp^3$  coupling beginning from **1** to give ethane, **4-2**, and **4-3**. Yields shown were obtained by  $^{31}\text{P}\{^1\text{H}\}$  NMR spectroscopy.

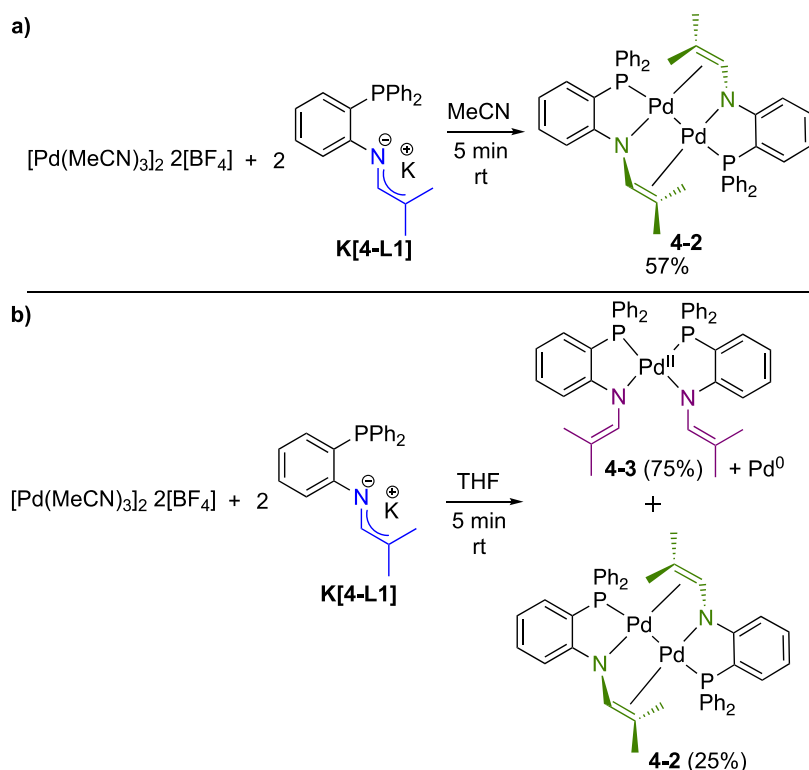
Encouraged by our discovery of an operative dinuclear  $[\text{Pd}^{\text{II}}(\mathbf{4-L1})(\text{R})]_2$  to  $[\text{Pd}^{\text{I}}(\mathbf{4-L1})]$  pathway, we sought to identify a catalytic reaction we could apply it to. Herein, we discuss an experimental investigation of dinuclear  $\text{Pd}^{\text{I}}$  complex **4-2**, including an improved synthesis and its reactivity towards Kumada cross coupling

## 4.2 Results

### 4.2.1 Improved Synthesis of **4-2**

Previously, we had shown the synthesis of complex **2** to be achievable through the thermolysis of **4-1** (Scheme 4.2).<sup>24</sup> However, because complex **4-2** was the minor product it was

only isolable in 24% yield. Thus, we attempted to access **4-2** via a direct synthesis. This was achieved by reacting 2.0 equiv **K[4-L1]** with  $[\text{Pd}(\text{MeCN})_3]_2[\text{BF}_4]_2$  (Scheme 4.3a). The *in-situ*  $^{31}\text{P}\{^1\text{H}\}$  NMR showed quantitative conversion to one product as evidenced by one signal at  $\delta_{\text{P}} = 15.0$ , consistent with formation of **4-2**. Complex **4-2** was isolable in moderate (57%) yields as a bright red powder. The formation of **4-2** was further confirmed through  $^1\text{H}$ , and  $^{13}\text{C}\{^1\text{H}\}$  NMR spectroscopy, and the observed signals were consistent with those previously reported.<sup>24</sup> A dinuclear complex was the sole product when the ligand coordination was attempted in acetonitrile. When non-coordinating THF was used the major product was mononuclear **4-3** in 75% yield by  $^{31}\text{P}\{^1\text{H}\}$  NMR spectroscopy, while **4-2** was the minor product in 25% yield (Scheme 4.3b).

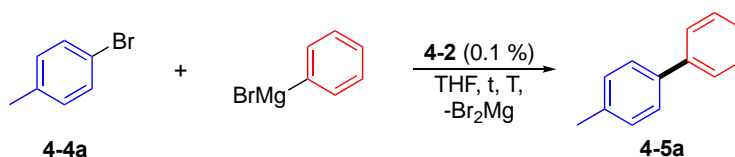


**Scheme 4.3.** a) Improved synthesis of complex **4-2** starting from a  $\text{Pd}^{\text{I}}$  dimer precursor. Isolated yields are shown. b) Attempted synthesis of **4-2** using non-coordinating solvent (*i.e.*, THF) **4-3** and **4-4**. *In-situ* yields relative to **K[4-L1]** are shown.

## 4.2.2 Kumada Cross Coupling

We first performed Kumada coupling between 4-bromotoluene (**4-4a**) and a minor excess of  $\text{PhMgBr}$  (1.5 equiv) with **4-2**, and product yields were determined *in-situ* by GC-FID (Scheme 4.4). Our initial reaction conditions were 0.1 mol% **4-2** at 50 °C. After 48 h, 40% **4-4a** was

remaining, with a yield of 53% for the heterocoupled product **4-5a** (Table 4.1, Entry 1). The only observed byproducts were from homocoupling of both substrates to give biphenyl (**4-6**) and 4,4-dimethylbiphenyl (**4-7a**). Elevating the temperature to 60 °C allowed for complete consumption of **4-4a** in 30 h with 85% yield of the cross coupled product (Entry 2). When **4-2** was absent no reaction was observed, confirming **4-2** is required for cross-coupling to occur (Entry 3). Likewise, when complex **4-2** was present but either **4-4a** or PhMgBr were excluded, homocoupling to give **4-6** and **4-7a** did not occur (Entries 4 and 5, respectively). The reaction was still successful when radical traps 1,4-cyclohexadiene and 1,1-diphenylethylene were added to the reaction solution (Entries 6 and 7, respectively). Although, slightly lower yields of **4-5a** (ca. 5–10%) were observed. Furthermore, no consumption of either radical trap was observed throughout the reaction. Radical pathways are therefore unlikely to be involved in the cross-coupling mechanism.



Scheme 4. 4. General scheme for the Kumada coupling between **4-4a** and PhMgBr with varying loadings of **4-2**, and temperatures.

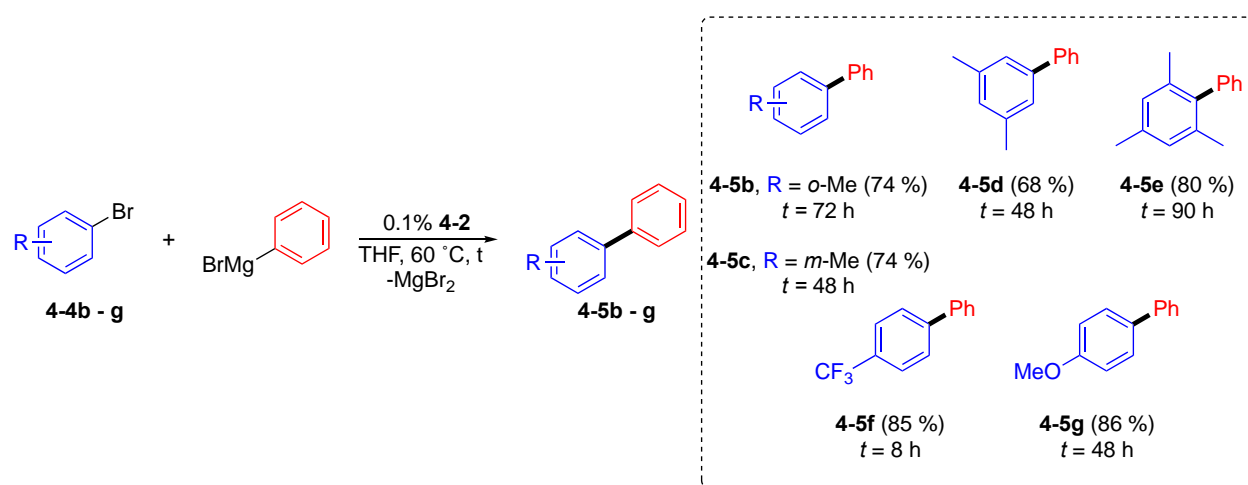
**Table 4.1.** Reaction optimization and control reactions for Kumada coupling between **4-4a** and PhMgBr at 0.1 mol% **4-2**, at varying times and temperatures.

| Entry          | Cat. (mol %)     | Temp. (°C) | Time (h) | <b>4-5a</b> (%) <sup>a</sup> | <b>4-7a</b> (%) <sup>b</sup> |
|----------------|------------------|------------|----------|------------------------------|------------------------------|
| 1              | <b>4-2</b> (0.1) | 50         | 48       | 53                           | 4                            |
| 2              | <b>4-2</b> (0.1) | 60         | 30       | 85                           | 8                            |
| 3              | None             | 60         | 48       | NR                           | NR                           |
| 4 <sup>c</sup> | <b>4-2</b> (0.1) | 60         | 48       | NR                           | NR                           |
| 5 <sup>d</sup> | <b>4-2</b> (0.1) | 60         | 48       | NR                           | NR                           |
| 6 <sup>e</sup> | <b>4-2</b> (0.1) | 60         | 30       | 79                           | 7                            |
| 7 <sup>f</sup> | <b>4-2</b> (0.1) | 60         | 30       | 72                           | 7                            |

<sup>a</sup> Yields obtained *in-situ* via GC-FID based on corrected response factors relative to **4-4a**. <sup>b</sup> **4-5aa** formed through homocoupling of **4-4a**. Yield based on corrected response factors relative to **4-4a**. <sup>c</sup> **4-4a** was not added to the reaction. <sup>d</sup> PhMgBr was not added to the reaction <sup>e</sup> 1,4 cyclohexadiene added (1.0 equiv). <sup>f</sup> 1,1 diphenylethylene added (1.0 equiv).

Kumada coupling with **4-2** was tested with a variety of Grignard-tolerant electrophiles (Figure 4.3). *o*-Bromotoluene (**4-4b**) reaches complete consumption in ca. 72 h with a yield of 74%. Comparatively, *m*-bromotoluene (**4-4c**) and 5-bromo-*m*-xylene (**4-4d**) reach complete

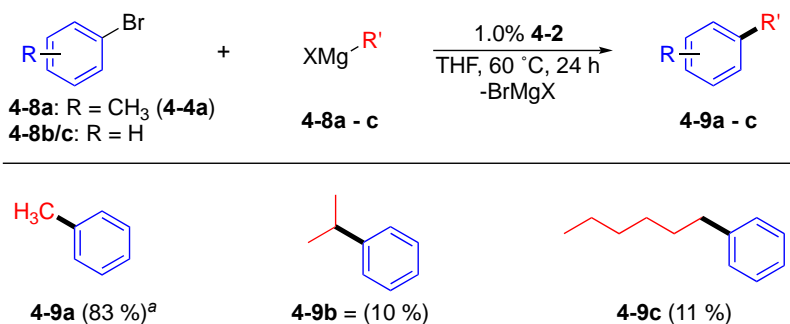
consumption in 48 h with 74 and 68% yields, respectively. When 2-bromomesitylene (**4-4e**) was used as the electrophile the reaction was exceedingly sluggish and reached a maximum conversion of 80% after 90 h. The homocoupled product **4-7e** (*i.e.*, 2,2' 4,4' 6,6'-hexamethyl-1,1'-biphenyl) produced from electrophile homocoupling was not observed. Therefore, steric bulk does not dramatically reduce reaction yields, though the reaction time increases with more steric bulk at the *ortho* position. Reaction time decreases to 8 h when electron-poor 4-trifluoromethylbromobenzene (**4-4f**) is used as the substrate, with a yield of 85%. While electron rich 4-bromoanisole (**4-4g**) reaches complete consumption in 48 h with 86% yield. Electron poor and sterically unencumbered aryl halides appear to be the best substrates for catalysis with **4-2**.



**Figure 4.3.** Kumada coupling between PhMgBr and aryl bromides **4-4b-g** using 0.1 mol % **4-2** at 60 °C.

Finally, Kumada coupling of carbon atoms with different hybridizations (*i.e.*, C<sub>sp</sub><sup>2</sup>-C<sub>sp</sub><sup>3</sup> coupling) was attempted by altering the Grignard reagent. Methyl (**4-8a**), isopropyl (**4-8b**), and *n*-hexyl (**4-8c**) Grignard reagents were used to determine if **4-2** can overcome  $\beta$ -H elimination and cross-couple C<sub>sp</sub><sup>3</sup> nucleophiles (Figure 4.4). Reactivity was initially tested between **4-4a**, and **4-8a**, with 0.1 mol% **4-2** at 60 °C. However, complete consumption of the aryl halide was not achieved under these conditions. Increasing the loading of **4-2** to 1 mol% allowed complete consumption of the aryl halide in 24 h affording the product *p*-xylene (**4-9a**) in 83% yield. Although, the reaction does not appear to be tolerant of alkyl groups susceptible to  $\beta$ -H elimination. Reactions with **4-8b** resulted in complete consumption of the aryl halide in 24 h, however only 10% conversion to the anticipated product was observed. Furthermore, one of the anticipated  $\beta$ -H elimination products, *n*-propylbenzene, was observed in 21% yield suggesting  $\beta$ -H elimination occurred from an intermediate bearing a 'Pd-CH(CH<sub>3</sub>)<sub>2</sub>' moiety. Reactions with **4-8c** also resulted

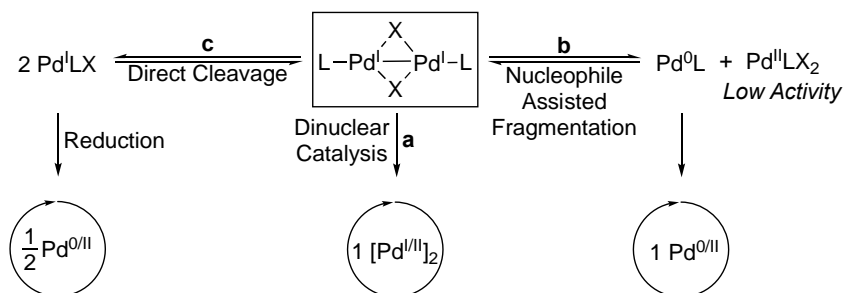
in complete consumption of the aryl halide in 24 h, however only an 11% yield of the expected heterocoupled product 1-phenylhexane (**4-9c**) was observed. One of the anticipated products from  $\beta$ -H elimination, 2-phenylhexane, was not observed by GC-FID.



**Figure 4.4.** Kumada coupling between PhBr and various  $C_{sp^3}$ -hybridized Grignard reagents using 1.0 mol % **4-2**. <sup>a</sup>: **4-4a** used as the coupling partner.

### 4.2.3 Determination of Catalyst and Substrate Order

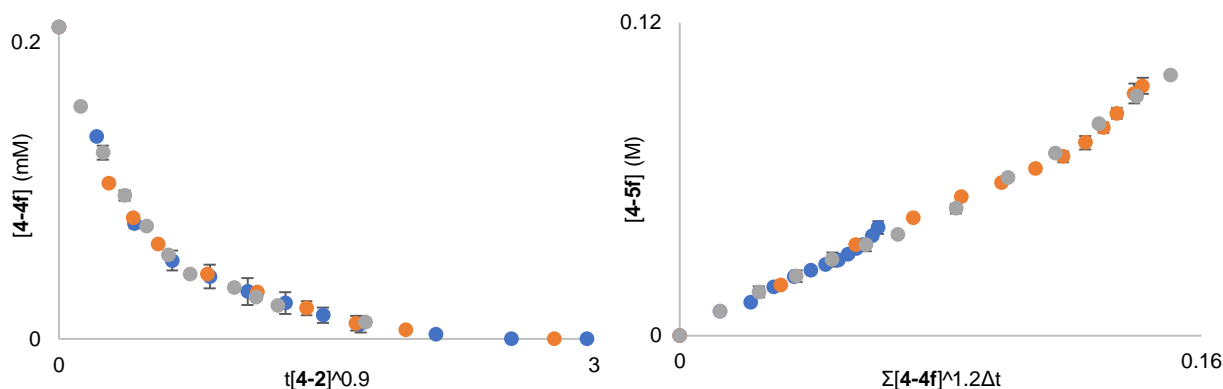
Three main routes for consumption of a dinuclear  $\text{Pd}^{\text{I}}$  complex into a catalytic cycle have been suggested (Figure 4.5).<sup>25, 26</sup> First, is direct entry into a dinuclear catalytic cycle (path **a**).<sup>15</sup> Second is disproportionation affording one equivalent of the highly active mononuclear  $\text{Pd}^{\text{0}}\text{L}$  catalyst (path **b**).<sup>19</sup> Third is direct cleavage of the dimer to give two equivalents of  $\text{Pd}^{\text{I}}$  monomer which are reduced to  $\text{Pd}^{\text{0}}$  (path **c**).<sup>27</sup> Whether the reaction is mono- or dinuclear will therefore have a notable impact on the order of the catalyst. If **4-2** follows path **a** or **b**, then an order of 1 in complex **4-2** is expected. Alternatively, if path **c** is followed then an order of 0.5 is expected.



**Figure 4.5.** Three plausible pathways for activation of a  $\mu\text{-X Pd}^{\text{I}}$  dimer to enter a catalytic cycle. Path a) Direct entry of the dinuclear complex that operates as an on-cycle catalyst. Expected order of **4-2** = 1.0. Path b) Nucleophile assisted fragmentation<sup>16</sup> which results in active  $\text{Pd}^{\text{0}}(\text{L})$  and  $\text{Pd}^{\text{II}}\text{LX}_2$  byproduct. Expected order of **4-2** = 1.0. Path c) Homolytic cleavage of the dinuclear  $\text{Pd}^{\text{I}}$  structure to give  $\text{Pd}^{\text{I}}\text{LX}$  monomers, followed by reduction to give 2 active  $\text{Pd}^{\text{0}}$  catalysts. Expected order in **4-2** = 0.5.



To this end, we determined the order in **4-2** by performing Kumada coupling with **4-4f** due to its fast reaction rate and good yield and mass balance. Kumada coupling was carried out with a consistent concentration of **4-4f** and PhMgBr (**4-4f** = 210 mM, PhMgBr = 315 mM). The concentration of **4-2** was varied between 210 (0.1 mol%), 520 (0.25 mol%), and 830  $\mu$ M (0.4 mol%) Reaction orders were determined using data collected by GC-FID, and the data was analyzed graphically using variable time normalization analysis (VTNA).<sup>28,29</sup> Excellent overlap of all three lines is observed with an order of 0.9 (Figure 4.6, left). Orders other than 0, 0.5, 1, and 2 have been observed in the literature,<sup>29</sup> and an order of 0.9 suggests that there are likely multiple operative mechanistic pathways, consistent with our previous studies on reductive elimination from **4-1**. While there may indeed be an operative path similar to **c**, the value close to 1.0 suggests it is not a dominant pathway and more likely the reaction proceeds via path **a** or **b**.



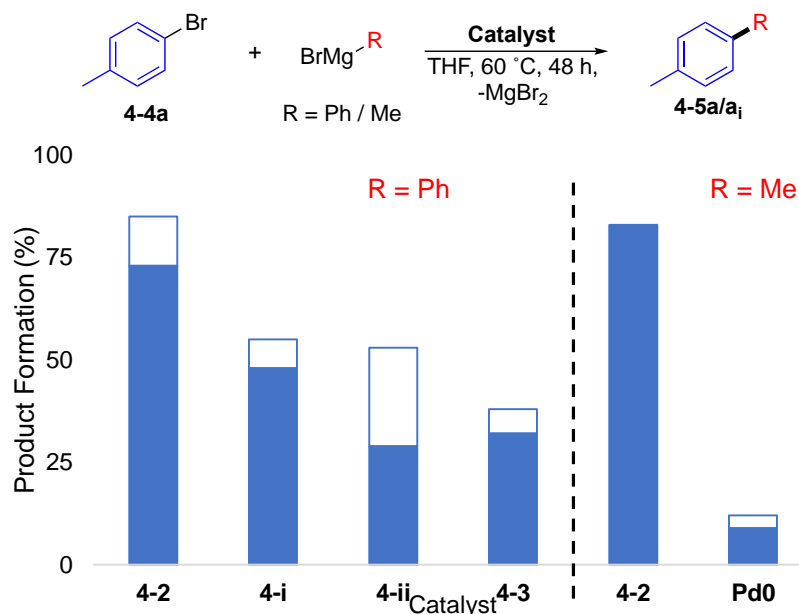
**Figure 4.6** Variable time normalization analysis: (left) concentration of **4-4f** and PhMgBr kept constant at 210 and 315 mM respectively. Concentration of **4-2** changed from 210  $\mu$ M (grey), 520  $\mu$ M (orange), and 830  $\mu$ M (blue). Consumption of **4-4f** is being tracked. (right) concentration of **4-2** and PhMgBr kept constant at 210  $\mu$ M and 315 mM respectively. Concentration of **4-4f** changed from 50 mM (grey), 110 mM (orange), and 220 mM (blue). Formation of **4-5f** is being tracked. Reactions ran in duplicate.

Next, we attempted to determine the order in substrates beginning with the electrophile. If the electrophile is involved in the rds then a non-zero order will be obtained. Kumada coupling was carried out with a consistent concentration of **4-2** and PhMgBr (**4-2** = 210  $\mu$ M, PhMgBr = 315 mM). The concentration of aryl bromide **4-4f** was varied between 50, 110, and 220 mM. Concentrations greater than 220 mM could not be used as homocoupling of the Grignard to give **4-6** consumes this substrate. If too much Grignard homocoupling occurs, then the reaction cannot reach completion. Excellent overlap of all three lines was observed with an order of 1.2 (Figure 4.6, right). Again, a partial order between 1 and 2 likely suggests that multiple mechanisms are operative. Regardless, a non-zero order suggests that **4** is involved in the rds, the likely step being

oxidative addition of **4-4**. Finally, we attempted to determine the order in nucleophile by keeping the concentration of **4-2** and **4-4f** constant (**4-2** = 210  $\mu$ M, **4-4f** = 210 mM). Unfortunately, reactivity at PhMgBr concentrations higher than 315 mM was exceedingly inconsistent and mass balance decreased with increasing concentration. As such, the order of PhMgBr could not be determined in this reaction.

#### 4.2.4 Assessment of Decomposition Products of **4-2** as Catalytically Active species

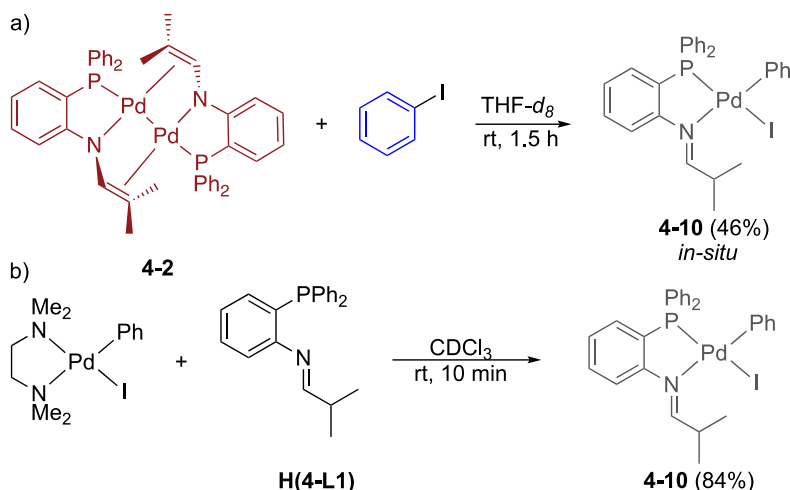
Complex **4-2** has previously been shown to decompose into **4-3** and Pd<sup>0</sup> over the course of 24 h at 70 °C.<sup>23</sup> We hypothesized that these two Pd species could potentially act the catalytically active species for Kumada coupling. Accordingly, we incubated two separate solutions of pure **4-2** at 60 °C for 3 h (**4-i**), and 70 °C for 24 h (**4-ii**). Conditions **i** are analogous to those used in catalysis and conditions **ii** are analogous to the conditions resulting in complete conversion of **4-2** to **4-3** and Pd<sup>0</sup>. Cross-coupling was then attempted at 60 °C with the incubated solutions (**4-i** and **4-ii**), and 55 and 53% yields of **4-5a** were obtained respectively (Figure 4.7). Catalysis was also attempted with a pure solution of **4-3** resulting in 37 % yield of **4-5a**. Comparatively when **4-2** is used under the same conditions **4-5a** is obtained in 85% yield in 30 h (Table 4.1, Entry 2). Catalysis was also attempted at 60 °C between **4-4a** and MeMgBr (**4-8a**) using a suspension of Pd<sup>0</sup> in THF. With Pd<sup>0</sup> the yields of **4-9a** are very poor, only reaching 12%, while **4-2** produces **4-9a** in 83% yield under the same conditions (Figure 4.4). Consequently, the products from thermolysis of **4-2** are not likely relevant to the observed catalysis, which is consistent with the observed order of 0.9 in **4-2**.



**Figure 4.7.** (Top) General reaction scheme for Kumada coupling of **4-4a** with PhMgBr or MeMgBr at 0.1 and 1.0 mol% respectively. Bar graph showing product formation vs. catalyst used, filled bar = formation after 24 h, unfilled and filled bar together = formation after 48 h. (Left) R = Ph 0.1 mol% catalyst used. i = 0.1 mol% of complex **4-2** heated for 3 h at 60 °C. ii = 0.1 mol% complex **4-2** heated for 24 h at 70 °C (Right) R = Me.

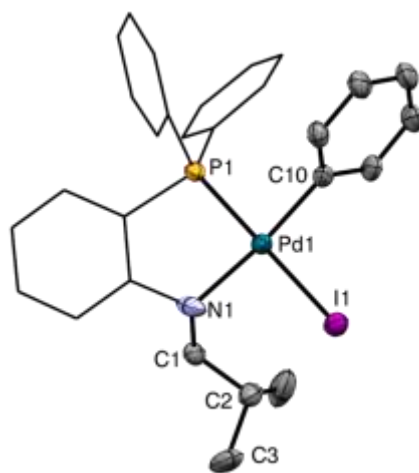
#### 4.2.5 Attempted Synthesis of Reaction Intermediates

We attempted to determine the product from oxidative addition of the electrophile to **4-2** via VT  $^{31}\text{P}\{^1\text{H}\}$  and  $^1\text{H}$  NMR spectroscopy. Phenyl iodide (PhI) was selected as the aryl halide in these reactions due to the ease of Ar-I bond activation compared to Ar-Br bonds.<sup>30</sup> Addition of one equivalent of PhI to complex **4-2** at room temperature (Scheme 4.5a) resulted in complete consumption of **4-2** in 1.5 h. One product was observed by  $^{31}\text{P}\{^1\text{H}\}$  NMR spectroscopy at  $\delta_{\text{P}} = 31.7$ . *In-situ* yield was determined to be 46% by  $^1\text{H}$  NMR spectroscopy relative to an internal standard. The  $^1\text{H}$  NMR spectrum of the isolated product has a doublet at  $\delta_{\text{H}} = 1.21$  and a septet at  $\delta_{\text{H}} = 4.40$  each with a coupling constant of  $J = 7.2$  Hz, consistent with protonation of the 1-azaallyl fragment to regenerate the phosphine-imine ligand **H(4-L1)**. Complex **10** was confirmed as the product through an independent synthesis between **H(4-L1)** and Pd(Ph)(I)(TMEDA) in 84% yield (Scheme 4.5b). All NMR spectroscopic data from the independently synthesized **4-10** matched the data acquired from the product obtained by oxidative addition of PhI to **4-2**.



**Scheme 4.5.** a) Addition of PhI (2.0 equiv) to **4-2** at room temperature resulting in 46% conversion in-situ to **4-10**. b) Independent synthesis of **4-10** via coordination of **H(4-L1)** to PdIPh(TMEDA).

The structure of **4-10** was further confirmed through X-ray diffraction, which confirmed the *cis* orientation of the aryl and phosphine groups (Figure 4.8). Furthermore the N(1)–C(1) and C(1)–C(2) bond lengths are 1.326(7) and 1.486(1) Å, consistent with a C–N double bond and C–C single bond, respectively. Additionally, the N(1)–C(1)–C(2) and C(1)–C(2)–C(3) bond angles are 121.80(6)° and 106.10(6)° respectively, which signify  $sp^2$  hybridization at C<sup>1</sup> and  $sp^3$  hybridization at C<sup>2</sup>. This data is consistent with protonation of **4-L1** to give the phosphine-imine ligand **H(4-L1)**.

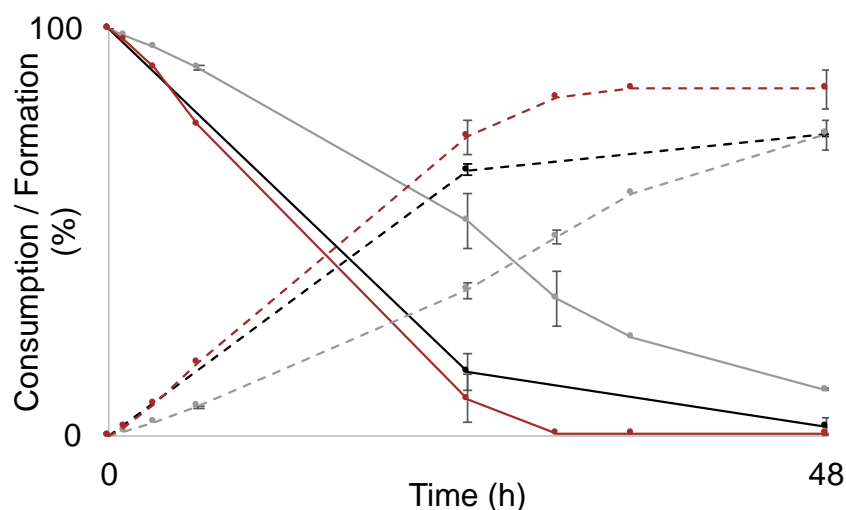
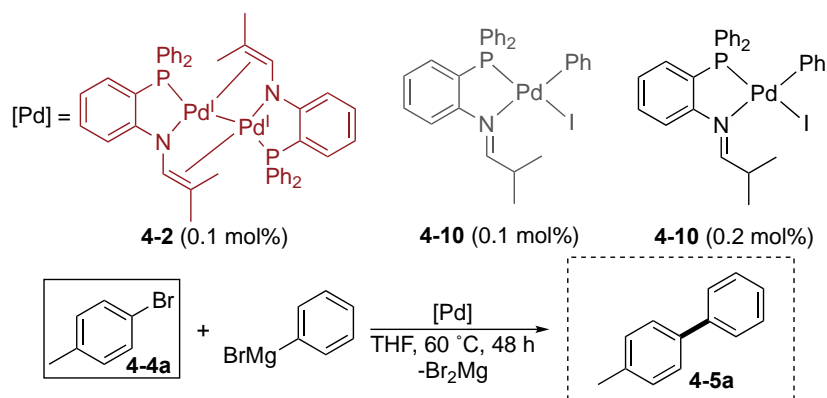


**Figure 4.8.** Thermal displacement plot of **4-10**. Displacement ellipsoid (50% probability). All hydrogen atoms and have been omitted for clarity. P(1)–Pd(1)–N(1) = 82.36(1)°, C(10)–Pd(1)–I(1) = 89.53(1)°, N(1)–C(1)–C(2) = 121.80(6)°, C(1)–C(2)–C(3) = 106.10(6)°,  $\tau^4 = 0.16$ ,<sup>31</sup> N(1)–C(1) = 1.326(7) Å, C(1)–C(2) = 1.486(1) Å, Pd(1)–P(1) = 2.231(1) Å, Pd(1)–N(1) = 2.201(4) Å, Pd(1)–I(1) = 2.654(7) Å, Pd(1)–C(10) = 2.008(5) Å.

There is no acidic proton in PhI, therefore **4-10** cannot be the initial product upon oxidative addition of the electrophile. To try and trap an intermediate between **4-2** and **4-10**, we performed the oxidative addition of PhI at lower temperatures. A solution of **4-2** and 1.0 equiv of PhI was prepared in THF-*d*<sub>8</sub> and analyzed at -25, -15, 0, 5, and 15 °C by <sup>31</sup>P{<sup>1</sup>H} and <sup>1</sup>H NMR spectroscopy. The solution was held at each temperature for 45 minutes, although no change was observed by NMR spectroscopy at any temperature lower than 20 °C. When the same solution was left at 25 °C, complete consumption of **4-2** was observed in 1.5 h and the only observed product was **4-10**. The signal for the methine in **H(4-L1)** is observed by <sup>1</sup>H NMR spectroscopy when **4-10** is generated *in-situ*, therefore the H does not come from the solvent THF-*d*<sub>8</sub>. Moreover, analysis of the solvents via the ketyl radical test determined the solvents were dry, so it is unlikely residual water in the solvent that caused **4-L1** protonation. Previous reports have shown that the C-H bond in one of methyl groups in **4-L1** can be activated via a C-H agostic interaction.<sup>23</sup> As such, it is possible that one of the **4-L1** ligands in **4-2** is the source of the proton via C-H activation. Transfer of the proton to the other **4-L1** ligand in **4-2** would account for the formation of **4-10**, ligated by **H(4-L1)**, in only 50% *in-situ* yield relative to **4-2**.

#### 4.2.6 Comparison of Kumada Coupling with **4-2** and **4-10**.

The performance of complex **4-2** was then compared to complex **4-10**, to assess if **4-2** operates as a precursor to **4-10** in solution (Figure 4.9). The NMR studies revealed a maximum 46% *in-situ* yield for the conversion of **4-2** to **4-10**. If **4-2** indeed acts as a precursor to **4-10** in solution, then catalysis beginning from **4-10** should be roughly twice as active as **4-2** at the same catalyst loading. Kumada coupling was performed with 0.1 mol% **4-2** and **4-10** at 60 °C and monitored over 48 h. With **4-2**, complete consumption of **4-4a** was observed after 30 h, with an 85% yield of **4-5a** (Figure 4.9, red). After 24 h complex **4-10** reaches ca. 47% consumption, forming 36% **4-5a**. While after 48 h 89% of **4-4a** has been consumed, with 75% yield **4-5a** (Figure 4.9, grey). When 0.2 mol% **4-5a** is used a 65% yield of **4-5a** is obtained after 24 h, and complete consumption of **4-4a** occurs in 48 h with 75% yield of **4-5a** (Figure 4.9, black). While the rates between **4-2** and **4-10** are similar at the same loading of Pd, at 0.1 mol% complex **4-2** outperforms **4-10**. Therefore, it is unlikely that **4-2** is a precatalyst to one equivalent of **4-10** which acts as the active mononuclear catalyst (Figure 4.5, path **b**).



**Figure 4.9.** Consumption of **4-4a** (solid line) and formation of **4-5a** (dotted line) following Kumada coupling with  $\text{PhMgBr}$  as the Grignard reagent, using 0.1 mol% **4-2** (red), 0.1 mol% **4-10** (grey), and 0.2 mol% **4-10** (black).

### 4.3 Conclusion

We have reported a rare example of a dinuclear  $[\text{Pd}^{\text{I}}]_2$  cross-coupling mechanism proceeding through the  $\text{Pd}^{\text{I}}$  dimer **4-2**. A fast, clean, and higher yielding pathway to synthesize **4-2** was described, allowing for the synthesis of **4-2** on scales suitable for reactivity assessment. Furthermore, complex **4-2** permits the Kumada coupling of aryl bromides and  $\text{PhMgBr}$  at 0.1 mol%. The reaction was tolerant of electron poor and electron rich substrates, as well as sterically congested substrates. Although, catalysis was most effective with electron poor and sterically uncongested substrates. Furthermore, the Grignard could be expanded to  $\text{MeMgBr}$  to allow  $\text{Csp}^2\text{-Csp}^3$  coupling although Grignard reagents susceptible to  $\beta\text{-H}$  elimination were not compatible with the reaction. Variable time normalization analysis (VTNA) revealed an order of 1.2 for the aryl

bromide, suggesting that a step involving the electrophile (such as oxidative addition) is the rate determining step. An order of 0.9 for the catalyst **4-2** was revealed, which suggests that a dinuclear mechanism is the dominant pathway. Consistent with the order of 0.9 results, dinuclear **4-2** outperforms an analogous mononuclear complex **4-10** at the same catalyst loading, as well as **4-2**'s decomposition products **4-3** and Pd<sup>0</sup>.

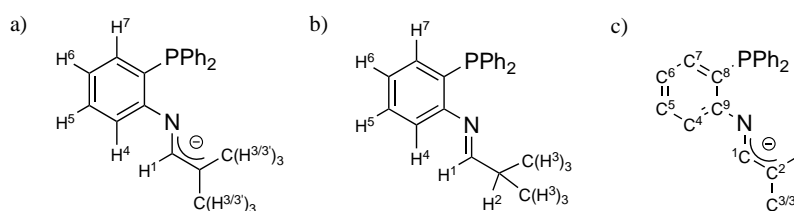
## 4.4 Experimental Section

### 4.4.1 General Considerations

All reactions were performed under an inert (Ar or N<sub>2</sub>) atmosphere using standard Schlenk line techniques and/or an MBRAUN glovebox, unless otherwise stated. Vials, flasks, and NMR tubes were oven dried (156 °C) and cooled under inert atmosphere before use. Unless otherwise stated, all reaction solvents were dried and degassed, and obtained from an Innovative Technology 400-5 Solvent Purification system and stored over 4 Å molecular sieves prior to use. Acetonitrile was dried using CaH<sub>2</sub>, distilled under vacuum, and stored over 3 Å molecular sieves. The following materials were prepared using literature procedures PdCl<sub>2</sub>(COD),<sup>32</sup> [PdCIME(COD)],<sup>33</sup> [Pd(MeCN)<sub>3</sub>]<sub>2</sub>[BF<sub>4</sub>]<sub>2</sub>,<sup>34</sup> Pd(Ph)(I)(TMEDA),<sup>35</sup> **4-1**,<sup>24</sup> **4-3**,<sup>24</sup> **K[4-L1]**,<sup>24</sup> and **H(4-L1)**.<sup>36</sup> All other reagents were purchased from commercial sources and used without further purification. Deuterated solvents were obtained from commercial sources and were degassed and stored over 4 Å molecular sieves. Toluene-*d*<sub>8</sub> was obtained in glass ampoules from Sigma Aldrich or Cambridge Isotope Laboratories and stored over 4 Å sieves under an inert atmosphere.

All NMR spectra were obtained on a 600 MHz Varian or 400 MHz Bruker spectrometer at 25 °C unless otherwise stated. <sup>1</sup>H and <sup>13</sup>C{<sup>1</sup>H} NMR spectra were referenced internally using residual solvent relative to TMS at δ = 0.0 as follows: CDCl<sub>3</sub> (δ<sub>H</sub> = 7.26; δ<sub>c</sub> = 77.4), C<sub>6</sub>D<sub>6</sub> (δ<sub>H</sub> = 7.16; δ<sub>c</sub> = 128.1), THF-*d*<sub>8</sub> (δ<sub>H</sub> = 4.58; δ<sub>c</sub> = 67.21), Toluene-*d*<sub>8</sub> (δ<sub>H</sub> = 2.09, δ<sub>c</sub> = 20.4). <sup>31</sup>P{<sup>1</sup>H} NMR spectra obtained in protio solvents were externally referenced to a sample of 85% H<sub>3</sub>PO<sub>4</sub> at δ<sub>P</sub> = 0. Multiplicities are described as s (singlet), d (doublet), t (triplet), sept (septet), and m (multiplet). Charge-transfer Matrix Assisted Laser Desorption/Ionization Mass Spectrometry data were collected on an AB Sciex 5800 TOF/TOF mass spectrometer using pyrene as the matrix in a 20:1 molar ratio to complex. Solutions were prepared in benzene and spotted on a sample plate under

an inert atmosphere and transferred to the instrument in a closed resealable plastic bag. The instrument is equipped with a 349 nm OptiBeam On-Axis laser. The laser pulse rate was 400 Hz and data were collected in reflectron positive mode. Reflectron mode was externally calibrated at 50 ppm mass tolerance. Each mass spectrum was collected as a sum of 500 shots. Infrared spectra were collected on solid samples using a Bruker ALPHA II ATR FTIR spectrometer. Quantification of catalytic reactivity was achieved using an Agilent 7890a gas chromatograph with a flame ionization detector (GC-FID). An HP-5 column was used. All substrates were calibrated relative to the internal standard (1,2,3,4)-tetrahydronaphthalene and product amounts were corrected based on elucidated response factors relative to the Ar-Br substrate.



**Figure 4.10.** General labelling scheme for a) phosphine 1-azaallyl (P<sup>AzA</sup>) ligand **4-L1**; b) phosphine amine ligand **H[4-L2]**; c) P<sup>AzA</sup> ligand **4-L1**. This scheme will be used consistently for all compounds throughout the experimental section. The denotations H<sup>3</sup>, H<sup>3'</sup>, C<sup>3</sup>, and C<sup>3'</sup> are used to distinguish between cases where atoms H<sup>3</sup> and C<sup>3</sup> are not equivalent.

#### 4.4.2 Improved Synthesis of [Pd<sup>I</sup>(**4-L1**)]<sub>2</sub>, **4-2**

In a glovebox, **K[4-L1]** (123 mg, 0.333 mmol) was suspended in acetonitrile (2.0 mL) and added to a stirring solution of [Pd(MeCN)<sub>3</sub>]<sub>2</sub>[BF<sub>4</sub>]<sub>2</sub> (100 mg, 0.183 mmol) in acetonitrile (2.5 mL). The vial containing ligand **K[4-L1]** was rinsed with 0.5 mL portions of acetonitrile until the washes were no longer yellow. A colour change from orange to red was immediately observed upon addition of **K[4-L1]** to the Pd precursor. The reaction solution was allowed to stir for 5 mins. The reaction solution was then filtered through a fritted funnel with a pad of Celite into a Büchner flask, and the reaction vial and celite were rinsed with 0.5 mL portions of acetonitrile until the red colour had disappeared. The funnel was removed, the Büchner flask was sealed, and the solvent of the filtrate was removed under vacuum. The black residue was then redissolved in a 1:1 benzene:acetonitrile mixture (2 mL total) and added to a round bottom flask. Cold pentane (15 mL) was added to the flask, and the solution was vigorously stirred for 10 min. The flask was then placed in a freezer at -20 °C for 1 h, over which time a red precipitate formed. The mixture was then swirled and filtered through a fritted funnel into a Büchner flask. The isolated solids were



washed with cold dichloromethane (1 mL), to produce a bright red powder. The solvent of the filtrate was then removed under vacuum in the flask, and the resulting black residue was redissolved in a 1:1 benzene:acetonitrile mixture (2 mL), and added to a round bottom flask. Cold pentane (15 mL) was added, and the biphasic solution was stored in a freezer at  $-20\text{ }^{\circ}\text{C}$  overnight. From this mixture 3 additional crops of **4-2** were obtained by repeating the above procedure. THF (0.5 mL) was added on top of the frit containing solid **4-2**, and the suspension was transferred to a 20 mL vial. The transfers were repeated until most of the red colour on the frit had disappeared. The solvent of the combined suspensions was removed under vacuum to afford **4-2** as a red powder. Yield: 49 mg (36%) from the first crop. Total yield: 77 mg (57%).  $^1\text{H}$  NMR (599 MHz  $\text{C}_6\text{D}_6$ ):  $\delta = 7.86$  (m, 4H, P( $\text{C}_6\text{H}_5$ )), 7.47 (m, 4H, P( $\text{C}_6\text{H}_5$ )), 7.22 (m, 4H, P( $\text{C}_6\text{H}_5$ )), 7.07 (m, 8H, P( $\text{C}_6\text{H}_5$ ),  $H^6$ ,  $H^5$ ), 6.97 (m, 2H,  $H^7$ ), 6.90 (m, 4H, P( $\text{C}_6\text{H}_5$ )), 6.57 (m, 2H,  $H^4$ ), 5.97 (s, 2H,  $H^1$ ), 2.20 (s, 6H,  $H^3$ ), 1.58 (s, 6H,  $H^3$ ).  $^{13}\text{C}\{^1\text{H}\}$  NMR (151 MHz,  $\text{C}_6\text{D}_6$ ):  $\delta = 133.0$  (P( $\text{C}_6\text{H}_5$ )), 132.9 (P( $\text{C}_6\text{H}_5$ )), 129.7 ( $\text{C}^5$ ), 128.5 ( $\text{C}^6$ ), 128.4 (P( $\text{C}_6\text{H}_5$ )), 128.3 (P( $\text{C}_6\text{H}_5$ )), 117.5 ( $\text{C}^4$ ), 114.7 (P( $\text{C}_6\text{H}_5$ )), 109.0 ( $\text{C}^1$ ), 74.5 ( $\text{C}^2$ ), 27.8 ( $\text{C}^3$ ), 20.8 ( $\text{C}^3$ ).  $^{31}\text{P}\{^1\text{H}\}$  NMR (243 MHz,  $\text{C}_6\text{D}_6$ ):  $\delta = 15.0$  (s, *P-4-L1*). All spectroscopic data acquired matches previously reported literature values.<sup>24</sup>

#### 4.4.3 Synthesis of [Pd(I)(Ph)(H(4-L1))], (**4-10**)

In a glovebox, ligand **H(4-L1)** (87 mg, 0.28 mmol) and Pd(I)(Ph)(TMEDA) (93 mg, 0.23 mmol) were added to two separate vials. Dichloromethane (1 mL) was added to each vial and **H(4-L1)** was added to the solution of Pd(I)(Ph)(TMEDA), and the vial containing **H(L1)** was rinsed with dichloromethane ( $3 \times 0.5$  mL) and the washings were added to the reaction vial. The reaction was stirred for 5 min at glovebox temperature, and the solvent was reduced to ca 0.5 mL under vacuum. Cold diethyl ether (6 mL) was added, and the beige mixture was vigorously stirred which resulted in precipitation of an orange solid over 10 min. The solids were allowed to settle, and the supernatant was removed via pipette. The solids were washed with cold ether ( $3 \times 3$  mL) to afford **4-10** as an orange solid. Yield 126 mg (90 %) Note: The *cis* P-Pd- $\text{CH}_3$  isomer of **4-10** is the major (80%) product, the *trans* P-Pd- $\text{CH}_3$  isomer represents the other 20% of the isolated material.  $^1\text{H}$  reported for *cis* isomer only (599 MHz,  $\text{C}_6\text{D}_6$ ):  $\delta = 7.51$  (d,  $J = 7.5$  Hz, 2H, Pd- $\text{C}_6\text{H}_5$ ), 7.34 – 7.23 (m, 4H,  $H^4$ ,  $H^5$ , P( $\text{C}_6\text{H}_5$ )), 7.04 – 6.86 (m, 10H,  $H^1$ ,  $H^6$ , P( $\text{C}_6\text{H}_5$ )), 6.85 – 6.81 (m, 2H, Pd- $\text{C}_6\text{H}_5$ ),

6.69 – 6.64 (m, 1H, Pd-C<sub>6</sub>H<sub>5</sub>), 6.49 – 6.45 (m, 1H, H<sup>7</sup>), 4.80 (sept, <sup>3</sup>J<sub>HH</sub> = 8.0 Hz, 1H, H<sup>2</sup>), 1.00 (d, J = 7.2 Hz, 6H, H<sup>3</sup>). <sup>13</sup>C{<sup>1</sup>H} NMR (101 MHz, C<sub>6</sub>D<sub>6</sub>): δ = 183.1 (C<sup>1</sup>), 157.7 (d, <sup>2</sup>J<sub>CP</sub> = 18.1 Hz, C<sup>9</sup>), 142.3 (P(C<sub>6</sub>H<sub>5</sub>)), 137.7 (d, <sup>3</sup>J<sub>CP</sub> = 5.1 Hz, Pd-C<sub>6</sub>H<sub>5</sub>), 133.7 (d, J<sub>CP</sub> = 13.1 Hz, P(C<sub>6</sub>H<sub>5</sub>)), 133.0 (C<sup>5</sup>), 132.3 (C<sup>4</sup>), 130.9 (d, J<sub>CP</sub> = 4 Hz, P(C<sub>6</sub>H<sub>5</sub>)), 129.1 (d, <sup>1</sup>J<sub>CP</sub> = 35.6 Hz, C<sup>8</sup>), 128.9 (d, J<sub>CP</sub> = 12.1 Hz, P(C<sub>6</sub>H<sub>5</sub>)), 127.1 (d, <sup>3</sup>J<sub>CP</sub> = 1.01 Hz, C<sup>6</sup>), 127.0 (Pd-C<sub>6</sub>H<sub>5</sub>), 122.8 (Pd-C<sub>6</sub>H<sub>5</sub>) 122.5 (Pd-C<sub>6</sub>H<sub>5</sub>), 119.8 (d, <sup>2</sup>J<sub>CP</sub> = 8.1 Hz, C<sup>7</sup>), 36.9 (C<sup>2</sup>), 19.5 (C<sup>3</sup>). <sup>31</sup>P{<sup>1</sup>H} NMR (243 MHz, CDCl<sub>3</sub>): δ = 22.7 (s, **P-4-L1**, *cis* P-Pd-Ph<sub>3</sub>). <sup>31</sup>P{<sup>1</sup>H} NMR (243 MHz, C<sub>6</sub>D<sub>6</sub>): δ = 21.8 (s, **P-4-L1**, *trans* P-Pd-Ph<sub>3</sub>). MALDI MS (pyrene): *m/z* found 563.9 calc [**4-10**-C<sub>6</sub>H<sub>5</sub>]<sup>+</sup> 563.9. ATR-FTIR (cm<sup>-1</sup>): ν 2955 (C<sub>sp</sub><sup>3</sup>-H, w), 1622 (C=C, m). X-ray quality crystals of **4-10** were obtained via slow vapour diffusion of diethyl ether into a 9:1 mixture of toluene:dichloromethane.

#### 4.4.4 General Procedure for Kumada Coupling Catalysis

In a glovebox, the aryl halide was weighed into a 4 mL vial and dissolved in THF (210 mM). Grignard Reagent (RMgBr) (1.5 equiv), and 1,2,3,4-tetrahydronaphthalene (1.0 equiv) were then added. An aliquot was removed from the reaction vial and added to hexanes to prepare a 10 mM solution of **4-4** for T<sub>0</sub> analysis. The T<sub>0</sub> solution was washed with water (1 × ½ the total volume of the solution of **4-4**, ca. 250 μL) to remove the magnesium salts. The organic layer was injected into the GC-FID to acquire a T<sub>0</sub>. A solution of the catalyst in C<sub>6</sub>H<sub>6</sub> (2.26 – 5.77 mM) was added to the reaction vial via a microliter syringe or micropipette. The reaction solution was then dispersed among 6 – 12 vials, depending on how many time points were required. For time points less than 6 h 150 μL was dispensed. For time points 6 – 12 h 300 μL was dispensed. For reactions longer than 12 h 500 μL was dispensed. A stir bar was added to each reaction vial. The vials were capped and sealed with electrical tape, removed from the glovebox, and placed in an aluminum heating block preheated to the desired temperature. The reaction vials were stirred at 80 rpm until the desired time point had arrived. Upon reaching the desired time the vial was removed from the aluminum block and while the solution was still warm an aliquot was removed from the reaction and added to a solution of hexanes to make a 10 mM solution of **4-4** based on its starting concentration. The hexanes solution was washed with water (1 × ½ the total volume of the solution of **4-4**, ca. 250 μL) to remove any magnesium salts, and the organic layer was injected into the

GC-FID. Reaction progress was monitored via calibrated GC-FID, product amounts were corrected based on elucidated response factors relative to the Ar-Br substrate.

#### 4.4.5 General Procedure for Variable Time Normalization Analysis (VTNA)

For VTNA analysis the following concentrations were used as the standard concentrations: 4-bromobenzotrifluoride (**4-4f**) 210 mM, PhMgBr 315 mM, **4-2**, 210  $\mu$ M. 1,2,3,4-tetrahydronaphthalene was added in the same concentration of **4-4f** as an internal standard. The concentrations of one component were altered while the concentrations of the other components were strictly maintained at the aforementioned values. The following concentrations were used to analyze each species: **4-4f** (mM): 210, 110, and 50. PhMgBr (mM): 315, 415, and 515 mM. **4-2** ( $\mu$ M): 210, 520, 830.

In a glovebox, **4-4f** was weighed into a 4 mL vial and dissolved in THF. 1,2,3,4-tetrahydronaphthalene (1.0 equiv.) was then added as an internal standard. PhMgBr was added, and an aliquot was removed from the solution and added to hexanes to quench the Grignard reagent and prepare a 10 mM solution of **4-4f** for a  $T_0$ . The  $T_0$  was removed from the glovebox, washed with water ( $1 \times \frac{1}{2}$  the volume) to remove any magnesium salts, and the organic layer was added to a GC vial and auto-injected into the GC-FID. A stock solution of **4-2** in  $C_6H_6$  was added to the reaction vial via a microliter syringe or micropipette. 150  $\mu$ L quantities of the solution were then dispensed into 11 individual vials. The vials were sealed with electrical tape, removed from the glovebox, and placed in an aluminum heating block that had been preheated to 60  $^{\circ}$ C. The reaction was stirred and assessed every 30 minutes for 5 h, and every hour for 2 h after that for 7 h total. Reaction progress was assessed removing one vial from the heating block. An aliquot was removed from that vial and added to hexanes to quench the Grignard reagent and prepare a 10 mM solution. The solution was washed with water ( $1 \times 0.5$  mL) to remove any magnesium salts, and the organic layer added to a GC vial and auto-injected into the GC-FID.

## 4.5 References

1. Korch, K. M.; Watson, D. A., *Chem. Rev.* **2019**, *119*, 8192-8228.
2. Jana, R.; Pathak, T. P.; Sigman, M. S., *Chem. Rev.* **2011**, *111*, 1417-1492.
3. Liu, C.; Zhang, H.; Shi, W.; Lei, A., *Chem. Rev.* **2011**, *111*, 1780-1824.
4. Esteruelas, M. A.; López, A. M.; Oñate, E.; San-Torcuato, A.; Tsai, J.-Y.; Xia, C., *Organometallics* **2017**, *36*, 699-707.
5. Turnbull, G.; Williams, J. A. G.; Kozhevnikov, V. N., *Chem. Commun.* **2017**, *53*, 2729-2732.
6. Li, G.; Zhu, D.; Wang, X.; Su, Z.; Bryce, M. R., *Chem. Soc. Rev.* **2020**, *49*, 765-838.
7. Pal, S.; Uyeda, C., *J. Am. Chem. Soc.* **2015**, *137*, 8042-8045.
8. Matsubara, K.; Yamamoto, H.; Miyazaki, S.; Inatomi, T.; Nonaka, K.; Koga, Y.; Yamada, Y.; Veiros, L. F.; Kirchner, K., *Organometallics* **2017**, *36*, 255-265.
9. Hruszkewycz, D. P.; Wu, J.; Hazari, N.; Incarvito, C. D., *J. Am. Chem. Soc.* **2011**, *133*, 3280-3283.
10. Xue, F.; Zhao, J.; Hor, T. S. A., *Dalton Trans.* **2013**, *42*, 5150-5158.
11. Yada, Y.; Miyake, Y.; Nishibayashi, Y., *Organometallics* **2008**, *27*, 3614-3617.
12. Hazari, N.; Hruszkewycz, D. P., *Chem. Soc. Rev.* **2016**, *45*, 2871-2899.
13. Powers, D. C.; Ritter, T., *Acc. Chem. Res.* **2012**, *45*, 840-850.
14. Xu, W.; Li, M.; Qiao, L.; Xie, J., *Chem. Commun.* **2020**, *56*, 8524-8536.
15. Bonney, K. J.; Proutiere, F.; Schoenebeck, F., *Chemical Science* **2013**, *4*, 4434-4439.
16. Aufiero, M.; Scattolin, T.; Proutière, F.; Schoenebeck, F., *Organometallics* **2015**, *34*, 5191-5195.
17. Scattolin, T.; Senol, E.; Yin, G.; Guo, Q.; Schoenebeck, F., *Angew. Chem. Int. Ed.* **2018**, *57*, 12425-12429.
18. Fricke, C.; Sperger, T.; Mendel, M.; Schoenebeck, F., *Angew. Chem. Int. Ed.* **2021**, *60*, 3355-3366.
19. Stambuli, J. P.; Kuwano, R.; Hartwig, J. F., *Angew. Chem. Int. Ed.* **2002**, *41*, 4746-4748.
20. Kolter, M.; Böck, K.; Karaghiosoff, K.; Koszinowski, K., *Angew. Chem. Int. Ed.* **2017**, *56*, 13244-13248.
21. Oderinde, M. S.; Frenette, M.; Robbins, D. W.; Aquila, B.; Johannes, J. W., *J. Am. Chem. Soc.* **2016**, *138*, 1760-1763.
22. Valente, C.; Pompeo, M.; Sayah, M.; Organ, M. G., *Org. Process Res. Dev.* **2014**, *18*, 180-190.
23. Jackman, K. M. K.; Liang, G.; Boyle, P. D.; Zimmerman, P. M.; Blacquiere, J. M., *Dalton Trans.* **2022**, *51*, 3977-3991.
24. Jackman, K. M. K.; Bridge, B. J.; Sauv e, E. R.; Rowley, C. N.; Zheng, C. H. M.; Stubbs, J. M.; Boyle, P. D.; Blacquiere, J. M., *Organometallics* **2019**, *38*, 1677-1681.
25. Inatomi, T.; Koga, Y.; Matsubara, K., *Molecules* **2018**, *23*, 140.
26. De, S.; Sivendran, N.; Maity, B.; Pirkel, N.; Koley, D.; Gooßen, L. J., *ACS Catal.* **2020**, *10*, 4517-4533.
27. Lee, C. L.; James, B. R.; Nelson, D. A.; Hallen, R. T., *Organometallics* **1984**, *3*, 1360-1364.
28. Bur s, J., *Angew. Chem. Int. Ed.* **2016**, *55*, 16084-16087.
29. Bur s, J., *Angew. Chem. Int. Ed.* **2016**, *55*, 2028-2031.

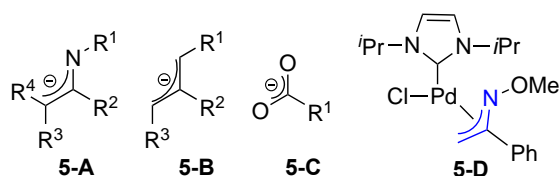
30. Davico, G. E.; Bierbaum, V. M.; DePuy, C. H.; Ellison, G. B.; Squires, R. R., *J. Am. Chem. Soc.* **1995**, *117*, 2590-2599.
31. Yang, L.; Powell, D. R.; Houser, R. P., *Dalton Trans.* **2007**, 955-964.
32. Pratihar, S.; Pegu, R.; Guha, A. K.; Sarma, B., *Dalton Trans.* **2014**, *43*, 17136-17144.
33. Salo, E. V.; Guan, Z., *Organometallics* **2003**, *22*, 5033-5046.
34. Murahashi, T.; Nagai, T.; Okuno, T.; Matsutani, T.; Kurosawa, H., *Chem. Commun.* **2000**, 1689-1690.
35. Witte, F.; Zucker, S. P.; Paulus, B.; Tzschucke, C. C., *Organometallics* **2021**, *40*, 591-599.
36. Stubbs, J. M.; Firth, K. F.; Bridge, B. J.; Berger, K. J.; Hazlehurst, R. J.; Boyle, P. D.; Blacquiere, J. M., *Dalton Trans.* **2017**, *46*, 647-650.

## 5.0 Assessing the Influence of Wider Bite Angles on P<sup>^</sup>AzA Coordination Chemistry

The synthesis of three new P<sup>^</sup>AzA ligands was attempted, in which the number of bonds between P and N was increased. The first ligand contained a phosphinite moiety rather than a phosphine. However, the P-O bond was unstable to the acidic conditions required for the synthesis of the P<sup>^</sup>I precursor, precluding further investigation of the phosphinite ligand. The other two ligands contain a naphthalene and biaryl backbone, which increases the number of bonds between P and N to 3, and 4 respectively. The two P<sup>^</sup>I precursors were coordinated to Pd, and their bite angles were inspected by X-Ray crystallography. The bite angle for the biaryl-linked ligand was *ca.* 15° wider than the naphthalene ligand, proving a positive correlation between ligand bite angle and the number of bonds between P and N. P<sup>^</sup>AzA complexes were isolated with both ligands. A complex coordinated with the naphthyl linked ligand could only be isolated when the ligand was deprotonated in the presence of pyridine, affording the 1-AzA coordinated  $\kappa^1$ -N. Alternatively, coordination of the biaryl 1-AzA salt to Pd allowed for the isolation of the first Pd(P<sup>^</sup>AzA) complex with the 1-AzA coordinated  $\eta^3$ -NCC.

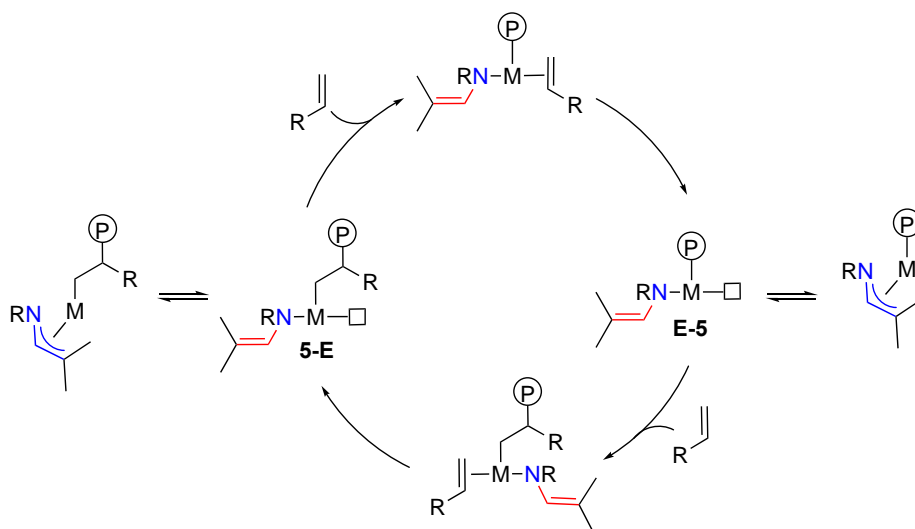
### 5.1 Introduction

Structurally responsive ligands (SRLs) are an advantageous class of ligand that have been shown to positively impact catalyst performance, rate, and reactivity.<sup>1</sup> Monoanionic functional groups capable of adopting numerous coordination modes are prevalent SRLs that have been used in catalysis. One such group is the 1-azaallyl (1-AzA) moiety (Figure 1 **5-A**) which is isoelectronic and structurally similar to other prevalent functional groups such as allyls (**5-B**) and carboxylates (**5-C**),<sup>2-4</sup> but its use is underexplored in catalysis.<sup>5-7</sup> One example is Pd<sup>II</sup> 1-AzA complex **5-D** (Figure 5.1b), which demonstrated higher catalyst performance for Suzuki-Miyaura coupling reactions than the directly analogous allyl catalyst.<sup>6</sup>



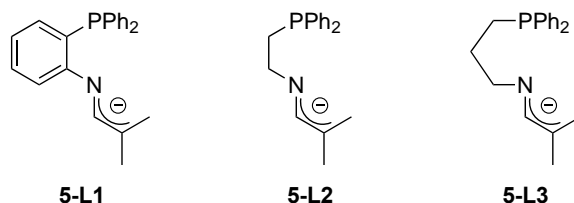
**Figure 5.1.** a) Selected monoanionic ligand groups: 1-AzA (**5-A**), allyl (**5-B**), carboxylate (**5-C**) and a Pd 1-AzA catalyst (**5-D**) used in Suzuki-Miyaura coupling catalysis. <sup>i</sup>Pr = 2,6-diisopropylphenyl.

A number of coordination modes are observed with the 1-AzA unit on binding to a metal (*i.e.*,  $\kappa^1\text{-N}$ ,  $\kappa^1\text{-C}$ ,  $\eta^3\text{-NCC}$ ,  $\kappa^2\text{-N,C}$ ) and the favoured structure depends on the steric bulk of the substituents ( $\text{R}^1\text{-R}^4$ ), the metal centre, and the other ancillary ligands.<sup>3</sup> It has previously been shown that 1-AzA ligands coordinated to Ni isomerize between a  $\kappa^1\text{-N}$  and  $\eta^3\text{-NCC}$  coordination mode, which occupy one and two coordination sites respectively.<sup>3</sup> The isomerization between  $\eta^3\text{-NCC}$  and  $\kappa^1\text{-N}$  is of particular interest for polymerization with group 10  $d^8$  complexes, as this isomerization can accompany monomer coordination and insertion steps. Ideally, this would lead to a longer lifetime catalyst through stabilization of the reactive three-coordinate species formed upon insertion of the monomer into the growing polymer chain (Figure 5.2, **5-E**).



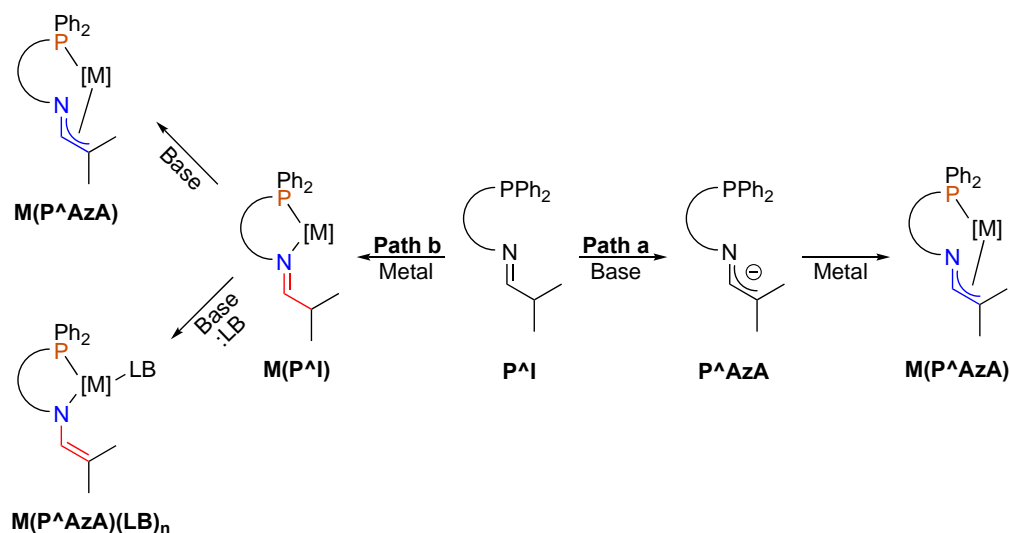
**Figure 5.2.** Representative scheme for a migratory-insertion polymerization mechanism, showing isomerization of the 1-AzA between  $\kappa^1\text{-N}$  and  $\eta^3\text{-NCC}$  potentially stabilizing the low coordinate species **5-E**.

We have previously created a ligand family that contains a strongly  $\sigma$  donating phosphine and a structurally responsive 1-AzA moiety ( $\text{P}^{\wedge}\text{AzA}$ ). Thus far, three entries have been designed for this ligand class: **5-L1**, **5-L2**, and **5-L3** (Figure 5.3). We have been able to successfully isolate several metal complexes coordinated by **5-L1**, however isolation of complexes coordinated by **5-L2** and **5-L3** were unsuccessful (*vide infra*).<sup>7-9</sup>



**Figure 5.3.** Three  $\text{P}^{\wedge}\text{AzA}$  ligands that have been designed thus far, a phenyl linked ligand **5-L1**, and two alkyl linked ligands **5-L2** and **5-L3**.

Successful preparation of P<sup>^</sup>AzA complexes have been achieved via two routes (Scheme 5.1).<sup>7, 8, 10</sup> Path **a** proceeds via deprotonation of the P<sup>^</sup>I precursor with a strong base (i.e., KH) affording the P<sup>^</sup>AzA ligand salt. This salt can then be coordinated to the metal precursor affording the M(P<sup>^</sup>AzA) complex. In path **b** the P<sup>^</sup>I ligand is coordinated to the metal precursor affording M(P<sup>^</sup>I). This complex is then treated with base producing the M(P<sup>^</sup>AzA) complex. It has been found that path **a** is often higher yielding and more reliable than path **b**.<sup>8</sup> It has been proposed that prolonged exposure of the M(P<sup>^</sup>AzA) complex to excess base and conjugate acid leads to decomposition of M(P<sup>^</sup>AzA) resulting in low yields and complex mixtures of products. Alternatively, if a P<sup>^</sup>AzA complex cannot be obtained through **a** or **b**, deprotonation of M(P<sup>^</sup>I) in the presence of a Lewis base (i.e., pyridine) can be a successful route.<sup>7</sup> The Lewis base helps to stabilize the P<sup>^</sup>AzA complex by binding to open coordination site(s) on the metal, effectively locking the 1-AzA moiety in the κ<sup>1</sup>-N coordination mode.<sup>3, 7, 8</sup> Coordination of the Lewis base has been found to be reversible<sup>10</sup> and irreversible depending on the complex.<sup>7, 8</sup>

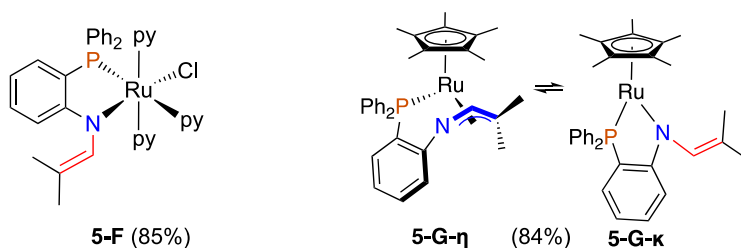


**Scheme 5.1.** The two paths that have been successfully used to obtain a P<sup>^</sup>AzA-metal complex beginning from P<sup>^</sup>I. Path **a**: deprotonation of the P<sup>^</sup>I followed by coordination to M generating M(P<sup>^</sup>AzA). Path **b**: Coordination of P<sup>^</sup>I to M followed by deprotonation affording M(P<sup>^</sup>AzA). Alternatively, the deprotonation can be attempted in the presence of a Lewis base (:LB) affording a Lewis base stabilized M(P<sup>^</sup>AzA) complex M(P<sup>^</sup>AzA)(LB)<sub>n</sub>.

Ligand **5-L1** contains a rigid phenyl donor between the two heteroatoms, and has been coordinated to both Ru<sup>7</sup> and Pd<sup>8</sup>. When RuCl<sub>2</sub>(PPh<sub>3</sub>)<sub>3</sub> was used as the metal precursor a P<sup>^</sup>AzA complex was only accessible via the Lewis base addition in path **b** affording (**5-F**) (Figure 5.4). Lewis base (i.e. pyridine) coordination was irreversible, and as such the only 1-AzA coordination

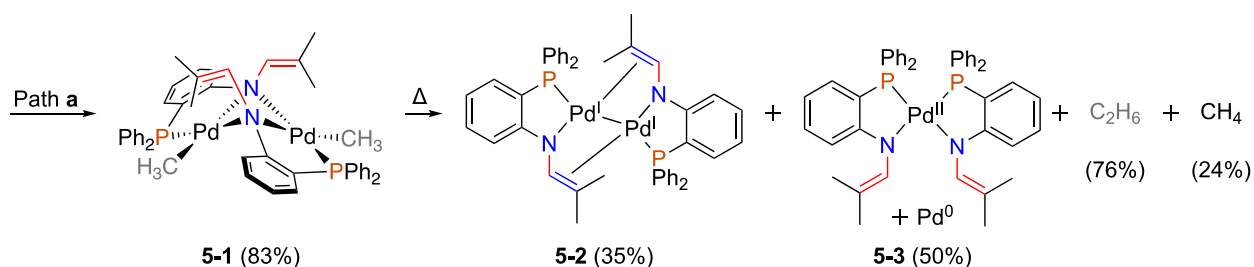


mode observed was  $\kappa^1\text{-N}$ .<sup>7</sup> When the precursor was changed to  $[\text{RuCl}(\text{Cp}^*)(\text{PPh}_3)_2]$ , in turn making the Ru centre more electron rich, a P<sup>^</sup>AzA complex could still only be acquired via the Lewis base addition in path **b**. However, pyridine coordination was determined to be reversible with the more electron rich Ru centre. By removing excess pyridine from solution, a Ru(P<sup>^</sup>AzA) species could be isolated with the 1-AzA ligand in equilibrium between a  $\kappa^1\text{-N}$  (**5-G- $\kappa$** ) mode in resulting in a low-coordinate Ru complex, and an  $\eta^3\text{-NCC}$  (**5-G- $\eta$** ) coordination mode. Although, computations and spectroscopic data indicate that **5-G- $\kappa$**  is the dominant species in solution.<sup>10</sup>



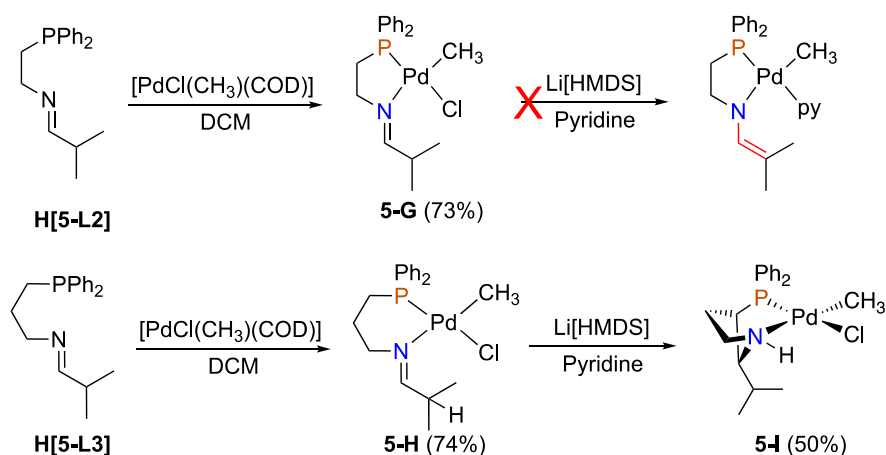
**Figure 5.4.** Isolated Ru(**5-L1**) complexes showing  $\kappa^1\text{-N}$  (**5-F** and **5-G- $\kappa$** ) and  $\eta^3\text{-NCC}$  (**5-G- $\eta$** ) coordination.

Coordination of **5-L1** to Pd afforded **5-1**,<sup>8</sup> a dinuclear complex bridged through the anionic amido in a  $\mu\text{-N}$  fashion (Scheme 5.2). Thermolysis of this complex results in reductive elimination of ethane, and the formation of dinuclear **5-2** and mononuclear **5-3**. In **5-2** the 1-AzA moiety is coordinated  $\mu\text{-}(\kappa^1\text{-N};\eta^2\text{-CC})$  and in **5-3** the 1-AzA moiety is coordinated  $\kappa^2\text{-PN}$ . The  $\mu\text{-}(\kappa^1\text{-N};\eta^2\text{-CC})$  motif, where the N and the C-C  $\pi$ -bond are simultaneously coordinated to two different metal centres is the first example of a 1-AzA moiety coordinated in this fashion. Computational investigations into the mechanism of C–C reductive elimination revealed  $\eta^3\text{-NCC}$ ,  $\eta^2\text{-CC}$ ,  $\kappa^1\text{-N}$ ,  $\mu\text{-}(\kappa^1\text{-N};\eta^2\text{-CC})$ , and  $\mu\text{-N}$  coordination modes operative throughout a dinuclear mechanism highlighting the structural diversity of the 1-AzA functional group.<sup>11</sup> Computationally, it was determined a species with a 1-AzA group coordinated  $\eta^3\text{-NCC}$  was instrumental to one of the reductive elimination pathways from **5-1**. However, a Pd complex with **5-L1** coordinated in the  $\eta^3\text{-NCC}$  mode was not isolated experimentally.



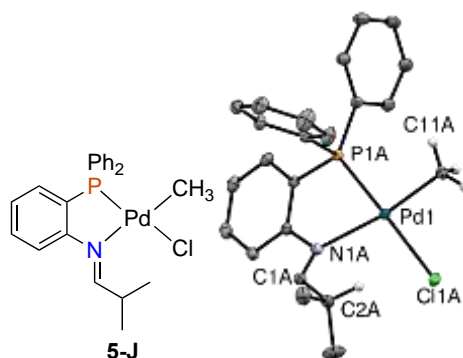
**Scheme 5.2.** a) Coordination of **H[5-L1]** to Pd via path **a** to afford P<sup>AzA</sup> complex **5-1** in excellent yields. Thermolysis of **5-1** gives dinuclear **5-2** and mononuclear **5-3**, each with distinct coordination modes of the 1-AzA

Ligands **5-L2** and **5-L3** contain flexible ethyl and propyl linkages respectively.<sup>9</sup> The synthesis of a P<sup>AzA</sup> complex with **5-L2** was attempted via path **a** and **b**. While P<sup>I</sup> complex **5-H** was acquired in good yields, all attempts at deprotonating the ligand were unsuccessful (Scheme 5.3a), and NMR spectroscopy suggested deprotonation did not occur. Likewise, path **a** was unsuccessful with **5-L3**. The synthesis of the P<sup>I</sup> Pd complex **5-H** was achievable in good yields however deprotonation of **H[5-L3]** was only possible in the presence of a Lewis base (Scheme 5.3b). Successful deprotonation of ligand **H[5-L3]** was only observed when the phosphine-imine precursor **H[5-L3]** was first coordinated to Pd (Scheme 5.3b). This resulted in backbone deprotonation at the carbon  $\alpha$ - to the phosphine, generating **5-I**. Complex **5-I** no longer contains an imine moiety and has formed a six- and five-member metallocycle rather than the target 1-AzA moiety. As such, it was determined that flexible alkyl linkages and backbones with protons  $\alpha$  to P must be avoided for access to a P<sup>AzA</sup> species.



**Scheme 5.3.** Attempted synthesis of a P<sup>AzA</sup> complex containing a) ethyl linked ligand **5-L2**. Coordination of **H[5-L2]** to Pd affording **5-G**, followed by attempted deprotonation with Li[HMDs]. b) propyl linked ligand **5-L3**. Coordination of **H[5-L3]** to Pd generates **5-H**. Complex **5-H** is treated with Li[HMDs] in pyridine affording **5-I**.

While our reported [M(P<sup>AzA</sup>)] complexes portray a diverse range of coordination modes including proposed  $\eta^3$ -NCC coordination mode with Ru, we have not yet obtained any experimental data suggestive of an  $\eta^3$ -NCC coordination mode with Pd. X-ray crystallography of the complex **5-J** coordinated by **H[5-L1]** revealed that the bite angle between P–Pd–N was 80.10° (Figure 5.5). In perfect square planar geometry there is a 90° angle between each L–Pd–L bond.<sup>12</sup> A bite angle of 80.10° suggests the rigidity of **5-L1** imparts a fair amount of strain on the complex. It was hypothesized that this strain makes  $\eta^3$ -NCC coordination unfavourable. As such, we sought to increase the number of bonds between phosphorus and nitrogen, as it was proposed this would lead to a subsequent increase in the bite angle and reduction in ligand induced strain. Herein, the design and synthesis of three new P<sup>AzA</sup> ligands, and the coordination chemistry of both the P<sup>AzA</sup> and P<sup>Imine</sup> precursor ligands with Pd<sup>II</sup> is discussed.

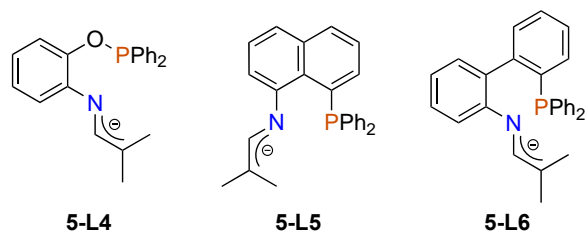


**Figure 5.5.** Pd(H(**5-L1**)) complex **5-J** and its thermal ellipsoid plot. Thermal ellipsoids are shown at the 50% probability level. For clarity, hydrogens have been omitted except on C2 and C11. The hydrogen atoms were introduced at idealized positions and were allowed to ride on the parent atom. P(1)–Pd(1)–N(1) = 80.10(2)°, C(11)–Pd(1)–Cl(1) = 90.35(3)°, N(1)–C(1)–C(2) = 124.85(9)°, C(1)–C(2)–C(3) = 109.10(1)°,  $\tau^4$  = 0.10,<sup>13</sup> N(1)–C(1) = 1.284(1) Å, C(1)–C(2) = 1.488(2) Å, Pd(1)–P(1) = 2.190(7) Å, Pd(1)–N(1) = 2.199(9) Å, Pd(1)–Cl(1) = 2.381(7) Å, Pd(1)–C(11) = 2.038(1) Å.

## 5.2 Result and Discussion

### 5.2.1 Ligand Synthesis

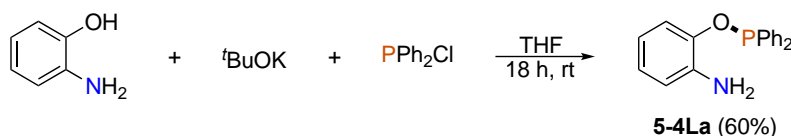
Three ligands were considered, which have rigid aryl backbones that are not susceptible to deprotonation (Figure 5.6). Ligand **5-L4** has a phenyl linker, but the phosphorus functional group has been changed to a phosphinite. This not only increases the number of bonds between P and N to three but it also makes the phosphorus more electron poor. Ligand **5-L5** contains a naphthalene linkage between P and N, and has three bonds between P and N. Finally, in **5-L6** the heteroatoms are connected by a biaryl backbone increasing the distance between P and N to four bonds.



**Figure 5.6.** The three ligands designed to have wider bite angles compared to **5-L1**.

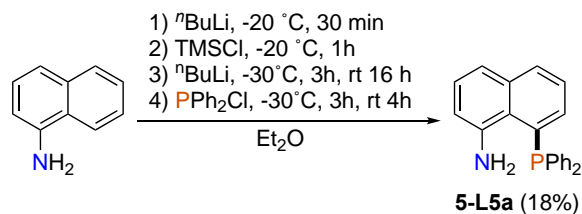
### 5.2.1.1 Phosphin(it)e-Amine Synthesis (**5-L4a**, **5a**, and **6a**)

The phosphinite-amine precursor **5-L4a** was synthesized via a modified literature procedure.<sup>14</sup> 2-Aminophenol was deprotonated with <sup>t</sup>BuOK in THF, followed by the addition of chlorodiphenylphosphine (Scheme 5.4). After workup, **5-L4a** was isolated as an air-stable pale pink solid in 60% yield. The <sup>31</sup>P{<sup>1</sup>H} NMR spectrum of **5-L4a** reveals a single peak at  $\delta_P = 108.3$ , consistent with the formation of a phosphinite.<sup>15,16</sup> Additionally, in the <sup>1</sup>H NMR spectrum a broad singlet at  $\delta_H = 4.76$  that integrates to two is the most upfield signal, this signal was determined to be the amine protons.



**Scheme 5.4.** Synthesis of phosphinite-amine precursor **5-L4a**.

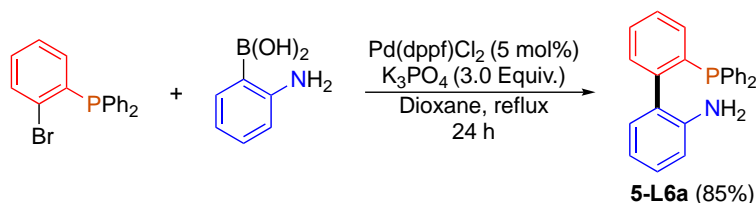
The known phosphine-amine precursor **5-L5a** was synthesized via literature procedure (Scheme 5.5).<sup>17</sup> 1-Aminonaphthalene was deprotonated with <sup>n</sup>BuLi and then reacted with chlorodiphenylphosphine. Following purification via column chromatography **5-L5a** was synthesized in poor yields. The reaction was consistently low yielding, with an average yield of 18%, compared to literature yields of 30%.<sup>17</sup>



**Scheme 5.5.** Synthesis of phosphine-amine precursor **5-L5a**.

The known phosphine amine precursor (**5-L6a**) was synthesized following a literature procedure.<sup>18</sup> A Suzuki cross coupling was carried out between 2-bromophenyldiphenylphosphine

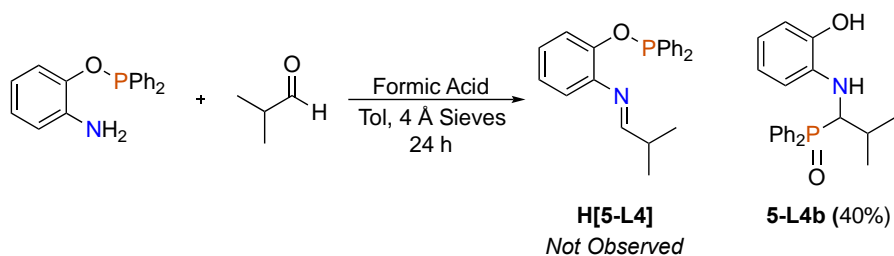
and 2-aminophenylboronic acid using Pd(dppf)Cl<sub>2</sub> as the catalyst (Scheme 5.6). The product was purified by column chromatography, affording **5-L6a** as a yellow solid with an average yield of 85%. The <sup>31</sup>P{<sup>1</sup>H} NMR spectrum of the product displayed a singlet at δ = -13.0, which matched literature value.<sup>18</sup> The formation of **5-L4 – L6a** was further confirmed via multinuclear 1D and 2D NMR and IR spectroscopy.



**Scheme 5.6.** Synthesis of **5-L6a** following literature procedures.

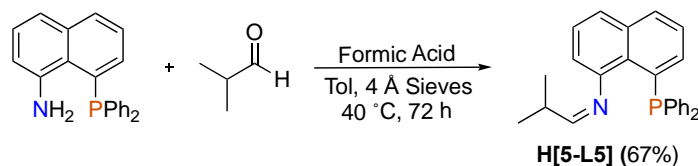
### 5.2.1.2 Phosphin(it)e-Imine Synthesis (**H[5-L4, 5, and 6]**)

A condensation reaction was attempted between **5-L4a** and isobutyraldehyde (Scheme 5.7). Upon workup a white powder was isolated, and it was determined that this product was in fact **5-L4b** and not **H[5-L4]** as anticipated. The <sup>31</sup>P{<sup>1</sup>H} NMR of **5-L4b** has a single peak at δ<sub>P</sub> = 35.4, consistent with formation of a phosphine oxide.<sup>19</sup> Furthermore, the IR spectrum of **5-L4b** has a band at 3370 cm<sup>-1</sup> and there are no signals observed at 1690–1640 cm<sup>-1</sup>, indicating that a secondary amine is present and not an imine. Moreover, there is a strong stretch at 1156 cm<sup>-1</sup>, which is indicative of a P=O bond. In the <sup>1</sup>H NMR spectrum, signals are observed for the -OH, -NH, and methine protons at δ<sub>H</sub> = 10.09, 5.53, 4.36, and 2.16, respectively. The signal at δ<sub>H</sub> = 4.36 is significantly downfield from what is typically expected for a methine moiety. However, deshielding from P and N results in a notable downfield chemical shift. A common drawback of phosphinites is facile hydrolysis of the P-O bond.<sup>20, 21</sup> Despite previous reports on the stability of the P-O bond in **5-L4a**,<sup>14</sup> it is likely that acid-catalyzed cleavage of this bond occurred in the attempted synthesis of **H[L-4]** resulting in cleavage of the P-O bond and formation of a hydroxyl group. Hydrophosphination of the imine<sup>22</sup> followed by oxidation results in formation of **5-L4b**. As the acidic conditions required for the condensation reaction to proceed are incompatible with the phosphinite function group the synthesis of **5-L4** was not pursued further.



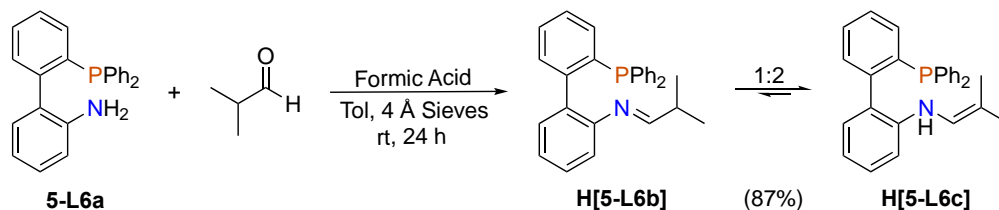
**Scheme 5.7.** Attempted synthesis of phosphinite-imine **H[5-L4]** instead affording **5-L4b**.

The precursor **5-L5a** was reacted with isobutyraldehyde to give **H[5-L5]** as a yellow solid in good yield (Scheme 5.8). Typically, condensation reactions to give the phosphine-imine precursors reach completion within 24 h at room temperature,<sup>8,9</sup> however the synthesis of **H[5-L5]** required heating at 40 °C and an increased reaction time of 72 h. The <sup>1</sup>H NMR spectrum of **H[5-L5]** has a diagnostic doublet (<sup>3</sup>J<sub>HH</sub> = 10.2 Hz) at δ<sub>H</sub> = 1.02, corresponding to the methyl protons of the isopropyl moiety. The imine proton (H<sup>1</sup>) was found via <sup>1</sup>H-<sup>13</sup>C HSQC at δ<sub>H</sub> = 7.44, a location that overlapped with aromatic signals. A small (0.2 ppm) downfield shift in the <sup>31</sup>P{<sup>1</sup>H} NMR spectrum is observed for **H[5-L5]** as compared to **5-L5a**. Furthermore, the IR spectrum of **H[5-L5]** has a band at 1648 cm<sup>-1</sup>, consistent with an imine while no bands are seen above 3000 cm<sup>-1</sup> confirming the amine is no longer present. The successful synthesis of **H[5-L5]** was further confirmed using <sup>1</sup>H-<sup>1</sup>H COSY, <sup>13</sup>C{<sup>1</sup>H}, and <sup>1</sup>H-<sup>13</sup>C HSQC/HMBC spectroscopies.



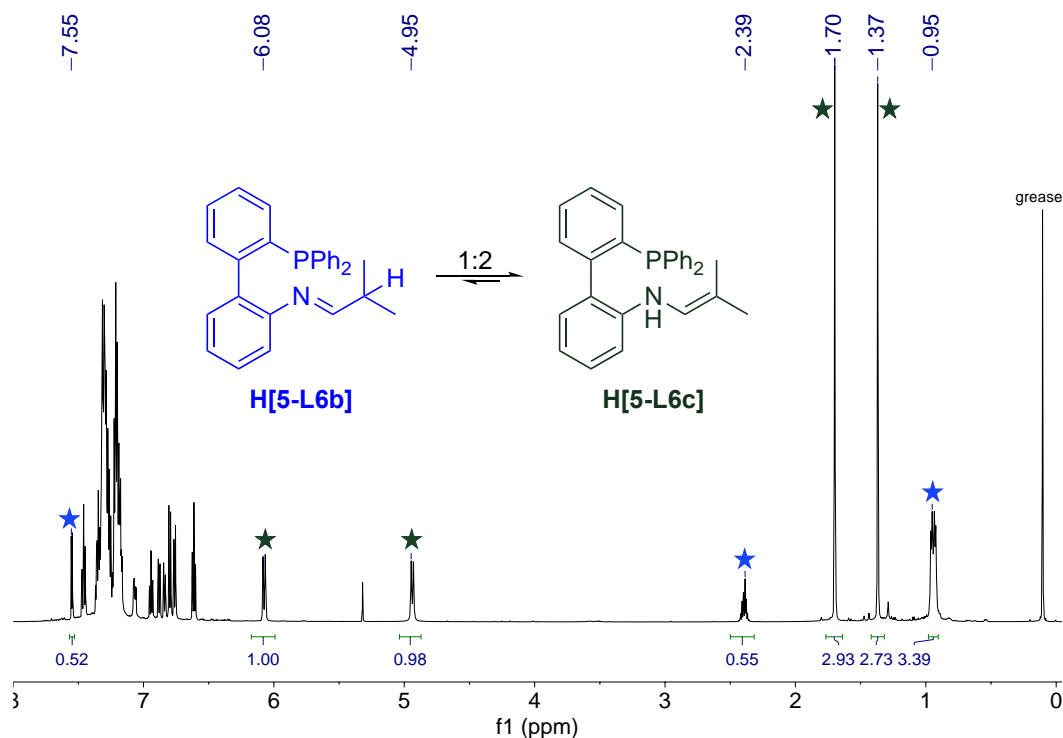
**Scheme 5.8.** Synthesis of phosphine-imine precursor **H[5-L5]**.

The phosphine imine precursor **H[5-L6]** was performed through a condensation reaction with isobutyraldehyde, affording **H[5-L6]** as a white solid with an average yield of 87% (Scheme 5.9).



**Scheme 5.9.** Synthesis of **H[5-L6]** from precursor **5-L6a**. **H[5-L6]** is in equilibrium with tautomers **H[5-L6a]** and **H[5-L6b]**.

The  $^{31}\text{P}\{^1\text{H}\}$  NMR spectrum of the isolated product no longer has a signal at  $\delta_{\text{P}} = -13.0$ , confirming consumption of **5-L6a**. Instead, two singlets are found at  $\delta_{\text{P}} = -12.4$  and  $-13.3$ , in a 1:2 ratio, respectively, suggesting two distinct products have formed. There are two sets of signals in  $^1\text{H}$  NMR spectrum that were key to assigning the structure of **H[5-L6]**. First, a doublet ( $J = 4.8$  Hz), a doublet of septets ( $J = 2.1$  Hz,  $6.9$  Hz), and a broad multiplet are found at  $\delta_{\text{H}} = 7.53$ ,  $2.37$ , and  $0.92$ , consistent with formation of the target imine **H[5-L6b]** (Figure 5.7). The second set of signals are two singlets at  $\delta_{\text{H}} = 1.68$ , and  $1.35$ , that implies that the methyls are inequivalent, and two doublets ( $^3J_{\text{HH}} = 9.0$ ,  $10.5$  Hz), at  $\delta_{\text{H}} = 6.06$ ,  $4.92$ . The  $^1\text{H}$ - $^{13}\text{C}$  HSQC spectrum shows that only the signal at  $\delta_{\text{H}} = 6.06$  is attached to a carbon, which helped to confirm the signal at  $\delta_{\text{H}} = 4.92$  is the N-H signal, confirming the structure of the enamine **H[5-L6c]**.

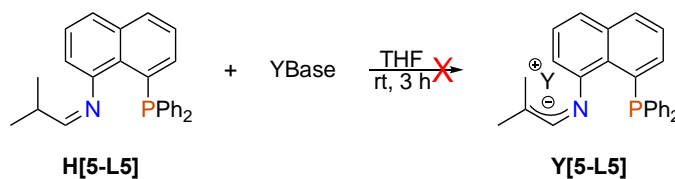


**Figure 5.7.**  $^1\text{H}$  NMR spectrum of **H[5-L6]** in  $\text{CDCl}_3$  with an example of the tautomerization between **H[5-L6b]** and **H[5-L6c]**.

### 5.2.1.3 Phosphine-Imine Deprotonation

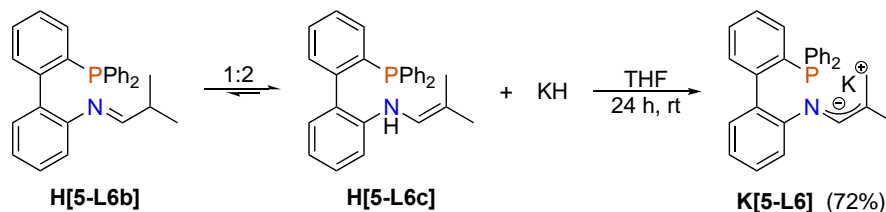
The deprotonation of **H[5-L5]** was attempted with a wide variety of bases (Scheme 5.10). Initially, the reaction was carried out with  $\text{KH}$  in THF as these are the conditions that successfully

gave **K[5-L1]**.<sup>8</sup> Upon addition of the base the colour immediately changed from yellow to red, however the NMR spectra of the recovered material showed no change from **H[5-L5]**. Deprotonation was then attempted with stronger bases such as <sup>t</sup>BuLi, <sup>t</sup>BuLi, and LDA, and in each scenario a colour change from yellow to red was observed. However, no change was observed by *in-situ* <sup>31</sup>P{<sup>1</sup>H} NMR spectroscopy or in the <sup>1</sup>H NMR spectrum of the isolated material. As such the formation of a [Pd<sup>II</sup>(**5-L5**)] complex was attempted via coordination of **H[5-L5]** to Pd<sup>II</sup> followed by deprotonation (Section 5.2.2.2).



**Scheme 5.10.** Attempted deprotonation of **H[5-L5]** to give **Y[5-L5]** Y = Li/K, Base = H, <sup>t</sup>BuOK, <sup>n</sup>Bu, <sup>t</sup>Bu, N(Si(CH<sub>3</sub>)<sub>2</sub>), N(CH<sub>2</sub>(CH<sub>3</sub>)<sub>2</sub>).

Deprotonation of **H[5-L6]** with potassium hydride was performed to afford the phosphine 1-azaallyl ligand **K[5-L6]**, as an orange solid with an average yield of 72% (Scheme 5.11). The <sup>31</sup>P{<sup>1</sup>H} NMR spectrum of **K[5-L6]**, shows one peak at  $\delta_P = -13.6$ , confirming deprotonation of both tautomers to give one species. The <sup>1</sup>H NMR spectrum has three singlets at  $\delta_H = 6.15$ , 1.66 and 1.32 that correspond to the H<sup>1</sup> proton and the two methyls of the 1-AzA moiety, respectively. Furthermore, the signals previously observed for the N-H and H<sup>1</sup> in **H[5-L6b]** and **H[5-L6c]**, respectively are no longer observed. A negative ion MALDI-MS spectrum was also acquired of **K[5-L6]**, and the molecular ion peak was observed for [**5-L6**]<sup>-</sup>.



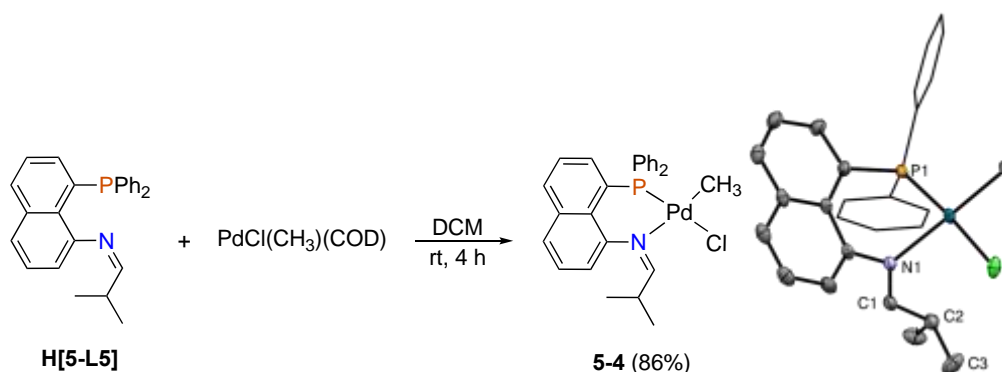
**Scheme 5.11.** Synthesis of **K[5-L6]** via deprotonation of the two tautomers of **H[5-L6]** with KH.



## 5.2.2 Palladium Complex Synthesis

### 5.2.2.1 Synthesis of Pd Phosphine-Imine Complexes **5-4** and **5-5**

Ligand **H[5-L5]** was coordinated to Pd<sup>II</sup> following a reaction with [PdCl(CH<sub>3</sub>)(COD)] affording **5-4** as a yellow solid in excellent yield (Scheme 5.12). The <sup>31</sup>P{<sup>1</sup>H} NMR spectrum showed a significant downfield shift from -3.20 ppm for the free ligand to 36.6 ppm, consistent with phosphine coordination to Pd. The diagnostic signal for the Pd bound methyl was observed as a doublet at δ<sub>H</sub> = 0.64 with a small coupling constant (*J* = 3.9 Hz). The small coupling constant is consistent with *cis* coordination of the phosphine and methyl.<sup>23-25</sup>



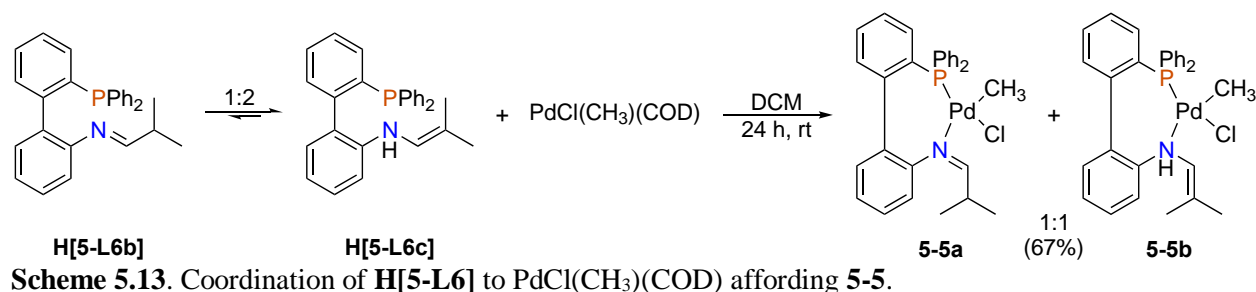
**Scheme 5.12.** Coordination of **H[5-L5]** to [PdCl(CH<sub>3</sub>)(COD)] affording **5-4**. Thermal Ellipsoid plot of **5-4**. Thermal ellipsoids are shown at the 50% probability level. For clarity, all hydrogens have been omitted. P(1)-Pd(1)-N(1) = 81.94(3)°, C(27)-Pd(1)-Cl(1) = 89.08(4)°, N(1)-C(1)-C(2) = 124.31(1)°, C(1)-C(2)-C(3) = 109.03(1)°, τ<sup>4</sup> = 0.06,<sup>13</sup> N(1)-C(1) = 1.280(1) Å, C(1)-C(2) = 1.490(2) Å, Pd(1)-P(1) = 2.206(7) Å, Pd(1)-N(1) = 2.144(9) Å, Pd(1)-Cl(1) = 2.371(7) Å, Pd(1)-C(27) = 2.060(1) Å.

Crystals of **5-4** suitable for X-ray diffraction were grown via slow vapour diffusion of pentane into a solution of **5-4** in DCM at -20 °C. The structure confirmed the square planar geometry of **5-4**, with very minimal distortion according to the τ<sup>4</sup> value<sup>13</sup> of 0.06 (for a perfect square plane τ<sup>4</sup> = 0) (Scheme 5.12, right). The crystal structure also confirms the *cis* orientation of the phosphine and methyl substituents. The N(1)-C(1) bond length is 1.280(1) Å, characteristic of a C-N double bond. The C(1)-C(2) bond length is 1.490(2) Å which is expected for a C-C single bond. There is also evidence in solution of a moderate<sup>26</sup> hydrogen-bonding interaction between the chlorine atom and the protons on C<sup>3</sup>. In the <sup>1</sup>H NMR spectrum the two methyls of the 1-AzA group are found as separate doublets with the same coupling constant from coupling to the methine (<sup>3</sup>J<sub>HH</sub> = 6.6 Hz). The bond length between H(2) and Cl(1) is 2.875 Å while the Cl(1)-H-C(3) bond angle

is 137.92°. In a typical moderate-strength hydrogen bond the X–H distance is between 2.5 – 3.2 Å, while the Cl–H–C angle is >130°.<sup>26</sup> The P(1)–Pd–N(1) bite angle was 81.94°, suggesting there is a fair amount of strain caused by the chelating ligand. Comparatively, ligand **H[5-L1]** when coordinated to Pd has a bite angle of 80.10°.<sup>8</sup> As such, merely increasing the distance between P and N does not appear to be sufficient in reducing the ligand bite angle.

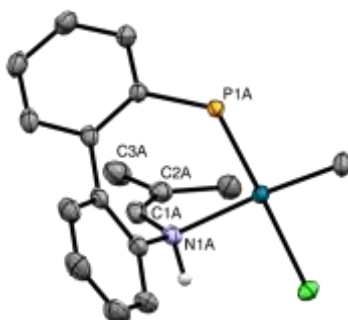
The tautomeric mixture of **H[5-L6b]** and **H[5-L6c]** was coordinated to [PdCl(CH<sub>3</sub>)(COD)] affording complex **5-5** in 67% yield (Scheme 5.13). The <sup>31</sup>P{<sup>1</sup>H} NMR spectrum shows two distinct species at δ<sub>P</sub> = 36.2 and 35.4, signifying again there are two different <sup>31</sup>P environments. The <sup>1</sup>H NMR spectrum has two doublets and a septet at δ<sub>H</sub> = 3.56, 1.18, and 0.69 consistent with H<sup>2</sup> and H<sup>3/3'</sup> of the target imine. H<sup>3</sup> and H<sup>3'</sup> are likely inequivalent due to hydrogen bonding with the adjacent chloro ligand observed in other P^Imine Pd complexes such as **5-4**. Additionally, three broad signals are seen at δ<sub>H</sub> = 5.67, 1.60 and 1.50 which correspond to N–H and H<sup>3/3'</sup> in **H[5-L6c]**. The diagnostic doublets for the Pd bound methyls are seen at δ<sub>H</sub> = 0.61 and 0.49, with coupling constants of *J* = 3.4 and 3.5 Hz, respectively. The small coupling constants are consistent with *cis* coordination of the phosphine and methyls for both tautomeric products **5-5a** and **5-5b**.<sup>23-</sup>

25



Crystals of **5-5** suitable for X-ray diffraction were grown via slow vapour diffusion of pentane into a solution of **5-5** in a 9:1 mixture of toluene and DCM at –20 °C (Figure 5.8). The crystallized structure was determined to be **5-5b**, the enamine form of **5-5**. Two units of **5-5b** crystallized in the unit cell, but only one will be discussed. The square planar geometry of **5-5b** was confirmed, with very minimal distortion according to the τ<sup>4</sup> value of 0.07.<sup>13</sup> The N(1B)–C(1B) bond length is 1.440 Å, characteristic of a C–N single bond. While the C(1B)–C(2B) bond length is 1.332 Å which is expected for a C–C double bond and confirms crystallization of the enamine tautomer. The crystal structure also confirms the *cis* orientation of the phosphine and methyl substituents. Although complex **5-5b** is coordinated by an enamine and not an imine, the P(1B)–

Pd–N(1B) bite angle with **H[5-L6c]** was determined to be 95.18°, which is significantly wider than either **H[5-L1]**<sup>8</sup> or **H[5-L4]**, and the angle is comparable to those of the flexible ligands **H[5-L2]** and **H[5-L3]**.<sup>9</sup> Confirming our hypothesis that increasing the distance between P and N will result in an increase of the bite angle. Therefore, **H[5-L4]** imparts less conformational strain on the metal centre and may allow for isolation of a Pd species with the phosphine 1-azaallyl form of the ligand coordinated  $\eta^3$ -NCC.

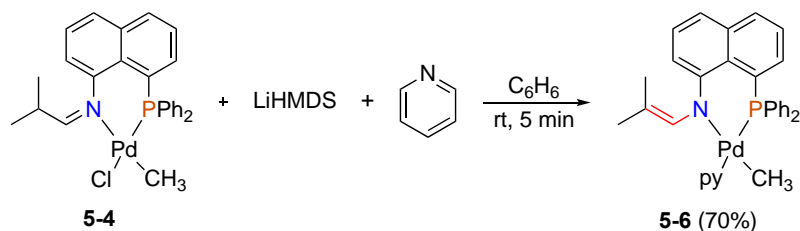


**Figure 5.8.** Thermal ellipsoid plot of **5-5b**, for clarity only one unit of crystallized **5-5b** is shown, additionally and all hydrogens except for the N-H and all phenyl substituents were omitted. The hydrogen atoms were introduced at idealized positions and were allowed to ride on the parent atom. Thermal ellipsoids are shown at the 50% probability level. Only values for A crystal are reported. P(1)-Pd(1)-N(1) = 95.18(4)°, C(27)-Pd(1)-Cl(1) = 91.68(5)°, N(1)-C(1)-C(2) = 125.67(2)°, C(1)-C(2)-C(3) = 119.31(2)°,  $\tau^4$  = 0.07,<sup>13</sup> N(1)-C(1) = 1.440(2) Å, C(1)-C(2) = 1.332(3) Å, Pd(1)-P(1) = 2.208(9) Å, Pd(1)-N(1) = 2.248(2) Å, Pd(1)-Cl(1) = 2.387(1) Å, Pd(1)-C(27) = 2.035(2) Å.

### 5.2.2.2 P<sup>A</sup>AzA Complex Synthesis

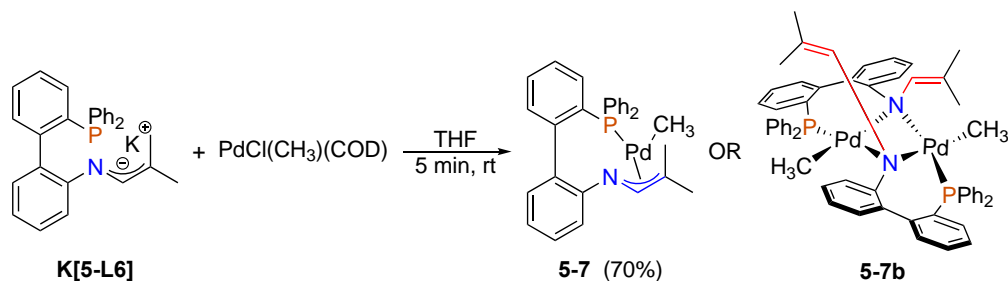
Since the free ligand **H[5-L5]** could not be deprotonated (Section 5.2.1.3) the synthesis of a P<sup>A</sup>AzA complex was instead attempted via deprotonation of the phosphine-imine complex **5-4**. Deprotonation was attempted with Li[HMDS] in C<sub>6</sub>H<sub>6</sub> as these were the conditions that gave conversion of the P<sup>A</sup>I complex of **H[5-L1]** to **5-1**.<sup>8</sup> Deprotonation of **5-4** was attempted with 1.2 and 1.5 equivalents of Li[HMDS] and while there was an immediate colour change from yellow to red, the <sup>1</sup>H NMR spectra in C<sub>6</sub>D<sub>6</sub> still had a septet at  $\delta_{\text{H}} = 3.92$ . This signal is characteristic of H<sup>2</sup>, which is where deprotonation would be anticipated, indicating deprotonation to give a 1-AzA did not occur. Deprotonation was instead attempted in the presence of pyridine (Scheme 5.14). Pyridine is a Lewis base and can therefore occupy the fourth coordination site that is vacated following deprotonation, thereby stabilizing the complex. Most commonly 1-AzA ligands are coordinated  $\kappa^1$ -N in these scenarios.<sup>3</sup> Again, the solution immediately changed colour from yellow to red upon addition of Li[HMDS]. The *in-situ* <sup>31</sup>P{<sup>1</sup>H} NMR spectrum shows complete

consumption of **5-4** and formation of a new signal at  $\delta_P = 36.4$ . Additionally, the  $^1\text{H}$  NMR spectrum does not have any signals consistent with  $\text{H}^2$  and the signals for  $\text{H}^{3/3'}$  are found as two distinct singlets at  $\delta_H = 1.57$  and  $1.36$ , validating deprotonation has occurred at  $\text{H}^2$  as desired. The diagnostic doublet ( $^3J_{\text{HP}} = 1.2$  Hz) at  $\delta_H = 0.47$  with a small coupling constant confirms the *cis* orientation of P and  $-\text{CH}_3$ . Furthermore, a broad signal can be observed in the room temperature NMR of **5-6** at  $\delta_H = 8.45$  representing coordinated pyridine. At  $10^\circ\text{C}$  the signal begins to decoalesce with complete decoalescence occurring at  $-10^\circ\text{C}$ , and two distinct broad signals are seen at  $\delta_H = 8.53$  and  $8.28$  representing free pyridine and coordinated py, respectively. Through 2D  $^1\text{H}$ - $^{13}\text{C}$  NMR spectroscopy the  $^{13}\text{C}$  signal for  $\text{C}^2$  was found at  $\delta_C = 110.2$ , consistent with  $\kappa^1\text{-N}$  coordination of the 1-AzA moiety.<sup>7</sup> All of this data confirms deprotonation of **5-L5** to afford the target P^AZA species **5-6**.



**Scheme 5.14.** Deprotonation of **5-4** with Li[HMDS] in pyridine, affording P^AZA complex **5-6** in 70% yield with the 1-AzA coordinated  $\kappa^1\text{-N}$ .

Ligand **K[5-L6]** was coordinated to Pd following a reaction with  $[\text{PdCl}(\text{CH}_3)(\text{COD})]$ , and complex **5-7** was isolated as an orange solid in 70% yield (Scheme 5.15). The  $^{31}\text{P}\{^1\text{H}\}$  NMR spectrum of **5-7** has one singlet at  $\delta_P = 25.7$ , consistent with ligand coordination to Pd. Two proposed products are possible from this reaction: complex **5-7b** which is structurally analogous to **5-1** in which the anionic nitrogen bridges the two metal centres, or a complex with the 1-AzA ligand coordinated  $\eta^3\text{-NCC}$  (**5-7**).

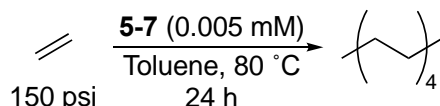


**Scheme 5.15.** Synthesis of P^AZA complex **5-7** via coordination of **K[5-L6]**. The 1-AzA moiety is proposed to be coordinated  $\eta^3\text{-NCC}$ .

$^1\text{H}$ - $^{31}\text{P}$  HMBC NMR spectroscopy was used to help determine the coordination mode of **5-L6**. If the 1-AzA in **5-L6** is coordinated  $\kappa^1\text{-N}$  the distance between P and  $\text{H}^{3/3'}$  is 6 bonds, while in  $\eta^3\text{-NCC}$  coordination mode P and  $\text{H}^{3/3'}$  are only 4 bonds apart through the Pd centre. The  $^1\text{H}$ - $^{31}\text{P}$  HMBC NMR spectrum of **5-7** revealed a correlation between P and  $\text{H}^{3/3'}$  (Figure D.30). By comparison, no analogous correlation was observed with **5-1** ( $\mu\text{-N}$ ), or **5-3** ( $\kappa^1\text{-N}$ ). A correlation is also observed in **5-2** between P and  $\text{H}^{3/3'}$  with the 1-AzA coordinated  $\eta^2\text{-CC}$ . Furthermore, the  $^{13}\text{C}$  NMR shift for  $\text{C}^2$  in **5-7** was determined to be  $\delta_{\text{C}} = 88.4$ , which is not in the ranges reported for  $\kappa^1\text{-N}$  (117.3–118.9) with other  $\text{P}^{\wedge}\text{AzA}$  ligands, or  $\eta^3\text{-NCC}$  (42.0–64.5) coordination modes.<sup>7,8</sup> The  $^{13}\text{C}$  NMR shift for  $\text{C}^2$  is downfield of the expected range of an  $\eta^3\text{-NCC}$  coordination mode, although **5-L6** is a new class of ligand and a representative range for  $\eta^3\text{-NCC}$  coordination has not yet been established. Comparatively, the same signal in **5-1** and **5-2** was found at  $\delta_{\text{C}} = 117.2$  and 74.5, respectively. The MALDI-MS spectrum of **5-7** does not show any peaks in the range of  $m/z = 1026 - 1056$ , which would be expected for a dinuclear analogue of **5-7** (i.e., **5-7b**), although due to the ionization and ablation techniques in MALDI a dinuclear structure cannot be ruled out via this result. It is therefore proposed that **5-7** exists as a mononuclear complex with ligand **5-L6** coordinated  $\eta^3\text{-NCC}$ . Crystals were attempted to be grown via slow vapour diffusion of pentane into a solution of **5-7** in THF, as well as slow evaporation of a saturated solution of **5-7** in pentane. Unfortunately, crystals suitable for X-ray diffraction could not be obtained.

### 5.2.3 Ethylene Homopolymerization

Palladium complex **5-7** was used to catalyze the polymerization of pressurized ethylene (Scheme 5.16). A solution of **5-7** in toluene was added to a Parr Reactor with pressurized ethylene and heated at 80 °C for 24 h. After 24 h, MeOH was added to the solution to try and precipitate any polymers formed, the solution was filtered however no solids were obtained. As such, the solvents were removed to afford a white solid with an average mass of 11 mg.



**Scheme 5.16.** Synthesis of polyethylene catalyzed by **5-7**.

The  $^1\text{H}$  NMR spectrum of the isolated material in  $\text{CDCl}_3$  had signals at  $\delta_{\text{H}} = 1.40, 1.28$ , which represent the methylene units, as well as a signal at  $\delta_{\text{H}} = 0.88$ . These signals are consistent

with other reported  $^1\text{H}$  NMR spectra of polyethylene in  $\text{CDCl}_3$ .<sup>27</sup> The peaks corresponding to the terminal end groups in the  $^1\text{H}$  NMR spectrum were set to 6H and the methylene signals were integrated to determine the chain length of the product. The methylene signals integrated to 16, correlating to four repeating units. As such the organic products were oligomers, and not polymers.<sup>28</sup> Due to time constraints, polymerization was not attempted with **5-1**, **5-4**, **5-5**, or **5-6**. However, future work should include polymerization with these species.

### 5.3 Conclusions

We have designed three new P<sup>^</sup>AzA ligands differing in the linkers between the P and N heteroatoms. It was hypothesized that increasing the distance between the P and N relative to **H-L1** would result in a larger ligand bite angle, thereby imposing less strain on the complex with the goal of isolating a species with the 1-AzA functional group in an  $\eta^3$ -NCC coordination mode. Ligand **5-L4** with a phosphinite functionality was not compatible with the synthetic process of generating a P<sup>^</sup>AzA ligand, as the acid catalyst required for the phosphine-imine precursor synthesis results in cleavage of the O–P bond. Ligand **H[5-L5]** and **H[5-L6]** containing 1,8-naphthyl and 2,2-biaryl linkages between P and N, respectively. Ligand **H[5-L5]** was determined to have a bite angle of 81.94°, comparatively **H[5-L1]** has a bite angle of 80.10°. This suggests that exclusively increasing the distance between P and N by a single carbon is not sufficient to increase the bite angle of the ligand, and factors other than distance between P and N should be considered. Consequently, a P<sup>^</sup>AzA species with **5-L5** could only be isolated with the 1-AzA moiety coordinated  $\kappa^1$ -N. When **H[5-L6]** was coordinated to Pd its bite angle was substantially wider at 95.97°, which suggests little to no stress is imposed by **H[5-L6]**. Additionally, the spectroscopic data acquired from **5-7** suggests that the 1-AzA moiety is coordinated in an  $\eta^3$ -NCC coordination mode. Accordingly, this confirms our hypothesis that increasing the ligand bite angle allows for the isolation of a Pd(P<sup>^</sup>AzA) complex with the 1-AzA coordinated  $\eta^3$ -NCC. Finally, complex **5-7** was capable of oligomerizing ethylene, generating oligomers with 4 repeat units.

## 5.4 Experimental

### 5.4.1 Synthetic Procedures

#### 5.4.1.1 General Considerations

All reactions were conducted in a nitrogen atmosphere glove box or using standard Schlenk line techniques under an argon atmosphere, unless otherwise indicated. All glassware was oven dried and cooled under nitrogen atmosphere prior to use, unless otherwise stated. Ground-glass syringes were stored in a desiccator containing DrieRite. All reagents used were obtained from commercially available sources and used without further purification, unless otherwise indicated. Potassium hydride was purchased from Alfa Aesar as a 30% w/w suspension in mineral oil, and was purified by filtration through a fritted funnel, the solid KH was washed with dry hexanes and diethyl ether (20 mL/g KH), the solid was dried under vacuum and inside a nitrogen atmosphere glovebox for use. The following materials were prepared following literature procedures: PdCl(CH<sub>3</sub>)(COD),<sup>29</sup> **5-L4a**,<sup>17</sup> and **5-L5a**.<sup>18</sup> All reaction solvents were obtained from an Innovative Technology 400-5 Solvent Purification system, and stored over activated 4 or 3 Å molecular sieves under N<sub>2</sub> prior to use, unless stated otherwise. Pyridine was dried over CaH<sub>2</sub>, distilled under dynamic vacuum, and stored in an inert atmosphere over activated 4 Å. Deuterated NMR solvents were obtained from commercial sources and stored over activated 4 Å sieves in an inert atmosphere. Molecular sieves were activated by heating the sieves at 160 °C under vacuum overnight.

All NMR spectra were obtained on a 600 or 400 MHz Bruker or 600 MHz Varian spectrometer at 25 °C unless otherwise stated. <sup>1</sup>H and <sup>13</sup>C{<sup>1</sup>H} spectra were referenced internally, using residual solvent values, to TMS at 0 ppm as follows: benzene-*d*<sub>6</sub> (<sup>1</sup>H, 7.16 ppm; <sup>13</sup>C{<sup>1</sup>H}, 128.1 ppm), CDCl<sub>3</sub> (<sup>1</sup>H, 7.26 ppm; <sup>13</sup>C{<sup>1</sup>H} 77.2 ppm), and acetone-*d*<sub>6</sub> (<sup>1</sup>H, 2.05 ppm; <sup>13</sup>C{<sup>1</sup>H}, 29.8 ppm). <sup>31</sup>P{<sup>1</sup>H} spectra obtained in deuterated solvents were referenced internally to H<sub>3</sub>PO<sub>4</sub> at 0.0 ppm. <sup>31</sup>P{<sup>1</sup>H} spectra obtained in non-deuterated solvents were externally referenced to a sample of 85% H<sub>3</sub>PO<sub>4</sub>. Multiplicities are described as s (singlet), d (doublet), t (triplet), sept (septet), m (multiplet), and br (broad). Chemical shift assignments were obtained using 1D NMR

spectroscopy, and hetero- and homonuclear 2D NMR spectroscopy (i.e.  $^1\text{H}$ - $^1\text{H}$  COSY,  $^1\text{H}$ - $^{13}\text{C}$  HSQC, and  $^1\text{H}$ - $^{13}\text{C}/^{31}\text{P}$  HMBC). X-ray diffraction measurements were made on a Bruker Kappa Axis Apex2 diffractometer at a temperature of 110 K. Further details are provided in Appendix D.IV. Infrared spectra were collected on solid samples using a Bruker ALPHA II FTIR spectrometer. Charge-transfer Matrix Assisted Laser Desorption/Ionization (MALDI) mass spectrometry data were collected on an AB Sciex 5800 TOF/TOF mass spectrometer using pyrene as the matrix in a 20:1 molar ratio to complex. Solutions were prepared in  $\text{C}_6\text{H}_6$  and spotted on a sample plate under an inert atmosphere and transferred to the instrument in a sealed Ziplock<sup>®</sup> bag. The instrument is equipped with a 349 nm OptiBeam On-Axis laser. The laser pulse rate was 400 Hz and data were collected in reflectron positive mode unless otherwise indicated. Reflectron mode was externally calibrated at 50 ppm mass tolerance. Each mass spectrum was collected as a sum of 500 shots. The acquired data sets were plotted in Microsoft Excel, and simulations for peaks of interest were acquired from [envipat.eawag.ch](http://envipat.eawag.ch)<sup>30</sup> and plotted in Microsoft Excel. Gas chromatography mass spectrometry (GC-MS) measurements formation were obtained on a Shimadzu GCMS-QP2010 instrument, fitted with a HP-Plot/U column.

## 5.4.1.2 Ligand Synthesis

### 5.4.1.2.1 Phosphinite-Amine Synthesis (**5-L4a**)

In a glovebox, two separate 20 mL vials were charged with 2-aminophenol (372 mg, 3.41 mmol) and potassium *tert*-butoxide (421 mg, 3.75 mmol). THF (2 mL) was added to each vial containing the separate reactants. The suspension of *t*BuOK was added dropwise to a stirring solution of 2-aminophenol. The *t*BuOK vial was rinsed with THF (0.5 mL) until all of the white solids were transferred, and the reaction was stirred for 30 min. Over this time a colour change from brown to black to grey was observed. After 30 min. chlorodiphenylphosphine (752 mg, 610  $\mu\text{L}$ , 3.41 mmol) was added dropwise over 6 minutes with vigorous stirring resulting in a colour change to deep purple. The reaction was stirred overnight (ca. 16 h), after which the pink solution was filtered through a 60 mL frit with a mixture of Celite and alumina to prevent clogging. The reaction vials were rinsed with DCM ( $3 \times 15$  mL) and filtered through the Celite/alumina. The filtrates were collected in the same Büchner flask, and the volume of the combined filtrate was reduced to 1 mL in the flask. The solution was filtered through a silica plug into a 20 mL vial. The vial was rinsed



with THF (3 × 0.5 mL), filtered through the silica plug and the solvent of the combined filtrate was reduced under vacuum to 0.5 mL. Cold pentane (5 mL) was added to precipitate a white solid. The white solid was washed with pentane (3 × 3 mL) and dried under vacuum to afford **5-L4a** as a white powder. Yield: 571 mg, 57%. All <sup>1</sup>H, <sup>31</sup>P, <sup>13</sup>C NMR and IR spectroscopic data match literature values.<sup>14</sup>

#### 5.4.1.2.2 Attempted Phosphinite-Imine Synthesis (**H[5-L4]**)

In a glovebox, **5-L4a** (196 mg, 0.668 mmol) was dissolved in toluene (20 mL) in a 100 mL Schlenk flask with 4 Å sieves. The Schlenk flask was removed from the glovebox and connected to the Schlenk line. Argon-sparged isobutyraldehyde (63 mg, 80 μL, 0.87 mmol) and formic acid (5 drops) were added via plastic syringe, and the reaction solution was stirred at room temperature under argon for 24 h. The brown mixture was then filtered through a pad of celite. The reaction flask was washed with toluene (3 × 15 mL) and filtered through the pad of celite into the same reaction flask. The solvent of the combined filtrate was removed at 60 °C under vacuum to produce a brown oil. The brown oil was then brought back into the glovebox, redissolved in DCM (2 mL), transferred to a new 20 mL vial, and the solvent was reduced under vacuum to 0.5 mL. Cold pentane (4 mL) was added to precipitate a white solid. The white solid was washed with pentane (3 × 4 mL) affording **5-L4b** as a white powder. Yield: 90 mg, 39%. <sup>1</sup>H NMR (400 MHz, CDCl<sub>3</sub>): δ 10.06 (s, 1H, OH), 7.97 – 7.89 (m, 2H, P(C<sub>6</sub>H<sub>5</sub>)), 7.86 – 7.75 (m, 2H, P(C<sub>6</sub>H<sub>5</sub>)), 7.64 – 7.50 (m, 3H, P(C<sub>6</sub>H<sub>5</sub>)), 7.40 – 7.29 (m, 1H, P(C<sub>6</sub>H<sub>5</sub>)), 7.30 – 7.21 (m, 2H, P(C<sub>6</sub>H<sub>5</sub>)), 6.92 (dd, <sup>3</sup>J<sub>HH</sub> = 1.4 Hz, 7.6 Hz, 1H, H<sup>6</sup>), 6.62 (td, <sup>3</sup>J<sub>HH</sub> = 0.8 Hz, 7.64 Hz, 1H, H<sup>7</sup>), 6.55 – 6.42 (m, 2H, H<sup>5</sup>, H<sup>8</sup>), 5.52 (dd, <sup>3</sup>J<sub>HH/HP</sub> = 2.6 Hz, 11.6 Hz, 1H, N-H), 4.42 – 4.29 (m, 1H, H<sup>1</sup>), 2.15 (dsept, <sup>3</sup>J<sub>HH/HP</sub> = 2.6 Hz, 6.8 Hz, 1H, H<sup>2</sup>), 1.04 (d, <sup>3</sup>J<sub>HH</sub> = 6.8 Hz, 3H, H<sup>3</sup>), 0.90 (d, <sup>3</sup>J<sub>HH</sub> = 6.8 Hz, 3H, H<sup>3'</sup>). <sup>13</sup>C{<sup>1</sup>H} NMR (101 MHz, CDCl<sub>3</sub>): δ 145.2 (s, C<sup>9</sup>), 137.2 (d, J = 7.2 Hz, C<sup>4</sup>), 131.4 (d, J<sub>CP</sub> = 9.3 Hz, P(C<sub>6</sub>H<sub>5</sub>)), 131.2 (d, J<sub>CP</sub> = 8.3 Hz, P(C<sub>6</sub>H<sub>5</sub>)), 129.0 (d, J<sub>CP</sub> = 11.2 Hz, P(C<sub>6</sub>H<sub>5</sub>)), 128.6 (d, J<sub>CP</sub> = 11.7 Hz, P(C<sub>6</sub>H<sub>5</sub>)), 132.2 (d, J<sub>CP</sub> = 2.6 Hz, P(C<sub>6</sub>H<sub>5</sub>)), 131.81 (d, J<sub>CP</sub> = 3.0 Hz, P(C<sub>6</sub>H<sub>5</sub>)), 119.4 (s, C<sup>7</sup>), 117.1 (s, C<sup>8</sup>), 114.5 (s, C<sup>6</sup>), 110.3 (s, C<sup>5</sup>), 57.5 (d, <sup>1</sup>J<sub>CP</sub> = 78.3 Hz, C<sup>1</sup>), 30.7 (d, <sup>2</sup>J<sub>CP</sub> = 5.8 Hz, C<sup>2</sup>), 22.5 (d, <sup>3</sup>J<sub>CP</sub> = 2.5 Hz, C<sup>3</sup>), 17.6 (s, C<sup>3</sup>). <sup>31</sup>P{<sup>1</sup>H} NMR (2162 MHz, CDCl<sub>3</sub>): δ 35.4 (s, P-**5-L4b**). ATR-FTIR (cm<sup>-1</sup>): ν 3370 (N-H, w), 1156 (P=O, m).

### 5.4.1.2.3 Naphthalene Phosphine-Imine Synthesis (**H[5-L5]**)

**5-L5a** (272 mg, 0.831 mmol) was dissolved in 20 mL of toluene and added to a 100 mL Schlenk flask containing Å sieves. The reaction flask was set up on the Schlenk line and heated to 40 °C under argon. Argon-sparged isobutyraldehyde (0.152 mL, 1.66 mmol) was added dropwise via a plastic syringe to the stirring pale-yellow solution. Five drops of argon-sparged formic acid were then added via plastic syringe, and the reaction was allowed to proceed for 72 h. The reaction was filtered through a plug of celite via cannula to produce a clear yellow solution. The sieves and celite plug were washed with toluene (3 × 10 mL), the rinse solution was filtered, and the solvent of the combined filtrate was removed under reduced pressure to afford a yellow solid which was washed with cold pentane (3 × 1 mL) to produce **H[5-L5]** as a yellow powder. Yield: 210 mg, 66% yield. <sup>1</sup>H NMR (400 MHz, CDCl<sub>3</sub>): δ 7.79 – 7.76 (m, 1H, C<sub>10</sub>H<sub>6</sub>), 7.71 – 7.68 (m, 1H, C<sub>10</sub>H<sub>6</sub>), 7.44 – 7.41 (m, 1H, C<sub>10</sub>H<sub>6</sub>), 7.41 – 7.39 (m, 1H, C<sub>10</sub>H<sub>6</sub>), 7.29 – 7.23 (m, 7H, H<sup>1</sup> and P(C<sub>6</sub>H<sub>5</sub>)), 7.23 – 7.19 (m, 4H, P(C<sub>6</sub>H<sub>5</sub>)), 6.93 – 6.88 (m, 1H, C<sub>10</sub>H<sub>6</sub>), 6.76, - 6.71 (dd, *J* = 7.3 Hz, 1.2 Hz, 1H, C<sub>10</sub>H<sub>6</sub>), 2.37 (dsept, *J* = 6.8 Hz, 5.3 Hz, 1H, H<sup>2</sup>), 1.02 (d, *J* = 6.8 Hz, 6H, H<sup>3</sup>). <sup>13</sup>C{<sup>1</sup>H} NMR (151 MHz, CDCl<sub>3</sub>): δ 170.3 (s, C<sup>1</sup>), 150.8 (d, *J*<sub>CP</sub> = 4.2 Hz, C<sub>10</sub>H<sub>6</sub>), 140.9 (d, *J*<sub>CP</sub> = 14.0 Hz, P(C<sub>6</sub>H<sub>5</sub>)), 135.01 (d, *J*<sub>CP</sub> = 3.7 Hz, C<sub>10</sub>H<sub>6</sub>), 134.2 (d, *J*<sub>CP</sub> = 19.9 Hz, P(C<sub>6</sub>H<sub>5</sub>)), 134.3 (d, *J*<sub>CP</sub> = 1.1 Hz, C<sub>10</sub>H<sub>6</sub>), 131.5 (d, *J*<sub>CP</sub> = 9.3 Hz, C<sub>10</sub>H<sub>6</sub>), 131.0 (s, C<sub>10</sub>H<sub>6</sub>), 129.3 (s, C<sub>10</sub>H<sub>6</sub>), 128.4 (s, C<sub>10</sub>H<sub>6</sub>), 128.3 (s, P(C<sub>6</sub>H<sub>5</sub>)), 128.1 (s, P(C<sub>6</sub>H<sub>5</sub>)), 126.7 (d, *J*<sub>CP</sub> = 1.5 Hz, C<sub>10</sub>H<sub>6</sub>), 125.9 (s, C<sub>10</sub>H<sub>6</sub>), 115.7 (s, C<sub>10</sub>H<sub>6</sub>), 34.57 (s, C<sup>2</sup>), 18.9 (s, C<sup>3</sup>). <sup>31</sup>P{<sup>1</sup>H} NMR (243 MHz, CDCl<sub>3</sub>): δ – 3.20 (s, *P*-**H[5-L5]**). ATR-FTIR (cm<sup>-1</sup>): ν 2960 (C<sub>sp</sub><sup>3</sup>-H), 1647 (C=N). LRMS: *m/z* found: 338.2, calc: [**H[5-L5]** – C<sub>3</sub>H<sub>8</sub>]<sup>+</sup> 338.1.

### 5.4.1.2.4 Biaryl Phosphine-Imine Synthesis (**H[5-L6]**)

In a glovebox, **5-L6a** (118 mg, 0.330 mmol) was dissolved in toluene (20 mL) and added to a 100 mL Schlenk flask containing a magnetic stir bar and 4 Å molecular sieves. The Schlenk flask was then removed from the glovebox and attached to the Schlenk line. Degassed isobutyraldehyde (0.040 mL, 0.43 mmol) and five drops of degassed formic acid were individually added to the Schlenk flask via plastic syringe, and the flask was left to stir for 24 h at room temperature. After 24 h, the solution was filtered through Celite via cannula. The original flask was washed with toluene (3 × 15 mL) and the washings were filtered through Celite. The solvent of the combined

filtrates was removed under vacuum at 60 °C to afford a yellow solid. The Schlenk flask was brought into the glovebox and DCM (2 mL) was added to dissolve the yellow solid. The yellow solution was transferred to a 20 mL vial, the Schlenk flask was rinsed with DCM (3 × 1 mL) and the combined solvent was reduced under vacuum to afford a yellow solid that was washed with pentane (3 × 4 mL) affording **H[5-L6]**. Yield: 118 mg, 0.290 mmol (87%). <sup>1</sup>H NMR (599 MHz, CDCl<sub>3</sub>): δ **H[5-L6b]**: 7.55 (d, <sup>3</sup>J<sub>HH</sub> = 4.8, 1H, *H*<sup>1</sup>), 7.37 – 7.15 (m, 14 H, C<sub>12</sub>H<sub>8</sub>, P(C<sub>6</sub>H<sub>5</sub>)), 7.08 – 7.05 (m, 1H, C<sub>12</sub>H<sub>8</sub>), 6.96 – 6.93 (m, 1H, C<sub>12</sub>H<sub>8</sub>), 6.89 – 6.87 (m, 1H, C<sub>12</sub>H<sub>8</sub>), 6.85 – 6.83 (m, 1H, C<sub>12</sub>H<sub>8</sub>), 2.39 (dsept, <sup>3</sup>J<sub>HH</sub> = 2.1, 7.2 Hz, 1H, *H*<sup>2</sup>), 0.98 – 0.89 (m, 6H, *H*<sup>3</sup>). **H[5-L6c]**: 7.48 – 7.43 (m, 1H, C<sub>12</sub>H<sub>8</sub>), 7.37 – 7.15 (m, 14H, C<sub>12</sub>H<sub>8</sub>, P(C<sub>6</sub>H<sub>5</sub>)), 6.80 (d, <sup>3</sup>J<sub>HH</sub> = 8.4 Hz, 1H, C<sub>12</sub>H<sub>8</sub>), 6.77 – 6.75 (dd, <sup>3</sup>J<sub>HH</sub> = 1.5, 7.4 Hz, 1H, C<sub>12</sub>H<sub>8</sub>), 6.63 – 6.59 (m, 1H, C<sub>12</sub>H<sub>8</sub>), 6.06 (d, <sup>3</sup>J<sub>HH</sub> = 9.0 Hz, 1H, *H*<sup>1</sup>), 4.92 (d, <sup>3</sup>J<sub>HH</sub> = 10.5 Hz, 1H, *N-H*), 1.70 (s, 3H, *H*<sup>3</sup>), 1.37 (s, 3H, *H*<sup>3'</sup>). <sup>13</sup>C{<sup>1</sup>H} NMR (151 MHz, CDCl<sub>3</sub>): δ **H[5-L6b]**: 171.2 (s, C<sup>1</sup>) 150.7 (s, C<sub>12</sub>H<sub>8</sub>), 145.9 (d, J<sub>CP</sub> = 30.6 Hz, C<sub>12</sub>H<sub>8</sub>), 138.8 (d, J<sub>CP</sub> = 13.6 Hz, C<sub>12</sub>H<sub>8</sub>), 137.3 (d, J<sub>CP</sub> = 6.9 Hz, P(C<sub>6</sub>H<sub>5</sub>)), 133.9 (d, J<sub>CP</sub> = 5.2 Hz, C<sub>12</sub>H<sub>8</sub>), 133.4 (s, C<sub>12</sub>H<sub>8</sub>) 131.3 (d, J<sub>CP</sub> = 4.2 Hz, P(C<sub>6</sub>H<sub>5</sub>)), 130.9 (d, J<sub>CP</sub> = 5.3 Hz, C<sub>12</sub>H<sub>8</sub>), 128.6 (s, C<sub>12</sub>H<sub>8</sub>), 128.5 (s, C<sub>12</sub>H<sub>8</sub>), 128.4 (s, P(C<sub>6</sub>H<sub>5</sub>)), 128.3 (s, C<sub>12</sub>H<sub>8</sub>), 128.2 (s, P(C<sub>6</sub>H<sub>5</sub>)) 127.3, (s, C<sub>12</sub>H<sub>8</sub>), 123.8 (s, C<sub>12</sub>H<sub>8</sub>), 119.6 (s, C<sub>12</sub>H<sub>8</sub>), 34.6 (s, C<sup>2</sup>), 18.0 (s, C<sup>3</sup>). **H[5-L6c]**: 144.2 (d, J<sub>CP</sub> = 30.5 Hz, C<sub>12</sub>H<sub>8</sub>) 141.3 (s, C<sub>12</sub>H<sub>8</sub>), 137.4 (d, J<sub>CP</sub> = 7.8 Hz, C<sub>12</sub>H<sub>8</sub>), 137.0 (d, J<sub>CP</sub> = 11.7 Hz, P(C<sub>6</sub>H<sub>5</sub>)), 134.3 (s, C<sub>12</sub>H<sub>8</sub>), 134.0 (d, J<sub>CP</sub> = 5.9 Hz, C<sub>12</sub>H<sub>8</sub>), 131.0 (d, J<sub>CP</sub> = 3.4 Hz, P(C<sub>6</sub>H<sub>5</sub>)), 130.8 (d, J<sub>CP</sub> = 4.5 Hz, C<sub>12</sub>H<sub>8</sub>), 129.6 (s, C<sub>12</sub>H<sub>8</sub>), 129.1 (s, C<sub>12</sub>H<sub>8</sub>), 129.8 (d, J<sub>CP</sub> = 6.9 Hz, P(C<sub>6</sub>H<sub>5</sub>)), 128.4 (s, C<sub>12</sub>H<sub>8</sub>), 128.3 (s, P(C<sub>6</sub>H<sub>5</sub>)), 126.7 (d, J<sub>CP</sub> = 6.9 Hz C<sub>12</sub>H<sub>8</sub>), 121.3 (s, C<sup>1</sup>), 117.3 (s, C<sub>12</sub>H<sub>8</sub>), 110.7 (s, C<sub>12</sub>H<sub>8</sub>), 109.7 (s, C<sup>2</sup>) 22.5 (s, C<sup>3</sup>), 16.1 (s, C<sup>3'</sup>). <sup>31</sup>P{<sup>1</sup>H} NMR (243 MHz, CDCl<sub>3</sub>): δ **H[5-L6b]**: –12.4 (s, *P-H[5-L6b]*). **H[5-L6c]**: –13.3 (s, *P-H[5-L6c]*). ATR-FTIR (cm<sup>-1</sup>): ν 3067 (C<sub>sp</sub><sup>3</sup>-H, w), 1680 (C=N). ESI MS: *m/z* found: 408.1865, calc: [**H[5-L6]**]<sup>+</sup> 408.1881.

### 5.4.1.3 P<sup>^</sup>AzA Ligand Synthesis

#### 5.4.1.2.3.1 Biaryl P<sup>^</sup>AzA Synthesis (**K[5-L6]**)

In a glovebox, **H[5-L6]** (112 mg, 0.270 mmol) and KH (44 mg, 1.1 mmol) were added to two separate vials, THF (2 mL) was added to each vial. The **H[5-L6]** solution was added dropwise to the stirring mixture of KH, resulting in a slow colour change from yellow to light red. The reaction

solution was left to stir for 24 h at room temperature, during which the solution became dark red. The solution was passed through a Kimwipe/Celite glass pipette filter to remove excess KH. The reaction vial was rinsed with THF (0.5 mL) until the rinses were no longer yellow. Each rinse was filtered through the pipette filter and combined. The solvent of the filtrate was then reduced to ca. 0.5 mL under vacuum and cold pentane (3 mL) was added to the vial to precipitate an orange powder. The pentane was removed via pipette, the remaining solid was washed with cold pentane (3 × 4 mL) and dried under vacuum to produce **K[5-L6]** as an orange powder. NOTE: **K[5-L6]** is thermally unstable and should be stored in the freezer. Yield: 73 mg, 60%. <sup>1</sup>H NMR (599 MHz, (CD<sub>3</sub>)<sub>2</sub>CO): δ 7.53 – 7.49 (m, 1H, C<sub>12</sub>H<sub>8</sub>), 7.43 – 7.37 (m, 1H, C<sub>12</sub>H<sub>8</sub>), 7.37 – 7.28 (m, 7H, C<sub>12</sub>H<sub>8</sub>, P(C<sub>6</sub>H<sub>5</sub>)), 7.20 – 7.09 (m, 6H, C<sub>12</sub>H<sub>8</sub>, P(C<sub>6</sub>H<sub>5</sub>)), 6.82 (d, <sup>3</sup>J<sub>HH</sub> = 8.4 Hz, C<sub>12</sub>H<sub>8</sub>), 6.71 (d, <sup>3</sup>J<sub>HH</sub> = 7.2 Hz, C<sub>12</sub>H<sub>8</sub>), 6.56 – 6.50 (m, 1H, C<sub>12</sub>H<sub>8</sub>), 6.15 (s, 1H, H<sup>1</sup>), 1.66 (s, 3H, H<sup>3</sup>), 1.32 (s, 3H, H<sup>3'</sup>). <sup>13</sup>C{<sup>1</sup>H} NMR (151 MHz, CDCl<sub>3</sub>): δ 145.0 (d, J<sub>CP</sub> = 31.5, C<sub>12</sub>H<sub>8</sub>), 142.0 (s, C<sub>12</sub>H<sub>8</sub>), 139.2 (d, J<sub>CP</sub> = 13.9 Hz, C<sub>12</sub>H<sub>8</sub>), 138.2 (d, J<sub>CP</sub> = 3.3 Hz, P(C<sub>6</sub>H<sub>5</sub>)), 134.9 (s, C<sub>12</sub>H<sub>8</sub>), 134.4 (d, J<sub>CP</sub> = 9.8 Hz, P(C<sub>6</sub>H<sub>5</sub>)), 134.3 (s, C<sub>12</sub>H<sub>8</sub>), 134.2 (s, C<sub>12</sub>H<sub>8</sub>), 131.5 (d, J<sub>CP</sub> = 5.3 Hz, C<sub>12</sub>H<sub>8</sub>), 131.4 (d, J<sub>CP</sub> = 3.0 Hz, C<sub>12</sub>H<sub>8</sub>), 130.5 (s, C<sub>12</sub>H<sub>8</sub>), 129.6 (s, C<sub>12</sub>H<sub>8</sub>), 129.3 (d, J<sub>CP</sub> = 10.6 Hz, P(C<sub>6</sub>H<sub>5</sub>)), 129.1 (d J<sub>CP</sub> = 6.04 Hz, P(C<sub>6</sub>H<sub>5</sub>)), 122.0 (s, C<sup>1</sup>), 117.9 (s, C<sub>12</sub>H<sub>8</sub>), 111.3 (s, C<sub>12</sub>H<sub>8</sub>), 109.1 (s, C<sup>2</sup>), 22.4 (s, C<sup>3</sup>) 15.9 (s, C<sup>3'</sup>). <sup>31</sup>P{<sup>1</sup>H} NMR (243 MHz, CDCl<sub>3</sub>): δ –13.6. ATR-FTIR (cm<sup>-1</sup>): ν 3049 (C<sub>sp</sub><sup>3</sup>-H, w), 1090 (P-Ar, m). MALDI MS (pyrene) collected in negative ion mode *m/z* found: 406.2, calc. [**5-L6**]<sup>-</sup>: 406.2.

### 5.4.1.3. Complex Synthesis

#### 5.4.1.3.1 Phosphine-Imine Complex Synthesis

##### 5.4.1.3.1.1 Naphthalene P<sup>^</sup>I Complex Synthesis (**5-4**)

Ligand **H[5-L5]** (50 mg, 0.13 mmol) was dissolved in DCM (2 mL) and added to a solution of [PdCl(CH<sub>3</sub>)(COD)] (35 mg, 0.13 mmol) and stirred for 4 h. A colour change from grey to yellow was observed immediately upon addition of the ligand. The reaction volume was reduced to 1 mL and cold pentane (6 mL) was added to produce a pale-yellow precipitate. The solvent was decanted via pipette, the yellow solid was washed with cold pentane, (3 × 4 mL) and dried overnight under vacuum to yield **5-4** as a yellow powder. Yield: 70 mg, 92%. <sup>1</sup>H NMR (599 MHz, CDCl<sub>3</sub>): δ 8.06 – 7.99 (m, 1H, C<sub>10</sub>H<sub>6</sub>), 7.93 – 7.87 (m, 1H, C<sub>10</sub>H<sub>6</sub>), 7.76 – 7.66 (m, 2H, C<sub>10</sub>H<sub>6</sub>), 7.54 – 7.34 (m, 10H, Ph-H), 7.20 (d, J = 3.9 Hz, H, H<sup>1</sup>), 7.18 – 7.14 (m, 2H, C<sub>10</sub>H<sub>6</sub>), 3.57 (dsept, J = 4.8 Hz, 6.6

Hz, 1H,  $H^2$ ), 1.32 (d,  $J = 6.6$  Hz, 3H,  $H^3$ ), 0.64 (d,  $J = 3.9$  Hz, 3H, Pd- $CH_3$ ), 0.20 (d,  $J = 6.6$  Hz, 3H,  $H^3$ ).  $^{13}C\{^1H\}$  NMR (151 MHz,  $CDCl_3$ ):  $\delta$  181.4 (s,  $C^1$ ), 146.6 (d,  $J_{CP} = 3.6$  Hz,  $C_{10}H_6$ ), 136.4 (s, P( $C_6H_5$ )), 134.2 (d,  $J_{CP} = 12.2$  Hz,  $C_{10}H_6$ ), 133.9 (d,  $J_{CP} = 13.6$  Hz, P( $C_6H_5$ )), 133.6 (d,  $J_{CP} = 11.3$  Hz,  $C_{10}H_6$ ), 132.8 (s,  $C_{10}H_6$ ), 130.8 (d,  $J_{CP} = 14.0$  Hz,  $C_{10}H_6$ ), 129.3 (d,  $J_{CP} = 10.9$  Hz,  $C_{10}H_6$ ), 129.0 (s,  $C_{10}H_6$ ), 128.6 (d,  $J_{CP} = 11.2$  Hz, P( $C_6H_5$ )), 127.2 (s, P( $C_6H_5$ )), 125.5 (d,  $J_{CP} = 8.7$  Hz,  $C_{10}H_6$ ), 123.3 (s,  $C_{10}H_6$ ), 119.9 (s,  $C_{10}H_6$ ), 36.7 (s,  $C^2$ ), 19.9 (s,  $C^3$ ), 18.0 (3,  $C^{3'}$ ), 2.98 (s, Pd- $CH_3$ ).  $^{31}P\{^1H\}$  NMR (243 MHz,  $CDCl_3$ ):  $\delta$  36.6 (s, P-**H(5-L5)**). ATR-FTIR ( $cm^{-1}$ ):  $\nu$  2958 ( $C_{sp^3}-H$ ), 1635 ( $C=N$ ). MALDI MS (pyrene)  $m/z$  found: 524.1, calc: [**H(5-L5)**- $CH_3$ ] $^{+}$  524.0.

### 5.4.1.3.1.2 Biaryl P<sup>^</sup>I Complex Synthesis (5-5)

Ligand **H[5-L6]** (65 mg, 0.16 mmol) was dissolved in DCM (2 mL) and added to a solution of [ $PdCl(CH_3)(COD)$ ] (38 mg, 0.15 mmol) and stirred for 24 h. The reaction volume was reduced to 0.5 mL and placed in a freezer at  $-20$  °C for 10 min. Cold pentane (6 mL) was added to produce a white precipitate. The solvent was decanted via pipette and the white solid was washed with cold pentane ( $3 \times 4$  mL) and dried under vacuum to yield **5-5** as a white powder. Yield: 55 mg, 67%.

$^1H$  NMR (599 MHz,  $CDCl_3$ ):  $\delta$  **5-5a**: 7.39 – 7.34 (m, 4H,  $C_{12}H_4$ , P( $C_6H_5$ )), 7.26 – 7.15 (m, 11 H,  $C_{12}H_4$ , P( $C_6H_5$ )), 6.94 – 6.87 (m, 1H,  $C_{12}H_8$ ), 6.83 – 6.75 (m, 1H,  $C_{12}H_8$ ), 6.32 (d,  $J = 7.7$  Hz, 1H,  $C_{12}H_4$ ), 3.53 (dsept,  $^3J_{HH} = 1.0$  Hz, 6.6 Hz, 1H,  $H^2$ ), 1.19 (d,  $^3J_{HH} = 6.6$  Hz, 3H,  $H^3$ ), 0.68 (d,  $^3J_{HH} = 6.6$  Hz, 3H,  $H^3$ ), 0.47 (d,  $^3J_{HP} = 3.4$  Hz, 3H, Pd- $CH_3$ ).

**5-5b**: 7.63 – 7.52 (m, 4H,  $C_{12}H_8$ , P( $C_6H_5$ ))), 7.52 – 7.40 (m, 8H, P( $C_6H_5$ ))), 7.33 – 7.26 (m, 2H,  $C_{12}H_8$ ), 7.10 – 7.03 (m, 1H,  $C_{12}H_8$ ), 7.01 – 6.95 (m, 1H,  $C_{12}H_8$ ), 6.64 – 6.52 (m, 1H,  $C_{12}H_8$ ), 6.13 (dd,  $^3J_{HH} = 1.4$  Hz, 7.6 Hz, 1H,  $C_{12}H_8$ ), 5.90 (br, 1H,  $N-H$ ), 1.65 (br, 3H,  $H^3$ ), 1.47 (s, 3H,  $H^3$ ), 0.60 (d,  $^3J_{HP} = 3.6$  Hz, 3H, Pd- $CH_3$ ).  $^{13}C\{^1H\}$  NMR (151 MHz,  $CDCl_3$ ):  $\delta$  **5-5a**: 179.5 (s,  $C^1$ ), 148.6 (s,  $C_{12}H_8$ ), 35.3 ( $C^2$ ), 19.0 (s,  $C^3$ ), 18.5 (s,  $C^{3'}$ ), 0.76 (d,  $J_{CP} = 2.9$  Hz, Pd- $CH_3$ ). **5-5b**: 121.4 (s,  $C^1$ ), 119.7 (s,  $C^2$ ), 22.5 (s,  $C^3$ ), 22.5 (s,  $C^{3'}$ ), 1.26 (d,  $J_{CP} = 2.7$ , Pd- $CH_3$ ). The following signals cannot be assigned to specifically **5-5a** or **5-5b**. 136.0 (d,  $J = 14.0$  Hz,  $C_{12}H_8$ ), 134.2 (d,  $J_{CP} = 12.5$  Hz,  $C_{12}H_8$ ), 132.5 (s, P( $C_6H_5$ )), 132.4 (s, P( $C_6H_5$ )), 132.3 (s, P( $C_6H_5$ )), 132.3 (s, P( $C_6H_5$ )), 132.3 (s,  $C_{12}H_8$ ), 132.3 (s,  $C_{12}H_8$ ), 132.2 (s,  $C_{12}H_8$ ), 132.2 (s,  $C_{12}H_8$ ), 131.6 (s,  $C_{12}H_8$ ), 131.0 (s,  $C_{12}H_8$ ), 130.9 (d,  $J_{CP} = 2.3$  Hz,  $C_{12}H_8$ ), 130.8 (d,  $J_{CP} = 2.3$  Hz,  $C_{12}H_8$ ), 129.8 (s,  $C_{12}H_8$ ), 129.4 (s,  $C_{12}H_8$ ), 129.1 (s,  $C_{12}H_8$ ), 129.0 (s,  $C_{12}H_8$ ), 128.8 (s,  $C_{12}H_8$ ), 128.8 (s,  $C_{12}H_8$ ), 128.7 (s,  $C_{12}H_8$ ), 128.6 (s,

$C_{12}H_8$ ), 128.5 (s, P( $C_6H_5$ )), 128.4 (s, P( $C_6H_5$ )), 128.4 (s, P( $C_6H_5$ )), 128.3 (s, P( $C_6H_5$ )), 127.4 (d,  $J_{CP} = 8.2$  Hz,  $C_{12}H_8$ ), 126.4 (s,  $C_{12}H_8$ ), 125.4 (s,  $C_{12}H_8$ ), 124.0 (s,  $C_{12}H_8$ ), 122.5 (s,  $C_{12}H_8$ ).  $^{31}P\{^1H\}$  NMR (243 MHz,  $CDCl_3$ ):  $\delta$  **5-5a**: 35.4 (s, *P*-**5-5a**). **5-5b**: 36.2 (s, *P*-**5-5b**). ATR-FTIR ( $cm^{-1}$ ):  $\nu$  3306 (N-H, w), 1671 (C=N, m). MALDI MS (pyrene)  $m/z$  found: 337.1, calc: [**H(5-L6)**- $C_4H_8N$ ] $^{+}$  337.1, found: 347.0, calc: [**5-5-CH<sub>3</sub>**] $^{+}$  347.0.

### 5.4.1.3.2 P<sup>A</sup>AzA Complex Synthesis

#### 5.4.1.3.2.1 Naphthalene P<sup>A</sup>AzA Synthesis (**5-6**)

In a glovebox **5-4** (25 mg, 0.046 mmol) and Li[HMDS] (12 mg, 0.070 mmol) were added to two separate vials and dissolved in  $C_6H_6$  (1 mL). 1 drop of pyridine was added to the vial containing **5-4**. The Li[HMDS] solution was added to the solution of **5-4** dropwise resulting in an immediate colour change from yellow to red. The vial containing Li[HMDS] was rinsed with  $C_6H_6$  ( $2 \times 0.5$  mL) and added to the reaction vial. The reaction was allowed to stir for 5 min. The red solution was then filtered through a glass kimwipe/celite pipette filter and the reaction vial was rinsed with  $C_6H_6$  ( $3 \times 0.5$  mL) and filtered through the pipette filter. The solvent of the combined filtrates was removed under vacuum to afford a red solid. The red solid was washed with pentane ( $3 \times 2$  mL) to afford **5-6** as a pink powder. Yield: 19 mg, 76%.  $^1H$  NMR (400 MHz,  $C_6D_6$ , 298 K):  $\delta$  7.85 – 7.80 (m, 1H,  $C_{10}H_6$ ), 7.56 – 7.45 (m, 5H,  $C_{10}H_6$ ), 7.06 – 6.94 (m, 10H, P( $C_6H_5$ )), 5.90 (s, 1H,  $H^1$ ), 1.57 (s, 3H,  $H^3$ ), 1.36 (s, 3H,  $H^{3'}$ ), 0.48 (d,  $^3J_{HP} = 1.0$  Hz, 3H, Pd- $CH_3$ ). (400 MHz,  $C_6D_5(CD_3)$ , 243 K):  $\delta$  8.42 (m, 1H,  $NC_5H_5$ ), 6.59 (m, 2H,  $NC_5H_5$ ), 6.31 (m, 2H,  $NC_5H_5$ ).  $^{13}C\{^1H\}$  NMR (101 MHz,  $C_6D_6$ ):  $\delta$  153.9 (s,  $C_{10}H_6$ ), 137.5 (d,  $J_{CP} = 8.6$  Hz,  $C_{10}H_6$ ), 136.3 (s,  $C^1$ ), 134.6 (d,  $J_{CP} = 11.6$  Hz,  $C_{10}H_6$ ), 133.2 (d,  $J_{CP} = 2.6$  Hz, P( $C_6H_5$ )), 132.7 (s, P( $C_6H_5$ )), 132.2 (s,  $C_{10}H_6$ ), 130.3 (d,  $J_{CP} = 11.5$  Hz,  $C_{10}H_6$ ), 129.7 (d,  $J_{CP} = 2.4$  Hz,  $C_{10}H_6$ ), 129.6 (d,  $J_{CP} = 4.2$  Hz, P( $C_6H_5$ )), 128.8 (s,  $C_{10}H_6$ ), 128.2 (s, P( $C_6H_5$ )), 127.9 (s,  $C_{10}H_6$ ), 123.8 (s,  $C_{10}H_6$ ), 123.5 (s,  $C_{10}H_6$ ), 110.1 (s,  $C^2$ ), 23.5 (s,  $C^3$ ), 19.1 (s,  $C^{3'}$ ), 6.2 (s, Pd- $CH_3$ ).  $^{31}P\{^1H\}$  NMR (162 MHz,  $C_6D_6$ ):  $\delta$  37.5. ATR-FTIR ( $cm^{-1}$ ):  $\nu$  2958 ( $C_{sp^3}-H$ ), 1635 (C=N). MALDI MS (pyrene)  $m/z$  found: 380.1, calc: [**L5-5**] $^{+}$  380.2, found: 485.0, calc: [**5-6**-(py)( $CH_3$ ), 485.0.

### 5.4.1.3.2.2 Biaryl P<sup>A</sup>AzA Synthesis (5-7)

Prior to the initiation of the reaction all components were stored in the freezer at  $-20\text{ }^{\circ}\text{C}$  for at least 30 minutes. In a glovebox, two separate solutions of **K[5-L6]** (32 mg, 0.072 mmol) and PdCl(CH<sub>3</sub>)(COD) (15 mg, 0.060 mmol) were prepared in THF (1 mL). **K[5-L6]** was added dropwise to the stirring solution of PdCl(CH<sub>3</sub>)(COD), resulting in an immediate colour change to orange. The orange solution was stirred for five minutes and filtered through a Kimwipe/Celite glass pipette filter into a 20 mL vial. The reaction vial was rinsed with THF (0.5 mL) until the rinses were no longer yellow. The rinses were filtered, and the filtrates were combined. The solvent of the filtrate was removed under vacuum to give an orange solid which was washed with pentane (3 × 4 mL) affording **5-7**. Yield: 22 mg, 70%. <sup>1</sup>H NMR (599 MHz, C<sub>6</sub>D<sub>6</sub>): δ 7.57 – 7.50 (m, 5H, C<sub>12</sub>H<sub>8</sub>), 7.09 – 6.95 (m, 10H, P(C<sub>6</sub>H<sub>5</sub>)), 6.80 – 6.76 (m, 1H, C<sub>12</sub>H<sub>8</sub>), 6.65 – 6.60 (m, 1H, C<sub>12</sub>H<sub>8</sub>), 6.46 (d, <sup>3</sup>J<sub>HH</sub> = 7.3 Hz, C<sub>12</sub>H<sub>8</sub>), 5.58 (s, 1H, H<sup>1</sup>), 1.82 (d, <sup>3</sup>J<sub>HH</sub> = 3.45, 3H, H<sup>3</sup>), 1.73 (d, <sup>3</sup>J<sub>HH</sub> = 6.9 Hz, 3H, H<sup>3'</sup>), 0.51 (d, <sup>3</sup>J<sub>HP</sub> = 3.8 Hz, 3H, Pd-CH<sub>3</sub>). <sup>13</sup>C{<sup>1</sup>H} NMR (151 MHz, CDCl<sub>3</sub>): δ 153.1 (s, C<sub>12</sub>H<sub>8</sub>), 148.1 (s, C<sub>12</sub>H<sub>8</sub>), 136.2 (d, J<sub>CP</sub> = 14.1 Hz, ), 135.4 (d, J<sub>CP</sub> = 12.2 Hz, C<sub>12</sub>H<sub>8</sub>), 134.7 (d, J<sub>CP</sub> = 7.0 Hz, P(C<sub>6</sub>H<sub>5</sub>)), 133.0 (s, C<sub>12</sub>H<sub>8</sub>), 132.7 (s, C<sub>12</sub>H<sub>8</sub>), 131.1 (s, C<sub>12</sub>H<sub>8</sub>), 131.0 (d, J<sub>CP</sub> = 7.6 Hz, P(C<sub>6</sub>H<sub>5</sub>)), 130.6 (d, J<sub>CP</sub> = 18.0 Hz, C<sub>12</sub>H<sub>8</sub>), 129.7 (d, J<sub>CP</sub> = 4.7 Hz, C<sub>12</sub>H<sub>8</sub>), 128.8 (s, C<sub>12</sub>H<sub>8</sub>), 128.7 (d, J<sub>CP</sub> = 10.1 Hz, P(C<sub>6</sub>H<sub>5</sub>)), 128.4 (s, C<sub>12</sub>H<sub>8</sub>), 126.6 (d, J<sub>CP</sub> = 7.0 Hz, P(C<sub>6</sub>H<sub>5</sub>)), 121.9 (s, C<sub>12</sub>H<sub>8</sub>), 113.9 (s, C<sub>12</sub>H<sub>8</sub>), 88.7 (d, <sup>2</sup>J<sub>CP</sub> = 28.2 Hz, C<sup>2</sup>), 22.2 (s, C<sup>3</sup>), 21.2 (s, C<sup>3</sup>), -1.3 (d, J<sub>CP</sub> = 11.8 Pd-CH<sub>3</sub>). <sup>31</sup>P{<sup>1</sup>H} NMR (243 MHz, C<sub>6</sub>D<sub>6</sub>): δ 25.8. ATR-FTIR (cm<sup>-1</sup>): ν 2957 (C<sub>sp</sub><sup>2</sup>-H, w), 1098 (P-Aryl, m). MALDI MS (pyrene) *m/z* found: 406.1, calc: [**5-L6**]<sup>+</sup> 406.2, found: 512.1, calc: [**5-7-CH<sub>3</sub>**]<sup>+</sup> 512.1.

## 5.5 References

1. Blacquiere, J. M., *ACS Catal.* **2021**, *11*, 5416-5437.
2. Hitchcock, P. B.; Lappert, M. F.; Layh; Marcus, Z. *Anorg. Allg. Chem.* **2000**, *626*, 1081-1086.
3. Caro, C. F.; Lappert, M. F.; Merle, P. G., *Coord. Chem. Rev.* **2001**, *219-221*, 605-663.
4. Avent, A. G.; Hitchcock, P. B.; Lappert, M. F.; Sablong, R.; Severn, J. R., *Organometallics* **2004**, *23*, 2591-2600.
5. Deelman, B.-J.; Hitchcock, P. B.; Lappert, M. F.; Leung, W.-P.; Lee, H.-K.; Mak, T. C. W., *Organometallics* **1999**, *18*, 1444-1452.

6. Shen, A.; Ni, C.; Cao, Y.-C.; Zhou, H.; Song, G.-H.; Ye, X.-F., *Tetrahedron Lett.* **2014**, *55*, 3278-3282.
7. Stubbs, J. M.; Firth, K. F.; Bridge, B. J.; Berger, K. J.; Hazlehurst, R. J.; Boyle, P. D.; Blacquiere, J. M., *Dalton Trans.* **2017**, *46*, 647-650.
8. Jackman, K. M. K.; Bridge, B. J.; Sauv , E. R.; Rowley, C. N.; Zheng, C. H. M.; Stubbs, J. M.; Boyle, P. D.; Blacquiere, J. M., *Organometallics* **2019**, *38*, 1677-1681.
9. Jackman, K. M. K.; Fogh, A. A.; Stubbs, J. M.; Blacquiere, J. M., *J. Organomet. Chem.* **2019**, *880*, 56-61.
10. Kindervater, M.; Jackman, K. M. K.; Fogh, A. A.; Stareoverov, V.; Boyle, P. D.; Blacquiere, J. M., *Manuscript in Preperation* **2022**.
11. Jackman, K. M. K.; Liang, G.; Boyle, P. D.; Zimmerman, P. M.; Blacquiere, J. M., *Dalton Trans.* **2022**, *51*, 3977-3991.
12. Shriver, D. F.; Weller, M. T.; Overton, T.; Rourke, J.; Armstrong, F. A., *Inorganic Chemistry*. Freeman: New York, NY, 2014.
13. Yang, L.; Powell, D. R.; Houser, R. P., *Dalton Trans.* **2007**, 955-964.
14. Firouzabadi, H.; Iranpoor, N.; Gholinejad, M., *Tetrahedron* **2009**, *65*, 7079-7084.
15. Benito-Garagorri, D.; Lackner-Warton, W.; Standfest-Hauser, C. M.; Mereiter, K.; Kirchner, K., *Inorg. Chim. Acta* **2010**, *363*, 3674-3679.
16. Vabre, B.; Canac, Y.; Duhayon, C.; Chauvin, R.; Zargarian, D., *Chem. Commun.* **2012**, *48*, 10446-10448.
17. Yu, S.-B.; Huang, J.-D.; Wang, D.-Y.; Hu, X.-P.; Deng, J.; Duan, Z.-C.; Zheng, Z., *Tetrahedron: Asymmetry* **2008**, *19*, 1862-1866.
18. Li, X.-G.; Zhou, Q.-L., *Adv. Synth. Catal.* **2021**, *363*, 3471-3475.
19. Hilliard, C. R.; Bhuvanesh, N.; Gladysz, J. A.; Bl mel, J., *Dalton Trans.* **2012**, *41*, 1742-1754.
20. Pryjomska, I.; Bartosz-Bechowski, H.; Ciunik, Z.; Trzeciak, A. M.; Zi lkowski, J. J., *Dalton Trans.* **2006**, 213-220.
21. Zhang, B.; Jiao, H.; Michalik, D.; Klo , S.; Deter, L. M.; Selent, D.; Spannenberg, A.; Franke, R.; B rner, A., *ACS Catal.* **2016**, *6*, 7554-7565.
22. Koshti, V.; Gaikwad, S.; Chikkali, S. H., *Coord. Chem. Rev.* **2014**, *265*, 52-73.
23. Zhou, X.; Lau, K.-C.; Petro, B. J.; Jordan, R. F., *Organometallics* **2014**, *33*, 7209-7214.
24. Contrella, N. D.; Sampson, J. R.; Jordan, R. F., *Organometallics* **2014**, *33*, 3546-3555.
25. Kochi, T.; Noda, S.; Yoshimura, K.; Nozaki, K., *J. Am. Chem. Soc.* **2007**, *129*, 8948-8949.
26. Steiner, T., *Angew. Chem. Int. Ed.* **2002**, *41*, 48-76.
27. Allen, K. E.; Campos, J.; Daugulis, O.; Brookhart, M., *ACS Catal.* **2015**, *5*, 456-464.
28. Naka, K., Monomers, Oligomers, Polymers, and Macromolecules (Overview). In *Encyclopedia of Polymeric Nanomaterials*, Kobayashi, S.; M llen, K., Eds. Springer Berlin Heidelberg: Berlin, Heidelberg, 2021; pp 1-6.
29. Salo, E. V.; Guan, Z., *Organometallics* **2003**, *22*, 5033-5046.
30. Loos, M.; Gerber, C. enviPat: Isotope Pattern, Profile and Centroid Calculation for Mass Spectrometry. <https://www.envipat.eawag.ch/>.



## 6.0 Conclusions and Future Work

### 6.1 Summary and Conclusion

A systematic study into the coordination chemistry of a series of phosphine 1-azaallyl (P<sup>^</sup>AzA) ligands with palladium has been presented. Through various ligand design strategies, the ligand coordination mode and complex reactivity could be modulated.

Chapter two investigated our initial ligand design **2-L1**, with phosphorus and nitrogen *ortho* to each other on a phenyl ring. Coordination of **K[2-L1]** to [Pd(CH<sub>3</sub>)Cl(COD)] afforded dinuclear **2-2**. Thermolysis of **2-2** affords the dinuclear Pd<sup>I</sup> complex **2-3** and mononuclear Pd<sup>II</sup> complex **2-4**. A distinct coordination mode of the 1-AzA moiety is observed in each complex, and the coordination mode observed in **2-3** is the first example of this coordination between a 1-AzA ligand and a metal reported in the literature. The formation of **2-3** and **2-4** is accompanied by the reductive elimination of ethane in 76% yield. This reaction is unique as it proceeds without the need for an oxidant, it is not mediated by radicals, the ligand is not redox active, and in at least one pathway the dinuclear motif is maintained. As such, we proposed that this reductive elimination mechanism is distinct from currently established pathways and may offer new means to access C–C coupling reactions. Furthermore, we strongly believe that the capacity of **2-L1** to change coordination modes is imperative to the observed reactivity.

In Chapter 3 the mechanism for Csp<sup>3</sup>-Csp<sup>3</sup> reductive elimination introduced in Chapter 2 was investigated through a combined experimental and computational approach. Performing thermolysis with **3-4** coordinated by a reduced form of the ligand bearing an alkyl amine rather than a 1-AzA moiety afforded methane in 80% yield confirming the importance of the 1-AzA to the unique Csp<sup>3</sup>-Csp<sup>3</sup> coupling pathway. A monomer-dimer equilibrium was determined to be operative when **3-1** is in solution, and the monomer was stabilized by a C–H agostic interaction that was determined to be the source of methane observed in 26% yield. Thermolysis of mononuclear **K[3-7]** affords methane in 72% yield, discounting reductive elimination occurring from a mononuclear dimethyl intermediate. Computationally, it was determined there are three operative dinuclear pathways for reductive elimination beginning from **3-1**, and a myriad of 1-AzA coordination modes are observed throughout all pathways. Overall, it was confirmed that the 1-AzA group is crucial to the observed reactivity. Ligand **3-L1** maintains the unique dinuclear motif in the reaction and prevents cleavage of **3-1** into monomers. Therefore, P<sup>^</sup>AzA ligands can

be used to access rare dinuclear reaction pathways. Furthermore, **3-L1** helps to reduce barriers for methyl transfer and reductive elimination steps, which permits the difficult  $Csp^3-Csp^3$  coupling observed and prevents pathways resulting in C–H activation. As such, P<sup>^</sup>AzA ligands can also be used to access reactions that are inaccessible or difficult via current pathways with non-SRLs.

The fourth chapter assesses a dinuclear  $[Pd^{II}]_2$  cross-coupling mechanism proceeding through the Pd<sup>I</sup> dimer **4-2**. A fast, and higher yielding pathway to synthesize **4-2** was reported, allowing for the synthesis of **4-2** on scales suitable for reactivity assessment. At 0.1 mol% loading, complex **4-2** permits the Kumada coupling of aryl bromides with PhMgBr. The reaction is tolerant of sterically hindered, electron rich and electron poor electrophiles, and proceeds fastest with sterically uncongested and electron poor substrates. The reaction also proceeded when the nucleophile was changed to MeMgBr, allowing  $Csp^2-Csp^3$  coupling. Variable time normalization analysis (VTNA) revealed an order of 0.9 for **4-2**, which suggests a dinuclear mechanism is operative. Catalysis with a mononuclear **4-2** and stoichiometric reactions between **4-2** and PhI also suggested that cross-coupling proceeds through a unique dinuclear pathway. The obtained experimental data strongly suggests that Kumada coupling with **4-2** proceeds through a highly unique dinuclear  $[Pd^{II}]_2$  cross-coupling mechanism. Thus, confirming our hypothesis in Chapter 3 that P<sup>^</sup>AzA ligands can be used to access dinuclear catalytic cycles. Consequently, dinuclear Pd<sup>I</sup>(P<sup>^</sup>AzA) complexes are likely applicable to a wide variety of cross-coupling reactions such as Suzuki coupling.

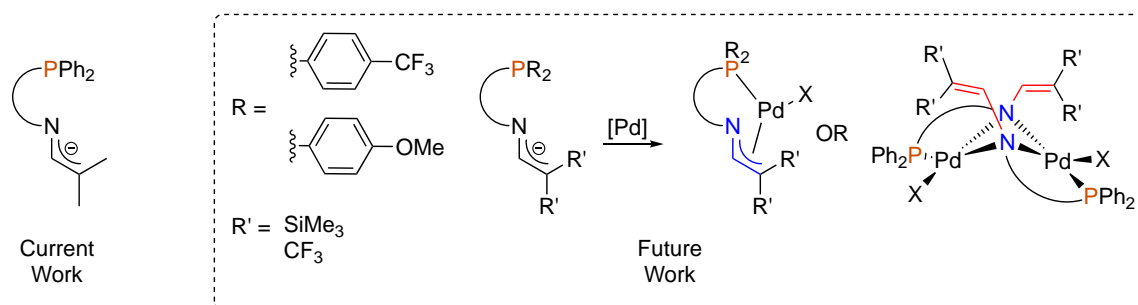
In the fifth chapter the influence of the backbone on 1-AzA binding was investigated. Three ligands were designed with increased distance between P and N compared to phenyl-linked **5-L1**. Ligands **5-L5** and **5-L6** were synthesized containing naphthalene and biaryl backbones, respectively. The P<sup>^</sup>I precursors for **H[5-L5]** and **H[5-L6]** were coordinated to Pd, and their bite angles were determined to be 81.94° and 95.97°, respectively. Comparatively, phenyl-linked **H[5-L1]** has a bite angle of 80.1°. A P<sup>^</sup>AzA complex with **5-L5** could only be obtained when the P<sup>^</sup>I complex was deprotonated in the presence of pyridine, affording **5-6** with the 1-AzA group coordinated  $\kappa^1$ -N. Remarkably, the first example of a Pd(P<sup>^</sup>AzA) complex with the 1-AzA moiety coordinated  $\eta^3$ -NCC (**5-7**) was obtained when **5-L6** is coordinated to Pd. It was therefore proposed that increasing the bite angle likely allowed for the isolation of the 1-AzA in the unique  $\eta^3$ -NCC coordination mode. However, the difference in bite angle between **H[5-L1]** and **H[5-L5]** (1.84°) and **H[5-L1]** and **H[5-L6]** (15.87°) suggests that simply increasing the distance between P and N

is not sufficient to dramatically increase the bite angle. Instead, the ligand backbone likely also requires some rotational freedom to increase the bite angle, which consequently allows for isolation of a Pd(P<sup>^</sup>AzA) complex coordinated  $\eta^3$ -NCC. Furthermore, the facile isomerization of the 1-AzA group from  $\eta^3$ -NCC to  $\kappa^1$ -N likely enables the oligomerization of ethylene with complex **5-7**.

Overall, the diverse coordination chemistry and the myriad of unique reactions accessible via the P<sup>^</sup>AzA family of ligands has been thoroughly established. The structurally responsive nature of the phosphine 1-AzA ligands permits reactions proceeding through rare dinuclear pathways that are not often observed in the literature. They also reduce energy barriers for steps foundational to catalysis and can consequently perform reactions that are difficult with current reported catalytic systems. Furthermore, the relationship between the P<sup>^</sup>AzA ligand backbone and coordination mode of the 1-AzA moiety has been established, allowing for the isolation of Pd(P<sup>^</sup>AzA) species with the 1-AzA group in the rare  $\eta^3$ -NCC coordination mode.

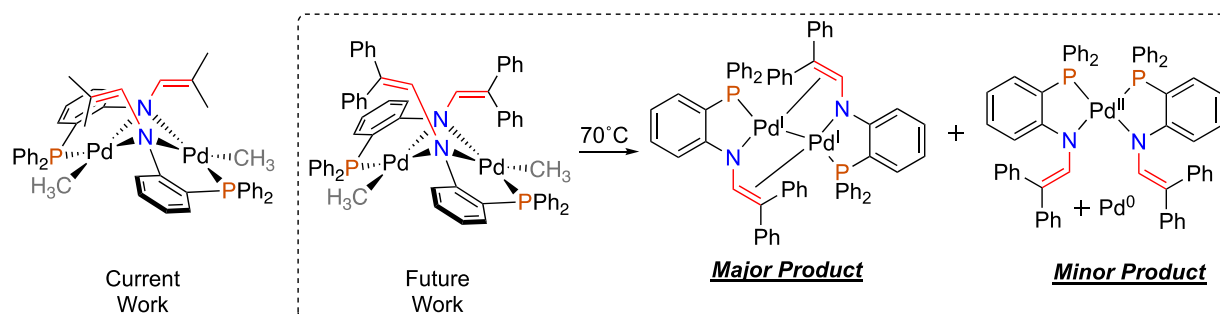
## 6.2 Future Work

The P<sup>^</sup>AzA ligands contain several sites for structural variation, including: the backbone, the phosphine substituents, and the C<sup>1</sup> and C<sup>2</sup> positions of the 1-AzA group. We have established that simultaneously increasing the distance between P and N and introducing rotational freedom can allow for the isolation of an  $\eta^3$ -NCC coordination mode, therefore structural variations should next be done at the PR<sub>2</sub> and 1-AzA sites to assess their impact on the 1-AzA coordination chemistry. When the 1-AzA ligand is coordinated  $\eta^3$ -NCC the 1-AzA occupies sites *cis* and *trans* relative to the phosphine, and the phosphine electronics will therefore have a profound effect on metal to 1-AzA bonding due to the trans-effect. As such, changing the phosphine substituents should be performed to investigate the impact of electron poor, and rich phosphine substituents on 1-AzA coordination. Similarly, changing the substituents at the C<sup>2</sup> position of the 1-AzA should be investigated to determine the electronic influences of 1-AzA to metal binding (Scheme 6.1).



**Scheme 6.1.** Left: Current P<sup>^</sup>AzA ligands bearing phenyl phosphine substituents. Right: Future phosphine substituents that should be investigated including electron rich and poor groups. X = X-type ligand.

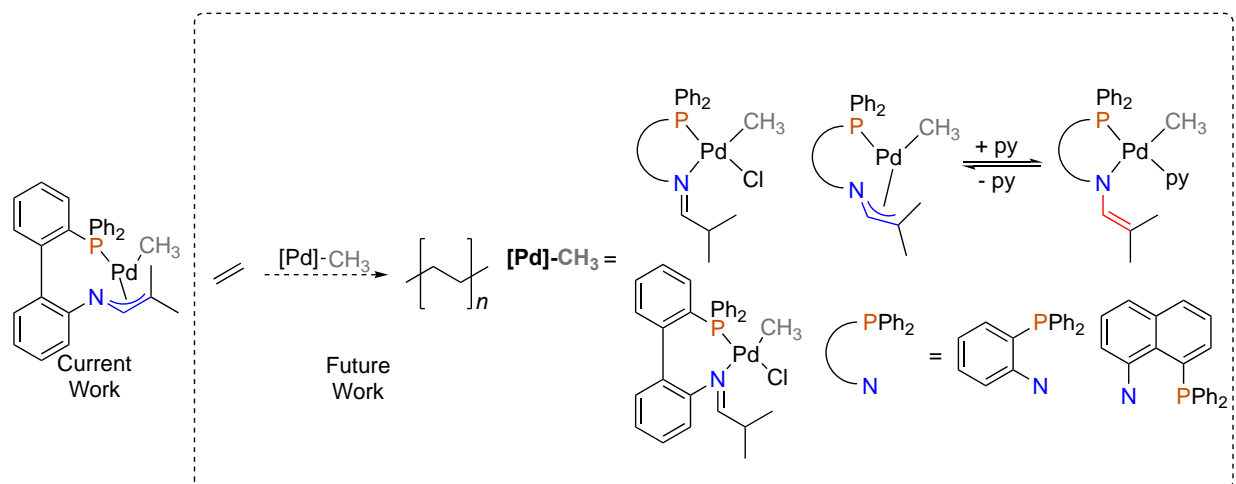
In the third chapter natural bond order computations revealed that metal-alkene bonding dramatically influences the reductive elimination step (Scheme B.12). As such, with sufficient electronic influence (i.e., via substitution at the C<sup>2</sup> positions) thermolysis of the resulting complexes may lower the energy barriers for the pathway affording the [Pd<sup>I</sup>(P<sup>^</sup>AzA)]<sub>2</sub> dimer. In turn, this would allow easier access to the Pd<sup>I</sup> dimer and operative [Pd<sup>II</sup>]<sub>2</sub> dinuclear cycles. To ensure that a dramatic change in electronic influence does not preclude formation of a dinuclear complex, mildly donating or withdrawing groups (e.g., phenyl), should be used.



**Scheme 6.2.** Left: Current P<sup>^</sup>AzA ligands bearing methyl substituents at the C<sup>2</sup> position and its coordination complex with Pd. Right: Phenyl substitution at C<sup>2</sup> and the proposed change in Pd product selectivity favouring formation of the Pd<sup>I</sup> dimer instead of the mononuclear Pd<sup>II</sup> complex.

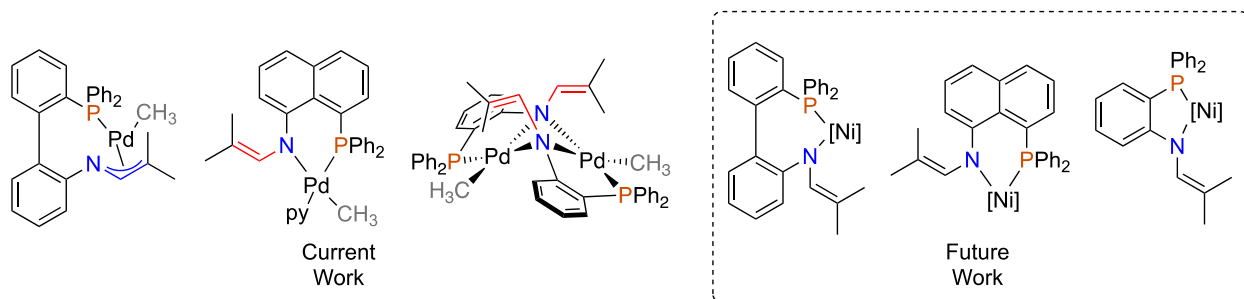
Furthermore, the impact of the 1-AzA moiety on polymerization must be assessed. Currently, polyethylene homopolymerization has only been attempted with biaryl linked **5-7**. However, to determine if the structurally responsive 1-AzA is beneficial to polymerization then a control reaction with the P<sup>^</sup>I precursor **H[5-L6]** coordinated to Pd must be attempted (Scheme 6.3). Additionally, polymerization should also be attempted with the P<sup>^</sup>AzA complexes coordinated by **5-L1** and **5-L5**, as well as their P<sup>^</sup>I precursors coordinated to Pd to establish the best catalyst for homopolymerization of ethylene. The copolymerization of ethylene with

industrially relevant polar monomers such as methyl acrylate and vinyl acetate should also be performed.



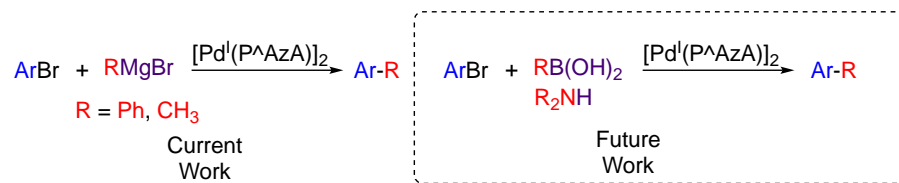
**Scheme 6.3.** Left: Biaryl P<sup>A</sup>AzA complex used for homopolymerization of ethylene. Right: Future polyethylene polymerization using the other P<sup>A</sup>AzA ligands reported in this document and their P<sup>I</sup> analogues.

The metal centre in the P<sup>A</sup>AzA metal complexes can also be varied. A substantial body of work has previously been dedicated to Ni(1-AzA) coordination chemistry, and  $\eta^3$ -NCC coordination modes have been isolated with Ni. As such the P<sup>A</sup>AzA ligands should be coordinated to Ni and their coordination modes and subsequent reactivity reported (Scheme 6.4).



**Scheme 6.4.** Left: Currently synthesized P<sup>A</sup>AzA ligands and their coordination complexes with Pd. Right: Currently synthesized P<sup>A</sup>AzA ligands and future work of coordinating them to Ni.

Finally, the [Pd<sup>I</sup>(P<sup>A</sup>AzA)]<sub>2</sub> dimers have also been proven to be capable of cross-coupling reactions requiring milder nucleophiles such as a boronic acid to allow for easier reaction assessment, wider range of compatible functional groups, and easier reaction handling (Scheme 6.5).



**Scheme 6.5.** Left: Kumada coupling using a  $[\text{Pd}^{\text{I}}(\text{P}^{\wedge}\text{AzA})]_2$  dimer reported in chapter 4. Right: Different potential cross coupling uses for the  $[\text{Pd}^{\text{I}}(\text{P}^{\wedge}\text{AzA})]_2$  including Suzuki-Miyaura cross coupling and Buchwald-Hartwig Amination.

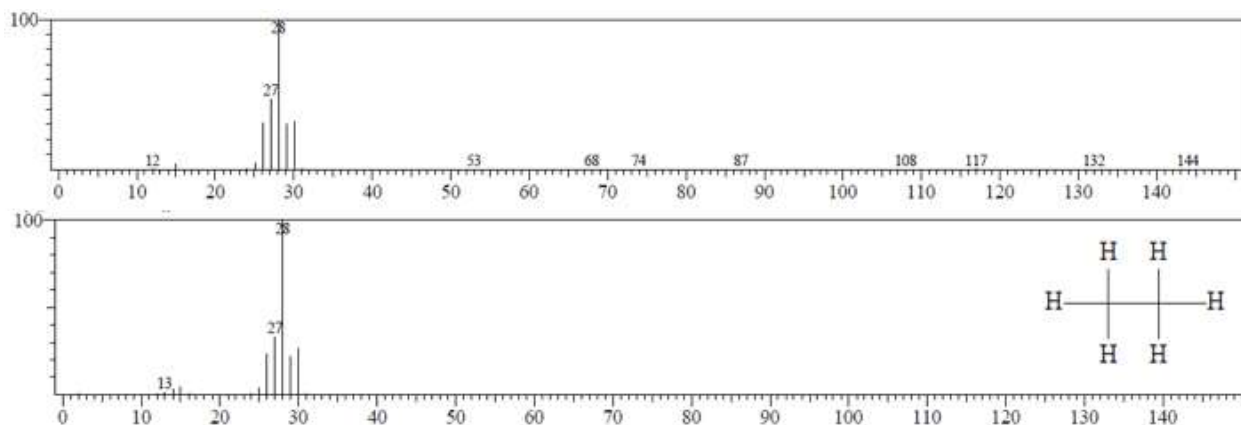
## Appendices

### Appendix A: Supplementary Information for Chapter 2

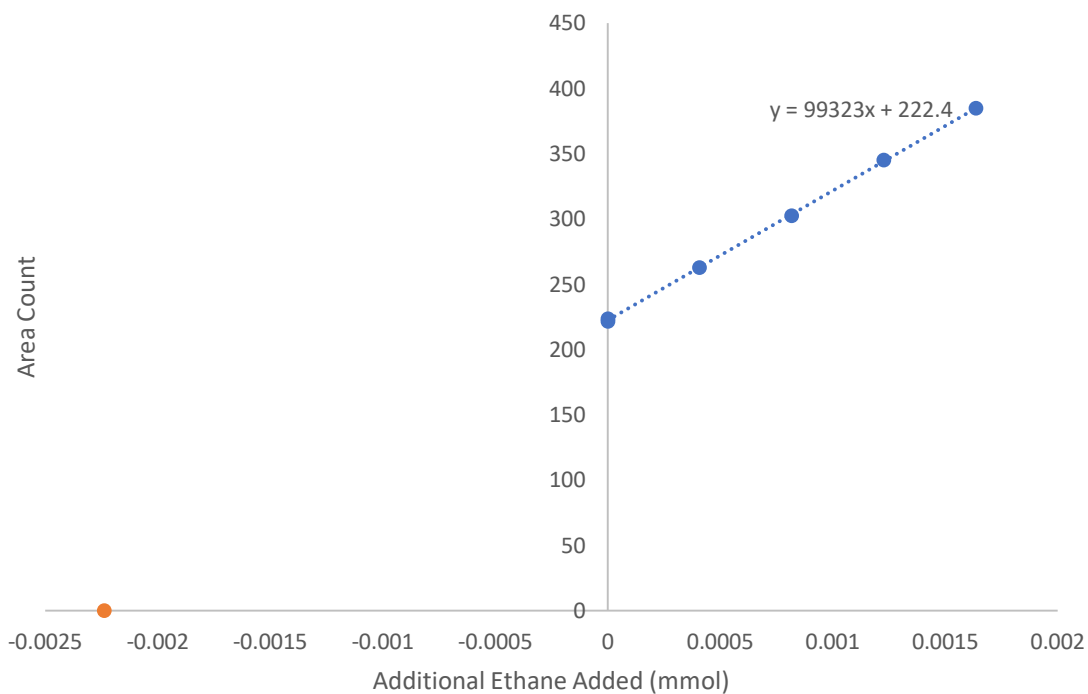
**Table A.1.** Summary of Selected  $^1\text{H}$ ,  $^{13}\text{C}\{^1\text{H}\}$  and  $^{31}\text{P}\{^1\text{H}\}$  NMR Spectroscopy Data for Complexes **2-1-2-5**.

|  | $\text{H}^1$ | $\text{H}^2$ | $\text{C}^1$ | $\text{C}^2$ | P     |
|--|--------------|--------------|--------------|--------------|-------|
| <b>H[2-L1]</b> ( $\text{C}_6\text{D}_6$ )  | 7.29         | 2.15         | 170.0        | 34.8         | -14.4 |
| <b>K[L1]</b> ( $(\text{CD}_3)_2\text{O}$ ) | 6.68         | –            | 122.3        | 111.0        | -21.5 |
| <b>2-1</b> ( $\text{CD}_2\text{Cl}_2$ )    | 7.80         | 4.19         | 182.6        | 34.7         | 36.2  |
| <b>2-2</b> ( $\text{C}_6\text{D}_6$ )      | 6.60         | –            | 141.5        | 117.2        | 43.7  |
| <b>2-3</b> ( $\text{C}_6\text{D}_6$ )      | 6.35         | –            | 133.5        | 118.3        | 45.5  |
| <b>2-4</b> ( $\text{C}_6\text{D}_6$ )      | 5.97         | –            | 109.0        | 74.5         | 15.0  |
| <b>2-5</b> ( $\text{C}_6\text{D}_6$ )      | 6.78         | –            | 135.4        | 118.0        | 47.7  |
| $\kappa^1\text{-N}^1$                      | 7.28         | –            | 149.8-187.5  | 66.3-114.8   | –     |
| $\eta^3\text{-NCC}^1$                      | N/A          | –            | 151.9-184.9  | 42.0-64.5    | –     |

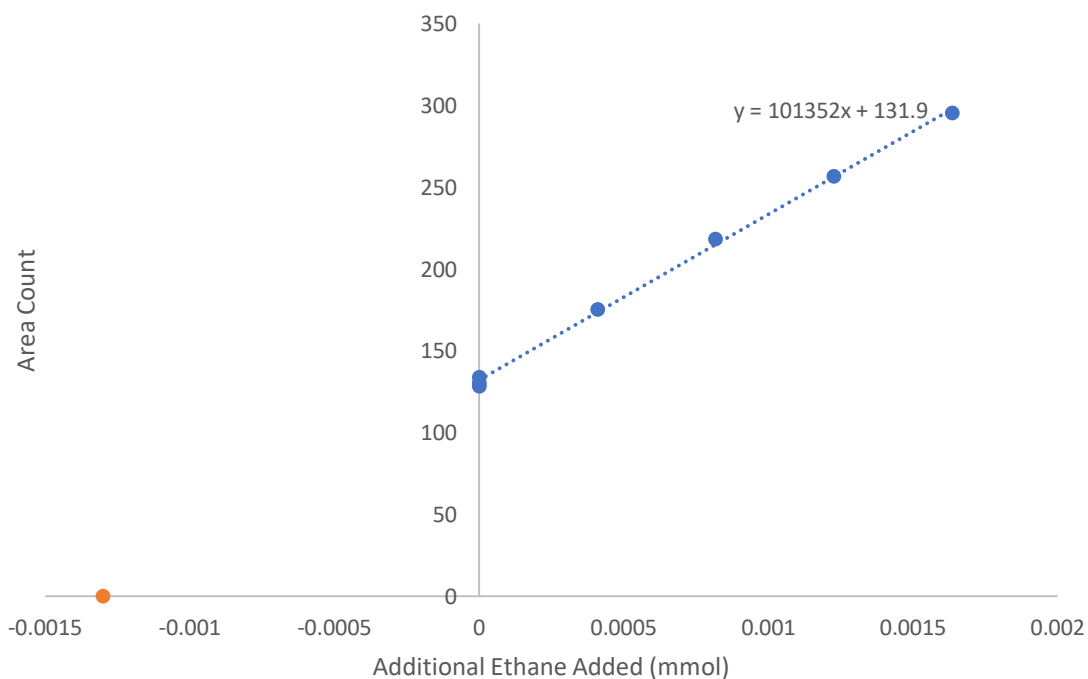
### I – GC-MS and GC-FID Data



**Figure A.1.** Headspace GC-MS analysis obtained from a solution sample of **2-2** that was at room temperature. Depicted are: the MS from the observed chromatogram (top), and library spectrum for ethane (bottom).

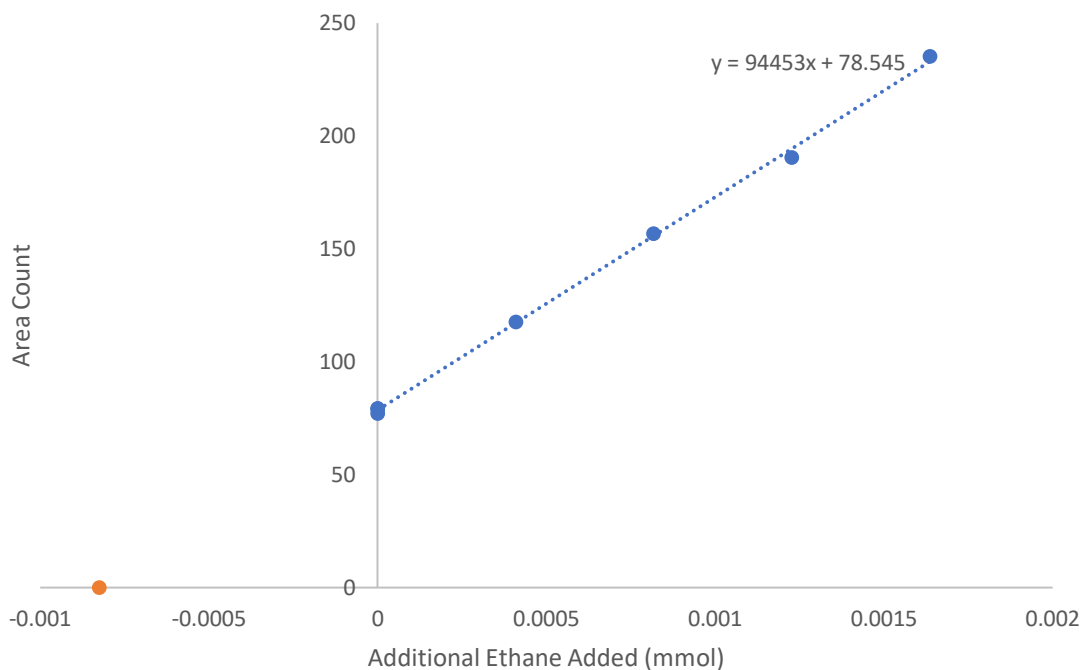


**Figure A.2.** Standard addition plot generated from NMR tube **A** containing 81  $\mu\text{L}$  of ethane. The orange marker indicates the molar amount of ethane present in the headspace.

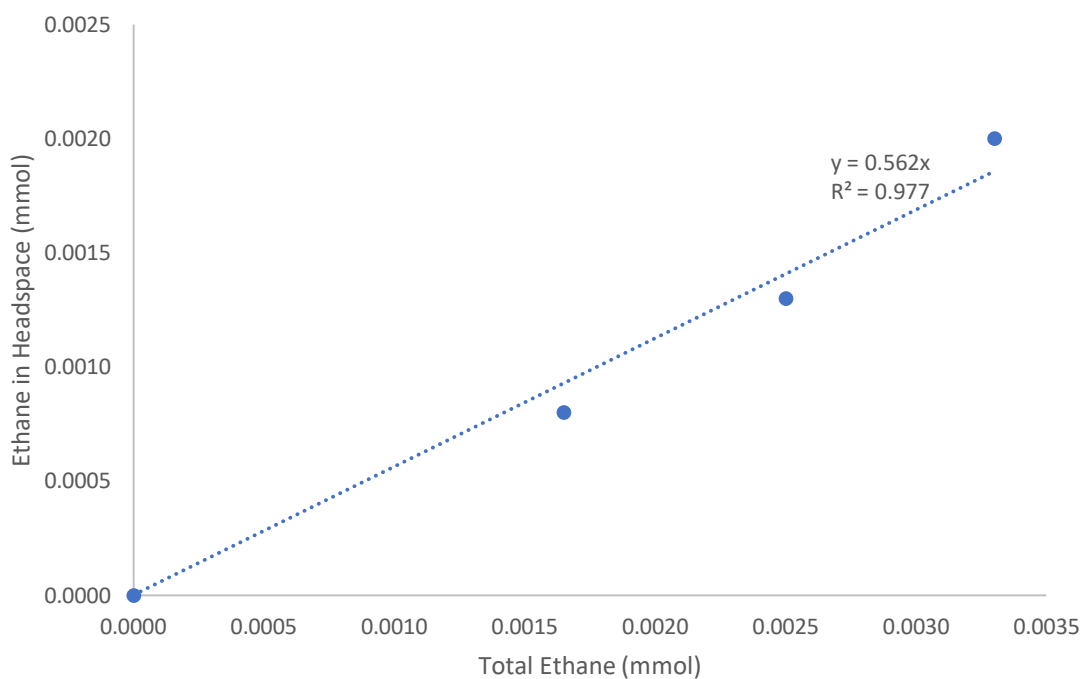


**Figure A.3.** Standard addition plot generated from NMR tube **B** containing 62  $\mu\text{L}$  of ethane. The orange marker indicates the molar amount of ethane present in the headspace.

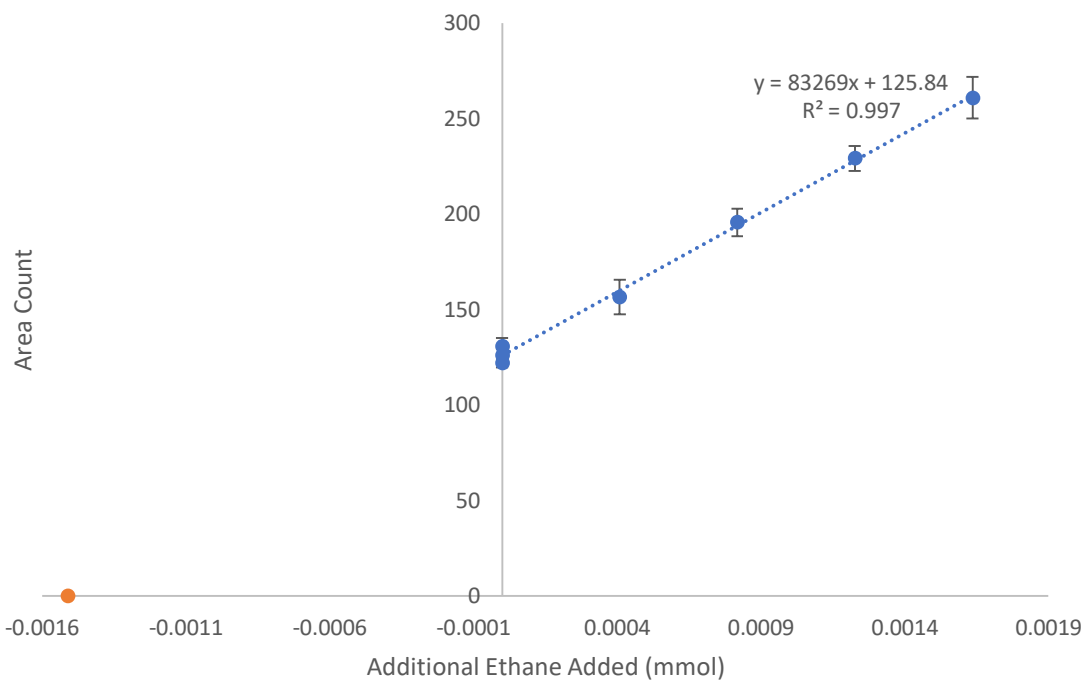




**Figure A.4.** Standard addition plot generated from NMR tube **C** containing 42  $\mu\text{L}$  of ethane. The orange marker indicates the molar amount of ethane present in the headspace.

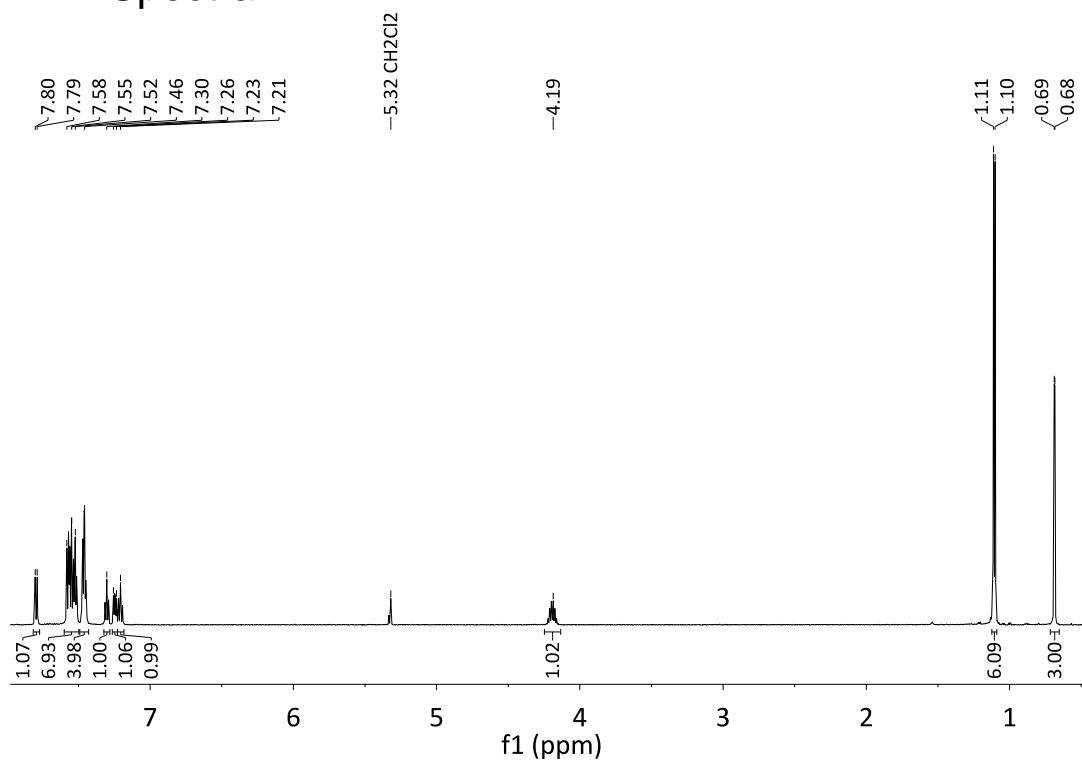


**Figure A.5.** Calibration curve that correlates ethane in the headspace to total molar amount of ethane in the tube, generated using the data obtained in Figures S3-S5 in combination with equation (1).

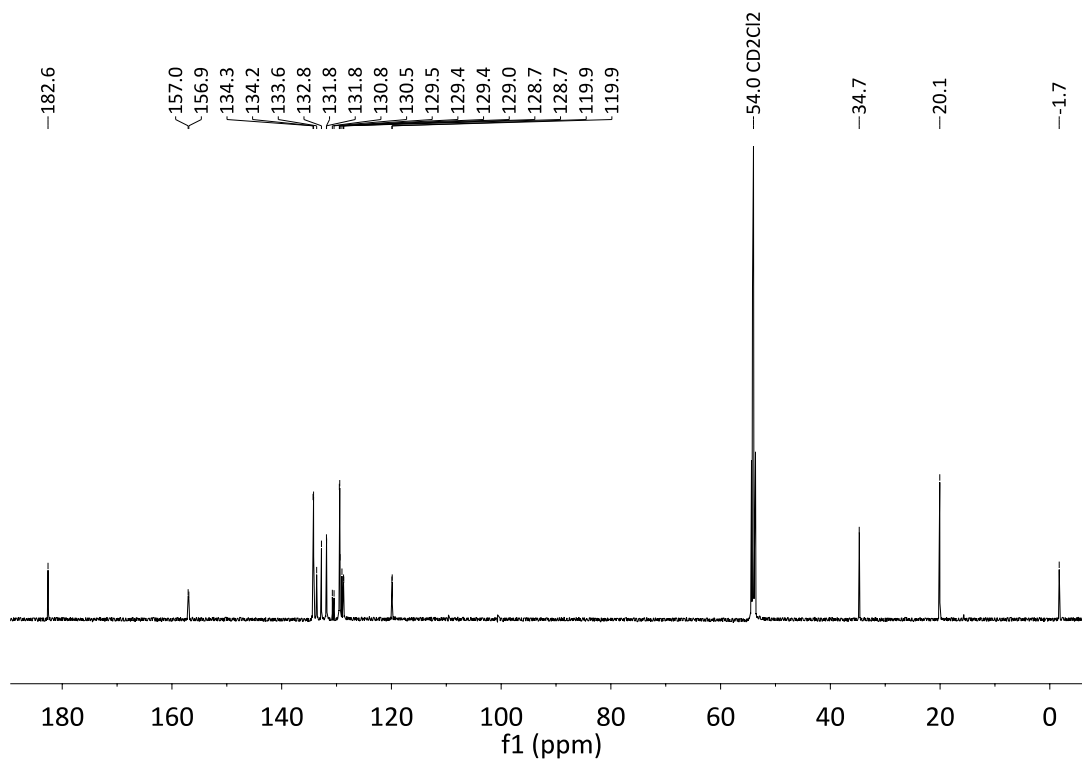


**Figure A.6.** Standard addition plot used to quantify the amount of ethane formed upon dimerization of **2-2**.

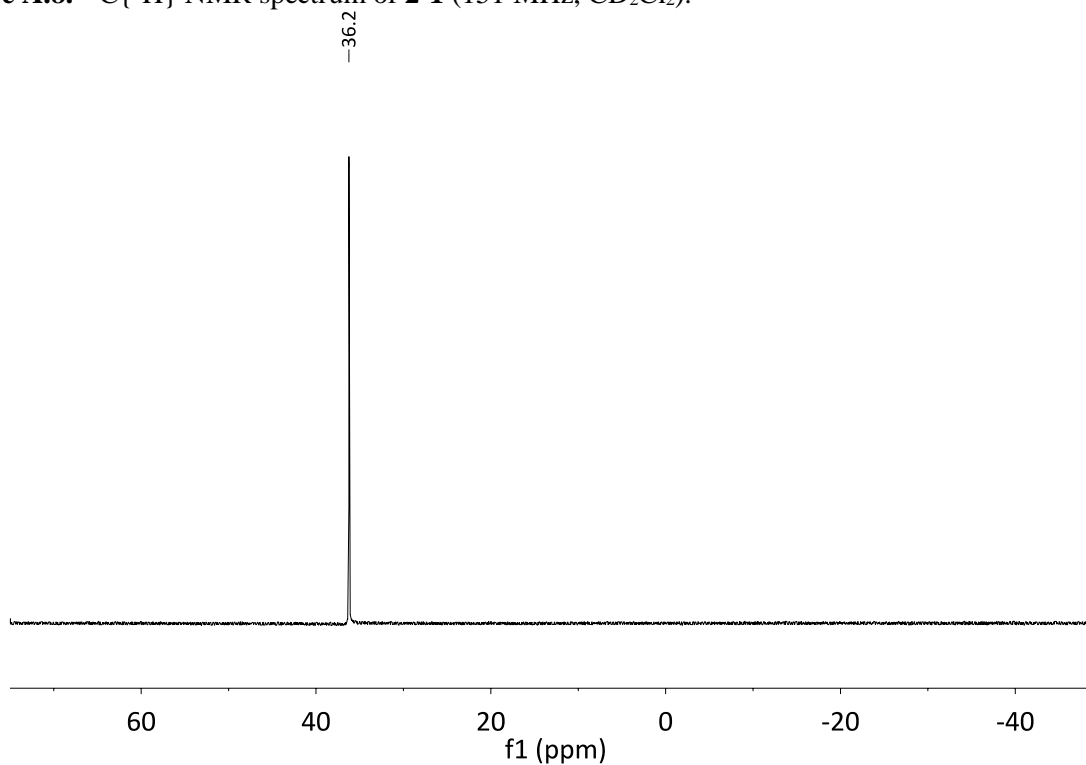
## II – NMR Spectra



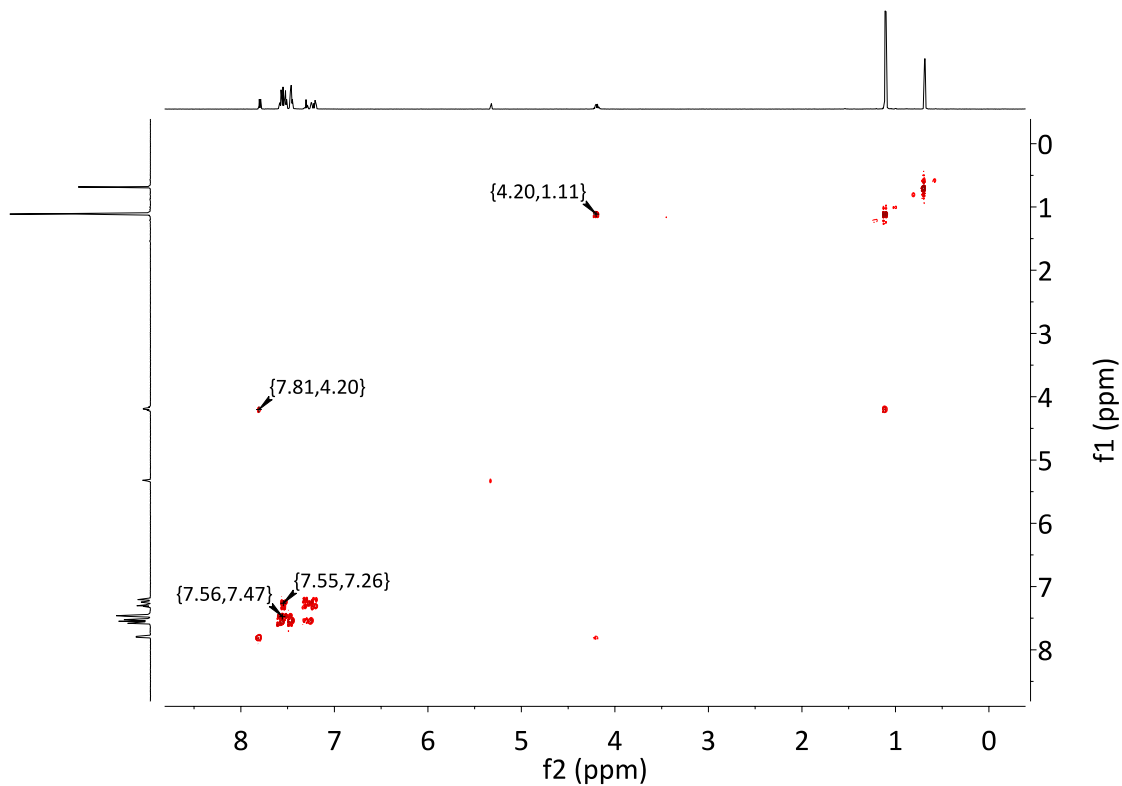
**Figure A.7.** <sup>1</sup>H NMR spectrum of **2-1** (599 MHz, CD<sub>2</sub>Cl<sub>2</sub>).



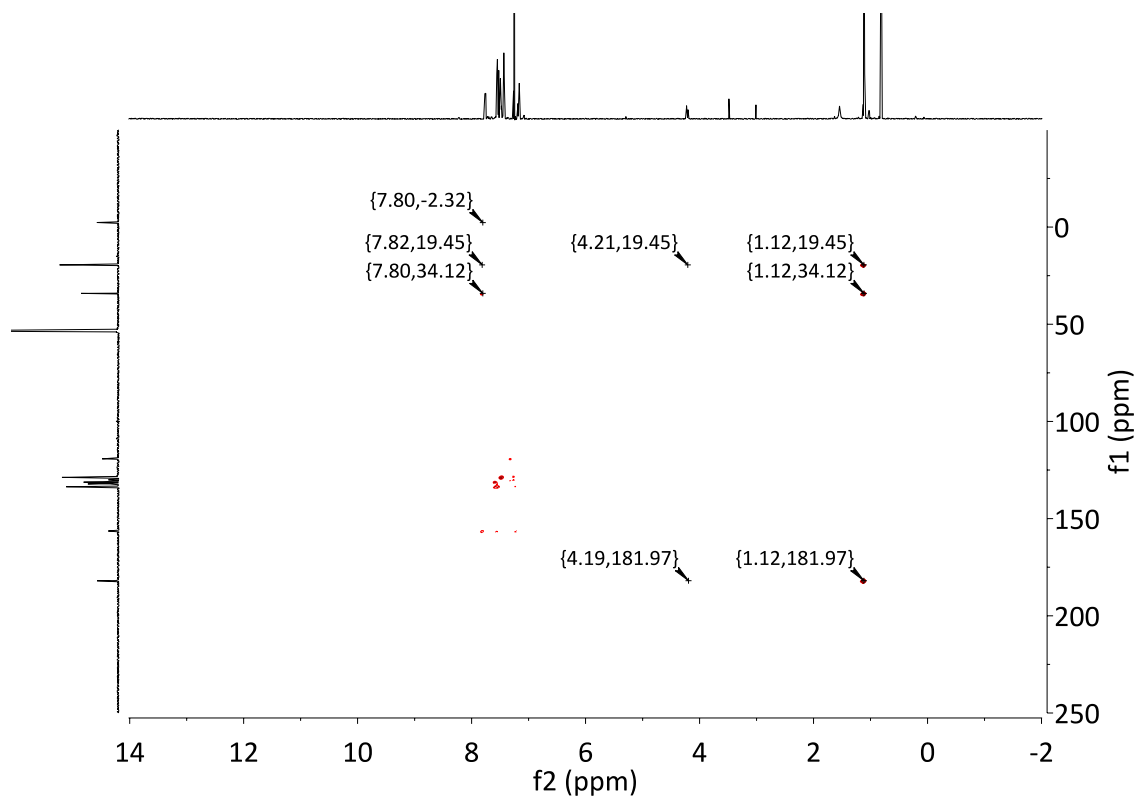
**Figure A.8.**  $^{13}\text{C}\{^1\text{H}\}$  NMR spectrum of **2-1** (151 MHz,  $\text{CD}_2\text{Cl}_2$ ).



**Figure A.9.**  $^{31}\text{P}\{^1\text{H}\}$  NMR spectrum of **2-1** (243 MHz,  $\text{CD}_2\text{Cl}_2$ ).



**Figure A.10.**  $^1\text{H}$ - $^1\text{H}$  COSY NMR spectrum of **2-1** (599 MHz,  $\text{CD}_2\text{Cl}_2$ ).



**Figure A.11.**  $^1\text{H}$ - $^{13}\text{C}$  HMBC NMR spectrum of **2-1** (599 MHz,  $\text{CD}_2\text{Cl}_2$ ).

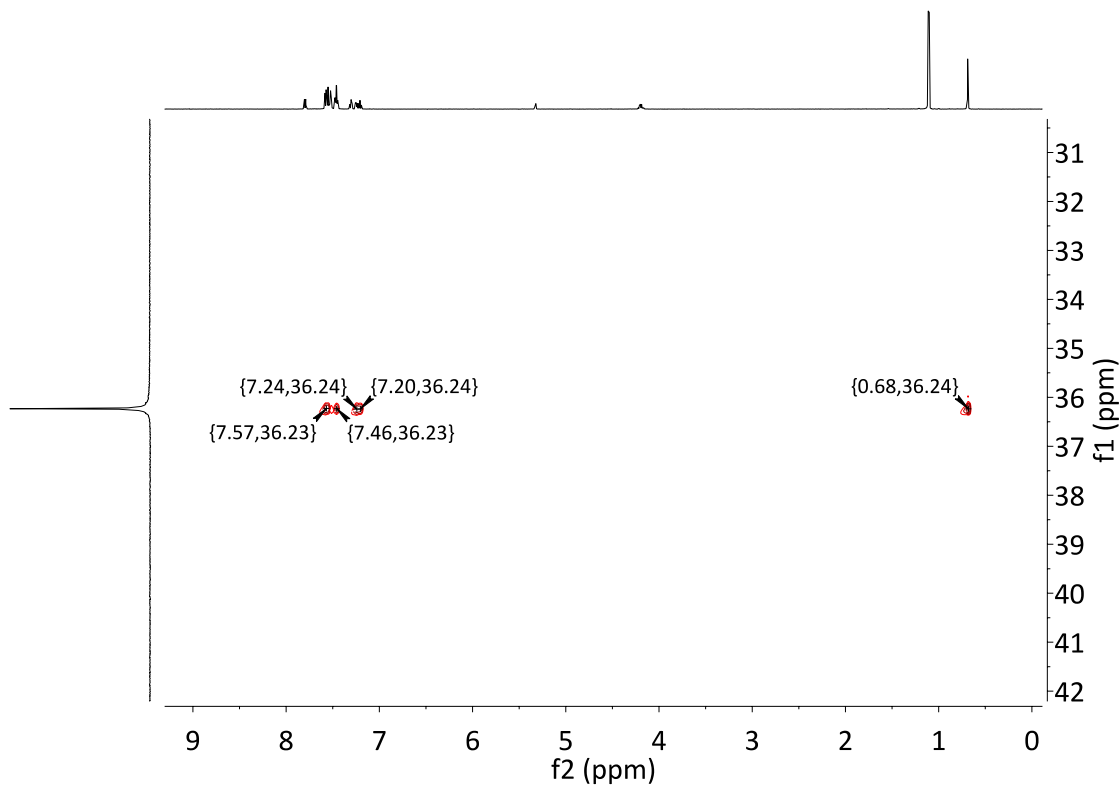


Figure A.12.  $^1\text{H}$ - $^{31}\text{P}$  HMBC NMR spectrum of **2-1** (599 MHz,  $\text{CD}_2\text{Cl}_2$ ).

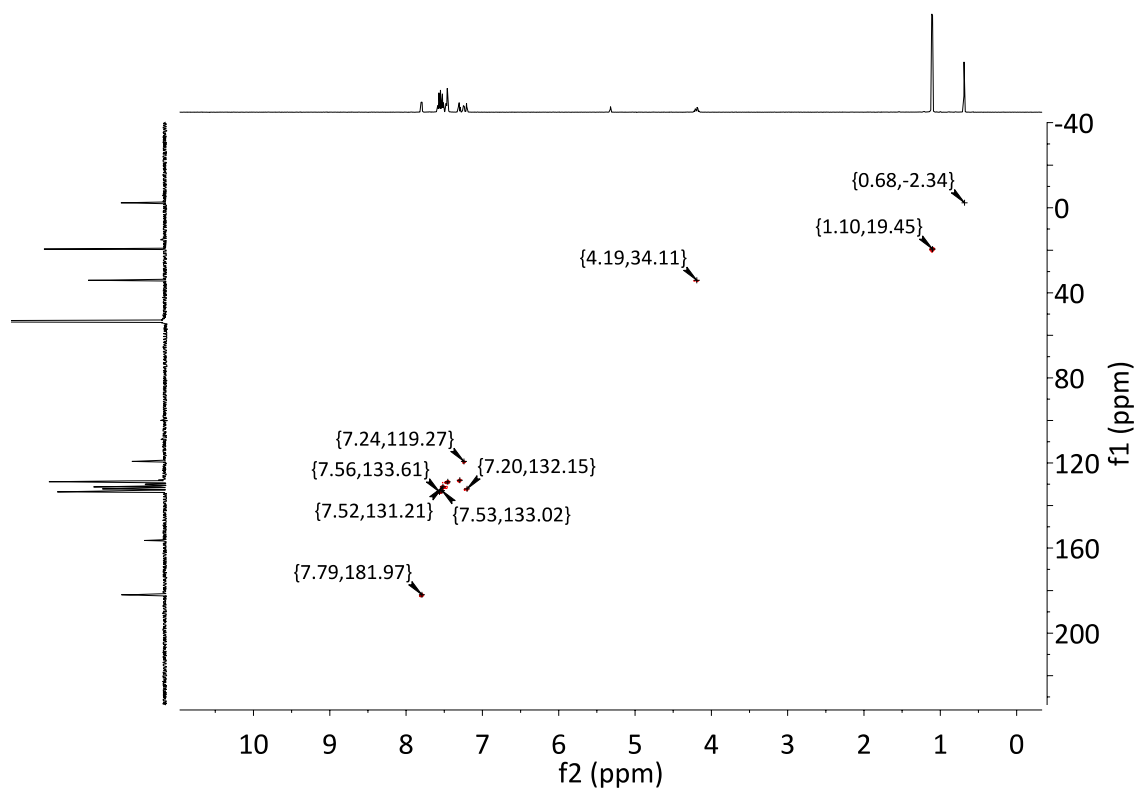
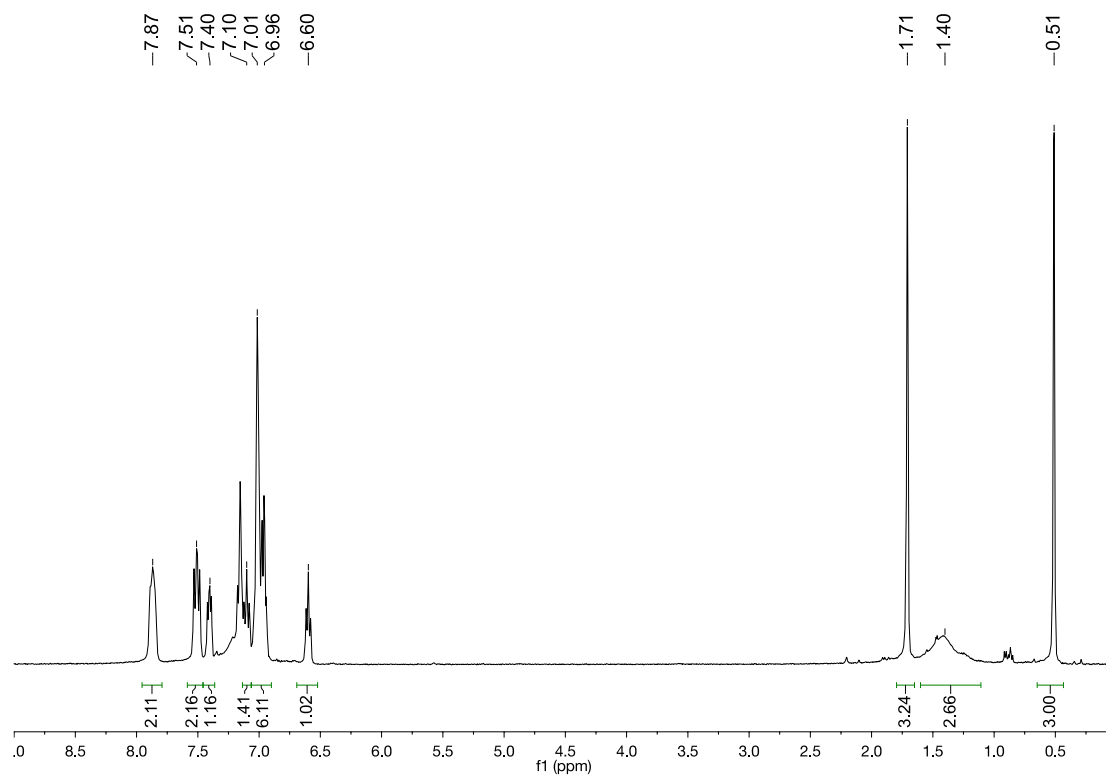
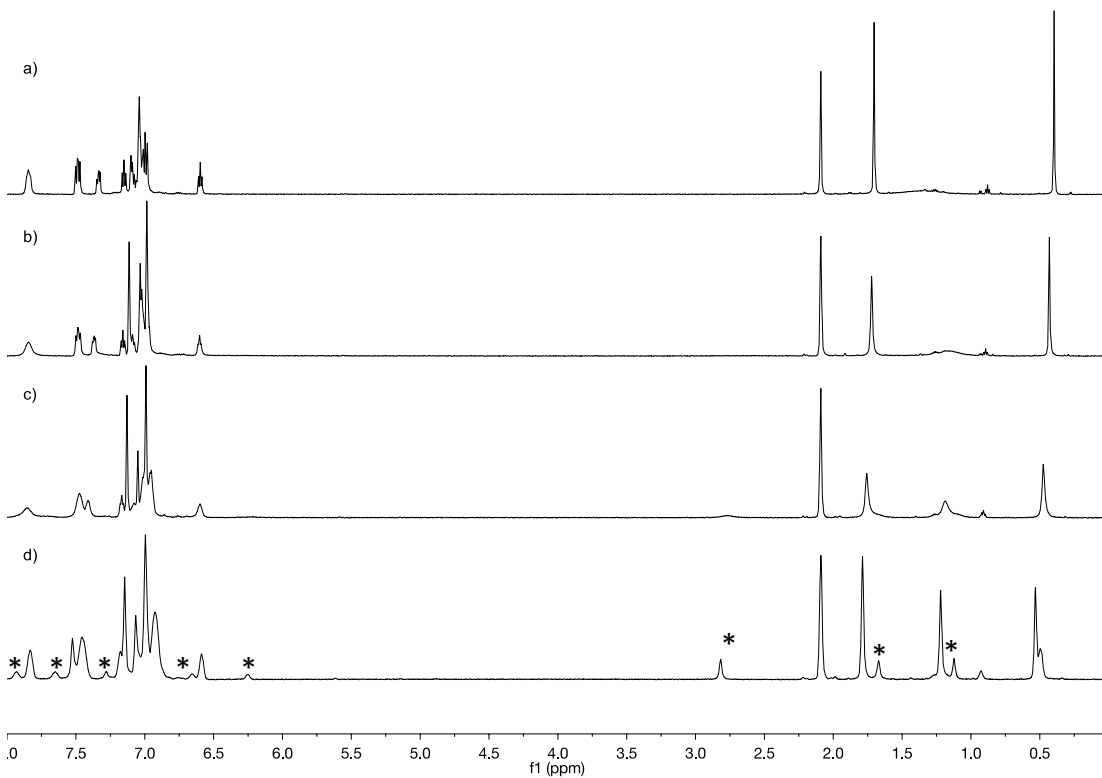


Figure A.13.  $^1\text{H}$ - $^{13}\text{C}$  HSQC NMR spectrum of **2-1** (599 MHz,  $\text{CD}_2\text{Cl}_2$ ).



**Figure A.14.** <sup>1</sup>H NMR spectrum of **2-2** (599 MHz, C<sub>6</sub>D<sub>6</sub>).



**Figure A.15.** VT  $^1\text{H}$  NMR stack plots of **2-2**, a) 25 °C b) 0 °C c) -25 °C d) -50 °C (599 MHz, toluene- $d_8$ ). The agostic methyl resonance ( $\text{H}^3$ ) is broad at 25 °C and sharpens to a singlet at -50 °C. The emergence of a minor isomer (\*) indicates that a second dynamic process occurs in addition to freezing-out the agostic interaction. The multiple dynamic events precludes line shape analysis and extraction of activation parameters.

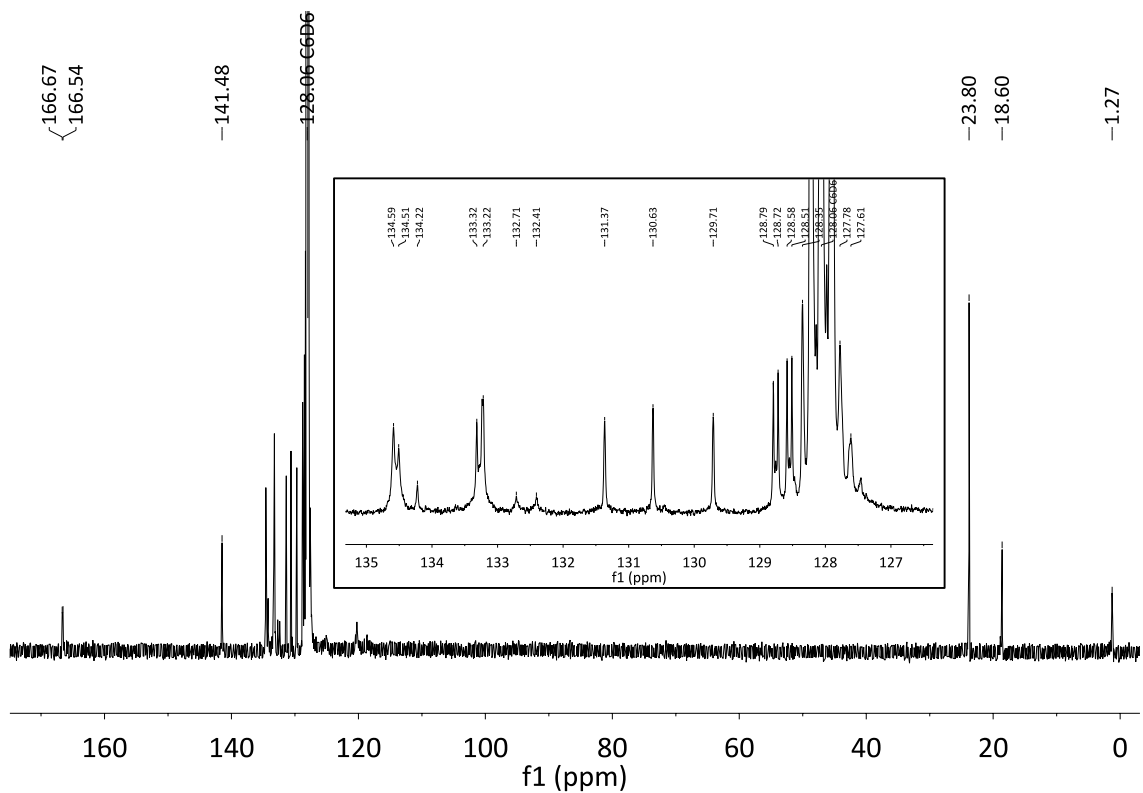


Figure A.16.  $^{13}\text{C}\{^1\text{H}\}$  NMR spectrum of **2-2** (151 MHz,  $\text{C}_6\text{D}_6$ ).

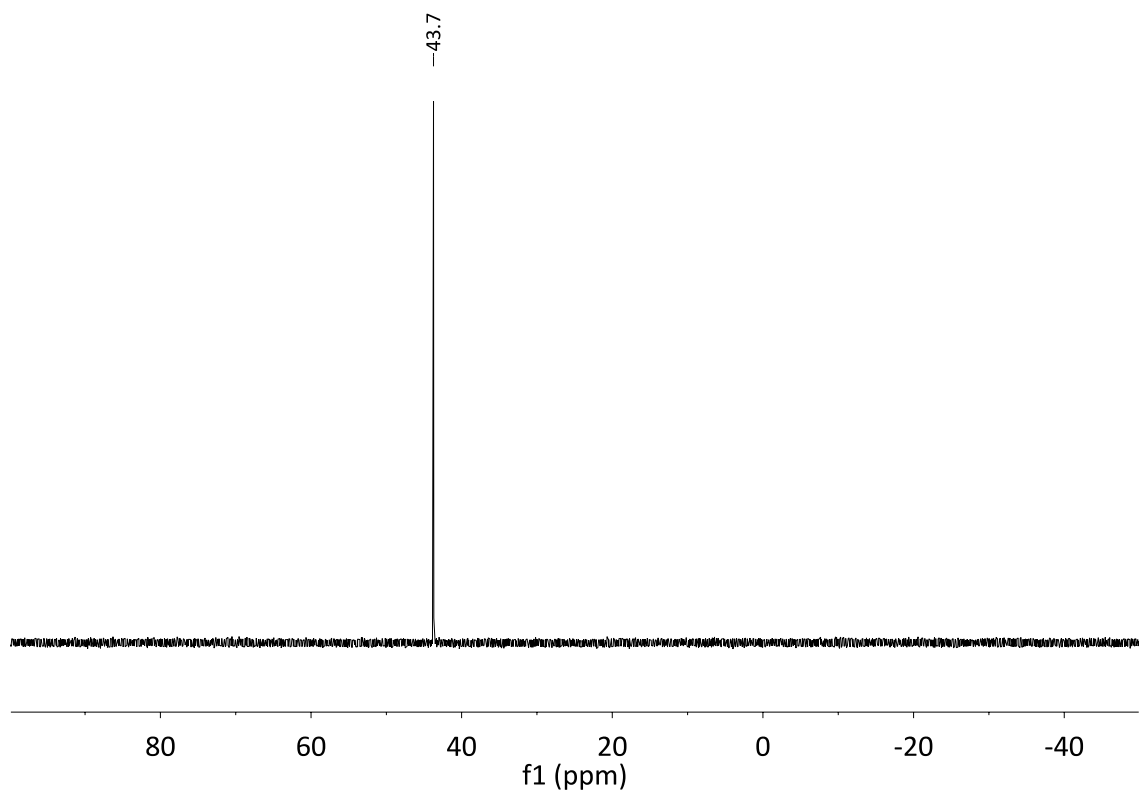
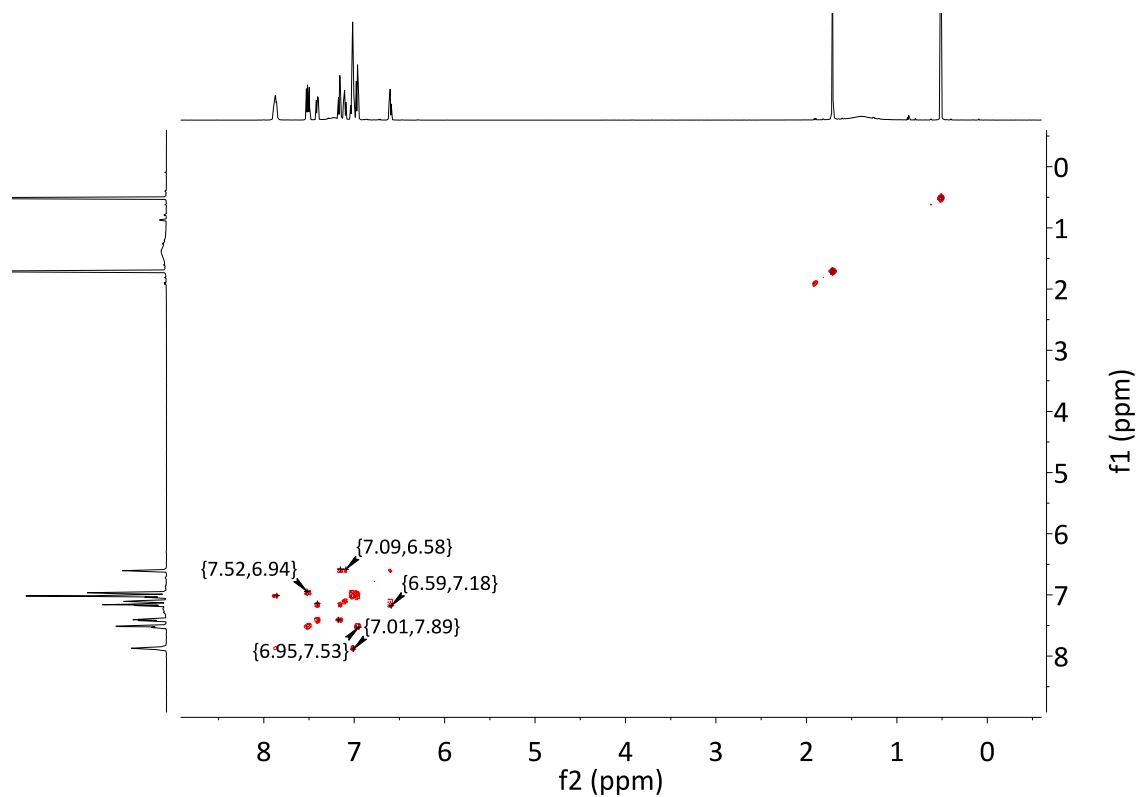
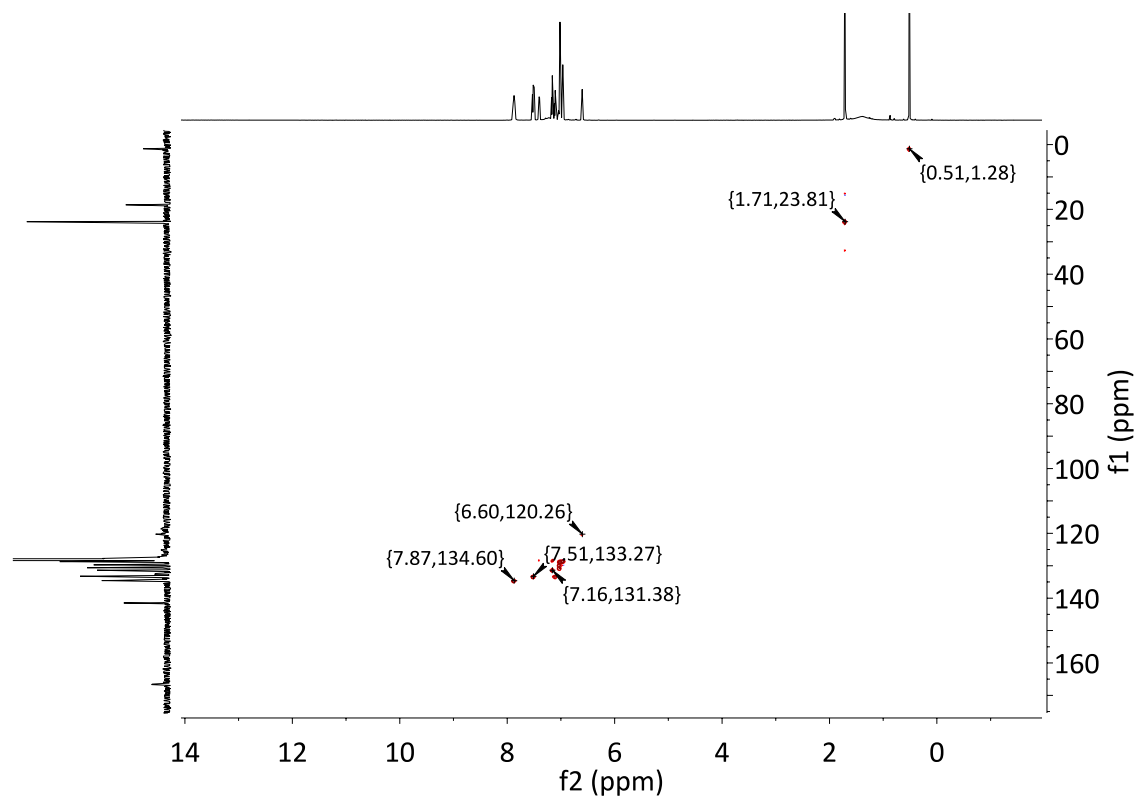


Figure A.17.  $^{31}\text{P}\{^1\text{H}\}$  NMR spectrum of **2-2** (243 MHz,  $\text{C}_6\text{D}_6$ ).





**Figure A.18.**  $^1\text{H}$ - $^1\text{H}$  COSY NMR spectrum of **2-2** (599 MHz,  $\text{C}_6\text{D}_6$ ).



**Figure A.19.**  $^1\text{H}$ - $^{13}\text{C}$  HSQC NMR spectrum of **2-2** (599 MHz,  $\text{C}_6\text{D}_6$ ).

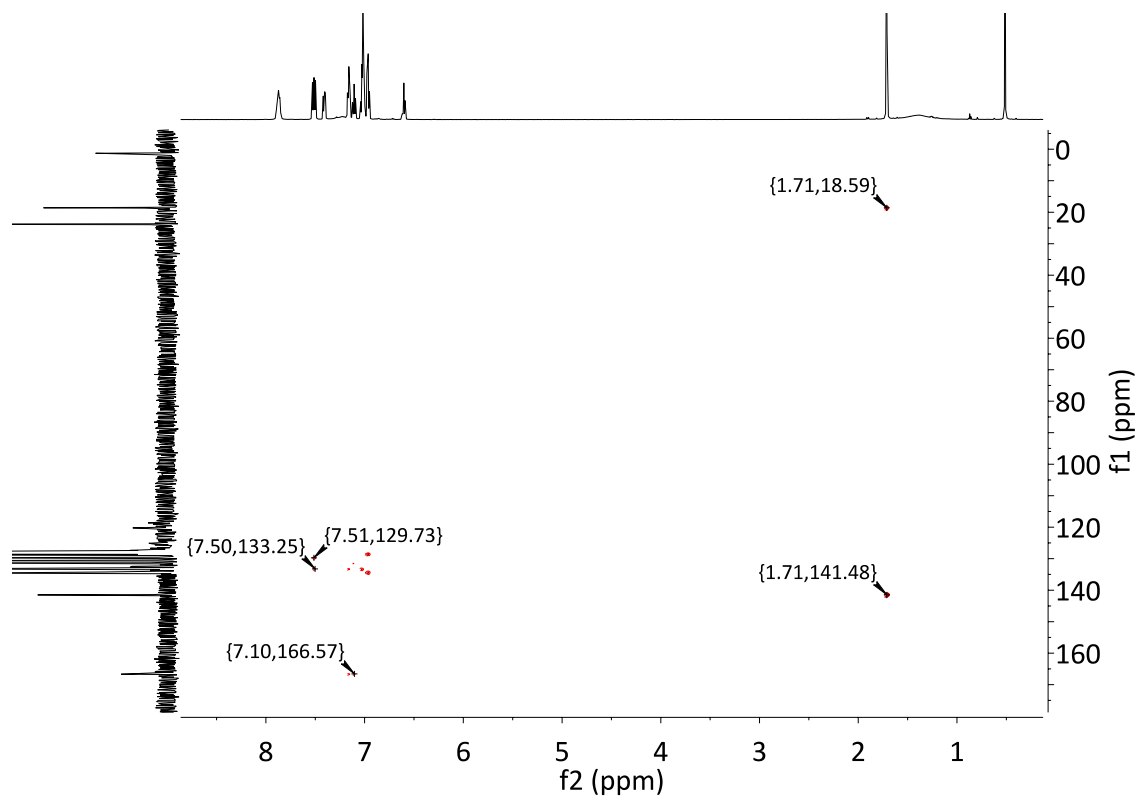


Figure A.20.  $^1\text{H}$ - $^{13}\text{C}$  HMBC NMR spectrum of **2-2** (599 MHz,  $\text{C}_6\text{D}_6$ ).

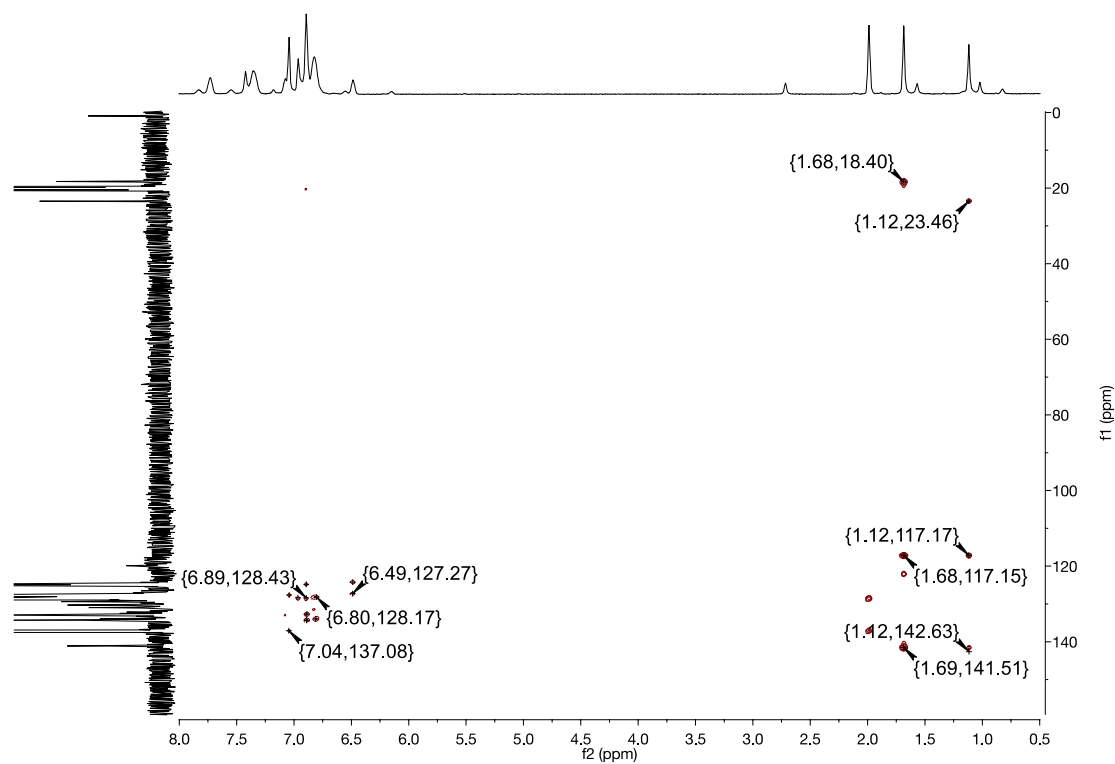


Figure A.21.  $^1\text{H}$ - $^{13}\text{C}$  HMBC NMR spectrum of **2-2** acquired at  $-50^\circ\text{C}$  (599 MHz,  $\text{toluene-d}_8$ ).

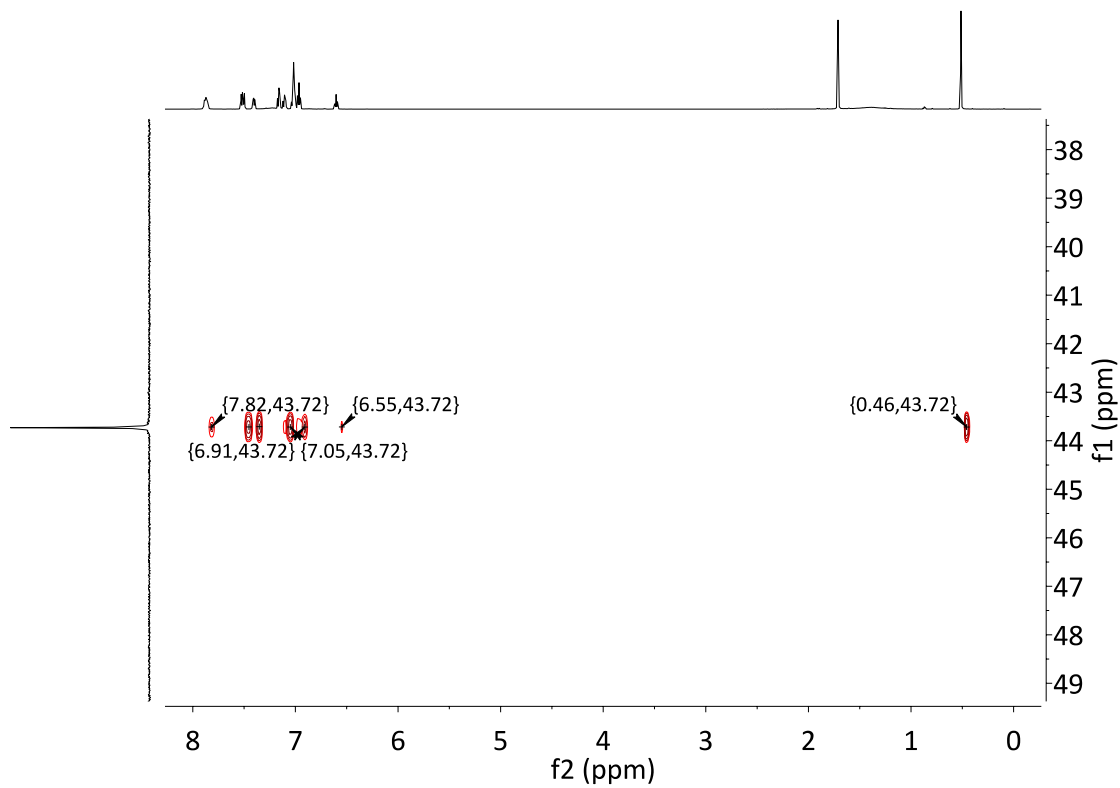


Figure A.22.  $^1\text{H}$ - $^{31}\text{P}$  HMBC NMR spectrum of **2-2** (599 MHz,  $\text{C}_6\text{D}_6$ ).

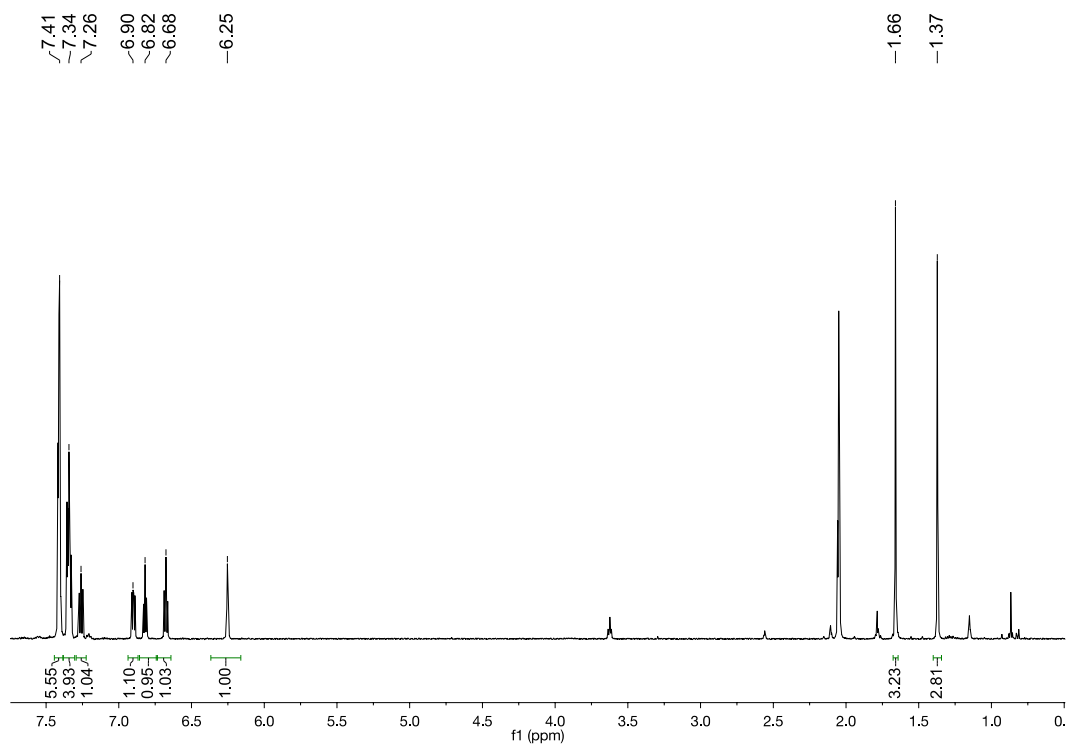


Figure A.23  $^1\text{H}$  NMR spectrum of **K[2-L1]** (599 MHz,  $(\text{CD}_3)_2\text{O}$ ).

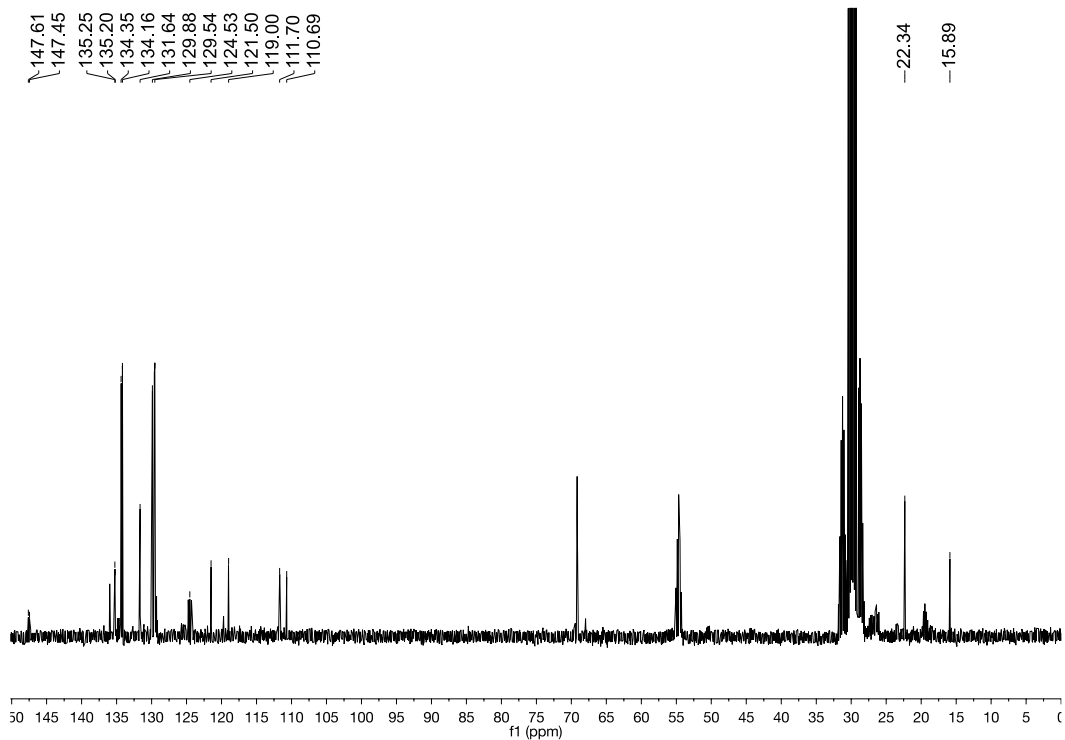


Figure A.24  $^{13}\text{C}\{^1\text{H}\}$  NMR spectrum of **K[2-L1]** (151 MHz,  $(\text{CD}_3)_2\text{O}$ ).

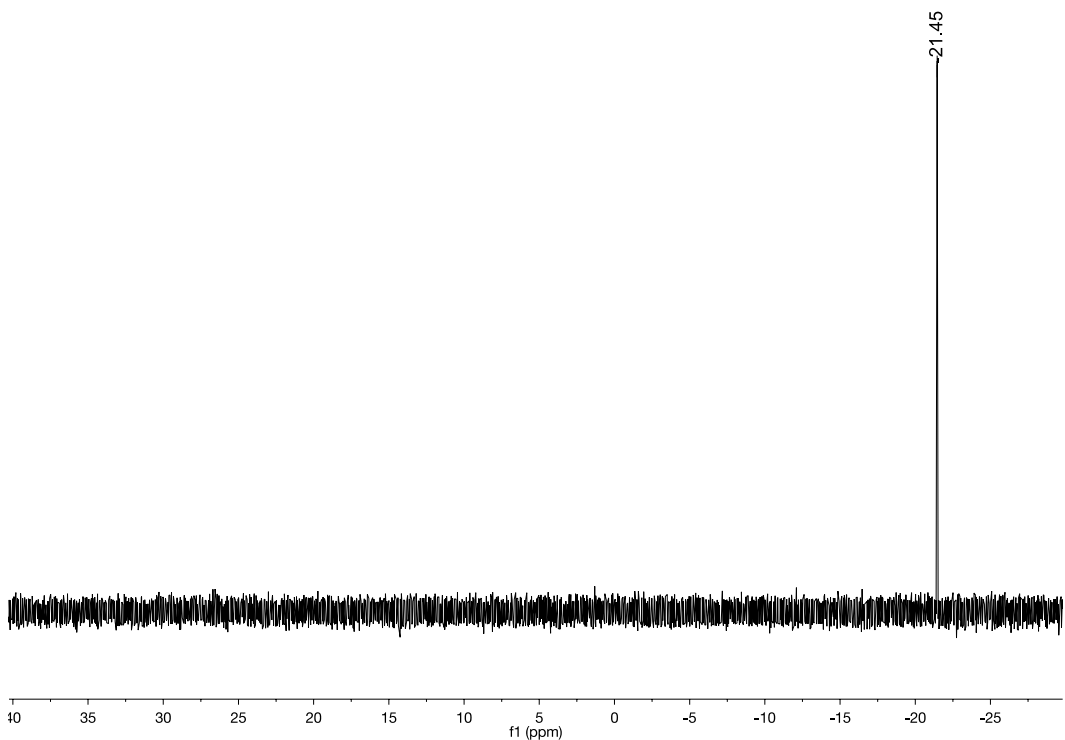
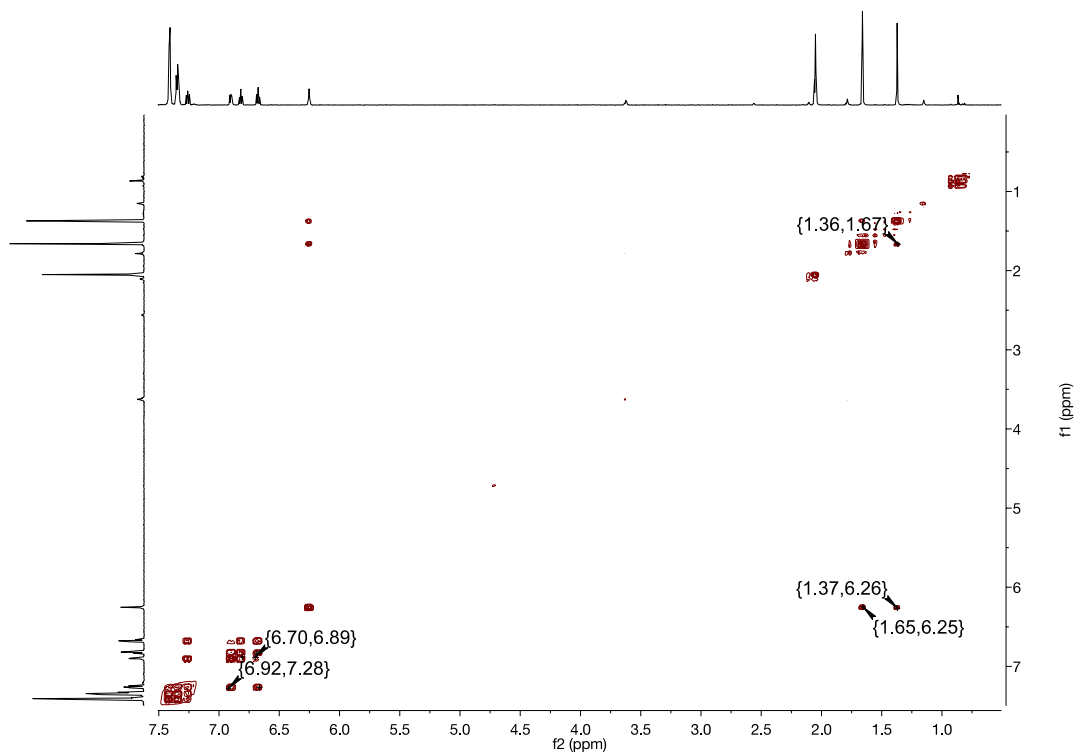
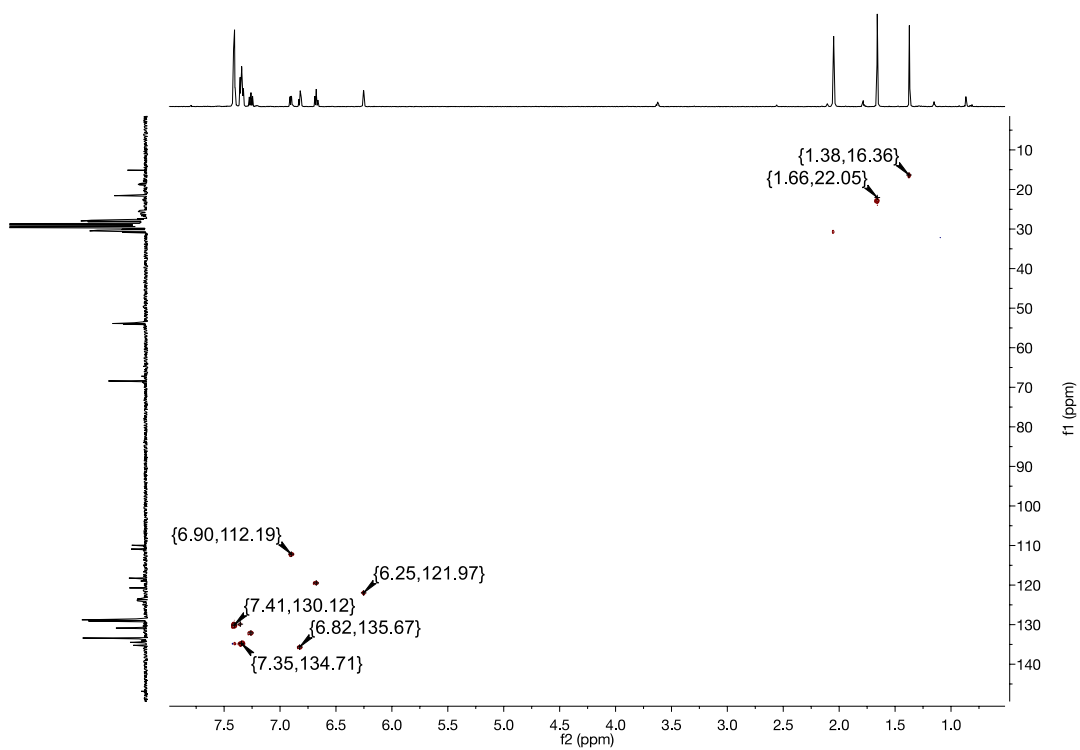


Figure A.25  $^{31}\text{P}\{^1\text{H}\}$  NMR spectrum of **K[2-L1]** (243 MHz,  $(\text{CD}_3)_2\text{O}$ ).



**Figure A.26.**  $^1\text{H}$ - $^1\text{H}$  COSY NMR spectrum of **K[2-L1]** (599 MHz,  $(\text{CD}_3)_2\text{O}$ ).



**Figure A.27.**  $^1\text{H}$ - $^{13}\text{C}$  HSQC NMR spectrum of **K[2-L1]** (599 MHz,  $(\text{CD}_3)_2\text{O}$ ).

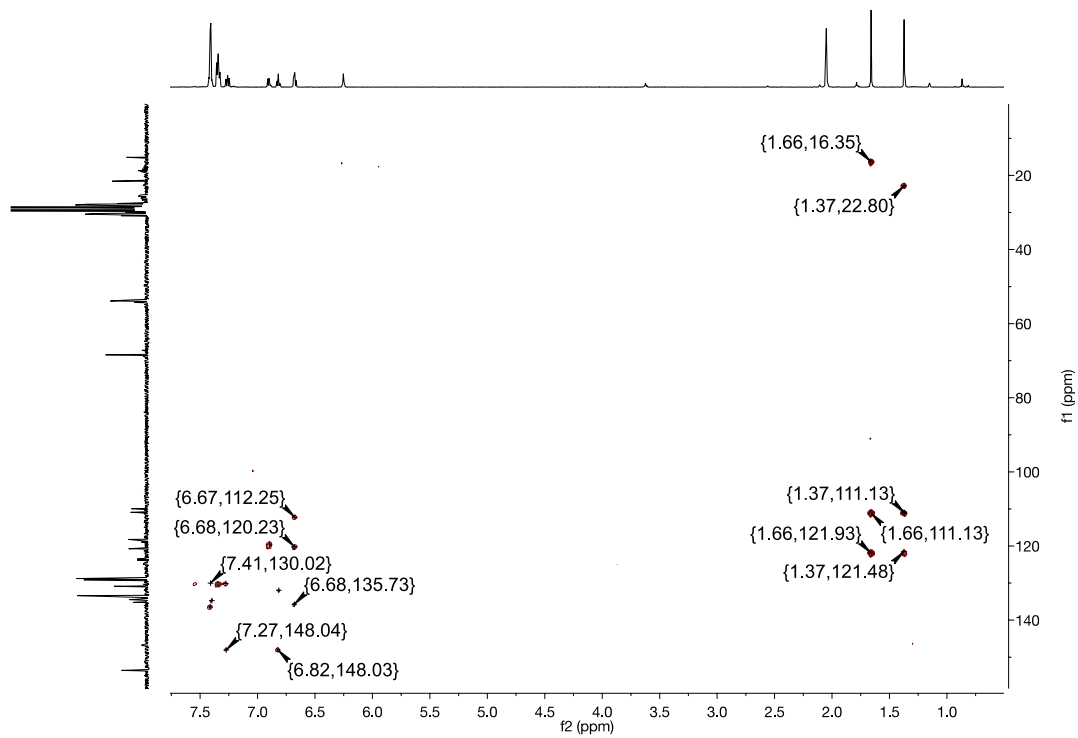


Figure A.28.  $^1\text{H}$ - $^{13}\text{C}$  HMBC NMR spectrum of **K[2-L1]** (599 MHz,  $(\text{CD}_3)_2\text{O}$ ).

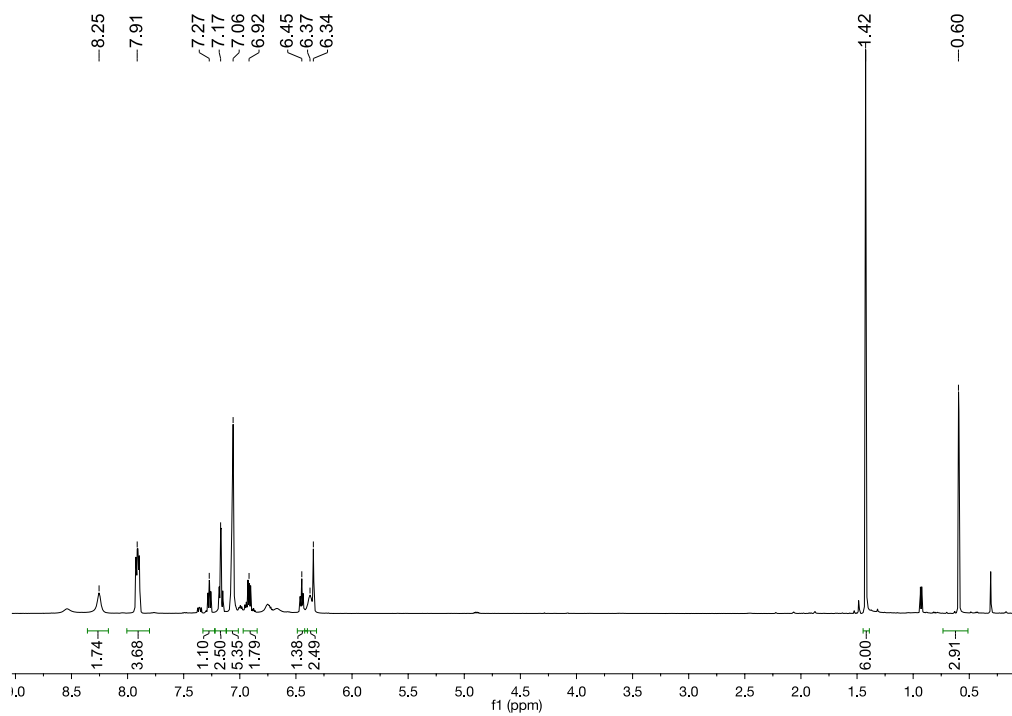


Figure A.29.  $^1\text{H}$  NMR spectrum of **2-3** (599 MHz,  $\text{C}_6\text{D}_6$ ).

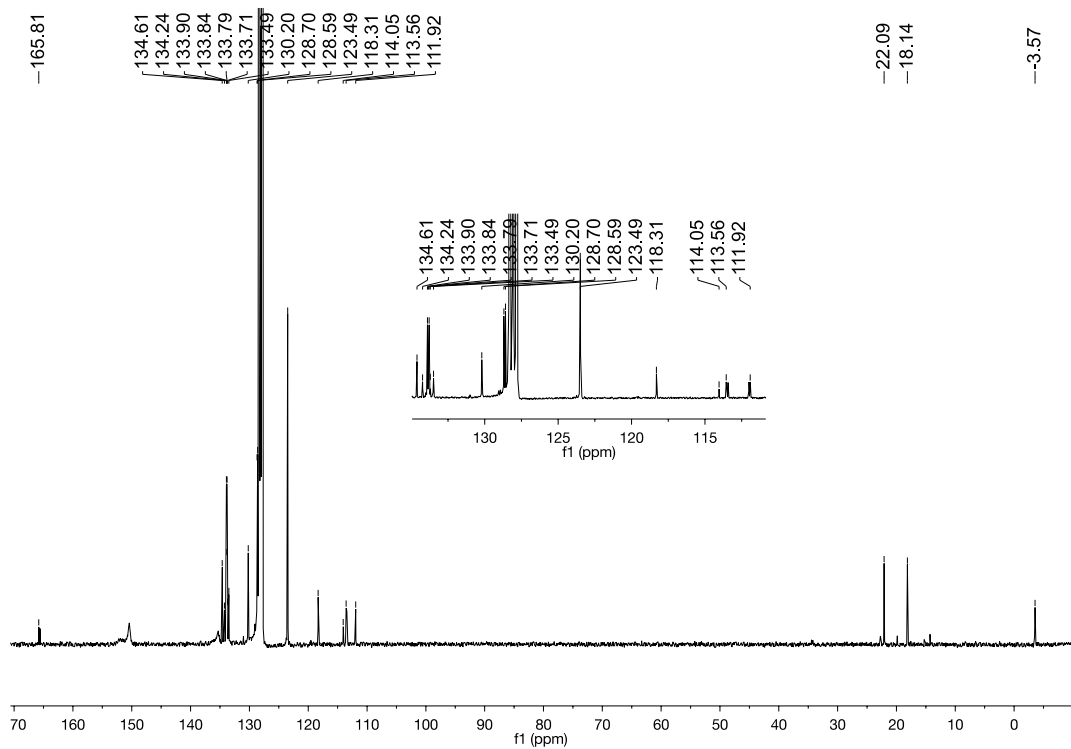


Figure A.30.  $^{13}\text{C}\{^1\text{H}\}$  NMR spectrum of **2-3** (599 MHz,  $\text{C}_6\text{D}_6$ ).

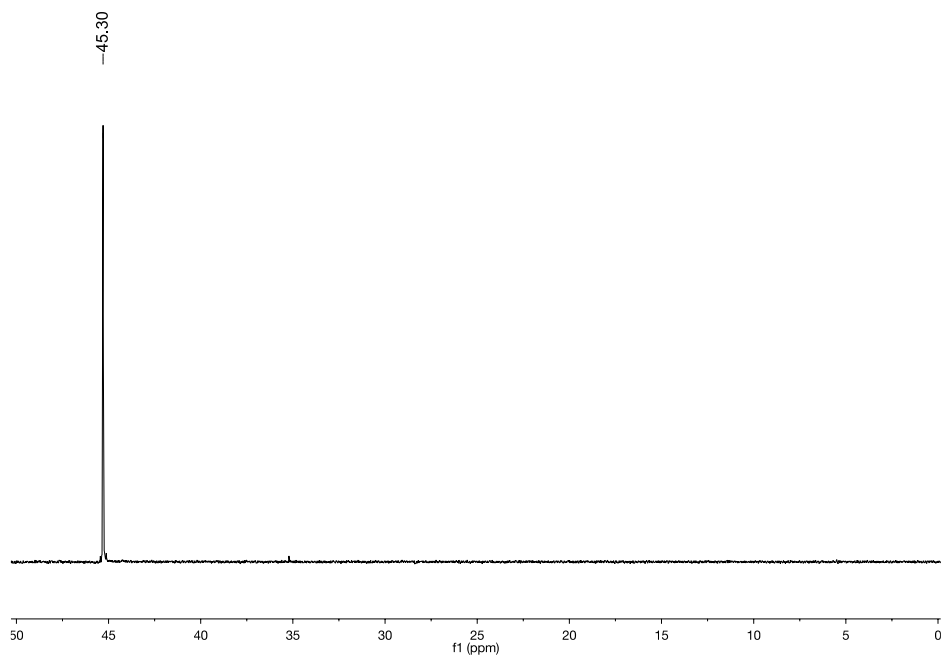
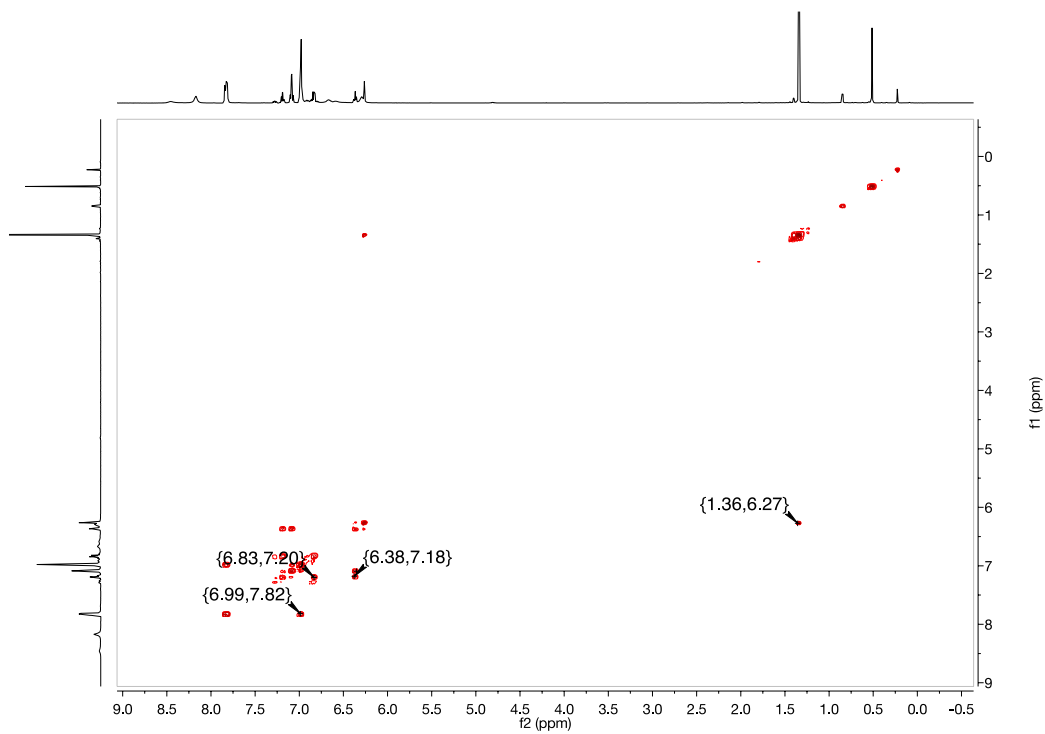
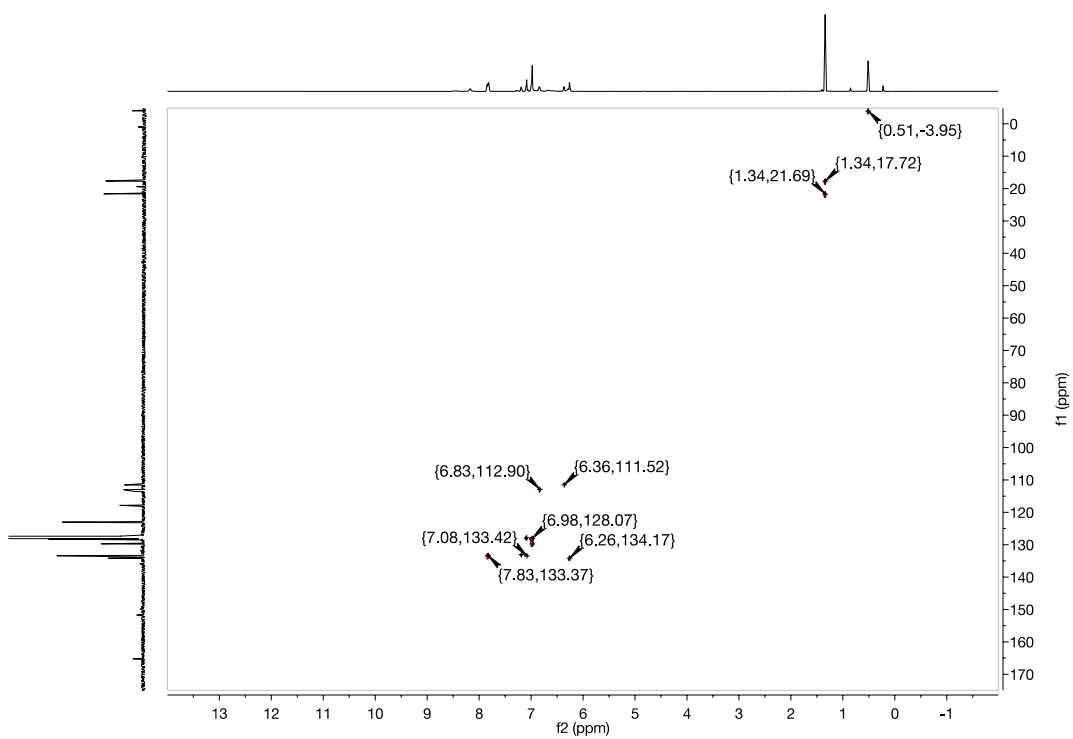


Figure A.31.  $^{31}\text{P}\{^1\text{H}\}$  NMR spectrum of **2-3** (599 MHz,  $\text{C}_6\text{D}_6$ )

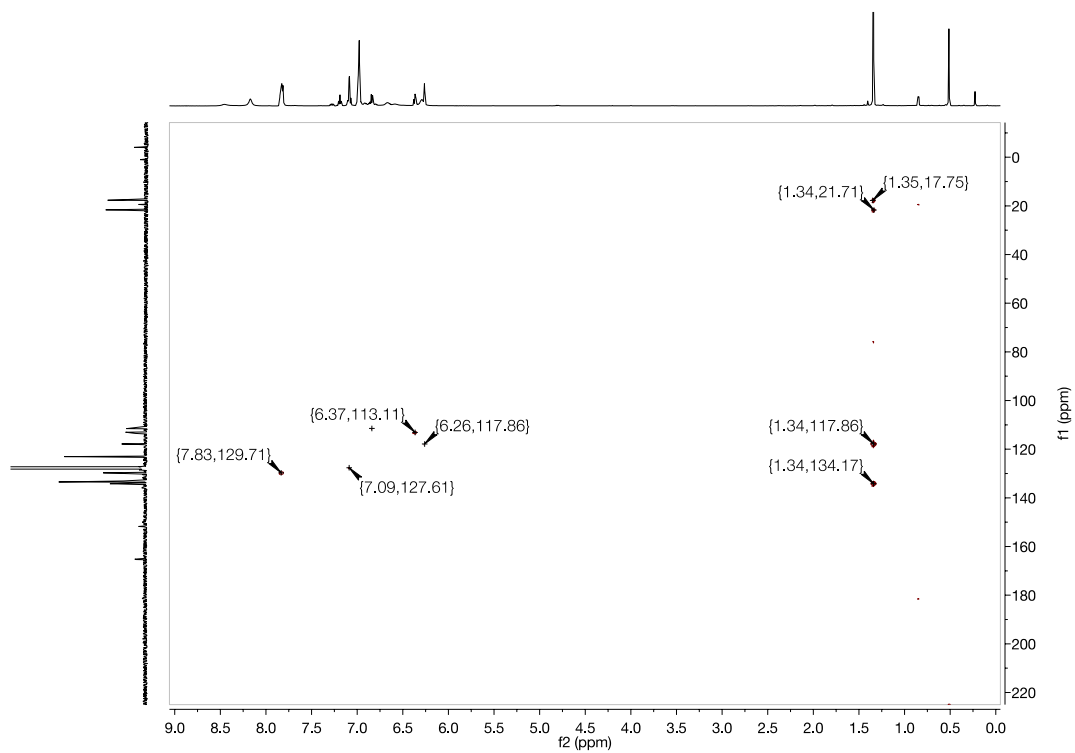


**Figure A.32.**  $^1\text{H}$ - $^1\text{H}$  COSY NMR spectrum of **2-3** (599 MHz,  $\text{C}_6\text{D}_6$ ).

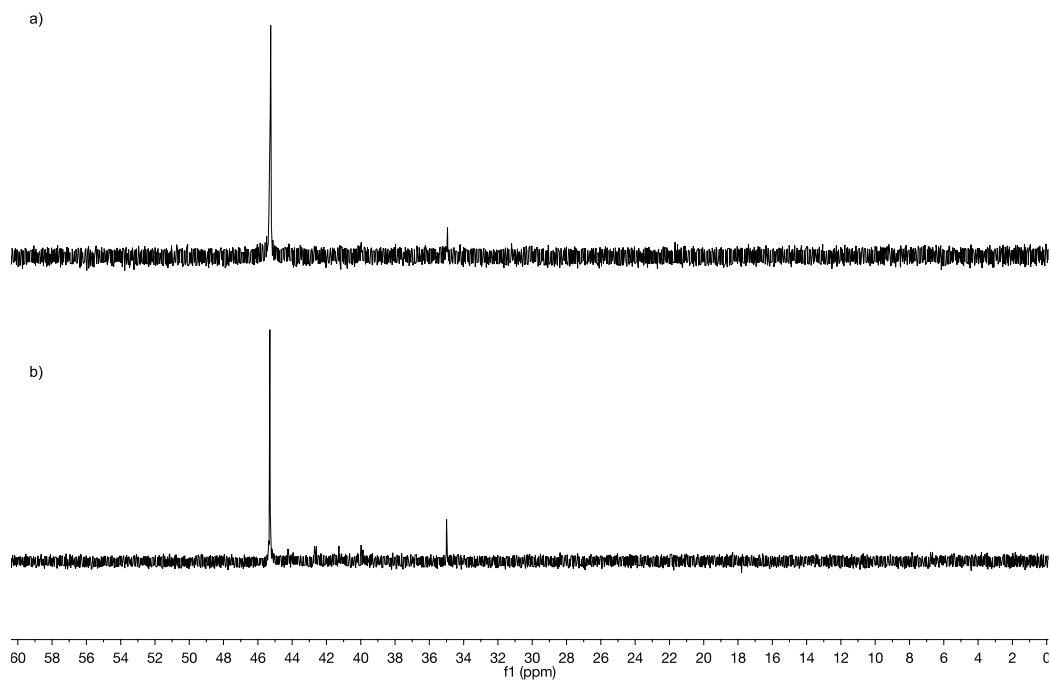


**Figure A.33.**  $^1\text{H}$ - $^{13}\text{C}$  HSQC NMR spectrum **2-3** (599 MHz,  $\text{C}_6\text{D}_6$ ).

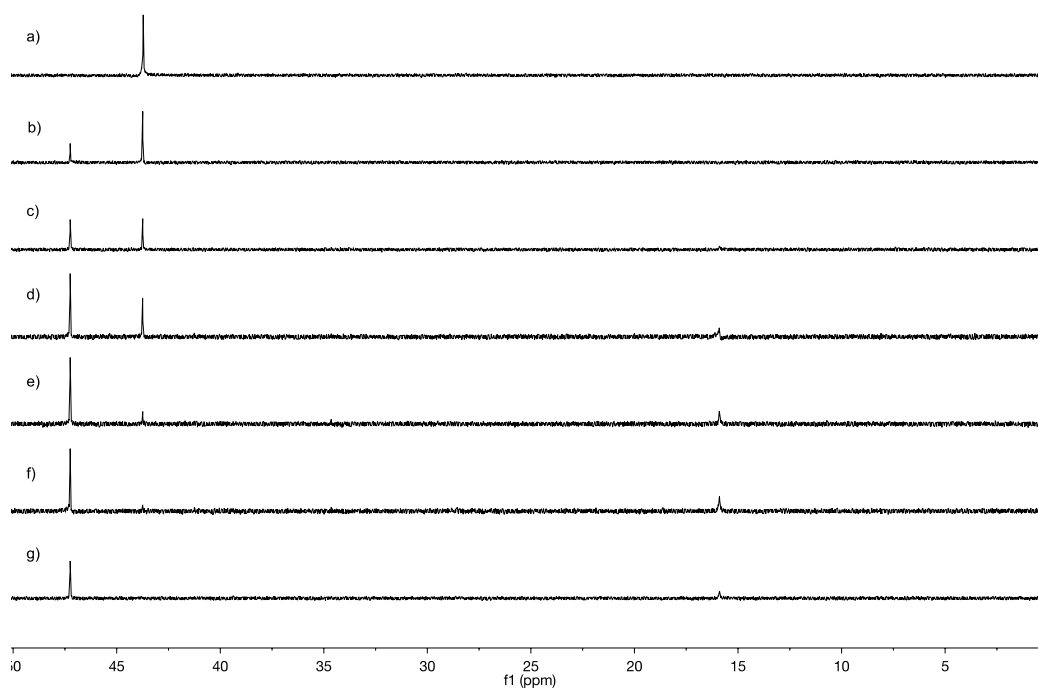




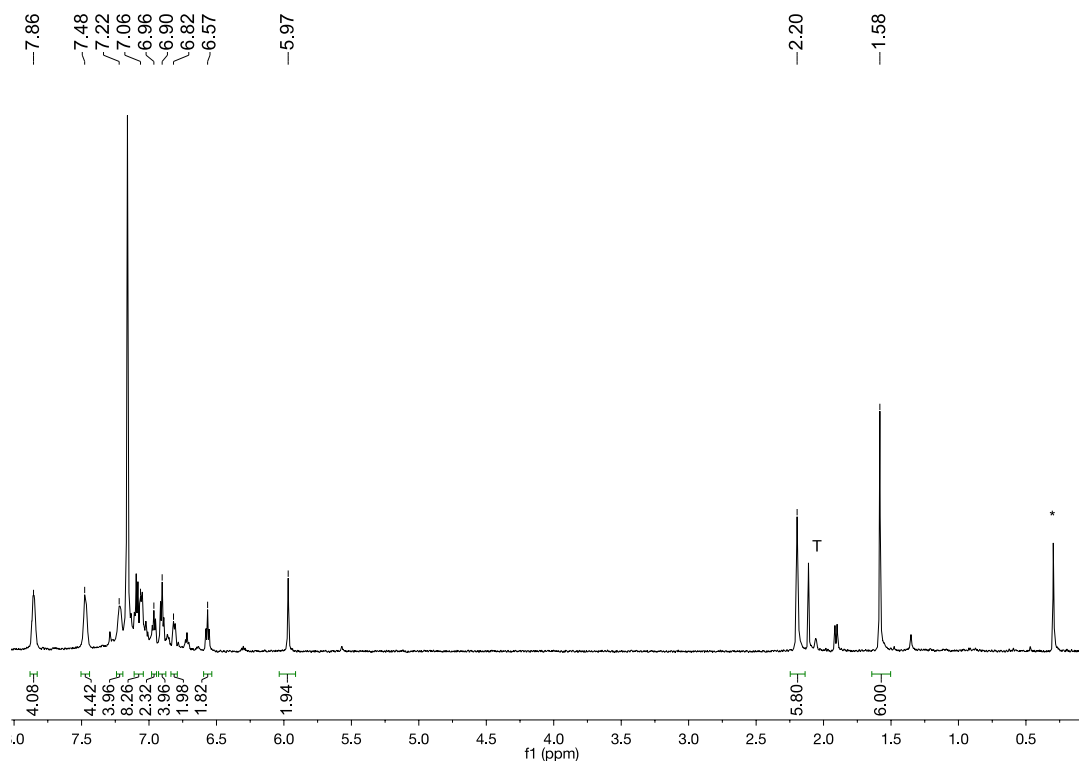
**Figure A.34.**  $^1\text{H}$ - $^{13}\text{C}$  HMBC NMR spectrum **2-3** (599 MHz,  $\text{C}_6\text{D}_6$ ).



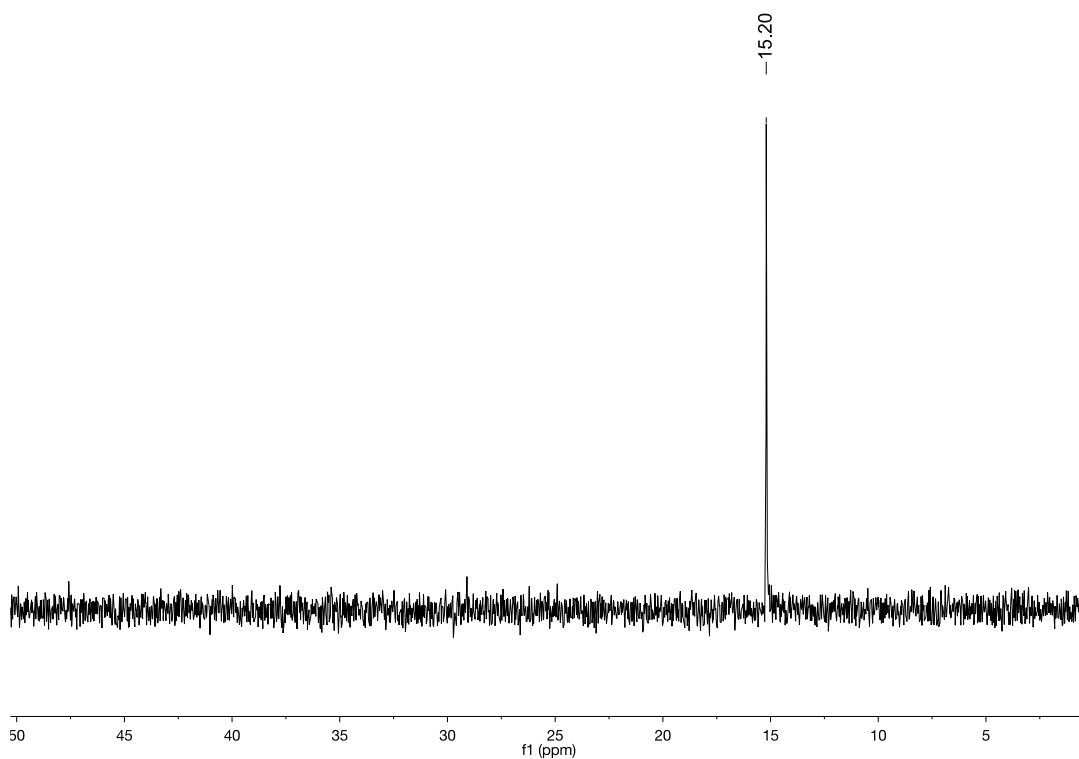
**Figure A.35.**  $^{31}\text{P}\{^1\text{H}\}$  NMR spectrum of **2-3** upon heating at  $70^\circ\text{C}$  for a) 0 h and b) 7 h (243 MHz,  $\text{C}_6\text{D}_6$ ).



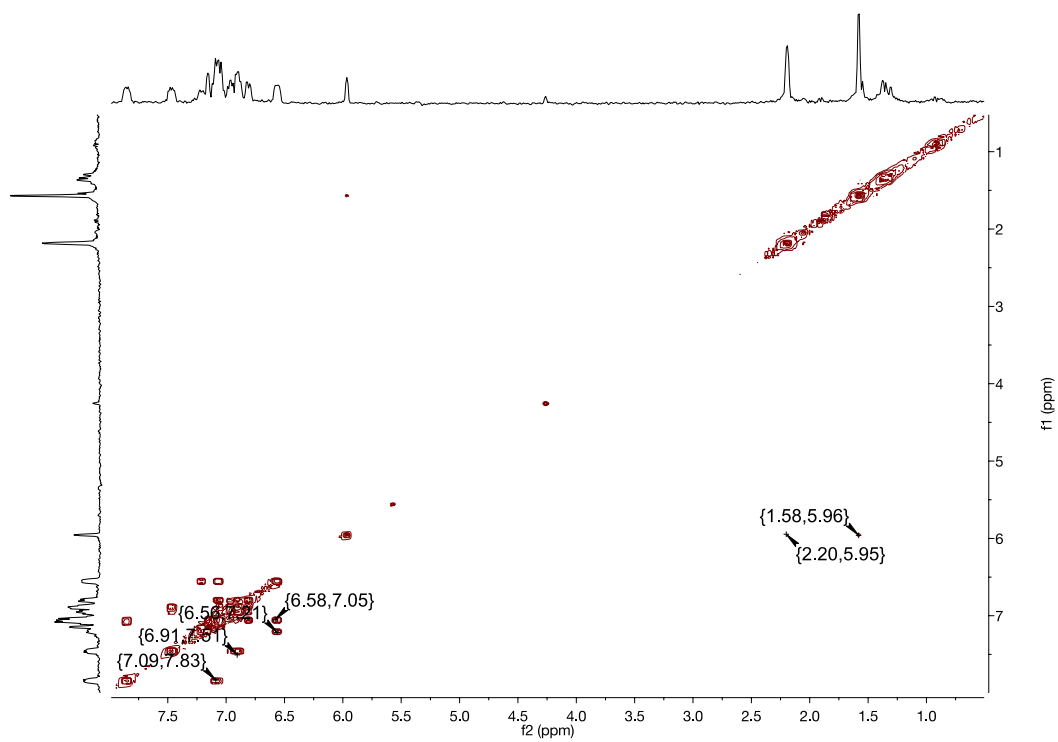
**Figure A.36.**  $^{31}\text{P}\{^1\text{H}\}$  NMR spectra obtained of **2-3** at a) 25 °C; and heating to 70 °C in the NMR spectrometer after: b) 5 min. c) 30 min. d) 60 min. e) 120 min. f) 150 min. g) 180 min (243 MHz,  $\text{C}_6\text{D}_6$ ). The product signals are assigned to **2-4** (15 ppm) and **2-5** (47.7 ppm).



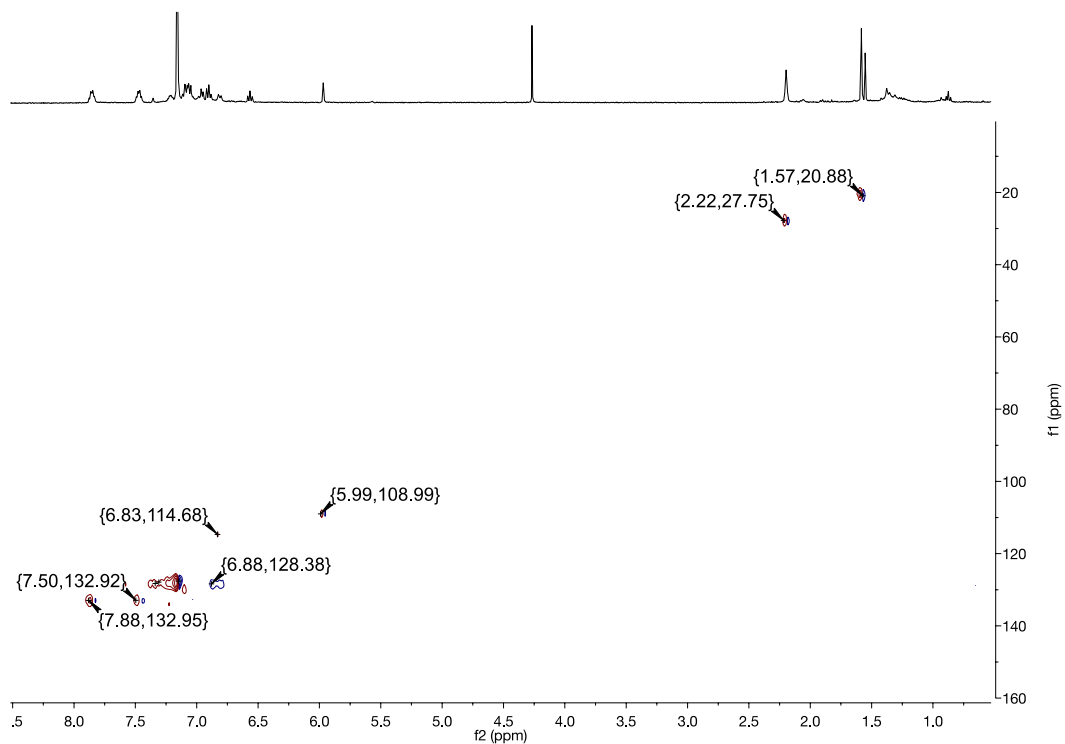
**Figure A.37.**  $^1\text{H}$  NMR spectrum of **2-4** (400 MHz,  $\text{C}_6\text{D}_6$ ). \* Denotes silicon grease. T denotes toluene.



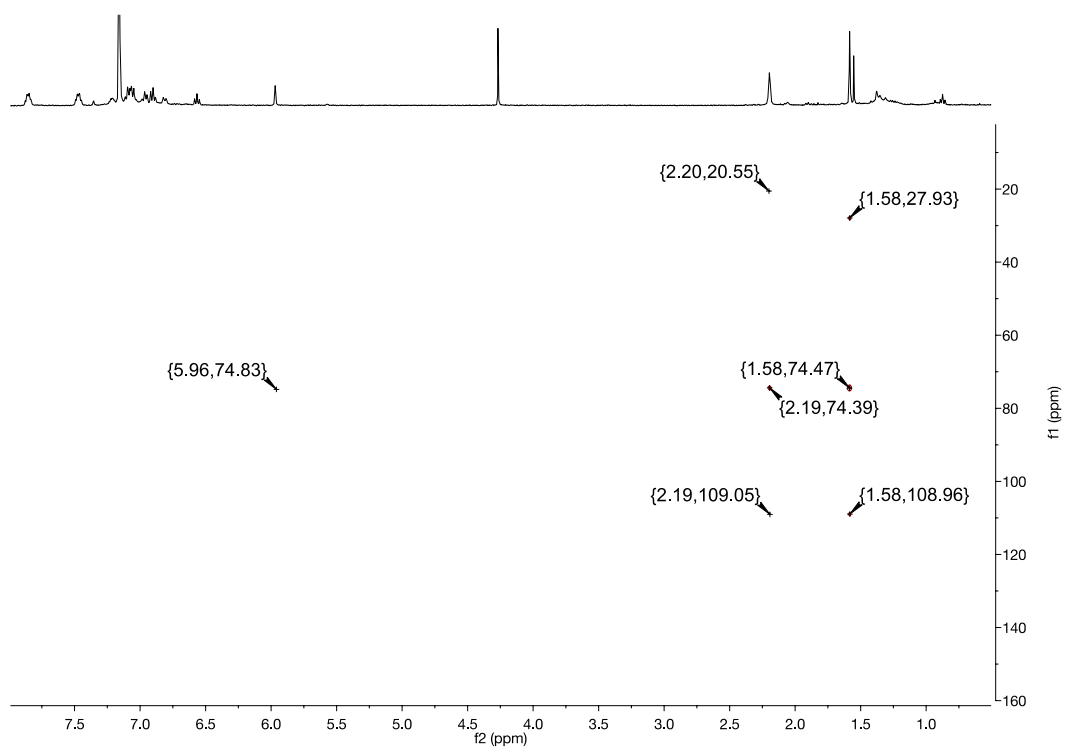
**Figure A.38.**  $^{31}\text{P}\{^1\text{H}\}$  NMR spectrum of **2-4** (243 MHz,  $\text{C}_6\text{D}_6$ ).



**Figure A.39.**  $^1\text{H}\text{-}^1\text{H}$  COSY NMR spectrum of **2-4** (400 MHz,  $\text{C}_6\text{D}_6$ ).



**Figure A.40.**  $^1\text{H}$ - $^{13}\text{C}$  HSQC NMR spectrum of **2-4** (151 MHz,  $\text{C}_6\text{D}_6$ ).



**Figure A.41.**  $^1\text{H}$ - $^{13}\text{C}$  HMBC NMR spectrum of **2-4** (151 MHz,  $\text{C}_6\text{D}_6$ ).

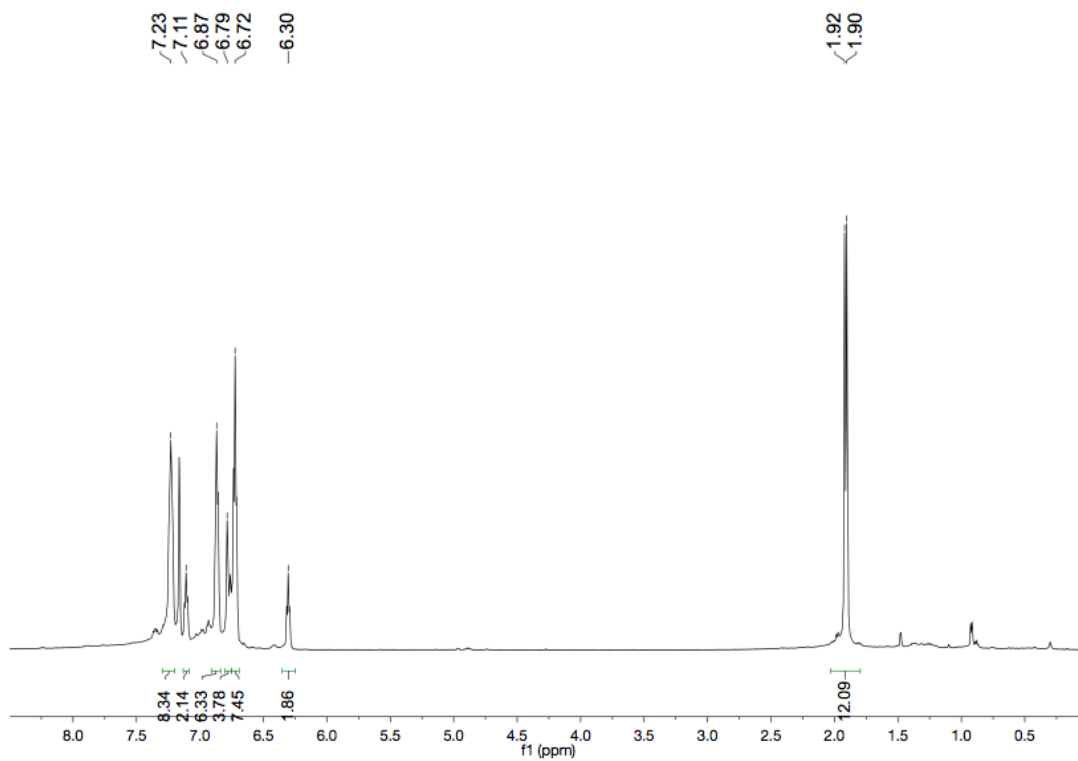


Figure A.42.  $^1\text{H}$  NMR spectrum of **2-5** (599 MHz,  $\text{C}_6\text{D}_6$ ).

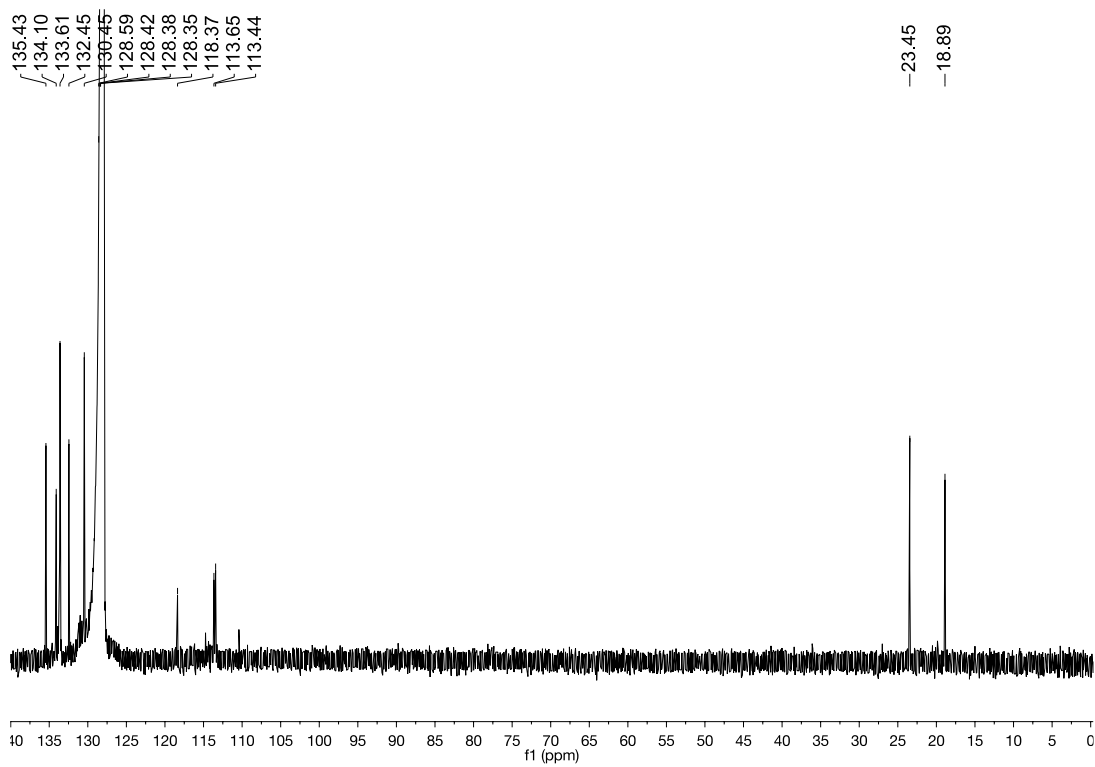
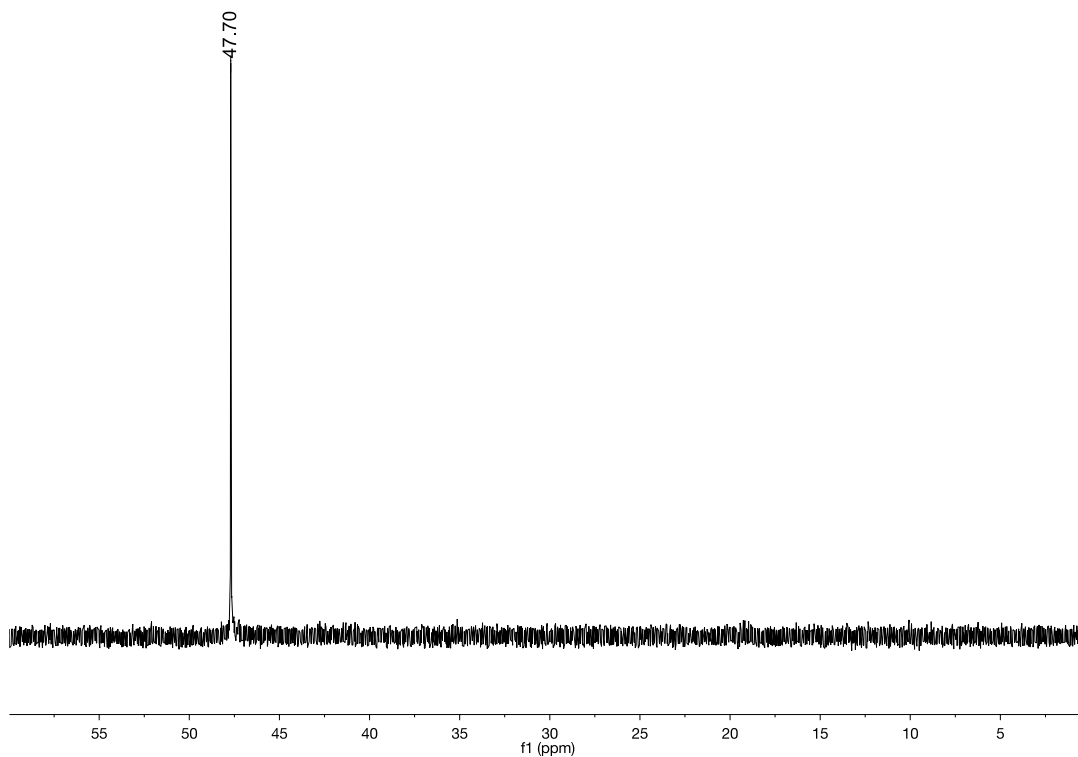
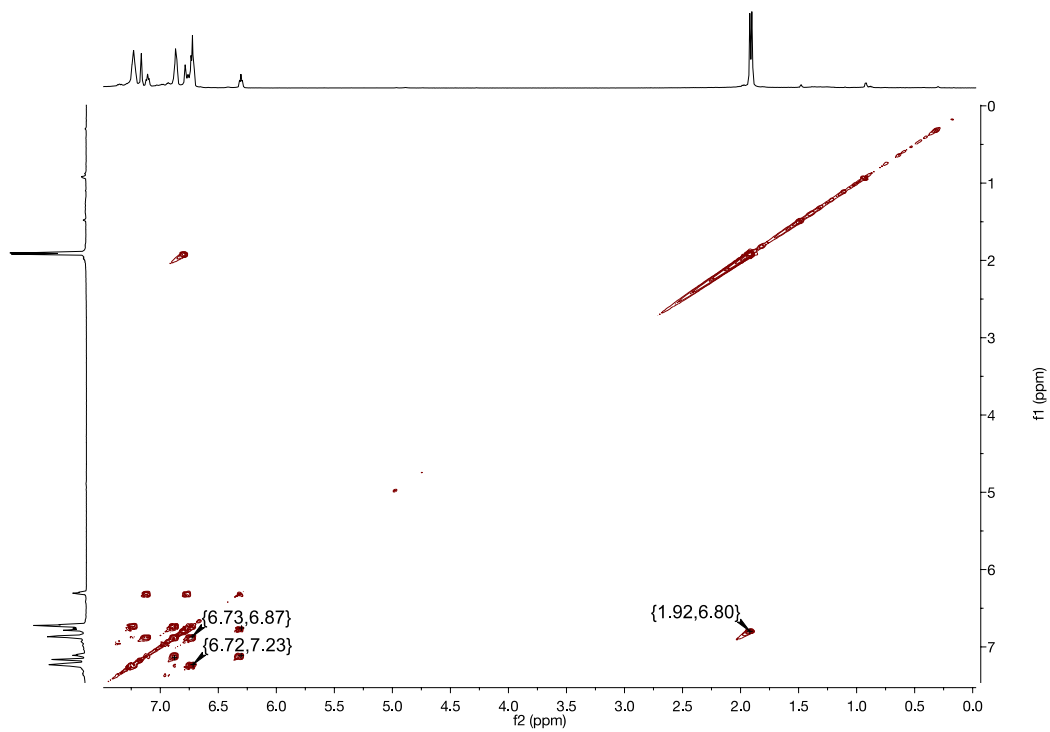


Figure A.43.  $^{13}\text{C}\{^1\text{H}\}$  NMR spectrum of **2-5** (151 MHz,  $\text{C}_6\text{D}_6$ ).



**Figure A.44.**  $^{31}\text{P}\{^1\text{H}\}$  NMR spectrum of **2-5** (243 MHz,  $\text{C}_6\text{D}_6$ ).



**Figure A.45.**  $^1\text{H}$ - $^1\text{H}$  COSY NMR spectrum of **2-5** (599 MHz,  $\text{C}_6\text{D}_6$ ).

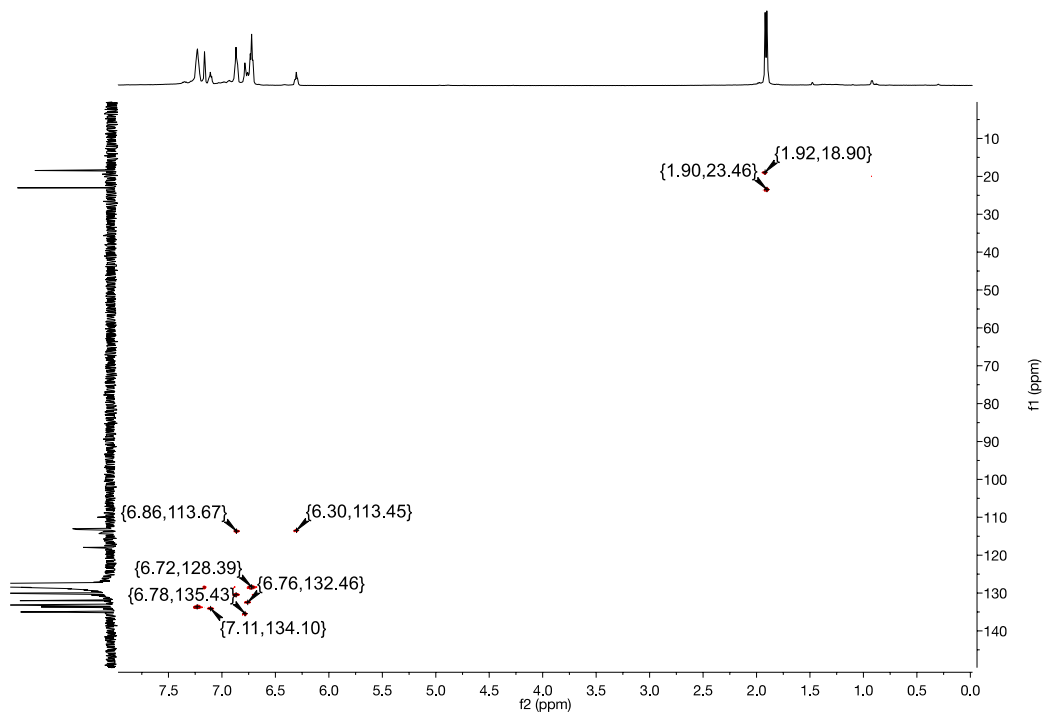


Figure A.46.  $^1\text{H}$ - $^{13}\text{C}$  HSQC NMR spectrum of **2-5** (599 MHz  $\text{C}_6\text{D}_6$ ).

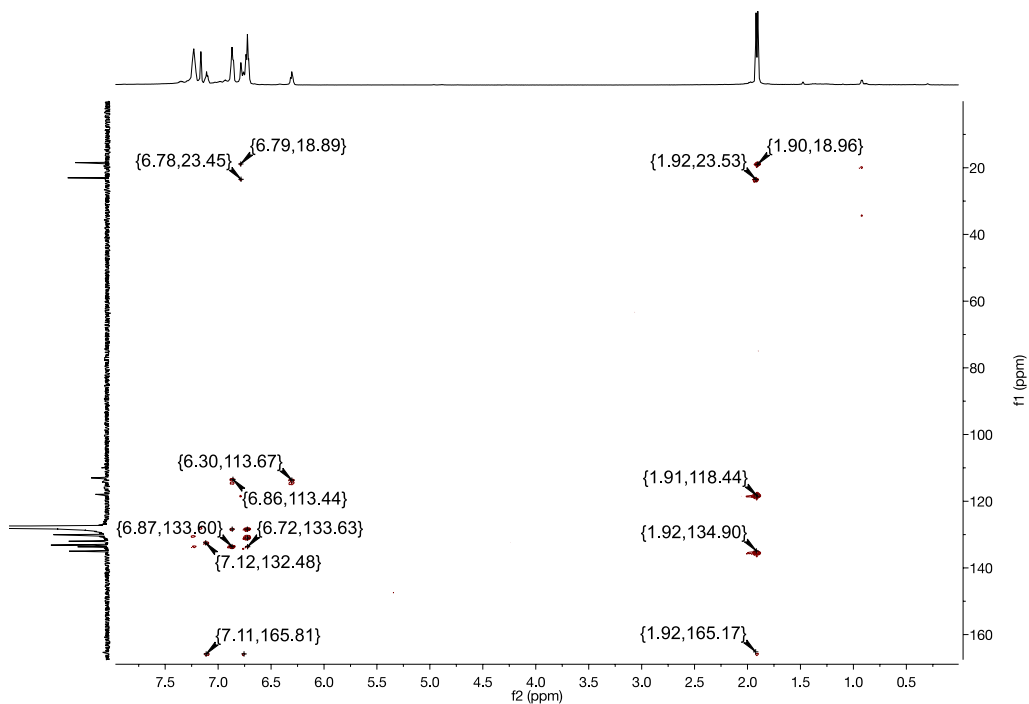


Figure A.47.  $^1\text{H}$ - $^{13}\text{C}$  HMBC NMR spectrum of **2-5** (599 MHz,  $\text{C}_6\text{D}_6$ ).

### III – IR Spectra

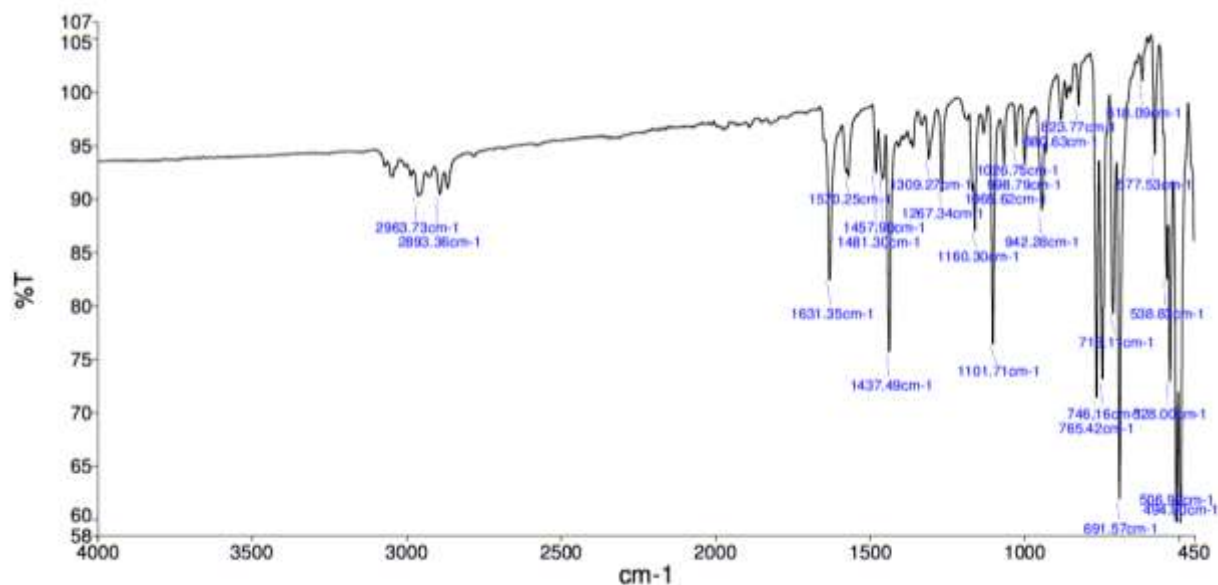
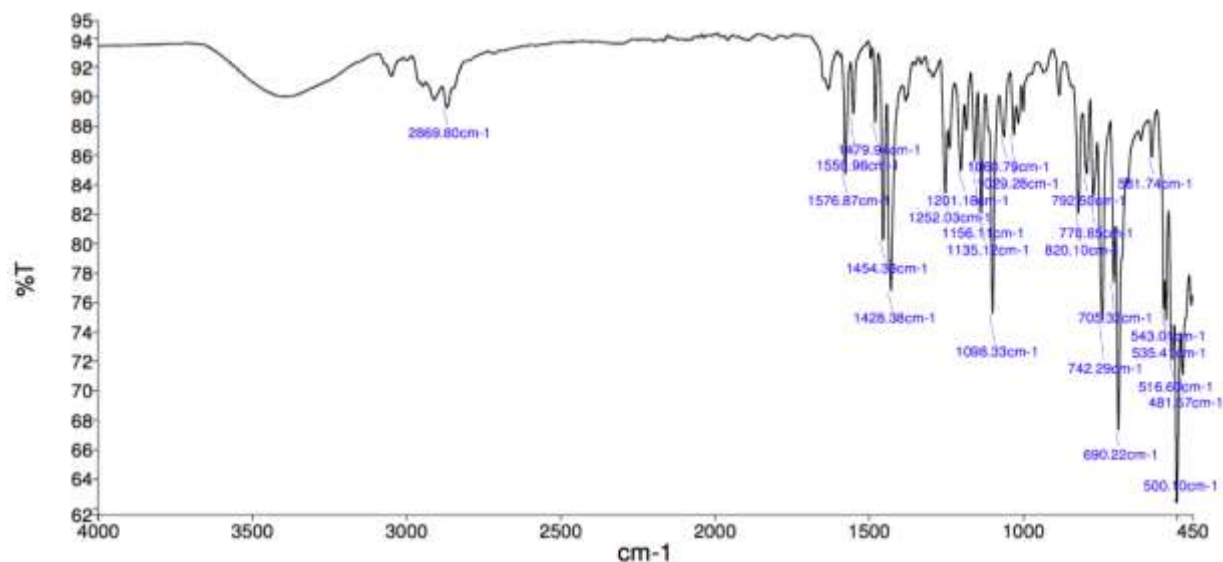


Figure A.48. ATR-FTIR spectrum of solid 2-1.



**Figure A.49.** ATR-FTIR spectrum of solid 2-2. Note that the broad signal at ca. 3400 cm<sup>-1</sup> is likely due to coordination of atmospheric H<sub>2</sub>O that ligates to the open coordination site of 2-2 due to the affinity of the complex for a ligand forming a water adduct with 2-2.



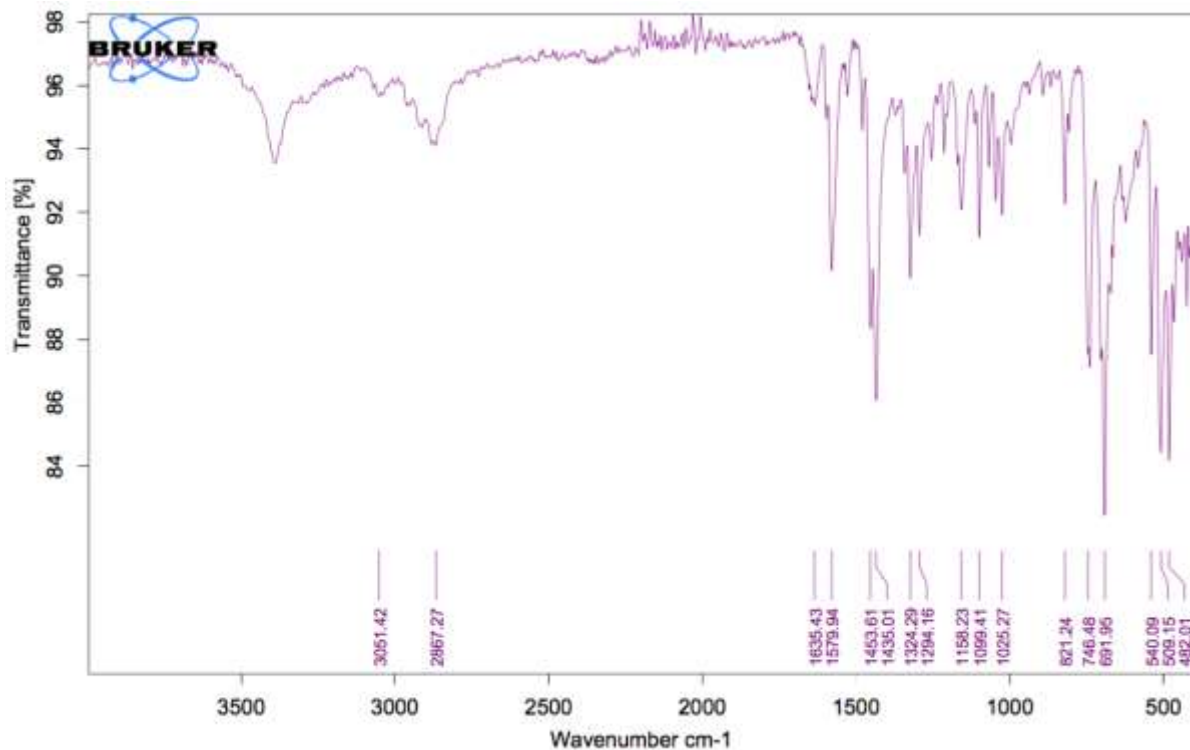


Figure A.50. ATR-FTIR spectrum of solid 2-3.

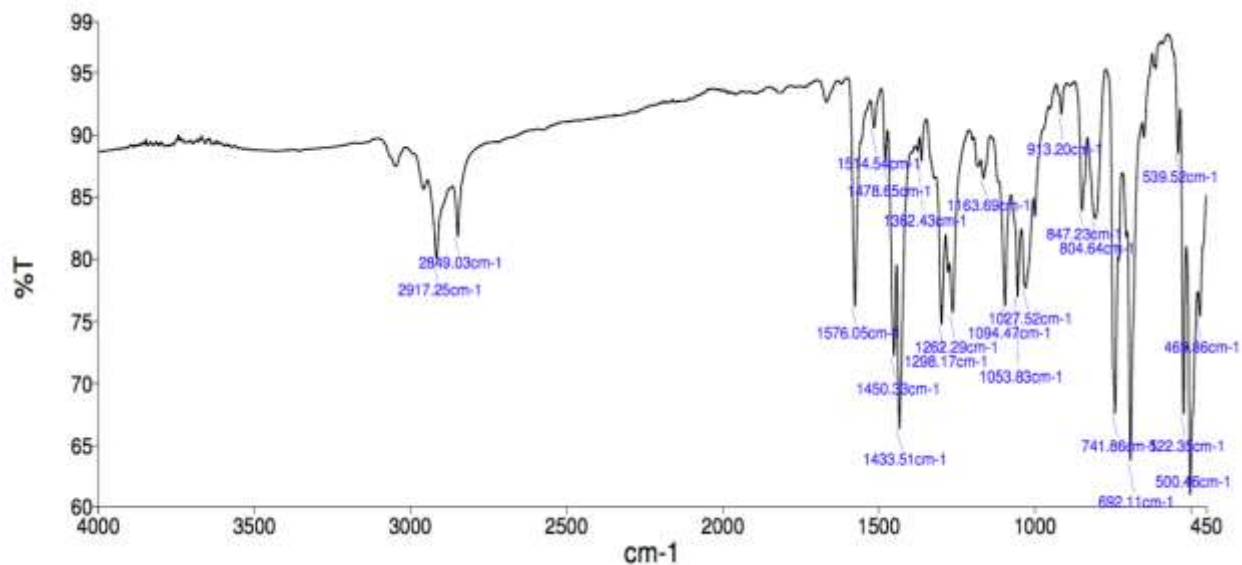


Figure A.51. ATR-FTIR spectrum of solid 2-4.

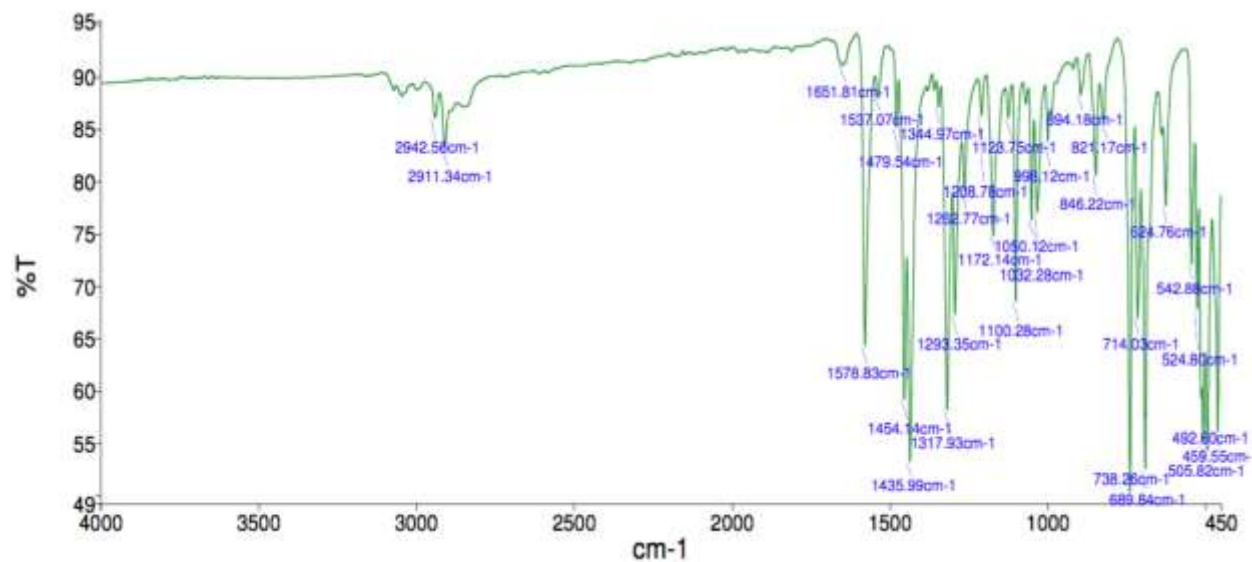


Figure A.52. ATR-FTIR spectrum of solid 2-5.

#### IV – MALDI Mass Spectrometry Data

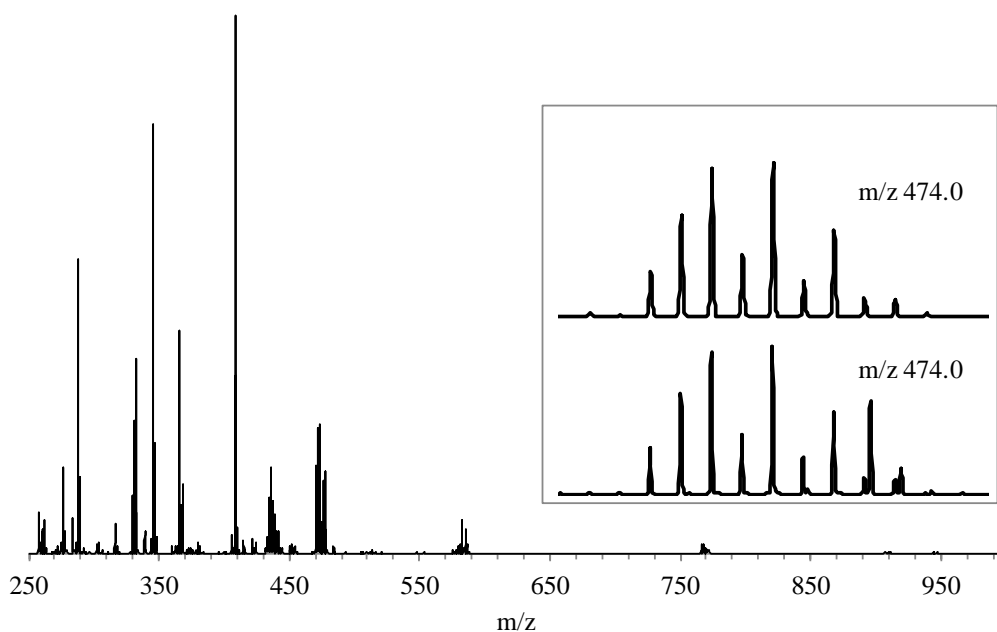
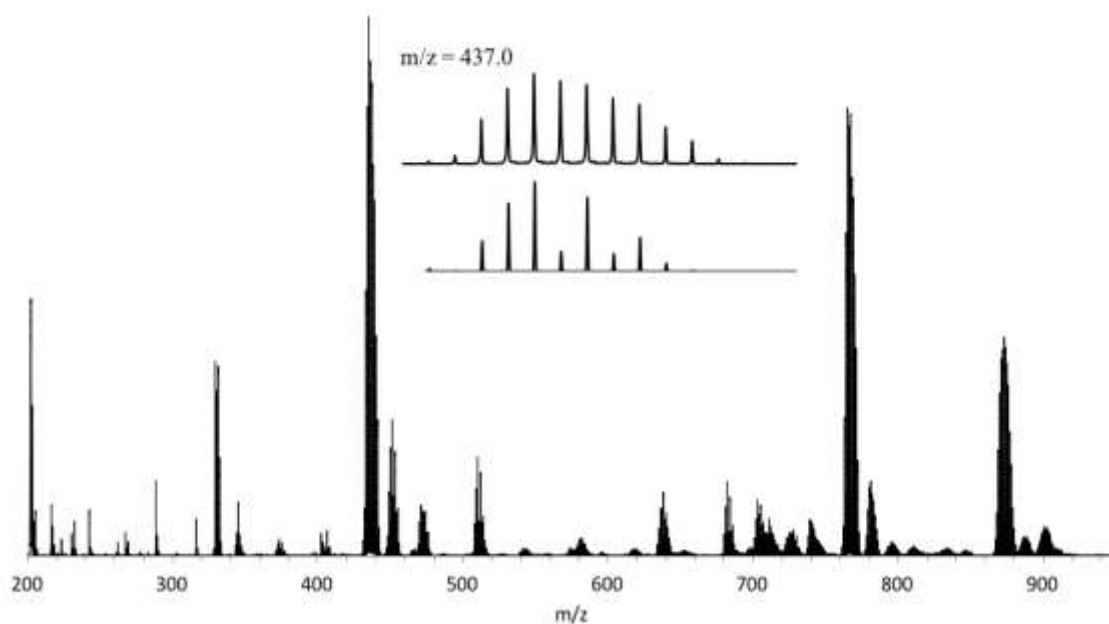
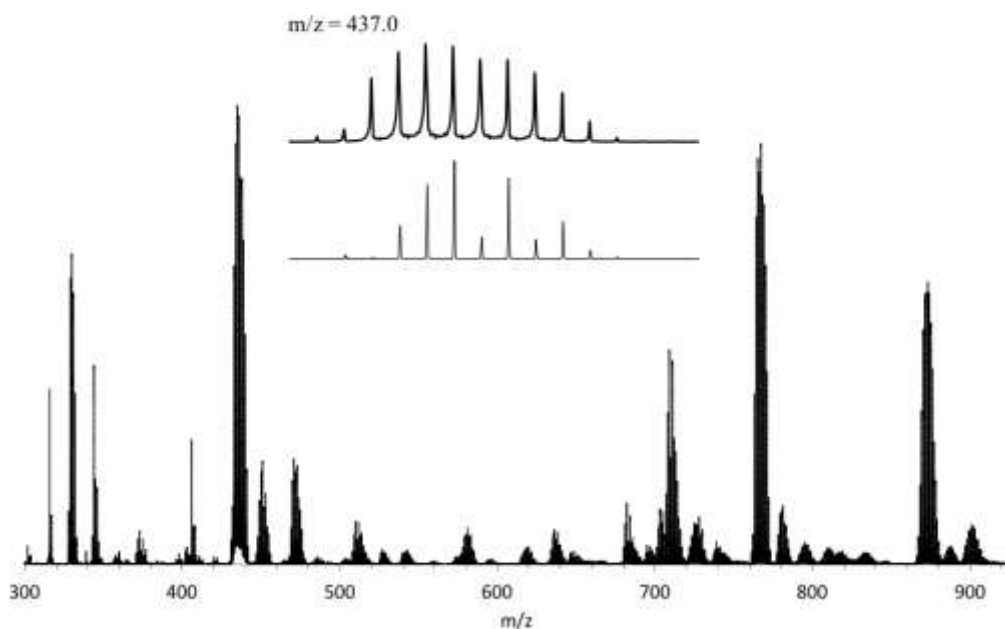


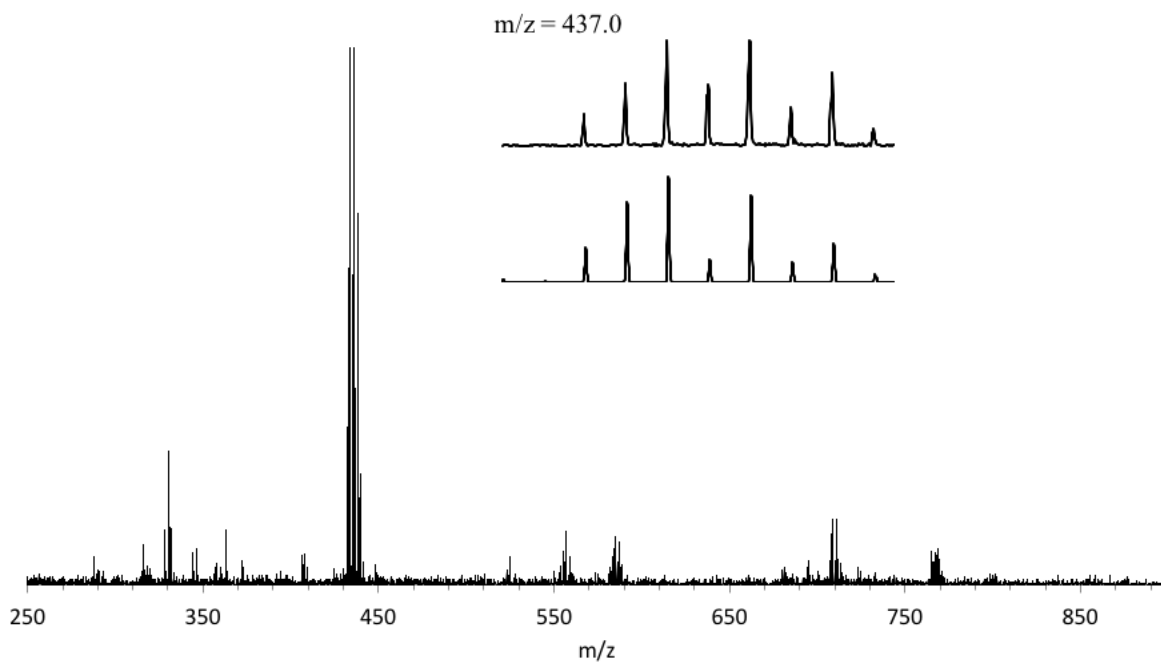
Figure A.53. MALDI mass spectrum of 2-1 with pyrene as the matrix. Inset simulation<sup>2</sup> pattern (top) for [2-1-CH<sub>3</sub>]<sup>++</sup> and observed (bottom) signal at m/z 474.0.



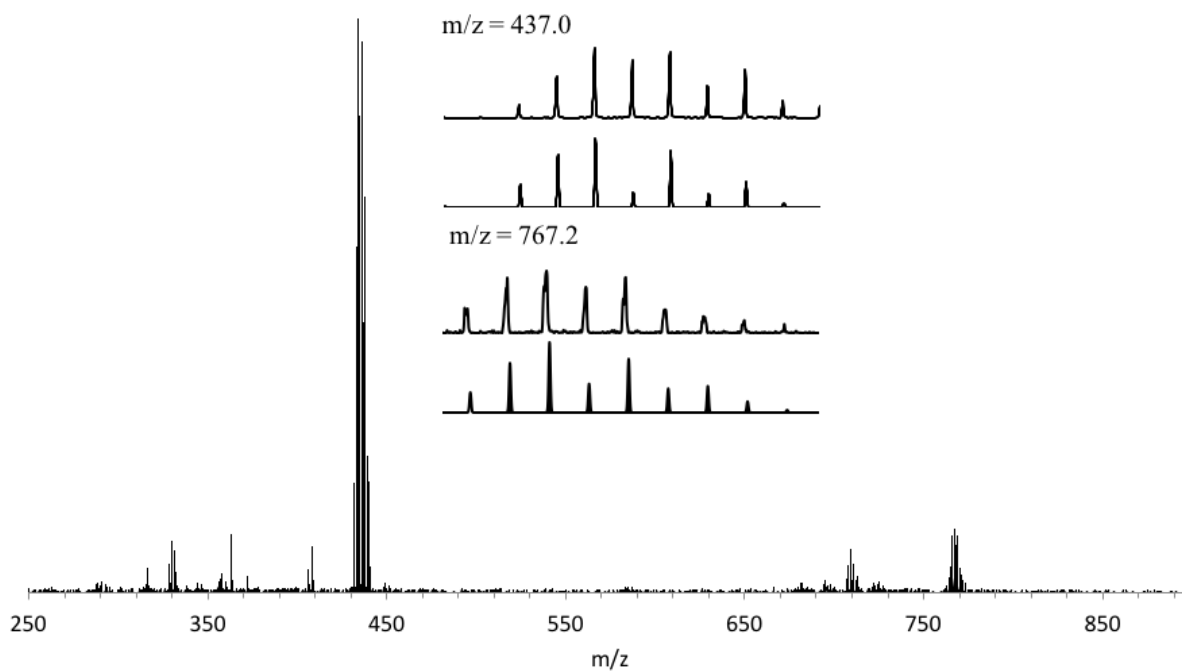
**Figure A.54.** MALDI-MS analysis of **2-2** with a pyrene matrix. Inset simulation<sup>2</sup> (bottom), and observed (top) for  $[\text{Pd}(\mathbf{2-L1})]^{+}$   $m/z = 437.0$ . Additional major signals, likely due to gas phase aggregation/fragmentation are:  $m/z = 873.0$ ,  $[\text{Pd}_2(\mathbf{2-L1})_2]^{+}$ ;  $m/z = 763.0$ ,  $[\text{Pd}_2(\text{C}_{18}\text{H}_{14}\text{NP})_2]^{+}$



**Figure A.55.** MALDI-MS analysis of **2-3** with a pyrene matrix. Inset simulation<sup>2</sup> (bottom), and observed (top) for  $[\text{Pd}(\mathbf{2-L1})]^{+}$   $m/z = 437.0$ . Additional major signals, likely due to gas phase aggregation/fragmentation are:  $m/z = 873.0$ ,  $[\text{Pd}_2(\mathbf{2-L1})_2]^{+}$ ;  $m/z = 767.2$ ,  $[\text{Pd}_2(\text{C}_{18}\text{H}_{14}\text{NP})_2]^{+}$ .



**Figure A.56.** MALDI-MS analysis of **2-4** with a pyrene matrix. Inset simulation<sup>2</sup> (bottom) and observed (top) for  $[Pd(2-L1)]^+$   $m/z = 437.0$ .



**Figure A.57.** MALDI-MS analysis of **2-5** with a pyrene matrix. Inset simulation<sup>4</sup> (bottom) and observed (top) for  $[Pd(2-L1)]^+$   $m/z = 437.0$ .  $[Pd(2-L1)_2]^+$   $m/z = 767.1$ .

## V – Crystallographic Details

*Data Collection and Processing.* Samples of **2-1**, **2-2**, **2-4** and **2-5** were each mounted on a Mitegen polyimide micromount with a small amount of Paratone N oil. All X-ray measurements were made on a Bruker Kappa Axis Apex2 diffractometer at a temperature of 110 K. The unit cell dimensions were determined from a symmetry-constrained fit with reflections and dimensions listed in Table S3. The data collection strategy was a number of  $\omega$  and  $\phi$  scans which collected data up to  $2\theta_{\max}$  as listed in Table S3. The frame integration was performed using SAINT.<sup>3</sup> The resulting raw data was scaled and absorption corrected using a multi-scan averaging of symmetry equivalent data using SADABS<sup>4</sup> for **2-1** and **2-5** and TWINABS<sup>5</sup> for **2-4**.

*Twinning.* During the course of the structure analysis of **2-4**, the refinement displayed symptoms of mild twinning. The TwinRotMat function in PLATON<sup>6,7</sup> indicated there was some twinning (approximately in a 90:10 ratio for the scattering volumes) and proposed a possible twin law. As a consequence, reflections were re-harvested from the original frame data and indexed using CELL\_NOW<sup>8</sup> to yield the same twin law as had been suggested in the output of PLATON. The twin operation was an approximately 180° rotation about the  $b^*$  axis and yielded the following twin law:

```
-0.99994 -0.00100 0.00229  
-0.56192 0.99865 -0.40477  
-0.00200 -0.00528 -0.99870
```

The data were re-integrated using this 2-component twin model.

*General Structure Solution and Refinement.* The structures of **2-1**, **2-2**, **2-4** and **2-5** were solved by using a dual space methodology using the SHELXT program.<sup>9</sup> All non-hydrogen atoms were obtained from the initial solution. The hydrogen atoms were introduced at idealized positions and were allowed to ride on the parent atom. The structural model was fit to the data using full matrix least-squares based on  $F^2$ . The calculated structure factors for **2-2** included corrections for anomalous dispersion from the usual tabulation. The structures were refined using the SHELXL-2014 program from the SHELXTL suite of crystallographic software.<sup>9</sup> Graphic plots were produced using the NRCVAX program suite<sup>10</sup> or the SHELXL XP program suite.<sup>9</sup>

*Additional Structure Solution and Refinement Information for 2-1.* The asymmetric unit contains two symmetry independent molecules, designated by the suffixes A and B in the labeling scheme. The calculated structure factors included corrections for anomalous dispersion from the usual tabulation.

*Additional Structure Solution and Refinement Information for 2-4.* The molecule sits across a crystallographic centre of symmetry. Due to the aforementioned twinning, several refinement models were tested: **(A)** disregarding the twinning, **(B)** including the data from the minor twin fraction, and **(C)** using only the data from the major component. The results of the various refinements are tabulated in Table S2.

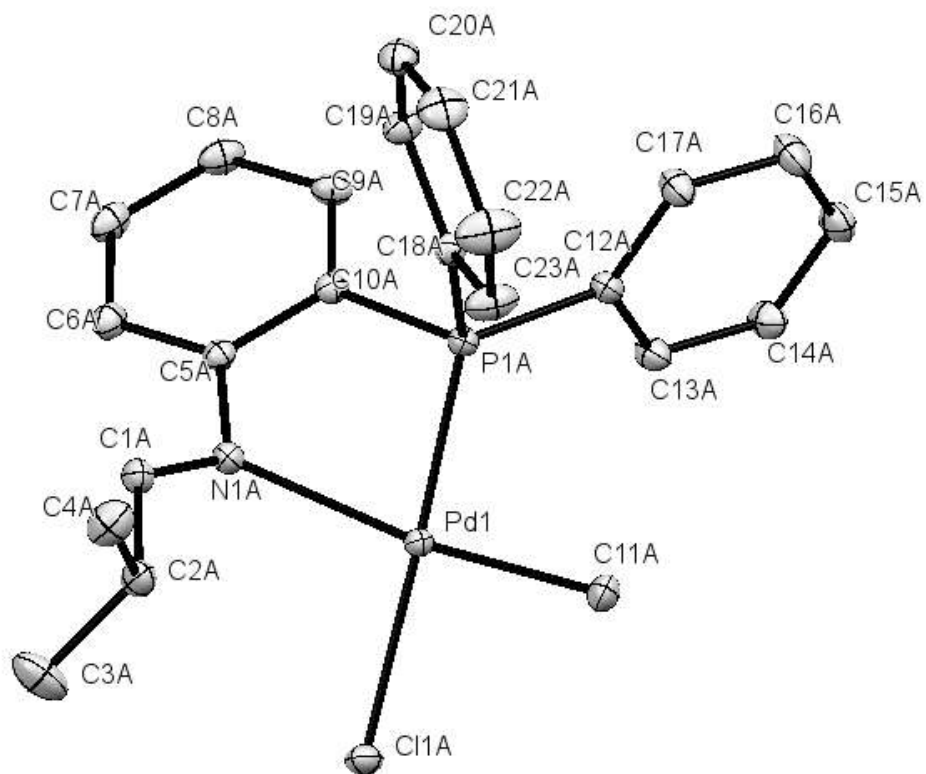
**Table A.2. Refinement Results for 2-4.**

|  | <b>Refinement (A)</b> | <b>Refinement (B)</b> | <b>Refinement (C)</b> |
|--|-----------------------|-----------------------|-----------------------|
| wR2, R1  | 0.1313, 0.0571        | 0.1364, 0.0561        | 0.1020, 0.0504        |
| Max, min, peaks in final $\Delta F$ map ( $e/\text{\AA}^3$ ) | 2.114, -1.556         | 2.565, -2.520         | 0.996, -1.575         |
| SHELX weight parameters $a$ and $b$                          | 0.0218, 5.145         | 0.0596, 0.1644        | 0.0502, 0.0000        |

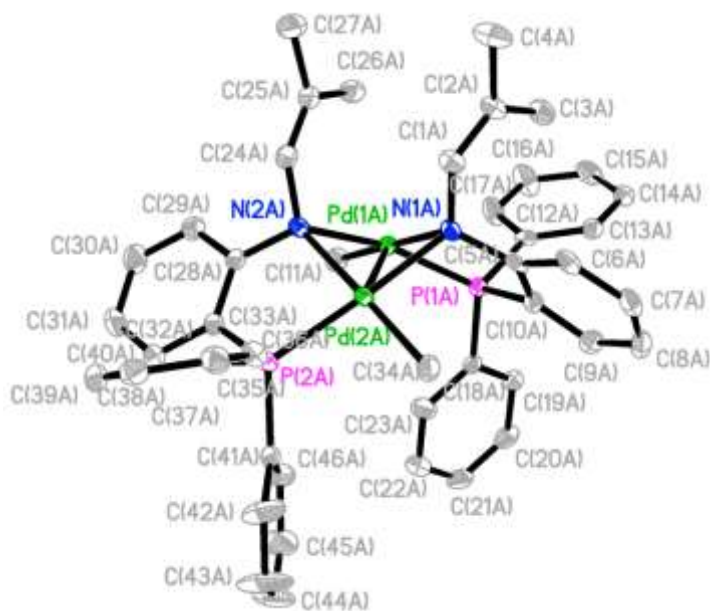
For refinement **(B)**, the twin fraction refined to a value of 0.0876(4). Refinement **(C)** was used in all subsequent refinements.

*Final Refinements for 2-4.* The calculated structure factors included corrections for anomalous dispersion from the usual tabulation.

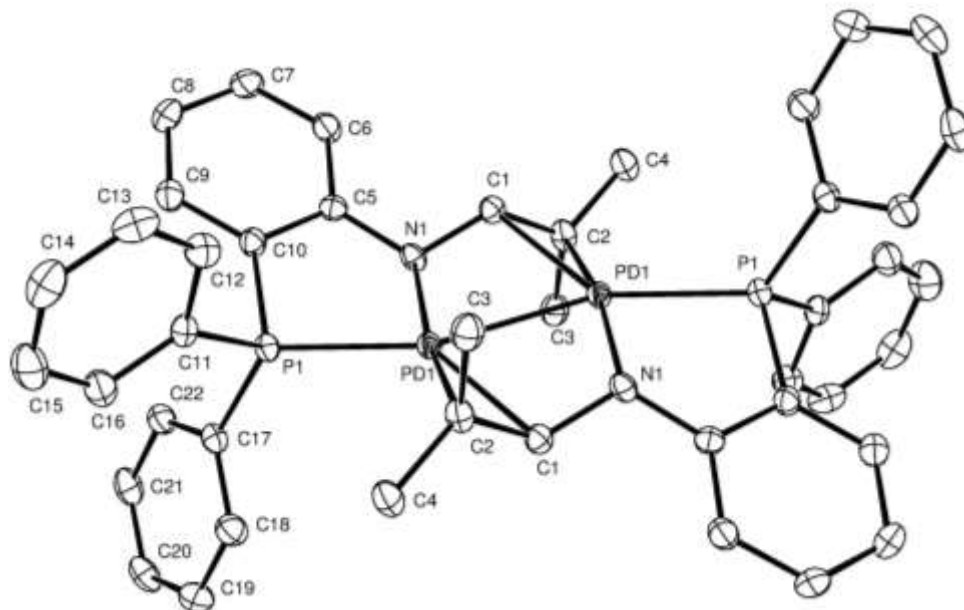
*Additional Structure Solution and Refinement Information for 2-5.* Analysis of the data by the TwinRotMat routine in PLATON<sup>6,7</sup> indicated that there was some slight twinning (~6%) present in the sample. Attempts to re-index and reintegrate the data to recover the presumed twin law were unsuccessful. The structure analysis was completed using a single domain model.



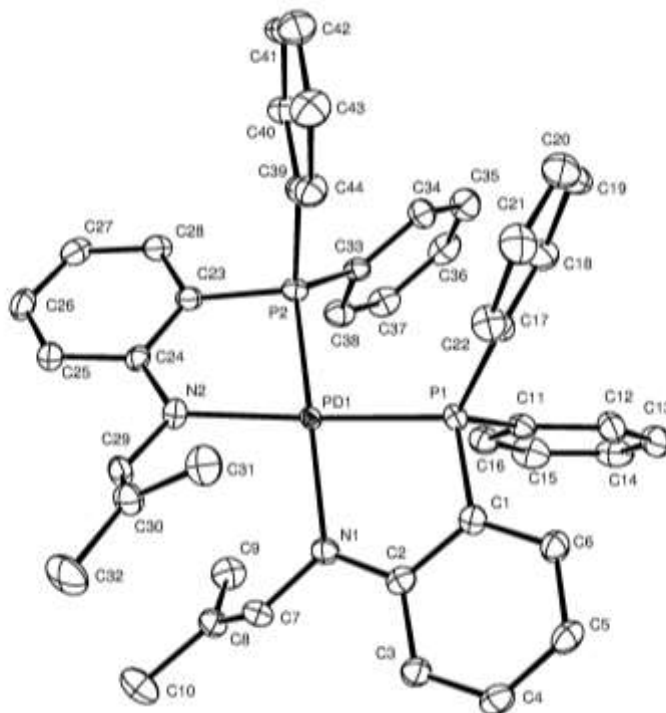
**Figure A.58.** ORTEP drawing of **2-1** showing naming and numbering scheme. Ellipsoids are at the 50% probability level and hydrogen atoms were omitted for clarity.



**Figure A.59.** ORTEP drawing of **2-2** showing naming and numbering scheme. Ellipsoids are at the 50% probability level and hydrogen atoms were omitted for clarity.



**Figure A.60.** ORTEP drawing of **2-4** showing naming and numbering scheme. Ellipsoids are at the 50% probability level and hydrogen atoms were omitted for clarity.



**Figure A.61.** ORTEP drawing of **2-5** showing naming and numbering scheme. Ellipsoids are at the 50% probability level and hydrogen atoms were omitted for clarity.



**Table A.3. Summary of Crystal Data for 2-1, 2-2, 2-4 and 2-5.**

| Compound  | 2-1                                    | 2-2   | 2-4   | 2-5  |
|---|--|---|---|--|
| Formula   | C <sub>23</sub> H <sub>25</sub> ClNPPd | C <sub>46</sub> H <sub>48</sub> N <sub>2</sub> P <sub>2</sub> Pd <sub>2</sub> | C <sub>44</sub> H <sub>42</sub> N <sub>2</sub> P <sub>2</sub> Pd <sub>2</sub> | C <sub>44</sub> H <sub>42</sub> N <sub>2</sub> P <sub>2</sub> Pd |
| CCDC  | 1839629                                | 1873060   | 1839630   | 1839631  |
| Formula Weight<br>( <i>g/mol</i> )                          | 488.26                                 | 903.60  | 873.53  | 767.13   |
| Crystal<br>Dimensions ( <i>mm</i> )                         | 0.335 × 0.212 ×<br>0.134               | 0.312 × 0.223 ×<br>0.114  | 0.153 × 0.048 ×<br>0.032  | 0.229 × 0.127 ×<br>0.027   |
| Crystal Color and<br>Habit                                  | yellow prism                           | yellow prism  | orange prism  | blue plate   |
| Crystal System  | triclinic                              | triclinic   | triclinic   | monoclinic   |
| Space Group   | P -1                                   | P -1  | P -1  | P 2 <sub>1</sub> /c  |
| Temperature, K  | 110                                    | 110   | 110   | 110  |
| <i>a</i> , Å  | 7.5990(14)                             | 10.399(3)   | 8.836(2)  | 15.497(5)  |
| <i>b</i> , Å  | 14.391(2)                              | 17.765(4)   | 9.653(2)  | 13.644(4)  |
| <i>c</i> , Å  | 20.311(5)                              | 22.834(6)   | 11.399(3)   | 17.339(7)  |
| $\alpha$ , °  | 98.33(2)                               | 108.602(8)  | 74.975(10)  | 90   |
| $\beta$ , °   | 99.789(11)                             | 95.082(10)  | 85.166(10)  | 90.055(12)   |
| $\gamma$ , °  | 98.066(12)                             | 91.992(13)  | 73.937(9)   | 90   |
| <i>V</i> , Å <sup>3</sup>                                   | 2134.5(8)                              | 3973.4(18)  | 902.3(4)  | 3666(2)  |
| Number of<br>reflections to<br>determine final<br>unit cell | 9658                                   | 9845  | 8528  | 9837   |
| Min and Max 2θ<br>for cell<br>determination, °              | 6.26, 84.54                            | 5.1, 72.4   | 6.52, 66.02   | 5.98, 59.9   |
| <i>Z</i>  | 4                                      | 4   | 1   | 4  |
| F(000)  | 992                                    | 1840  | 442   | 1584   |
| $\rho$ ( <i>g/cm</i> )                                      | 1.519                                  | 1.510   | 1.608   | 1.390  |
| $\lambda$ , Å, (MoK $\alpha$ )                              | 0.71073                                | 0.71073   | 0.71073   | 0.71073  |
| $\mu$ , ( <i>cm</i> <sup>-1</sup> )                         | 1.077                                  | 1.021   | 1.121   | 0.627  |
| Max 2θ for data<br>collection, °                            | 86.294                                 | 48.498  | 66.462  | 68.762   |
| Measured fraction<br>of data                                | 0.997                                  | 0.999   | 0.994   | 0.998  |

|  |   |   |   |  |
|--|---|---|---|--|
| Number of reflections measured                             | 117657  | 74766   | 6796  | 156935   |
| Unique reflections measured                                | 28206   | 12800   | 6796  | 15129  |
| R <sub>merge</sub>   | 0.0282  | 0.0332  | 0.0760  | 0.0763   |
| Number of reflections included in refinement               | 28206   | 12800   | 6796  | 15129  |
| Weighting Scheme   | w =<br>1/[σ <sup>2</sup> (Fo <sup>2</sup> )+(0.0230P) <sup>2</sup> +0.7079P]<br>where<br>P=(Fo <sup>2</sup> +2Fc <sup>2</sup> )/3 | w =<br>1/[σ <sup>2</sup> (Fo <sup>2</sup> )+(0.0232P) <sup>2</sup> +3.1471P]<br>where<br>P=(Fo <sup>2</sup> +2Fc <sup>2</sup> )/3 | w =<br>1/[σ <sup>2</sup> (Fo <sup>2</sup> )+(0.0232P) <sup>2</sup> +0.0502P]<br>where<br>P=(Fo <sup>2</sup> +2Fc <sup>2</sup> )/3 | w =<br>1/[σ <sup>2</sup> (Fo <sup>2</sup> )+(0.0232P) <sup>2</sup> +19.7380P]<br>where<br>P=(Fo <sup>2</sup> +2Fc <sup>2</sup> )/3 |
| Number of parameters in least-squares                      | 493   | 949   | 228   | 446  |
| R <sub>1</sub>   | 0.0280  | 0.0224  | 0.0504  | 0.0609   |
| wR <sub>2</sub>  | 0.0575  | 0.0505  | 0.1020  | 0.1266   |
| R <sub>1</sub> (all data)                                  | 0.0390  | 0.0273  | 0.0812  | 0.0965   |
| wR <sub>2</sub> (all data)                                 | 0.0612  | 0.0566  | 0.1092  | 0.1368   |
| GOF  | 1.025   | 1.082   | 1.073   | 1.118  |
| Maximum shift/error  | 0.006   | 0.003   | 0.001   | 0.002  |
| Min & Max peak heights on final ΔF Map (e <sup>-</sup> /Å) | -0.921, 1.040   | -0.357, 0.815   | -1.575, 0.996   | -1.226, 1.640  |

Diffraction Type: Bruker Kappa Axis Apex2; Scan Types: Φ and Ω scans; Cut off Threshold Expression: I > 2σ(I); Structure refined using full matrix least-squares using F2; Weighting Scheme: w=1/[σ<sup>2</sup>(Fo<sup>2</sup>)+(0.0230P)<sup>2</sup>+0.7079P] where P=(Fo<sup>2</sup>+2Fc<sup>2</sup>)/3

Where:

$$R_1 = \frac{\sum (|F_o| - |F_c|)}{\sum F_o}$$

$$wR_2 = \left[ \frac{\sum (w(F_o^2 - F_c^2))^2}{\sum (w F_o^4)} \right]^{1/2}$$

$$GOF = \left[ \frac{\sum (w(F_o^2 - F_c^2))^2}{(\text{No. of reflns.} - \text{No. of params.})} \right]^{1/2}$$

## VI – References

1. Stubbs, J. M.; Firth, K. F.; Bridge, B. J.; Berger, K. J.; Hazlehurst, R. J.; Boyle, P. D.; Blacquiere, J. M., *Dalton Trans.* **2017**, *46*, 647-650.
2. Patiny, L.; Borel, A., *J. Chem. Inf. Model.* **2013**, *53*, 1223-1228.
3. Bruker-Nonius; SAINT; version; 2012.12, **2012**, Bruker-Nonius, Madison, WI 53711, USA
4. Bruker-Nonius; SADABS; version; 2012.1, **2012**, Bruker-Nonius, Madison, WI 53711, USA.
5. Bruker-AXS; TWINABS; version; 2012.1, **2012**, Bruker-AXS, Madison, WI 53711, USA
6. Spek, A., *J. Appl. Crystallogr.* **2003**, *36*, 7-13.
7. Spek, A. L., *Acta Cryst.* **2009**, *D65*, 148-155.
8. Sheldrick, G. M.; CELL\_NOW; version; 208/4, **2008**, Bruker-AXS, Madison, WI 53711, USA
9. Sheldrick, G. M., *Acta Crystallogr. Sect. A* **2008**, *A64*, 112-122.
10. Gabe, E. J.; Le Page, Y.; Charland, J. P.; Lee, F. L.; White, P. S., *J. Appl. Crystallogr.* **1989**, *22*, 384-387.

## Appendices

### Appendix B: Supplementary Information for Chapter 3

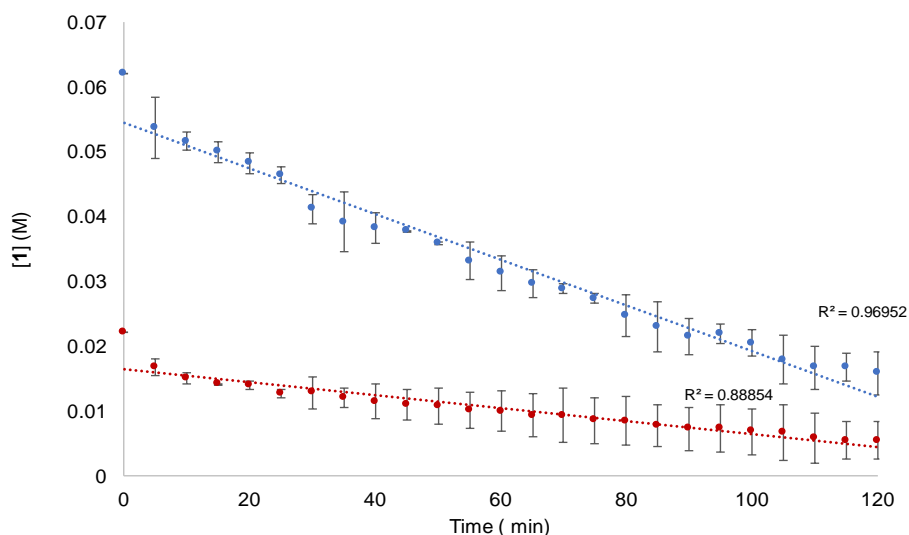
Table B.1. Summary of Selected  $^1\text{H}$ , and  $^{13}\text{C}\{^1\text{H}\}$  NMR Spectroscopy Data for Known 1-AzA complexes.

|   | $\text{H}^1$ | $\text{C}^1$ | $\text{C}^2$ | References |
|---|--------------|--------------|--------------|------------|
| $\kappa^1\text{-N}$                       | 7.28         | 149.8-187.5  | 66.3-114.8   | 3, 4       |
| $\eta^3\text{-NCC}$                       | N/A          | 151.9-184.9  | 42.0-64.5    | 3          |
| $\mu(\kappa^1\text{-N};\eta^2\text{-CC})$ | 5.97         | 109.0        | 74.5         | 4          |

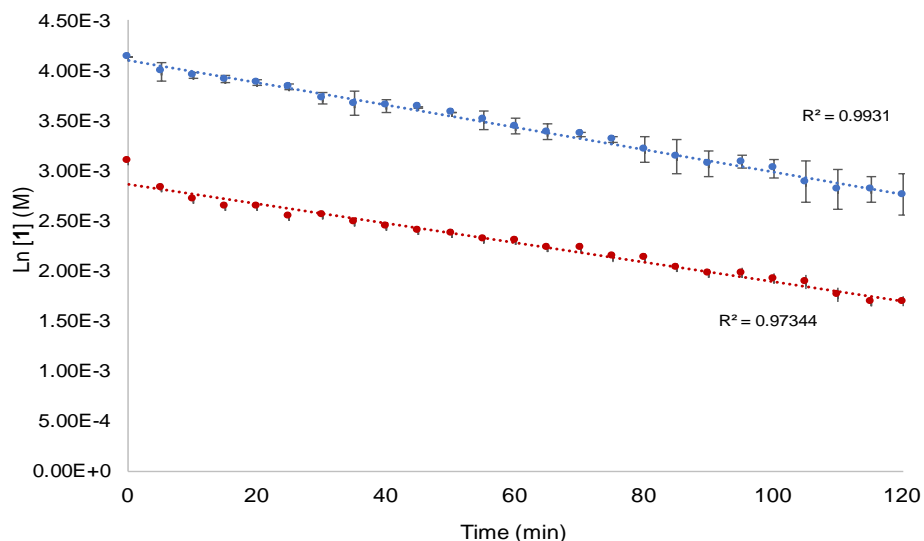
## I – Experimental Procedures

### I.1 – Kinetic Data

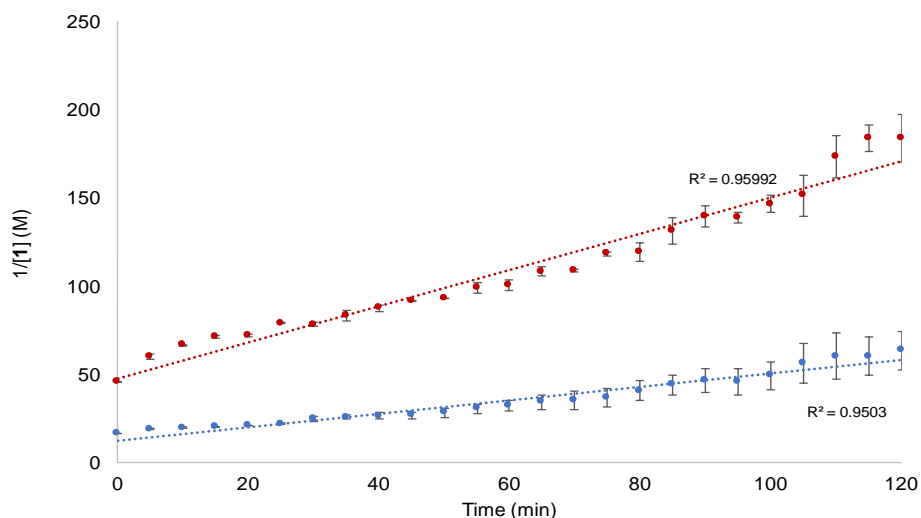
#### I.1.1 – Rate Data



**Figure B.1.** Zero order in **3-1** manipulation. Plot of concentration of **3-1** (M) vs. time (min) generated from  $^{31}\text{P}\{^1\text{H}\}$  NMR spectroscopy integrations from spectra of a solution of **3-1** in  $\text{C}_6\text{H}_6$  heated at  $70^\circ\text{C}$  for 2.5 h. A  $^{31}\text{P}\{^1\text{H}\}$  NMR spectrum was acquired every 5 min with a T1 delay = 5 s. Concentration of **3-1** determined by integration relative to TPPO (47 mM). Initial concentrations of **3-1** = 62 mM (blue), and 22 mM (red). Error bars are an average of two runs.

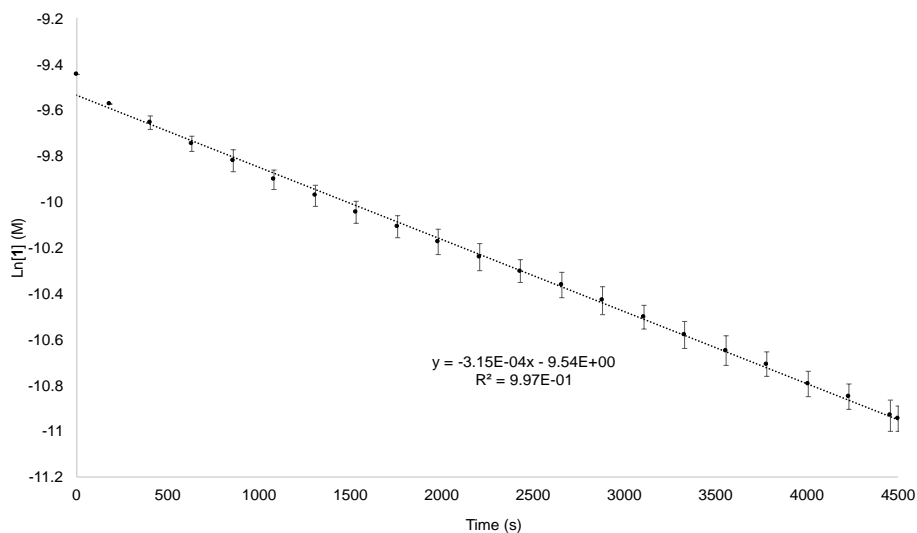


**Figure B.2.** First order in **3-1** manipulation. Plot of  $\text{Ln}[\mathbf{3-1}]$  (M) vs. time (min) generated by  $^{31}\text{P}\{^1\text{H}\}$  NMR spectroscopy integrations from spectra of a solution of **3-1** in  $\text{C}_6\text{H}_6$  heated at  $70^\circ\text{C}$  for 2.5 h. A  $^{31}\text{P}\{^1\text{H}\}$  NMR spectrum was acquired every 5 min with a  $T_1$  delay = 5 s. Concentration of **3-1** determined by integration relative to TPPO (47 mM). Initial concentrations of **3-1** = 62 mM (blue), and 22 mM (red). Error bars are an average of two runs.

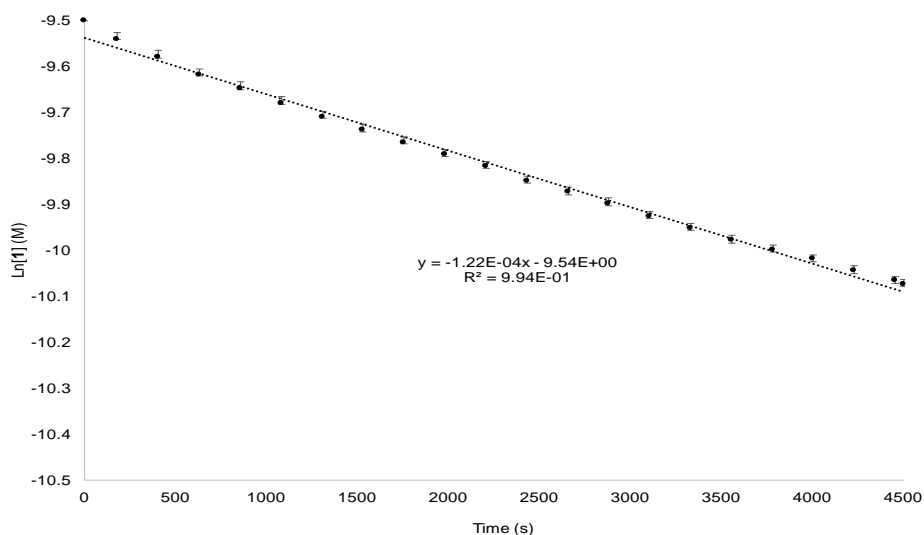


**Figure B.3.** Second order in **3-1** manipulation. Plot of concentration of  $1/[\mathbf{3-1}]$  (M) vs. time (min) generated by  $^{31}\text{P}\{^1\text{H}\}$  NMR spectroscopy integrations from spectra of **1** in  $\text{C}_6\text{H}_6$  heated at  $70^\circ\text{C}$  for 2.5 h. A  $^{31}\text{P}\{^1\text{H}\}$  NMR spectrum was acquired every 5 min with a  $T_1$  delay = 5 s. Concentration of **1** determined by integration relative to TPPO (47 mM). Initial concentrations of **3-1** = 62 mM (blue), and 22 mM (red).

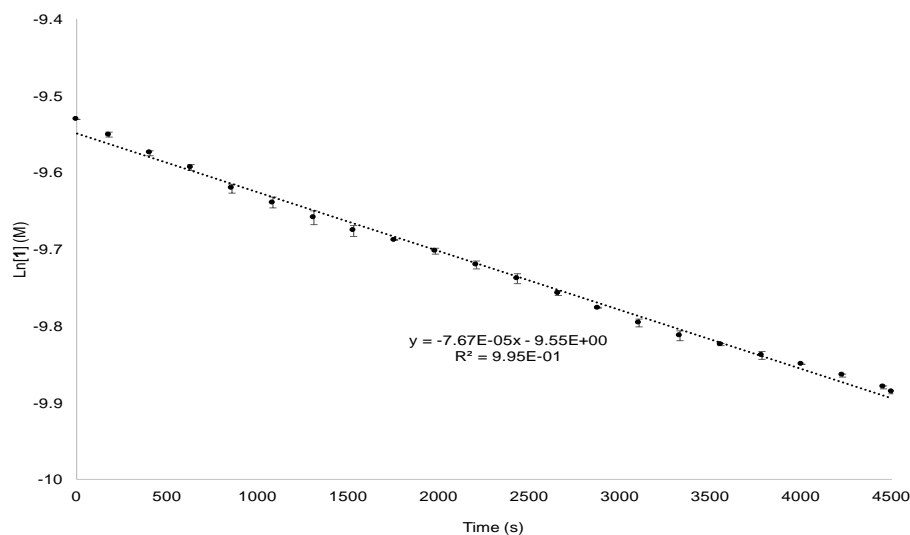
## I.I.II – Eyring Analysis



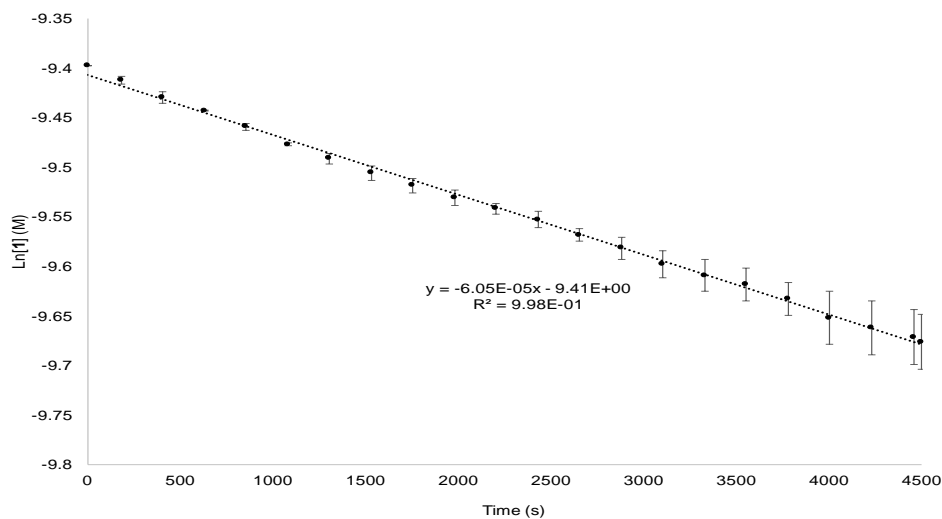
**Figure B.4.** Plot of Ln[**3-1**] (M) vs. time (s) generated by  $^1\text{H}$  NMR spectroscopy integrations from spectra of a solution of **3-1** in  $\text{C}_6\text{D}_6$  heated at  $70\text{ }^\circ\text{C}$  for 1.15 h heating a solution. A  $^1\text{H}$  NMR spectrum was acquired every 45 s. Concentration of **3-1** determined by integration relative to DMTP (31 mM). Error bars are an average of two runs.



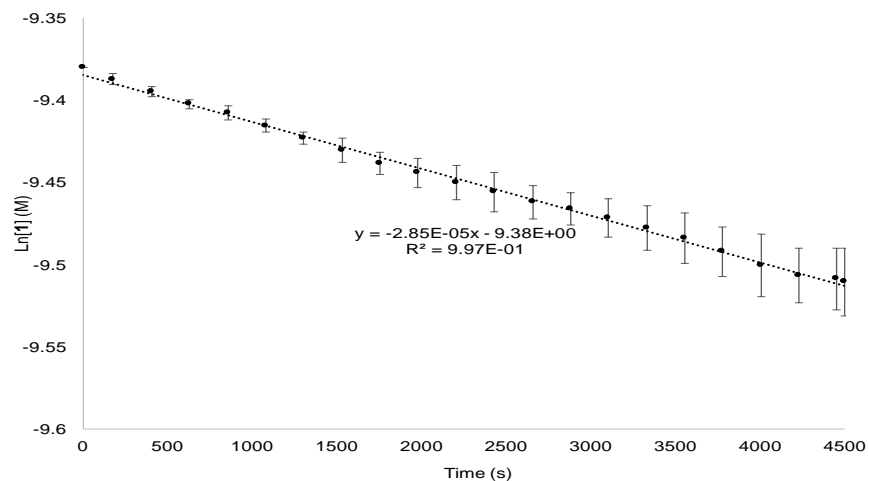
**Figure B.5.** Plot of Ln[**3-1**] (M) vs. time (s) generated by  $^1\text{H}$  NMR spectroscopy integrations from spectra of a solution of **3-1** in  $\text{C}_6\text{D}_6$  heated at  $60\text{ }^\circ\text{C}$  for 1.15 h heating a solution. A  $^1\text{H}$  NMR spectrum was acquired every 45 s. Concentration of **3-1** determined by integration relative to DMTP (31 mM). Error bars are an average of two runs.



**Figure B.6.** Plot of  $\text{Ln}[3-1]$  (M) vs. time (s) generated by  $^1\text{H}$  NMR spectroscopy integrations from spectra of a solution of **1** in  $\text{C}_6\text{D}_6$  heated at  $55^\circ\text{C}$  for 1.15 h heating a solution A  $^1\text{H}$  NMR spectrum was acquired every 45 s. Concentration of **3-1** determined by integration relative to DMTP (31 mM). Error bars are an average of two runs.

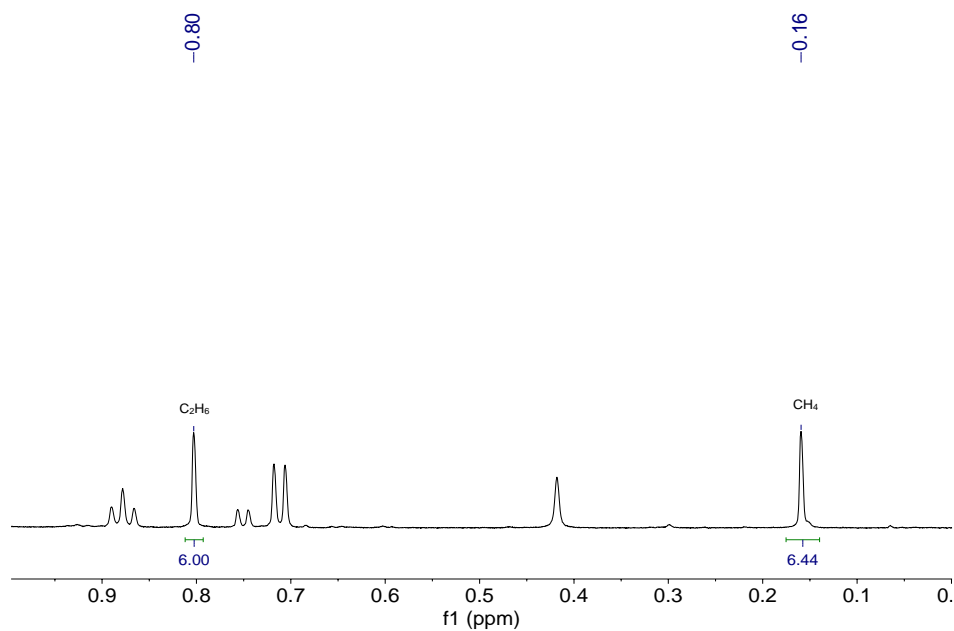


**Figure B.7.** Plot of  $\text{Ln}[3-1]$  (M) vs. time (s) generated by  $^1\text{H}$  NMR spectroscopy integrations from spectra of a solution of **3-1** in  $\text{C}_6\text{D}_6$  heated at  $50^\circ\text{C}$  for 1.15 h heating a solution A  $^1\text{H}$  NMR spectrum acquired was every 45 s. Concentration of **3-1** determined by integration relative to DMTP (31 mM). Error bars are an average of two runs.



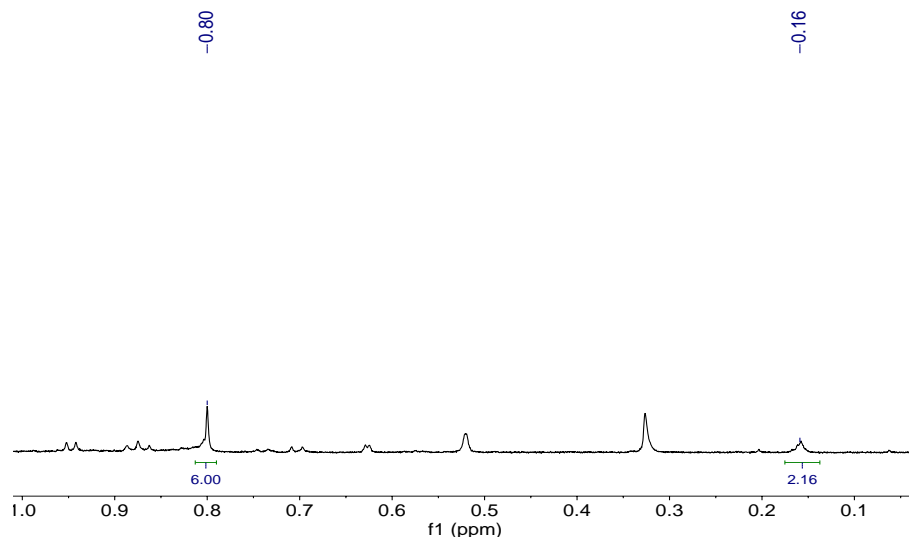
**Figure B.8.** Plot of Ln[**3-1**] (M) vs. time (s) generated by  $^1\text{H}$  NMR spectroscopy integrations from spectra of a solution of **3-1** in  $\text{C}_6\text{D}_6$  heated at  $40^\circ\text{C}$  for 1.15 h heating a solution. A  $^1\text{H}$  NMR spectrum was acquired every 45 s. Concentration of **3-1** determined by integration relative to DMTP (31 mM). Error bars are an average of two runs.

## I.II – Radical Tests



**Figure B.9.**  $^1\text{H}$  NMR spectrum of a solution of **3-1** and 35 equiv of 1,4-CHD in  $\text{C}_6\text{D}_6$  that was heated at  $70^\circ\text{C}$  for 2.5 h. The NMR tube was cooled to rt prior to obtaining the spectrum. The chemical shift range of 0-1 ppm is shown, which is the range for product signals of  $\text{C}_2\text{H}_6$ , and  $\text{CH}_4$  (599 MHz,  $\text{C}_6\text{D}_6$ ).

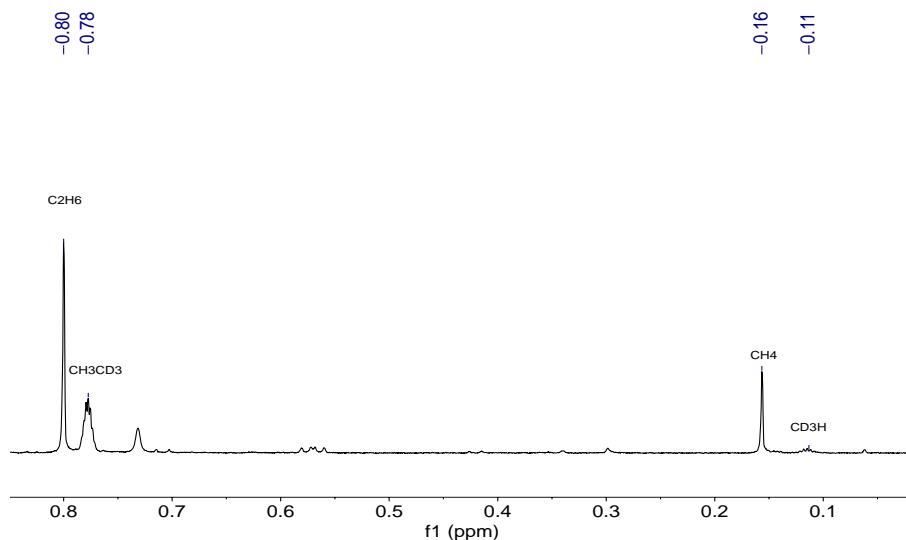




**Figure B.10.**  $^1\text{H}$  NMR spectrum of a solution of **3-1** and 35 equiv of 9,10-DHA in  $\text{C}_6\text{D}_6$  that was heated at  $70\text{ }^\circ\text{C}$  for 2.5 h. The NMR tube was cooled to rt prior to obtaining the spectrum. The chemical shift range of 0-1 ppm is shown, which is the range for product signals of  $\text{C}_2\text{H}_6$ , and  $\text{CH}_4$  (599 MHz,  $\text{C}_6\text{D}_6$ ).

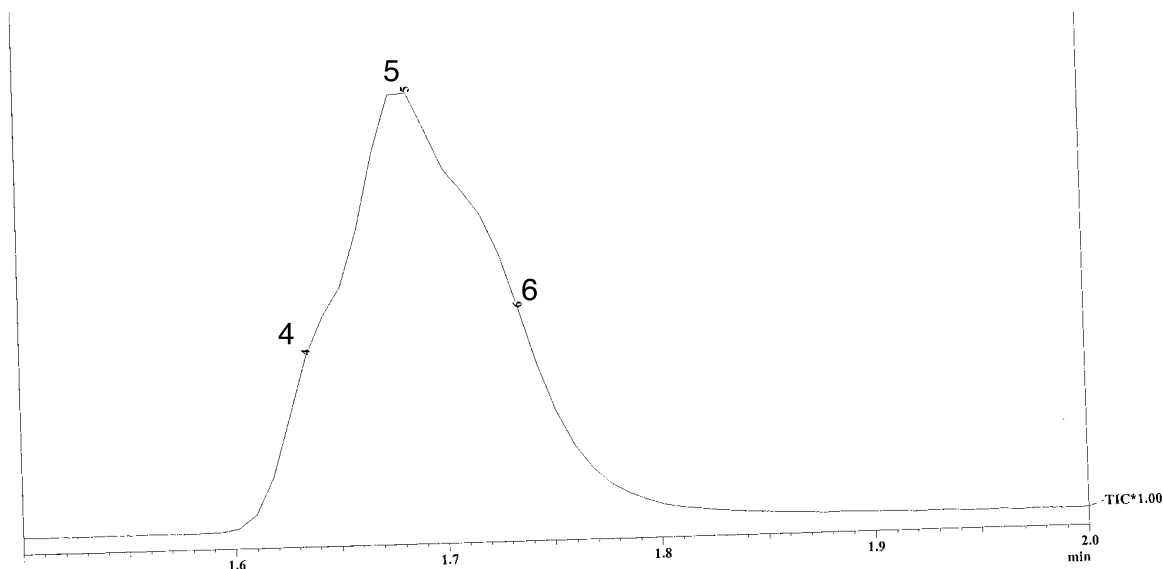
### I.III – Crossover Experiments

#### I.III.I – Filled Tube Experiment



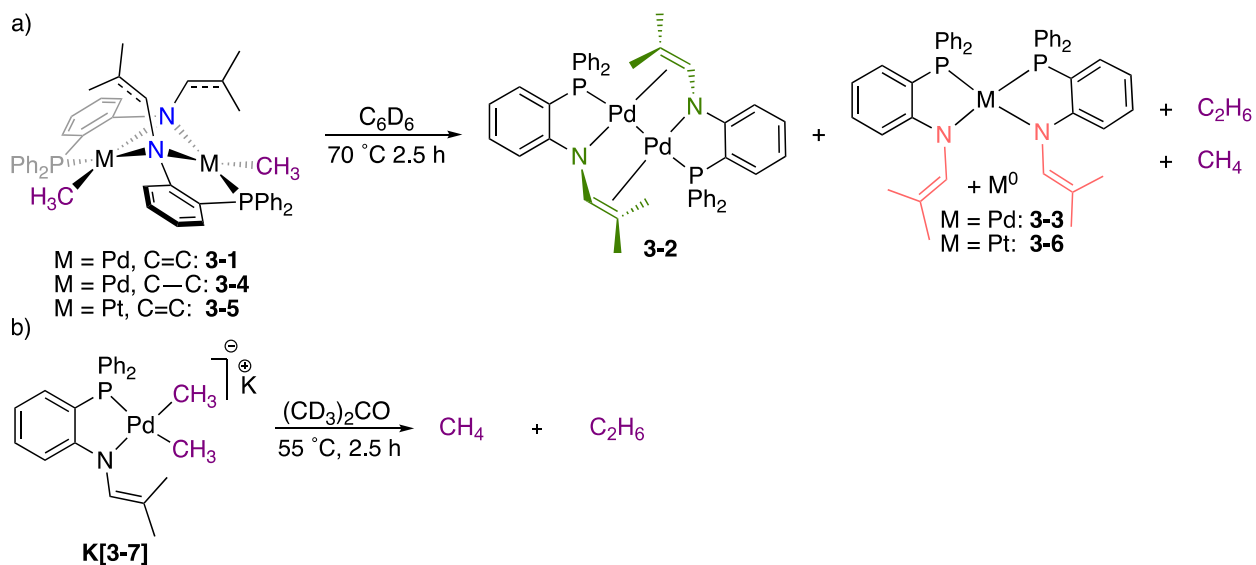
**Figure B.11.**  $^1\text{H}$  NMR spectrum of a solution of **3-1** and **3-1- $d_6$**  in  $\text{C}_6\text{D}_6$  that was heated at  $70\text{ }^\circ\text{C}$  for 2.5 h. The NMR tube was cooled to rt prior to obtaining the spectrum. The chemical shift range of 0-1 ppm is shown, which is the range for product signals of  $\text{C}_2\text{H}_6$ , and  $\text{CH}_4$  (599 MHz,  $\text{C}_6\text{D}_6$ ).

#### I.III.II – GC-MS Analysis

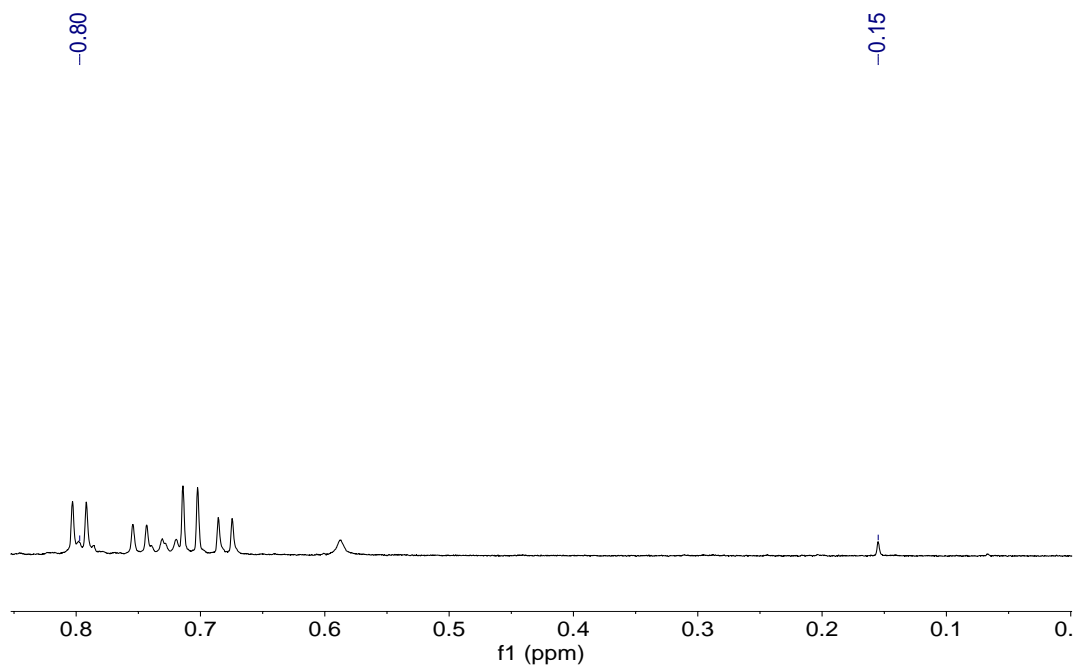


**Figure B.12.** GC-MS spectrum of the headspace after heating **3-1** and **3-1-*d*<sub>6</sub>** for 2.5 h at 70 °C, zoomed in to see the formation of C<sub>2</sub>H<sub>6</sub> (4), C<sub>2</sub>D<sub>6</sub> (5), and C<sub>2</sub>H<sub>3</sub>D<sub>3</sub> (6).

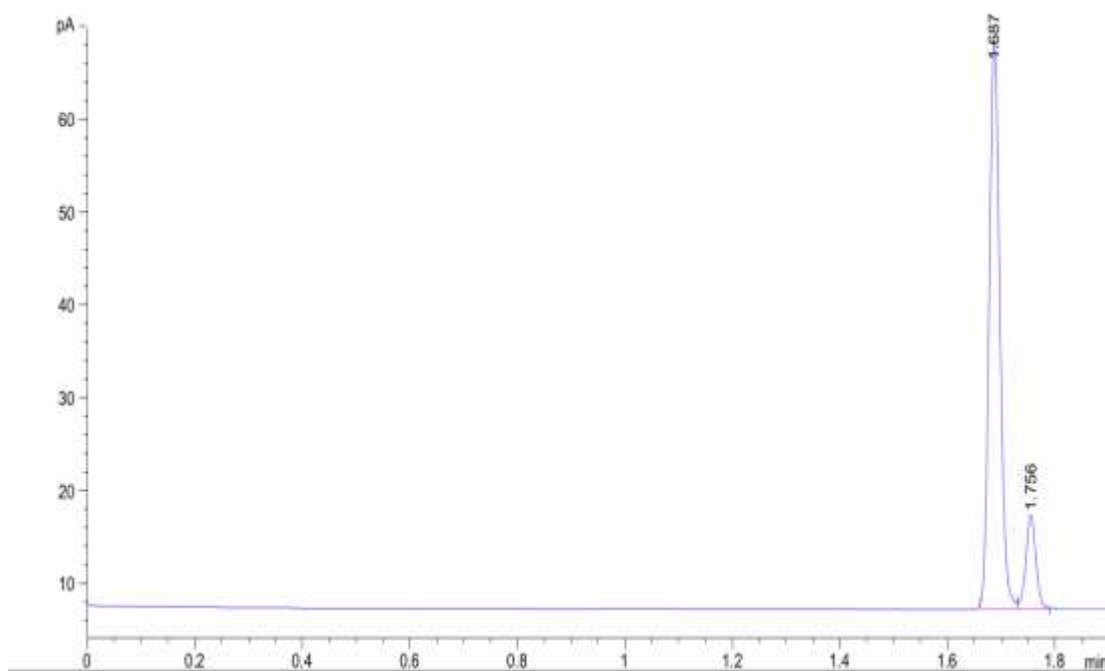
## I.IV – General Thermolysis Procedure



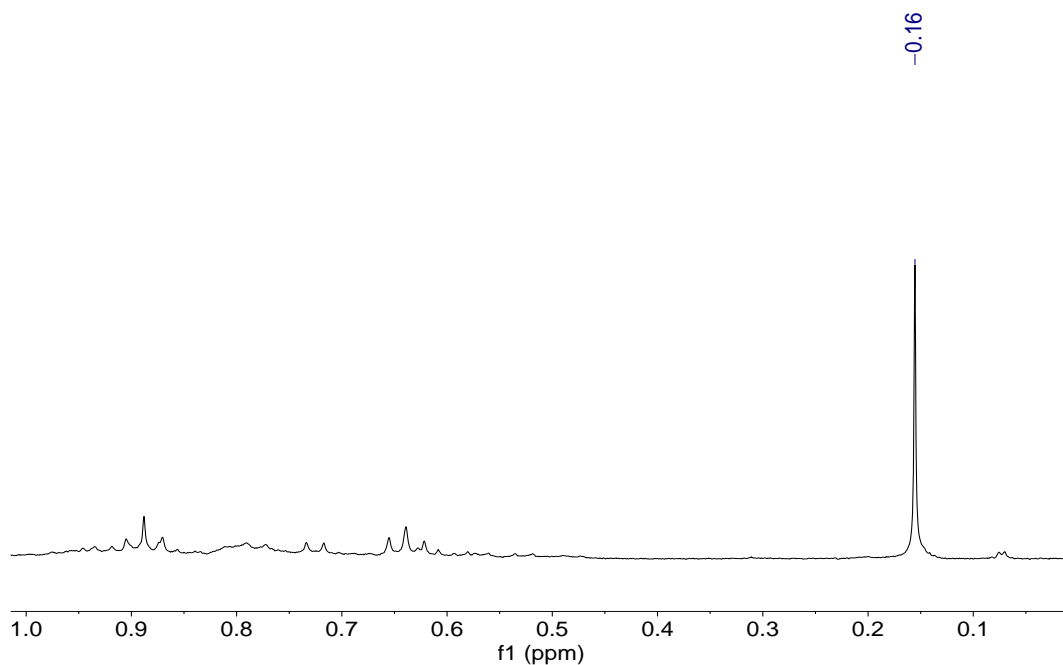
**Scheme B.1.** a) Solutions of **3-1**, **3-4**, and **3-5** in C<sub>6</sub>D<sub>6</sub> were heated at 70 °C for 2.5 h. b) A solution of K[**3-7**] in (CD<sub>3</sub>)<sub>2</sub>CO was heated at 50 °C for 2.5 h.



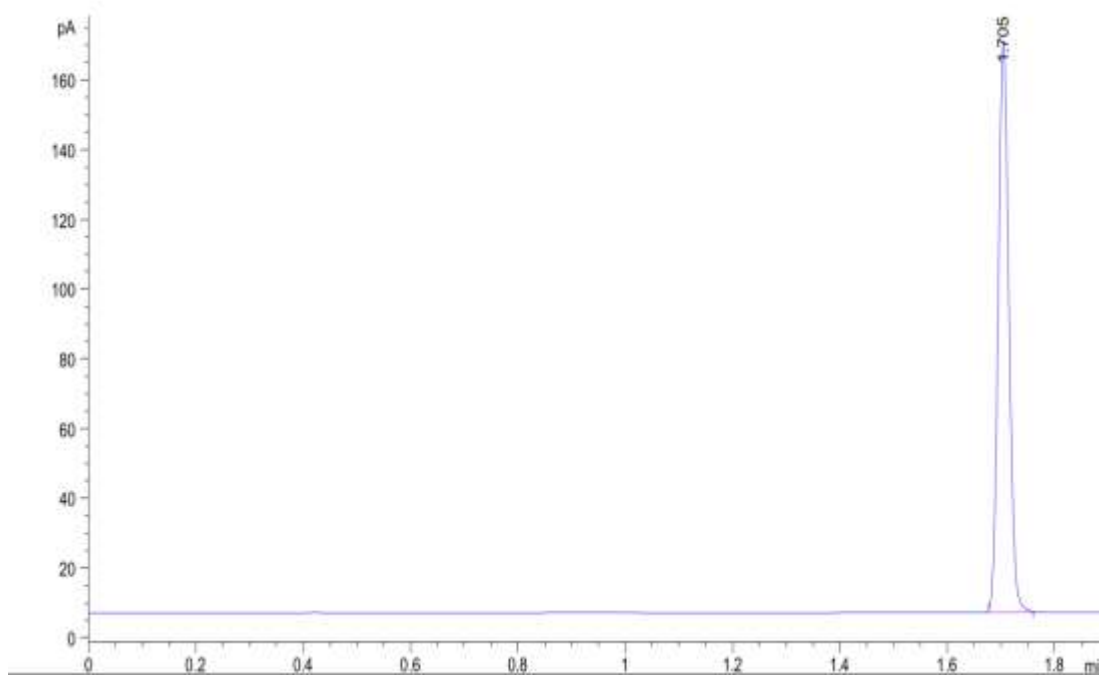
**Figure B.13.**  $^1\text{H}$  NMR spectrum of a solution of **3-4** in  $\text{C}_6\text{D}_6$  after heating at  $70\text{ }^\circ\text{C}$  for 2.5 h. The NMR tube was cooled to rt prior to data collection.  $\delta$ : 0.80 =  $\text{C}_2\text{H}_6$  (s), 0.15 =  $\text{CH}_4$  (s) (599 MHz,  $\text{C}_6\text{D}_6$ ).



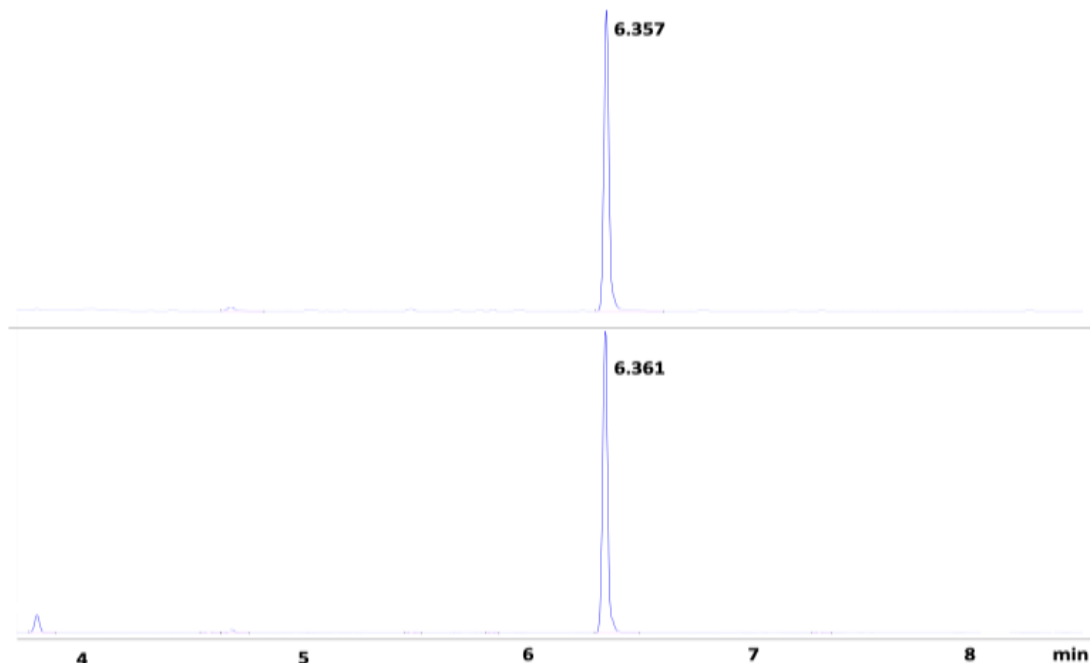
**Figure B.14.** GC-FID chromatogram of a solution of **3-4** heated in  $\text{C}_6\text{D}_6$  at  $70\text{ }^\circ\text{C}$  for 2.5 h. NMR tube was cooled to rt prior to injection into the instrument. Peak assignment: 1.687 min =  $\text{CH}_4$ , 80%; 1.756 min =  $\text{C}_2\text{H}_6$ , 20%.



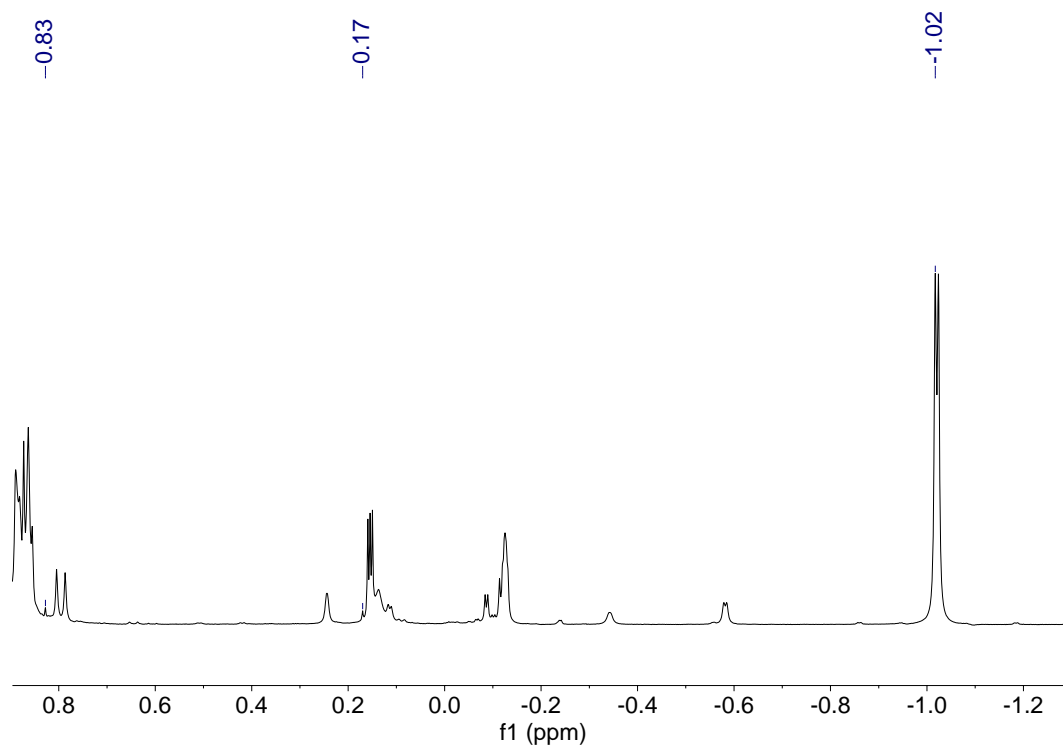
**Figure B.15.**  $^1\text{H}$  NMR spectrum of a solution of **3-5** in  $\text{C}_6\text{D}_6$  after heating at  $70\text{ }^\circ\text{C}$  for 2.5 h. The NMR tube was cooled to rt prior to data collection. 0.16 =  $\text{CH}_4$  (s) (599 MHz,  $\text{C}_6\text{D}_6$ ).



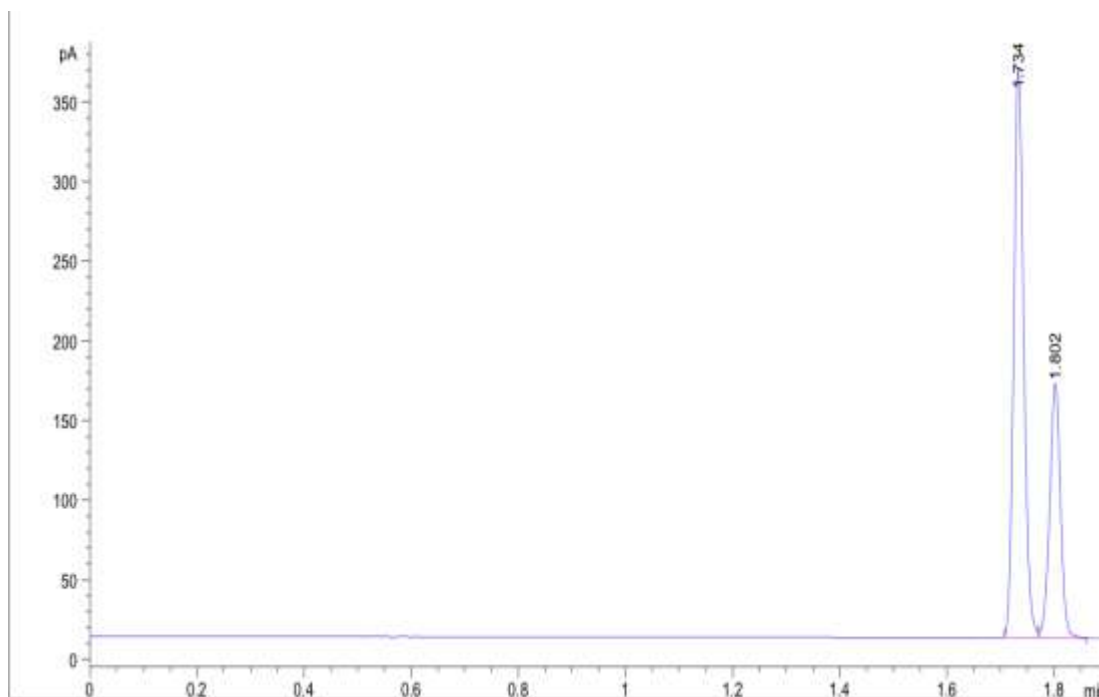
**Figure B.16.** GC-FID chromatogram of a solution of **3-5** heated in  $\text{C}_6\text{D}_6$  at  $70\text{ }^\circ\text{C}$  for 2.5 h. NMR tube was cooled to rt prior to injection into the instrument. Peak assignment: 1.705 min =  $\text{CH}_4$ , 100%.



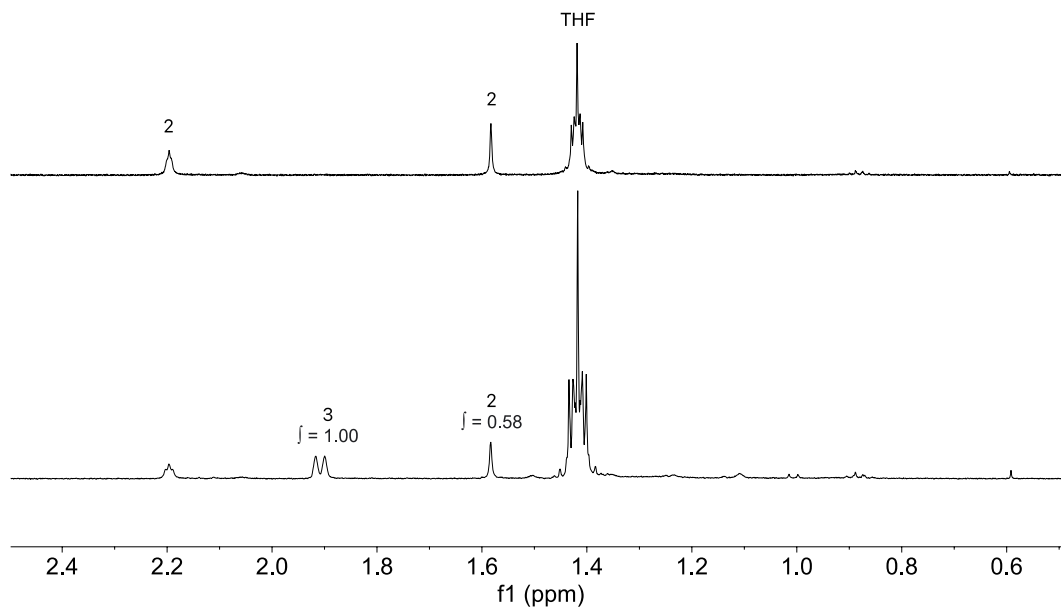
**Figure B.17.** GC-FID chromatogram from two separate solutions of **3-5** heated in  $C_6D_6$  (top) and  $C_6H_6$  (bottom) at  $70\text{ }^\circ\text{C}$  for 2.5 h. Reaction was cooled to rt prior to injection into the instrument. Peak assignment: 6.36 min =  $C_2H_{10}$ .



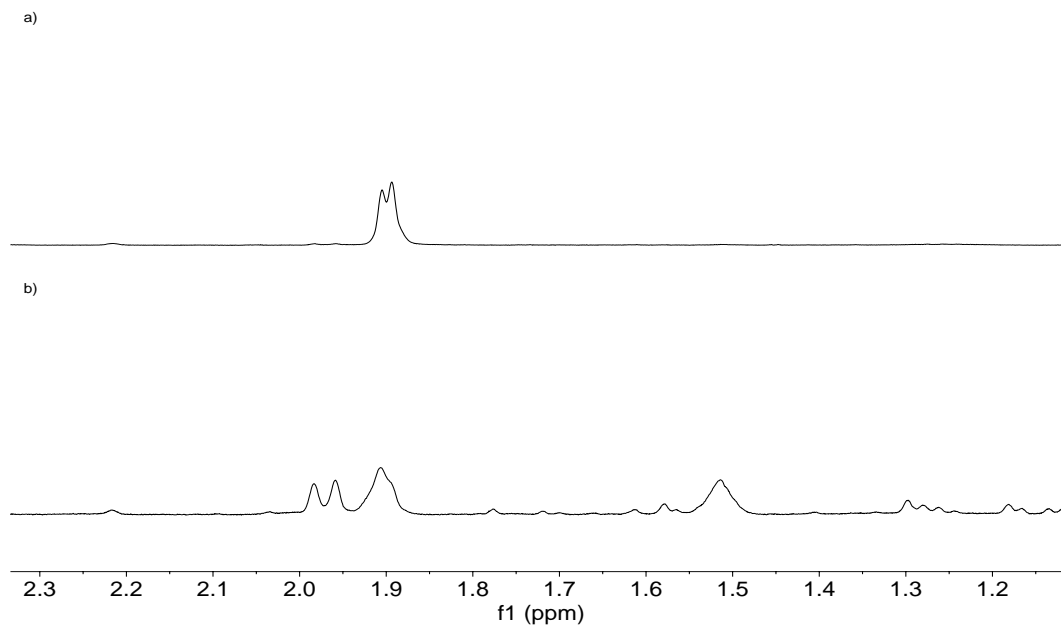
**Figure B.18.**  $^1\text{H}$  NMR spectrum of a solution of **K[3-7]** in  $(CD_3)_2CO$  at  $50\text{ }^\circ\text{C}$  for 2.5 h. The NMR tube was cooled to rt prior to data collection.  $\delta$ : 0.83 =  $C_2H_6$  (s), 0.17 =  $CH_4$  (s), -1.02 (d) = Pd- $CH_3$  (400 MHz,  $(CD_3)_2CO$ ).



**Figure B.19.** GC-FID chromatogram of a solution of **K[3-7]** heated in  $(\text{CD}_3)_2\text{CO}$  at  $50^\circ\text{C}$  for 2.5 h. NMR tube was cooled to rt prior to injection into the instrument. Peak assignment: 1.734 =  $\text{CH}_4$ ; 72%. Peak at 1.802 =  $\text{C}_2\text{H}_6$ , 28%.

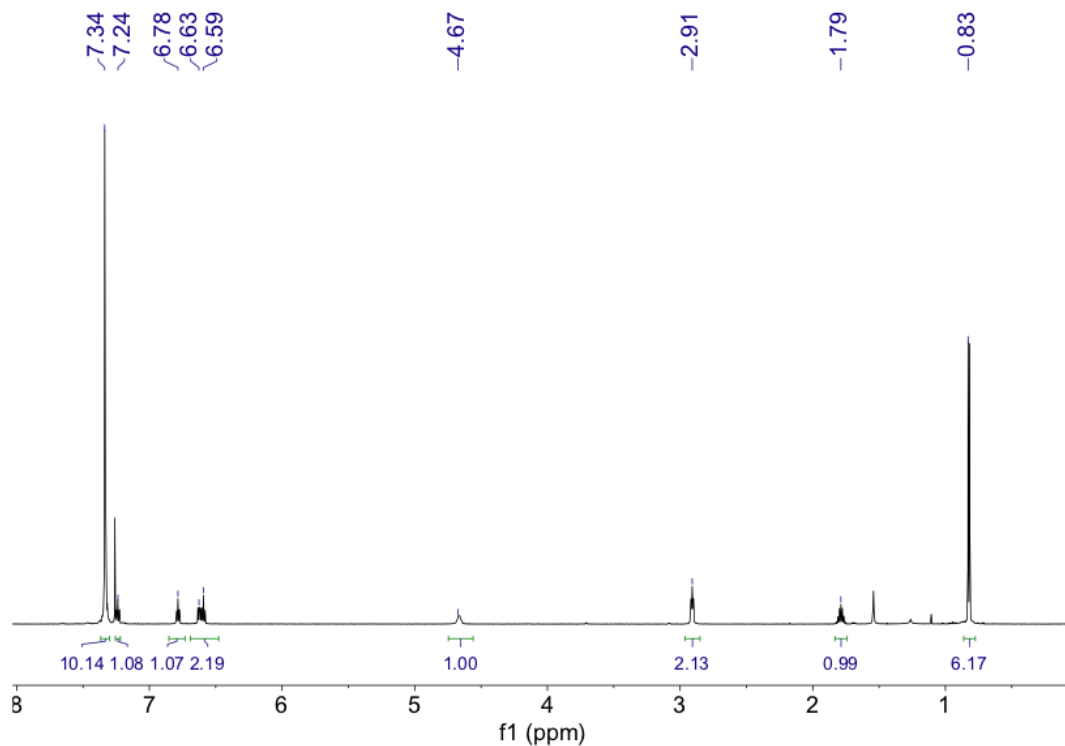


**Figure B.20.** Stack of  $^1\text{H}$  NMR spectra of **3-2** a) prior to heating ( $T_0$ ), and b) after heating at  $70\text{ }^\circ\text{C}$  for 2.5 h. The NMR tube was cooled to rt prior to obtaining the spectrum (599 MHz,  $\text{C}_6\text{D}_6$ ).

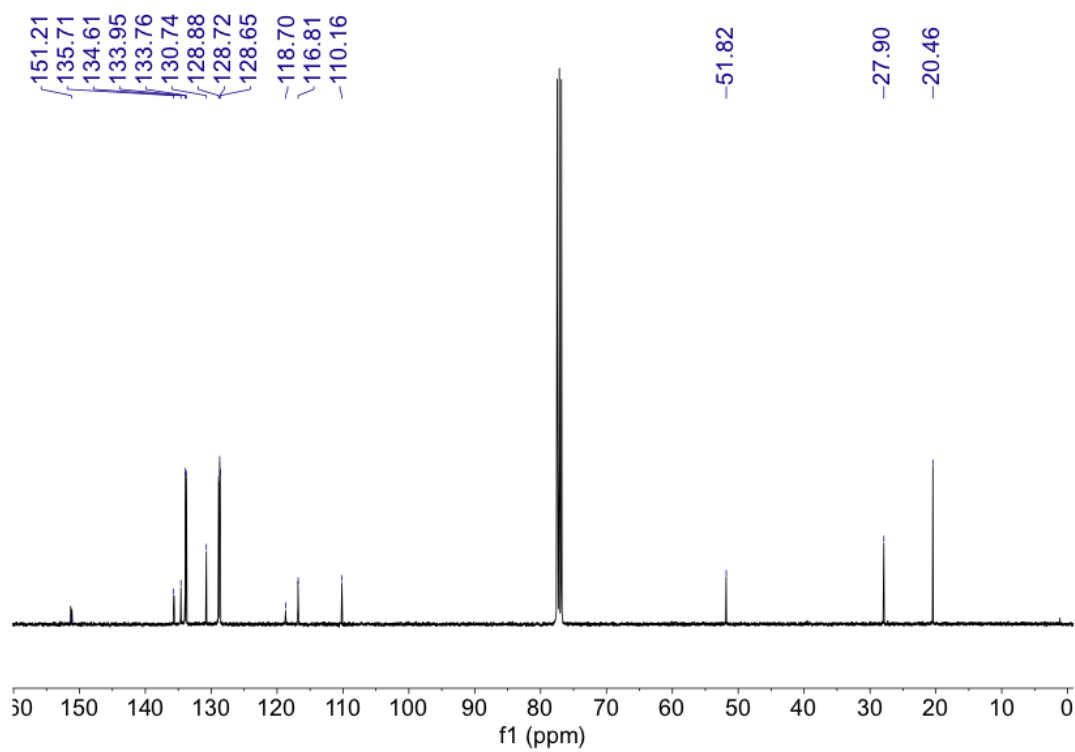


**Figure B.21.** Stack of  $^1\text{H}$  NMR spectra of **3-3** a) prior to heating ( $T_0$ ), and b) after heating at  $70\text{ }^\circ\text{C}$  for 2.5 h. The NMR tube was cooled to rt prior to obtaining the spectrum (599 MHz,  $\text{C}_6\text{D}_6$ ).

## II – Compound NMR Spectra

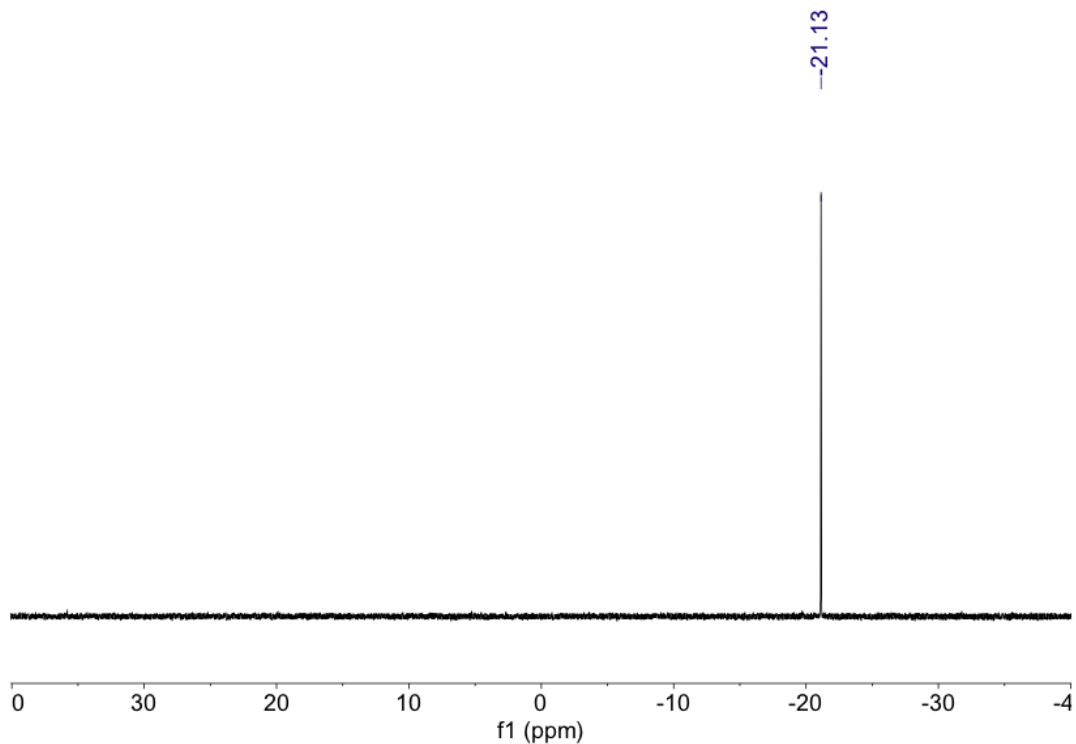


**Figure B.22.**  $^1\text{H}$  NMR spectrum of  $\text{Ph}_2\text{P}(o\text{-C}_6\text{H}_4)\text{NH}(i\text{-Bu})$ , **H[3-L2]** (599 MHz,  $\text{CDCl}_3$ ).

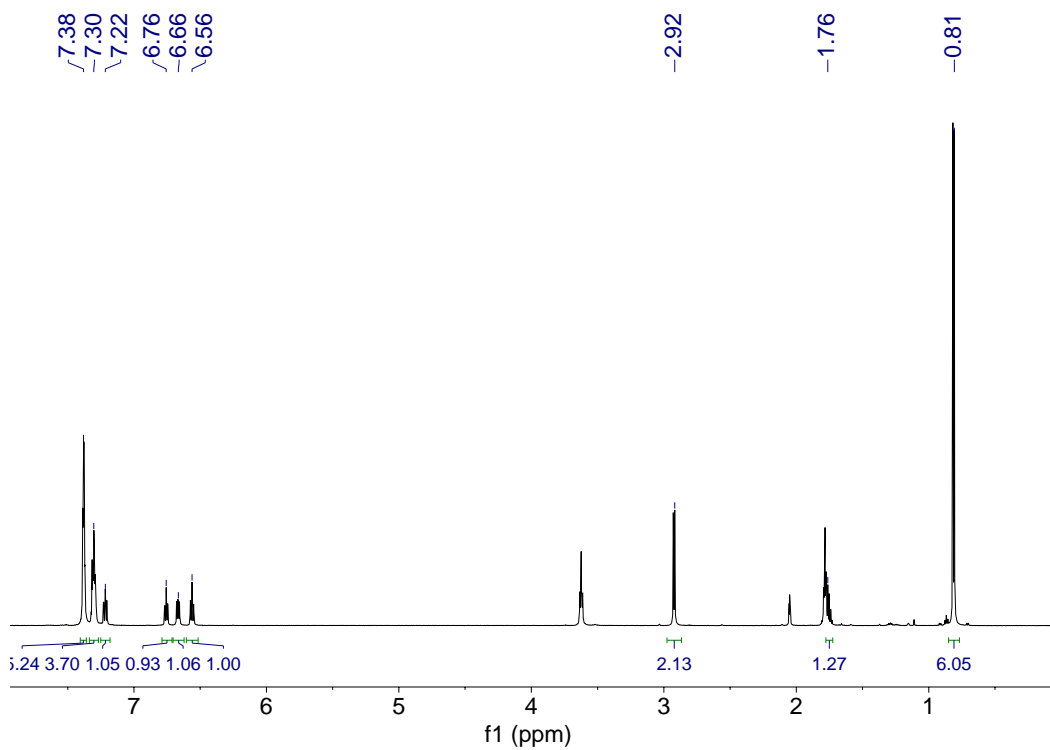


**Figure B.23.**  $^{13}\text{C}\{^1\text{H}\}$  NMR spectrum of  $\text{Ph}_2\text{P}(o\text{-C}_6\text{H}_4)\text{NH}(i\text{-Bu})$ , **H[3-L2]** (151 MHz,  $\text{CDCl}_3$ ).

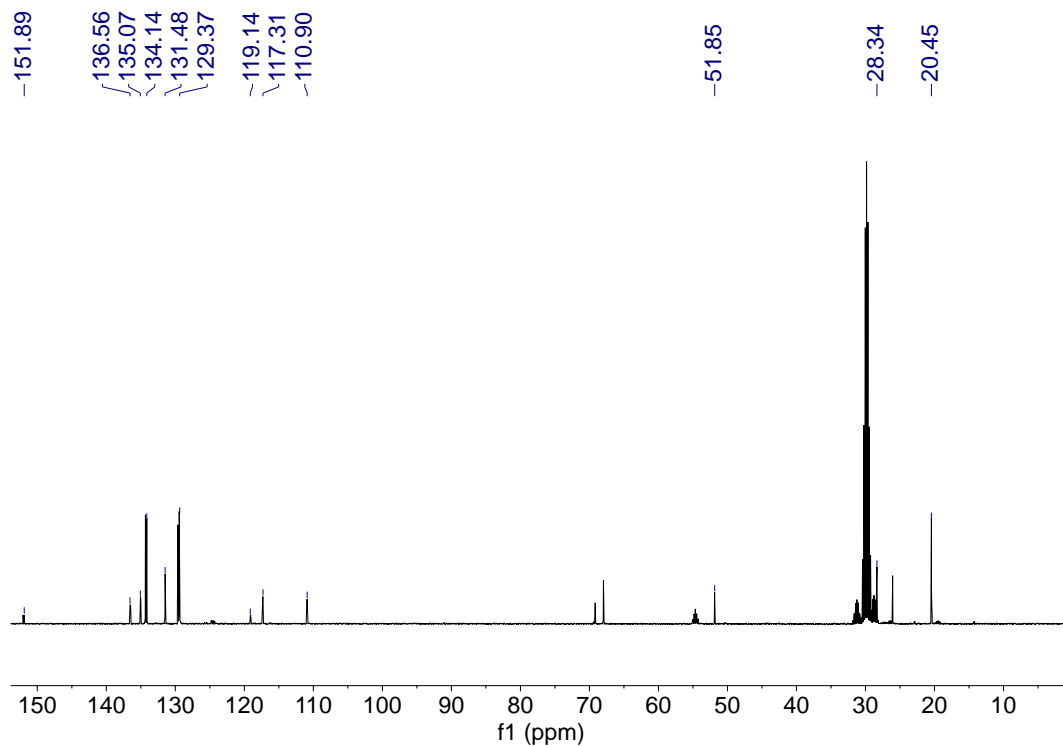




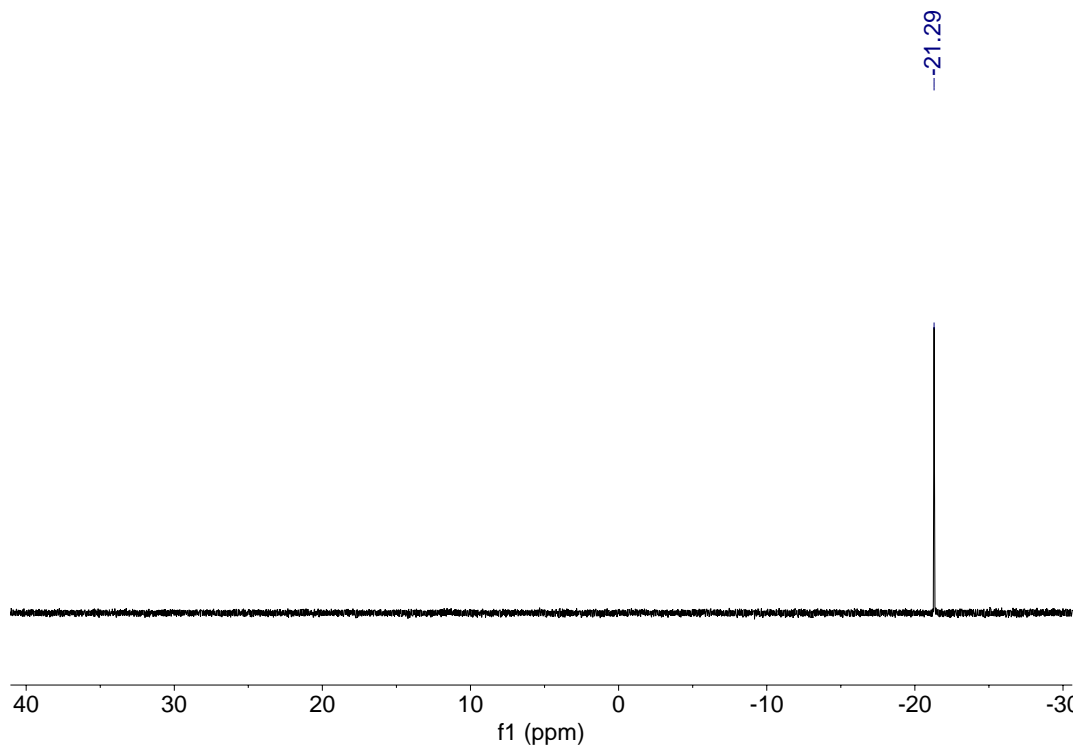
**Figure B.24.**  $^{31}\text{P}\{^1\text{H}\}$  NMR spectrum of  $\text{Ph}_2\text{P}(o\text{-C}_6\text{H}_4)\text{NH}(i\text{-Bu})$ , **H[3-L2]** (243 MHz,  $\text{CDCl}_3$ ).



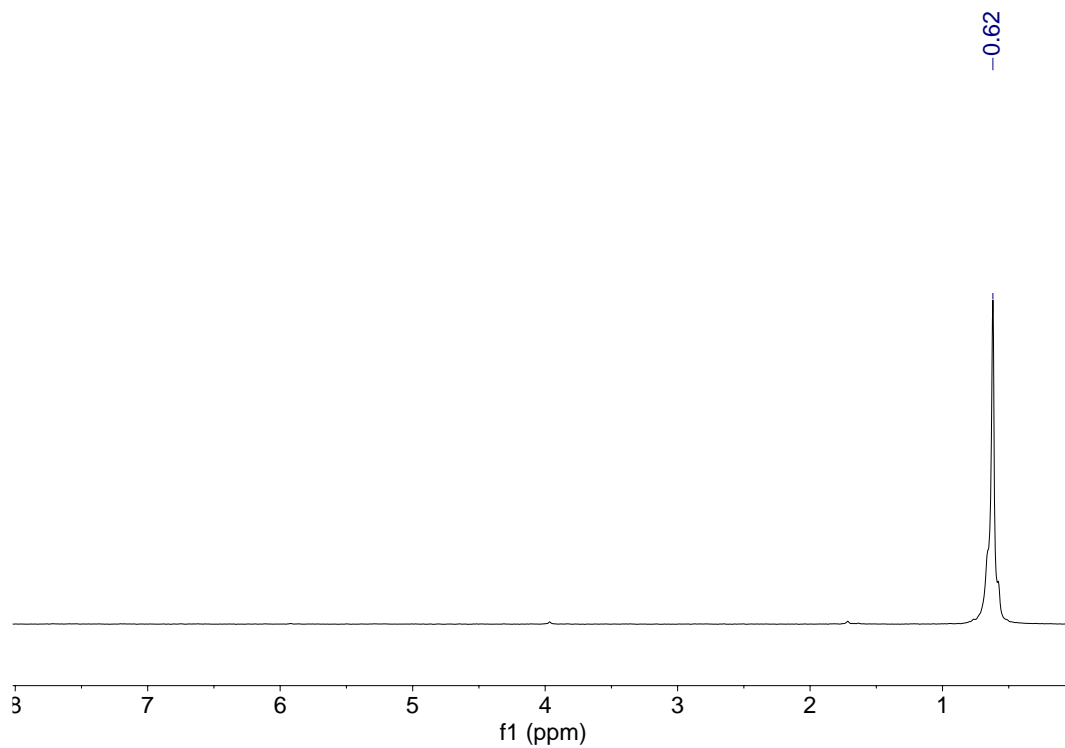
**Figure B.25.**  $^1\text{H}$  NMR spectrum of  $\text{K}[\text{Ph}_2\text{P}(o\text{-C}_6\text{H}_4)\text{N}(i\text{-Bu})]$ , **K[3-L2]** (599 MHz,  $(\text{CD}_3)_2\text{CO}$ ).



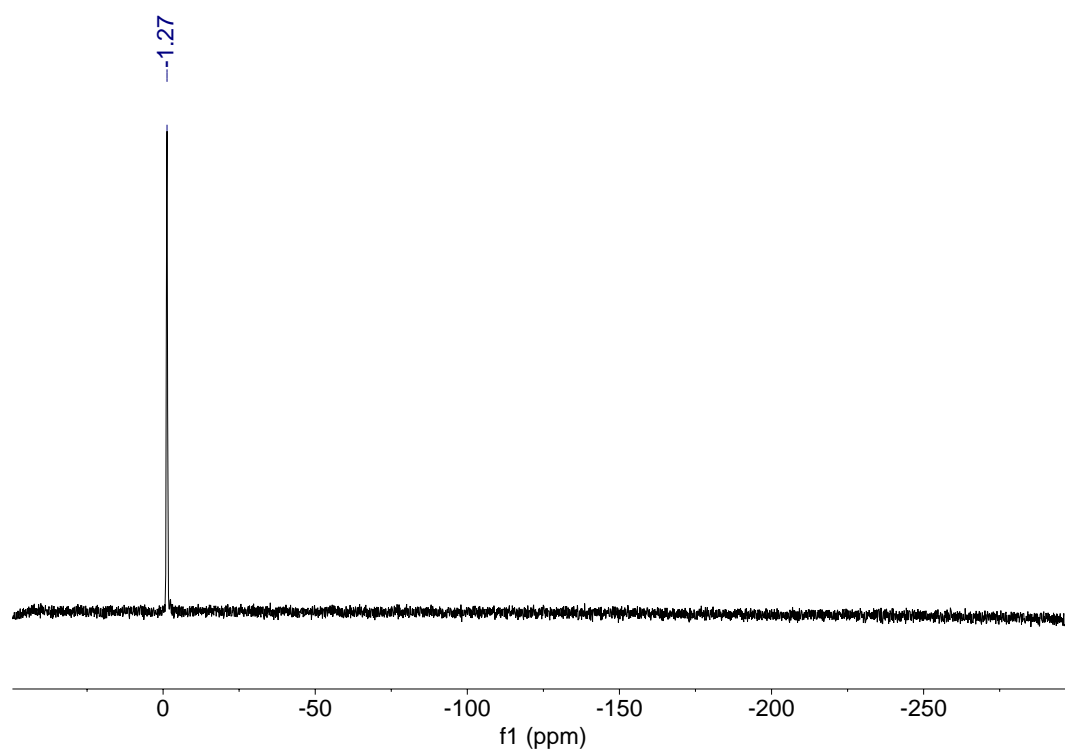
**Figure B.26.**  $^{13}\text{C}\{^1\text{H}\}$  NMR spectrum of  $\text{K}[\text{Ph}_2\text{P}(o\text{-C}_6\text{H}_4)\text{N}(i\text{-Bu})]$ , **K[3-L2]** (151 MHz,  $(\text{CD}_3)_2\text{CO}$ ).



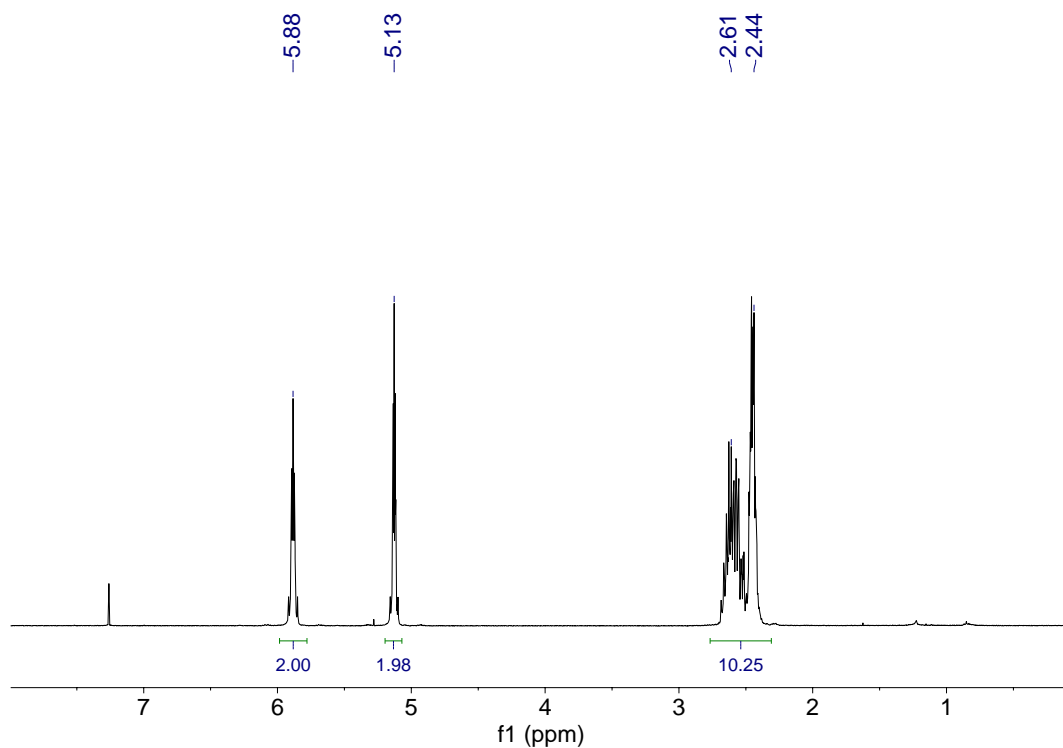
**Figure B.27.**  $^{31}\text{P}\{^1\text{H}\}$  NMR spectrum of  $\text{K}[\text{Ph}_2\text{P}(o\text{-C}_6\text{H}_4)\text{N}(i\text{-Bu})]$ , **K[3-L2]** (243 MHz,  $(\text{CD}_3)_2\text{CO}$ ).



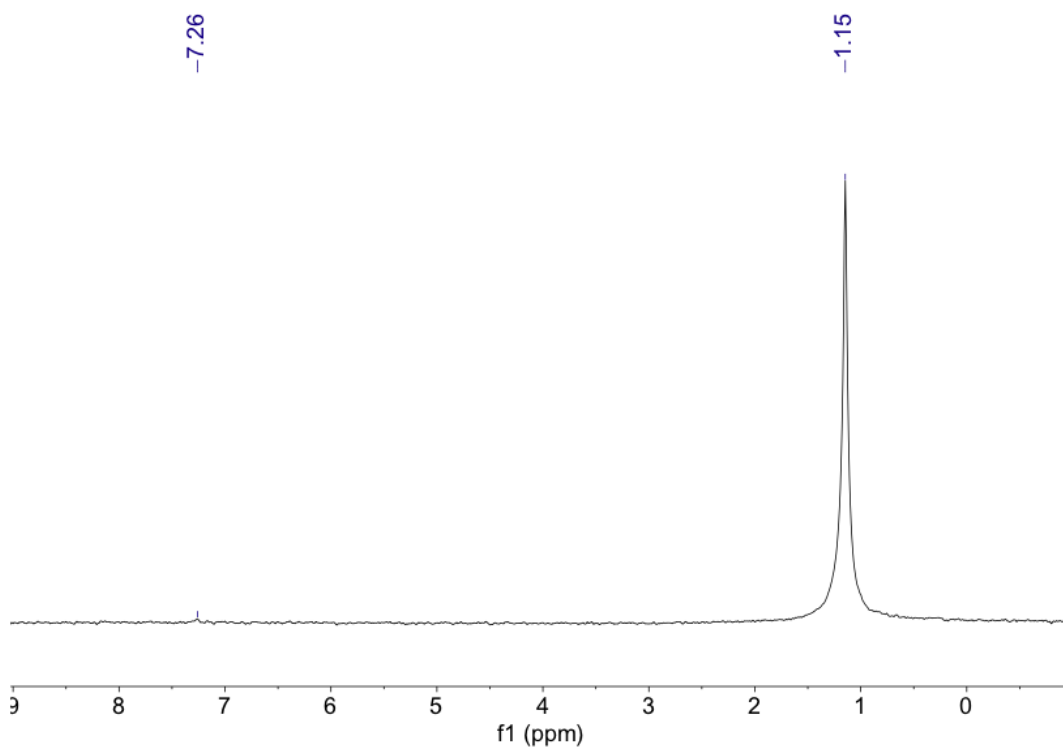
**Figure B.28.**  $^2\text{H}$  NMR spectrum of  $\text{Sn}(\text{CD}_3)_4$  (92.1 MHz,  $\text{CH}_2\text{Cl}_2$ ).



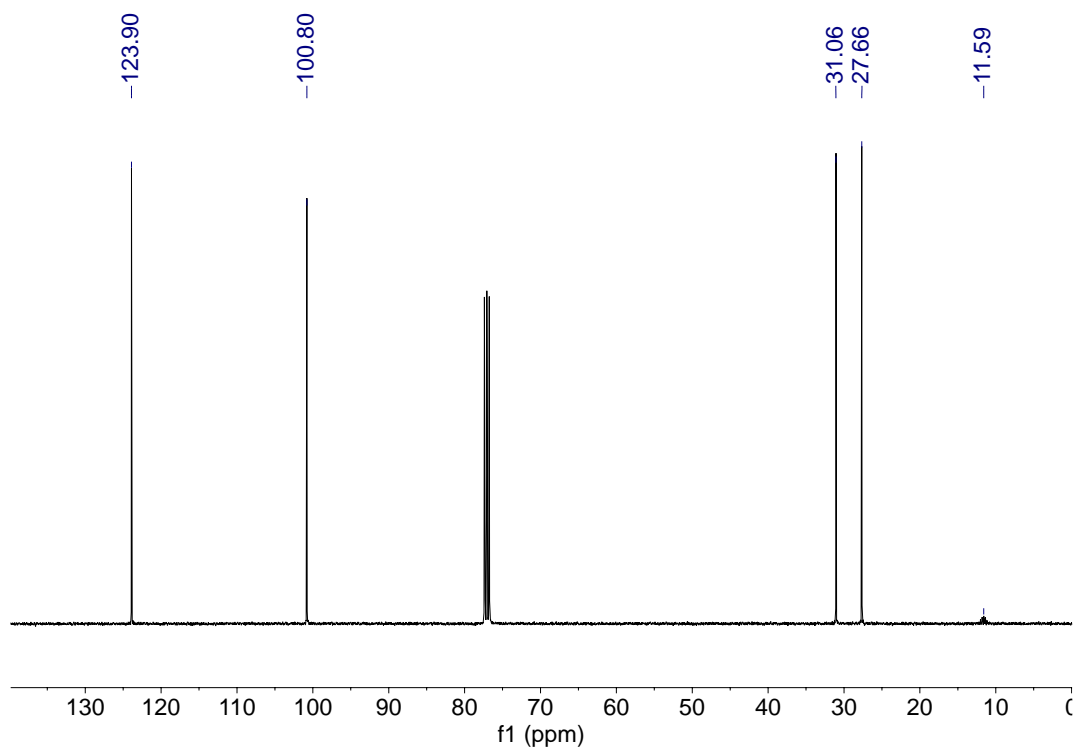
**Figure B.29.**  $^{119}\text{Sn}\{^1\text{H}\}$  NMR Spectrum of  $\text{Sn}(\text{CD}_3)_4$  (223.8 MHz,  $\text{CD}_2\text{Cl}_2$ ).



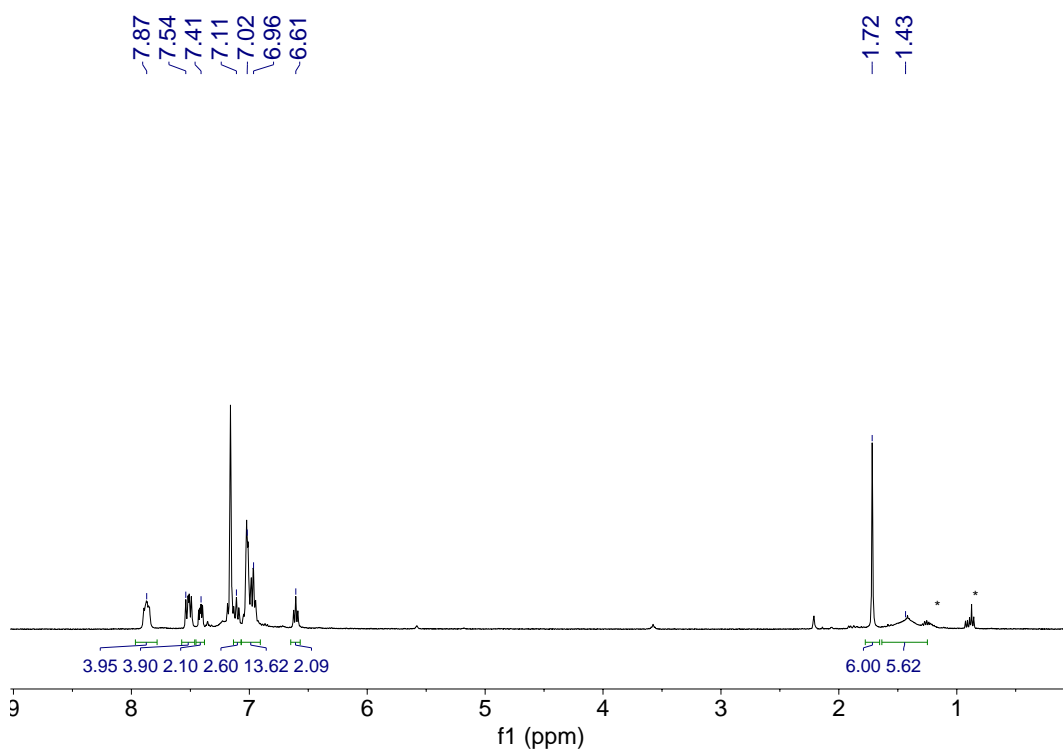
**Figure B.30.** <sup>1</sup>H NMR spectrum of [PdCl(CD<sub>3</sub>)(COD)] (599 MHz, CDCl<sub>3</sub>).



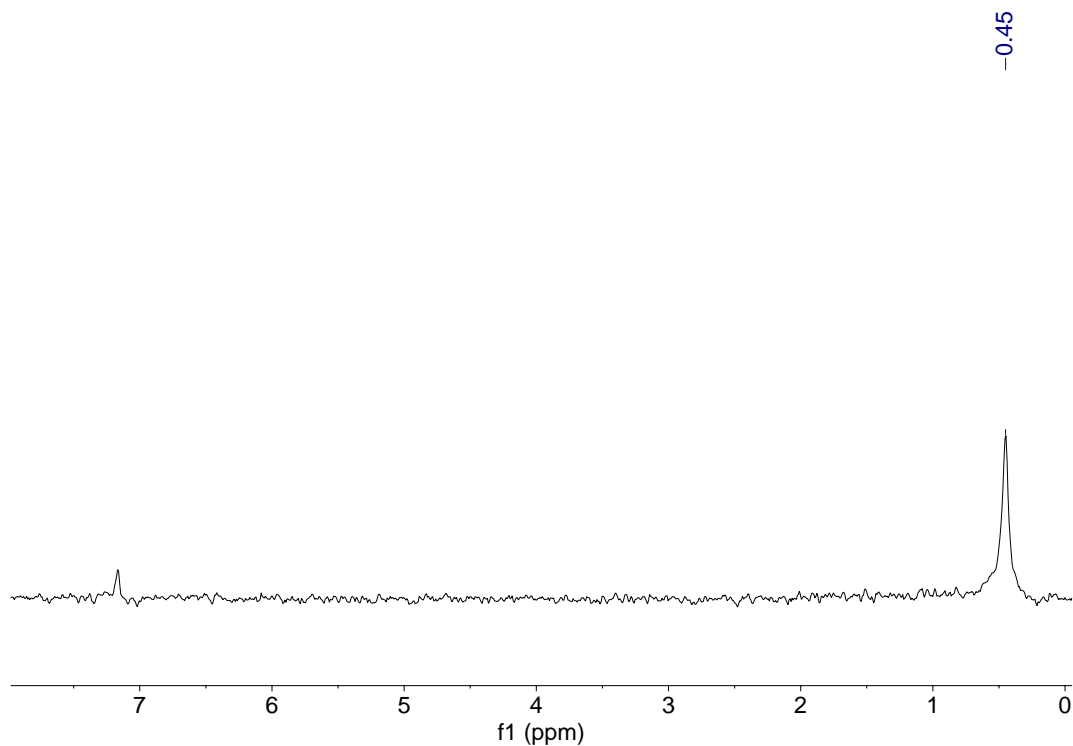
**Figure B.31.** <sup>2</sup>H NMR spectrum of [PdCl(CD<sub>3</sub>)(COD)] (92 MHz, CHCl<sub>3</sub>).



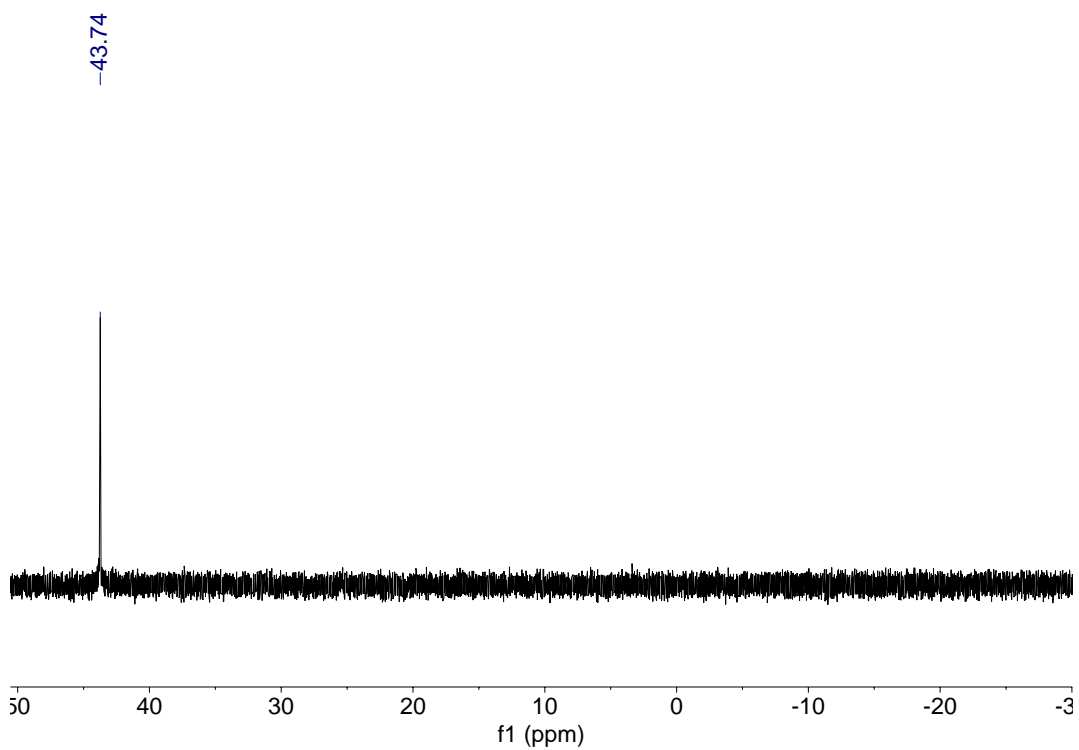
**Figure B.32.**  $^{13}\text{C}\{^1\text{H}\}$  NMR spectrum of  $[\text{PdCl}(\text{CD}_3)(\text{COD})]$  (151 MHz,  $\text{CDCl}_3$ ).



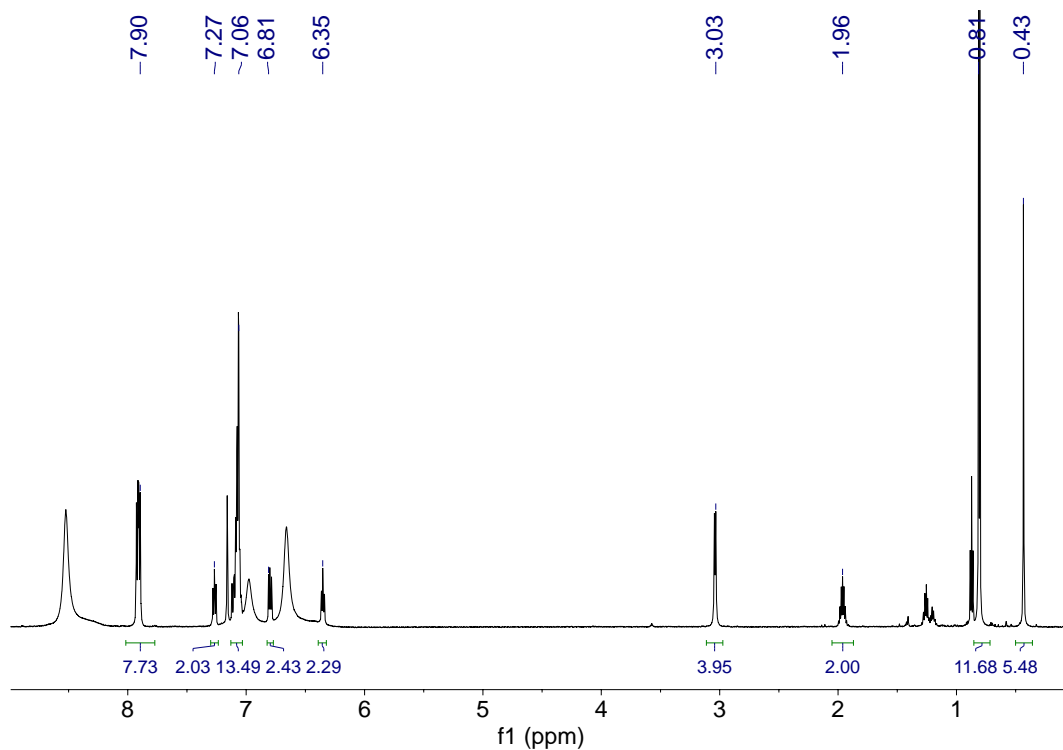
**Figure B.33.**  $^1\text{H}$  NMR spectrum of  $[\text{Pd}(\text{CD}_3)(\mathbf{3-L1})]_2$ ,  $\mathbf{3-1-d}_6$  (599 MHz,  $\text{C}_6\text{D}_6$ . \* denotes pentane).



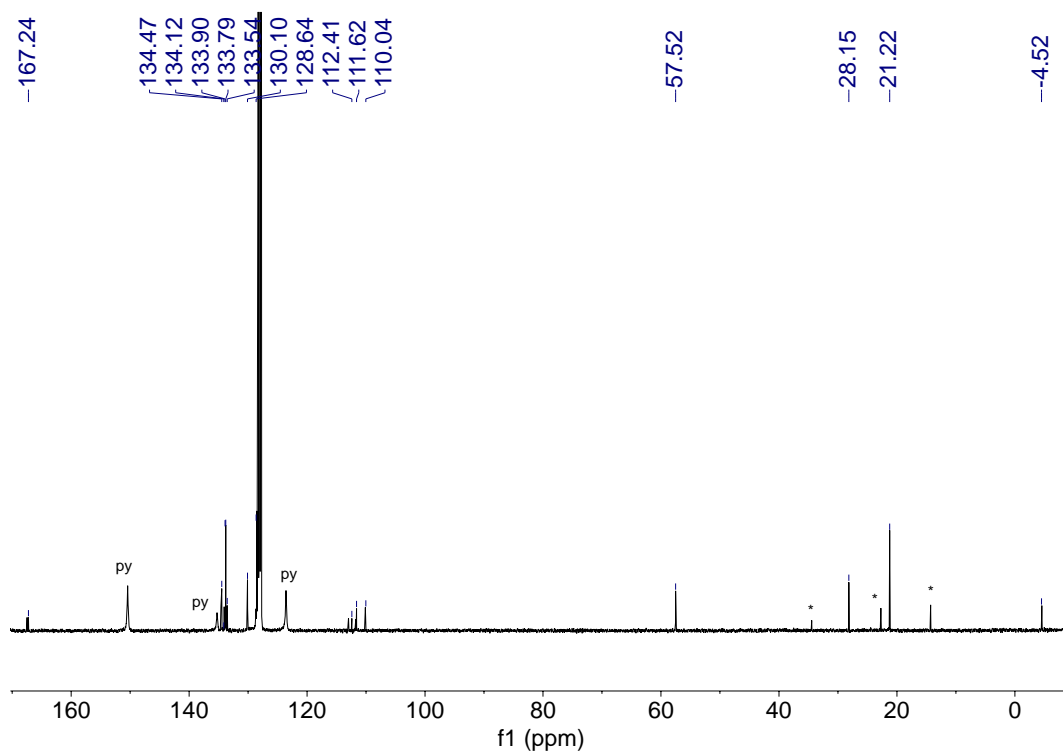
**Figure B.34.**  $^2\text{H}$  NMR spectrum of  $[\text{Pd}(\text{CD}_3)(\mathbf{3-1})]_2$ ,  $\mathbf{3-1-d}_6$  (92 MHz,  $\text{C}_6\text{D}_6$ ).



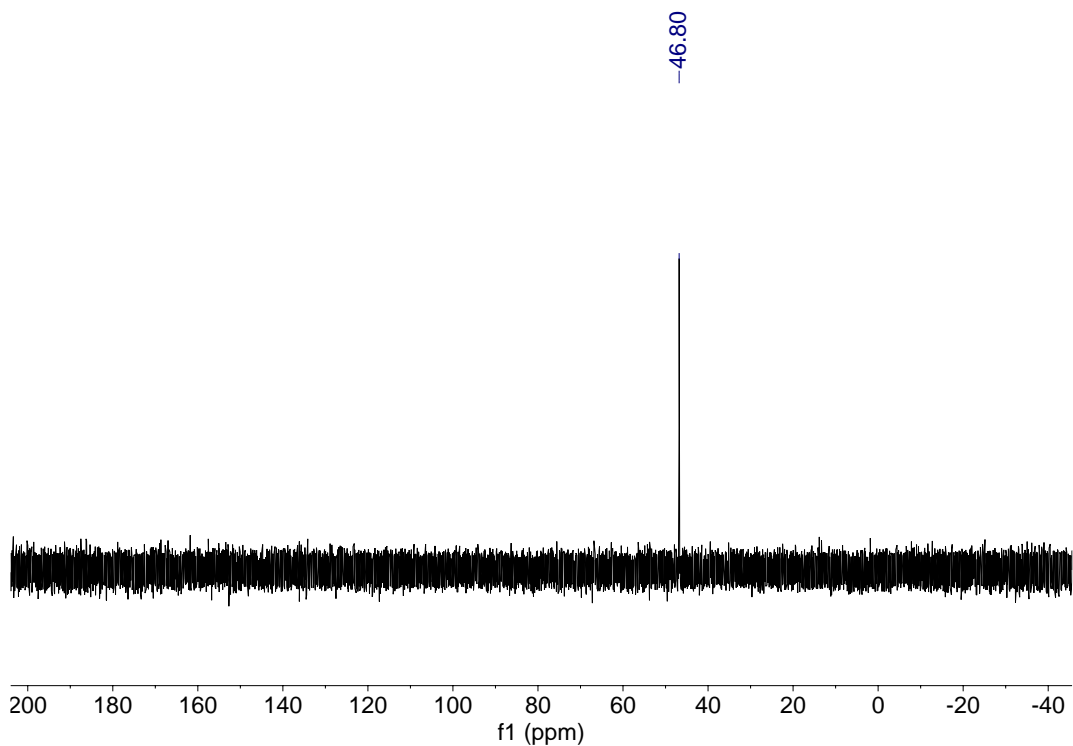
**Figure B.35.**  $^{31}\text{P}\{^1\text{H}\}$  NMR spectrum of  $[\text{Pd}(\text{CD}_3)(\mathbf{3-L1})]_2$ ,  $\mathbf{3-1-d}_6$  (243 MHz,  $\text{C}_6\text{D}_6$ ).



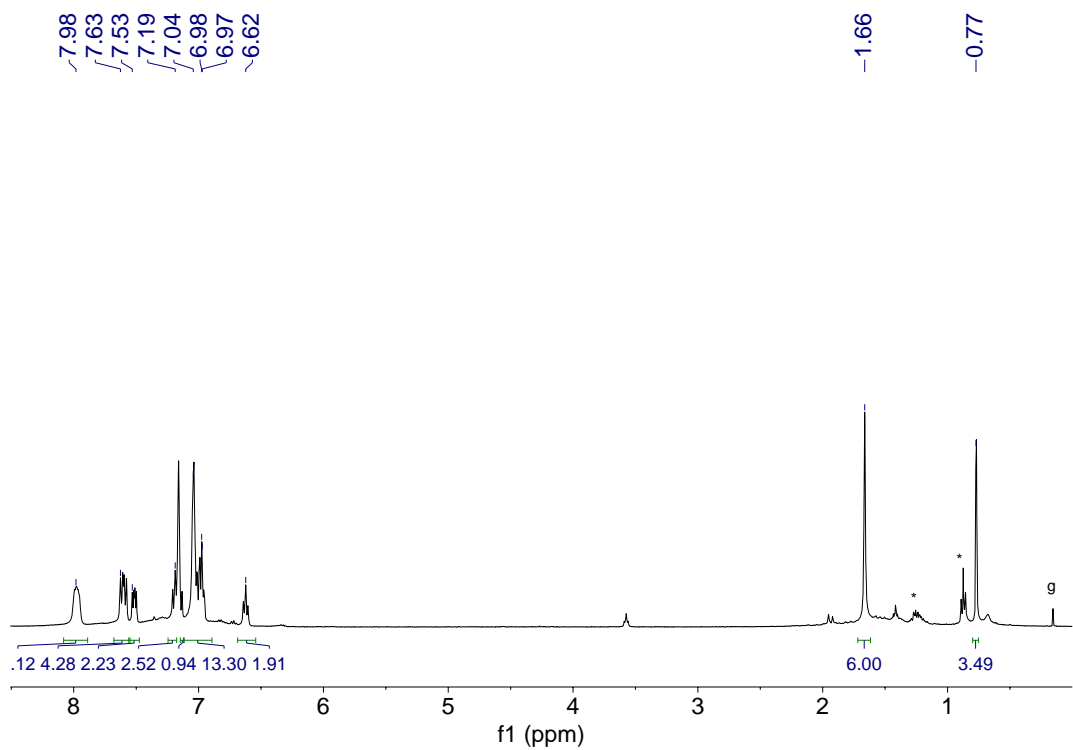
**Figure B.36.**  $^1\text{H}$  NMR spectrum of  $[\text{Pd}(\text{CH}_3)(\mathbf{3-L2})]_2$ , **3-4** (599 MHz,  $\text{C}_6\text{D}_6$ ).



**Figure B.37.**  $^{13}\text{C}\{^1\text{H}\}$  NMR spectrum of  $[\text{Pd}(\text{CH}_3)(\mathbf{3-L2})]_2$ , **3-4** (151 MHz,  $\text{C}_6\text{D}_6$ ). 'py' denotes pyridine, \* denotes pentane.

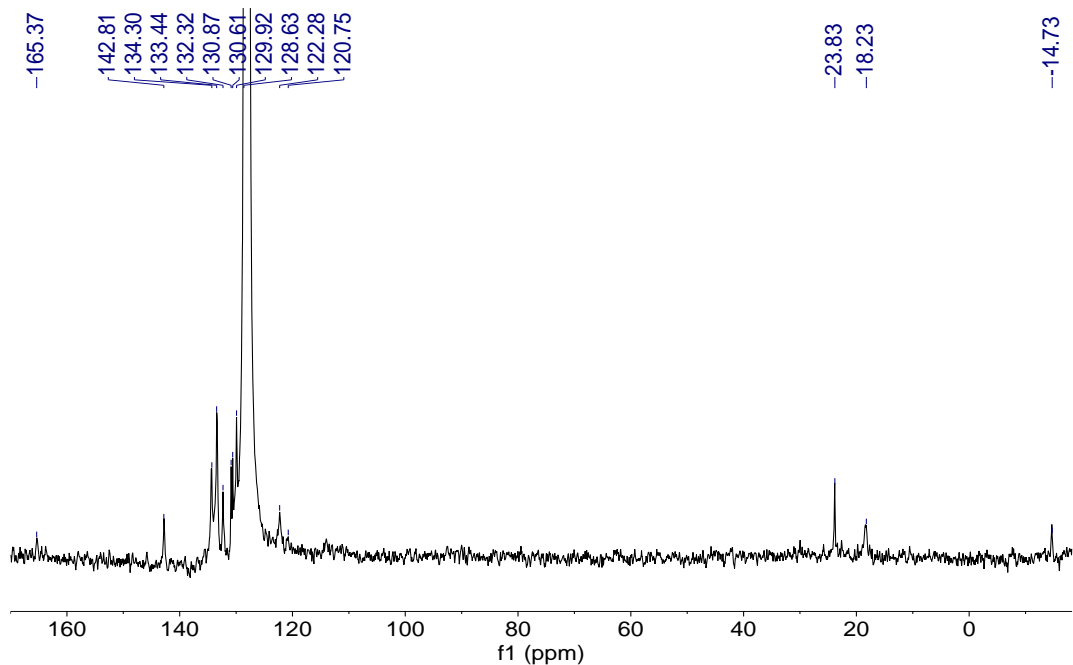


**Figure B.38.**  $^{31}\text{P}\{^1\text{H}\}$  NMR spectrum of  $[\text{Pd}(\text{CH}_3)(\mathbf{3-L2})]_2$ , **3-4** (243 MHz,  $\text{C}_6\text{D}_6$ ).

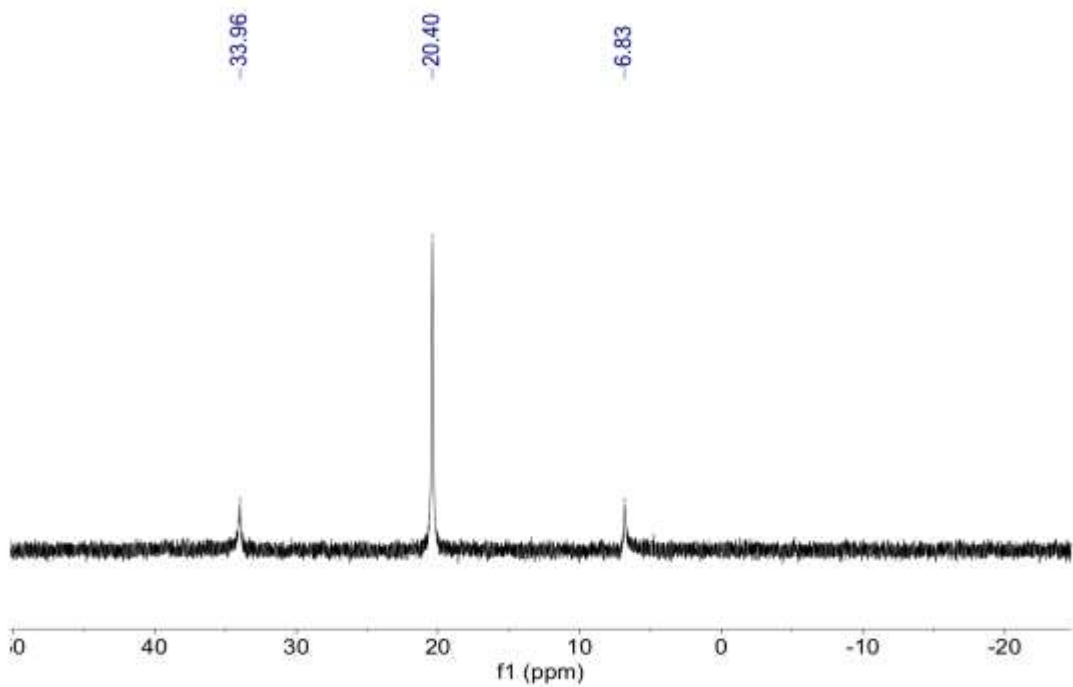


**Figure B.39.**  $^1\text{H}$  NMR spectrum of  $[\text{Pt}(\text{CH}_3)(\mathbf{3-L1})]_2$ , **3-5** (599 MHz,  $\text{C}_6\text{D}_6$ ). \* denotes pentane, 'g' denotes silicon grease.

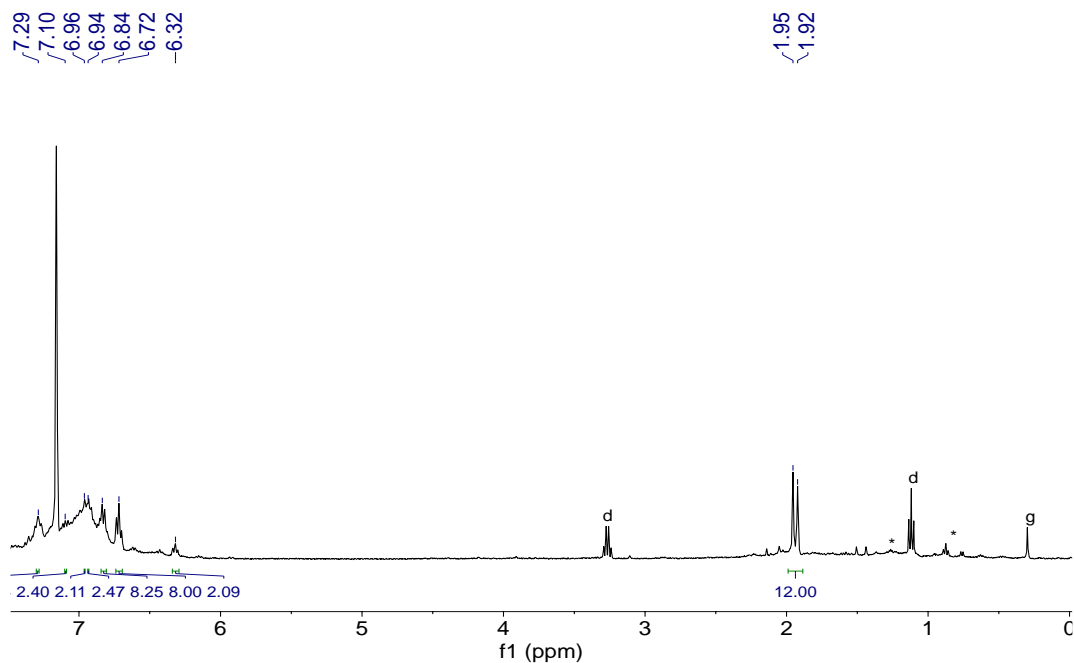




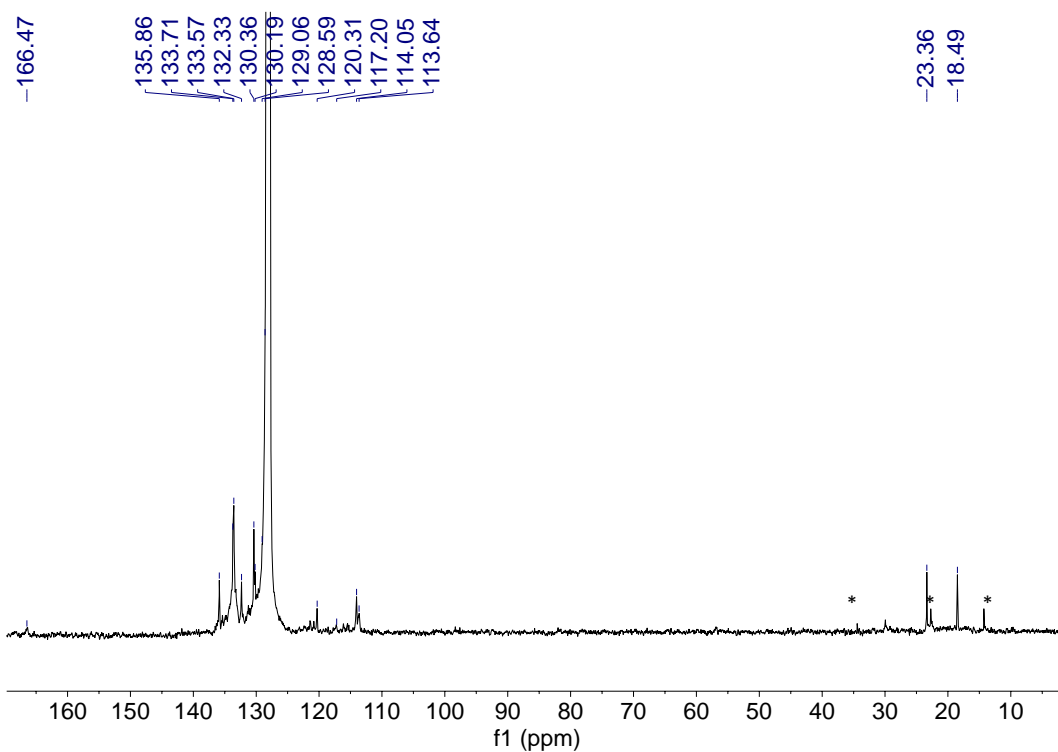
**Figure B.40.**  $^{13}\text{C}\{^1\text{H}\}$  NMR spectrum of  $[\text{Pt}(\text{CH}_3)(\mathbf{3-L1})]_2$ , **3-5** (599 MHz,  $\text{C}_6\text{D}_6$ ).



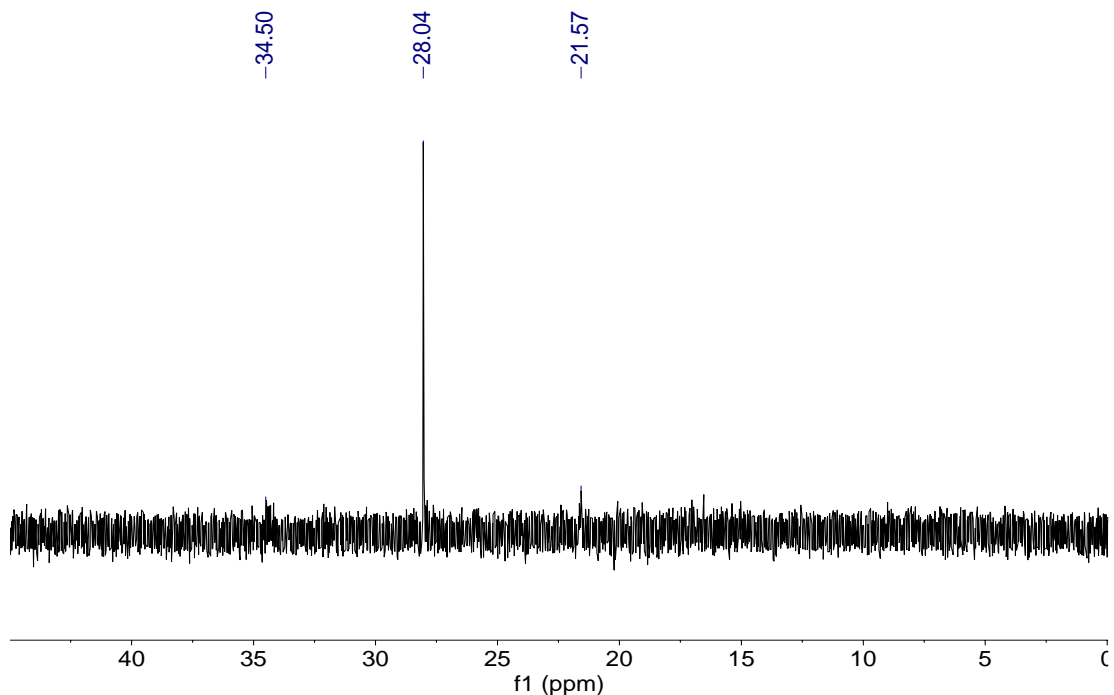
**Figure B.41.**  $^{31}\text{P}\{^1\text{H}\}$  NMR spectrum of  $[\text{Pt}(\text{CH}_3)(\mathbf{3-L1})]_2$ , **3-5** (243 MHz,  $\text{C}_6\text{D}_6$ ).



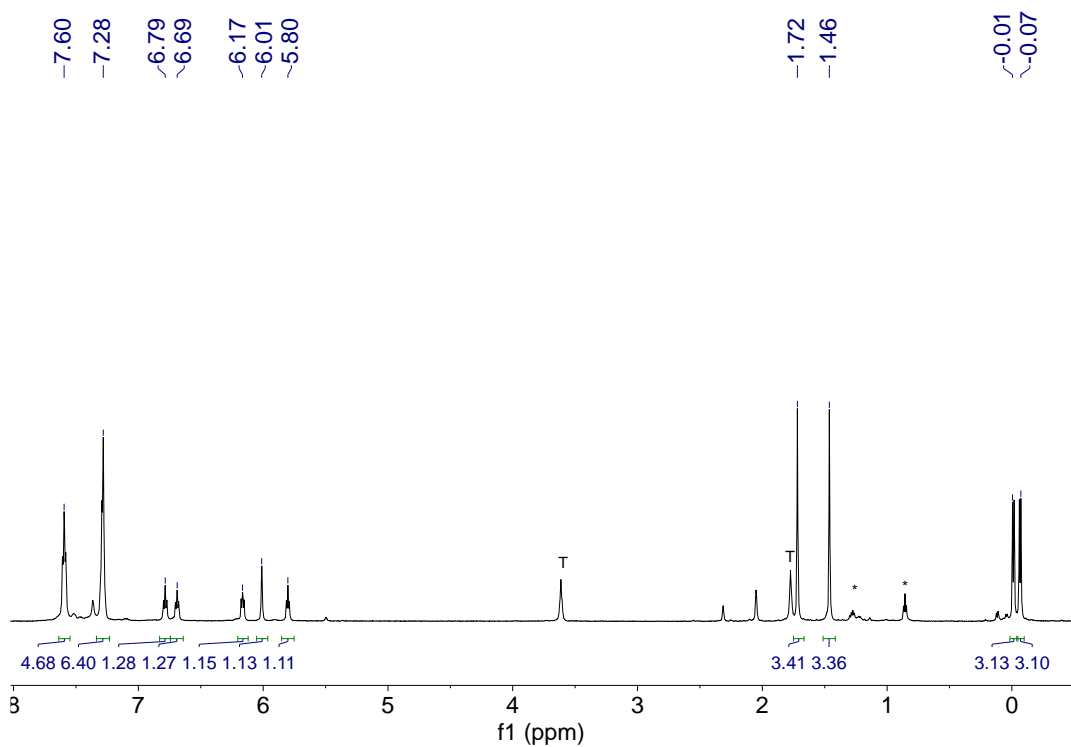
**Figure B.42.**  $^1\text{H}$  NMR spectrum of  $\text{Pt}(\mathbf{3-1})_2$ ,  $\mathbf{3-6}$  (599 MHz,  $\text{C}_6\text{D}_6$ ). \* denotes pentane, 'g' denotes silicon grease, 'd' denotes diethyl ether.



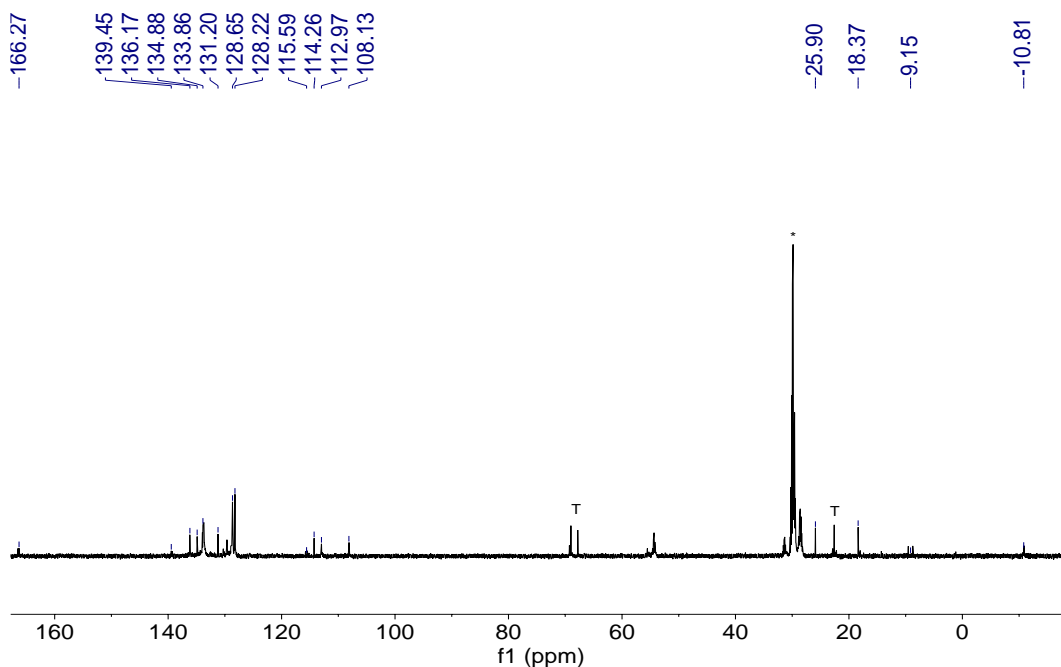
**Figure B.43.**  $^{13}\text{C}\{^1\text{H}\}$  NMR spectrum of  $\text{Pt}(\mathbf{3-L1})_2$ ,  $\mathbf{3-6}$  (151 MHz,  $\text{C}_6\text{D}_6$ ). \* denotes pentane.



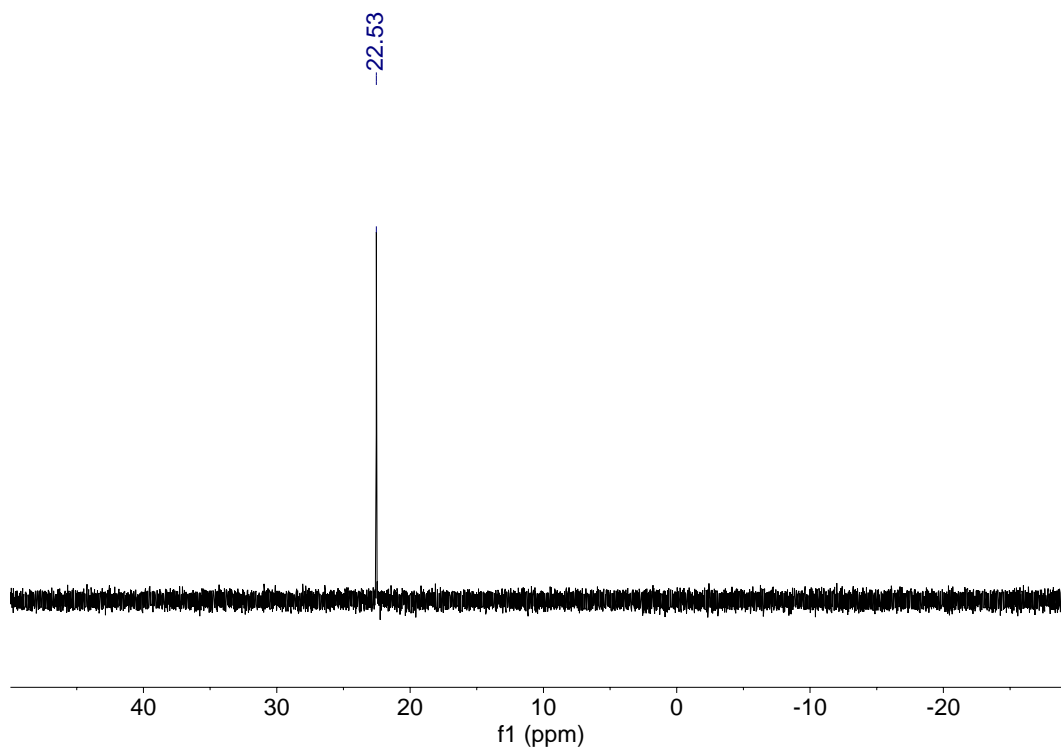
**Figure B.44.**  $^{31}\text{P}\{^1\text{H}\}$  NMR spectrum of  $\text{Pt}(\mathbf{3-L1})_2$ , **3-6** (243 MHz,  $\text{C}_6\text{D}_6$ ).



**Figure B.45.**  $^1\text{H}$  NMR spectrum of  $\text{K}[\text{Pd}(\text{CH}_3)_2(\mathbf{3-L1})]$ , **K[3-7]** (599 MHz,  $(\text{CD}_3)_2\text{CO}$ ). 'T' denotes THF, \* denotes pentane.

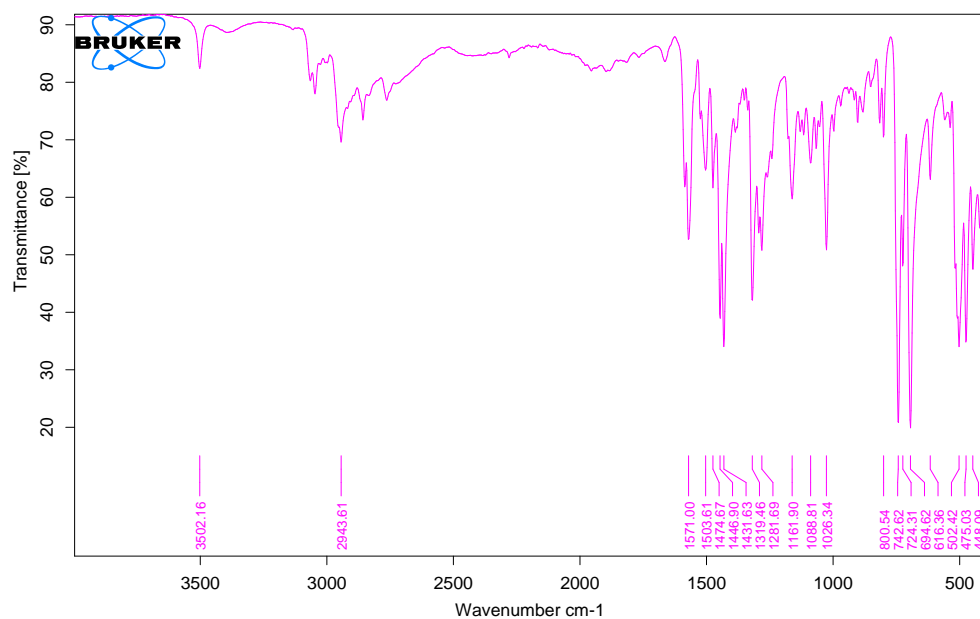


**Figure B.46.**  $^{13}\text{C}\{^1\text{H}\}$  NMR spectrum of  $\text{K}[\text{Pd}(\text{CH}_3)_2(\mathbf{3-L1})]$ ,  $\mathbf{K}[\mathbf{3-7}]$  (151 MHz,  $-20\text{ }^\circ\text{C}$   $(\text{CD}_3)_2\text{CO}$ ). 'T' denotes THF, \* denotes acetone.

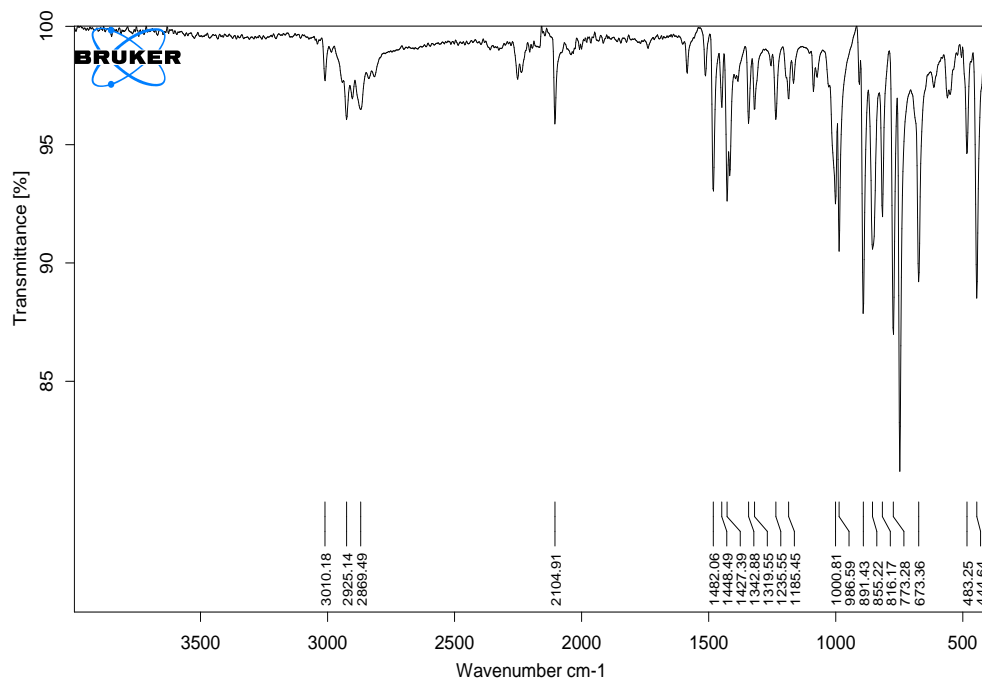


**Figure B.47.**  $^{31}\text{P}\{^1\text{H}\}$  NMR spectrum of  $\text{K}[\text{Pd}(\text{CH}_3)_2(\mathbf{3-L1})]$ ,  $\mathbf{K}[\mathbf{3-7}]$  (243 MHz,  $(\text{CD}_3)_2\text{CO}$ ).

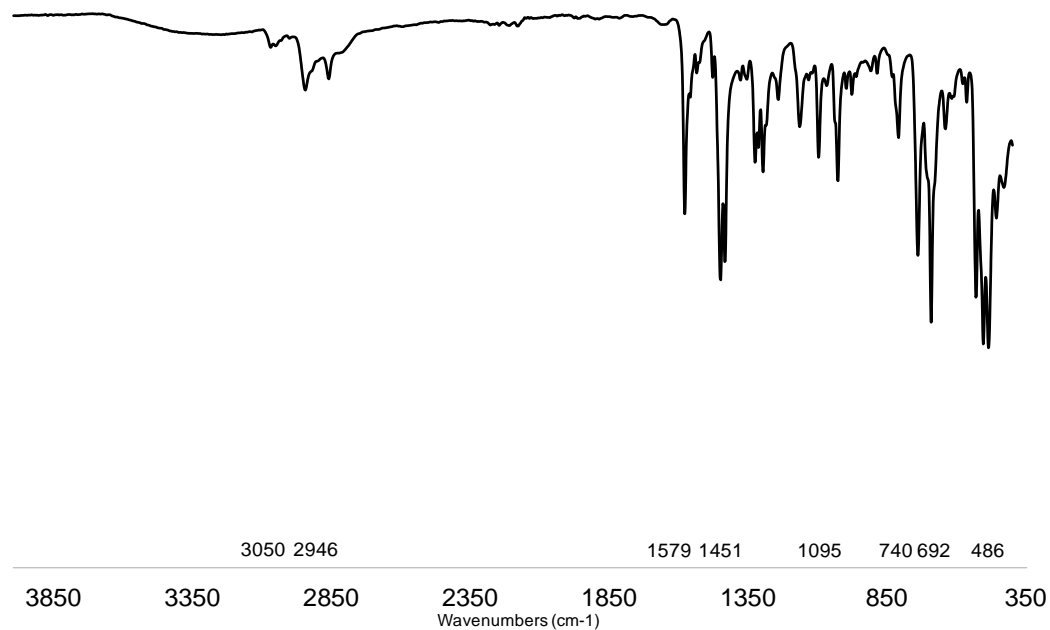
### III – IR Spectra



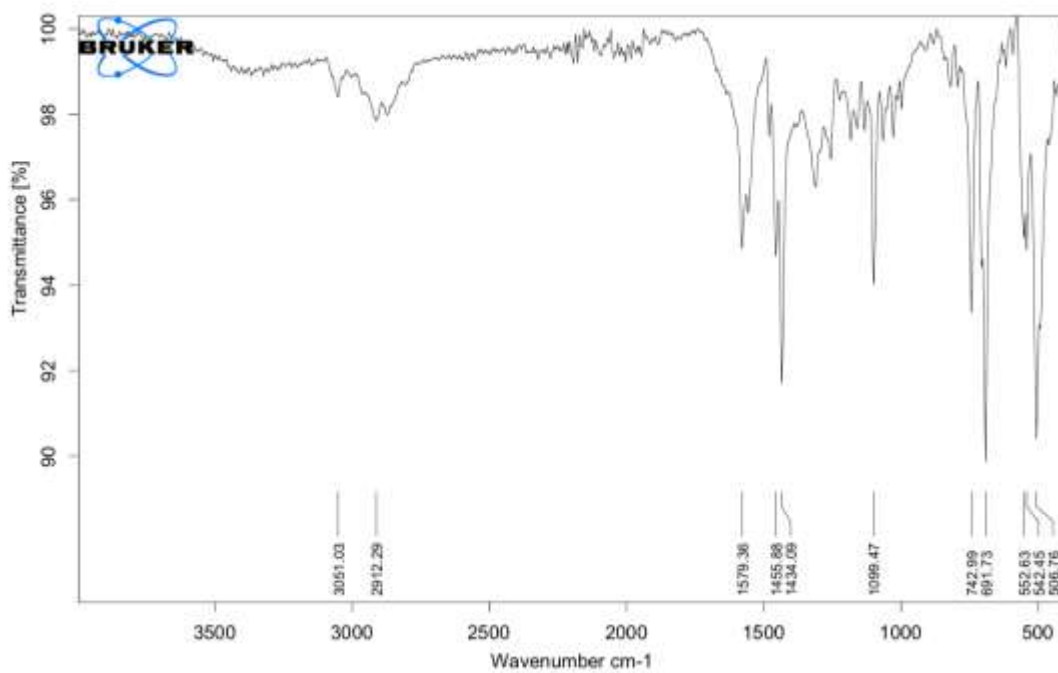
**Figure B.48.** ATR-FTIR of solid  $\text{Ph}_2\text{P}(o\text{-C}_6\text{H}_4)\text{NH}(i\text{-Bu})$ , **H[3-L2]**.



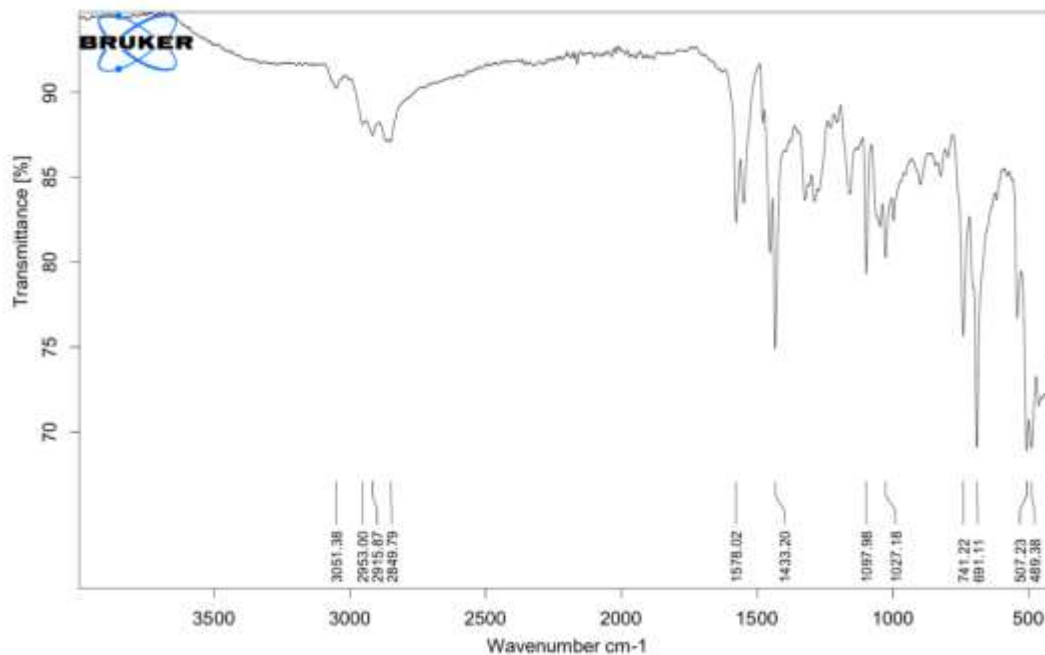
**Figure B.49.** ATR-FTIR of solid  $[\text{PdCl}(\text{CD}_3)(\text{COD})]$ .



**Figure B.50.** ATR-FTIR of solid  $[\text{Pd}(\text{CH}_3)(\mathbf{3-L2})]_2$ , **3-4**. Data acquired using Bruker Alpha II ATR-FTIR and plotted using Microsoft Excel.

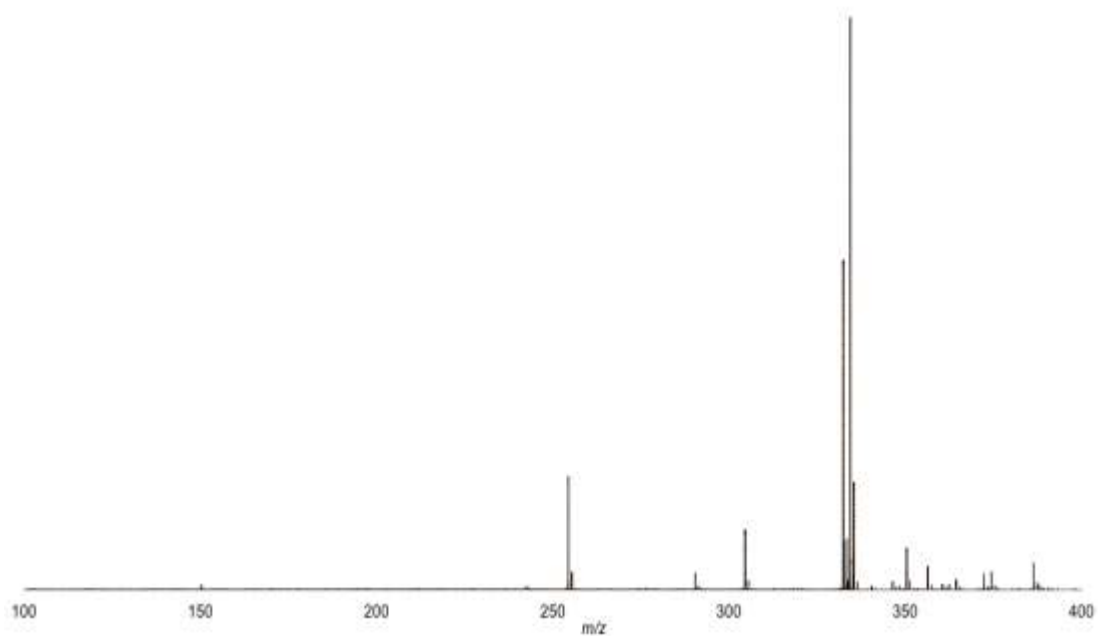


**Figure B.51.** ATR-FTIR of solid  $[\text{Pt}(\text{CH}_3)(\mathbf{3-L1})]_2$ , **3-5**.

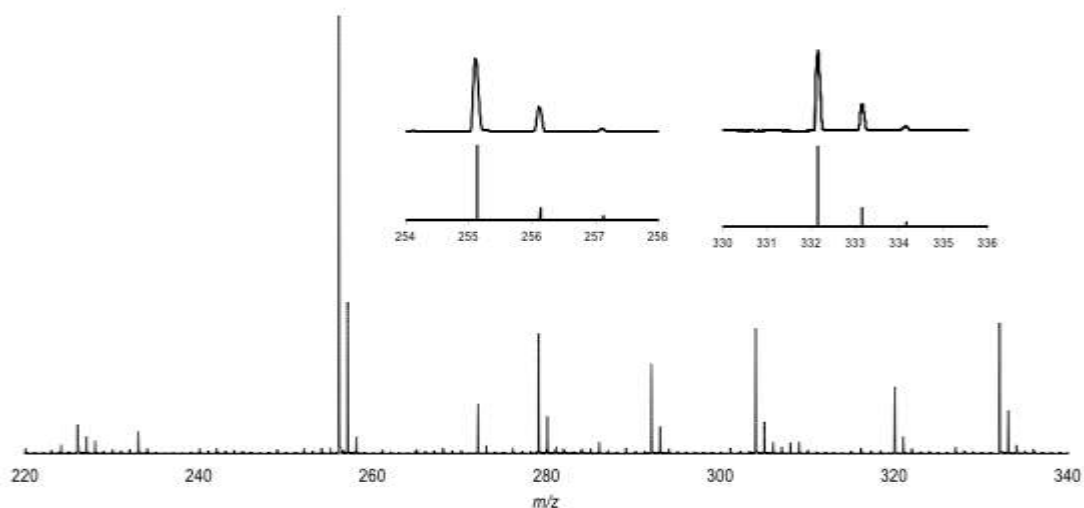


**Figure B.52.** ATR-FTIR of solid  $K[Pd(CH_3)_2(3-L1)]$ , **K[3-7]**.

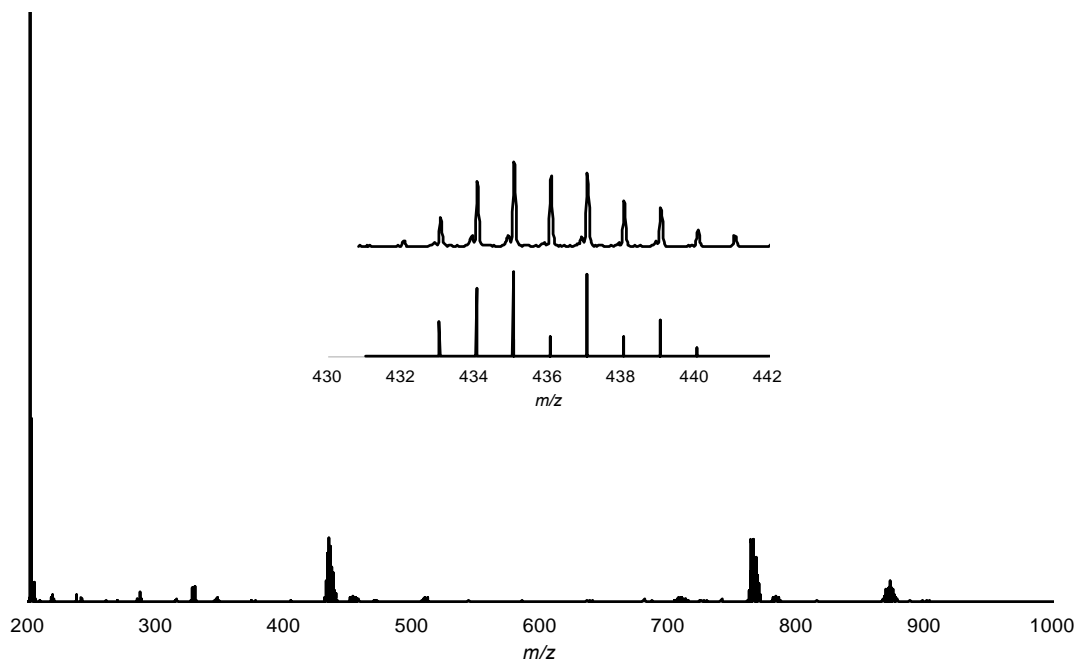
#### IV – Mass Spectra



**Figure B.53.** ESI mass spectrum of **H[3-L2]**.

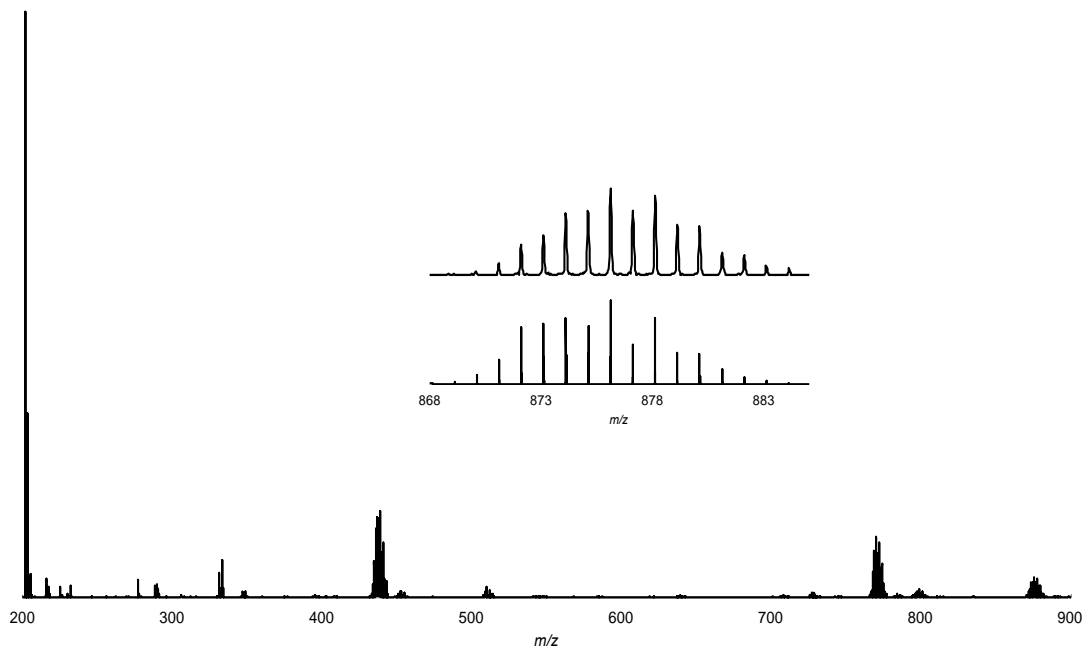


**Figure B.54.** MALDI mass spectrum of  $\text{K}[\text{Ph}_2\text{P}(o\text{-C}_6\text{H}_4)\text{N}(i\text{-Bu})]$ , **K[3-L2]** acquired in reflectron negative mode with pyrene as the matrix. Left inset: simulated spectrum (bottom) for  $[\mathbf{3-L2-C}_6\text{H}_5]^-$  and observed signal (top) at  $m/z = 255.1$ . Right inset: simulated (bottom) for  $[\mathbf{3-L2}]^-$  and observed signal (top) at  $m/z = 332.2$

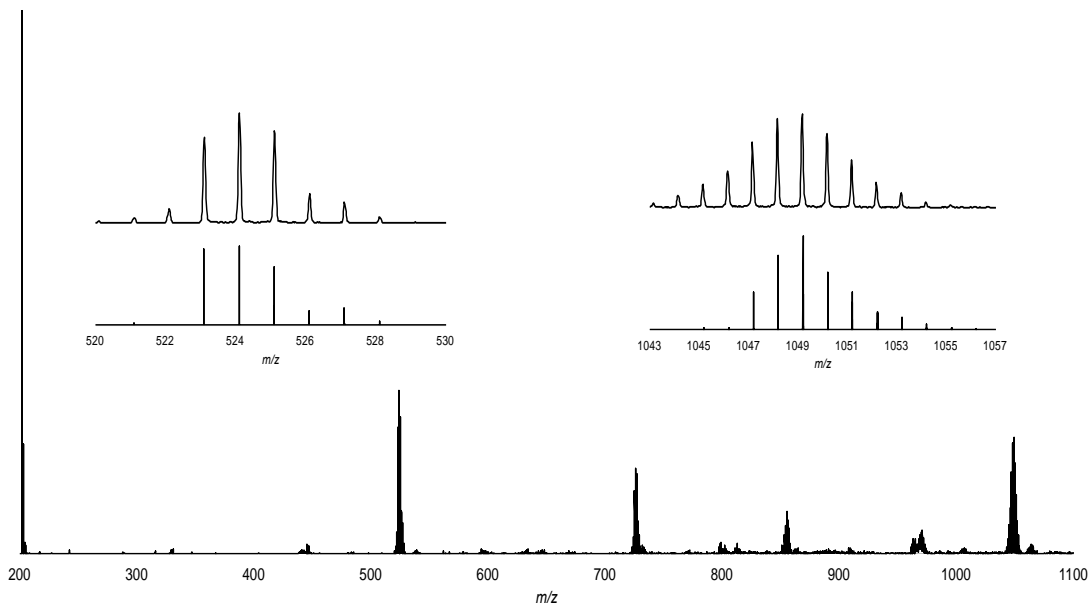


**Figure B.55.** MALDI mass spectrum of  $[\text{Pd}(\text{CD}_3)(\mathbf{3-L1})]_2$ , **3-1-*d*<sub>6</sub>** with pyrene as the matrix. Inset: simulated isotope pattern (bottom) for  $[\text{Pd}(\mathbf{3-L1})]^+$  and observed signal (top) at  $m/z = 435.0$ . Additional major signals likely due to gas phase aggregation/fragmentation; Signal at  $m/z = 766.2 = [\mathbf{3-3}]^+$ ; Signal at  $m/z = 874.1 = [\mathbf{3-2}]^+$ .

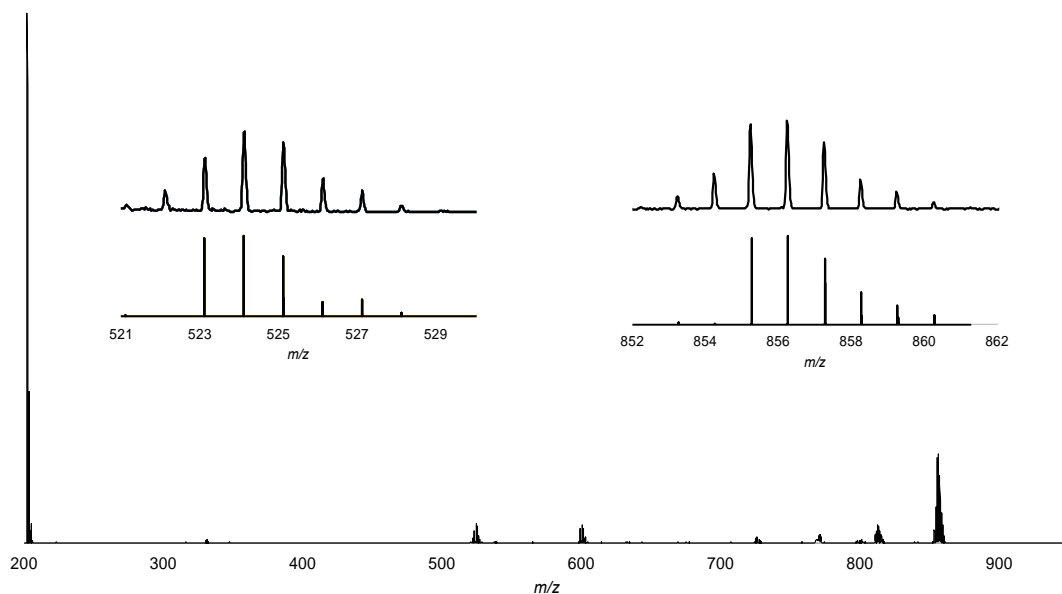




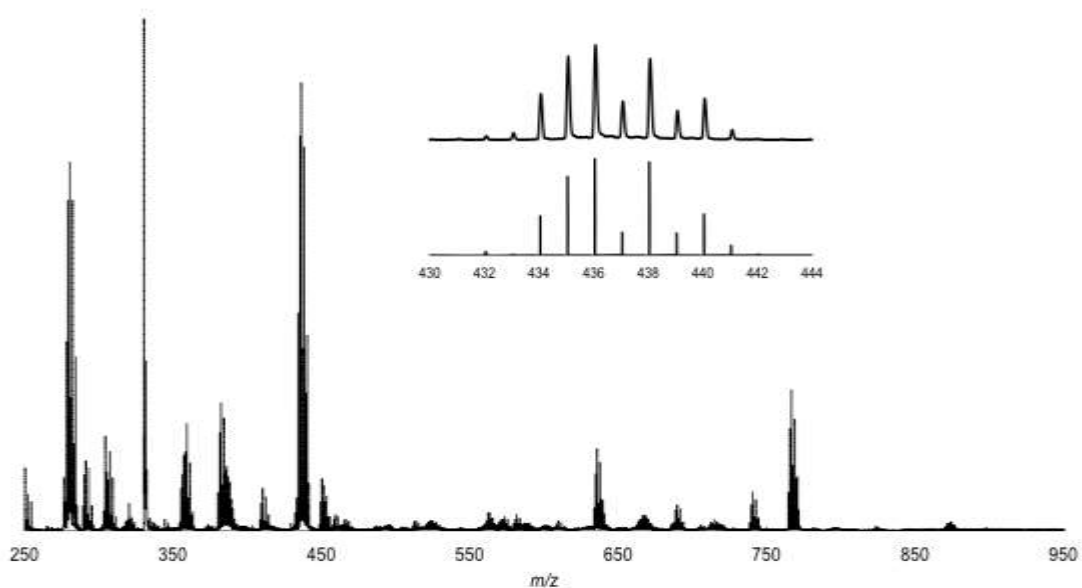
**Figure B.56.** MALDI mass spectrum of  $[\text{Pd}(\text{CH}_3)(\mathbf{3-L2})]_2$ , **3-4** with pyrene as the matrix. Inset: simulated isotope pattern (bottom) for  $[\mathbf{3-4-(CH_3)_2}]^{+}$  and observed signal (top) at  $m/z = 876.1$ .



**Figure B.57.** MALDI mass spectrum of  $[\text{Pt}(\text{CH}_3)(\mathbf{3-L1})]_2$ , **3-5** with pyrene as the matrix. Left inset: simulated isotop pattern (bottom) for  $[\text{Pt}(\mathbf{3-L1})]^{+}$  and observed signal (top) at  $m/z = 524.1$ . Right inset: simulated (bottom) for  $[\mathbf{3-5-(Me)_2}]^{+}$  and observed signal (top) at  $m/z = 1049.2$ .

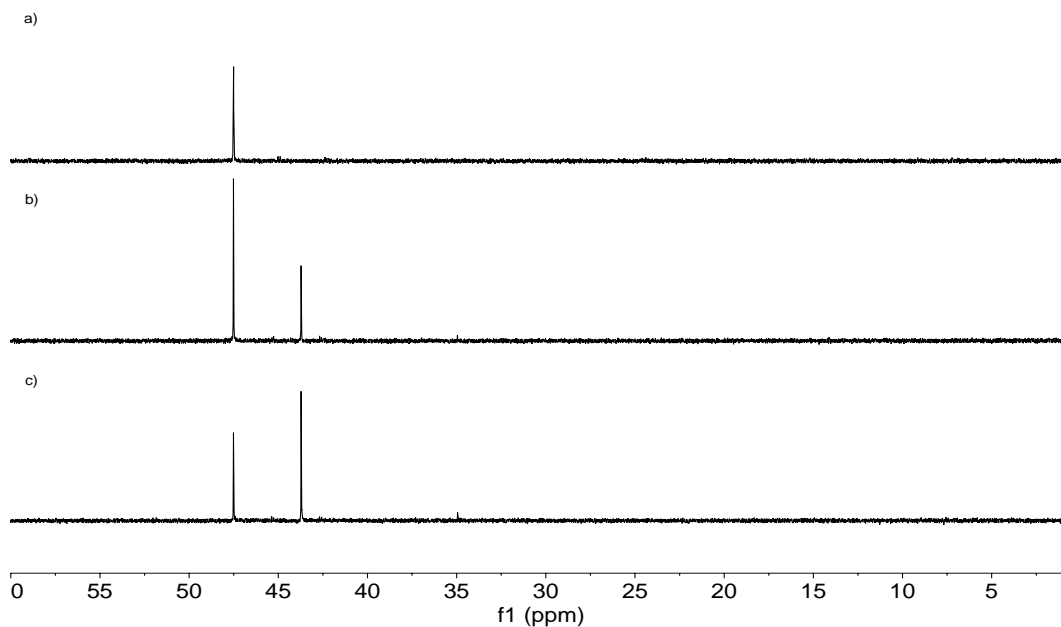


**Figure B.58.** MALDI mass spectrum of  $[\text{Pt}(\mathbf{3-L1})_2]$ , **3-6** with pyrene as the matrix. Left inset: simulated pattern (bottom) for  $[\text{Pt}(\mathbf{3-L1})]^+$  and observed signal (top) at  $m/z = 524.1$ . Right inset: simulated pattern (bottom) for  $[\mathbf{3-6}]^+$  and observed signal (top) at  $m/z = 855.3$ .



**Figure B.59.** Negative ion MALDI mass spectrum of  $\text{K}[\text{Pd}(\text{CH}_3)_2(\mathbf{3-L1})]$ , **3-7** acquired in reflectron negative mode with pyrene as the matrix. Inset: simulated pattern (bottom) for  $[\mathbf{3-7-(CH}_3)_2]^-$  and observed signal (top) at  $m/z = 436.1$ . Additional major signals likely due to gas phase aggregation/fragmentation; Signal at  $m/z = 766.2 = [\mathbf{3-3}]^-$ .

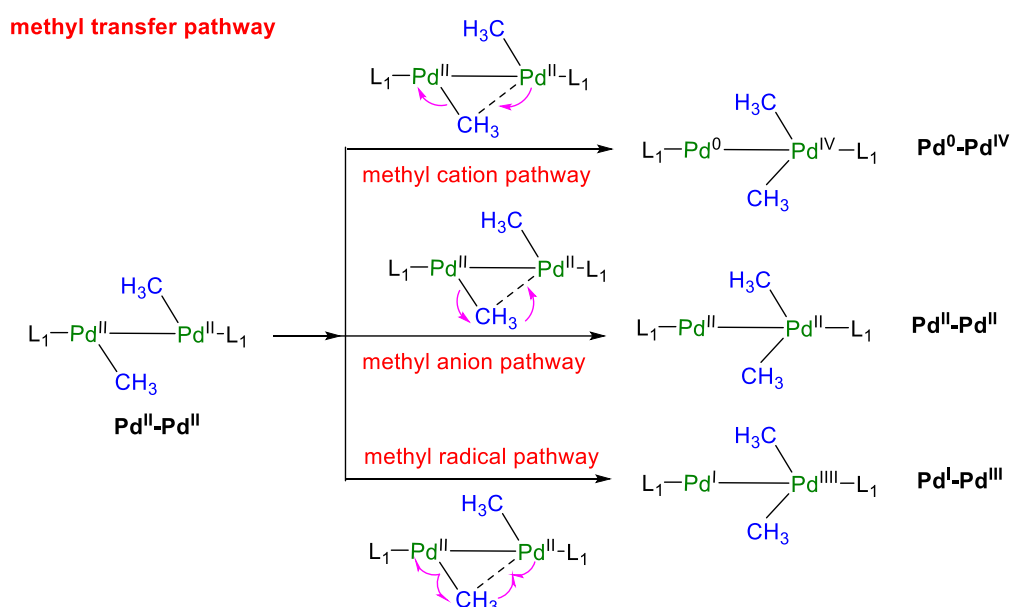
## V – Reaction NMR Spectra



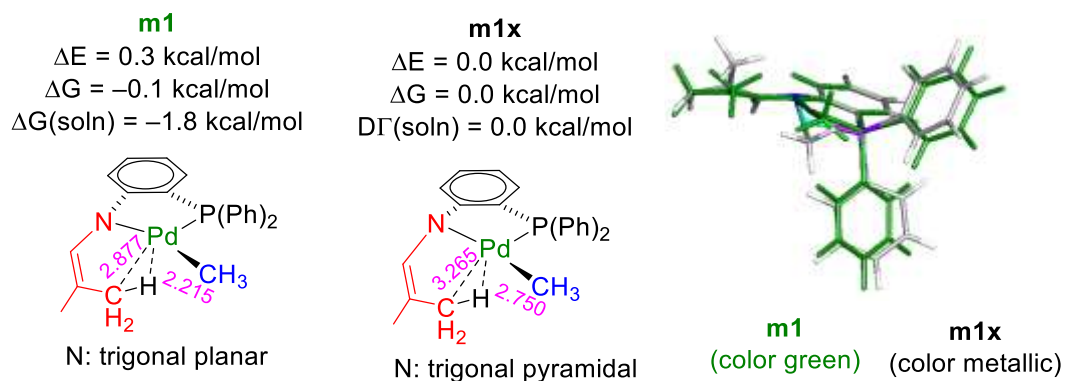
**Figure B.60.** Stack of  $^{31}\text{P}\{^1\text{H}\}$  NMR spectra of **3-3**: a) before the addition of  $[\text{Pd}(\text{CH}_3)_2(\text{COD})]$  ( $T_0$ ); b) After addition of 3.5 equiv  $\text{Pd}(\text{Me})_2(\text{COD})$  at rt for 10 min ( $\text{C}_6\text{D}_6$ ); and c) After addition of 3.5 equiv  $\text{Pd}(\text{Me})_2(\text{COD})$  at rt for 60 min (243 MHz,  $\text{C}_6\text{D}_6$ ). Complex **3-3** is the downfield signal at  $\delta$  47.7. Complex **3-1** is the upfield signal at  $\delta$  43.7.

## VI – Computational Details

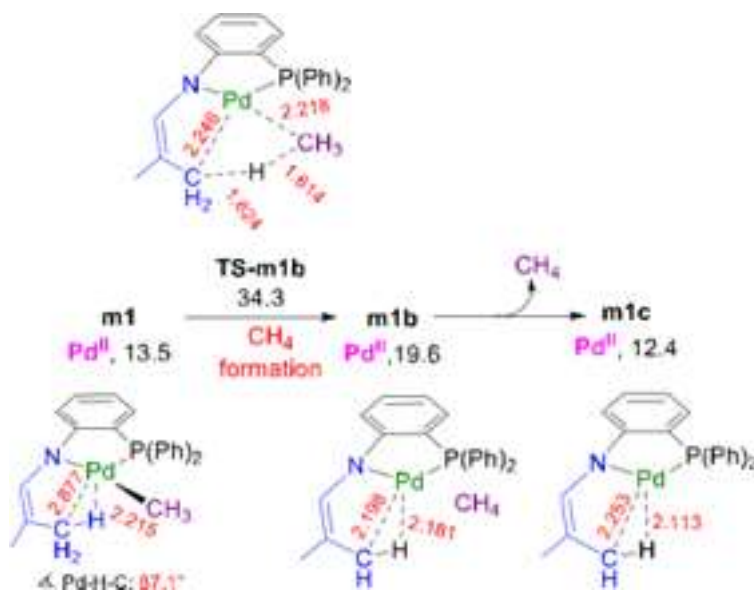
The proposed reaction pathways were optimized using the Growing String Method (GSM)<sup>7-9</sup> developed by the Zimmerman group, using the Q-Chem 5.2 software package<sup>10</sup>. The B97-D<sup>11,12</sup> density functional with basis BS1 [B97-D/BS1, BS1: 6-31G<sup>13</sup> for H, C, N, LANL2DZ and fit-LANL2DZ ECP<sup>14,15</sup> for P, and Pd] were utilized in the gas phase GSM computations. Following GSM optimizations, transition states were further refined using the B97-D density functional with basis BS2 [B97-D/BS2, BS2: 6-31G(d)<sup>13,16</sup> for H, C, N, LANL2DZ and fit-LANL2DZ ECP for P, and Pd]. ECP fitting<sup>17</sup> for the LANL2DZ basis set of P and Pd was used via keyword fit-LANL2DZ. Frequency computations (B97-D/BS2) were performed in order to verify the nature of all stationary points. A self-consistent field convergence of  $10^{-6}$  was used for all computations. Single-point energy computations in benzene (C<sub>6</sub>H<sub>6</sub>) used the SMD model<sup>18</sup> with BS3 (def-TZVP<sup>19</sup> for H, C, N and P, def2-TZVP<sup>20</sup> and related ECP<sup>21</sup> for Pd) to model the solvation effect of the chemical reactions in solution (SMD<sub>(C<sub>6</sub>H<sub>6</sub>)</sub>-B97-D/BS3//B97-D/BS2). The energies [SMD<sub>(C<sub>6</sub>H<sub>6</sub>)</sub>-B97-D/BS3//B97-D/BS2] are determined at 1 atm and 298.15 K, and Gibbs free energies of activation ( $\Delta G^\ddagger$ ) and Gibbs free energies of reaction ( $\Delta G^\circ$ ) are given in kcal mol<sup>-1</sup>. Oxidation states were computed using localized orbital bonding analysis (LOBA)<sup>22</sup> with the method of PM localization and analyzed via Löwdin population (keywords LOBA=12, and LOBA\_THRESH=6015). The second order perturbation energies ( $E^2$ , in kcal/mol) were obtained from natural bond orbital computations (NBO 5.0 package)<sup>23</sup> incorporated in Q-Chem 5.2 package<sup>10</sup>. Note for monomer **m1**: Two isomers of monomer **m1** and a higher energy species, **m1x**, were computed. Compared to **m1x**, a weak agostic interaction was present in isomer **m1**. The gas-phase electronic energy of **m1** is 0.3 kcal/mol higher than that of **m1x**, and the solvent-corrected Gibbs free energy of **m1** is -1.8 kcal/mol lower than that of **m1x**.



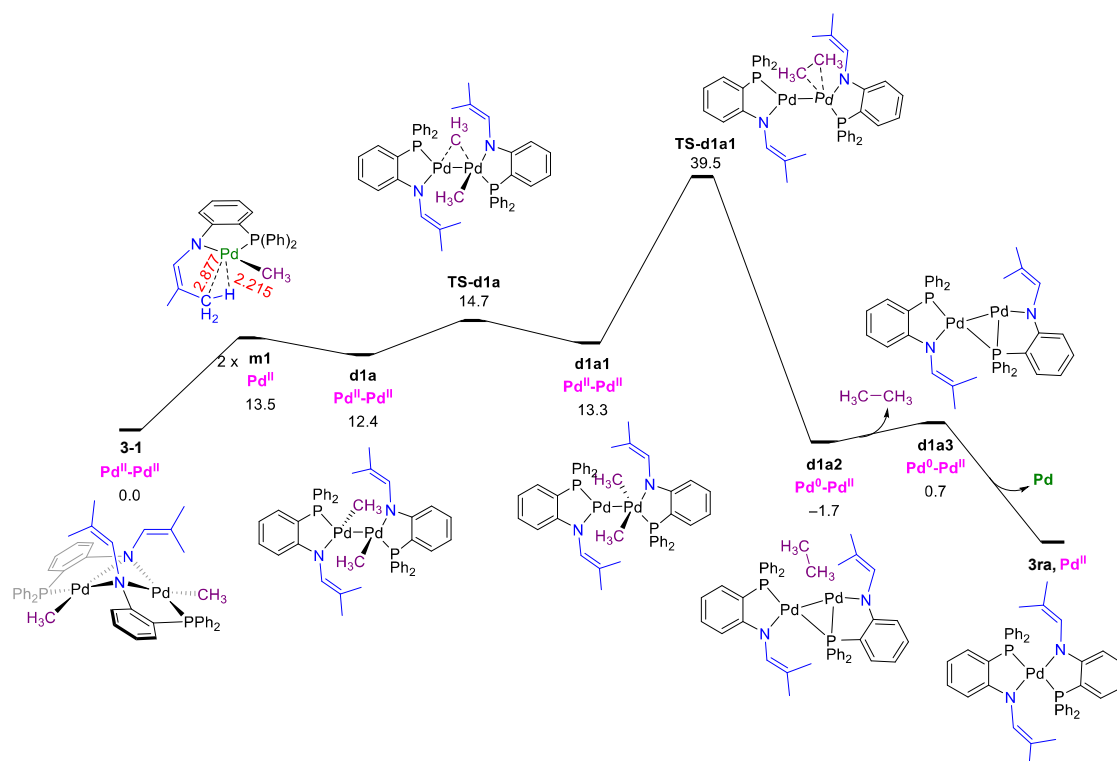
**Scheme B.2.** The oxidation states of the Pd centers in various methyl transfer pathways.



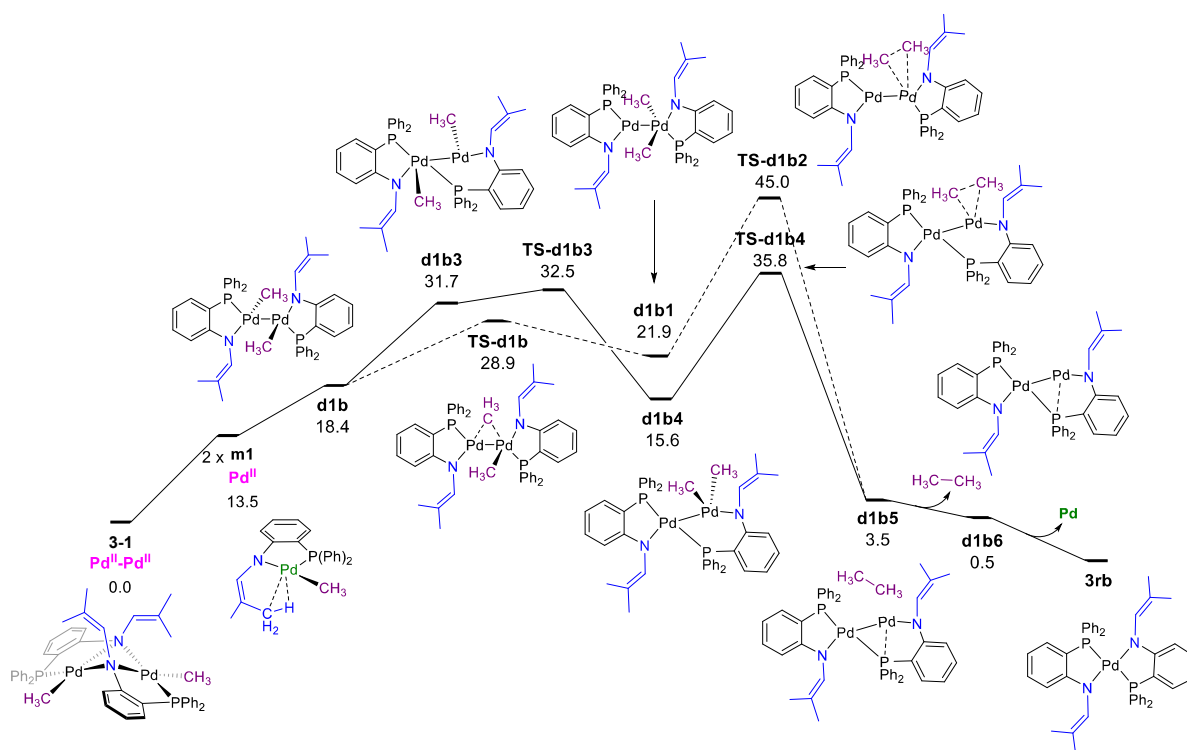
**Scheme B.3.** Details of **m1** and **m1x**.



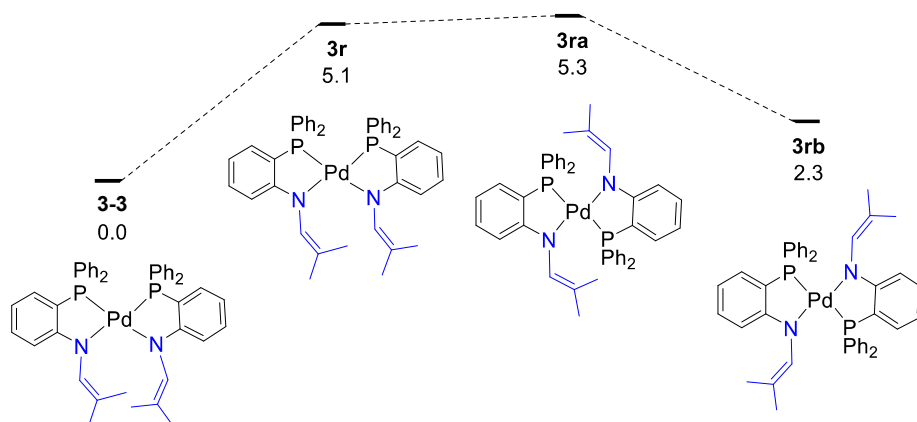
**Scheme B.4.** Formation of methane via the CMD-type (redox neutral) C-H activation.



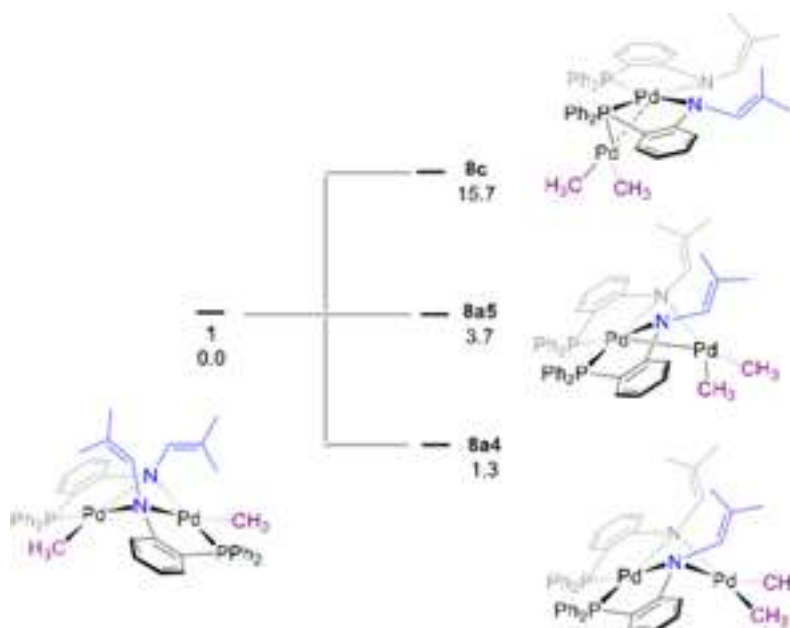
**Scheme B.5.** Alternative pathway for generation of ethane, Pd(0), and Pd<sup>II</sup>(L)<sub>2</sub> via dimer **d1a**.  $\Delta G^\circ/\Delta G^\ddagger$  are in kcal mol<sup>-1</sup>.



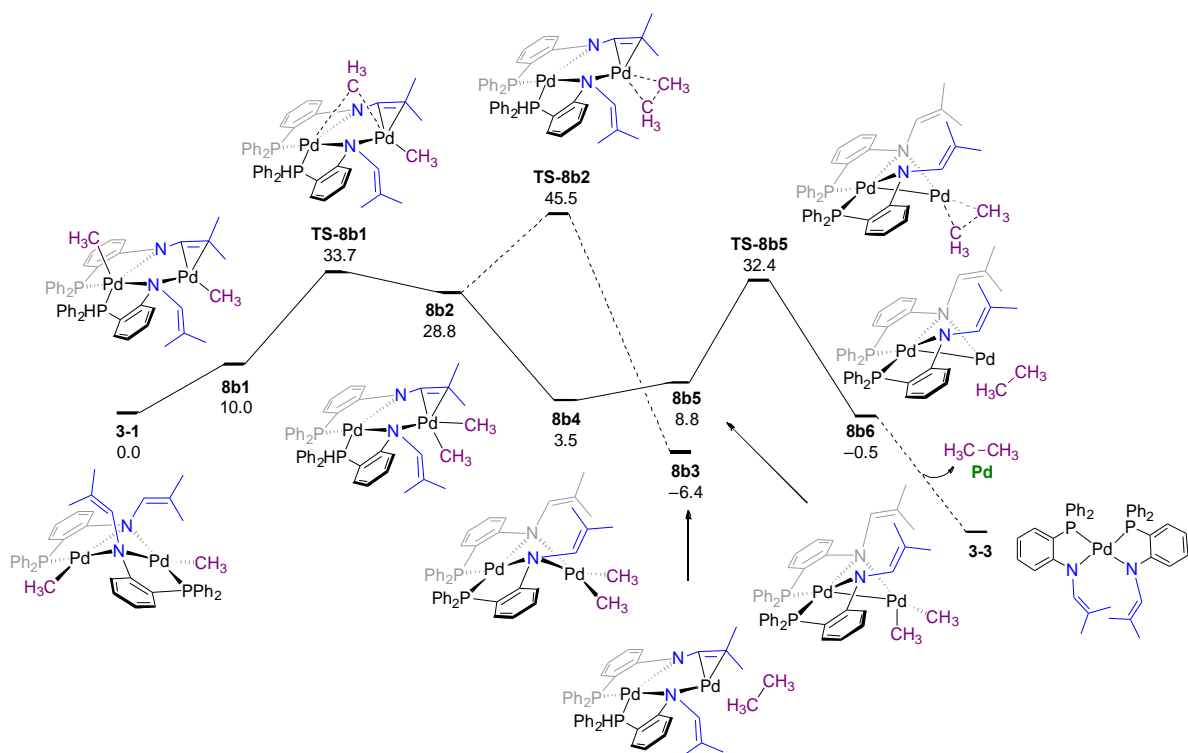
**Scheme B.6.** The generation of ethane, Pd(0), and Pd<sup>II</sup>(L)<sub>2</sub> via the rotamer of a pseudo methyl-bridged dimer **d1b**.  $\Delta G^\circ/\Delta G^\ddagger$  are in kcal mol<sup>-1</sup>.



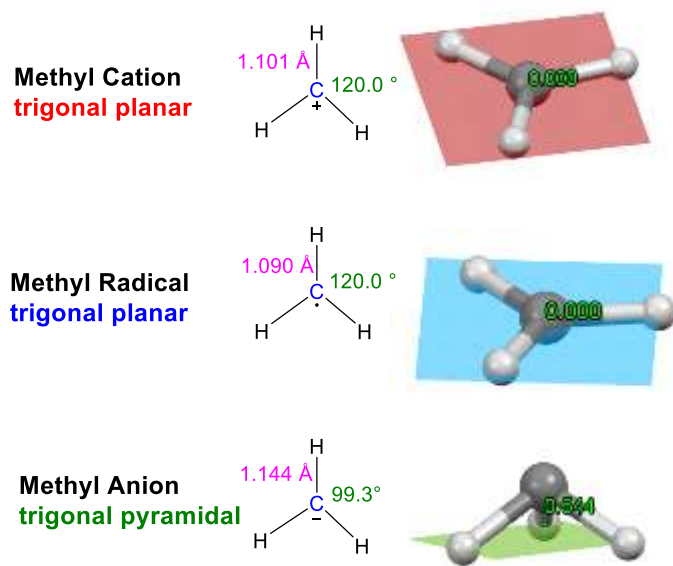
**Scheme B.7.** The relative energies of Pd<sup>II</sup>(L)<sub>2</sub> complex **3-3** and its rotamers.  $\Delta G^\circ$  are in kcal mol<sup>-1</sup>.



**Scheme B.8.** Comparisons of phosphine and nitrogen coordinated Pd(Me)<sub>2</sub> intermediates.

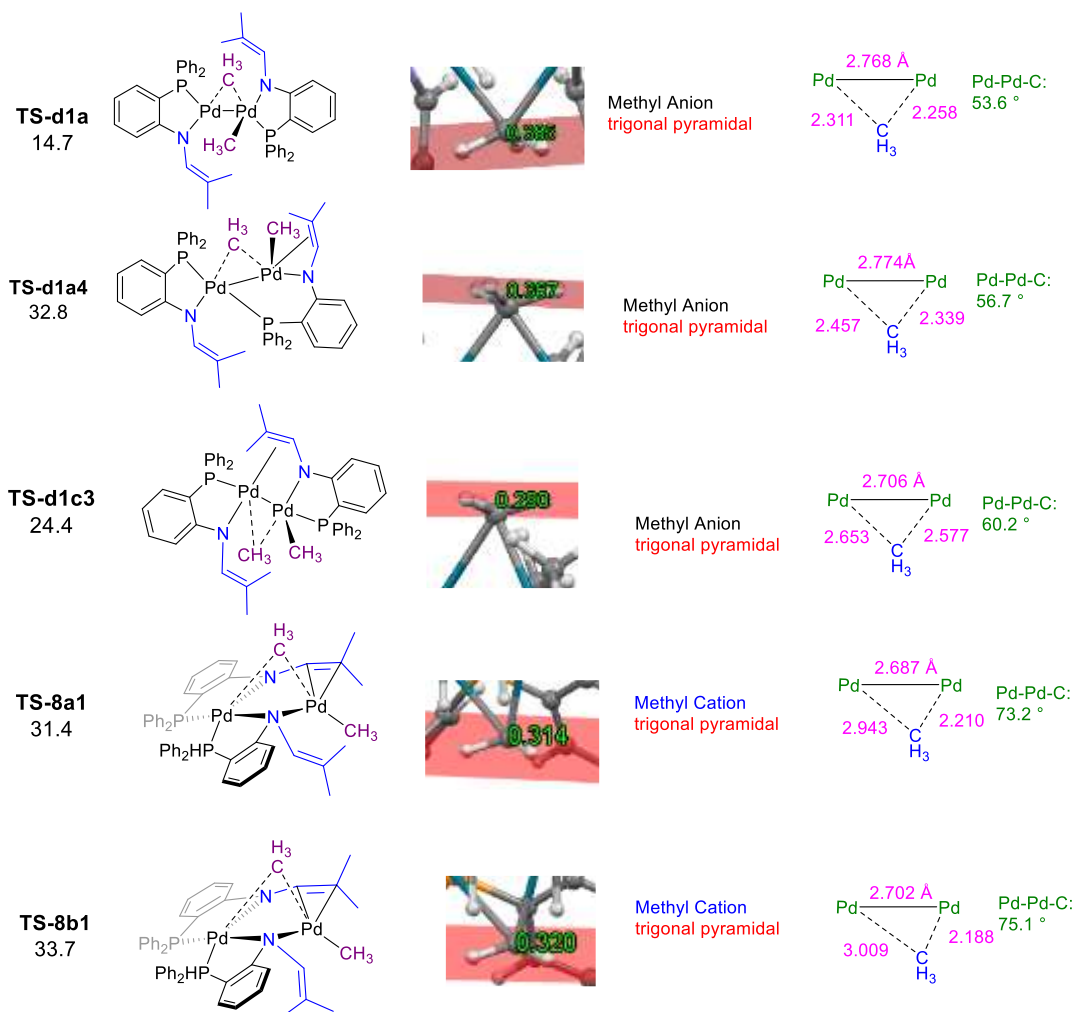


**Scheme B.9.** Ethane formation from a dimethyl dimer **8b5**.  $\Delta G^\circ/\Delta G^\ddagger$  are in kcal mol<sup>-1</sup>.

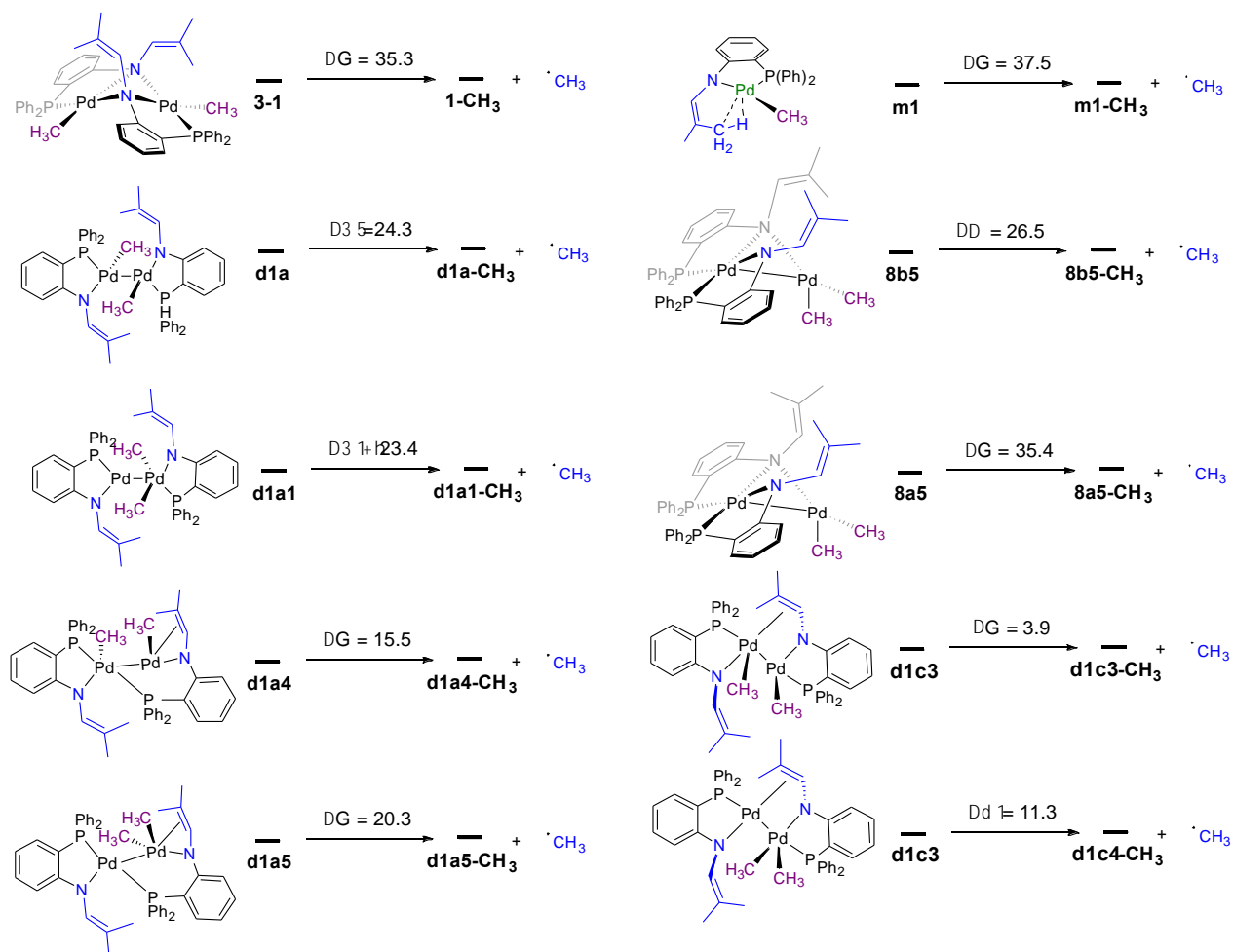


**Figure B.61.** The geometries of various CH<sub>3</sub> fragments. C-HHH out-of-plane distances are in Å.

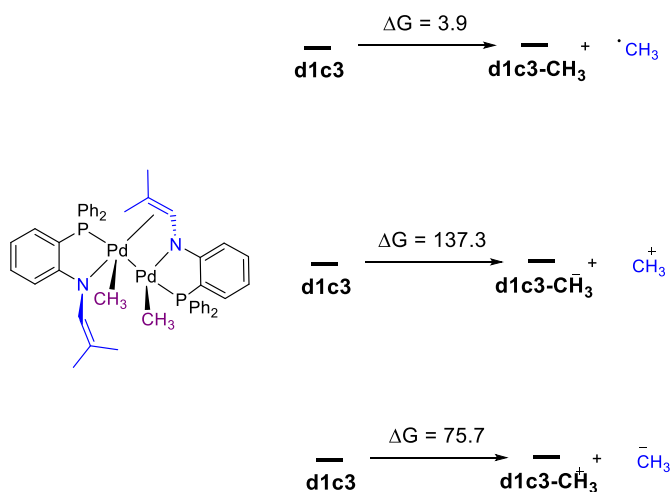




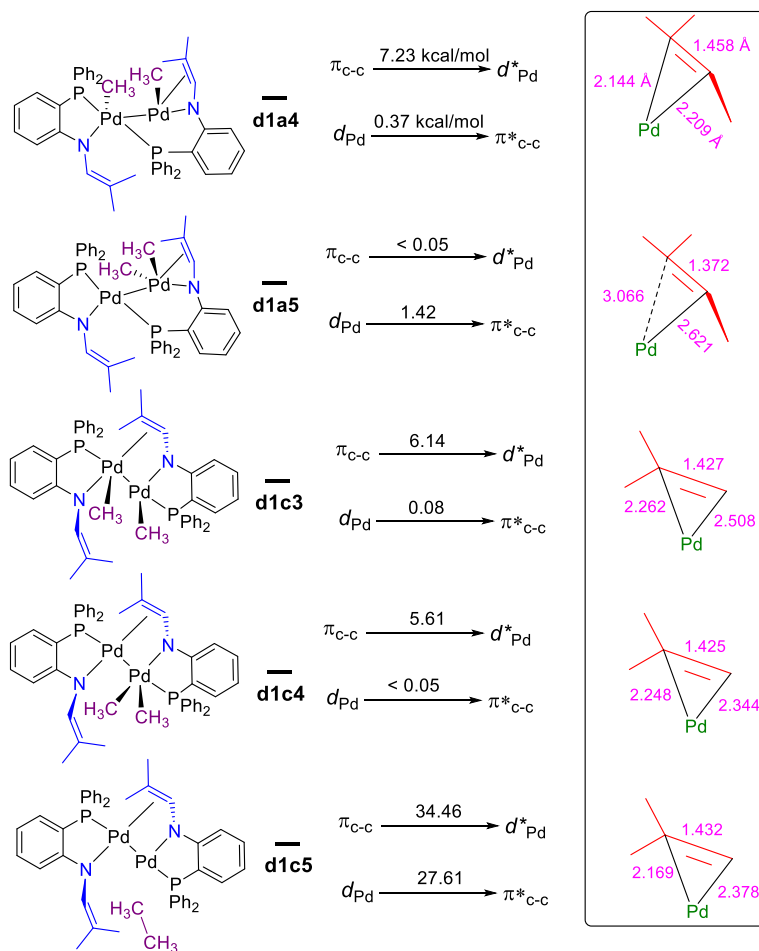
**Figure B.62.** The geometries of  $\text{CH}_3$  fragments in select transition states. C-HHH out-of-plane distances in  $\text{\AA}$ .



**Scheme B.10.** Reaction energies for methyl radical cleavage from Pd dimer **3-1**.



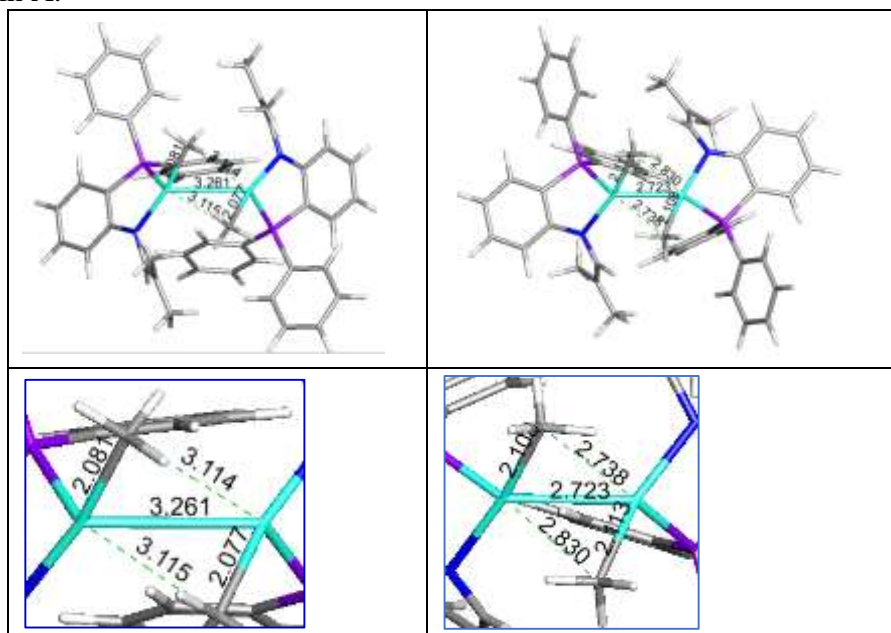
**Scheme B.11.** Reaction energies for the formation of methyl radical, methyl cation, and methyl anion from dimer **d1c3**.

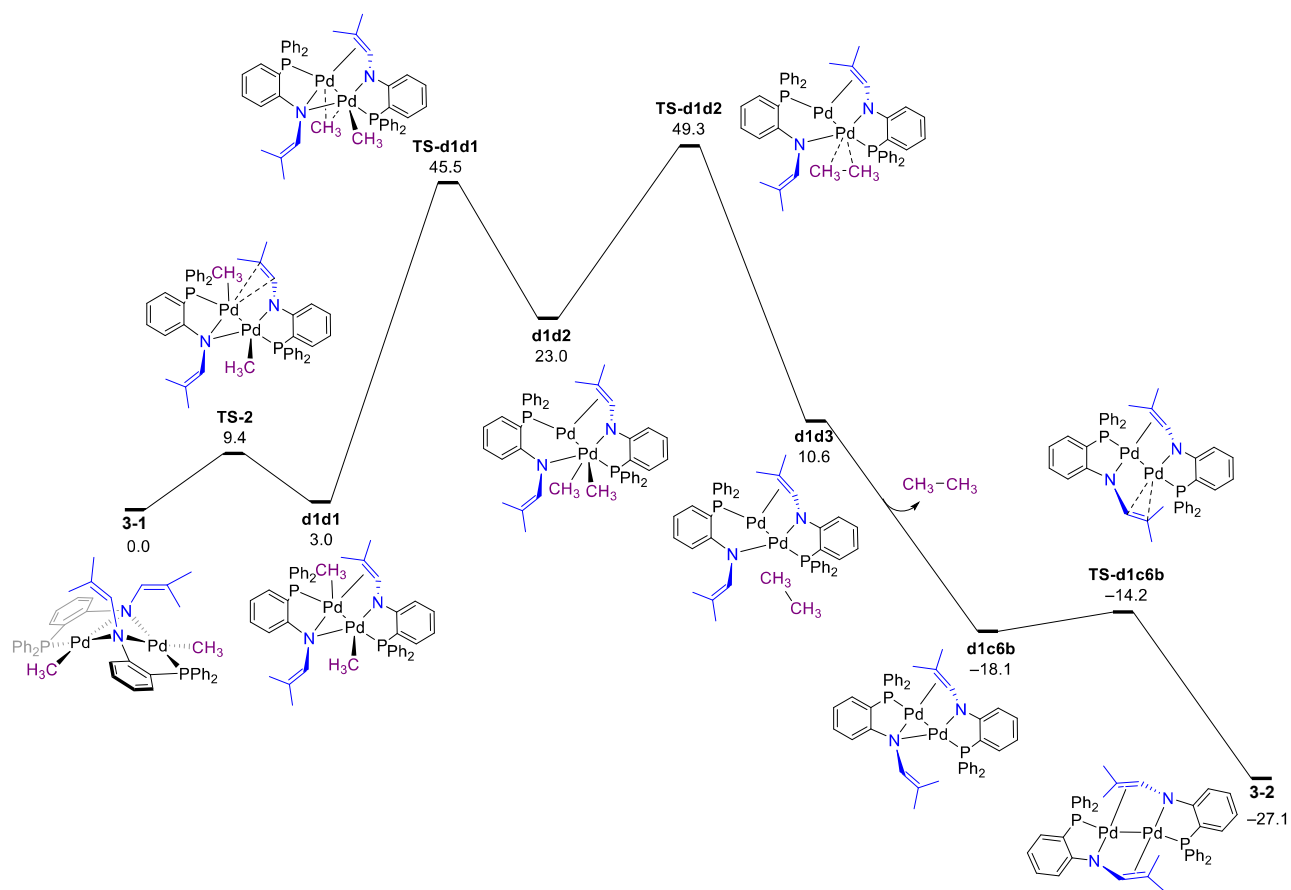


$E^2$ : second order perturbation energy (kcal/mol)

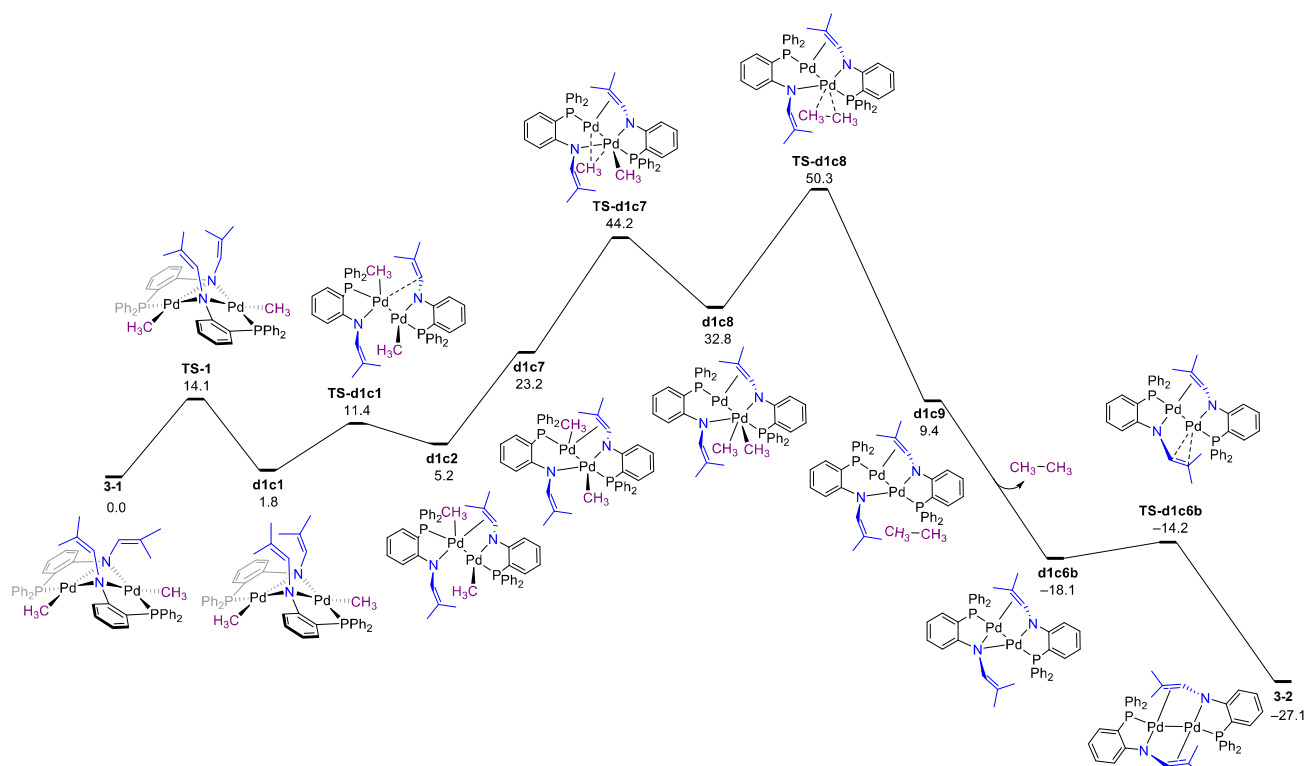
**Scheme B.12.** The second order perturbation energies ( $E^2$ , in kcal/mol) of Pd dimers from natural bond orbital (NBO) computations.

**Table B.2.** Select interatomic distances in the pseudo methyl-bridged dimers **d1a** and **d1b**. The distances are in Å.





**Scheme B.13.** Ethane formation from high energy ligand-bridged dimer **d1d1**.  $\Delta G^\circ/\Delta G^\ddagger$  are in kcal  $\text{mol}^{-1}$ .






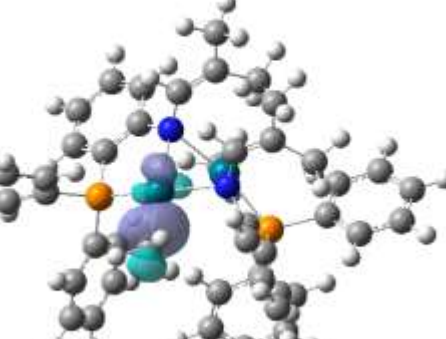
**Scheme B.14.** Ethane formation from the second-high energy ligand-bridged dimer **d1c2**.  $\Delta G^\circ/\Delta G^\ddagger$  are in kcal mol<sup>-1</sup>.

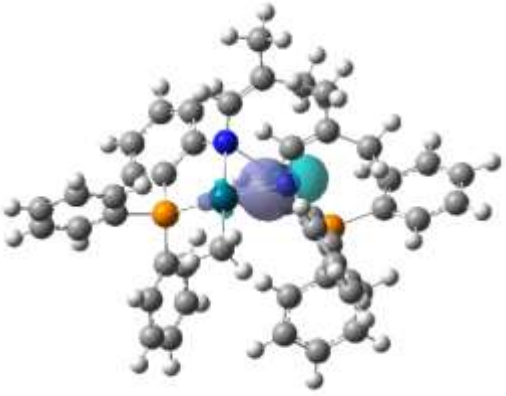

## Additional Discussion of Oxidation State Analysis

The primary challenge for the localized orbital bonding analysis (LOBA)<sup>22</sup> approach is the non-uniqueness of the localization procedure, and the fact that the orbitals in some systems do not localize cleanly, which may provide some incorrect assignments on the oxidation state of transition metal complexes.<sup>24</sup> While a new approach using oxidation state localized orbitals (OSLO) to obtain fragment-localized orbitals and to assign the oxidation state has been recently proposed,<sup>25</sup> the AdNDP approach was used herein.

The adaptive natural density partitioning (AdNDP)<sup>26</sup> was computed via the Multiwfn package (version 3.8)<sup>27, 28</sup> to verify the oxidation states from LOBA. First, analysis from the compositions of the AdNDP orbitals in **1** and **2** was performed to confirm its reliability (Table S3 and S4). **1** shows (1) four heterolytic Pd-N bonds are formed via the two electrons from N, which agree with the negatively charged amide; (2) two heterolytic Pd-C<sub>Me</sub> bonds are formed via the two electrons from C<sub>Me</sub>, which agree with the negatively charged methyl groups. The bond compositions of the AdNDP orbitals in **1** correspond to Pd(II)-Pd(II) oxidation states.

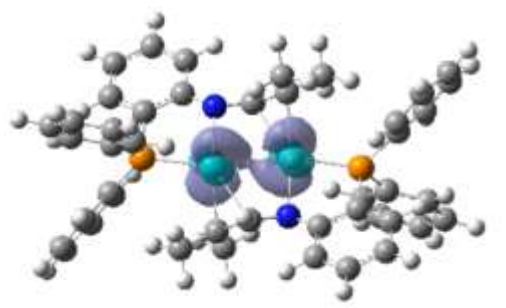
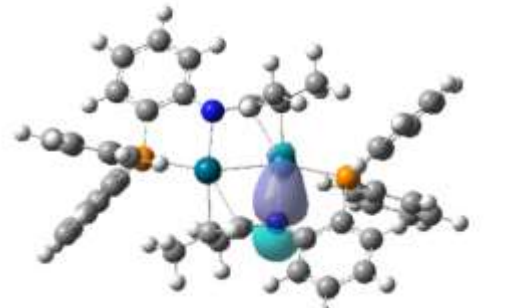
**Table S3.** Selected AdNDP orbitals in **1**. Isovalue of 0.05 for AdNDP orbitals presented in tables was used. Pd<sub>A</sub> represents the Pd atom on the left and Pd<sub>B</sub> represents the Pd atom on the right.


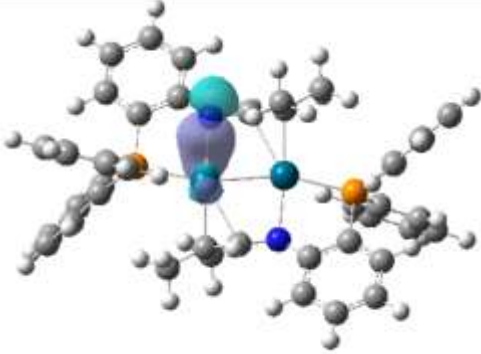
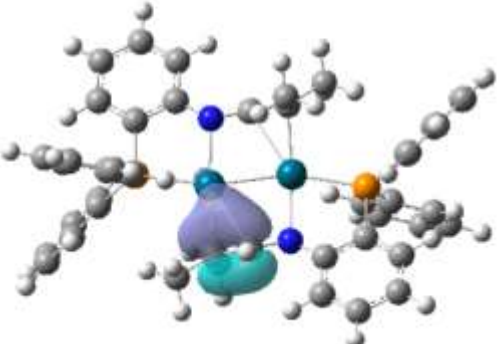
|   |  |
|---|--|
| <p>Pd-N bond: 1.8868 e-<br/>           (N) 75.498%<br/>           (Pd) 24.502%</p>   | <p>Pd-C bond: 1.7810 e-<br/>           (Pd) 36.783%<br/>           (C) 63.217%</p>   |
| <p>Pd-N bond: 1.8849 e-<br/>           (N) 74.381%<br/>           (Pd) 25.619%</p>  | <p>Pd-C bond: 1.7700 e-<br/>           (C) 63.221%<br/>           (Pd) 36.779%</p>  |
| <p>N-Pd bond: 1.7202 e-<br/>           (N) 88.145%<br/>           (Pd) 11.855%</p>  | <p>Pd-N bond: 1.7646 e-<br/>           (N) 88.685%<br/>           (Pd) 11.315%</p>   |

|  |   |
|--|---|
|   |   |
| <p><b>Lone pairs</b></p> <p>1.9492 e- Pd<sub>A</sub></p> <p>1.9627 e- Pd<sub>A</sub></p> <p>1.9762 e- Pd<sub>A</sub></p> <p>1.9866 e- Pd<sub>A</sub></p> | <p><b>Lone pairs</b></p> <p>1.9487 e- Pd<sub>B</sub></p> <p>1.9645 e- 9Pd<sub>B</sub></p> <p>1.9766 e- Pd<sub>B</sub></p> <p>1.9867 e- Pd<sub>B</sub></p> |

Analysis of **2** (Table S4) shows (1) two heterolytic Pd-N bonds are formed via the two electrons from N, which agree with the negatively charged amide; (2) two heterolytic  $h^2$ -alkenyl Pd bonds are formed via the two electrons from alkenyl groups; (3) a homolytic Pd-Pd bond is presented. The bond compositions of the AdNDP orbitals in **2** are consistent with Pd(I)-Pd(I) oxidation states.

**Table S4.** Selected AdNDP orbitals in **2**. Isovalue of 0.05 for AdNDP orbitals presented in tables was used. Pd<sub>A</sub> represents the Pd atom on the left and Pd<sub>B</sub> represents the Pd atom on the right.






|  |   |
|--|---|
| <p>Pd-Pd bond: 1.8804 e-</p> <p>(Pd) 50.286%</p> <p>(Pd) 49.714%</p>  | <p>Pd-N bond: 1.6059 e-</p> <p>(Pd) 13.721%</p> <p>(N) 86.279%</p>  |
| <p>Pd-C-C bond: 1.8245 e-</p> <p>(Pd) 8.553%</p> <p>(C) 38.723%</p>  | <p>Pd-N bond: 1.6177 e-</p> <p>(Pd) 14.180%</p> <p>(N) 85.820%</p>  |

|  |  |
|--|--|
| <p>(C) 52.724%</p>    |    |
| <p>Pd-C-C bond: 1.8231 e<sup>-</sup></p> <p>(C) 38.554%</p> <p>(C) 52.828%</p> <p>(Pd) 8.618%</p>  | <p><b>Lone pairs</b></p> <p>1.7535 e<sup>-</sup> for N<sub>A</sub></p> <p>1.7585 e<sup>-</sup> for N<sub>B</sub></p><br><p>1.9001 e<sup>-</sup> for Pd<sub>A</sub></p> <p>1.9624 e<sup>-</sup> for Pd<sub>A</sub></p> <p>1.9786 e<sup>-</sup> for Pd<sub>A</sub></p> <p>1.9873 e<sup>-</sup> for Pd<sub>A</sub></p><br><p>1.8968 e<sup>-</sup> for Pd<sub>B</sub></p> <p>1.9626 e<sup>-</sup> for Pd<sub>B</sub></p> <p>1.9789 e<sup>-</sup> for Pd<sub>B</sub></p> <p>1.9876 e<sup>-</sup> for Pd<sub>B</sub></p> |

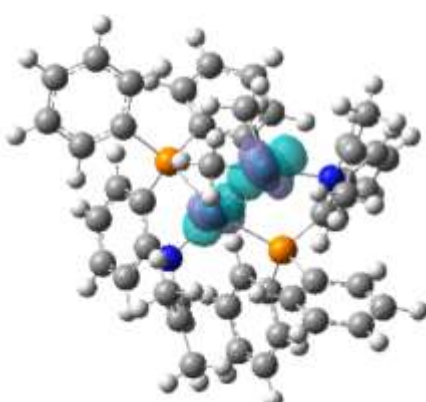
Analysis of **d1a1** (Table S5) in Scheme 18 shows (1) a heterolytic Pd-Pd bond is formed with one negatively charged Pd atom and one positively charged Pd atom; (2) two heterolytic Pd-N bonds are formed via the two electrons from N, which agree with the negatively charged amide; (3) two heterolytic Pd-C<sub>Me</sub> bonds are formed via the two electrons from C<sub>Me</sub>, which agree with the negatively charged methyl groups. Due to the heterolytic Pd-Pd bond, the Pd(II)-Pd(II) oxidation states in **d1a1** were assigned via AdNDP, and this assignment is consistent with LOBA. The unusual heterolytic Pd-Pd bond in **d1a5** (Table S6) is also obtained from the analysis of the bond compositions of the AdNDP orbitals, and Pd(II)-Pd(II) oxidation state in **d1a5** is assigned from the results of AdNDP and LOBA.



**Table S5.** Selected AdNDP orbitals in **d1a1**. Isovalue of 0.05 for AdNDP orbitals presented in tables was used. Pd<sub>A</sub> represents the Pd atom on the left and Pd<sub>B</sub> represents the Pd atom on the right.

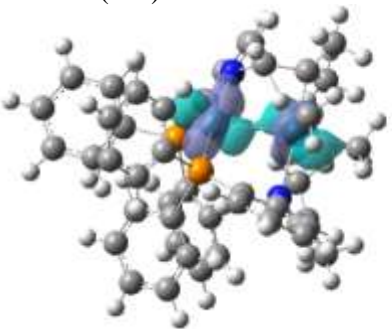

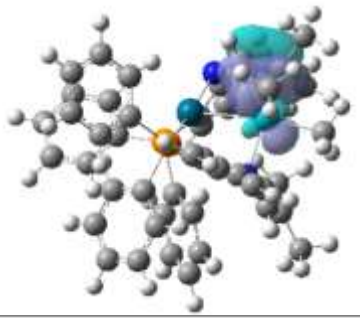

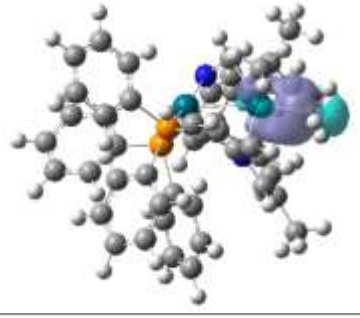

|  |  |
|--|--|
| <p>Pd-Pd bond: 1.9819 e-<br/> (Pd<sub>A</sub>) 26.095%<br/> (Pd<sub>B</sub>) 73.905%</p>  | <p>Pd-N bond: 1.8514 e-<br/> (N) 90.291%<br/> (Pd) 9.709%</p>    |
| <p>Pd-N bond: 1.9317 e-<br/> (N) 76.268%<br/> (Pd) 23.732%</p>                           | <p>Pd-C bond: 1.8286 e-<br/> (C) 57.290%<br/> (Pd) 42.710%</p>    |
| <p>Pd-C bond: 1.6793e-<br/> (Pd) 25.306%<br/> (C) 74.694%</p>                           | <p><i>Lone pairs</i></p> <p>1.9507 e- Pd<sub>A</sub><br/> 1.9612 e- Pd<sub>A</sub><br/> 1.9849 e- Pd<sub>A</sub><br/> 1.9899 e- Pd<sub>A</sub></p> <p>1.9648 e- Pd<sub>B</sub><br/> 1.9731 e- Pd<sub>B</sub><br/> 1.9873 e- Pd<sub>B</sub></p> |

**Table S6.** AdNDP orbitals of Pd-Pd bond in **d1a5**. Isovalue of 0.05 for AdNDP orbitals presented in tables was used. Pd<sub>A</sub> represents the Pd atom on the left and Pd<sub>B</sub> represents the Pd atom on the right.

|   |  |
|---|--|
| Pd-Pd bond: 1.9775 e-<br>(Pd <sub>A</sub> ) 66.304%<br>(Pd <sub>B</sub> ) 33.696% | <i>Lone pairs</i><br><br>1.9406 e- Pd <sub>A</sub><br>1.9643 e- Pd <sub>A</sub><br>1.9699 e- Pd <sub>A</sub><br>1.9802 e- Pd <sub>A</sub><br><br>1.9774 e- Pd <sub>B</sub><br>1.9840 e- Pd <sub>B</sub><br>1.9890 e- Pd <sub>B</sub> |
|  |  |

Analysis of **8a2** (Table S7) shows (1) a heterolytic Pd-Pd bond with one negatively charged Pd atom and one positively charged Pd atom; (2) two heterolytic Pd-N bond is formed via the two electrons from N, which agrees with the negatively charged amide; (3) the heterolytic  $h^2$ -alkenyl Pd bond is formed via the two electrons from alkenyl group; (4) two heterolytic Pd-C bond presented in the Pd(Me)<sub>2</sub> fragment with negatively charged methyl groups. The unusual heterolytic Pd-Pd bond in **8a2** is obtained from the analyses of the bond compositions of the AdNDP orbital, and Pd(0)-Pd(IV) oxidation state is assigned from the results of AdNDP and LOBA.

**Table S7.** Selected AdNDP orbitals in **8a2**. Isovalue of 0.05 for AdNDP orbitals presented in tables was used. Pd<sub>A</sub> represents the Pd atom on the left and Pd<sub>B</sub> represents the Pd atom on the right.

|  |   |
|--|---|
| <p>Pd-Pd bond: 1.8635 e-<br/>           (Pd<sub>A</sub>) 44.284%<br/>           (Pd<sub>B</sub>) 55.716%</p>      | <p>Pd-N bond: 1.8282 e-<br/>           (N) 94.949%<br/>           (Pd) 5.051%</p>       |
| <p>Pd-C-C bond: 1.8734 e-<br/>           (C) 18.882%<br/>           (C) 42.748%<br/>           (Pd) 38.370%</p>  | <p>Pd-C bond: 1.7491 e-<br/>           (Pd) 38.451%<br/>           (C) 61.549%</p>     |
| <p>Pd-C bond: 1.5816 e-<br/>           (Pd) 26.178%<br/>           (C) 73.822%</p>                              | <p>Pd-N bond: 1.8583 e-<br/>           3(N) 95.967%<br/>           92(Pd) 4.033%</p>  |
| <p><i>Lone pairs</i><br/>           1.9326 e- Pd<sub>A</sub><br/>           1.9498 e- Pd<sub>A</sub><br/>           1.9654 e- Pd<sub>A</sub><br/>           1.9774 e- Pd<sub>A</sub></p>           | <p><i>Lone pairs</i><br/>           1.9680 e- Pd<sub>B</sub><br/>           1.9835 e- Pd<sub>B</sub><br/>           1.9883 e- Pd<sub>B</sub></p>                          |

## VII – Crystallographic Details

### VII.I – Experimental for C<sub>50</sub>H<sub>60</sub>N<sub>2</sub>OP<sub>2</sub>Pd<sub>2</sub> (**3-4**)

*Data Collection and Processing.* The sample was mounted on a Mitegen polyimide micromount with a small amount of Paratone N oil. All X-ray measurements were made on a Bruker Kappa Axis Apex2 diffractometer at a temperature of 110 K. The unit cell dimensions were determined from a symmetry constrained fit of 9838 reflections with  $4.44^\circ < 2\theta < 61.28^\circ$ . The data collection strategy was a number of  $\omega$  and  $\phi$  scans which collected data up to  $75.604^\circ$  ( $2\theta$ ). The frame integration was performed using SAINT.<sup>24</sup> The resulting raw data was scaled and absorption corrected using a multi-scan averaging of symmetry equivalent data using SADABS.<sup>25</sup>

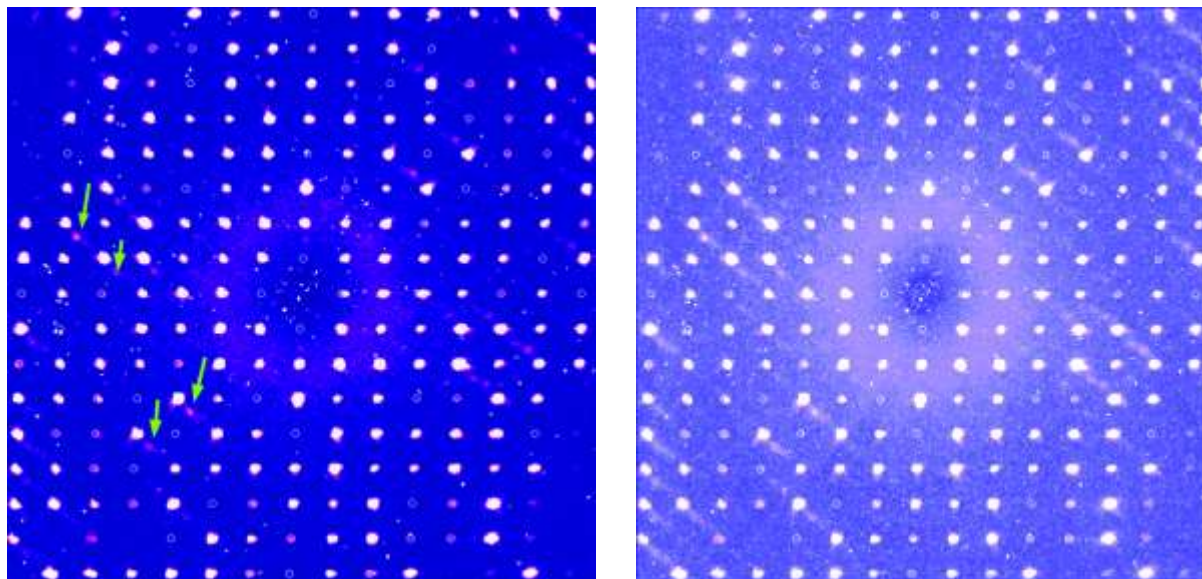
*Structure Solution and Refinement.* The structure was solved by using a dual space methodology using the SHELXT program.<sup>26</sup> Most non-hydrogen atoms were obtained from the initial solution. The remaining atomic positions were recovered from a difference Fourier map or calculated from the introduction of an idealized phenyl ring. The hydrogen atoms were introduced at idealized positions and were allowed to ride on the parent atom. The phenyl ring containing carbon atoms C41 through C46 was disordered. The atoms in the alternative orientation were designated C41' through C46'. The positions for C45' and C46' were obtained from a difference Fourier map. The positions of C41' and C44' were assumed to be co-incident with C41 and C44 respectively. However, the positions for C42' and C43' could not be obtained from a difference map. Therefore, the missing atomic positions were calculated using an idealized hexagon fit using the positions C41', C44', C45', and C46'. The disordered groups then refined normally. The occupancy for the predominant conformer refined to a value of 0.816(9). The structural model was fit to the data using full matrix least-squares based on  $F^2$ . The calculated structure factors included corrections for anomalous dispersion from the usual tabulation. The structure was refined using the SHELXL program from the SHELX suite of crystallographic software.<sup>27</sup> Graphic plots were produced using the NRCVAX program suite.<sup>28</sup>

An A-level checkCIF alert was detected for the structure of compound **3-4** because the final difference Fourier map shows large peaks in the vicinity of the Pd atom positions (approximately 0.6 Å away). A single origin for these peaks could not be determined, however, several possibilities exist, and do not contraindicate the determined space group or structure.

First, in some cases, series termination errors (“Fourier truncation”) gives large peaks in the difference map near the heavy atom positions. However, normally these occur about 0.8-1.0 Å from the heavy atoms and are not as large as the peaks observed in this structure.

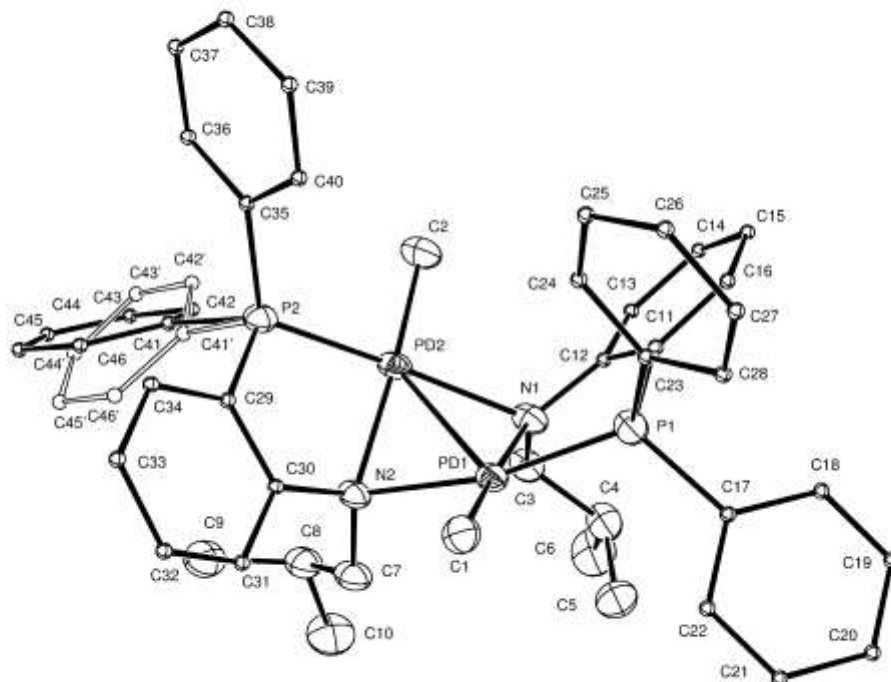
Two other possible reasons could be unaccounted for twinning or stacking faults. These cannot be unambiguously assessed from the collected data, though due diligence was applied in their consideration. To examine these possibilities, 1497 reflections with a minimum  $I/\sigma(I)$  of 4.0 were harvested and re-indexed from the first run of the data collection. Only 22 which were mostly weak reflections did not fit the indexed lattice and could not be indexed to their own lattice. In addition, the TwinRotMat function of the PLATON software (which is the program used by CheckCIF) could not find any unaccounted-for twinning. However, when creating synthetic

reciprocal lattice layer images some unaccounted-for Bragg reflections in the  $hk0$  layer were observed (Figure S63, Left), some of which are marked with green arrows. Enhancing the brightness of the PNG image reveals that these non-Bragg spots are associated with a weak diffuse scattering along the  $[110]$  direction (Figure S63, Right). It is well known that stacking faults can give rise to linear regions of diffuse scattering.<sup>29</sup>

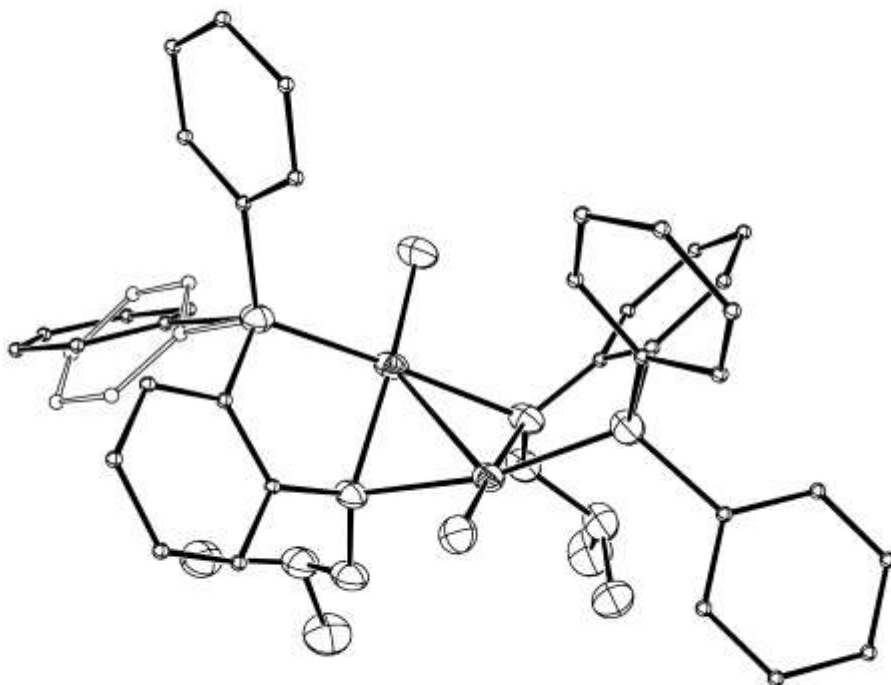


**Figure B.63.** : Left) Synthetic reciprocal lattice layer image with some unaccounted-for Bragg reflections in the  $hk0$  layer, which are marked with green arrows; and Right) Brightness enhanced image of the image on the left showing regions of weak diffuse scattering along the  $[110]$  direction.

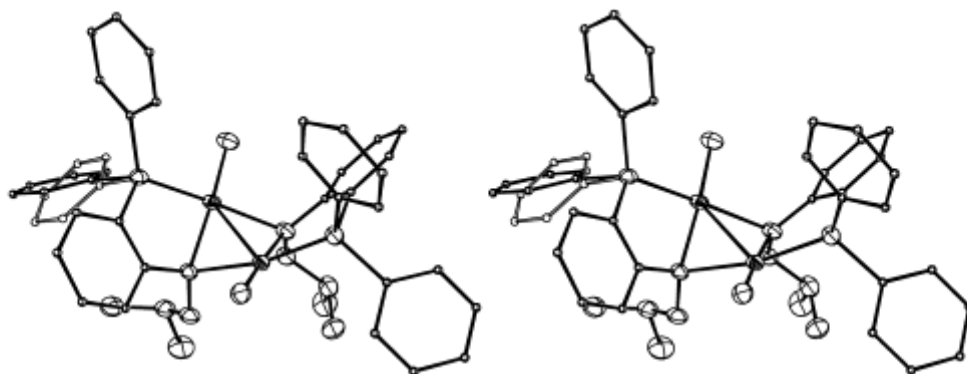
In some cases, both unaccounted for twinning or stacking faults can produce a “ghost” or “shadow” structure which can look like a disorder but cannot be successfully refined as a disorder. In fact, in the difference map there are also residual peaks in the vicinity of C7, C8, C9, C10 which suggest a disordered 2-methyl-propyl-amine group. However, all attempts to refine this as a disordered group were not successful. While the source of the large peaks in the difference map in the vicinity of the Pd atoms cannot be determined with certainty, the structure which is responsible for the dominant diffraction in this experiment has been duly reported.



**Figure B.64.** ORTEP Drawing of **3-4** showing naming and numbering scheme. Ellipsoids are at the 50% probability level. The aromatic carbon atoms were reduced to an arbitrary radii and hydrogen atoms are omitted for clarity. The minor disorder component is depicted using open circles and open bonds.



**Figure B.65.** ORTEP Drawing of **3-4**. Ellipsoids are at the 50% probability level. The aromatic carbon atoms were reduced to an arbitrary radii and hydrogen atoms are omitted for clarity. The minor disorder component is depicted using open circles and open bonds.



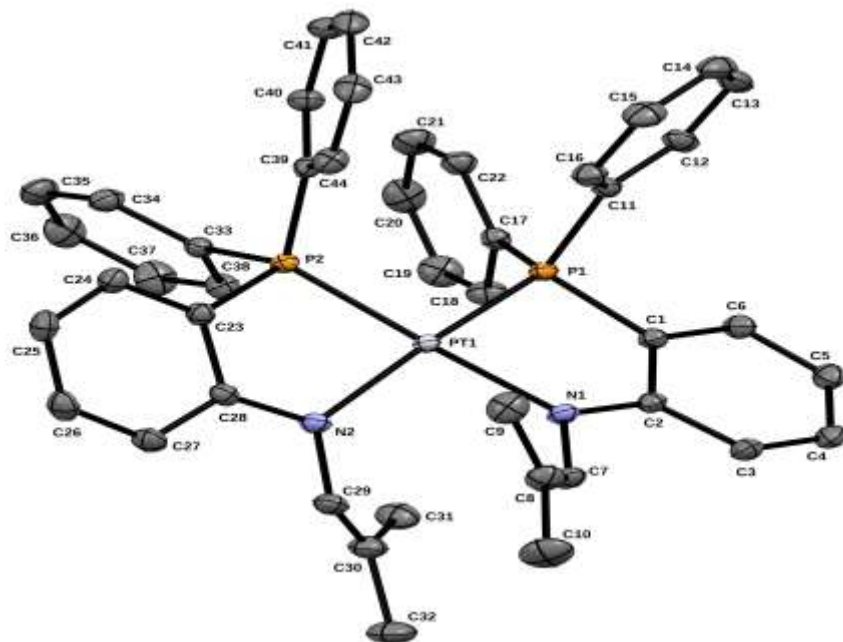
**Figure B.66.** Stereoscopic ORTEP Drawing of **3-4**. Ellipsoids are at the 50% probability level. The aromatic carbon atoms were reduced to an arbitrary radii and hydrogen atoms are omitted for clarity. The minor disorder component is depicted using open circles and open bonds.

## VII.II – Experimental for $C_{44}H_{42}N_2P_2Pt$ (**3-6**)

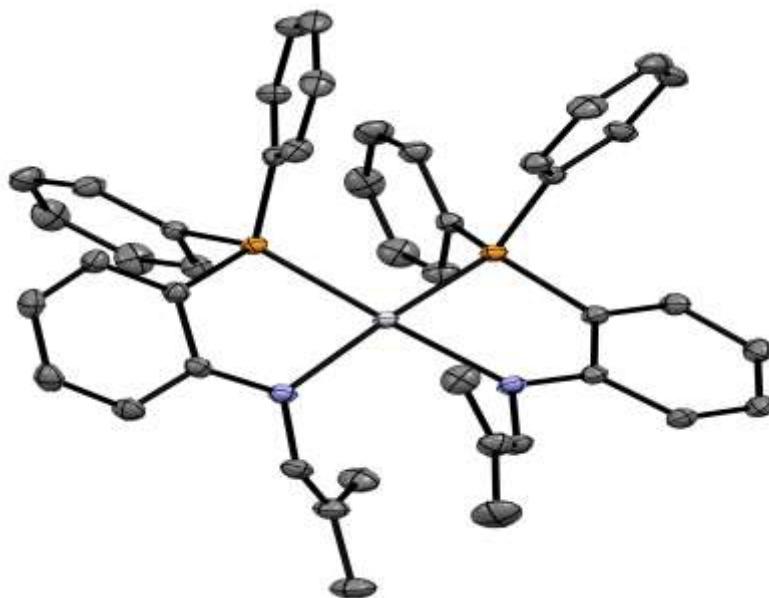
*Data Collection and Processing.* The sample was mounted on a Mitegen polyimide micromount with a small amount of Paratone N oil. All X-ray measurements were made on a Bruker Kappa Axis Apex2 diffractometer at a temperature of 110 K. The unit cell dimensions were determined from a symmetry constrained fit of 9678 reflections with  $5.38^\circ < 2\theta < 74.78^\circ$ . The data collection strategy was a number of  $\omega$  and  $\phi$  scans which collected data up to  $77.548^\circ$  ( $2\theta$ ). The frame integration was performed using SAINT.<sup>24</sup> The resulting raw data was scaled and absorption corrected using a multi-scan averaging of symmetry equivalent data using SADABS.<sup>25</sup>

*Structure Solution and Refinement.* The structure was solved by using a dual space methodology using the SHELXT program.<sup>26</sup> All non-hydrogen atoms were obtained from the initial solution. The hydrogen atoms were introduced at idealized positions and were allowed to ride on the parent atom. The structural model was fit to the data using full matrix least-squares based on  $F^2$ . The calculated structure factors included corrections for anomalous dispersion from the usual tabulation. The structure was refined using the SHELXL program from the SHELX suite of crystallographic software.<sup>27</sup> Graphic plots were produced using the Mercury program.<sup>30</sup>





**Figure B.67.** ORTEP Drawing of **3-6** showing naming and numbering scheme. Ellipsoids are at the 50% probability level.



**Figure B.68.** ORTEP Drawing of **3-6** without naming and numbering scheme. Ellipsoids are at the 50% probability level



**Table B.3.** Summary of Crystal Data for **3-4** and **3-6**

| Compound #<br>(CCDC)                               | <b>3-4</b> (2092272)              | <b>3-6</b> (2092271)              |
|--|-----------------------------------|-----------------------------------|
| Formula  | $C_{50}H_{60}N_2OP_2Pd_2$         | $C_{44}H_{42}N_2P_2Pt$            |
| Formula Weight (g/mol)                             | 979.74                            | 855.82                            |
| Crystal Dimensions (mm)                            | $0.288 \times 0.193 \times 0.087$ | $0.347 \times 0.279 \times 0.087$ |
| Crystal Color and Habit                            | yellow prism                      | red prism                         |
| Crystal System                                     | triclinic                         | monoclinic                        |
| Space Group  | P -1                              | P 2 <sub>1</sub> /c               |
| Temperature, K                                     | 110                               | 110                               |
| a, Å   | 10.568(4)                         | 15.551(4)                         |
| b, Å   | 11.581(3)                         | 13.574(4)                         |
| c, Å   | 18.826(5)                         | 17.328(4)                         |
| α, °   | 95.004(9)                         | 90                                |
| β, °   | 101.514(13)                       | 90.105(17)                        |
| γ, °   | 91.357(9)                         | 90                                |
| V, Å <sup>3</sup>                                  | 2247.3(12)                        | 3657.8(17)                        |
| Number of reflections to determine final unit cell | 9838                              | 9678                              |
| Min and Max 2θ for cell determination, °           | 4.44, 61.28                       | 5.38, 74.78                       |
| Z  | 2                                 | 4                                 |
| F(000)   | 1008                              | 1712                              |
| ρ (g/cm <sup>3</sup> )                             | 1.448                             | 1.554                             |
| λ, Å, (MoKα)                                       | 0.71073                           | 0.71073                           |
| μ, (cm <sup>-1</sup> )                             | 0.910                             | 3.958                             |
| Diffractometer Type                                | Bruker Kappa Axis Apex2           | Bruker Kappa Axis Apex2           |
| Scan Type(s)                                       | φ and ω scans                     | φ and ω scans                     |
| Max 2θ for data collection, °                      | 75.604                            | 77.548                            |
| Number of reflections measured                     | 171381                            | 260731                            |

|  |   |   |
|--|---|---|
| Unique reflections measured                                | 23901   | 20861   |
| R <sub>merge</sub>   | 0.0531  | 0.0611  |
| Number of reflections included in refinement               | 23901   | 20861   |
| Cut off  | I > 2σ(I)   | I > 2σ(I)   |
| Threshold Expression                                       |   |   |
| Structure refined using                                    | full matrix least-squares using F <sup>2</sup>  | full matrix least-squares using F <sup>2</sup>  |
| Weighting Scheme   | w=1/[σ <sup>2</sup> (Fo <sup>2</sup> )+(0.0464P) <sup>2</sup> +3.7992P]<br>where P=(Fo <sup>2</sup> +2Fc <sup>2</sup> )/3 | w=1/[σ <sup>2</sup> (Fo <sup>2</sup> )+(0.0199P) <sup>2</sup> +2.6085P]<br>where P=(Fo <sup>2</sup> +2Fc <sup>2</sup> )/3 |
| Number of parameters in least-squares                      | 575   | 446   |
| R <sub>1</sub>   | 0.0474  | 0.0277  |
| wR <sub>2</sub>  | 0.1073  | 0.0499  |
| R <sub>1</sub> (all data)                                  | 0.0779  | 0.0553  |
| wR <sub>2</sub> (all data)                                 | 0.1244  | 0.0571  |
| GOF  | 1.029   | 1.006   |
| Maximum shift/error  | 0.002   | 0.008   |
| Min & Max peak heights on final ΔF Map (e <sup>-</sup> /Å) | -2.443, 4.533   | -2.282, 2.168   |

Where:

$$R_1 = \frac{\sum (|F_o| - |F_c|)}{\sum F_o}$$

$$wR_2 = \left[ \frac{\sum (w(F_o^2 - F_c^2)^2)}{\sum (w F_o^4)} \right]^{1/2}$$

$$GOF = \left[ \frac{\sum (w(F_o^2 - F_c^2)^2)}{(\text{No. of reflns.} - \text{No. of params.})} \right]^{1/2}$$

## VIII References

1. Salo, E. V.; Guan, Z., *Organometallics* **2003**, 22, 5033-5046.
2. Dekker, G. P. C. M.; Buijs, A.; Elsevier, C. J.; Vrieze, K.; Van Leeuwen, P. W. N. M.; Smeets, W. J. J.; Spek, A. L.; Wang, Y. F.; Stam, C. H., *Organometallics* **1992**, 11, 1937-1948.
3. Stubbs, J. M.; Firth, K. F.; Bridge, B. J.; Berger, K. J.; Hazlehurst, R. J.; Boyle, P. D.; Blacquiere, J. M., *Dalton Trans.* **2017**, 46, 647-650.
4. Jackman, K. M. K.; Bridge, B. J.; Sauv e, E. R.; Rowley, C. N.; Zheng, C. H. M.; Stubbs, J. M.; Boyle, P. D.; Blacquiere, J. M., *Organometallics* **2019**, 38, 1677-1681.
5. Khusnutdinova, J. R.; Qu, F.; Zhang, Y.; Rath, N. P.; Mirica, L. M., *Organometallics* **2012**, 31, 4627-4630.

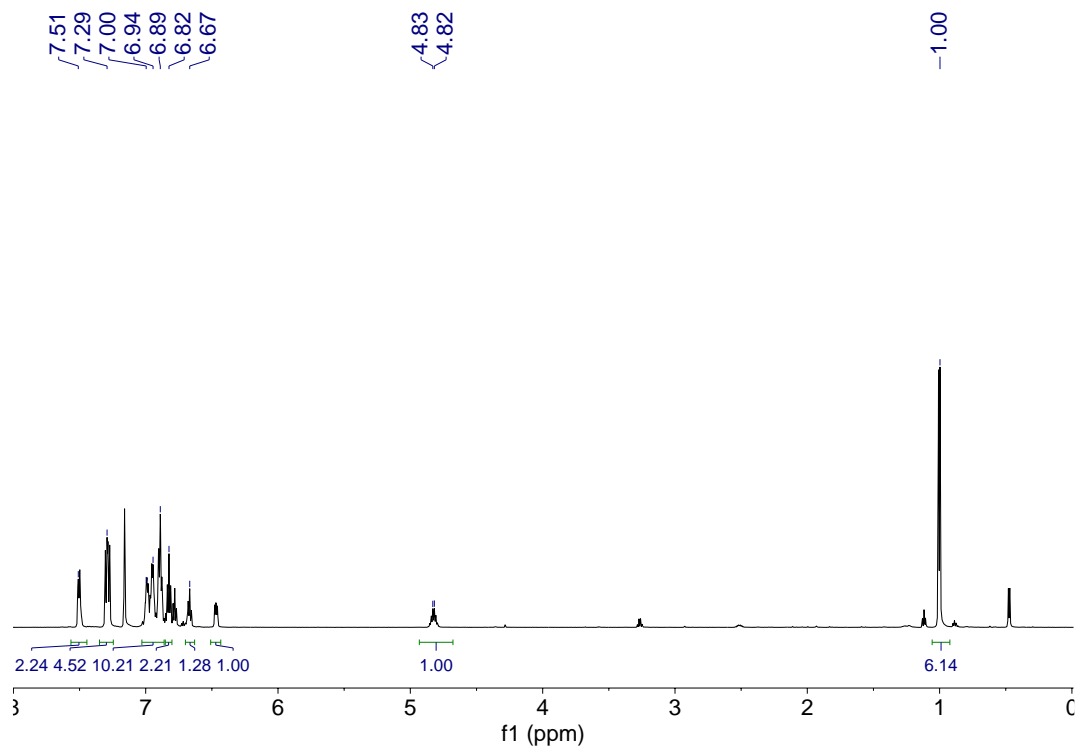
6. Patiny, L.; Borel, A., *J. Chem. Inf. Model.* **2013**, *53*, 1223-1228.
7. Zimmerman, P. M., *J. Chem. Phys.* **2013**, *138*, 184102.
8. Zimmerman, P. M., *J. Chem. Theory Comput.* **2013**, *9*, 3043-3050.
9. Zimmerman, P. M., *J. Comput. Chem.* **2015**, *36*, 601-611.
10. Shao, Y.; Gan, Z.; Epifanovsky, E.; Gilbert, A. T. B.; Wormit, M.; Kussmann, J.; Lange, A. W.; Behn, A.; Deng, J.; Feng, X.; Ghosh, D.; Goldey, M.; Horn, P. R.; Jacobson, L. D.; Kaliman, I.; Khaliullin, R. Z.; Kuš, T.; Landau, A.; Liu, J.; Proynov, E. I.; Rhee, Y. M.; Richard, R. M.; Rohrdanz, M. A.; Steele, R. P.; Sundstrom, E. J.; Woodcock, H. L.; Zimmerman, P. M.; Zuev, D.; Albrecht, B.; Alguire, E.; Austin, B.; Beran, G. J. O.; Bernard, Y. A.; Berquist, E.; Brandhorst, K.; Bravaya, K. B.; Brown, S. T.; Casanova, D.; Chang, C.-M.; Chen, Y.; Chien, S. H.; Closser, K. D.; Crittenden, D. L.; Diedenhofen, M.; DiStasio, R. A.; Do, H.; Dutoi, A. D.; Edgar, R. G.; Fatehi, S.; Fusti-Molnar, L.; Ghysels, A.; Golubeva-Zadorozhnaya, A.; Gomes, J.; Hanson-Heine, M. W. D.; Harbach, P. H. P.; Hauser, A. W.; Hohenstein, E. G.; Holden, Z. C.; Jagau, T.-C.; Ji, H.; Kaduk, B.; Khistyayev, K.; Kim, J.; Kim, J.; King, R. A.; Klunzinger, P.; Kosenkov, D.; Kowalczyk, T.; Krauter, C. M.; Lao, K. U.; Laurent, A. D.; Lawler, K. V.; Levchenko, S. V.; Lin, C. Y.; Liu, F.; Livshits, E.; Lochan, R. C.; Luenser, A.; Manohar, P.; Manzer, S. F.; Mao, S.-P.; Mardirossian, N.; Marenich, A. V.; Maurer, S. A.; Mayhall, N. J.; Neuscamman, E.; Oana, C. M.; Olivares-Amaya, R.; O'Neill, D. P.; Parkhill, J. A.; Perrine, T. M.; Peverati, R.; Prociuk, A.; Rehn, D. R.; Rosta, E.; Russ, N. J.; Sharada, S. M.; Sharma, S.; Small, D. W.; Sodt, A.; Stein, T.; Stück, D.; Su, Y.-C.; Thom, A. J. W.; Tsuchimochi, T.; Vanovschi, V.; Vogt, L.; Vydrov, O.; Wang, T.; Watson, M. A.; Wenzel, J.; White, A.; Williams, C. F.; Yang, J.; Yeganeh, S.; Yost, S. R.; You, Z.-Q.; Zhang, I. Y.; Zhang, X.; Zhao, Y.; Brooks, B. R.; Chan, G. K. L.; Chipman, D. M.; Cramer, C. J.; Goddard, W. A.; Gordon, M. S.; Hehre, W. J.; Klamt, A.; Schaefer, H. F.; Schmidt, M. W.; Sherrill, C. D.; Truhlar, D. G.; Warshel, A.; Xu, X.; Aspuru-Guzik, A.; Baer, R.; Bell, A. T.; Besley, N. A.; Chai, J.-D.; Dreuw, A.; Dunietz, B. D.; Furlani, T. R.; Gwaltney, S. R.; Hsu, C.-P.; Jung, Y.; Kong, J.; Lambrecht, D. S.; Liang, W.; Ochsenfeld, C.; Rassolov, V. A.; Slipchenko, L. V.; Subotnik, J. E.; Van Voorhis, T.; Herbert, J. M.; Krylov, A. I.; Gill, P. M. W.; Head-Gordon, M., *Mol. Phys.* **2015**, *113*, 184-215.
11. Grimme, S., *J. Comput. Chem.* **2006**, *27*, 1787-1799.
12. Becke, A. D., *J. Chem. Phys.* **1997**, *107*, 8554-8560.
13. Hehre, W. J.; Ditchfield, R.; Pople, J. A., *J. Chem. Phys.* **1972**, *56*, 2257-2261.
14. Wadt, W. R.; Hay, P. J., *J. Chem. Phys.* **1985**, *82*, 284-298.
15. Hay, P. J.; Wadt, W. R., *J. Chem. Phys.* **1985**, *82*, 299-310.
16. Hariharan, P. C.; Pople, J. A., *Theor. Chim. Acta* **1973**, *28*, 213-222.
17. McKenzie, S. C.; Epifanovsky, E.; Barca, G. M. J.; Gilbert, A. T. B.; Gill, P. M. W., *J. Phys. Chem. A* **2018**, *122*, 3066-3075.
18. Marenich, A. V.; Cramer, C. J.; Truhlar, D. G., *J. Phys. Chem. B* **2009**, *113*, 6378-6396.
19. Schäfer, A.; Huber, C.; Ahlrichs, R., *J. Chem. Phys.* **1994**, *100*, 5829-5835.
20. Weigend, F.; Ahlrichs, R., *Phys. Chem. Chem. Phys.* **2005**, *7*, 3297-3305.
21. Andrae, D.; Häußermann, U.; Dolg, M.; Stoll, H.; Preuß, H., *Theor. Chim. Acta* **1990**, *77*, 123-141.
22. Thom, A. J. W.; Sundstrom, E. J.; Head-Gordon, M., *Phys. Chem. Chem. Phys.* **2009**, *11*, 11297-11304.
23. Glendenning, E. D.; Badenhop, J. K.; Reed, A. E.; Carpenter, J. E.; Bohmann, J. A.; Morales, C. M.; Weinhold, F. NBO 5.0. *Theoretical Chemistry Institute, University of Wisconsin, Madison, WI.* **2001**.

24. Gimferrer, M.; Van der Mynsbrugge, J.; Bell, A. T.; Salvador, P.; Head-Gordon, M., *Inorg. Chem.* **2020**, *59* (20), 15410-15420.
25. Gimferrer, M.; Aldossary, A.; Salvador, P.; Head-Gordon, M., *J. Chem. Theory Comput.* **2022**, *18* (1), 309-322.
26. Zubarev, D. Y.; Boldyrev, A. I., *Phys. Chem. Chem. Phys.* **2008**, *10* (34), 5207-5217.
27. Multiwfn, version 3.8. <http://sobereva.com/multiwfn/> (accessed 2021).
28. Lu, T.; Chen, F., *J. Comput. Chem.* **2011**, *33* (5), 580-592.
29. Bruker-AXS, SAINT version 2013.8, **2013**, Bruker-AXS, Madison, WI 53711, USA
30. Bruker-AXS, SADABS version 2012.1, **2012**, Bruker-AXS, Madison, WI 53711, USA
31. Sheldrick, G. M., *Acta Cryst.* **2015**, *A71*, 3-8
32. Sheldrick, G. M., *Acta Cryst.* **2015**, *C71*, 3-8
33. Gabe, E. J.; Le Page, Y.; Charland, J. P.; Lee, F. L. and White, P. S. *J. Appl. Cryst.* **1989**, *22*, 384-387
34. Wellberry, T. R. *Diffuse Scattering and Models of Disorder*, IUCr Monographs on Crystallography 16, Oxford University Press, **2010**, p. 242
35. Macrae, C. F.; Bruno, I. J.; Chisholm, J. A.; Edington, P. R.; McCabe, P.; Pidcock, E.; Rodriguez-Monge, L.; Taylor, R.; van de Streek, J. and Wood, P. A. *J. Appl. Cryst.*, **2008**, *41*, 466-470

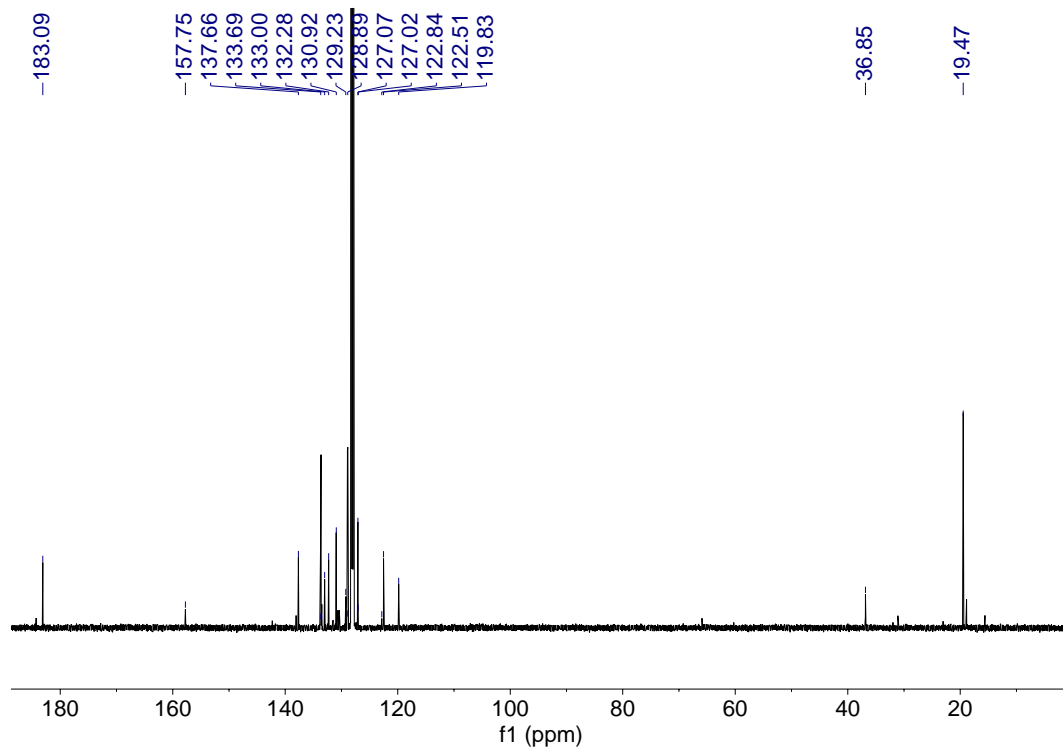
## Appendices

### Appendix C: Supplementary Information for Chapter 4

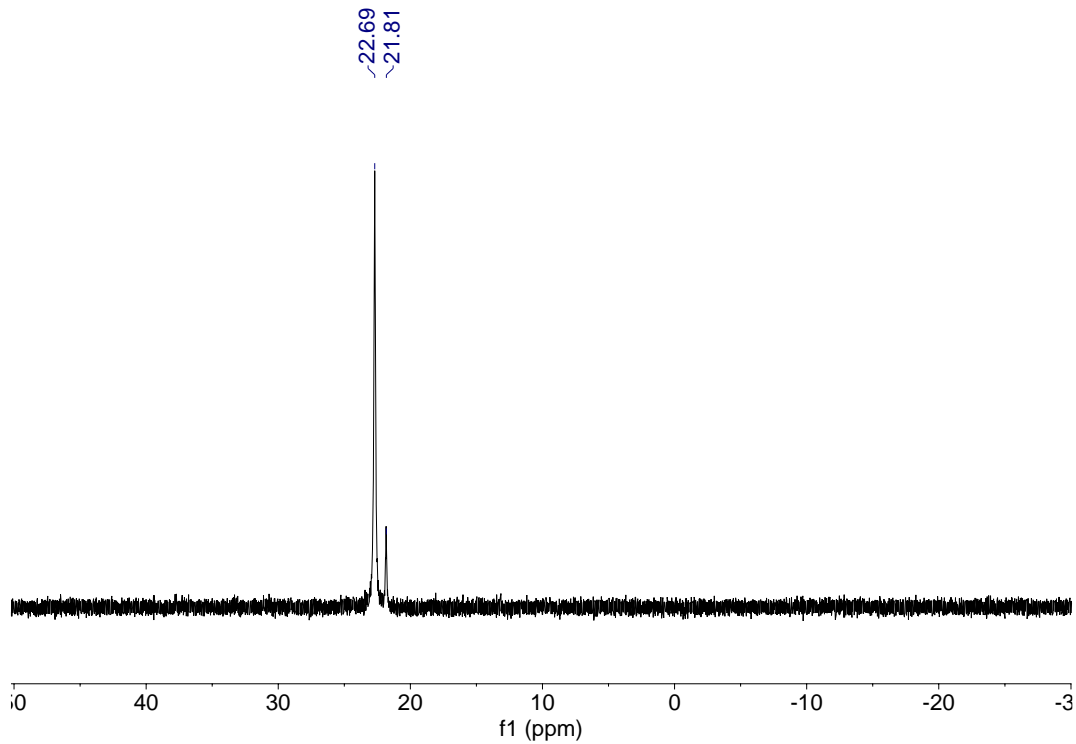
#### I Compound NMR Spectra



**Figure C.1.**  $^1\text{H}$  NMR spectrum of **4-10** (599MHz,  $\text{C}_6\text{D}_6$ ).

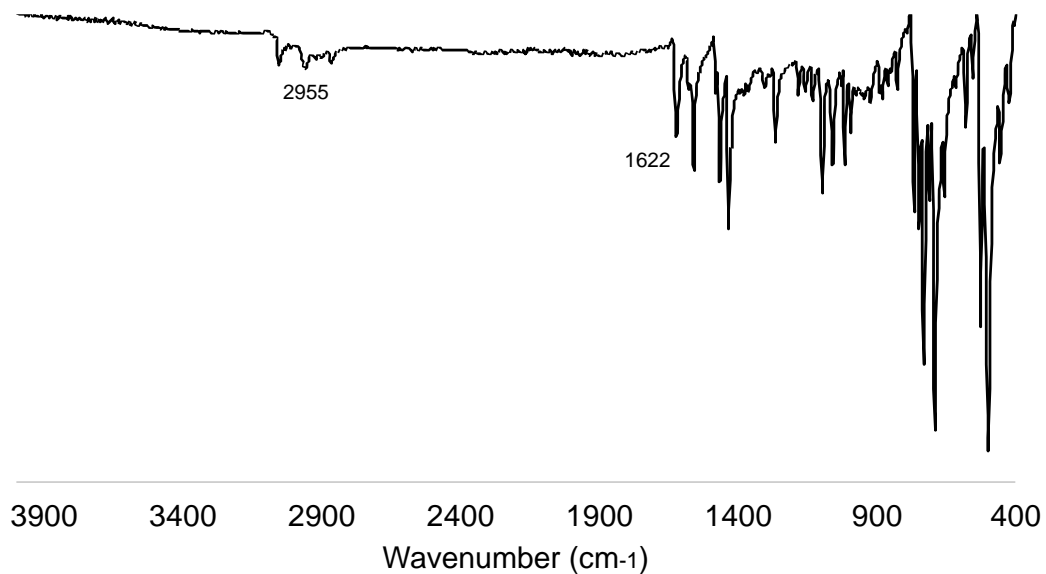


**Figure C.2.**  $^{13}\text{C}\{^1\text{H}\}$  NMR spectrum of **4-10** (151 MHz,  $\text{C}_6\text{D}_6$ ).



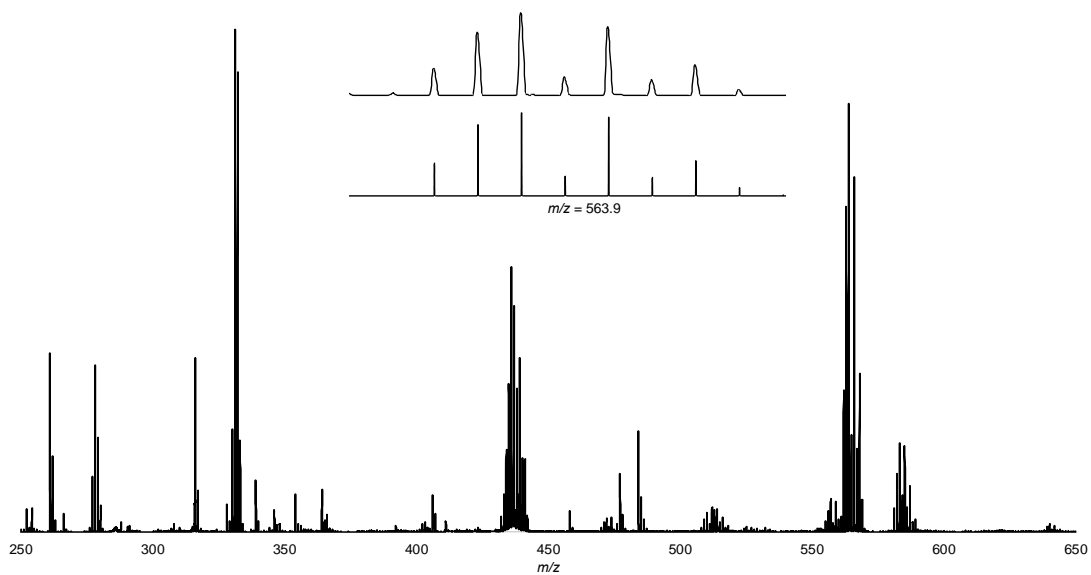
**Figure C.3.**  $^{31}\text{P}\{^1\text{H}\}$  NMR spectrum of **4-10** (243 MHz,  $\text{C}_6\text{D}_6$ ).

## II Compound IR Spectra



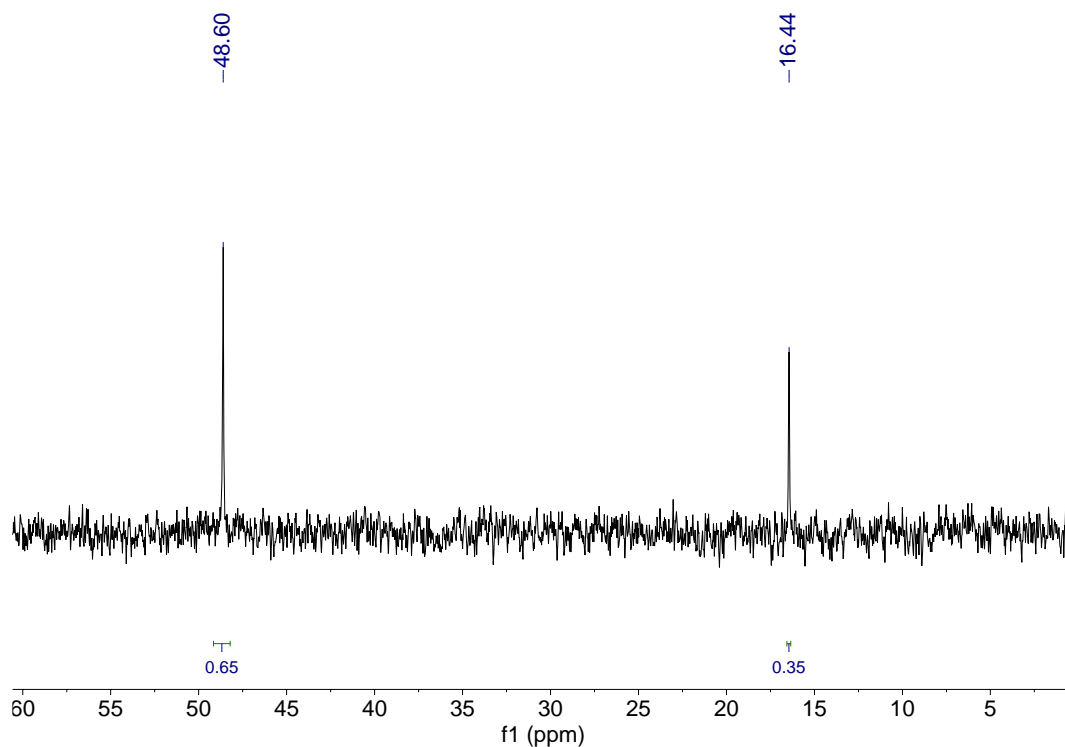
**Figure C.4.** ATR-FTIR spectrum of solid **4-10**. Data was acquired using a Bruker Alpha II ATR-FTIR and plotted using Microsoft Excel.

## III Compound Mass Spectra

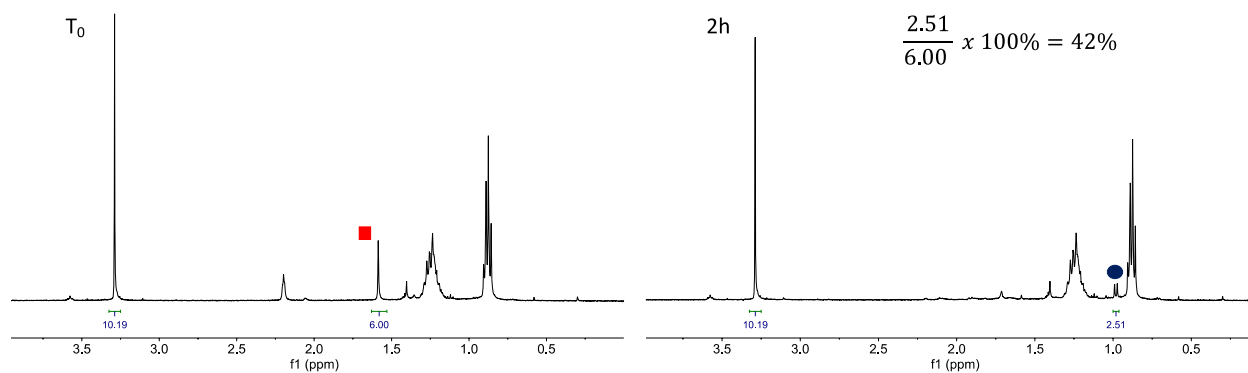
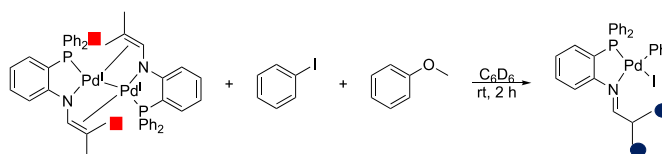


**Figure C.5.** MALDI mass spectrum of [Pd(I)(Ph)(H(4-L1))], **4-0** with pyrene as the matrix. Inset: simulated (bottom) for [Pd(I)(H(4-L1))]<sup>+</sup>, and observed (top) at  $m/z = 563.9$ .

## IV Reaction NMR Spectra

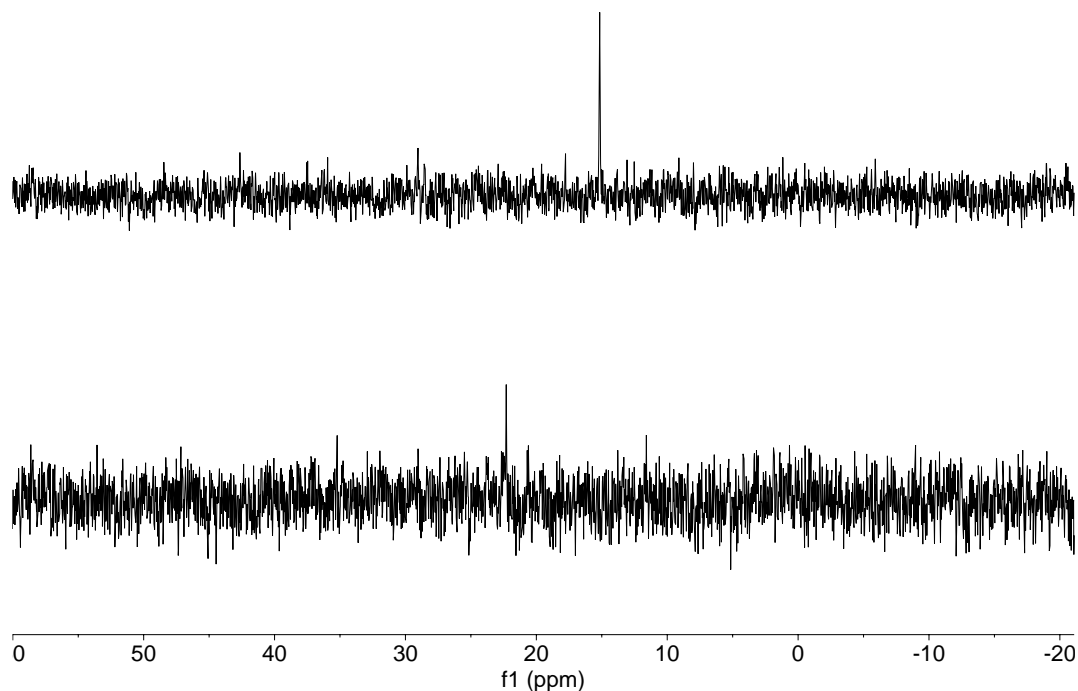


**Figure C.6.**  $^{31}\text{P}\{^1\text{H}\}$  NMR spectrum from the addition of **K[4-L1]** to  $[\text{Pd}(\text{MeCN})_3]_2 \cdot 2[\text{BF}_4]$  affording **4-2** and **4-3** (243 MHz, THF).

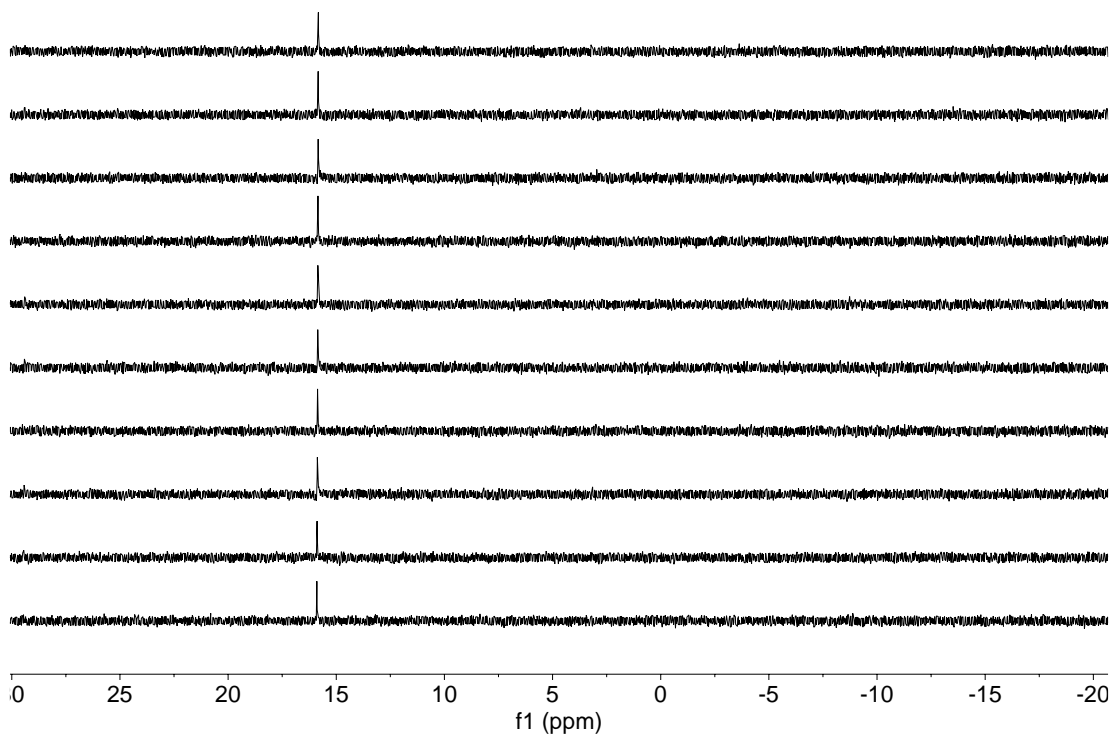


**Figure C.7.**  $^1\text{H}$  NMR spectrum of **4-2** in  $\text{C}_6\text{D}_6$  with anisole as an internal standard (left).  $^1\text{H}$  NMR spectrum 2 h after the addition of PhI to **4-2** in  $\text{C}_6\text{D}_6$  affording **4-10** in 47 % yield (right) (600 MHz,  $\text{C}_6\text{D}_6$ ).

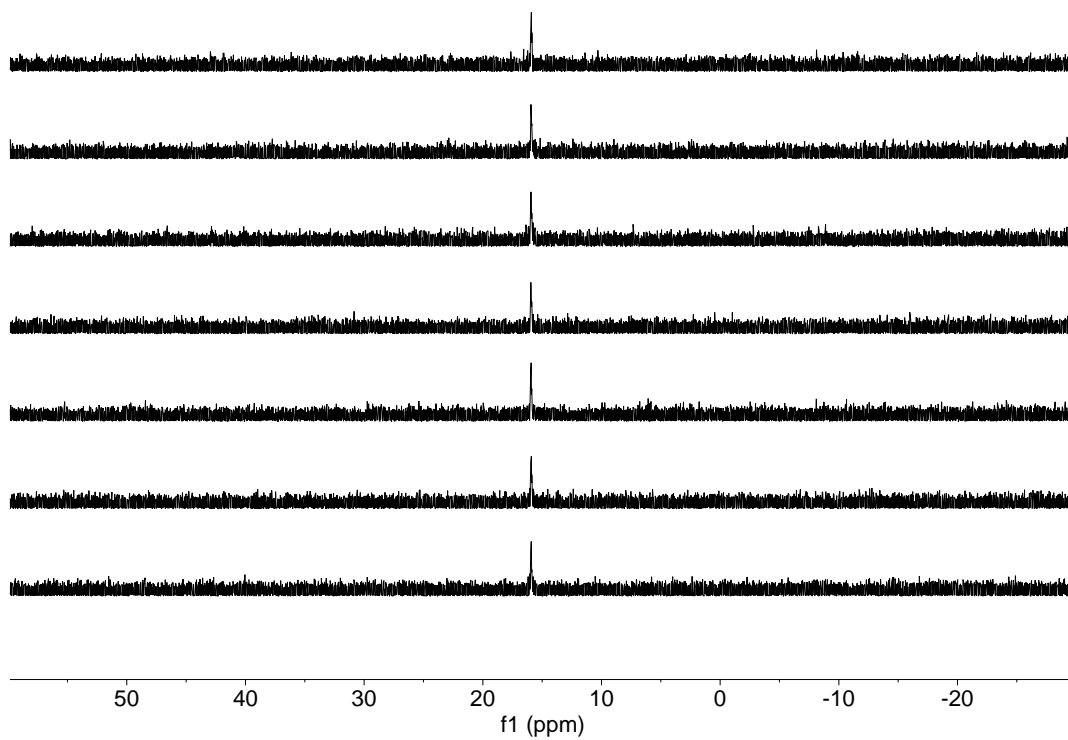




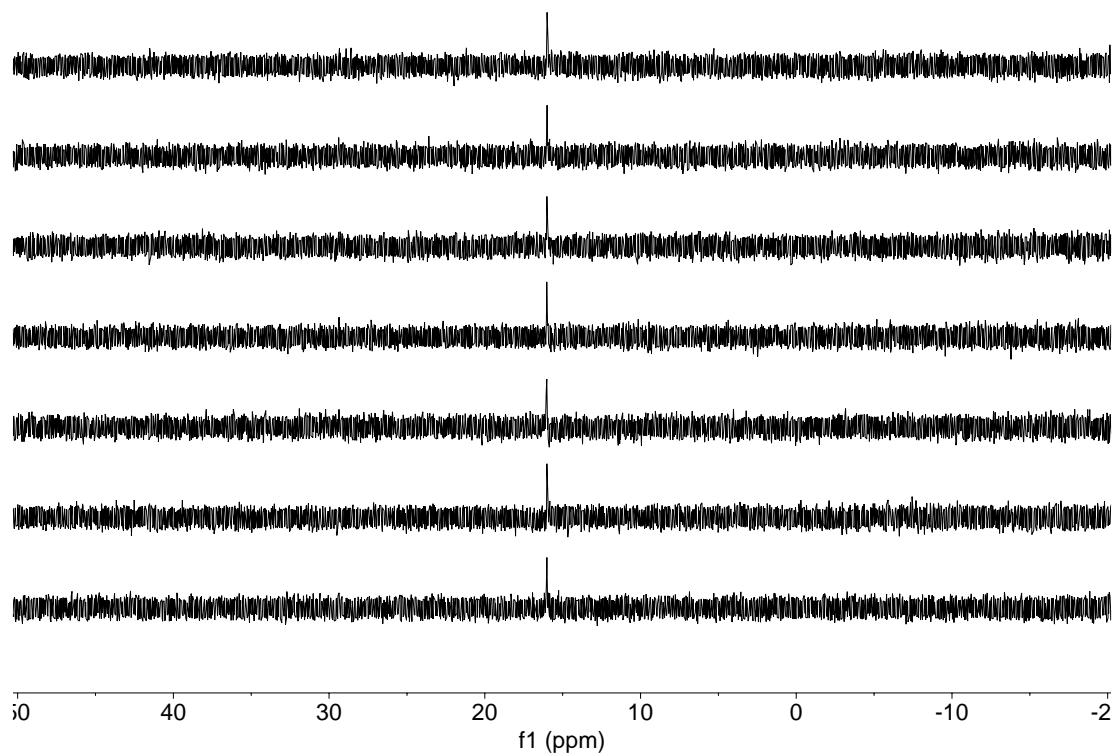
**Figure C.8.**  $^{31}\text{P}\{^1\text{H}\}$  NMR spectrum of **4-2** in  $\text{C}_6\text{D}_6$  (top).  $^{31}\text{P}\{^1\text{H}\}$  NMR spectrum 2 h after the addition of PhI to **4-2** in  $\text{C}_6\text{D}_6$  affording **4-10** (bottom) (243 MHz,  $\text{C}_6\text{D}_6$ , 298 K).



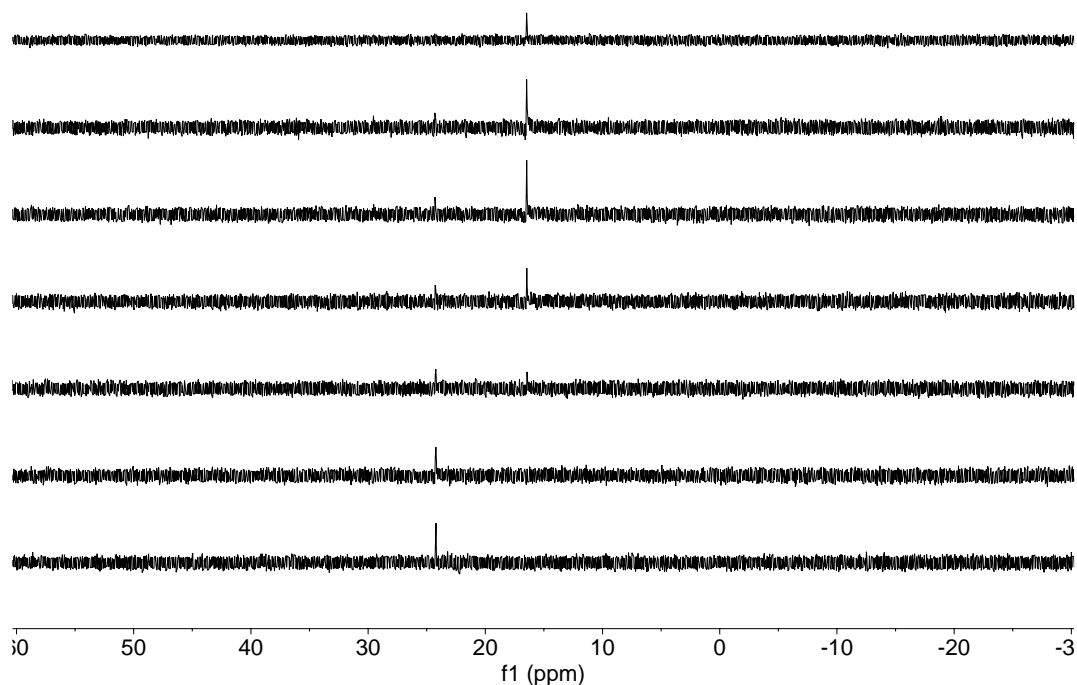
**Figure C.9.**  $^{31}\text{P}\{^1\text{H}\}$  NMR spectrum from the addition of 1.0 equiv PhI to **4-2** at  $-20\text{ }^\circ\text{C}$ . Scans acquired every 5 min for 120 min total. For clarity scans are shown every 10 mins and only 90 mins are shown.  $T_0 = \text{top } 90 \text{ min} = \text{bottom}$  (243 MHz, THF, 273 K).



**Figure C.10.**  $^{31}\text{P}\{^1\text{H}\}$  NMR spectrum from the addition of 1.0 equiv PhI to **4-2** at 0 °C, scans taken every 5 mins for 45 mins 2 scans have been omitted for clarity.  $T_0$  = top, 45 mins = bottom (243 MHz, THF, 278 K).



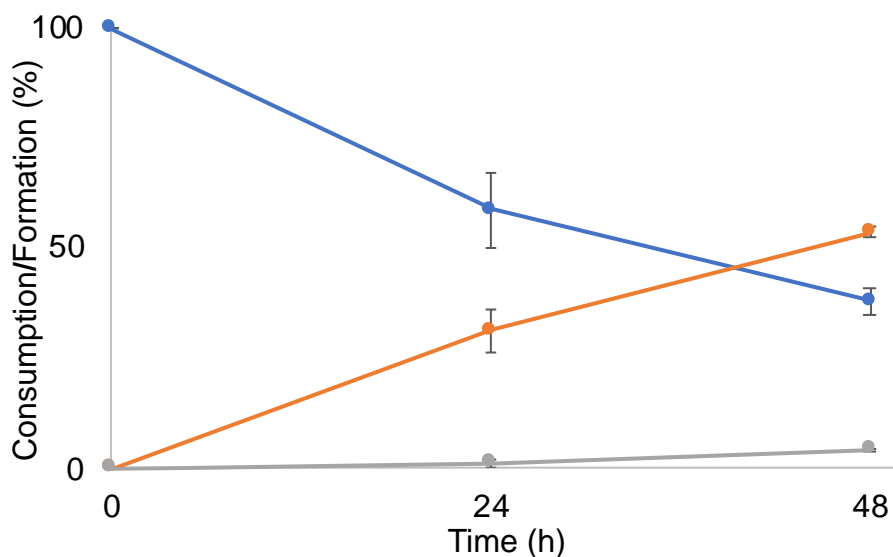
**Figure C.11.**  $^{31}\text{P}\{^1\text{H}\}$  NMR spectrum from the addition of 1.0 equiv PhI to **4-2** at 10 °C, scans taken every 5 mins for 45 mins 2 scans have been omitted for clarity. T<sub>0</sub> = top, 45 mins = bottom (243 MHz, THF, 283 K).



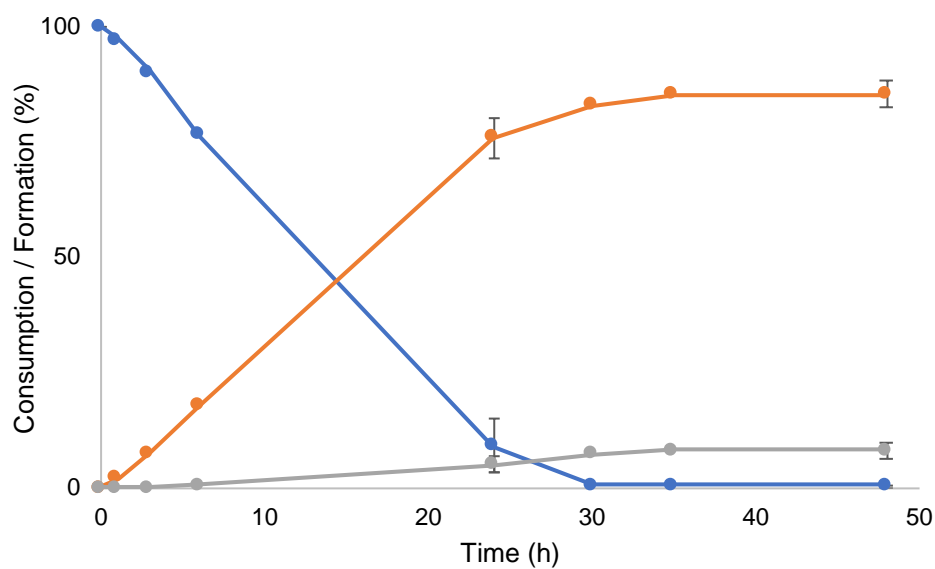
**Figure C.12.**  $^{31}\text{P}\{^1\text{H}\}$  NMR spectrum from the addition of 1.0 equiv of PhI to **4-2** at 25 °C, scans taken every 20 min for 100 min.  $T_0$  = top, 100 min = bottom. Second scan from the top is 5 min (243 MHz, THF, 298 K).

## V Kumada Coupling Conversion Plots

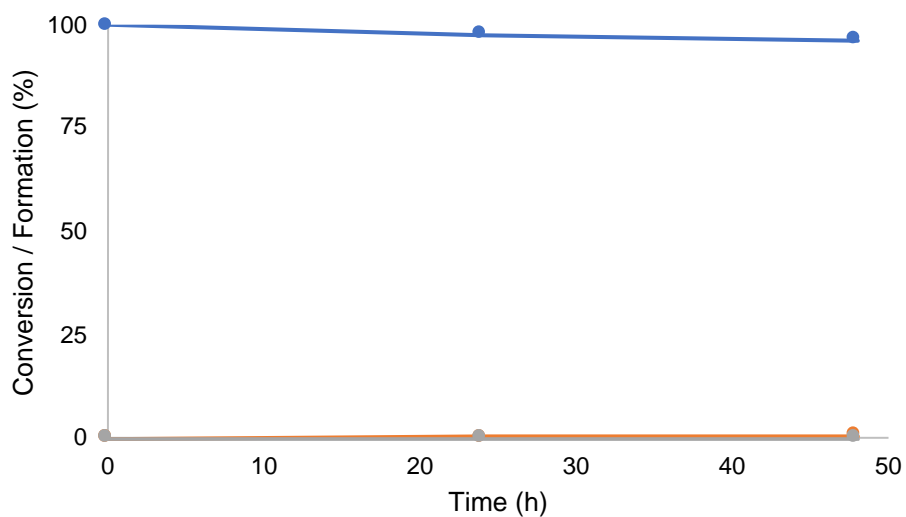
### V.I Kumada Coupling Optimization



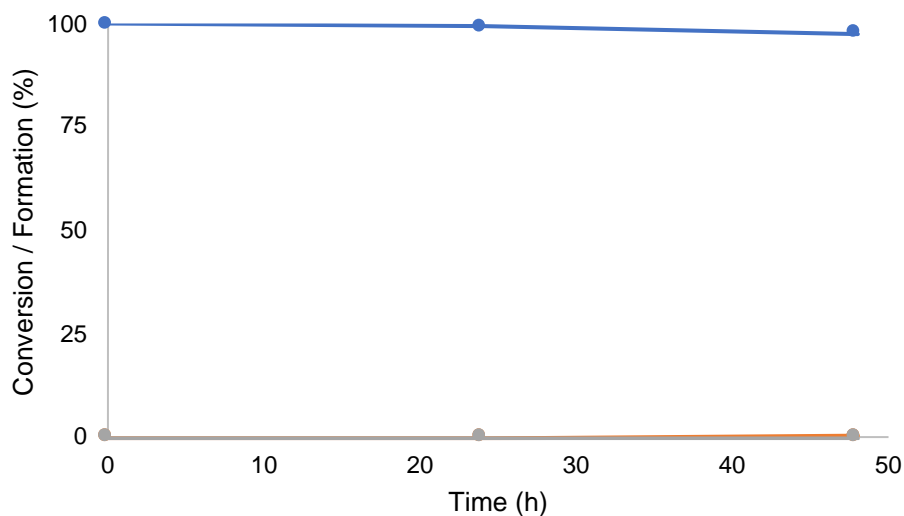
**Figure C.13.** Kumada coupling with **4-2** (0.1 mol%) and **4-4a** at 50°C. Reactions run in duplicate. Yields obtained *in-situ* via GC-FID based on corrected response factors relative to **4-4a**. Blue line is **4-4a**, orange line is **4-5a**, grey line is **4-7a**.



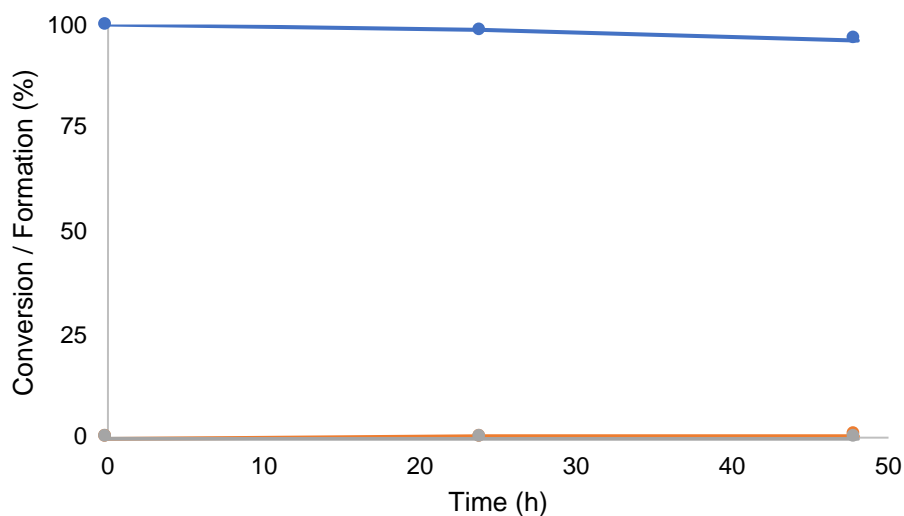
**Figure C.14.** Kumada coupling with **4-2** (0.1 mol%) and **4-4a** at 60°C. Reactions run in duplicate. Yields obtained *in-situ* via GC-FID based on corrected response factors relative to **4-4a**. Blue line is **4-4a**, orange line is **4-5a**, grey line is **4-7a**.



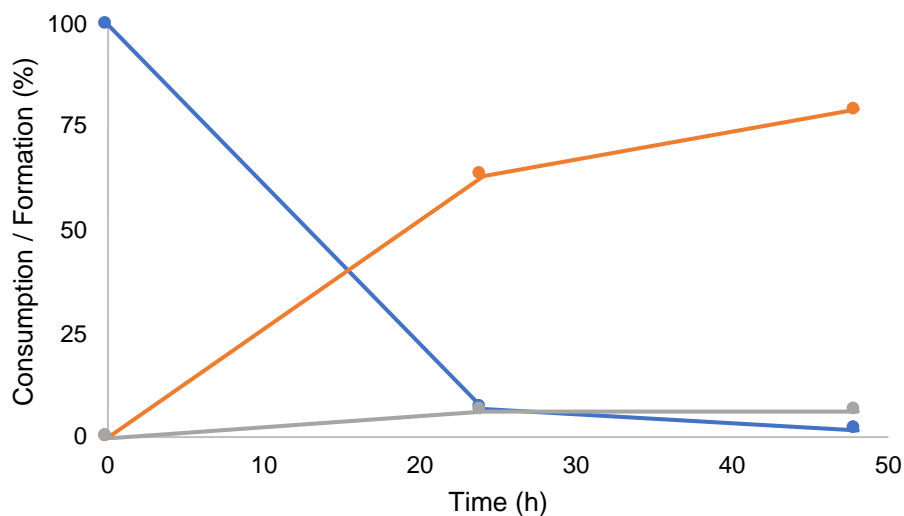
**Figure C.15.** Attempted Kumada coupling without **4-2** at 60°C. Yields obtained *in-situ* via GC-FID based on corrected response factors relative to **4-4a**. Blue line is **4-4a**, orange line is **4-5a**, grey line is **4-7a**.



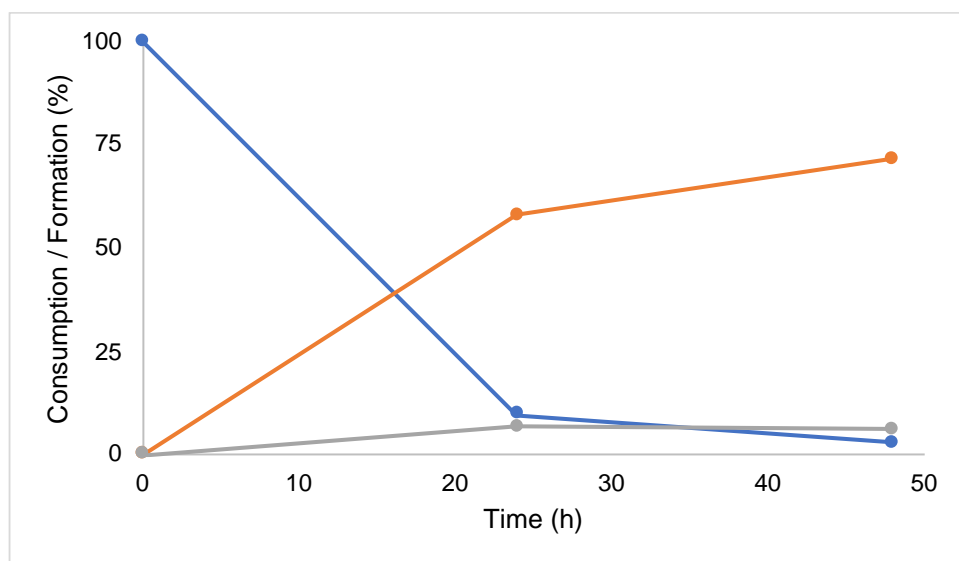
**Figure C.16.** Attempted Kumada coupling with **4-2** (0.1 mol%) at 60°C. Reaction was performed without **4-4a**. Yields obtained *in-situ* via GC-FID based on corrected response factors relative to 1,2,3,4-tetrahydronaphthalene. Blue line is **4-4a**, orange line is **4-5a**, grey line is **4-7a**.



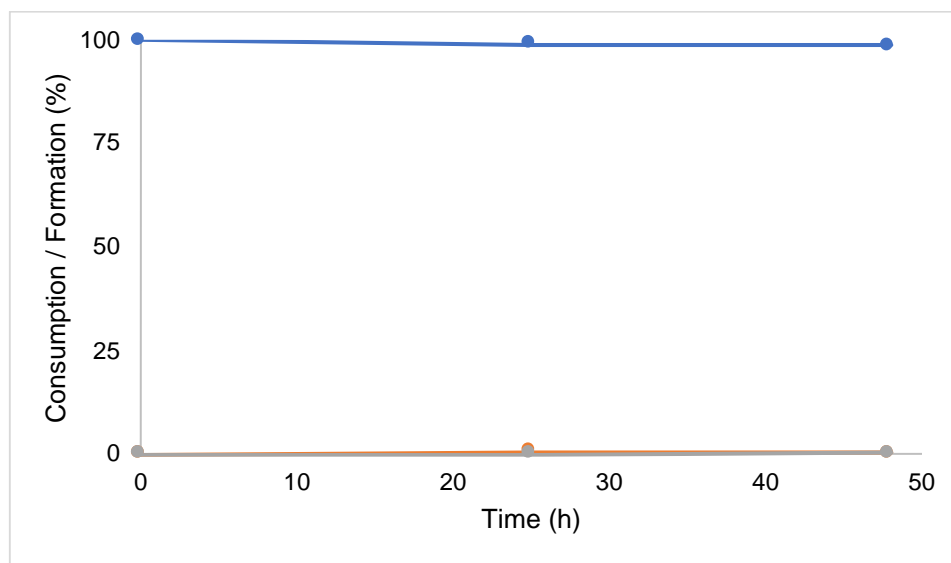
**Figure C.17.** Attempted Kumada coupling with **4-2** (0.1 mol%) at 60°C. Reaction was performed without PhMgBr. Yields obtained *in-situ* via GC-FID based on corrected response factors relative to **4-4a**. Blue line is **4-4a**, orange line is **4-5a**, grey line is **4-7a**.



**Figure C.18.** Kumada coupling with **2** (0.1 mol%) and **4-4a** at 60°C. Reaction was performed in the presence of 1,4-cyclohexadiene. Yields obtained *in-situ* via GC-FID based on corrected response factors relative to **4-4a**. Blue line is **4-4a**, orange line is **4-5a**, grey line is **4-7a**.

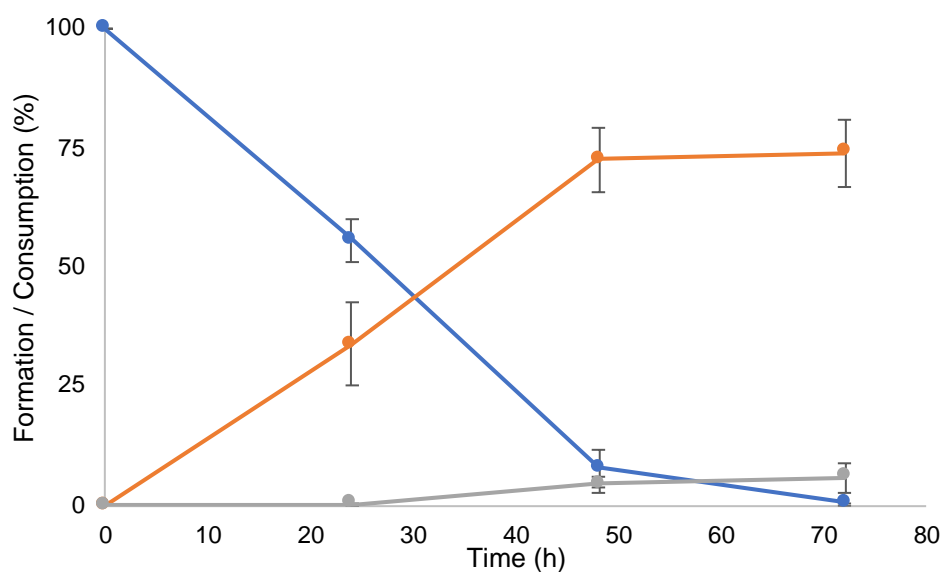


**Figure C.19.** Kumada coupling with **4-2** (0.1 mol%) and **4-4a** at 60°C. Reaction was performed in the presence of 1,1-diphenylethylene. Yields obtained *in-situ* via GC-FID based on corrected response factors relative to **4-4a**. Blue line is **4-4a**, orange line is **4-5a**, grey line is **4-7a**.



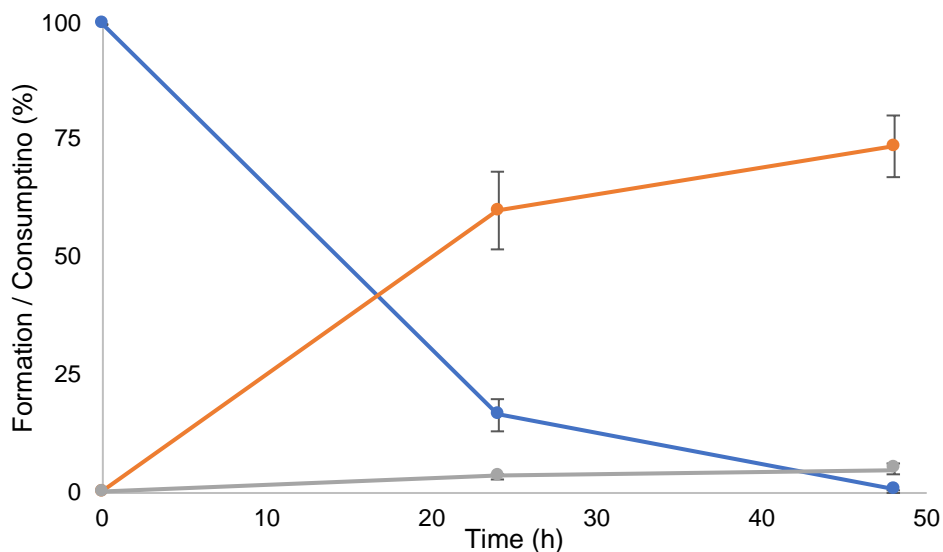
**Figure C.20.** Attempted Kumada coupling with **4-2** (0.1 mol%) and 4-chlorotoluene. Yields obtained *in-situ* via GC-FID based on corrected response factors relative to 4-chlorotoluene. Blue line is 4-chlorotoluene, orange line is 4-chlorobiphenyl, grey line is 4,4-dichlorobiphenyl.

## V.II Electrophile Scope

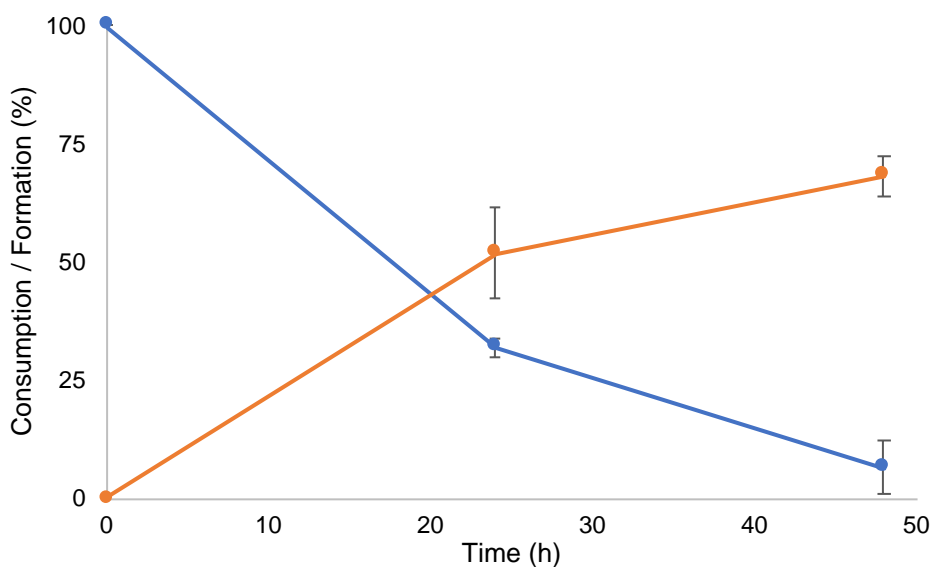


**Figure C.21.** Kumada coupling with **4-2** (0.1 mol%) and *o*-bromotoluene (**4-4b**) at 60°C. Error bars are the sum of two runs. Yields obtained *in-situ* via GC-FID based on corrected response factors relative to **4-4b**. Blue line is **4-4b**, orange line is **4-5b**, grey line is **4-7b**.

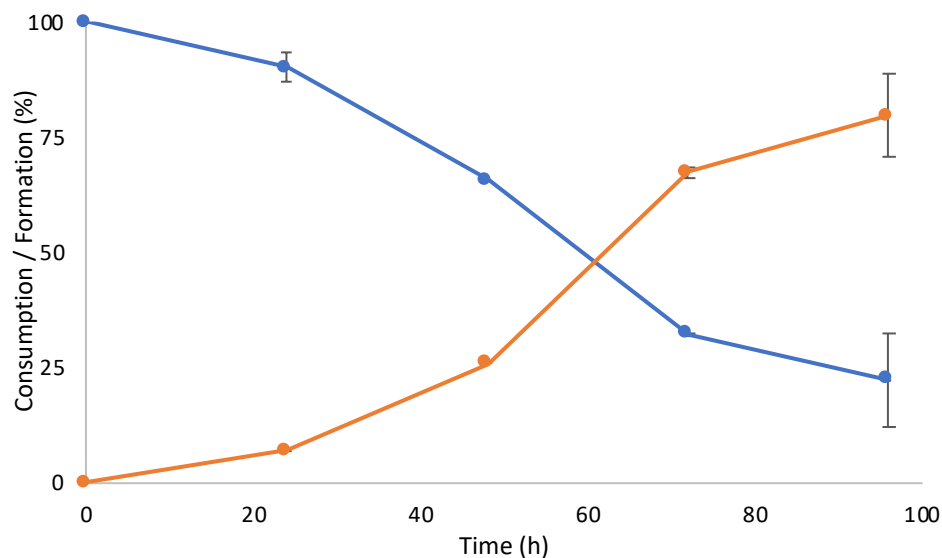




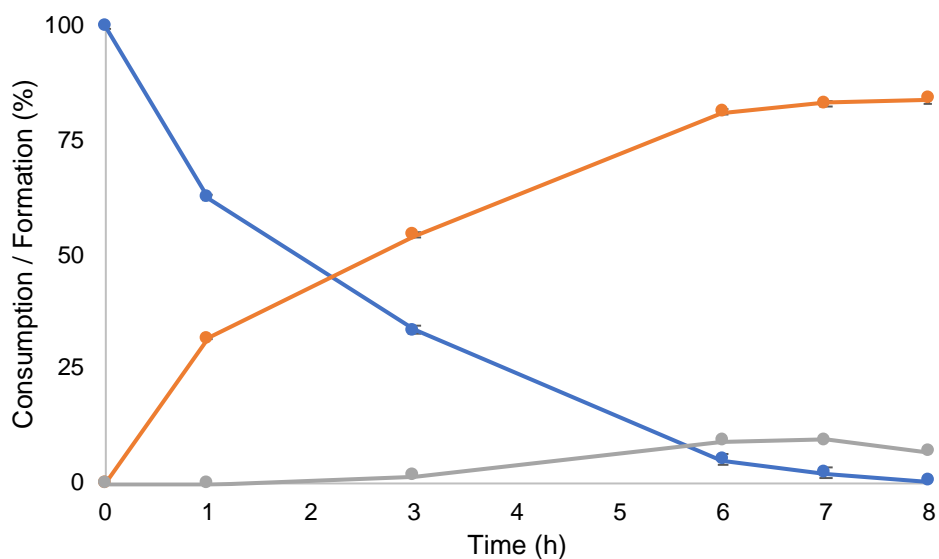
**Figure C.22.** Kumada coupling with **4-2** (0.1 mol%) and *m*-bromotoluene (**4-4c**) at 60°C. Error bars are the sum of two runs. Yields obtained *in-situ* via GC-FID based on corrected response factors relative to **4-4c**. Blue line is **4-4c**, orange line is **4-5c**, grey line is **4-7c**.



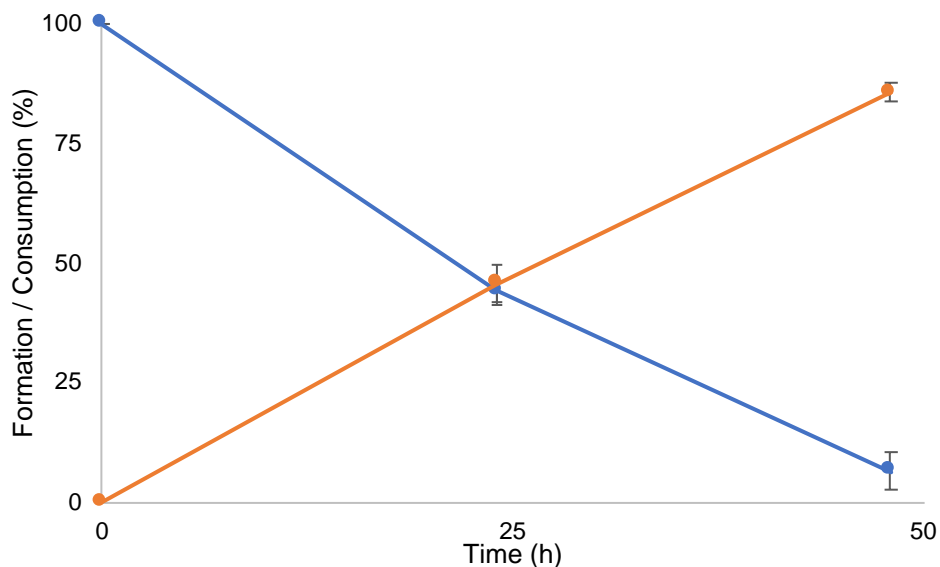
**Figure C.23.** Kumada coupling with **4-2** (0.1 mol%) and *m*-bromoxylene (**4-4d**) at 60°C. Error bars are the sum of two runs. Yields obtained *in-situ* via GC-FID based on corrected response factors relative to **4-4d**. Blue line is **4-4d**, orange line is **4-5d**, grey line is **4-7d**.



**Figure C.24.** Kumada coupling with **4-2** (0.1 mol%) and *m*-bromomesitylene (**4-4e**) at 60°C. Error bars are the sum of two runs. Yields obtained *in-situ* via GC-FID based on corrected response factors relative to **4-4e**. Blue line is **4-4e**, orange line is **4-5e**, grey line is **4-7e**.

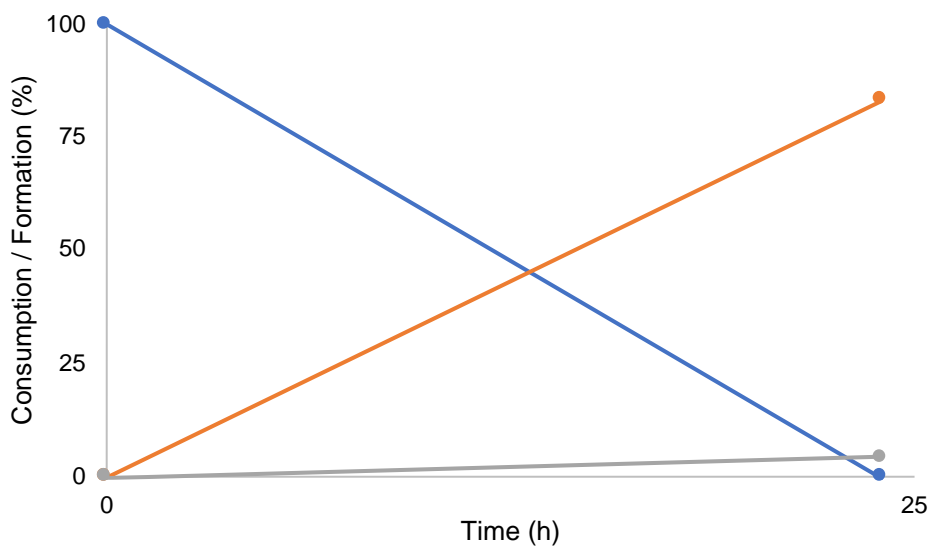


**Figure C.25.** Kumada coupling with **4-2** (0.1 mol%) and 4-bromobenzotrifluoride (**4-4f**) at 60°C. Error bars are the sum of two runs. Yields obtained *in-situ* via GC-FID based on corrected response factors relative to **4-4f**. Blue line is **4-4f**, orange line is **4-5f**, grey line is **4-7f**.

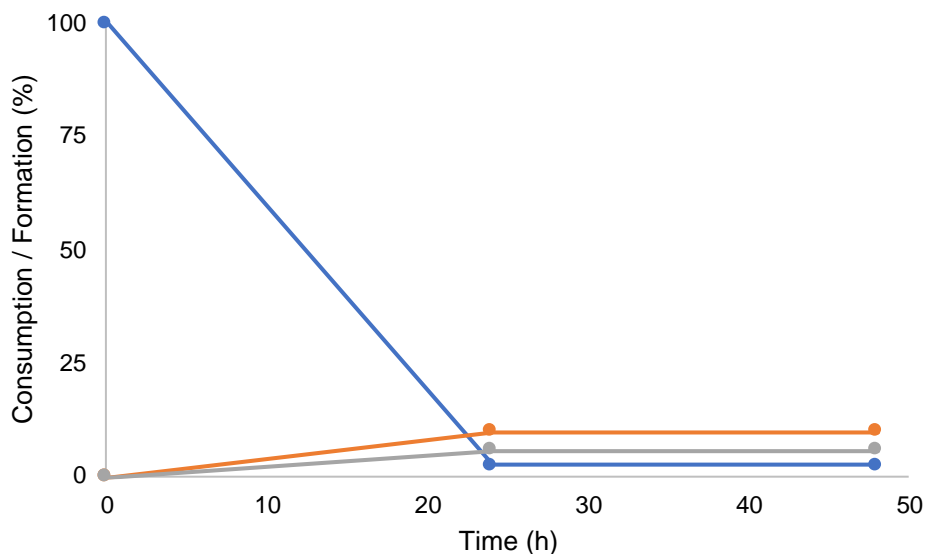


**Figure C.26.** Kumada coupling with **4-2** (0.1 mol%) and 4-bromoanisole (**4-4g**) at 60°C. Error bars are the sum of two runs. Yields obtained *in-situ* via GC-FID based on corrected response factors relative to **4-4g**. Blue line is **4-4g**, orange line is **4-5g**, grey line is **4-7g**.

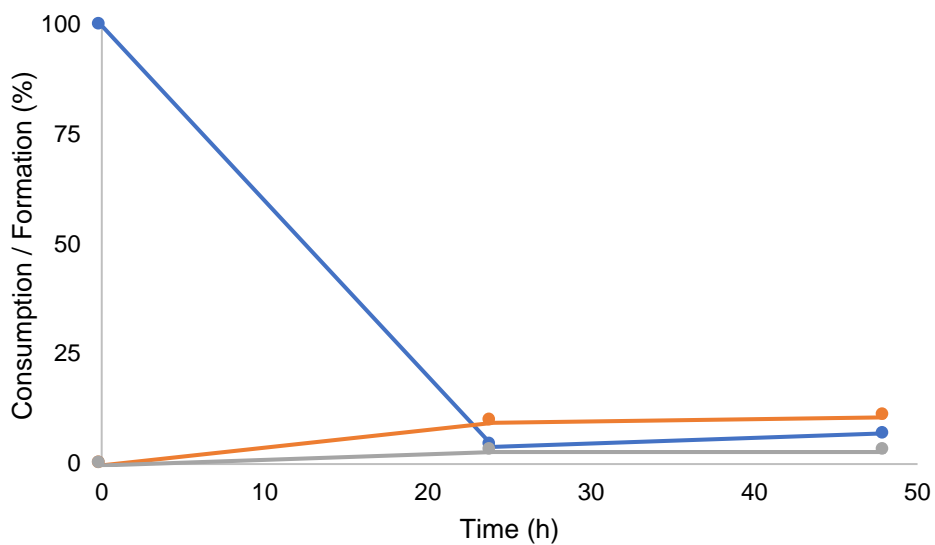
### V.III Nucleophile Scope



**Figure C.27.** Kumada coupling with **4-2** (0.1 mol%) **4-4a** and MeMgBr (**4-8a**) at 60°C. Yields obtained *in-situ* via GC-FID based on corrected response factors relative to **4-4a**. Blue line is **4-4a**, orange line is **4-9a**, grey line is **4-7a**.

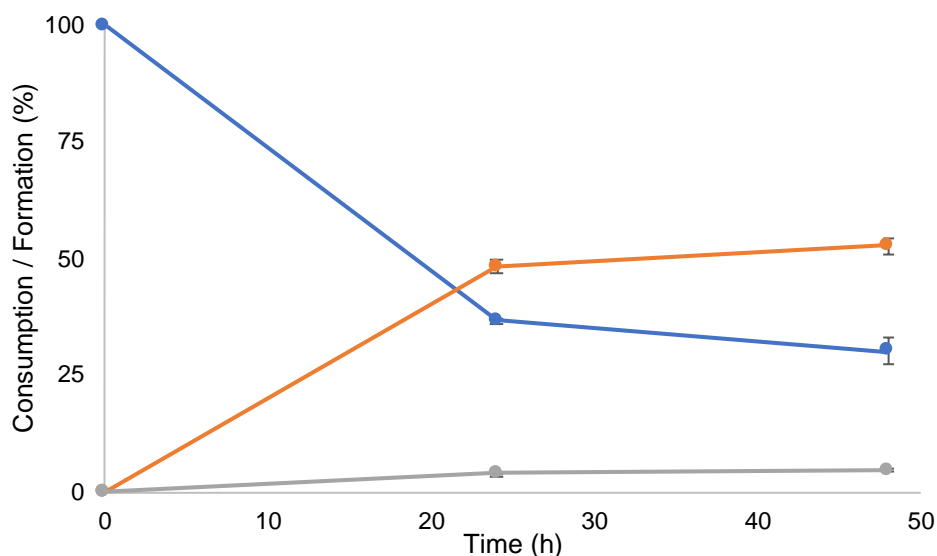


**Figure C.28.** Kumada coupling with **4-2** (0.1 mol%) **4-4a** and *i*PrMgBr (**4-8b**) at 60°C. Yields obtained *in-situ* via GC-FID based on corrected response factors relative to **4-4a**. Blue line is **4-4a**, orange line is **4-9a**, grey line is **4-7a**.

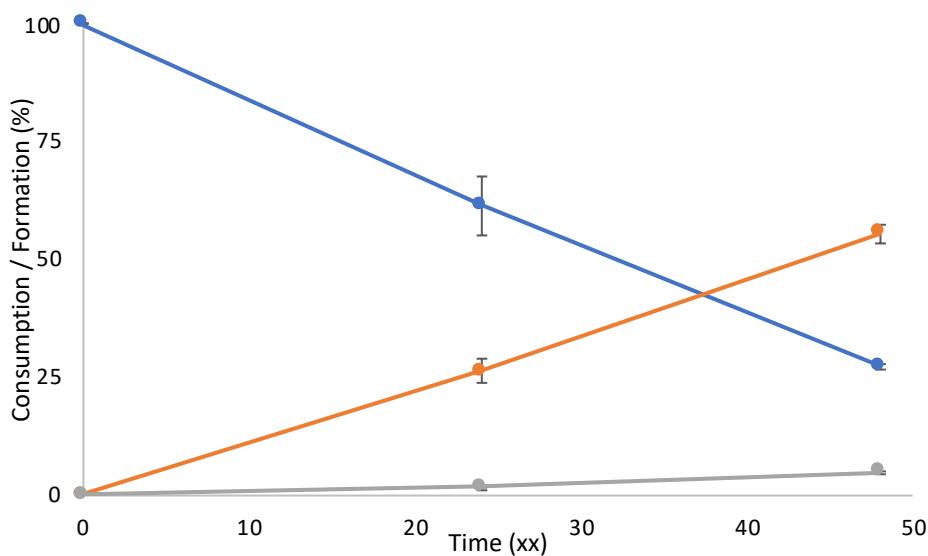


**Figure C.29.** Kumada coupling with **4-2** (0.1 mol%) **4-4a** and *i*PrMgBr (**4-8c**) at 60°C. Yields obtained *in-situ* via GC-FID based on corrected response factors relative to **4-4a**. Blue line is **4-4a**, orange line is **4-9a**, grey line is **4-7a**.

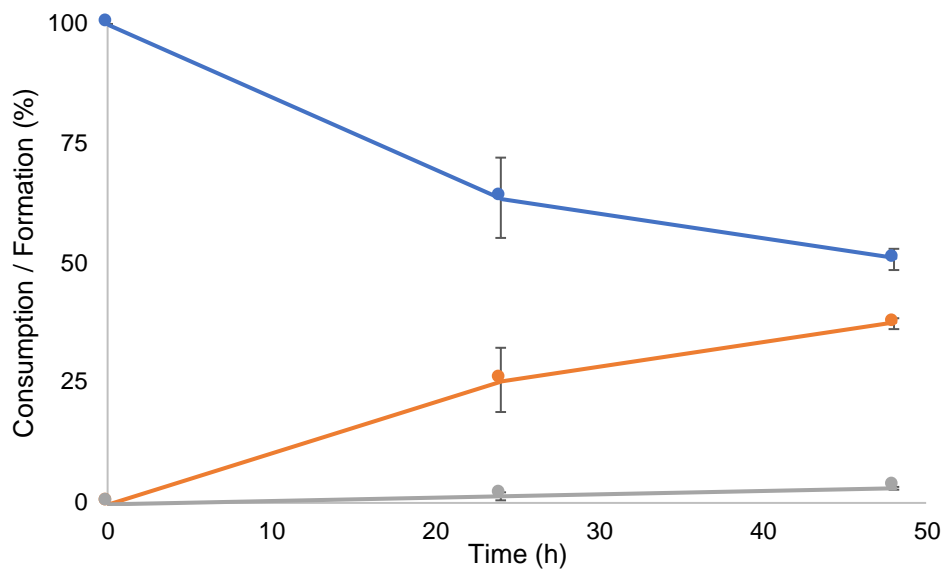
## V.IV Catalysis with Decomposition Products of 4-2



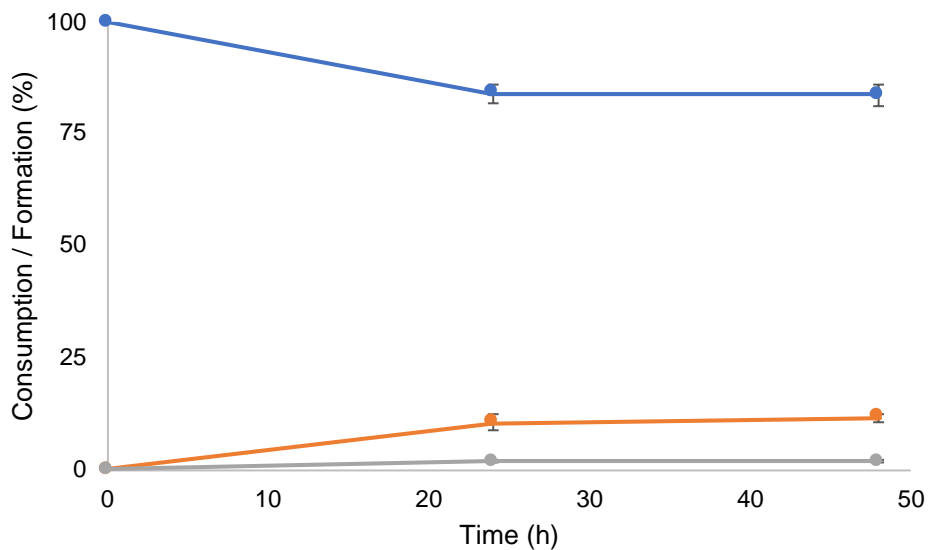
**Figure C.30.** Attempted Kumada coupling with **4-4a** after heating **4-2** (0.1 mol%) at 60 °C for 3 h. Yields obtained *in-situ* via GC-FID based on corrected response factors relative to **4-4a**. Blue line is **4-4a**, orange line is **4-5a**, grey line is **4-7a**.



**Figure C.31.** Attempted Kumada coupling with **4-4a** after heating **2** (0.1 mol%) at 70 °C for 48 h. Yields obtained *in-situ* via GC-FID based on corrected response factors relative to **4-4a**. Blue line is **4-4a**, orange line is **4-5a**, grey line is **4-7a**.

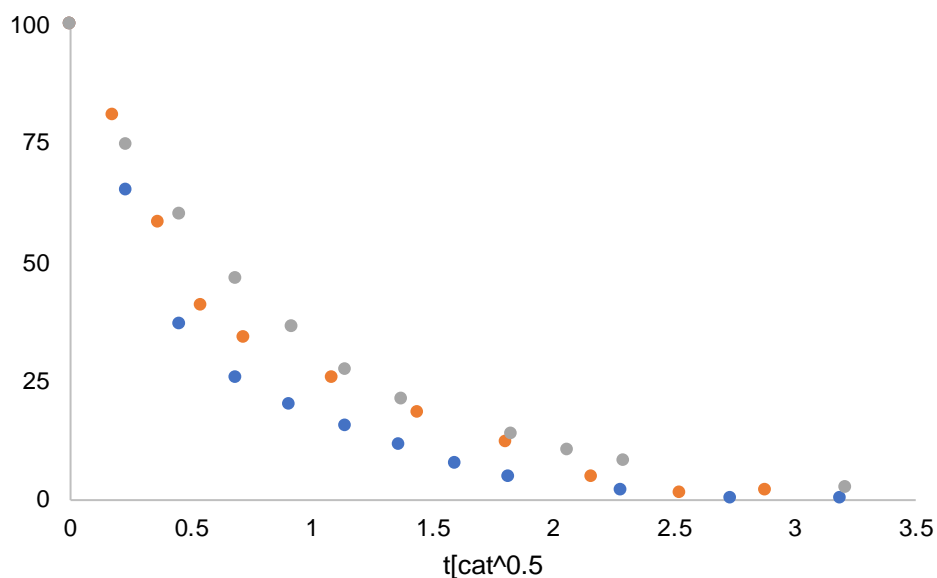


**Figure C.32.** Attempted Kumada coupling with **4-3** (0.1 mol%). Yields obtained *in-situ* via GC-FID based on corrected response factors relative to **4-4a**. Blue line is **4-4a**, orange line is **4-5a**, grey line is **4-7a**.

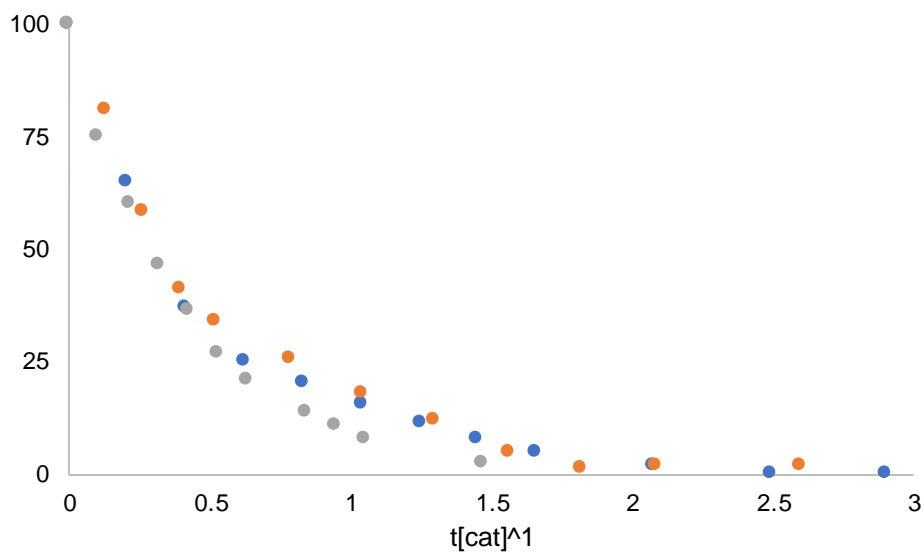


**Figure C.33.** Attempted Kumada coupling with Pd<sup>0</sup> (1 mol%), **4-4a** and MeMgBr. Yields obtained *in-situ* via GC-FID based on corrected response factors relative to **4-4a**. Blue line is **4-4a**, orange line is **4-5a**, grey line is **4-7a**.

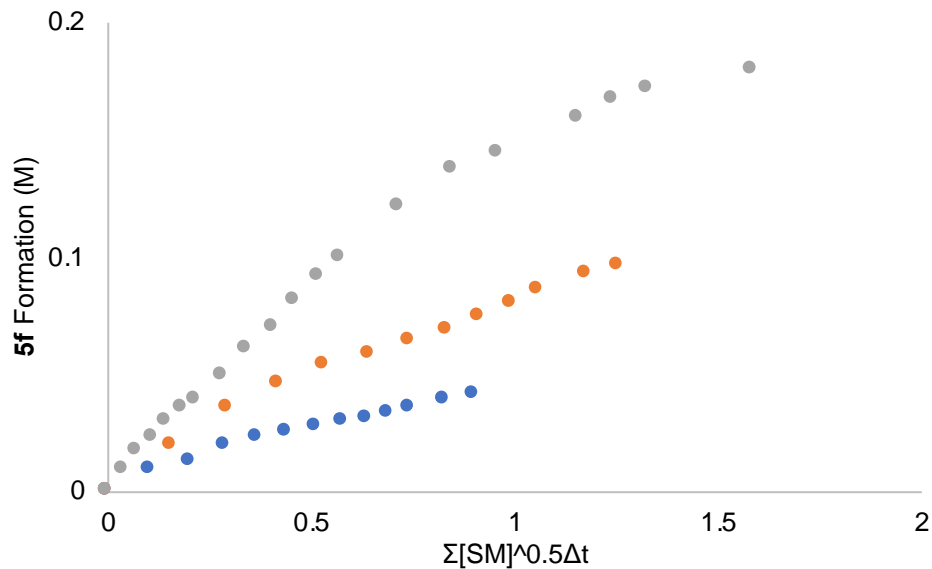
## VI VTNA



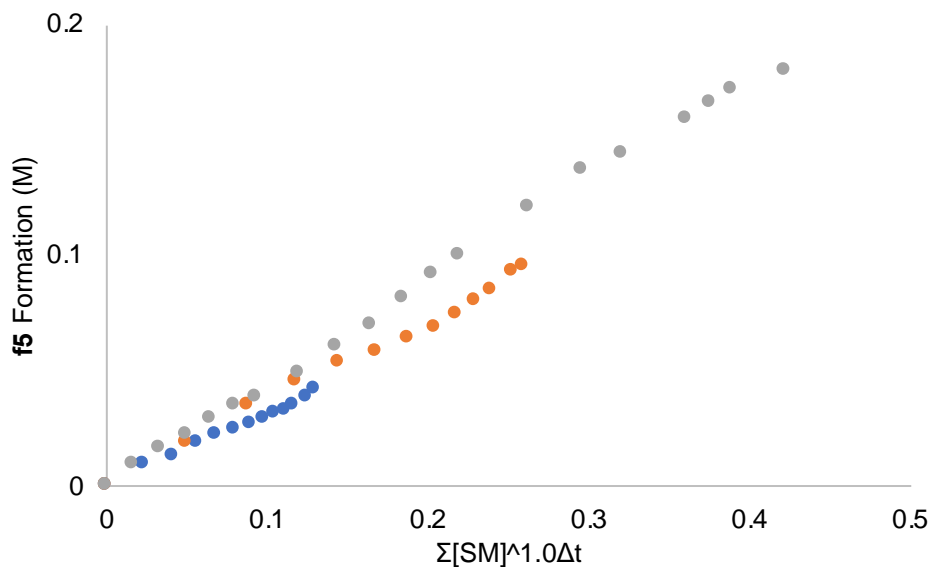
**Figure C.34.** Variable time normalization analysis, concentration of **4-4f** and PhMgBr kept constant at 210 mM and 315 mM respectively. Concentration of **4-2** changed from 210  $\mu\text{M}$  (blue), 520  $\mu\text{M}$  (orange), and 830  $\mu\text{M}$  (grey). Consumption of **4-4f** is being tracked. Order of 0.5 used.



**Figure C.35.** Variable time normalization analysis, concentration of **4-4f** and PhMgBr kept constant at 210 mM and 315 mM respectively. Concentration of **4-2** changed from 210  $\mu\text{M}$  (blue), 520  $\mu\text{M}$  (orange), and 830  $\mu\text{M}$  (grey). Consumption of **4-4f** is being tracked. Order of 1 used.

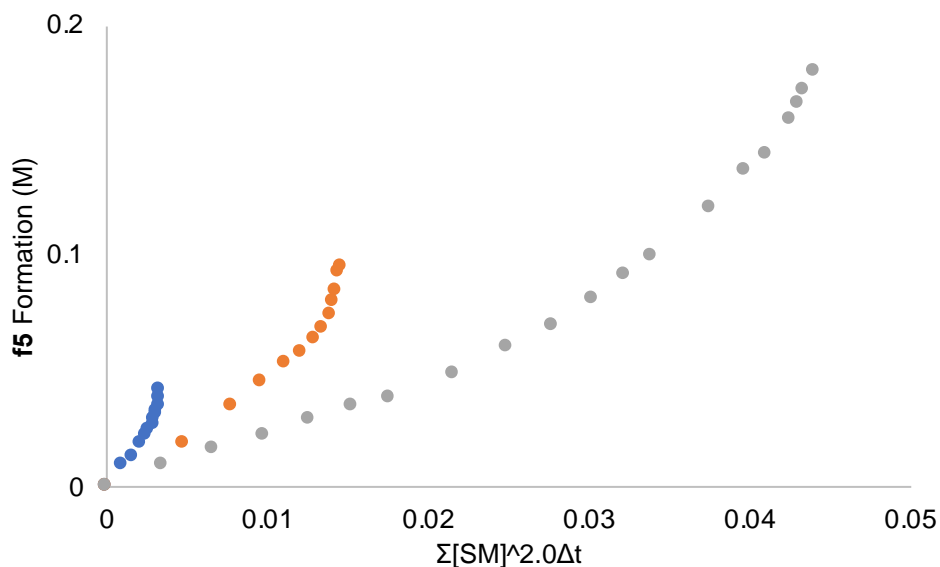


**Figure C.36.** Variable time normalization analysis, concentration of **4-2** and PhMgBr kept constant at 210  $\mu$ M and 315 mM respectively. Concentration of **4-4f** changed from 50 mM (blue) to 110 mM (orange), and 220 mM (grey). Formation of **4-5f** is being tracked. Reactions ran in duplicate. Order of 0.5 used.



**Figure C.37.** Variable time normalization analysis, concentration of **4-2** and PhMgBr kept constant at 210  $\mu$ M and 315 mM respectively. Concentration of **4-4f** changed from 50 mM (blue) to 110 mM (orange), and 220 mM (grey). Formation of **4-5f** is being tracked. Reactions ran in duplicate. Order of 1.0 used.





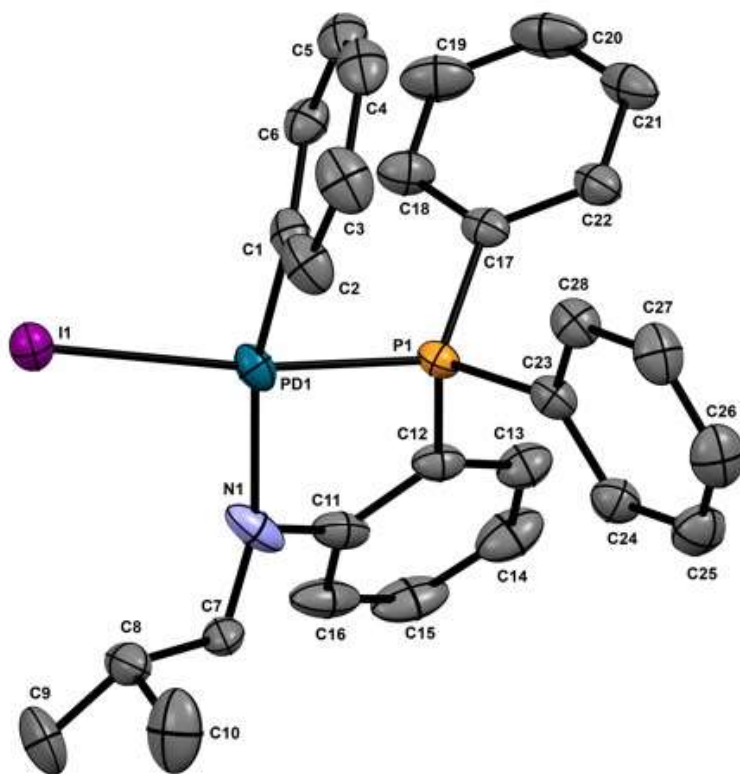
**Figure C.38.** Variable time normalization analysis, concentration of **4-2** and PhMgBr kept constant at 210  $\mu$ M and 315 mM respectively. Concentration of **4-4f** changed from 50 mM (blue) to 110 mM (orange), and 220 mM (grey). Formation of **4-5f** is being tracked. Reactions ran in duplicate. Order of 2.0 used.

## VII Crystallographic Details

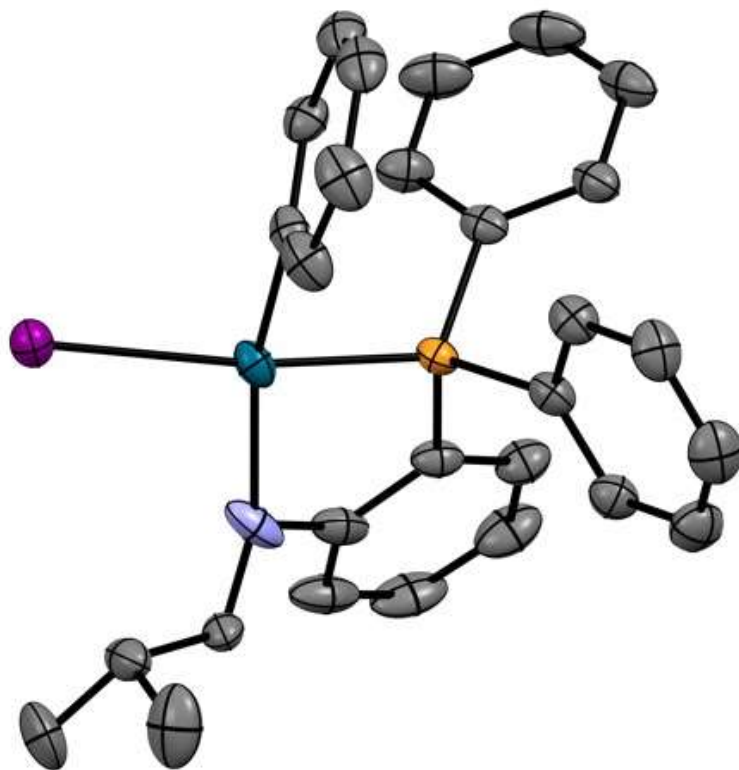
### Experimental for C<sub>28</sub>H<sub>27</sub>INPPd (**4-10**)

**Data Collection and Processing.** The sample (**4-10**) was submitted by Kyle Jackman of the Blacquiere research group at the University of Western Ontario. The sample was mounted on a Mitegen polyimide micromount with a small amount of Paratone N oil. All X-ray measurements were made on a Bruker Kappa Axis Apex2 diffractometer at a temperature of 110 K. The unit cell dimensions were determined from a symmetry constrained fit of 6481 reflections with  $4.72^\circ < 2\theta < 54.08^\circ$ . The data collection strategy was a number of  $\omega$  and  $\phi$  scans which collected data up to  $58.332^\circ$  ( $2\theta$ ). The frame integration was performed using SAINT.<sup>1</sup> The resulting raw data was scaled and absorption corrected using a multi-scan averaging of symmetry equivalent data using SADABS.<sup>2</sup>

**Structure Solution and Refinement.** The structure was solved by using a dual space methodology using the SHELXT program.<sup>3</sup> All non-hydrogen atoms were obtained from the initial solution. The hydrogen atoms were introduced at idealized positions and were allowed to ride on the parent atom. The isopropyl group was disordered over two orientations. The occupancy of the major orientation refined to a value of 0.676(9). The structural model was fit to the data using full matrix least-squares based on F<sub>2</sub>. The calculated structure factors included corrections for anomalous dispersion from the usual tabulation. The structure was refined using the SHELXL program from the SHELX suite of crystallographic software.<sup>4</sup> Graphic plots were produced using the Mercury program suite.<sup>5</sup>



**Figure C.39.** Thermal ellipsoid plot of **4-10** showing naming and numbering scheme. Ellipsoids are at the 50% probability level and hydrogen atoms were omitted for clarity. The minor component of the disordered isopropyl group was also omitted for clarity.



**Figure C.40.** Thermal ellipsoid plot of **4-10**. Ellipsoids are at the 50% probability level and hydrogen atoms were omitted for clarity. The minor component of the disordered isopropyl group was also omitted for clarity.

**Table C.1.** Summary of Crystal Data for **C<sub>28</sub>H<sub>27</sub>INPPd (4-10)**.

| Compound   | <b>4-10</b>                           |
|--|---------------------------------------|
| Formula  | C <sub>28</sub> H <sub>27</sub> INPPd |
| Formula Weight ( <i>g/mol</i> )                    | 641.77                                |
| Crystal Dimensions ( <i>mm</i> )                   | 0.134 × 0.127 × 0.046                 |
| Crystal Color and Habit                            | yellow plate                          |
| Crystal System                                     | triclinic                             |
| Space Group  | P -1                                  |
| Temperature, K                                     | 110                                   |
| <i>a</i> , Å                                       | 9.3501(18)                            |
| <i>b</i> , Å                                       | 11.520(3)                             |
| <i>c</i> , Å                                       | 13.117(3)                             |
| <i>a</i> , °                                       | 104.916(7)                            |
| <i>b</i> , °                                       | 109.003(12)                           |
| <i>g</i> , °                                       | 93.668(12)                            |
| <i>V</i> , Å <sup>3</sup>                          | 1273.8(5)                             |
| Number of reflections to determine final unit cell | 6481                                  |
| Min and Max 2 $\theta$ for cell determination, °   | 4.72, 54.08                           |
| <i>Z</i>   | 2                                     |

|   |   |
|---|---|
| F(000)  | 632   |
| $\rho$ (g/cm <sup>3</sup> )   | 1.673   |
| $\lambda$ , Å, (MoK $\alpha$ )  | 0.71073   |
| $\mu$ , (cm <sup>-1</sup> )   | 2.019   |
| Diffractometer Type   | Bruker Kappa Axis Apex2   |
| Scan Type(s)  | phi and omega scans   |
| Max 2 $\theta$ for data collection, °   | 58.332  |
| Measured fraction of data   | 0.999   |
| Number of reflections measured  | 52398   |
| Unique reflections measured   | 6851  |
| $R_{\text{merge}}$  | 0.0836  |
| Number of reflections included in refinement  | 6851  |
| Cut off Threshold Expression  | $I > 2\sigma(I)$  |
| Structure refined using   | full matrix least-squares using $F^2$                                     |
| Weighting Scheme  | $w=1/[\sigma^2(F_o^2)+(0.0255P)^2+2.8734P]$ where<br>$P=(F_o^2+2F_c^2)/3$ |
| Number of parameters in least-squares   | 330   |
| $R_1$   | 0.0418  |
| $wR_2$  | 0.0800  |
| $R_1$ (all data)  | 0.0634  |
| $wR_2$ (all data)   | 0.0863  |
| GOF   | 1.046   |
| Maximum shift/error   | 0.001   |
| Min & Max peak heights on final DF Map ( $e^-$ / $\text{Å}$ )                                 | -1.393, 0.861   |
| Where:  |   |
| $R_1 = \sum   F_o  -  F_c   / \sum F_o$   |   |
| $wR_2 = [ \sum (w(F_o^2 - F_c^2)^2) / \sum (w F_o^4) ]^{1/2}$                                 |   |
| $GOF = [ \sum (w(F_o^2 - F_c^2)^2) / (\text{No. of reflns.} - \text{No. of params.}) ]^{1/2}$ |   |

## VII References

1. Bruker-Nonius, *SAINTE*. Bruker-Nonius: Madison, WI 53771, USA, 2013; Vol. version; 2013.8.
2. Bruker-Nonius, *SADABS*. Bruker-Nonius: Madison, WI 53711, USA, 2012; Vol. version; 2012.1.
3. Sheldrick, G. M., *Acta Crystallogr A Found Adv* **2015**, *71*, 3-8.
4. Sheldrick, G., *Acta Crystallographica Section C* **2015**, *71*.
5. Macrae, C.; Bruno, I.; Chisholm, J.; Edgington, P.; McCabe, P.; Pidcock, E.; Rodriguez-Monge, L.; Taylor, R.; van de Streek, J.; Wood, P., *J. Appl. Cryst.* **2008**, *41*, 466-470.

## Appendices

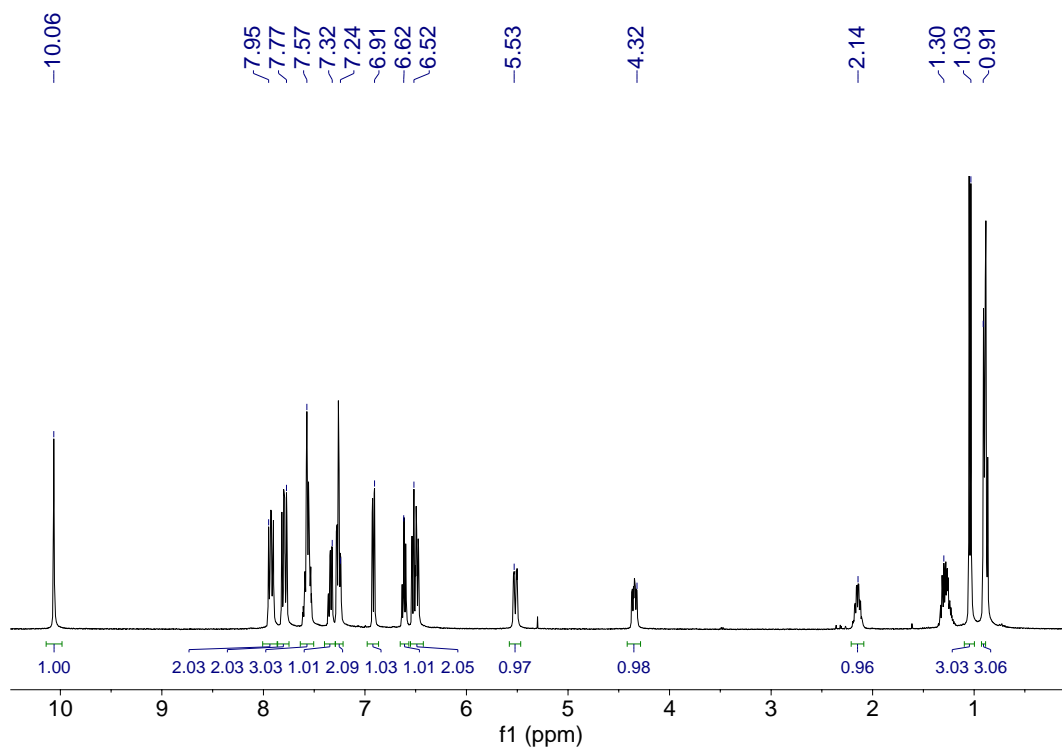
### Appendix D: Supplementary Information for Chapter 5

**Table D.1.** Summary of Selected  $^1\text{H}$ , and  $^{13}\text{C}\{^1\text{H}\}$  NMR Spectroscopy Data for Known 1-AzA complexes.

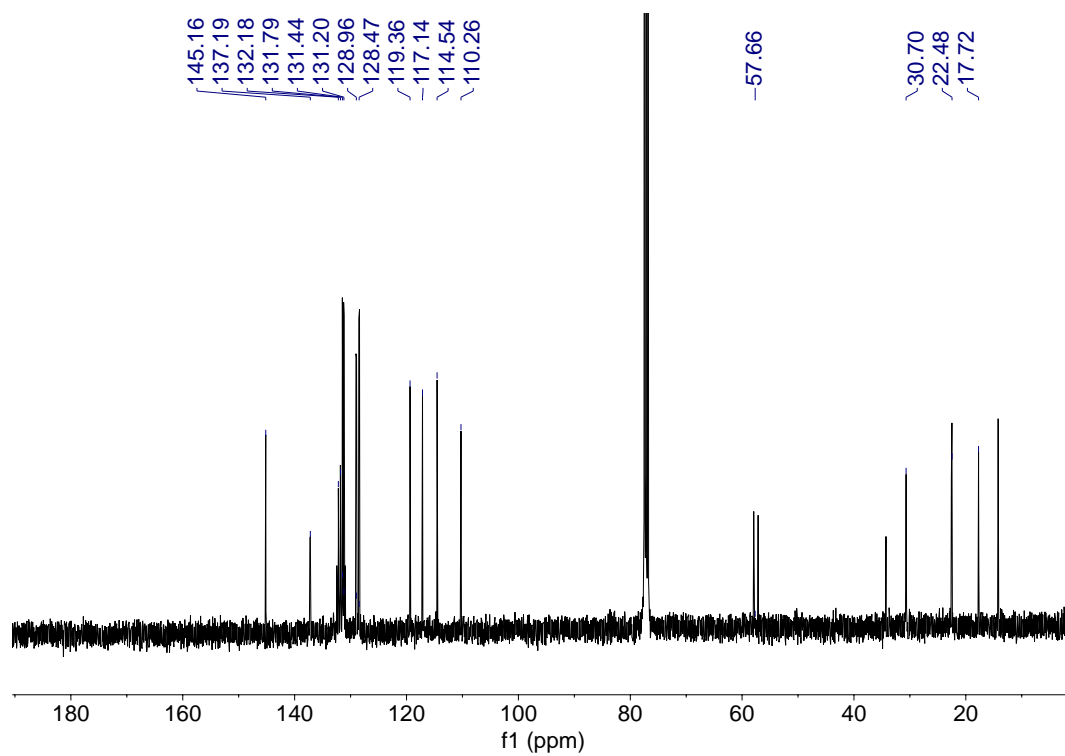
|   | $\text{H}^1$ | $\text{C}^1$ | $\text{C}^2$ | References |
|---|--------------|--------------|--------------|------------|
| $\kappa^1\text{-N}$                       | 7.28         | 149.8-187.5  | 66.3-114.8   | 1, 2       |
| $\eta^3\text{-NCC}$                       | N/A          | 151.9-184.9  | 42.0-64.5    | 1          |
| $\mu(\kappa^1\text{-N};\eta^2\text{-CC})$ | 5.97         | 109.0        | 74.5         | 2          |

## I NMR Spectra

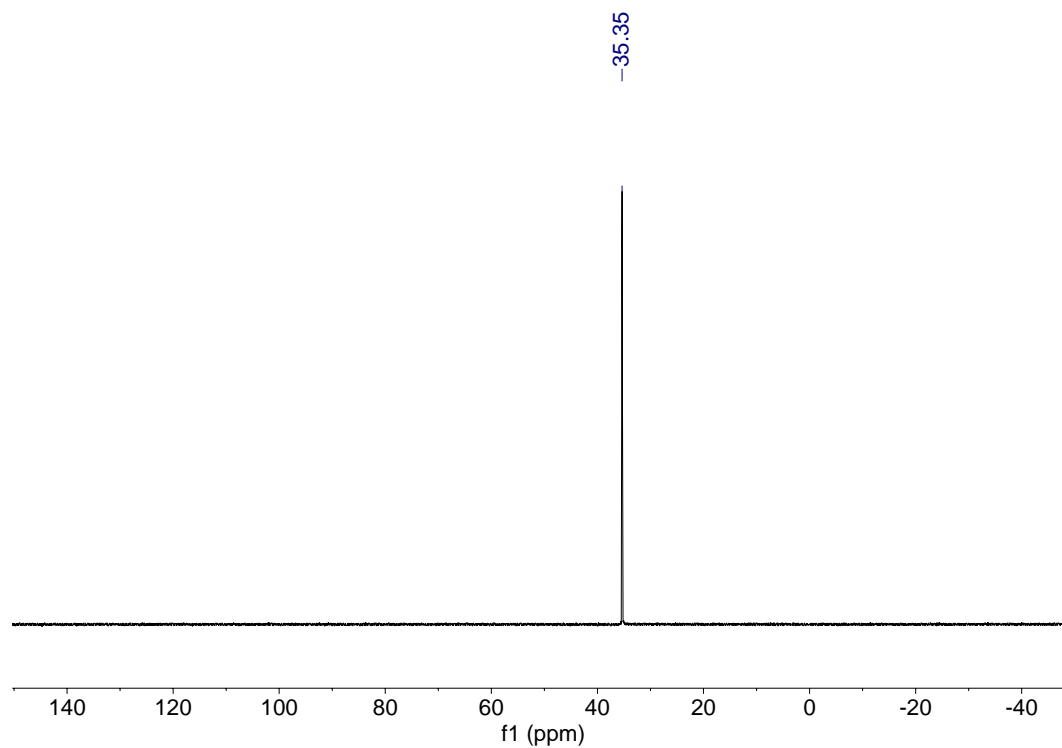
### I.I Phosphin(it)e-Imine NMR Spectra



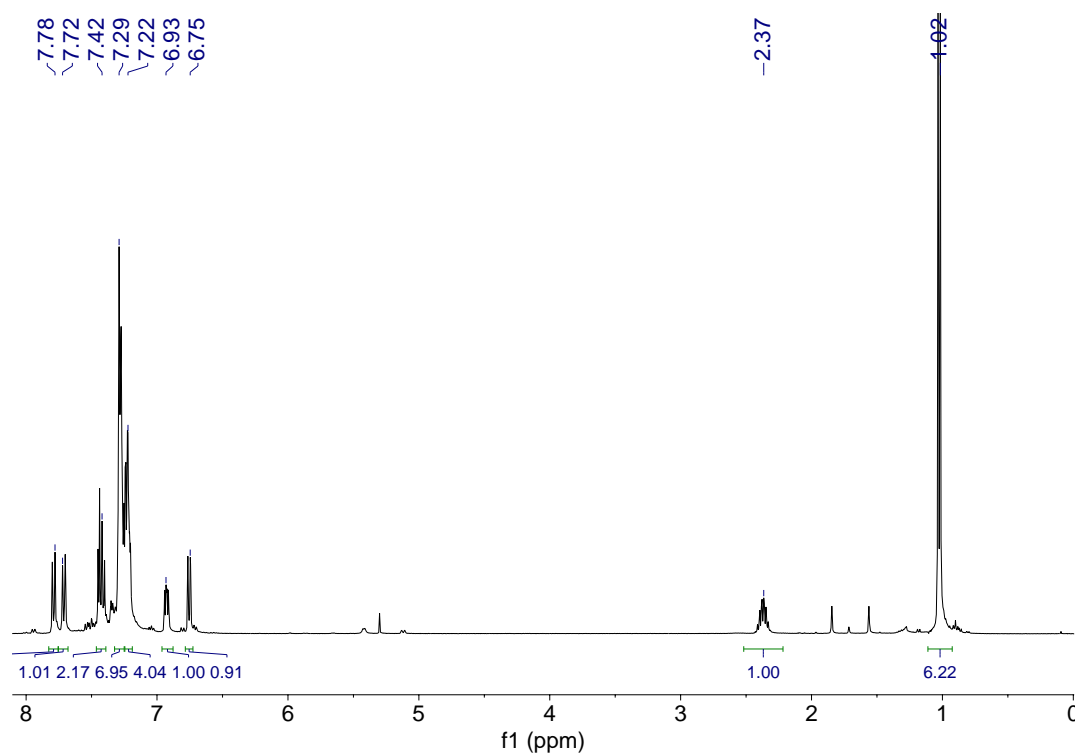
**Figure D.1.**  $^1\text{H}$  NMR spectrum of  $\text{HO}(o\text{-C}_6\text{H}_4)\text{NH}(\text{Ph}_2\text{P}=\text{O})(i\text{-Bu})$ , **5-L4b** ( $\text{CDCl}_3$ , 600 MHz).



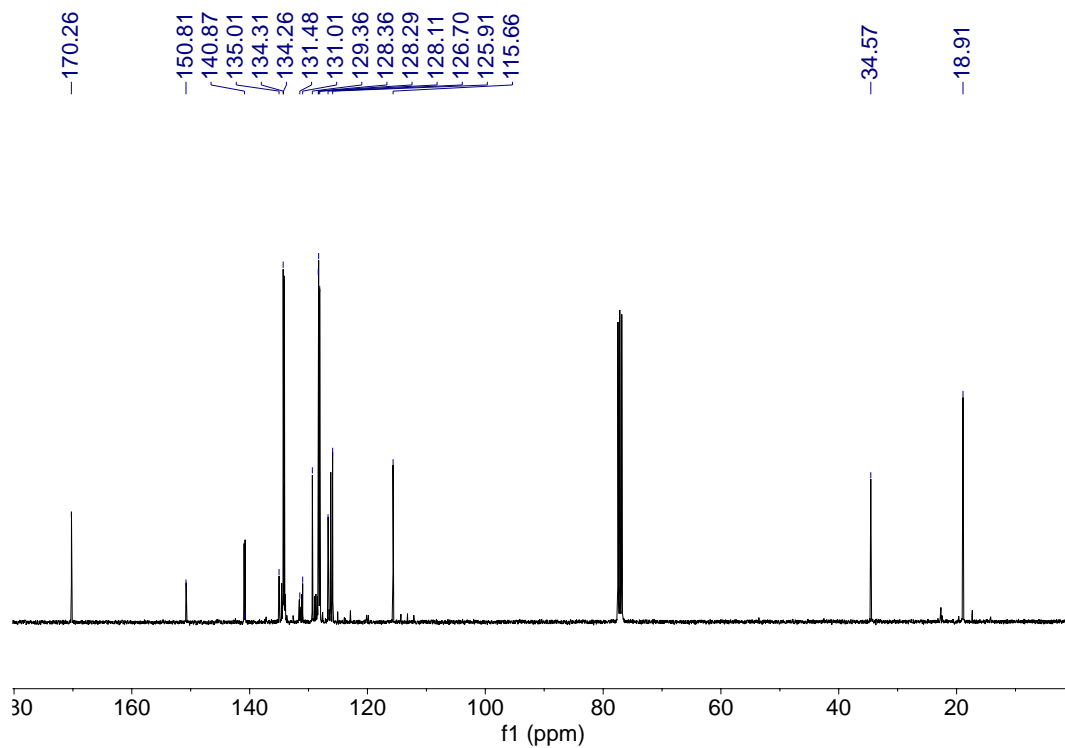
**Figure D.2.**  $^{13}\text{C}\{^1\text{H}\}$  NMR spectrum of  $\text{HO}(o\text{-C}_6\text{H}_4)\text{NH}(\text{Ph}_2\text{P}=\text{O})(i\text{-Bu})$ , **5-L4b** ( $\text{CDCl}_3$ , 151 MHz).



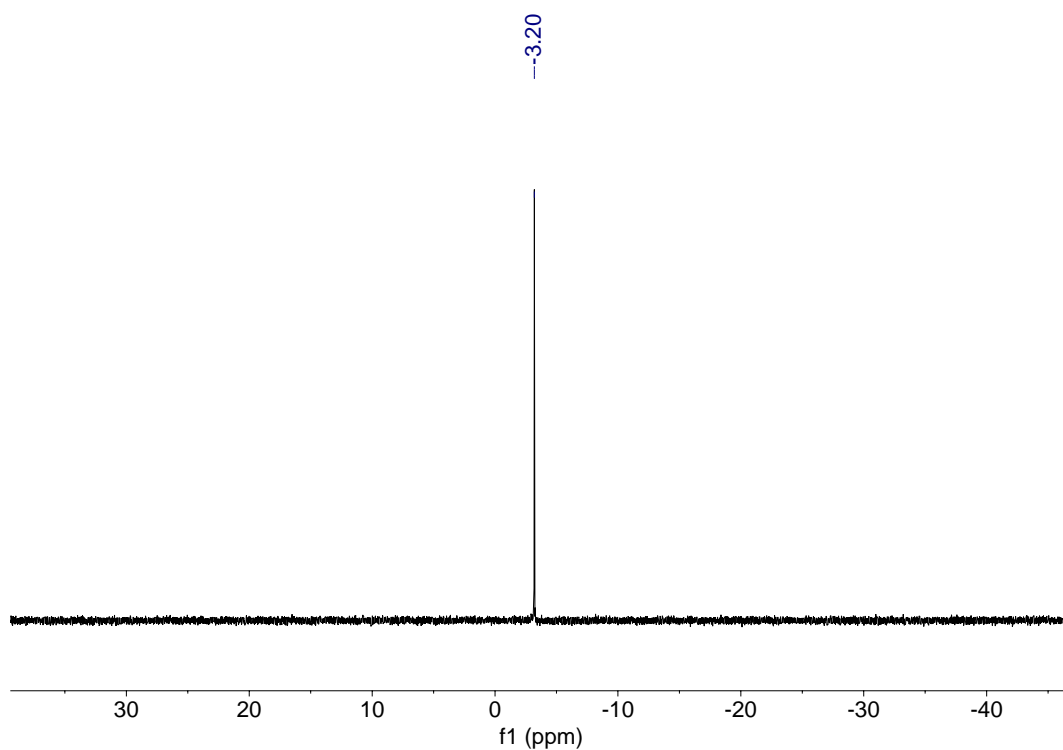
**Figure D.3.**  $^{31}\text{P}\{^1\text{H}\}$  NMR spectrum of  $\text{HO}(o\text{-C}_6\text{H}_4)\text{NH}(\text{Ph}_2\text{P}=\text{O})(i\text{-Bu})$ , **5-L4b** ( $\text{CDCl}_3$ , 243 MHz).



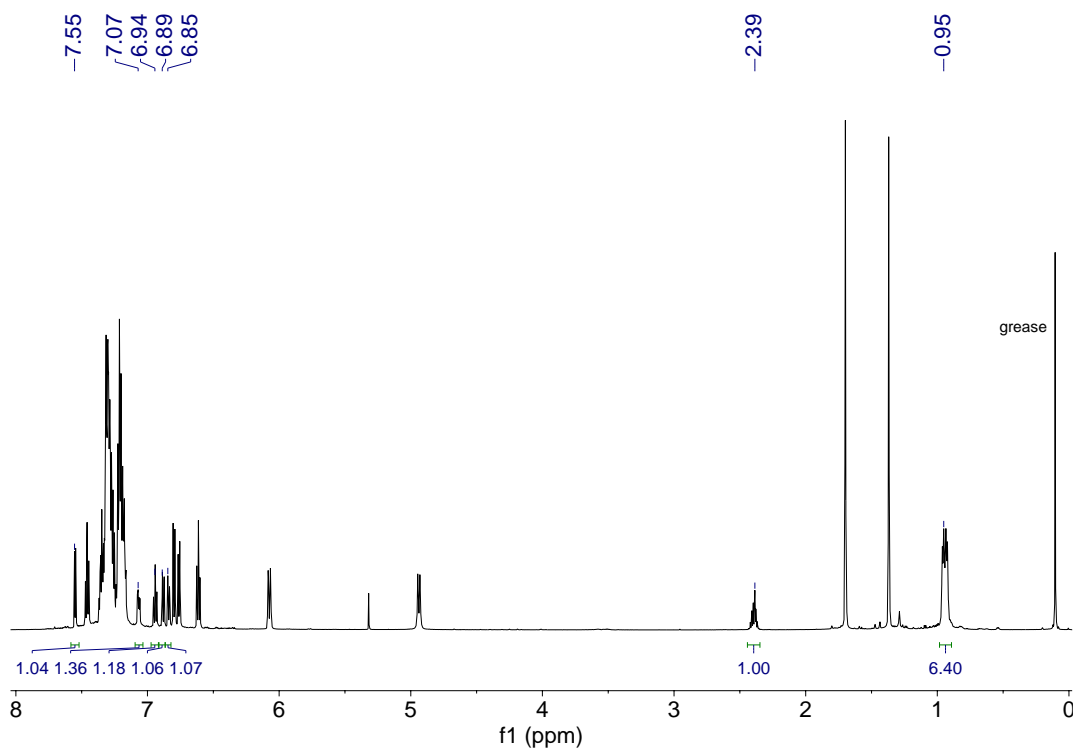
**Figure D.4.**  $^1\text{H}$  NMR spectrum of  $\text{Ph}_2\text{P-1-(C}_{10}\text{H}_6\text{)-8-N(3-Methyl-1-butene)}$ , **H(5-L5)** ( $\text{CDCl}_3$ , 600 MHz).



**Figure D.5.**  $^{13}\text{C}\{^1\text{H}\}$  NMR spectrum of  $\text{Ph}_2\text{P-1-(C}_{10}\text{H}_6\text{)-8-N(3-Methyl-1-butene)}$ , **H(5-L5)** ( $\text{CDCl}_3$ , 151 MHz).

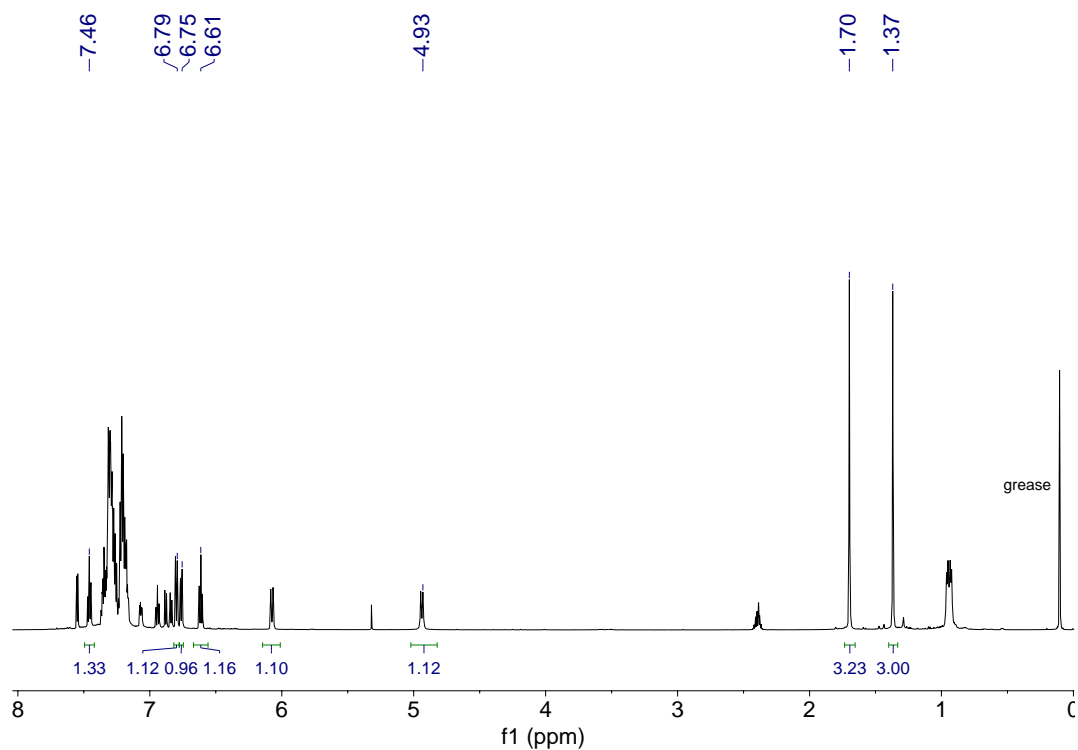


**Figure D.6.**  $^{31}\text{P}\{^1\text{H}\}$  NMR spectrum of  $\text{Ph}_2\text{P}-1-(\text{C}_{10}\text{H}_6)-8-\text{N}(3\text{-Methyl-1-butene})$ , **H(5-L5)** ( $\text{CDCl}_3$ , 243 MHz).

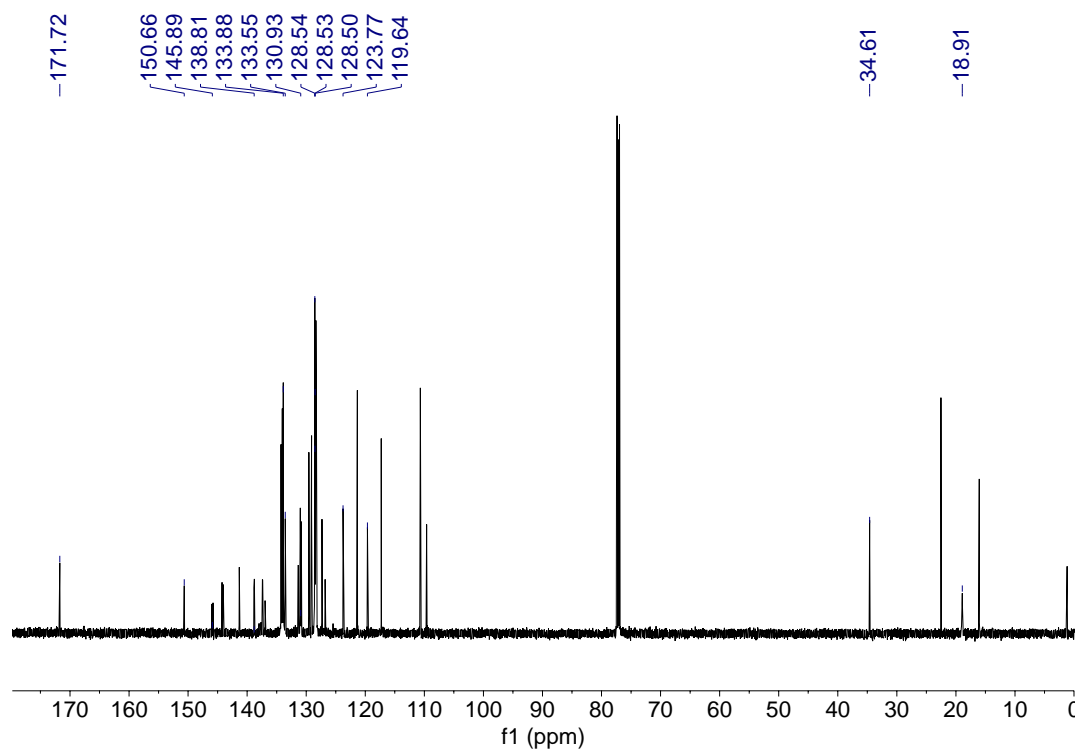


**Figure D.7.**  $^1\text{H}$  NMR spectrum of  $\text{Ph}_2\text{P}(o\text{-C}_6\text{H}_4)(o\text{-C}_6\text{H}_4)\text{N}(3\text{-Methyl-1-butene})$ , **H(5-L6b)** and  $\text{Ph}_2\text{P}(o\text{-C}_6\text{H}_4)(o\text{-C}_6\text{H}_4)\text{NH}(2\text{-Methyl-2-butene})$ , **H(5-L6c)**. Signals identified are for **H(5-L6b)**. ( $\text{CDCl}_3$ , 600 MHz).

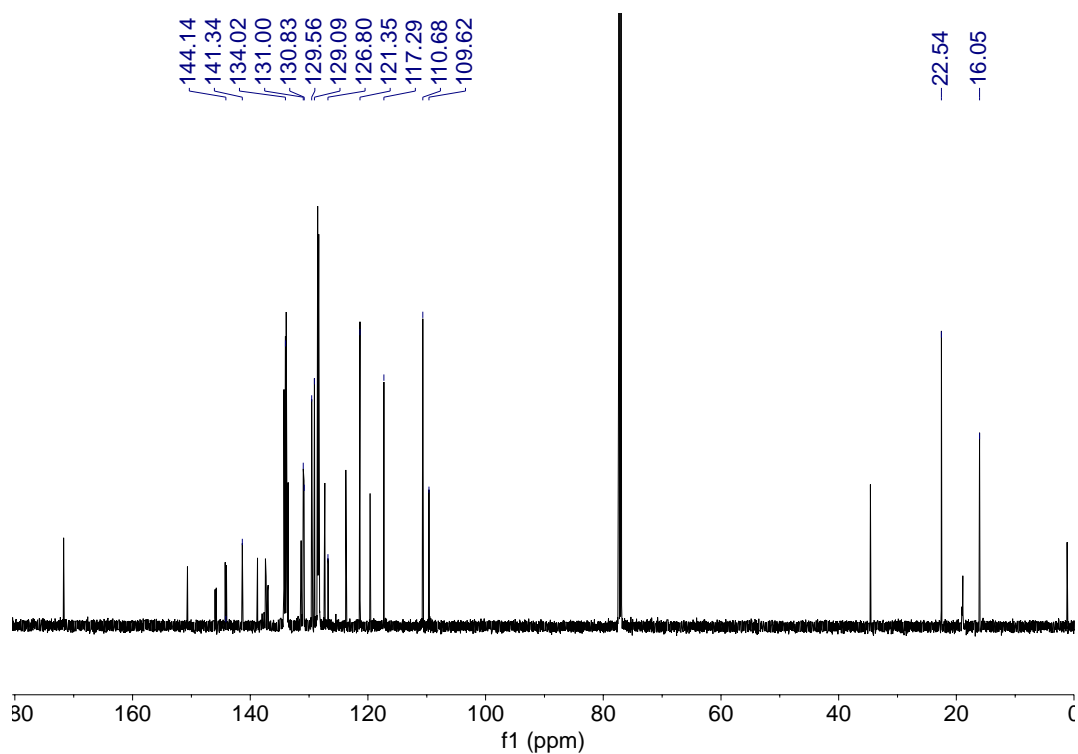




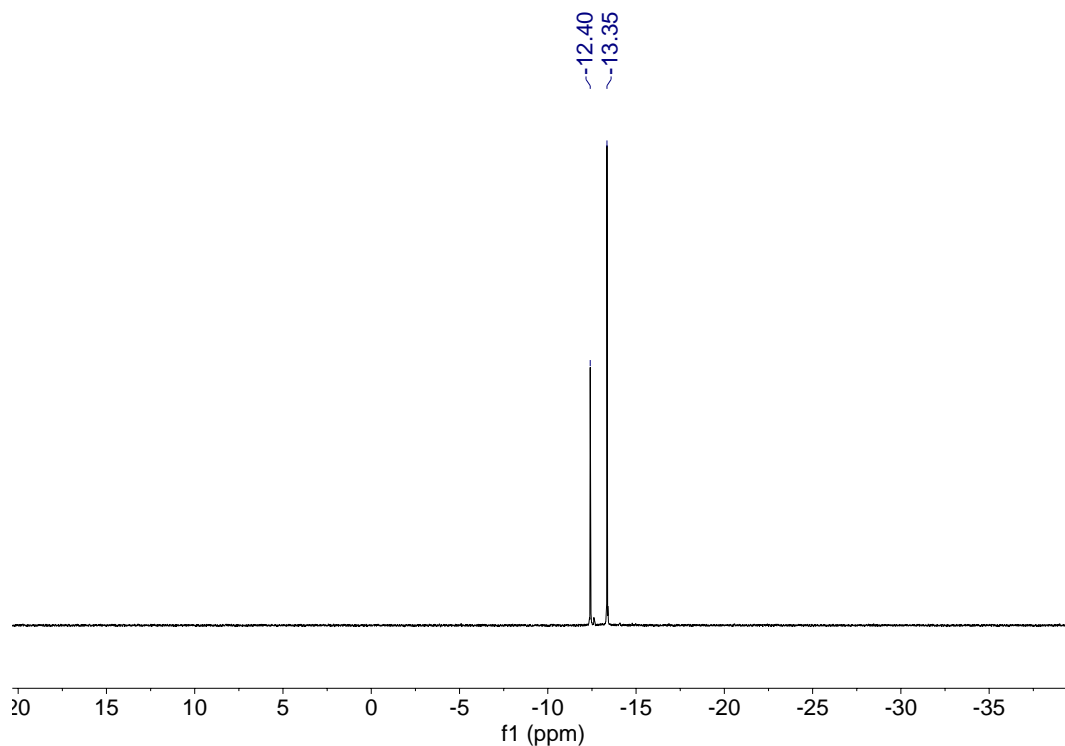
**Figure D.8.**  $^1\text{H}$  NMR spectrum of  $\text{Ph}_2\text{P}(o\text{-C}_6\text{H}_4)(o\text{-C}_6\text{H}_4)\text{N}(3\text{-Methyl-1-butene})$ , **H(5-L6b)** and  $\text{Ph}_2\text{P}(o\text{-C}_6\text{H}_4)(o\text{-C}_6\text{H}_4)\text{NH}(2\text{-Methyl-2-butene})$ , **H(5-L6c)**. Signals identified are for **H(5-L6c)**. ( $\text{CDCl}_3$ , 600 MHz).



**Figure D.9.**  $^{13}\text{C}\{^1\text{H}\}$  NMR spectrum of  $\text{Ph}_2\text{P}(o\text{-C}_6\text{H}_4)(o\text{-C}_6\text{H}_4)\text{N}(3\text{-Methyl-1-butene})$ , **H(5-L6b)**, and  $\text{Ph}_2\text{P}(o\text{-C}_6\text{H}_4)(o\text{-C}_6\text{H}_4)\text{NH}(2\text{-Methyl-2-butene})$ , **H(5-L6c)**. Signals identified are for **H(5-L6b)**. ( $\text{CDCl}_3$ , 151 MHz).

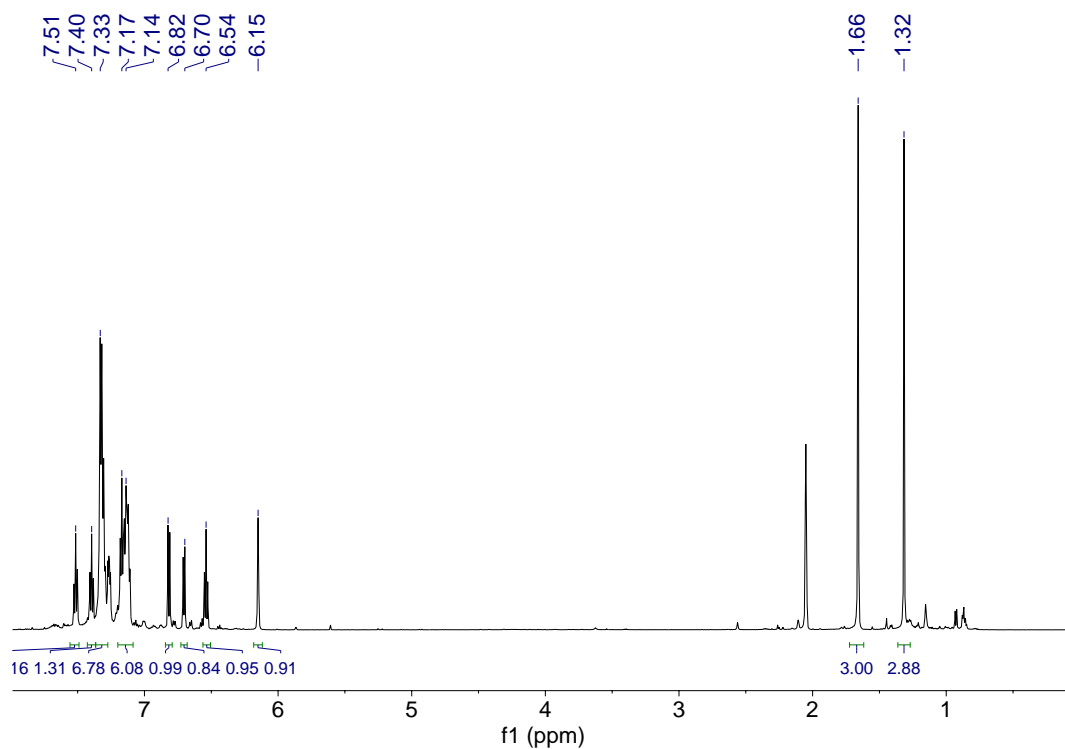


**Figure D.10.**  $^{13}\text{C}\{^1\text{H}\}$  NMR spectrum of  $\text{Ph}_2\text{P}(o\text{-C}_6\text{H}_4)(o\text{-C}_6\text{H}_4)\text{N}(3\text{-Methyl-1-butene})$ , **H(5-L6b)** and  $\text{Ph}_2\text{P}(o\text{-C}_6\text{H}_4)(o\text{-C}_6\text{H}_4)\text{NH}(2\text{-Methyl-2-butene})$ , **H(5-L6c)**. Signals identified are for **H(5-L6c)** ( $\text{CDCl}_3$ , 151 MHz).

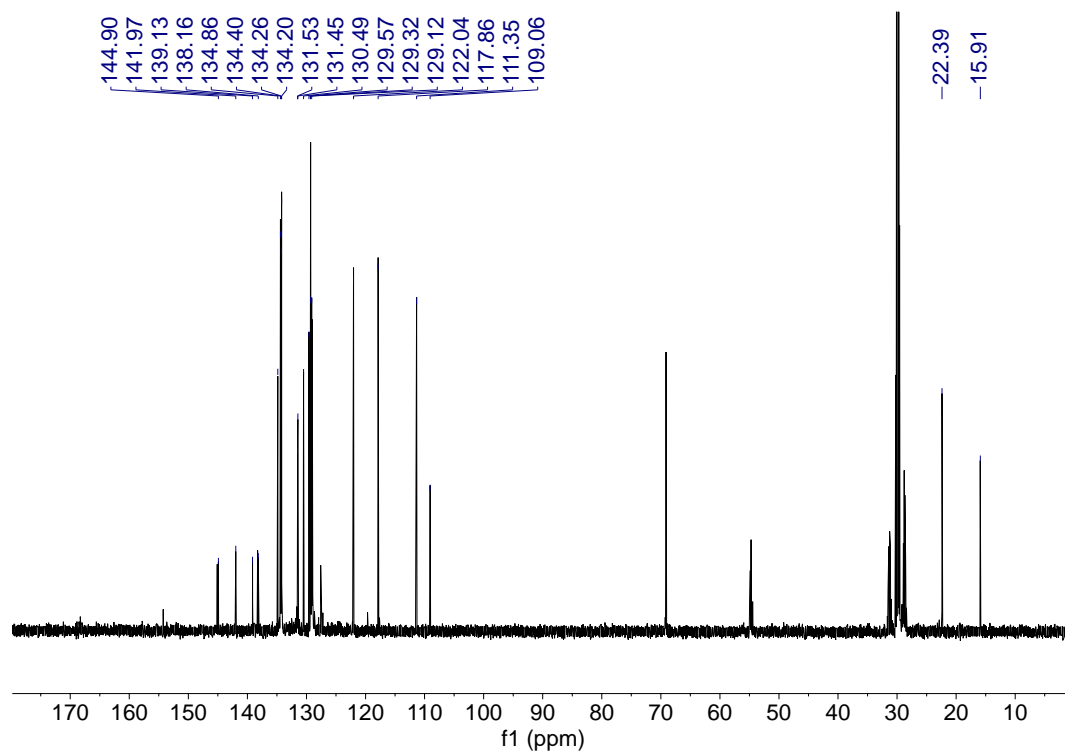


**Figure D.11.**  $^{31}\text{P}\{^1\text{H}\}$  NMR spectrum of  $\text{Ph}_2\text{P}(o\text{-C}_6\text{H}_4)(o\text{-C}_6\text{H}_4)\text{N}(3\text{-Methyl-1-butene})$ , **H(5-L6b)** and  $\text{Ph}_2\text{P}(o\text{-C}_6\text{H}_4)(o\text{-C}_6\text{H}_4)\text{NH}(2\text{-Methyl-2-butene})$ , **H(5-L6c)** ( $\text{CDCl}_3$ , 243 MHz).

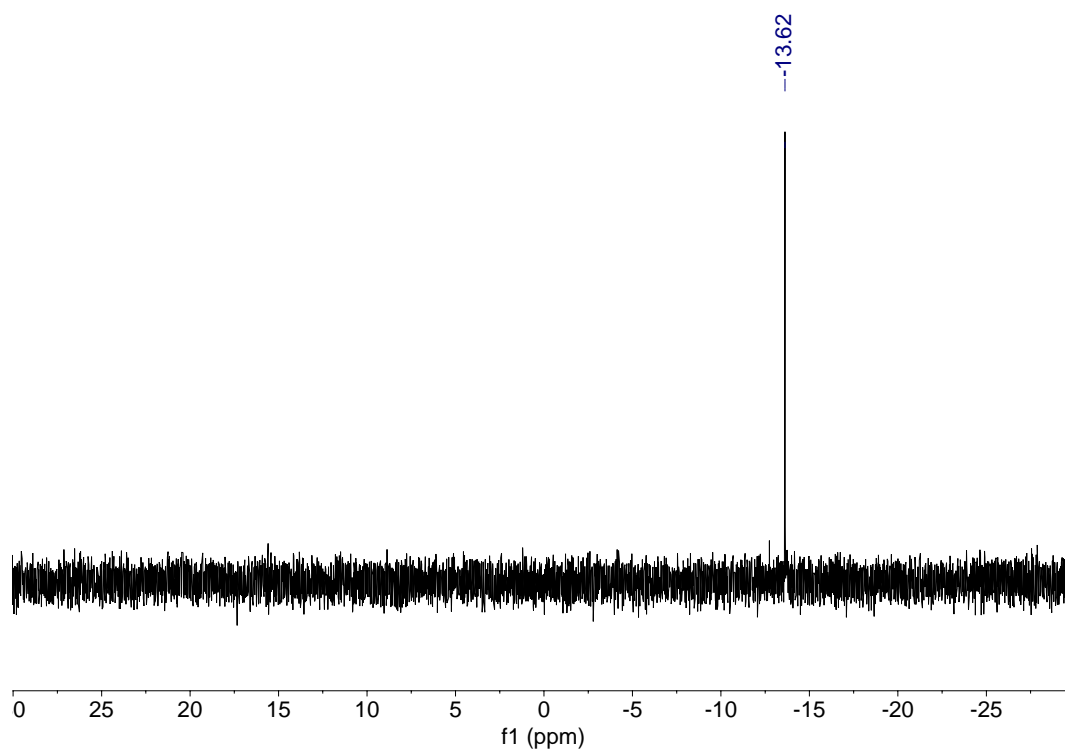
## I.II P<sup>AzA</sup> Ligand Salt NMR Spectra



**Figure D.12.** <sup>1</sup>H NMR spectrum of [Ph<sub>2</sub>P(*o*-C<sub>6</sub>H<sub>4</sub>)(*o*-C<sub>6</sub>H<sub>4</sub>)N(2-Methyl-2-butene)]K, **K(5-L6)** ((CD<sub>3</sub>)<sub>2</sub>CO, 600 MHz).

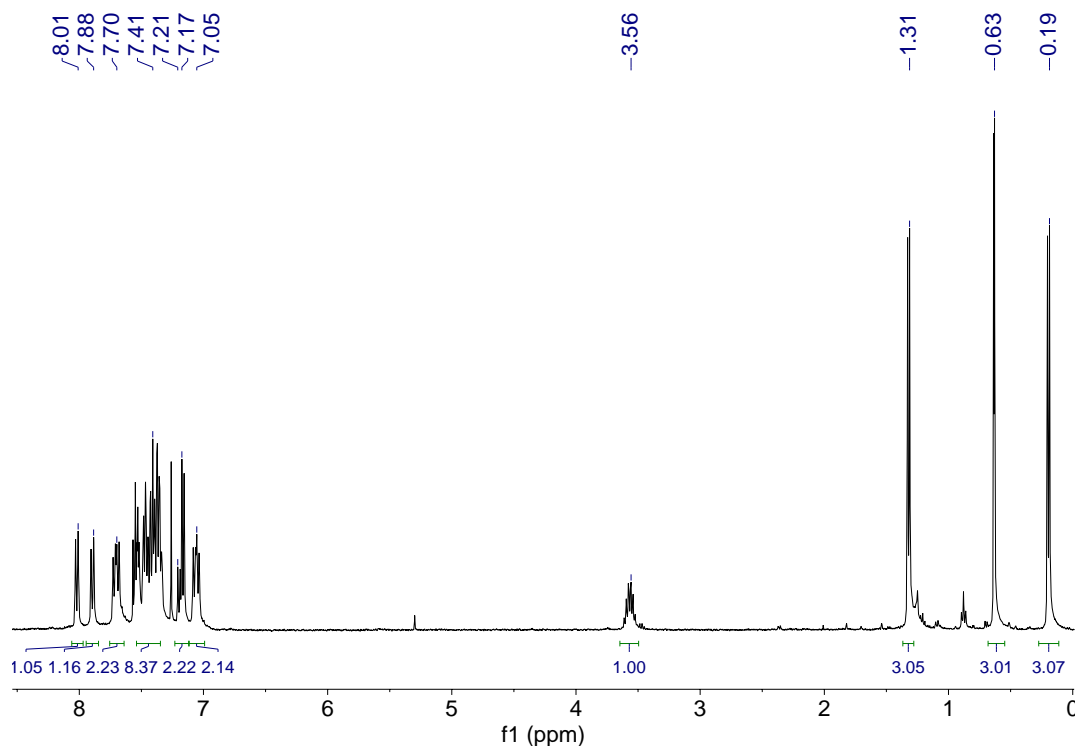


**Figure D.13.** <sup>13</sup>C{<sup>1</sup>H} NMR spectrum of [Ph<sub>2</sub>P(*o*-C<sub>6</sub>H<sub>4</sub>)(*o*-C<sub>6</sub>H<sub>4</sub>)N(2-Methyl-2-butene)]K, **K(5-L6)** ((CD<sub>3</sub>)<sub>2</sub>CO, 151 MHz).

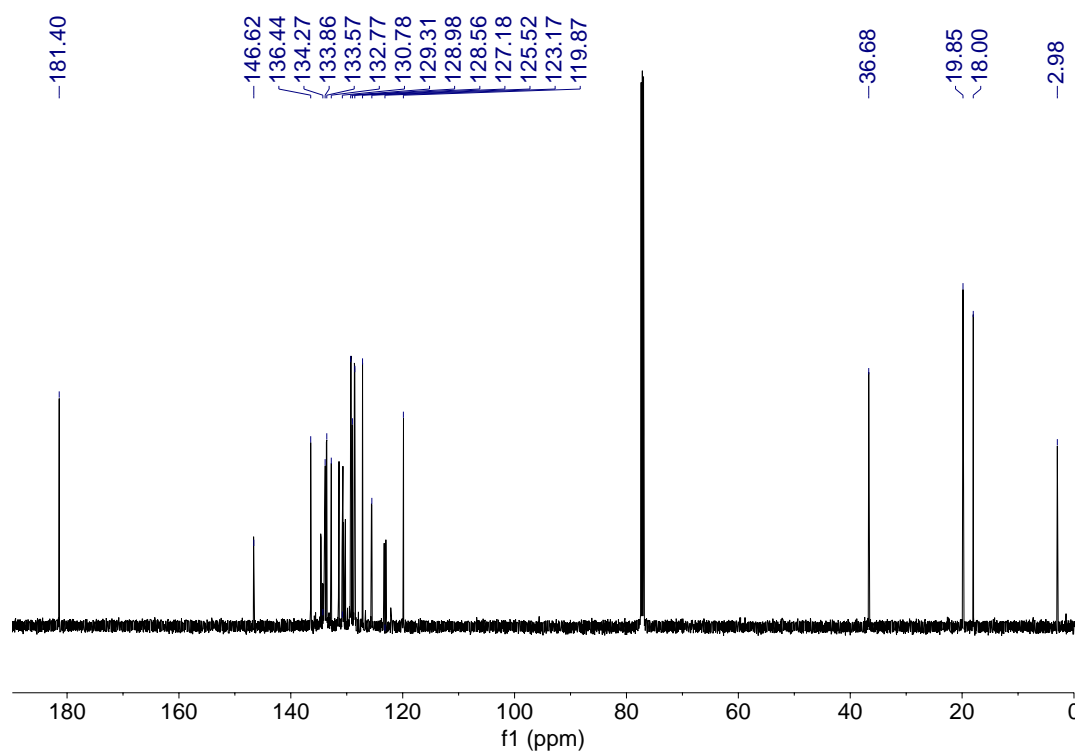


**Figure D.14.**  $^{31}\text{P}\{^1\text{H}\}$  NMR spectrum of  $[\text{Ph}_2\text{P}(o\text{-C}_6\text{H}_4)(o\text{-C}_6\text{H}_4)\text{N}(2\text{-Methyl-2-butene})]\text{K}$ , **K(5-L6)** ( $(\text{CD}_3)_2\text{CO}$ , 243 MHz).

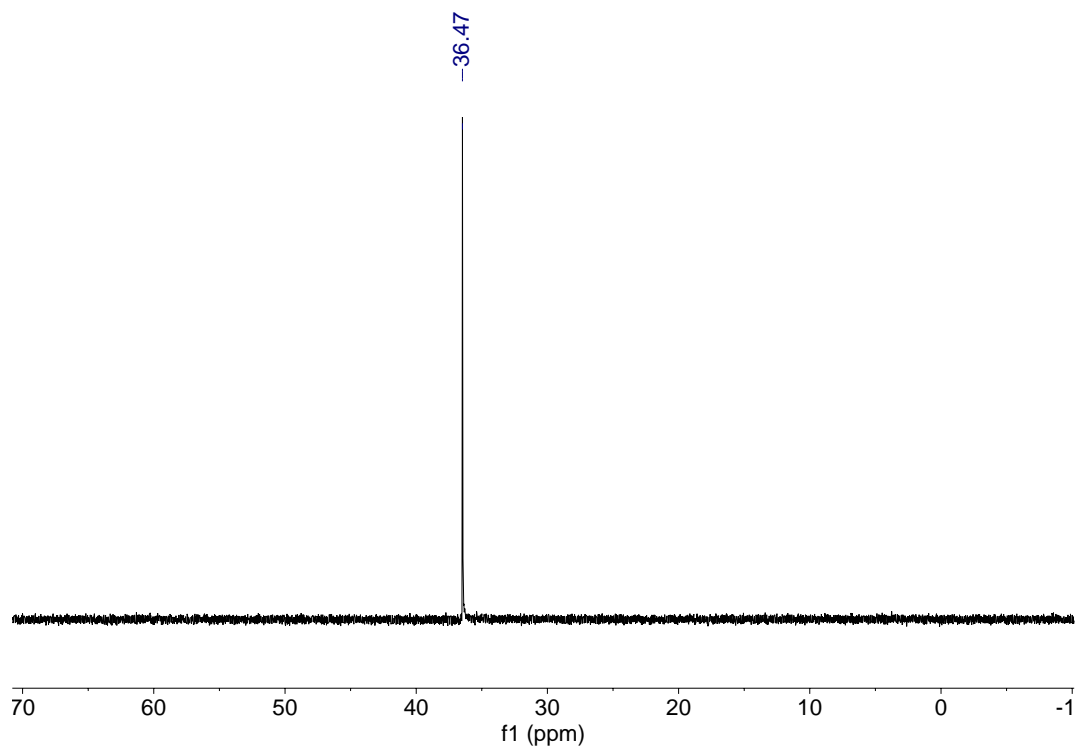
### I.III Palladium-Phosphine-Imine Complex NMR Spectra



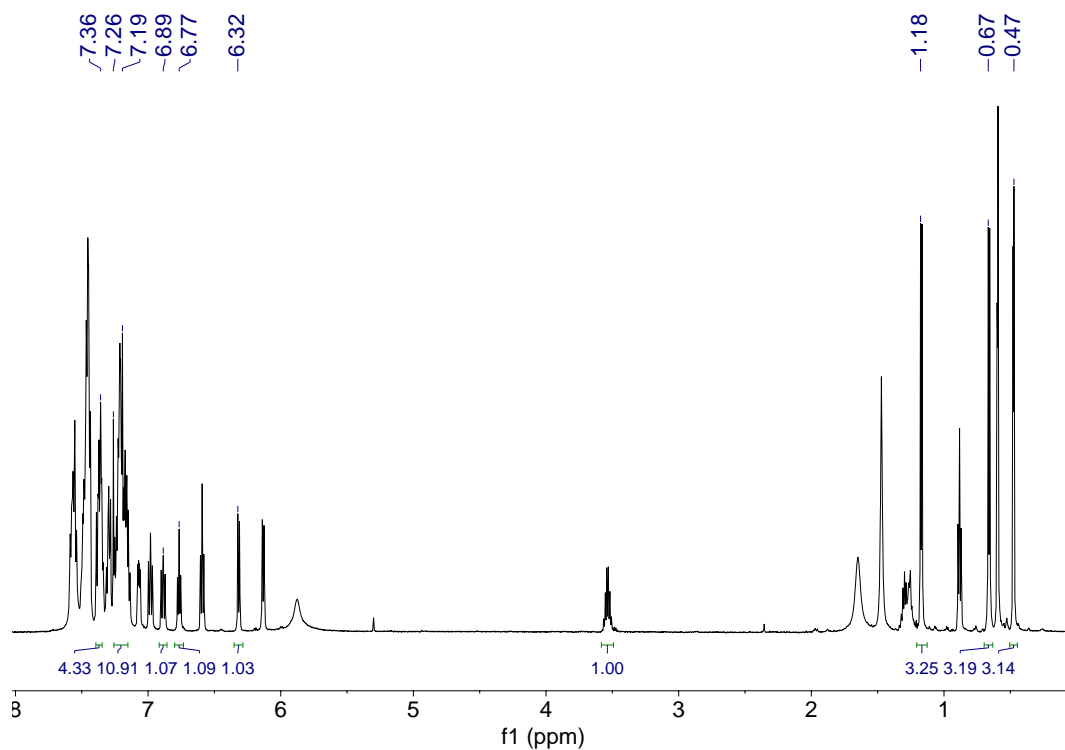
**Figure D.15.**  $^1\text{H}$  NMR spectrum of  $[\text{PdCl}(\text{CH}_3)(\text{H}(5\text{-L5}))]$ , **5-4** ( $\text{CDCl}_3$ , 600 MHz).



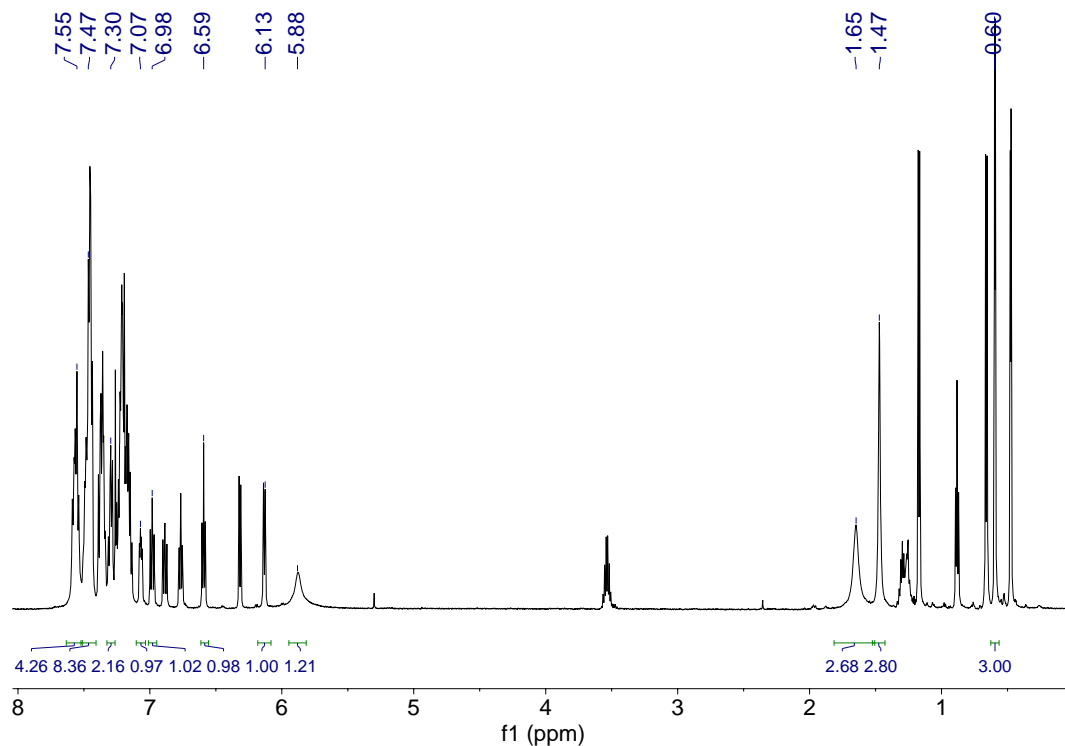
**Figure D.16.**  $^{31}\text{P}\{^1\text{H}\}$  NMR spectrum of  $[\text{PdCl}(\text{CH}_3)(\text{H}(\mathbf{5-L5}))]$ , **5-4** ( $\text{CDCl}_3$ , 151 MHz).



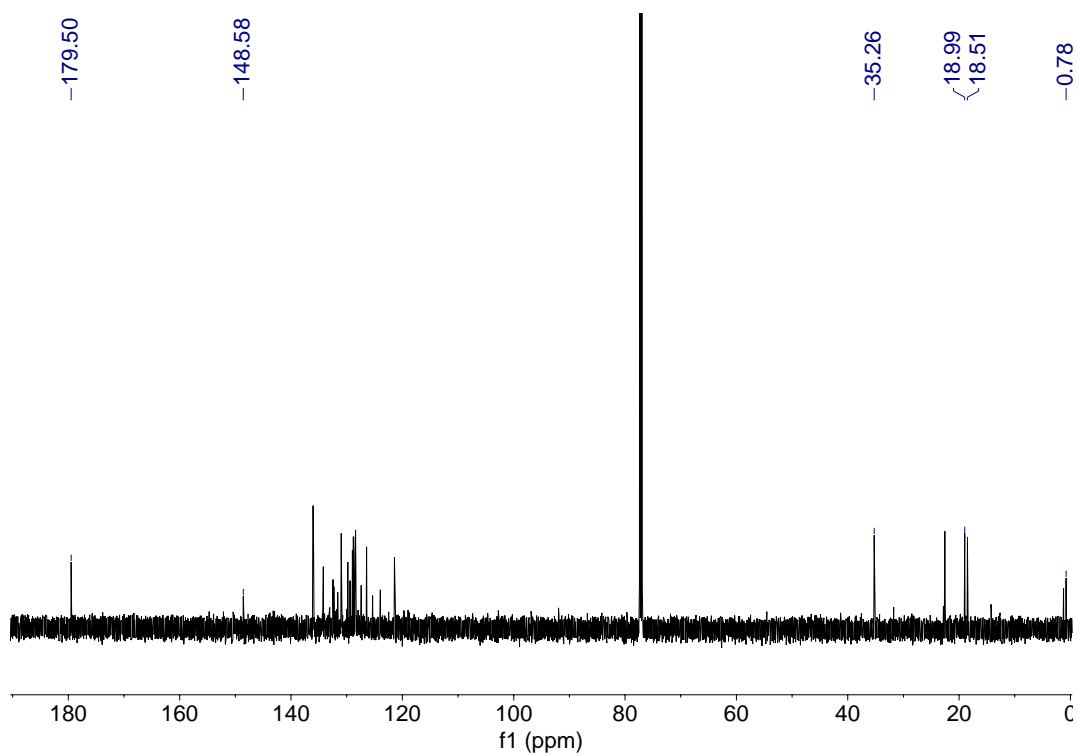
**Figure D.17.**  $^{31}\text{P}\{^1\text{H}\}$  NMR spectrum of  $[\text{PdCl}(\text{CH}_3)(\text{H}(\mathbf{5-L5}))]$ , **5-4** ( $\text{CDCl}_3$ , 243 MHz).



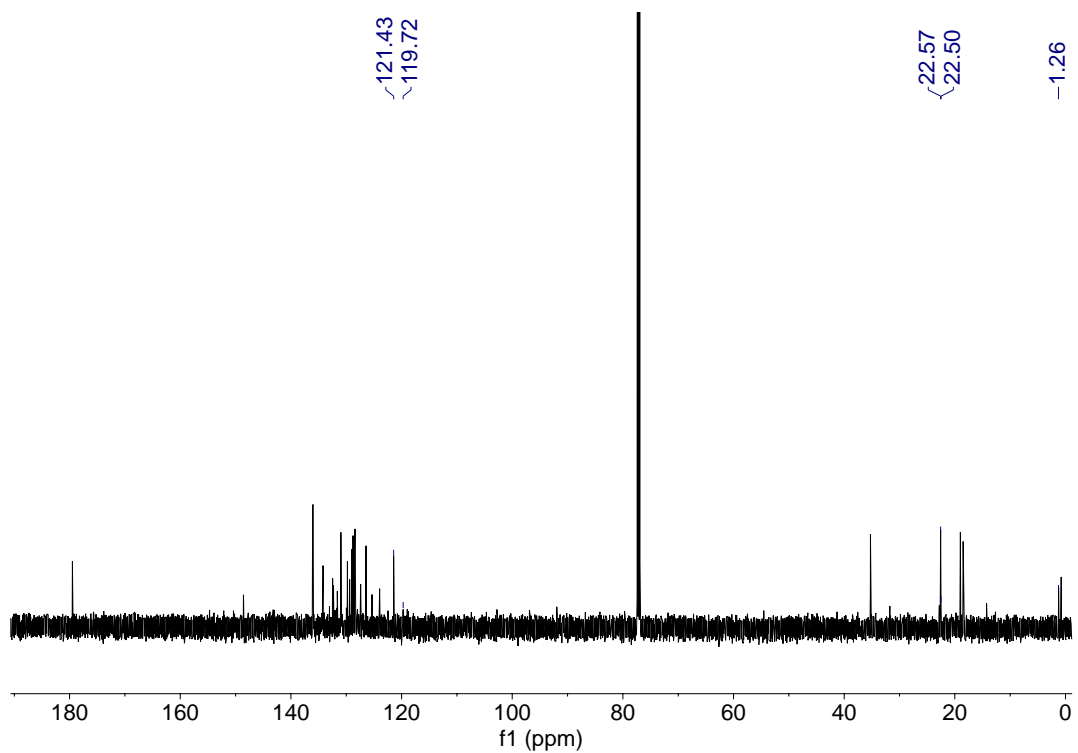
**Figure D.18.**  $^1\text{H}$  NMR spectrum of  $[\text{PdCl}(\text{CH}_3)(\text{H}(\mathbf{5-L6b}))]$ , **5-5a**, and  $[\text{PdCl}(\text{CH}_3)(\text{H}(\mathbf{5-Lbc}))]$ , **5-5b**. Signals shown are for **5-5a**. ( $\text{CDCl}_3$ , 600 MHz).



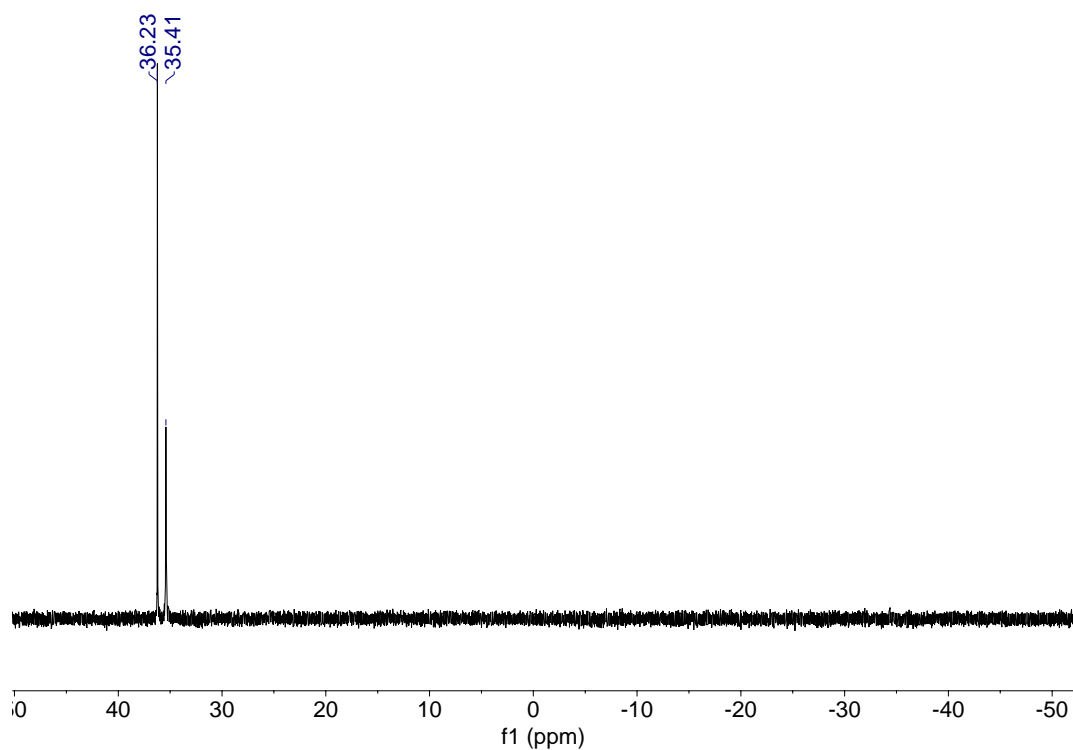
**Figure D.19.**  $^1\text{H}$  NMR spectrum of  $[\text{PdCl}(\text{CH}_3)(\text{H}(\mathbf{5-L6b}))]$ , **5-5a**, and  $[\text{PdCl}(\text{CH}_3)(\text{H}(\mathbf{5-Lbc}))]$ , **5-5b**. Signals shown are for **5-5b**. ( $\text{CDCl}_3$ , 600 MHz).



**Figure D.20.**  $^{13}\text{C}\{^1\text{H}\}$  NMR spectrum of  $[\text{PdCl}(\text{CH}_3)(\text{H}(\mathbf{5-L6b}))]$ ,  $\mathbf{5-5a}$ , and  $[\text{PdCl}(\text{CH}_3)(\text{H}(\mathbf{5-Lbc}))]$ ,  $\mathbf{5-5b}$ . Signals shown are for  $\mathbf{5-5a}$  ( $\text{CDCl}_3$ , 151 MHz).

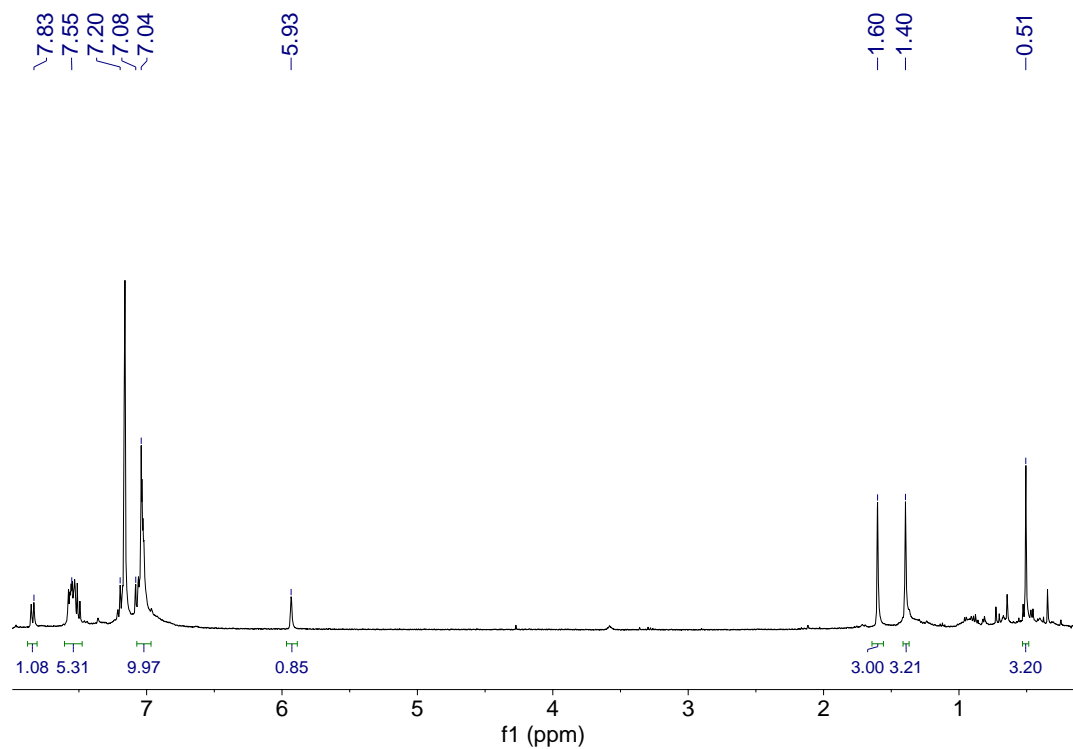


**Figure D.21.**  $^{13}\text{C}\{^1\text{H}\}$  NMR spectrum of  $[\text{PdCl}(\text{CH}_3)(\text{H}(\mathbf{5-L6b}))]$ ,  $\mathbf{5-5a}$ , and  $[\text{PdCl}(\text{CH}_3)(\text{H}(\mathbf{5-Lbc}))]$ ,  $\mathbf{5-5b}$ . Signals shown are for  $\mathbf{5-5b}$  ( $\text{CDCl}_3$ , 151 MHz).



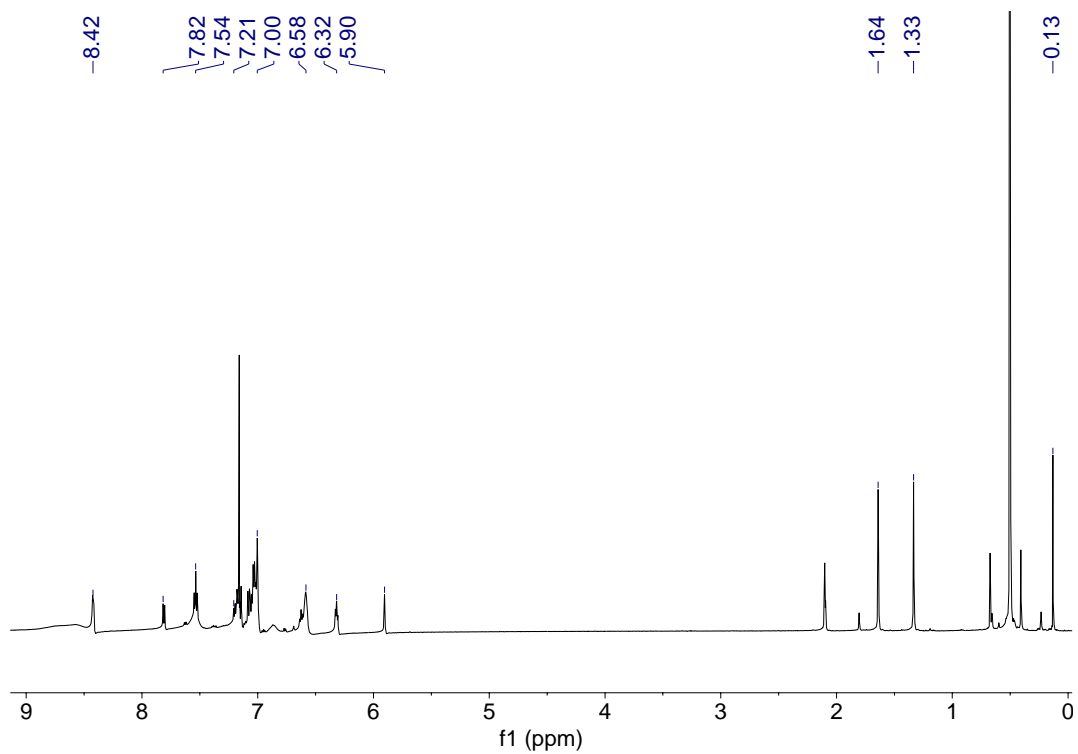
**Figure D.22.**  $^{31}\text{P}\{^1\text{H}\}$  NMR spectrum of  $[\text{PdCl}(\text{CH}_3)(\text{H}(\mathbf{5-L6b}))]$ , **5-5a** and  $[\text{PdCl}(\text{CH}_3)(\text{H}(\mathbf{5-L6c}))]$ , **5-5b** ( $\text{CDCl}_3$ , 243 MHz).

### I.IV Palladium-P<sup>AzA</sup> Complex NMR Spectra

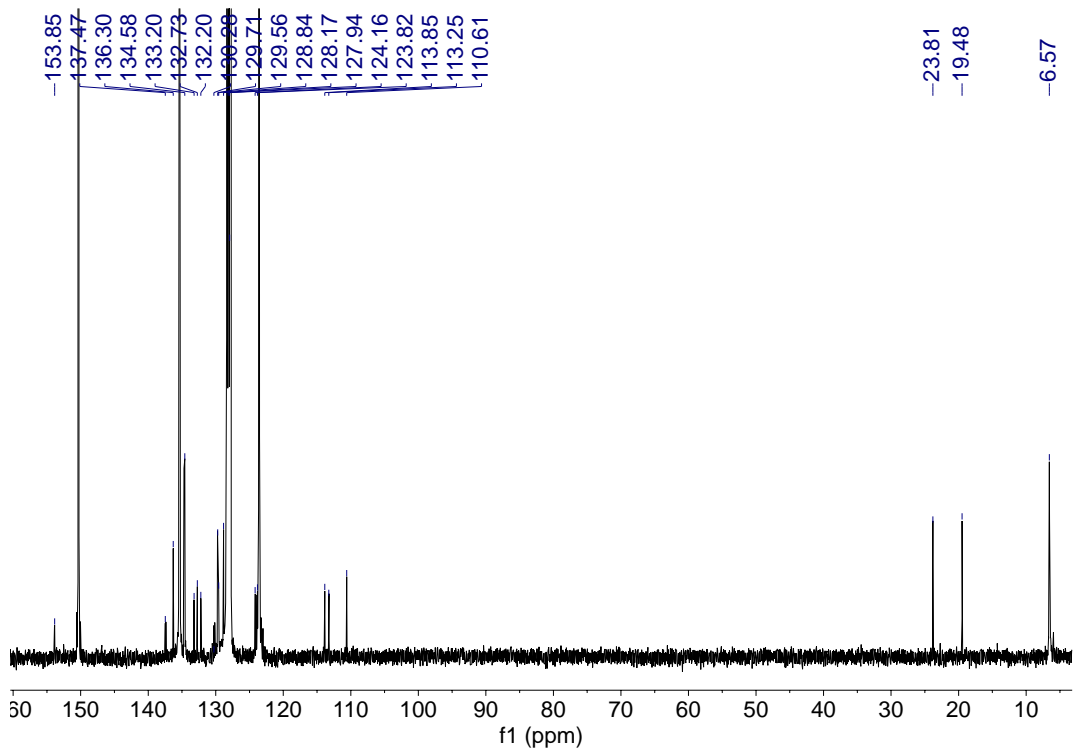


**Figure D.23.**  $^1\text{H}$  NMR spectrum of  $[\text{Pd}(\text{CH}_3)(\mathbf{5-L5})(\text{py-}d_5)]$ , **5-6** ( $\text{C}_6\text{D}_6$ , 600 MHz, 298 K).

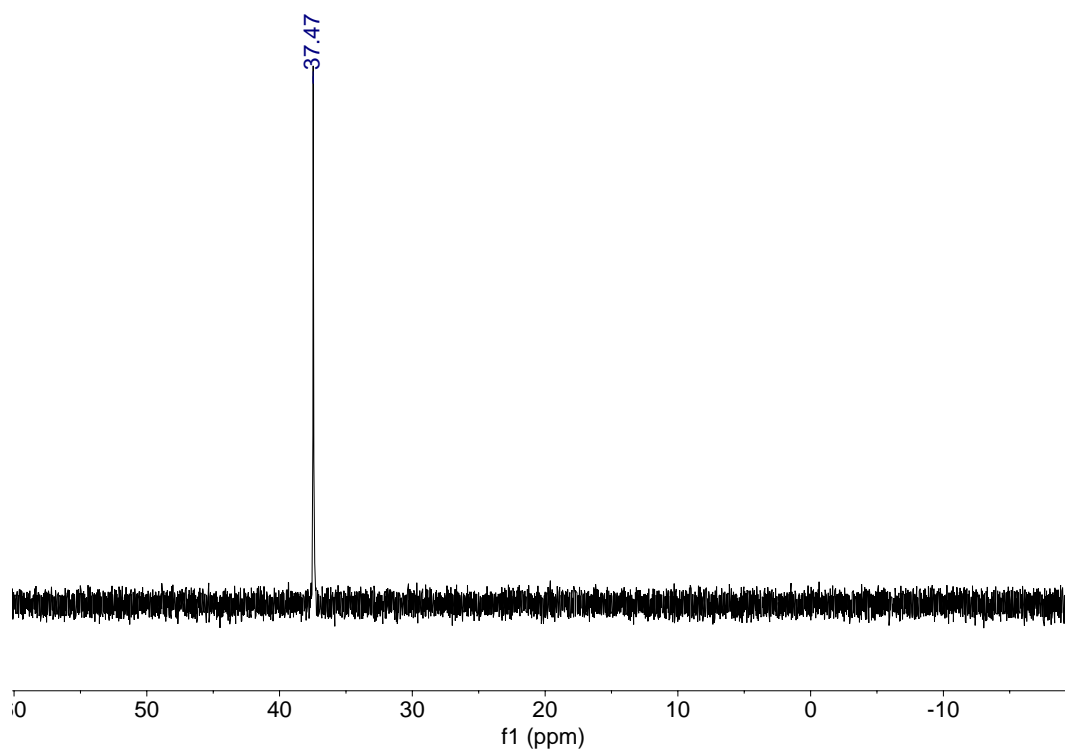




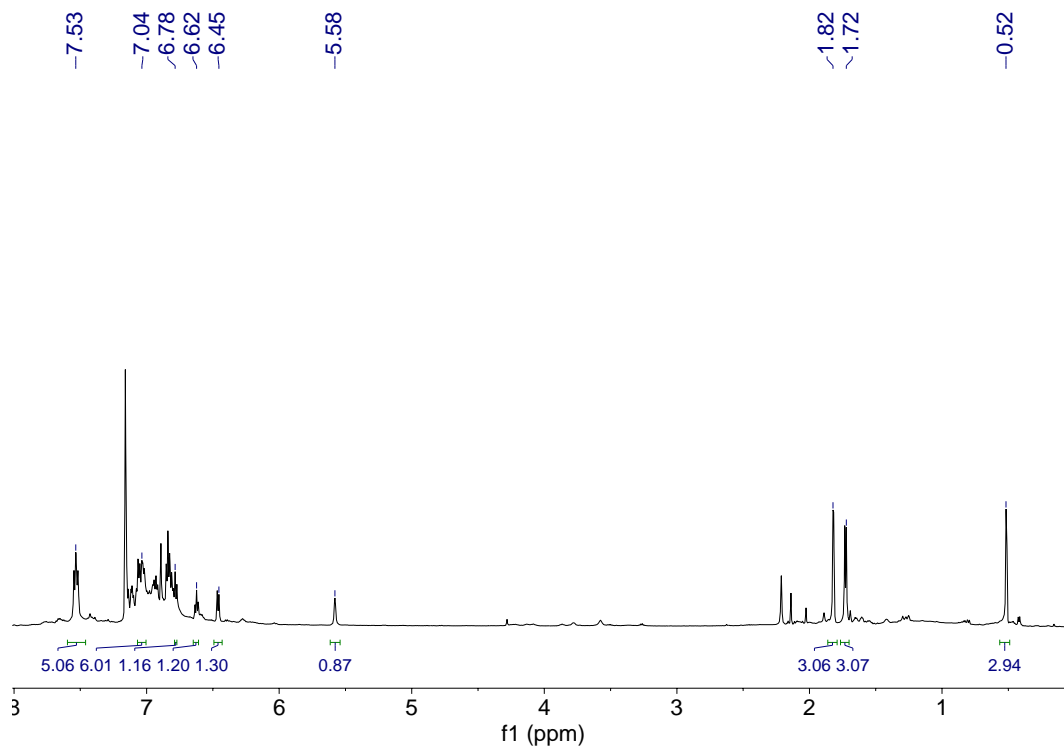
**Figure D.24.**  $^1\text{H}$  NMR spectrum of  $[\text{Pd}(\text{CH}_3)(\mathbf{5-L5})(\text{py})]$ , **5-6** ( $\text{C}_6\text{D}_5(\text{CD}_3)$ , 600 MHz, 243 K).



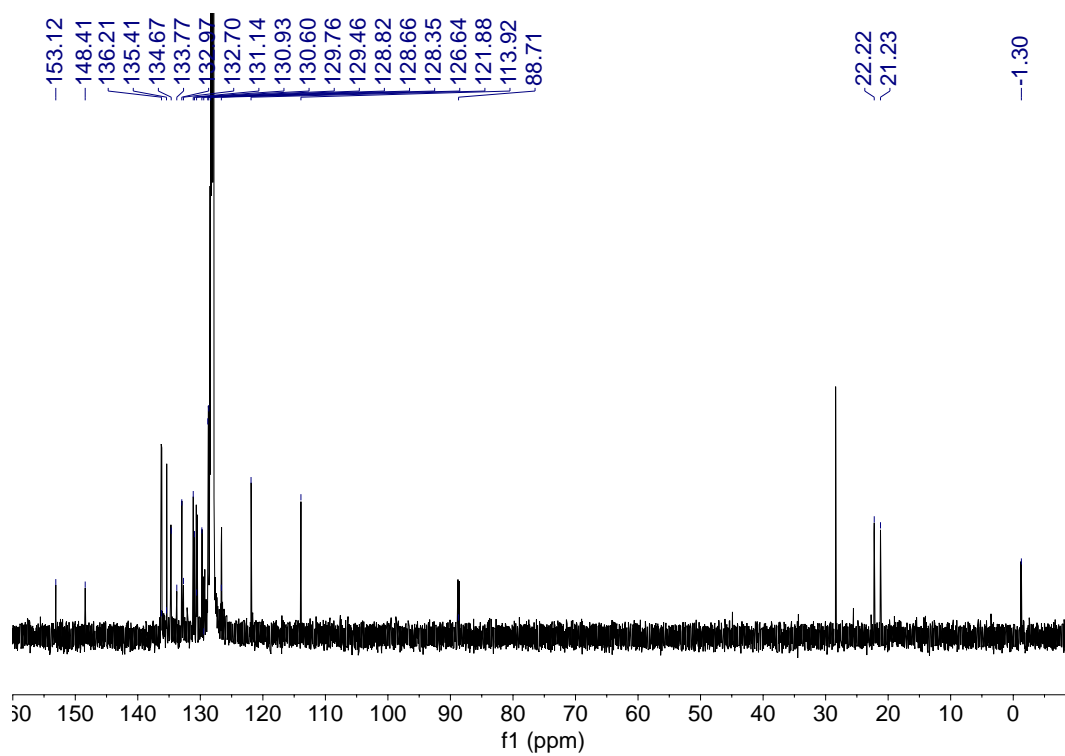
**Figure D.25.**  $^{13}\text{C}\{^1\text{H}\}$  NMR spectrum of  $[\text{Pd}(\text{CH}_3)(\mathbf{5-L5})(\text{py})]$ , **5-6** ( $\text{C}_6\text{D}_6$ , 151 MHz).



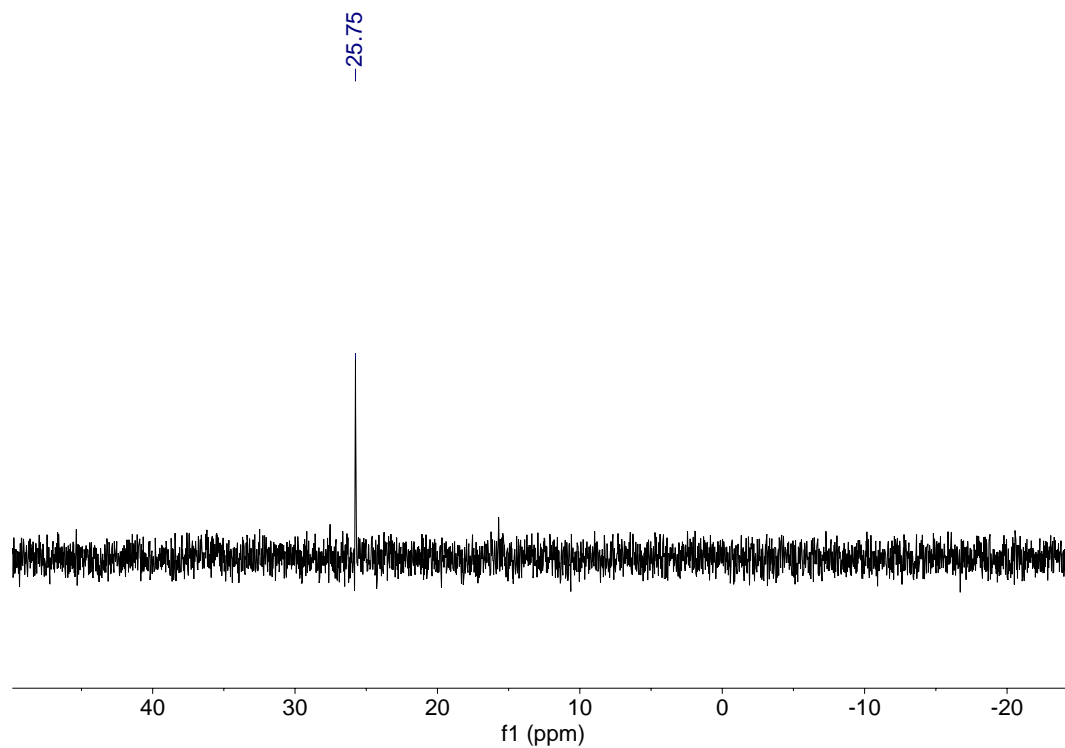
**Figure D.26.**  $^{31}\text{P}\{^1\text{H}\}$  NMR spectrum of  $[\text{Pd}(\text{CH}_3)(\mathbf{5-L5})(\text{py})]$ , **5-6** ( $\text{C}_6\text{D}_6$ , 243 MHz).



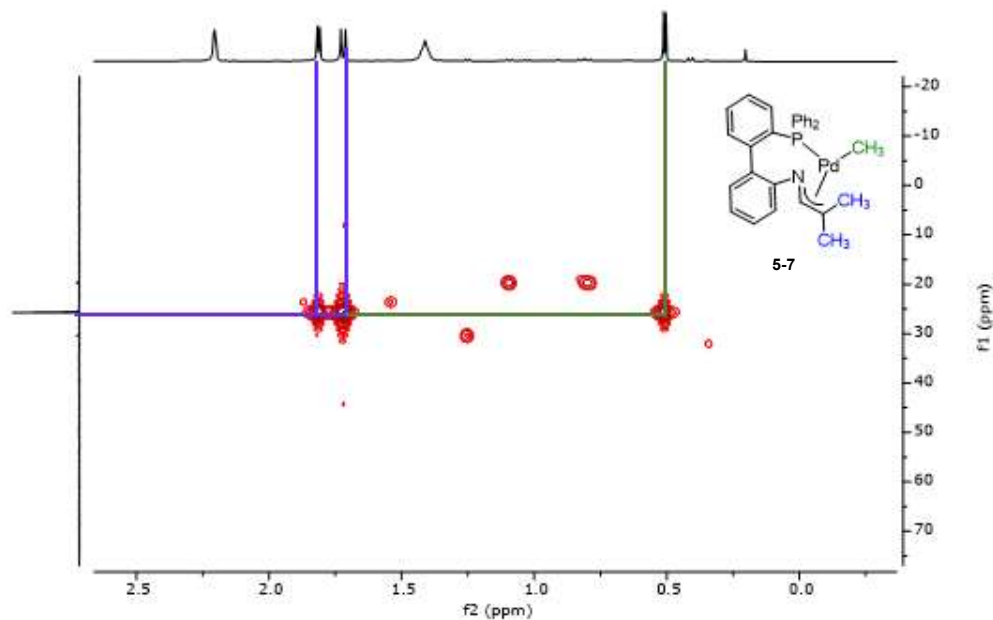
**Figure D.27.**  $^{31}\text{P}\{^1\text{H}\}$  NMR spectrum of  $[\text{Pd}(\text{CH}_3)(\mathbf{5-L6})]$ , **5-7** ( $\text{C}_6\text{D}_6$ , 243 MHz).



**Figure D.28.**  $^{31}\text{P}\{^1\text{H}\}$  NMR spectrum of  $[\text{Pd}(\text{CH}_3)(\mathbf{5-L6})]$ , **5-7** ( $\text{C}_6\text{D}_6$ , 243 MHz).

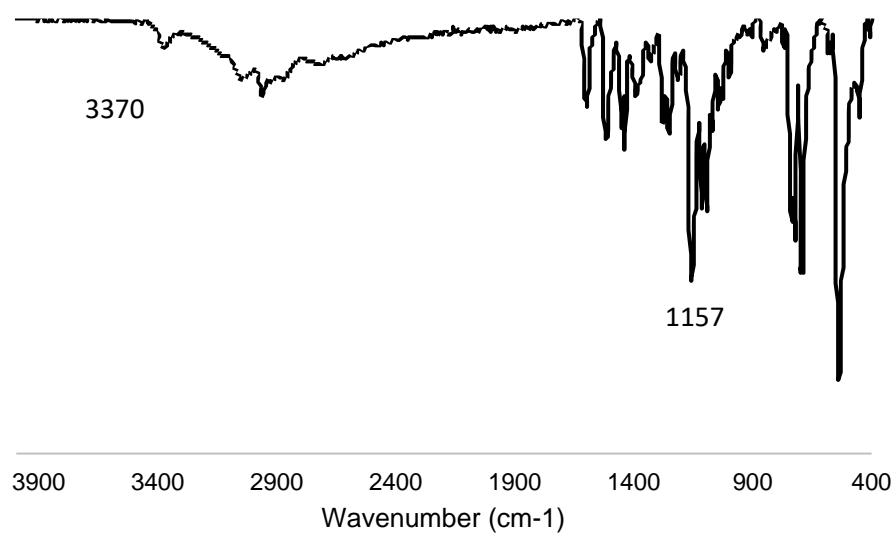


**Figure D.29.**  $^{31}\text{P}\{^1\text{H}\}$  NMR spectrum of  $[\text{Pd}(\text{CH}_3)(\mathbf{5-L6})]$ , **5-7** ( $\text{C}_6\text{D}_6$ , 243 MHz).

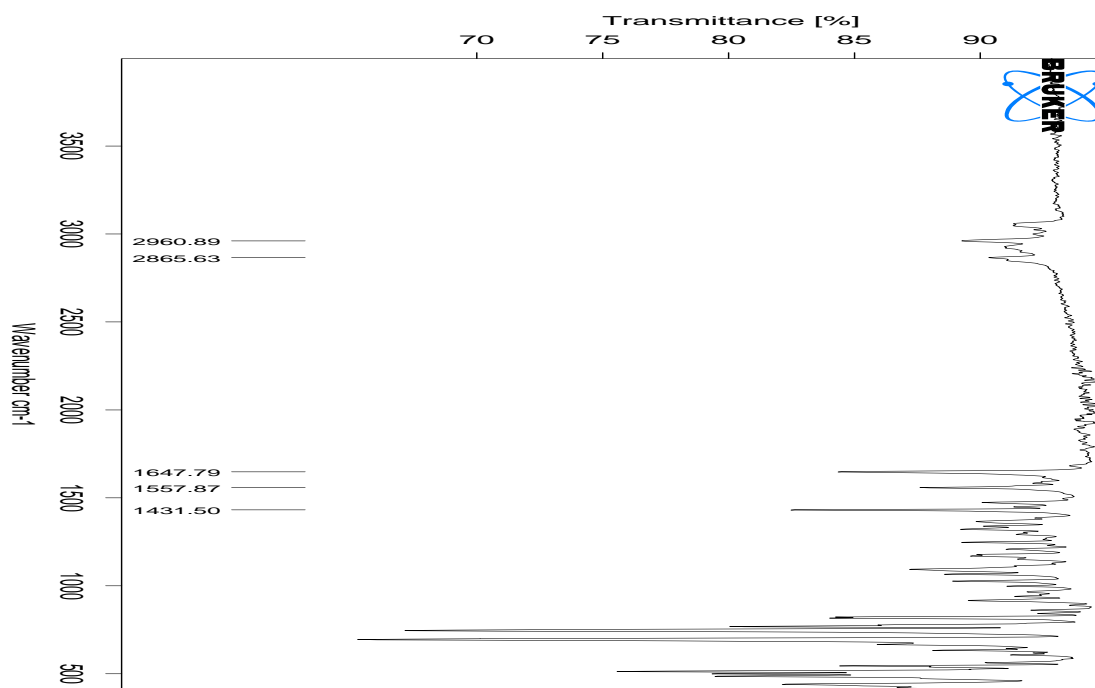


**Figure D.30.**  $^1\text{H}$ - $^{31}\text{P}$  HMBC spectrum of  $[\text{Pd}(\text{CH}_3)(\mathbf{5-L6})]$ , **5-7** ( $\text{C}_6\text{D}_6$ , 600 MHz).

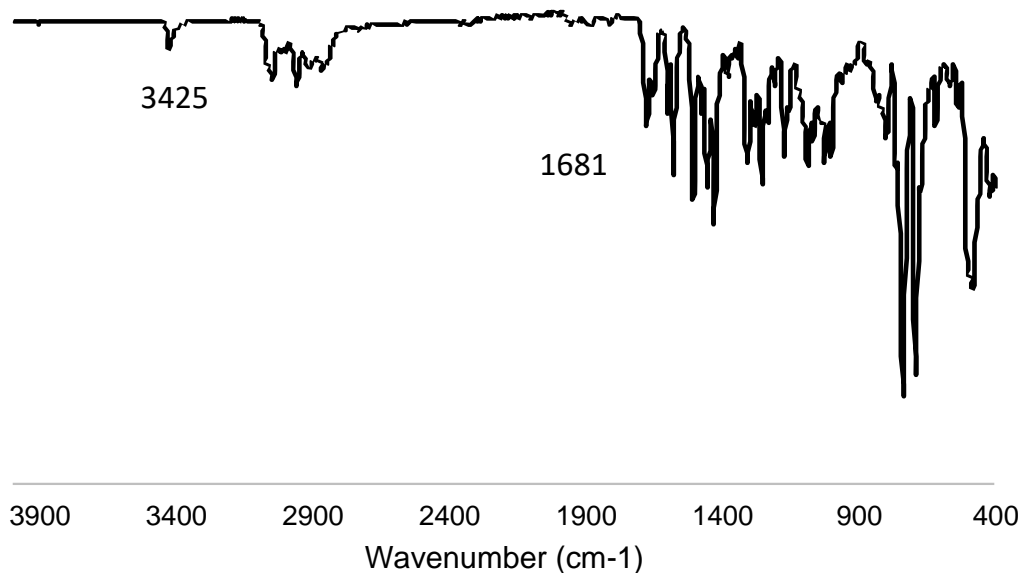
## II IR Spectra



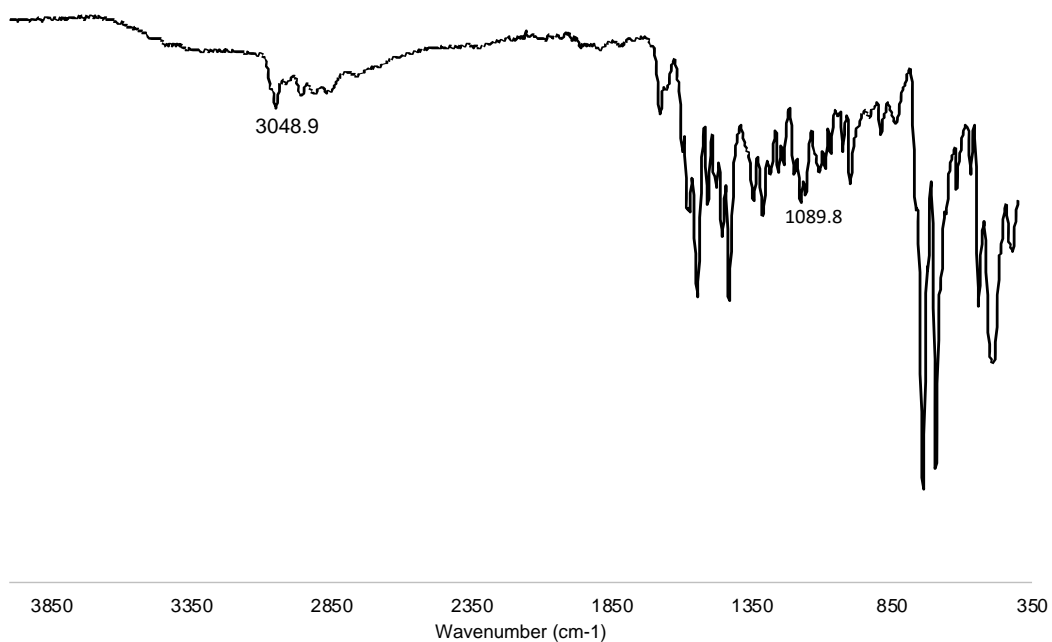
**Figure D.31.** ATR-FTIR of solid  $\text{HO}(o\text{-C}_6\text{H}_4)\text{NH}(\text{Ph}_2\text{P}=\text{O})(i\text{-Bu})$ , **5-L4b**. Data acquired using Bruker Alpha II ATR-FTIR and plotted using Microsoft Excel.



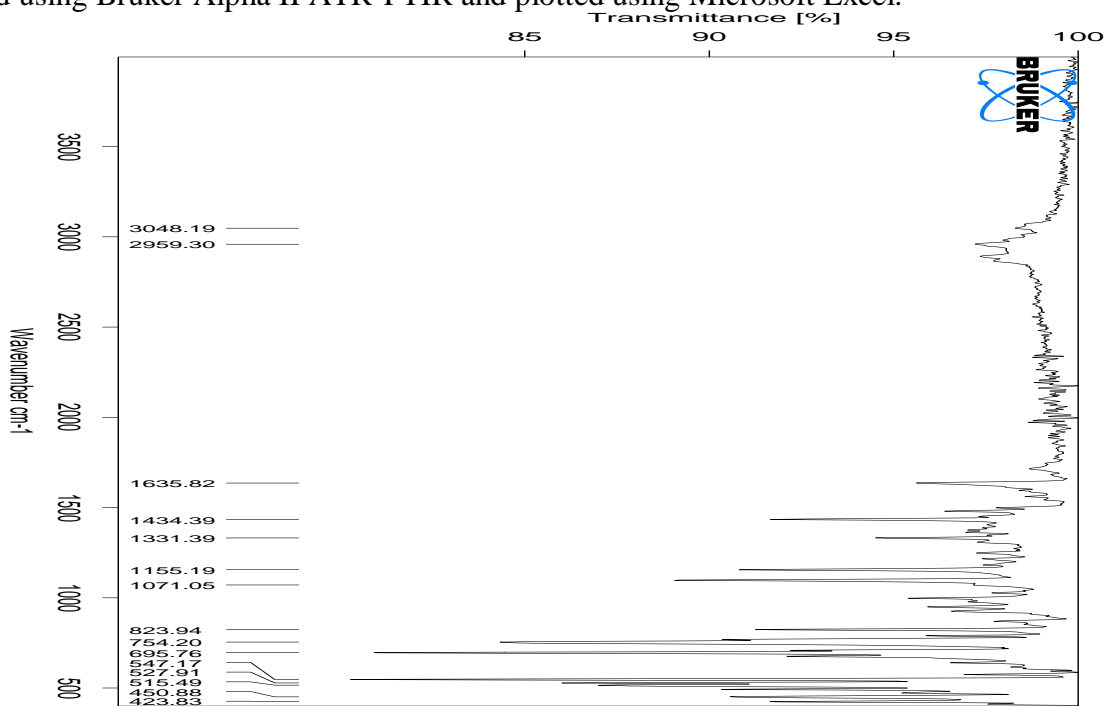
**Figure D.32.** ATR-FTIR of solid  $\text{Ph}_2\text{P-1-(C}_{10}\text{H}_6\text{)-8-N(3-Methyl-1-butene)}$ , **H(5-L5)**. Data acquired using Bruker Alpha II ATR-FTIR and plotted using Opus software.



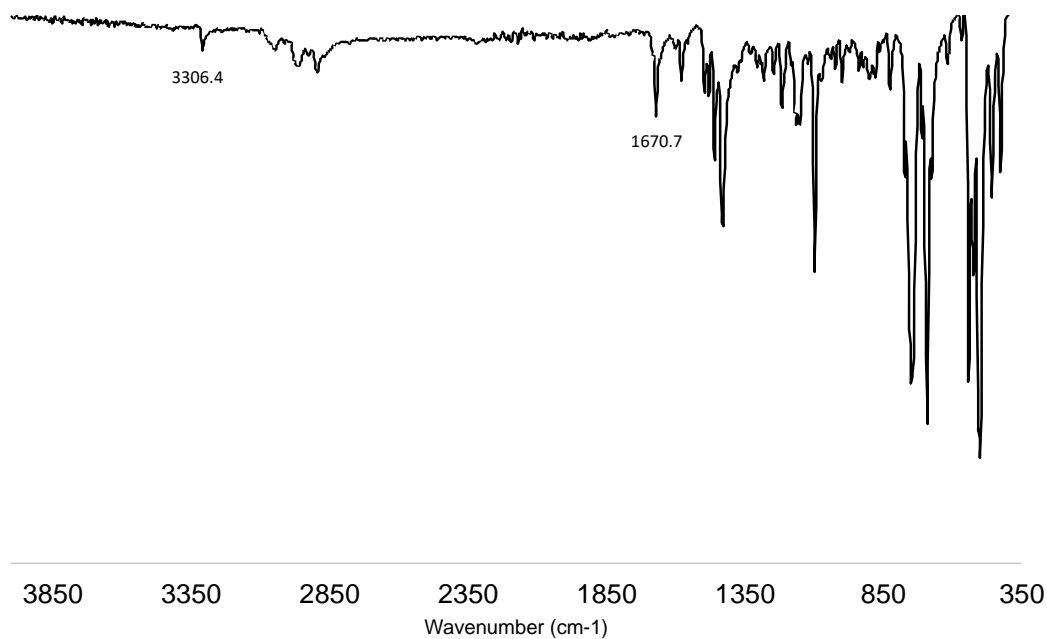
**Figure D.33.** ATR-FTIR of solid  $\text{Ph}_2\text{P}(o\text{-C}_6\text{H}_4)(o\text{-C}_6\text{H}_4)\text{N(3-Methyl-1-butene)}$ , **H(5-L6b)** and  $\text{Ph}_2\text{P}(o\text{-C}_6\text{H}_4)(o\text{-C}_6\text{H}_4)\text{NH(2-Methyl-2-butene)}$ , **H(5-L6c)**. Data acquired using Bruker Alpha II ATR-FTIR and plotted using Microsoft Excel.



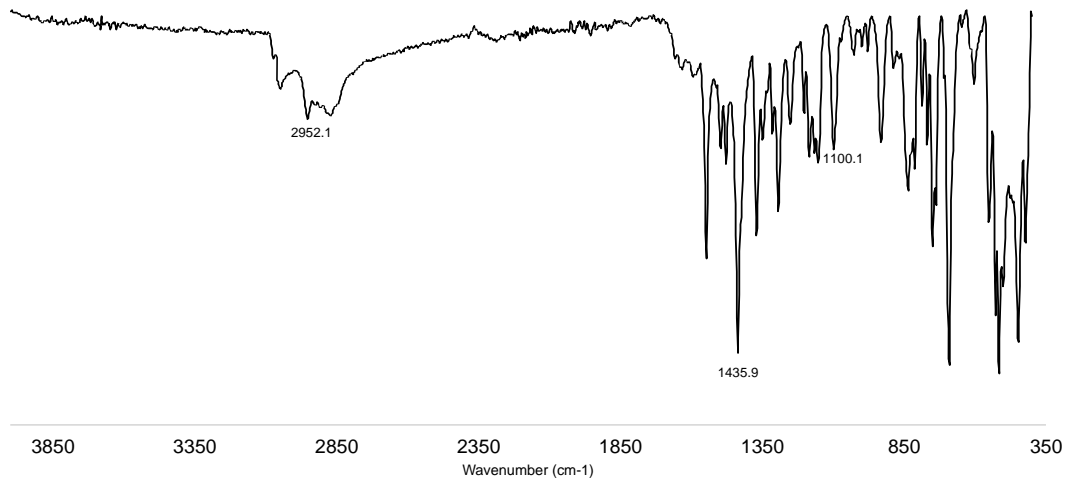
**Figure D.34.** ATR-FTIR of solid  $[\text{Ph}_2\text{P}(o\text{-C}_6\text{H}_4)(o\text{-C}_6\text{H}_4)\text{N}(2\text{-Methyl-2-butene})]\text{K}$ , **K(5-L6)**. Data acquired using Bruker Alpha II ATR-FTIR and plotted using Microsoft Excel.



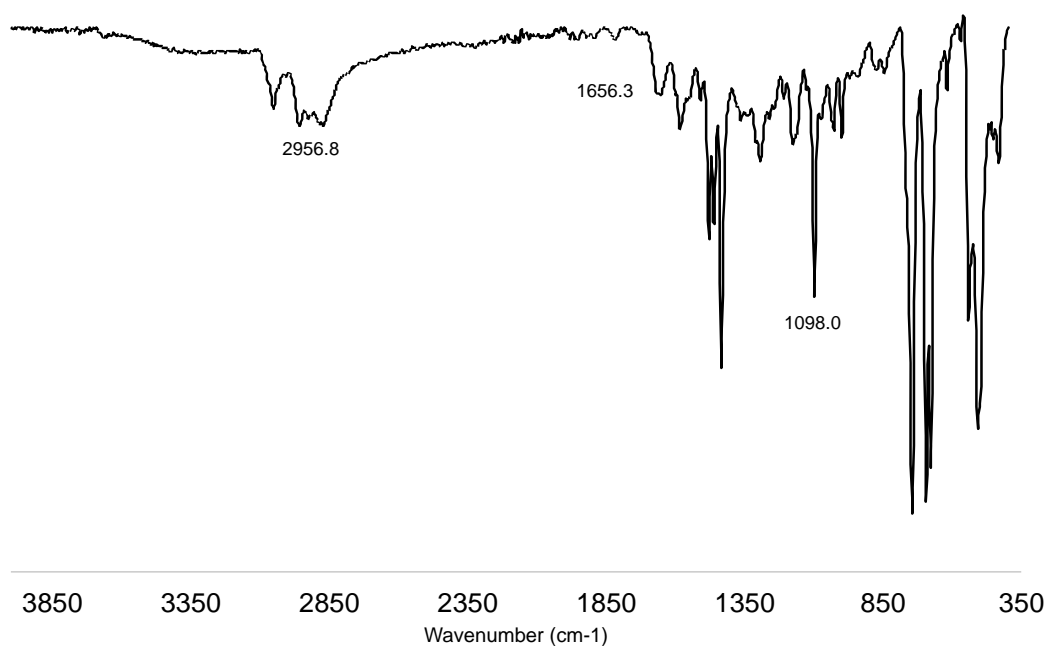
**Figure D.35.** ATR-FTIR of solid  $[\text{PdCl}(\text{CH}_3)(\text{H}(\mathbf{5-L5}))]$ , **5-4**. Data acquired using Bruker Alpha II ATR-FTIR and plotted using Opus software.



**Figure D.36.** ATR-FTIR of solid  $[\text{PdCl}(\text{CH}_3)(\text{H}(\mathbf{5-L6b}))]$ , **5-5a** and  $[\text{PdCl}(\text{CH}_3)(\text{H}(\mathbf{5-L6c}))]$ , **5-5b**. Data acquired using Bruker Alpha II ATR-FTIR and plotted using Microsoft Excel.

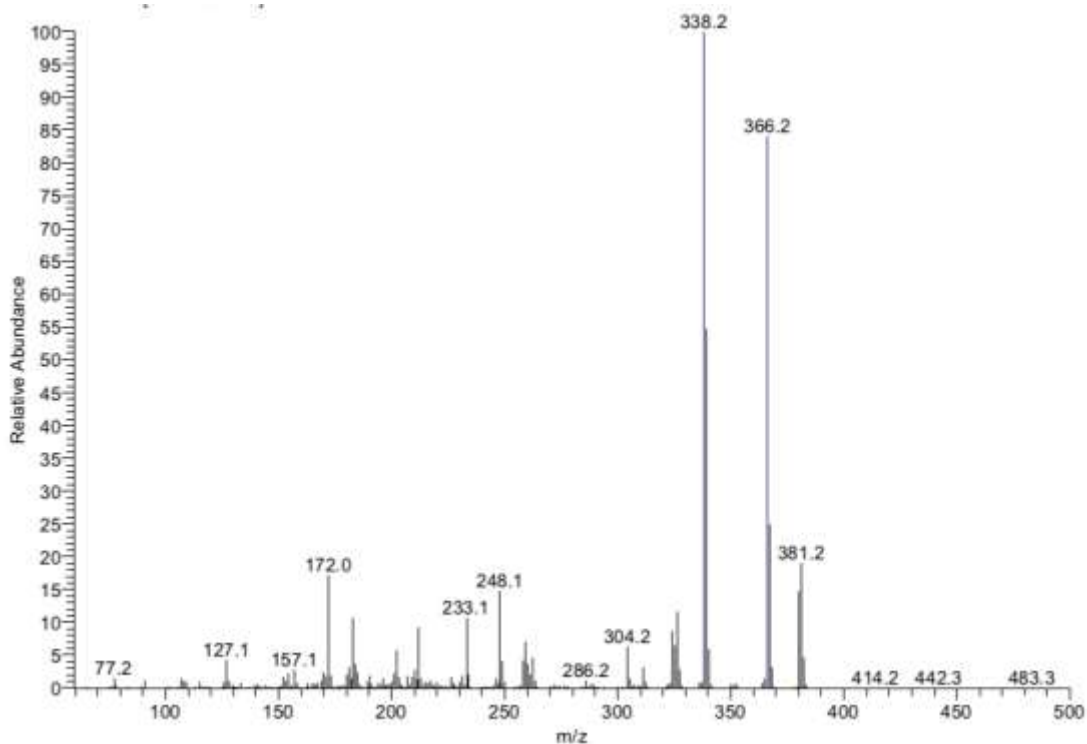


**Figure D.37.** ATR-FTIR of solid  $[\text{PdCl}(\text{CH}_3)(\mathbf{5-L5})(\text{py})]$ , **5-6**. Data acquired using Bruker Alpha II ATR-FTIR and plotted using Microsoft Excel.



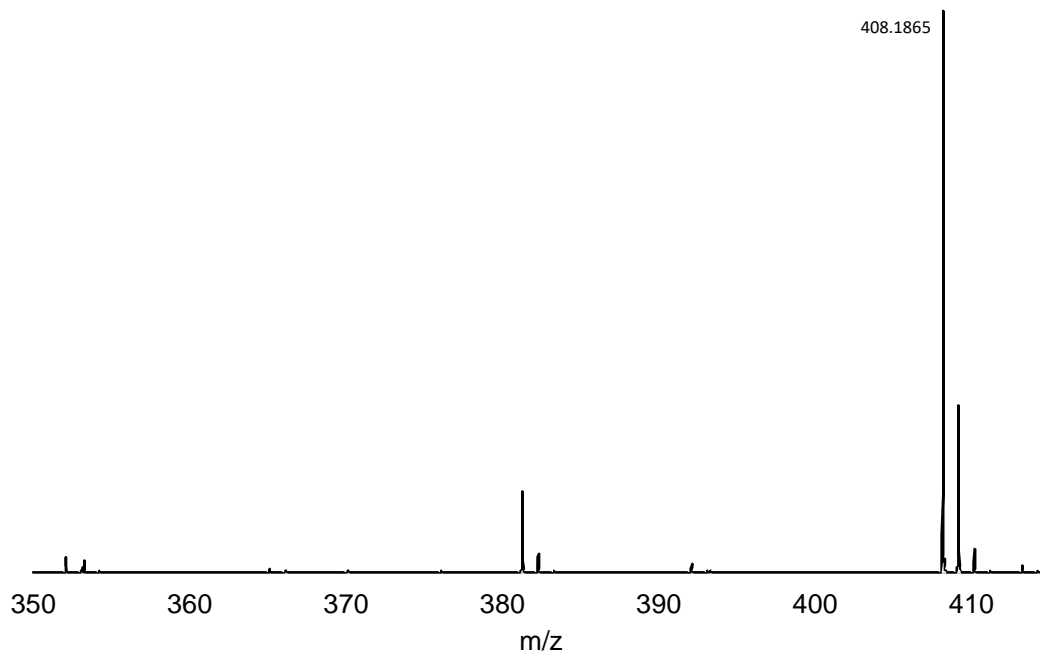
**Figure D.38.** ATR-FTIR of solid  $[\text{Pd}(\text{CH}_3)(\mathbf{5-L6})]$ , **5-7**. Data acquired using Bruker Alpha II ATR-FTIR and plotted using Microsoft Excel.

### III Mass Spectra

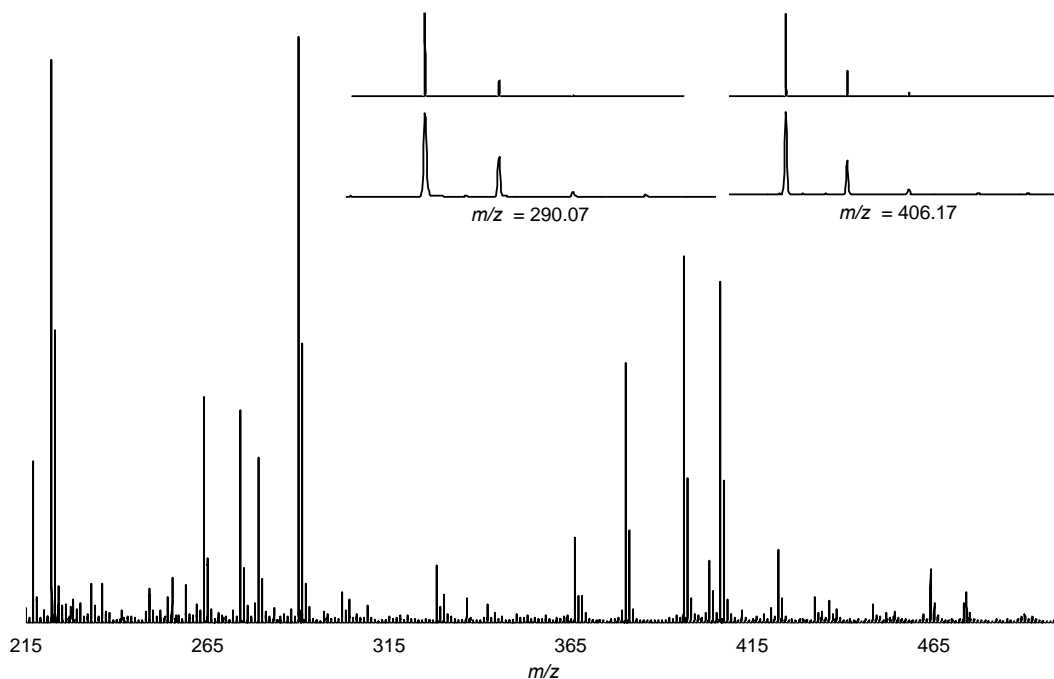


**Figure D.39.** Mass spectrum of  $\text{Ph}_2\text{P-1-(C}_{10}\text{H}_6\text{)-8-N(3-Methyl-1-butene)}$ , **H(5-L5)**. Found: 338.2, calc:  $[\text{H}[\mathbf{5-L5}] - \text{C}_3\text{H}_8]^+$  338.1

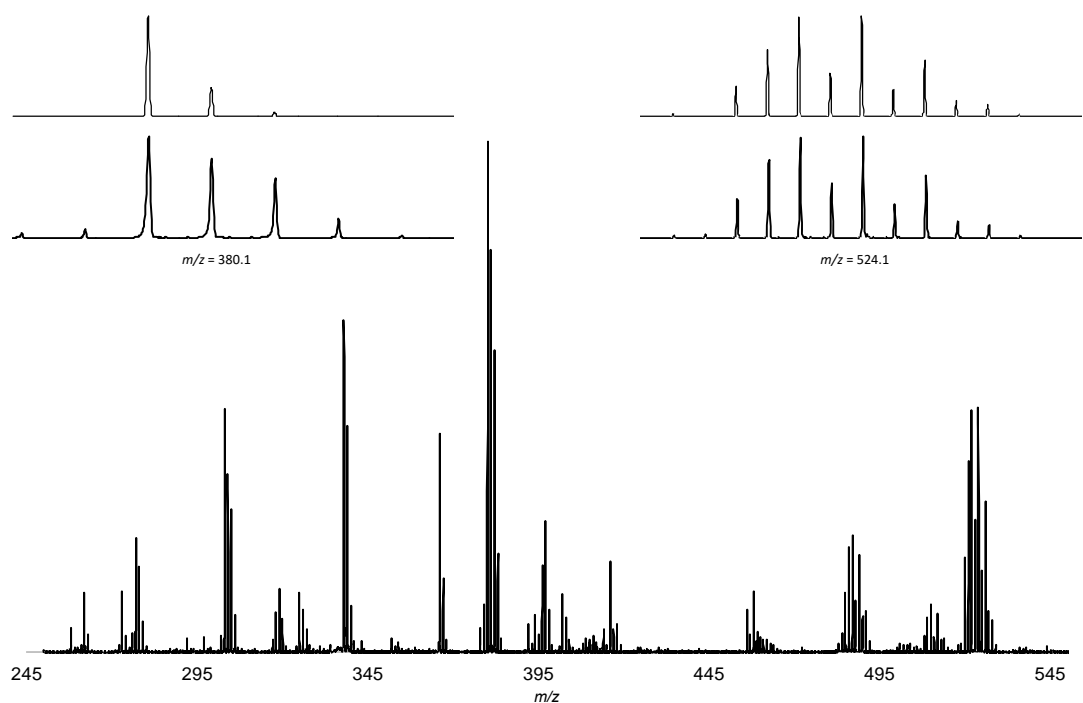




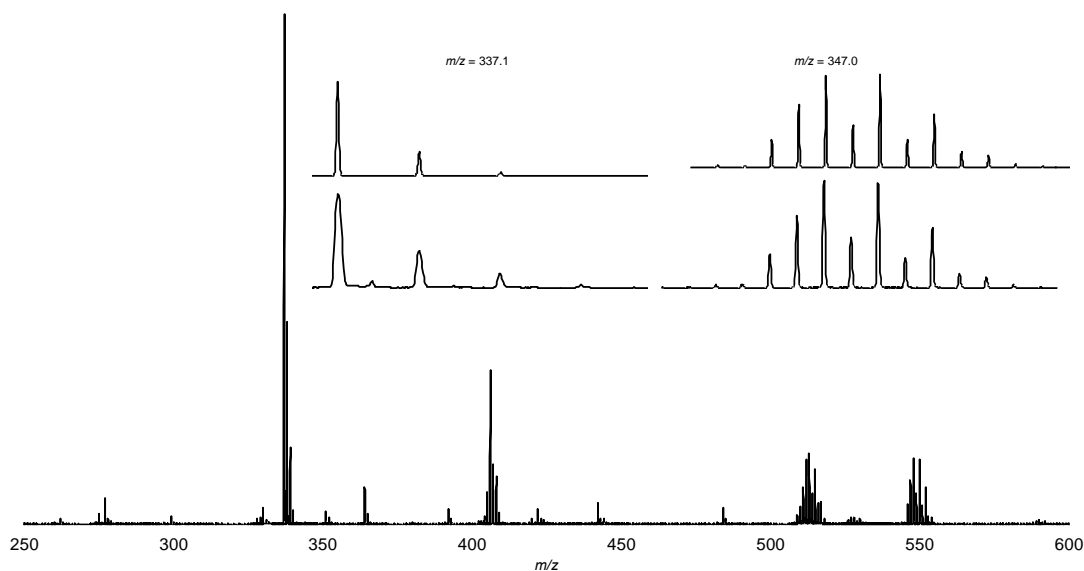
**Figure D.40.** ESI Mass spectrum of  $\text{Ph}_2\text{P}(o\text{-C}_6\text{H}_4)(o\text{-C}_6\text{H}_4)\text{N}(3\text{-Methyl-1-butene})$ , **H(5-L6b)** and  $\text{Ph}_2\text{P}(o\text{-C}_6\text{H}_4)(o\text{-C}_6\text{H}_4)\text{NH}(2\text{-Methyl-2-butene})$ , **H(5-L6c)**.  $m/z$  found: 408.1865, calc:  $[\text{H}[5\text{-L6}]]^+$  408.1881. Data plotted with Microsoft Excel.



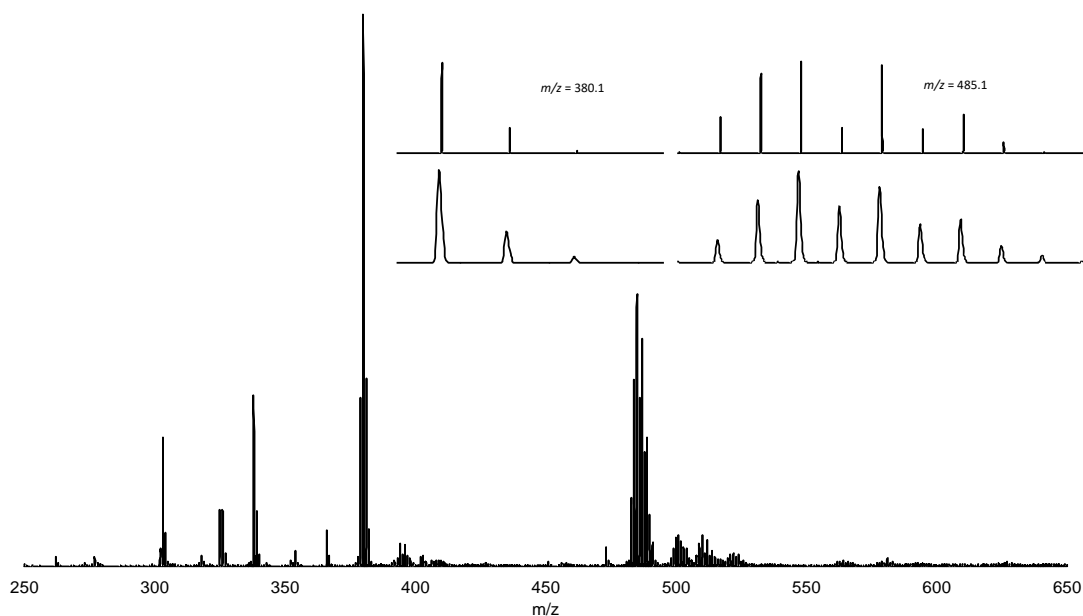
**Figure D.41.** MALDI mass spectrum collected in negative ion mode of  $[\text{Ph}_2\text{P}(o\text{-C}_6\text{H}_4)(o\text{-C}_6\text{H}_4)\text{N}(2\text{-Methyl-2-butene})]\text{K}$ , **K(5-L6)** with pyrene as the matrix. Left inset: simulated<sup>3</sup> isotope pattern (top) for  $[(\text{PhP}=\text{O})(\text{C}_{12}\text{H}_8)\text{N}]^-$  and observed signal (bottom) at  $m/z = 290.1$ . Right inset: simulated<sup>3</sup> isotope pattern (top) for  $[5\text{-L6}]^-$  and observed signal (bottom) at  $m/z = 406.2$ .



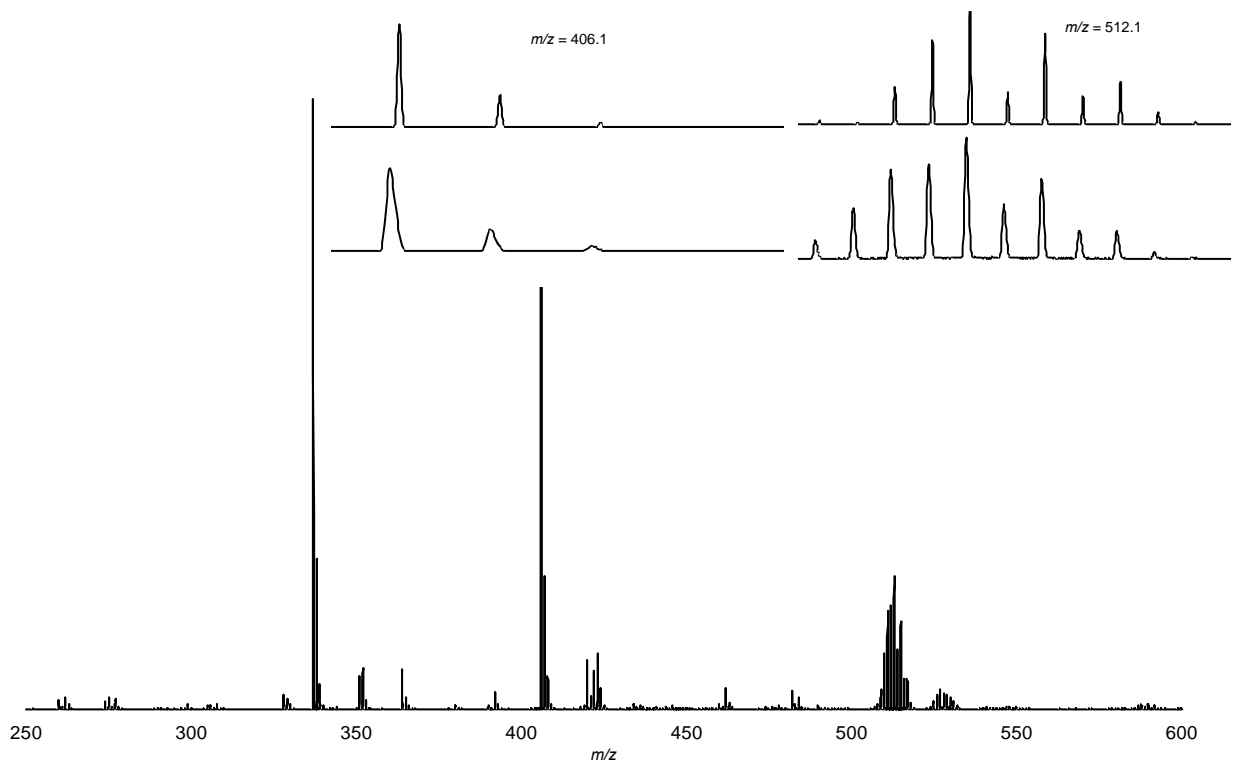
**Figure D.42.** MALDI mass spectrum mode of  $[\text{PdCl}(\text{CH}_3)(\text{H}(\mathbf{5-L5}))]$ , **5-4** with pyrene as the matrix. Left Inset: simulated<sup>3</sup> isotope pattern (top) for  $[\mathbf{5-L5}]^{++}$  and observed signal (bottom) at  $m/z = 380.1$ . Right Inset: simulated<sup>3</sup> isotope pattern (top) for  $[\mathbf{5-4-CH}_3]^{++}$  and observed signal (bottom) at  $m/z = 524.1$ .



**Figure D.43.** MALDI mass spectrum mode of  $[\text{PdCl}(\text{CH}_3)(\text{H}(\mathbf{5-L6b}))]$ , **5-5a** and  $[\text{PdCl}(\text{CH}_3)(\text{H}(\mathbf{5-L6c}))]$ , **5-5b** with pyrene as the matrix. Left inset: simulated<sup>3</sup> isotope pattern (top) for  $[\text{H}(\mathbf{5-L6})-\text{C}_4\text{H}_8\text{N}]^{++}$  and observed signal (bottom) at  $m/z = 337.1$ . Right inset: simulated<sup>3</sup> isotope pattern (top) for  $[\mathbf{5-5-CH}_3]^{++}$  and observed signal (bottom) at  $m/z = 347.0$ .



**Figure D.44.** MALDI mass spectrum mode of  $[\text{PdCl}(\text{CH}_3)(\mathbf{5-L5})(\text{py})]$ , **5-6** with pyrene as the matrix. Left inset: simulated<sup>3</sup> isotope pattern (top) for  $[\mathbf{L5-5}]^+$  and observed signal (bottom) at  $m/z = 380.1$ . Right inset: simulated<sup>3</sup> isotope pattern (top) for  $[\mathbf{5-6}(\text{py})(\text{CH}_3)]^+$  and observed signal (bottom) at  $m/z = 485.1$ .



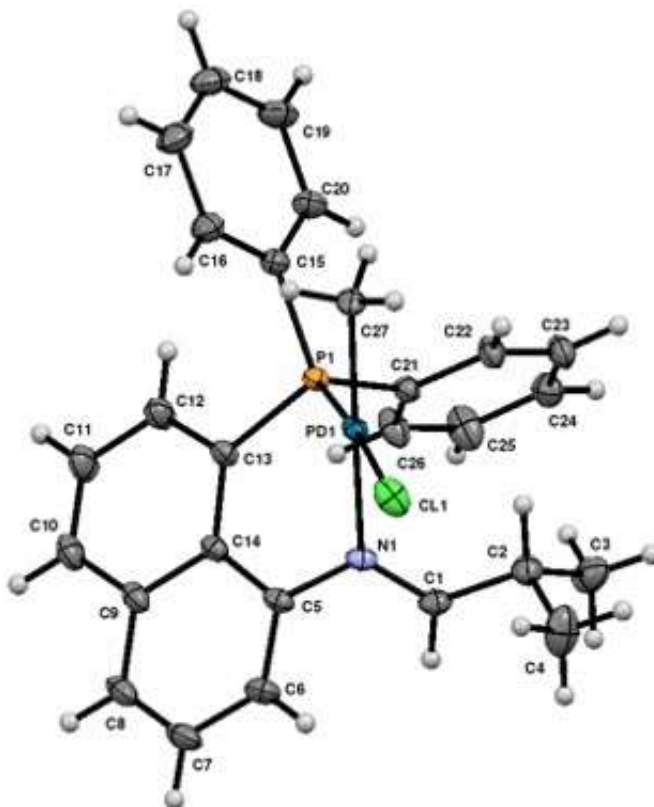
**Figure D.45.** MALDI mass spectrum mode of  $[\text{Pd}(\text{CH}_3)(\mathbf{5-L6})]$ , **5-7** with pyrene as the matrix. Left inset: simulated<sup>3</sup> isotope pattern (top) for  $[\mathbf{5-L6}]^+$  and observed signal (bottom) at  $m/z = 406.1$ . Right inset: simulated<sup>3</sup> isotope pattern (top) for  $[\mathbf{5-7-CH}_3]^+$  and observed signal (bottom) at  $m/z = 512.1$ .

## IV Crystallographic Details

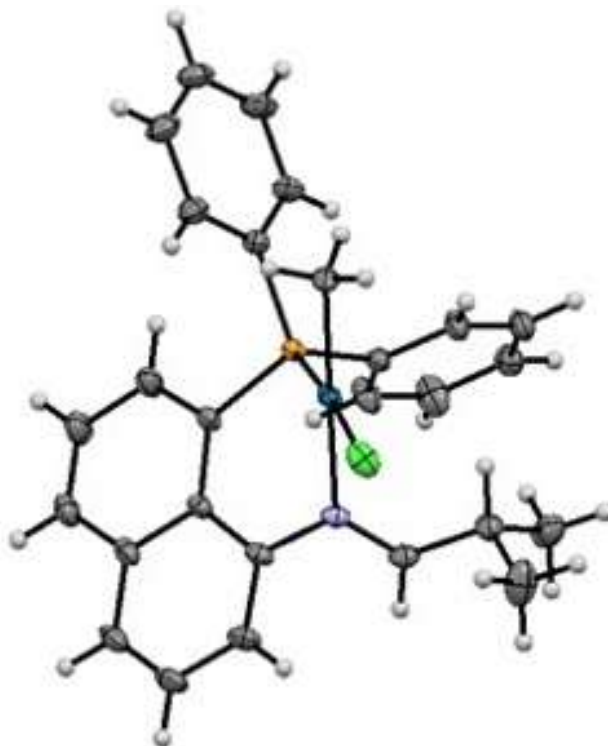
### IV.1 Experimental for C<sub>27</sub>H<sub>27</sub>CINPPd (5-4)

**Data Collection and Processing.** The sample (b5-4) was mounted on a Mitegen polyimide micromount with a small amount of Paratone N oil. All X-ray measurements were made on a Bruker Kappa Axis Apex2 diffractometer at a temperature of 110 K. The unit cell dimensions were determined from a symmetry constrained fit of 9236 reflections with  $5.28^\circ < 2\theta < 89.54^\circ$ . The data collection strategy was a number of  $\omega$  and  $\varphi$  scans which collected data up to  $90.822^\circ$  ( $2\theta$ ). The frame integration was performed using SAINT.<sup>4</sup> The resulting raw data was scaled and absorption corrected using a multi-scan averaging of symmetry equivalent data using SADABS.<sup>5</sup>

**Structure Solution and Refinement.** The structure was solved by using a dual space methodology using the SHELXT program.<sup>6</sup> All non-hydrogen atoms were obtained from the initial solution. The hydrogen atoms were introduced at idealized positions and were allowed to ride on the parent atom. The structural model was fit to the data using full matrix least-squares based on F<sub>2</sub>. The calculated structure factors included corrections for anomalous dispersion from the usual tabulation. The structure was refined using the SHELXL program from the SHELXTL suite of crystallographic software.<sup>7</sup> Graphic plots were produced using the NRCVAX program suite.<sup>8</sup>



**Figure D.46.** Thermal ellipsoid plot of 5-4 showing naming and numbering scheme. Ellipsoids are at the 50% probability level and hydrogen atoms were drawn with arbitrary radii for clarity.



**Figure D.47.** Thermal ellipsoid plot of **5-4**. Ellipsoids are at the 50% probability level and hydrogen atoms were drawn with arbitrary radii for clarity.



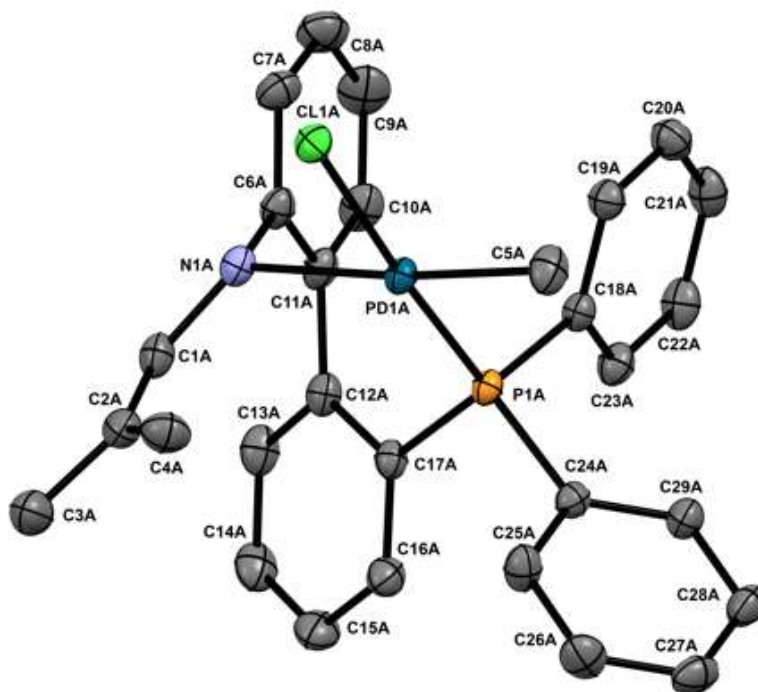
**Figure D.48.** Thermal ellipsoid plot of **5-4**. Ellipsoids are at the 50% probability level and hydrogen atoms.

## IV.II Experimental for $C_{29.50}H_{30}Cl_2NPPd$ (**5-5b**)

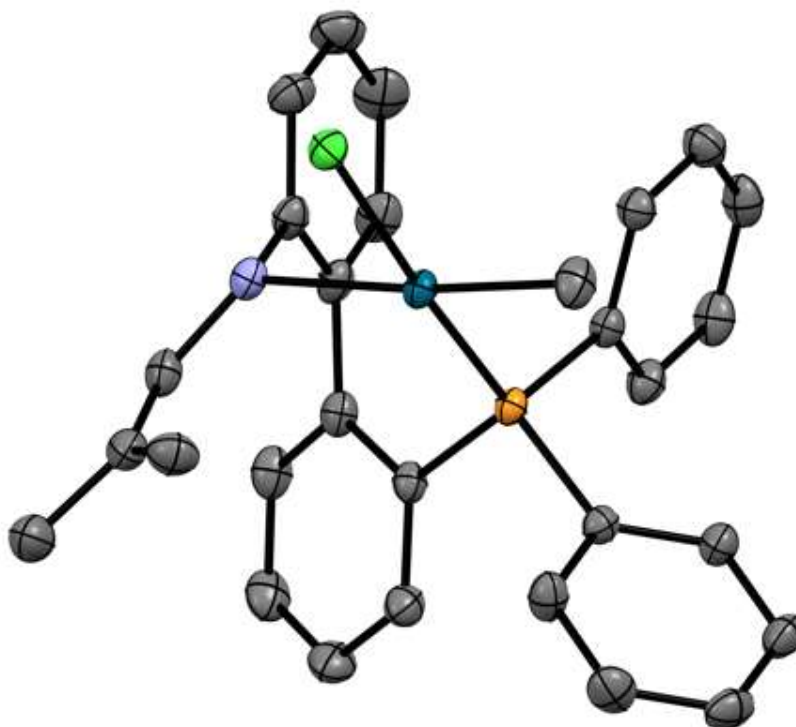
**Data Collection and Processing.** The sample (**5-5b**) was submitted by Kyle Jackman of the Blacquiere research group at the University of Western Ontario. The sample was mounted on a Mitegen polyimide micromount with a small amount of Paratone N oil. All X-ray measurements were made on a Bruker Kappa Axis Apex2 diffractometer at a temperature of 110 K. The unit cell dimensions were determined

from a symmetry constrained fit of 9246 reflections with  $5.06^\circ < 2\theta < 64.12^\circ$ . The data collection strategy was a number of  $\omega$  and  $\phi$  scans which collected data up to  $72.702^\circ$  ( $2\theta$ ). The frame integration was performed using SAINT.<sup>4</sup> The resulting raw data was scaled and absorption corrected using a multi-scan averaging of symmetry equivalent data using SADABS.<sup>5</sup>

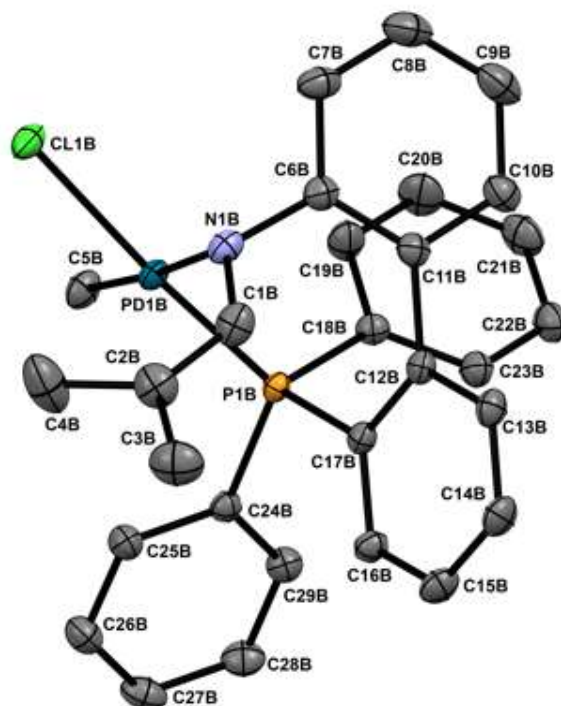
**Structure Solution and Refinement.** The structure was solved by using a dual space methodology using the SHELXT program.<sup>6</sup> All non-hydrogen atoms were obtained from the initial solution. The asymmetric unit contained two symmetry independent Pd complexes, designated A and B and one CH<sub>2</sub>Cl<sub>2</sub> molecule of solvation. The hydrogen atoms were introduced at idealized positions and were allowed to ride on the parent atom. The structural model was fit to the data using full matrix least-squares based on F<sup>2</sup>. The calculated structure factors included corrections for anomalous dispersion from the usual tabulation. The structure was refined using the SHELXL program from the SHELX suite of crystallographic software.<sup>7</sup> Graphic plots were produced using the Mercury program.<sup>9</sup>



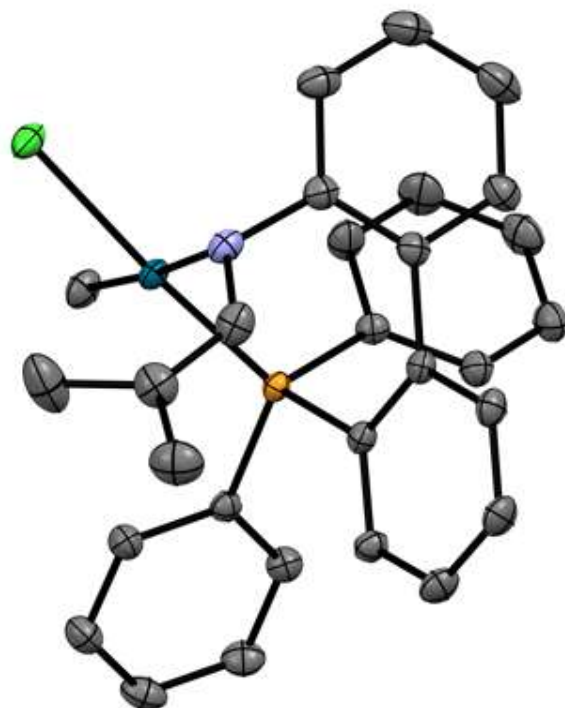
**Figure D.49.** Thermal ellipsoid plot of **5-5b molecule A** showing naming and numbering scheme. Ellipsoids are at the 50% probability level and hydrogen atoms were omitted for clarity.



**Figure D.50.** Thermal ellipsoid plot of **5-5b molecule A**. Ellipsoids are at the 50% probability level and hydrogen atoms were omitted for clarity.



**Figure D.51.** Thermal ellipsoid plot of **5-5b molecule B** showing naming and numbering scheme. Ellipsoids are at the 50% probability level and hydrogen atoms were omitted for clarity.



**Figure D.52.** Thermal ellipsoid plot of **5-5b molecule B**. Ellipsoids are at the 50% probability level and hydrogen atoms were omitted for clarity.

**Table D.2.** Summary of Crystal Data for  $C_{27}H_{27}ClNPPd$  (**5-4**) and  $C_{29.50}H_{30}Cl_2NPPd$  (**5-5b**)

| <b>Compound</b>             | <b>5-4</b>                        | <b>5-5b</b>                       |
|-----------------------------|-----------------------------------|-----------------------------------|
| Formula                     | $C_{27}H_{27}ClNPPd$              | $C_{29.50}H_{30}Cl_2NPPd$         |
| Formula Weight              | 538.31                            | 606.81                            |
| Crystal Dimensions ( $mm$ ) | $0.360 \times 0.290 \times 0.129$ | $0.372 \times 0.214 \times 0.094$ |
| Crystal Color and Habit     | yellow Prism                      | colourless prism                  |
| Crystal System              | monoclinic                        | triclinic                         |
| Space Group                 | $P 2_1/c$                         | $P - 1$                           |
| Temperature, K              | 110                               | 110                               |
| $a$ , Å                     | 8.6127(15)                        | 10.701(5)                         |
| $b$ , Å                     | 18.942(4)                         | 14.209(6)                         |
| $c$ , Å                     | 15.187(3)                         | 18.491(8)                         |
| $\alpha$ , °                | 90                                | 100.258(10)                       |
| $\beta$ , °                 | 101.720(9)                        | 94.936(14)                        |
| $\gamma$ , °                | 90                                | 94.487(14)                        |
| $V$ , Å <sup>3</sup>        | 2425.9(8)                         | 2744(2)                           |



|  |  |  |
|--|--|--|
| Number of reflections to determine final unit cell | 9236   | 9246   |
| Min and Max 2 $\theta$ for cell determination, °   | 5.28, 89.54  | 5.06, 64.12  |
| Z  | 4  | 4  |
| F(000)   | 1096   | 1236   |
| $\rho$ ( $g/cm^3$ )                                | 1.474  | 1.469  |
| $\lambda$ , Å, (MoK $\alpha$ )                     | 0.71073  | 0.71073  |
| $\mu$ , ( $cm^{-1}$ )                              | 0.955  | 0.948  |
| Diffractometer Type                                | Bruker Kappa Axis Apex2  | Bruker Kappa Axis Apex2  |
| Scan Type(s)                                       | phi and omega scans  | phi and omega scans  |
| Max 2 $\theta$ for data collection, °              | 90.822   | 72.702   |
| Measured fraction of data                          | 0.999  | 0.999  |
| Number of reflections measured                     | 168779   | 219806   |
| Unique reflections measured                        | 20356  | 26623  |
| $R_{merge}$  | 0.0709   | 0.0583   |
| Number of reflections included in refinement       | 20356  | 26623  |
| Cut off Threshold                                  | $I > 2\sigma(I)$   | $I > 2\sigma(I)$   |
| Expression Structure refined using                 | full matrix least-squares using $F^2$                                  | full matrix least-squares using $F^2$                                  |
| Weighting Scheme                                   | $w=1/[\sigma^2(F_o^2)+(0.0371P)^2+0.4468P]$ where $P=(F_o^2+2F_c^2)/3$ | $w=1/[\sigma^2(F_o^2)+(0.0393P)^2+0.9644P]$ where $P=(F_o^2+2F_c^2)/3$ |
| Number of parameters in least-squares              | 283  | 628  |
| $R_1$  | 0.0365   | 0.0362   |
| $wR_2$   | 0.0816   | 0.0813   |
| $R_1$ (all data)                                   | 0.0536   | 0.0544   |
| $wR_2$ (all data)                                  | 0.0874   | 0.0880   |
| GOF  | 1.027  | 1.026  |
| Maximum shift/error                                | 0.002  | 0.005  |

Min & Max peak heights on final DF Map ( $e^{-}/\text{\AA}$ ) -1.793, 0.947 -0.905, 0.950

Where:

$$R_1 = S \left| |F_o| - |F_c| \right| / S F_o$$

$$wR_2 = \left[ S(w(F_o^2 - F_c^2)^2) / S(w F_o^4) \right]^{1/2}$$

$$GOF = \left[ S(w(F_o^2 - F_c^2)^2) / (\text{No. of reflns.} - \text{No. of params.}) \right]^{1/2}$$

1. Stubbs, J. M.; Firth, K. F.; Bridge, B. J.; Berger, K. J.; Hazlehurst, R. J.; Boyle, P. D.; Blacquiere, J. M., *Dalton Trans.* **2017**, *46*, 647-650.
2. Jackman, K. M. K.; Bridge, B. J.; Sauv , E. R.; Rowley, C. N.; Zheng, C. H. M.; Stubbs, J. M.; Boyle, P. D.; Blacquiere, J. M., *Organometallics* **2019**, *38*, 1677-1681.
3. Loos, M.; Gerber, C. enviPat: Isotope Pattern, Profile and Centroid Calculation for Mass Spectrometry. <https://www.envipat.eawag.ch/>.
4. Bruker-Nonius, *SAINTE*. Bruker-Nonius: Madison, WI 53771, USA, 2013; Vol. version; 2013.8.
5. Bruker-Nonius, *SADABS*. Bruker-Nonius: Madison, WI 53711, USA, 2012; Vol. version; 2012.1.
6. Sheldrick, G. M., *Acta Crystallogr A Found Adv* **2015**, *71*, 3-8.
7. Sheldrick, G., *Acta Crystallographica Section C* **2015**, *71*.
8. Gabe, E. J.; Le Page, Y.; Charland, J.-P.; Lee, F. L.; White, P. S., *J. Appl. Crystallogr.* **1989**, *22*, 384-387.
9. Macrae, C.; Bruno, I.; Chisholm, J.; Edgington, P.; McCabe, P.; Pidcock, E.; Rodriguez-Monge, L.; Taylor, R.; van de Streek, J.; Wood, P., *J. Appl. Cryst.* **2008**, *41*, 466-470.

## Appendix E Copyright Material and Permissions

Chapter 2 - Reprinted with permission from K.M.K. Jackman, B. J. Bridge, E. R. Sauvé, C. N. Rowley, C. H. M. Zheng, J. M. Stubbs, P. D. Boyle, J. M. Blacquiere, *Organometallics*. Copyright 2019 American Chemical Society.

Chapter 3 - Royal Society of Chemistry Reproduction Permission  
K. M.K. Jackman, G. Liang, P. D. Boyle, P. M. Zimmerman J. M. Blacquiere, *Dalton Trans.*, 2022, 51, 3977-3991 - Reproduced by permission of The Royal Society of Chemistry.

# Appendix F Curriculum Vitae

## Education

**Ph.D. in Chemistry, Western University**

**2017–Present**

- Thesis: Coordination and Reactivity of Group 10 Phosphine 1-Azaallyl Complexes
  - Synthesis of air-sensitive phosphine-based ligands and their coordination modes with group 10 transition metals were analyzed. Characterization techniques include X-ray crystallography, multinuclear NMR spectroscopy, ATR-FTIR, GC-MS, and MALDI-MS. Investigation of catalytic behavior with the synthesized complexes towards cross-coupling was performed, and analyzed by GC-FID. An in-depth mechanistic study was carried out to determine a unique mechanism for  $C_{sp^2}$ - $C_{sp^3}$  coupling from a bimetallic  $Pd^{II}(alkyl)(P-AzA)$  complex.
- Supervisor: Johanna M. Blacquiere

**B.Sc. Honors Specialization in Chemistry, Western University**

**2013–2017**

- Thesis: Designing a Catalyst for the Long-Lifetime Polymerization of Polar Co-Monomers.
  - An air-sensitive bidentate P-N ligand was synthesized using standard Schlenk techniques, and coordinated to a monoalkyl  $Pd^{II}$  precursor in a glovebox. The complex and ligand were characterized using NMR and IR spectroscopy, mass spectrometry and x-ray crystallography. Homopolymerization of ethylene was attempted with this complex in a Parr reactor.
- Supervisor: Johanna M. Blacquiere

## Publications

1. K. M. K. Jackman, G. Liang, P. D. Boyle, P. M. Zimmerman, J. M. Blacquiere, *Dalton Trans.*, **2022**, 51, 3977.
2. K. M. K. Jackman, B. J. Bridge, E. R. Sauvé, C. N. Rowley, C. H. M. Zheng, J. M. Stubbs, P. D. Boyle, J. M. Blacquiere\* 'C $_{sp^2}$ -C $_{sp^3}$  Coupling with a Pd(II) Complex Bearing a Structurally Responsive Ligand', *Organometallics*, **2019**, 38, 1677.
3. K. M. K. Jackman, A. M. Fogh, J. M. Stubbs, J. M. Blacquiere\* 'Synthesis of Pd Phosphine-Imine Complexes and their Reactivity with Base.' *J. Organomet. Chem.* **2019**, 880, 56.

## Presentations (OP = Oral, PP = Poster)

1. OP: K. M. K. Jackman, G. Liang, P. M. Zimmerman, J. M. Blacquiere\* 'Bimetallic C–C Reductive Elimination Induced by Changes in Ligand Coordination Mode' *Virtual IUPAC | Canadian Chemistry Conference and Exhibition*, August 2021 (International).
2. OP: K. M. K. Jackman, J. M. Blacquiere\* 'Synthesis, Coordination, and Unusual Reactivity of Structurally Diverse P $^{\wedge}$ AzA Ligands' *G. Michael and Joan Bancroft Award Presentation*, London, ON, May 2020 (Departmental).
3. PP: K. M. K. Jackman, J. M. Blacquiere\* 'Synthesis and Coordination Chemistry of a Naphthalene Linked P $^{\wedge}$ AzA Ligand' *Canadian Chemistry Conference and Exhibition*, Quebec City, Qc, June 2019 (National).
4. OP: K. M. K. Jackman, B. B. Bridge, C. N. Rowley, J. M. Stubbs, J. M. Blacquiere\* 'Unusual C $_{sp^2}$ -C $_{sp^3}$  Bond Formation Promoted by the Diverse Coordination of a P $^{\wedge}$ AzA Ligand.' *Inorganic Discussion Weekend*, Waterloo, ON, November 2018 (National).
5. PP: K. M. K. Jackman, B. J. Bridge, D. G. Stephens, E. Sauvé, J. M. Blacquiere\* 'C $_{sp^2}$ -C $_{sp^3}$  Bond Formation Promoted by Versatile Ligand Coordination.' *International Conference on Organometallic Chemistry*, Florence, Italy, July 2018 (International).

6. PP: K. M. K. Jackman, A. A. Fogh, J. M. Stubbs, P. D. Boyle, J.M. Blacquiere\* ‘Design of Ligands with Flexible and Dynamic Bond Coordination Modes’, *100<sup>th</sup> Canadian Chemistry Conference and Exhibition*, Toronto, ON, June 2017 (National).
7. OP: K. M. K. Jackman, J. M. Blacquiere\* ‘Synthesis of a Long-Lifetime Catalyst for the Copolymerization of Olefins.’ *Southern Ontario Undergraduate Student Chemistry Conference*. Toronto, ON, March 2017 (Provincial).

## Awards and Scholarships

- Ontario Graduate Scholarship **2019**
- G. Michael and Joan Bancroft Research Award **2019**
- Dean’s Honor List, Western University **2017**
- Ontario Scholar, Corpus Christi Catholic Secondary School **2013**

## Mentoring / Teaching

### Graduate Student Mentor

**2017 – Present**

- Primary in lab mentor for Inorganic Chemistry Exchange student Emily Traver
- Primary in lab mentor for 4<sup>th</sup> year research project undergraduates David Stephens, Ethan Lidsky, and Leslie Kelley.
- Provided additional secondary support and assistance to 4491 students and undergraduate volunteers
- Offered technical assistance and trained new students in laboratory techniques

### Laboratory and Marking Teaching Assistant

**2017 – Present**

- Chemistry 1302B – Discovering Chemical Energetics **Winter 2022**
- Chemistry 2271A – Structure and Bonding in Inorganic Chemistry **Fall 2021**
- Chemistry 1302B – Discovering Chemical Energetics **Winter 2021**
- Chemistry 2271A – Structure and Bonding in Inorganic Chemistry **Fall 2020**
- Chemistry 2271A – Structure and Bonding in Inorganic Chemistry **Fall 2019**
- Chemistry 2223B – Organic Chemistry for Biological Molecules **Winter 2019**
- Chemistry 2271A – Structure and Bonding in Inorganic Chemistry **Fall 2018**
- Chemistry 2281G – Inorganic Chemistry of the Main Group Elements **Winter 2018**
- Chemistry 2213A – Organic Chemistry for Life Sciences **Fall 2017**

### Outreach Program Volunteer

**2018 – Present**

- Visited four universities in Nova Scotia to discuss graduate school at Western University with prospective candidates.
- Prepared a report in collaboration with a fellow graduate student proposing improvements to the recruitment program and documenting our efforts during our recruitment trip in Nova Scotia that was shared with the Chemistry Recruitment Committee Chair.
- Assisted in the operation of experiments for several groups of 25 – 30 high school and elementary students at Western University.
- Travelled to Lambeth Community Centre and performed demonstrations for 60 day-camp children with the City of London.

## Graduate Courses (2.0 of Required 2.0 Credits complete)

|    |   |              |
|----|---|--------------|
| 1. | 9658Y – Graduate Seminar Course – 87%         | Completed    |
| 2. | 9653S – Polymers: Synthesis to Function – 94% | 0.25 Credits |
| 3. | 9671T – Synthesis with Organometallics – 90%  | 0.25 Credits |
| 4. | 9651S – Organometallic Bond Activation – 90%  | 0.25 Credits |
| 5. | 9503R – ADV. NMR Spectroscopy – 78%           | 0.25 Credits |
| 6. | 9603S – ADV. NMR Spectroscopy. II – 86%       | 0.25 Credits |
| 7. | 9521S – Catalysis – 86%                       | 0.25 Credits |
| 8. | 9541A – Crystallography I – 80%               | 0.25 Credits |